

# IPP-Report



Max-Planck-Institut  
für Plasmaphysik

Thomas Pütterich

## **Control and Diagnostic of High-Z Impurities in Fusion Plasmas**

**IPP 17/44**  
**April, 2015**

# Control and Diagnostic of High-Z Impurities in Fusion Plasmas



Kumulative  
Habilitationsschrift  
für das Fach  
Experimentalphysik  
an der  
Ludwig-Maximilians-Universität München

vorgelegt von

Dr. Thomas Pütterich

---

Juli 2014



**for my father**



# Contents

<b>Contents</b>	<b>I</b>
<b>1 Introduction</b>	<b>1</b>
1.1 Nuclear Fusion as an Energy Source . . . . .	1
1.2 Plasma Confinement in a Tokamak Device . . . . .	2
1.2.1 Coil Configuration of a Tokamak . . . . .	3
1.2.2 Divertor Concept . . . . .	6
1.3 The Choice of the Wall Material . . . . .	8
1.4 Sources of Impurities . . . . .	13
1.5 The Burn Condition of a Fusion Reactor . . . . .	14
1.5.1 Without Impurities . . . . .	16
1.5.2 With Impurities . . . . .	16
1.6 Structure of This Thesis . . . . .	22
<b>2 Diagnostic of Impurities in Fusion Plasmas</b>	<b>25</b>
2.1 Spectroscopy . . . . .	25
2.1.1 Passive Spectroscopy . . . . .	25
2.1.2 Charge Exchange Recombination Spectroscopy . . . . .	31
2.2 Bolometry . . . . .	33
2.3 Soft X-ray Cameras . . . . .	34
2.4 Atomic Data for Tungsten Ions . . . . .	37
2.4.1 What Types of Data are Needed? . . . . .	37
2.4.2 Most Recent Developments and Limitations . . . . .	42
<b>3 Control of High-Z Impurities in Fusion Plasmas</b>	<b>43</b>
3.1 Erosion of Tungsten . . . . .	43
3.2 Transport of Tungsten on Open Field Lines (Divertor, SOL) . . . . .	46

3.3	Transport Processes in the Confined Plasma . . . . .	48
3.3.1	Collisional Transport . . . . .	48
3.3.2	Mixing of Collisional and Anomalous Transport . . . . .	54
3.4	Plasma Edge and Pedestal . . . . .	55
3.4.1	H-mode Regime . . . . .	56
3.4.2	ELMs and Their Impact on Impurity Control . . . . .	58
3.5	Impurity Control in the Plasma Core . . . . .	59
<b>4</b>	<b>Summary Bringing the Featured Publications into Context</b>	<b>63</b>
<b>5</b>	<b>Major Publications</b>	<b>69</b>
5.1	Publication 1 . . . . .	69
5.2	Publication 2 . . . . .	100
5.3	Publication 3 . . . . .	118
5.4	Publication 4 . . . . .	131
5.5	Publication 5 - (not refereed) . . . . .	151
5.6	Publication 6 . . . . .	160
5.7	Publication 7 . . . . .	174
5.8	Publication 8 . . . . .	203
5.9	Publication 9 . . . . .	208
5.10	Publication 10 . . . . .	233
5.11	Publication 11 . . . . .	244
5.12	Publication 12 . . . . .	264
<b>Bibliography</b>		<b>285</b>

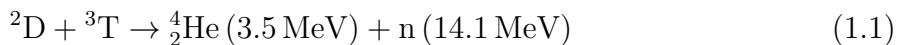
# Chapter 1

## Introduction

### 1.1 Nuclear Fusion as an Energy Source

The world's energy consumption is still mostly sustained by the burning of vast amounts of fossil fuels, the supply of which is limited. A change to renewable energy sources brings up issues with the pure volume of the energy consumption, the storage and transport of produced energy and costs. Thus, an additional option for producing energy featuring no carbon emissions, predictable availability and acceptable costs is of high interest. Possibly this will be provided by controlled nuclear fusion of hydrogen isotopes to helium. While an economical feasibility study is not the scope of this work, it is clear that the potential impact of the 'nuclear fusion' on the energy markets of the future may be considerable.

The physical energy source of nuclear fusion is given by the strong interaction. The especially large nuclear binding energy of the  ${}^4\text{He}$  nucleus is apparent from the difference in mass between the  ${}^4\text{He}$  nucleus and the unbound constituents of the nucleus. Thus, a fusion process arriving at the  ${}^4\text{He}$  nucleus, i.e. an energetic  $\alpha$ -particle, provides one of the largest energy gains possible via fusion. This is the case for the fusion of deuterium  ${}^2\text{D}$  and tritium  ${}^3\text{T}$  (cf. equation 1.1). This reaction is predominately considered for fusion on earth, because a resonance between the kinetic energy and an excited state of the  ${}^5\text{He}$  nucleus exists leading to an exceptionally large fusion cross-section already at energies of 10-20 keV (maximum at 64 keV).



The released energy is available as kinetic energy of the products. The considerable collision energies are required, because the fusion partners have to be brought close together despite both particles being positively charged and hence repulsed by the Coulomb force. A beam target concept using accelerated ions, e.g. tritium, colliding with a deuterium target, cannot achieve a net energy gain, because the large cross section for Coulomb

scattering with mostly electrons in the target leads to an energy transfer into thermal velocities, while the number of fusion processes is minuscule. Thus, a more promising approach is confining a plasma containing the deuterium and tritium, which is heated to high temperatures in the range of 10-30 keV<sup>1</sup>, such that a considerable fraction of the deuterium and tritium particles collide at sufficient collision energies to fuse. In order to illustrate the superiority of D-T fusion, the rate coefficient  $\langle\sigma v\rangle$ , i.e. the Maxwell average of the product of cross-section  $\sigma$  and relative velocity  $v$  for several reactions are presented in figure 1.1.

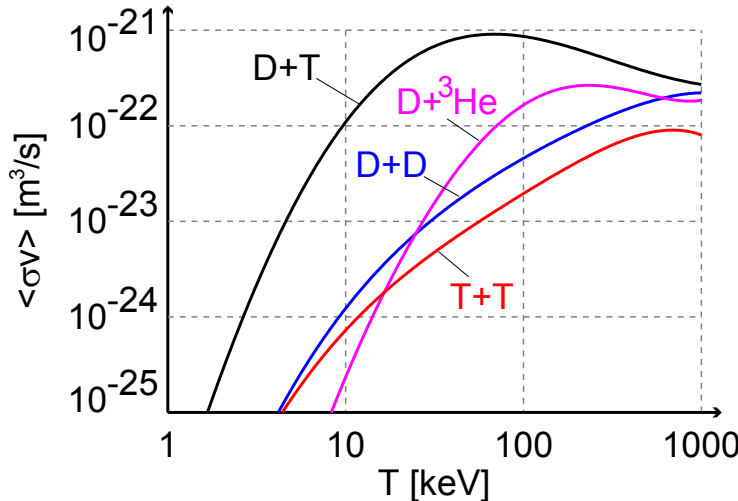


Figure 1.1: Rate coefficients for various fusion reactions. The DT-reaction features the highest rate coefficient, which is close to its maximum value already at temperatures of 10-30 keV. (adapted from [1])

This thesis is concerned with the properties of magnetically confined plasmas, and in particular with the plasma confinement in a Tokamak device, which is explained in the next section.

## 1.2 Plasma Confinement in a Tokamak Device

A magnetically confined plasma requires confinement perpendicular to the magnetic field lines but also along the field lines. The transport along field lines cannot easily be suppressed, which brings up naturally the option of bending field lines into circles. In practice this provides the topology of a torus. However, this implies a radial gradient in the magnetic field such that the plasma particles start drifting according to the  $\vec{\nabla}B$ -drift which ultimately means a loss of confinement due to transport perpendicular to the magnetic

<sup>1</sup>In plasma physics often the temperature  $T$  is denoted in energy units, i.e.  $kT$ , where  $k$  is Boltzmann's constant.

field lines. This can be avoided by implementation of helical field lines such that the  $\vec{\nabla}B$ -drift, which is constant in direction (either upward or downward), leads to a drift away from the plasma center for particles above/below the center, while particles below/above the center drift towards it. As the vast majority of particles move fast along field lines they spend half of the time above and below the center such that the  $\vec{\nabla}B$ -drift compensates. While the purely toroidal magnetic field is may be produced by external coils, helical field lines may be obtained by driving a current in the direction of the magnetic field, i.e. the so-called toroidal direction, which leads to a magnetic field component perpendicular to the toroidal direction, i.e. the so-called poloidal direction. The respective magnetic field components are called the toroidal and poloidal magnetic fields. The superposition of the fields leads to helical field lines spanning whole surfaces, which are called flux surfaces. In figure 1.2, the flux surface structure of such a configuration is presented. The flux surfaces do not intersect each other such that they form a nested set of surfaces. Note that driving a current is not the only option for obtaining a poloidal field component, however, if a current is used for providing the confining poloidal field the device can be axisymmetric and then it is called a tokamak. Note that helical field lines and plasma confinement can

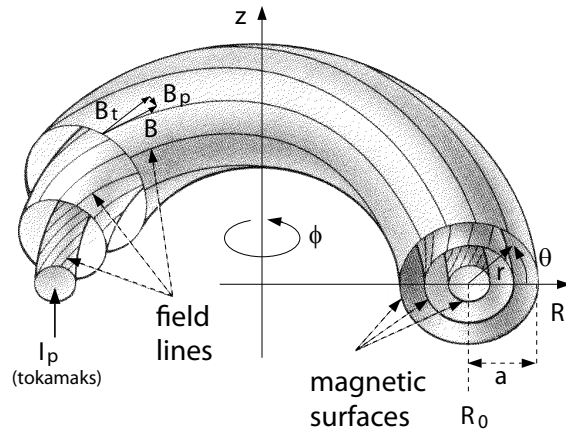


Figure 1.2: Magnetic surfaces are defined by helical field lines, i.e. field lines with a poloidal field component  $B_p$  on top of a toroidal field  $B_t$ . The poloidal field component is produced in a tokamak by a toroidal plasma current. (reprinted from [1])

also be obtained by purely externally produced magnetic fields, e.g. stellarators, however, for such a configuration the toroidal symmetry must be sacrificed.

### 1.2.1 Coil Configuration of a Tokamak

In figure 1.3 the basic setup of a tokamak is presented. The current in the blue coils provide a stationary toroidal field  $B_t$ . The current in the green coil is varied such that

a toroidal electric field exists in the volume of the plasma chamber giving rise to the so-called loop voltage. Due to that electric field plasma break down is achieved and a toroidal plasma current can be driven providing the poloidal field  $B_p$ . This principle is analogous to a transformer in which the green coil is acting as the primary circuit, while the plasma is the secondary circuit. Note that the plasma is only confined while the plasma current is driven such that after one ramp of the transformer coil the plasma discharge needs to be stopped making tokamaks, in the absence of additional current drive, inherently pulsed devices. The red coils provide a vertical field, which is necessary to counteract the radial

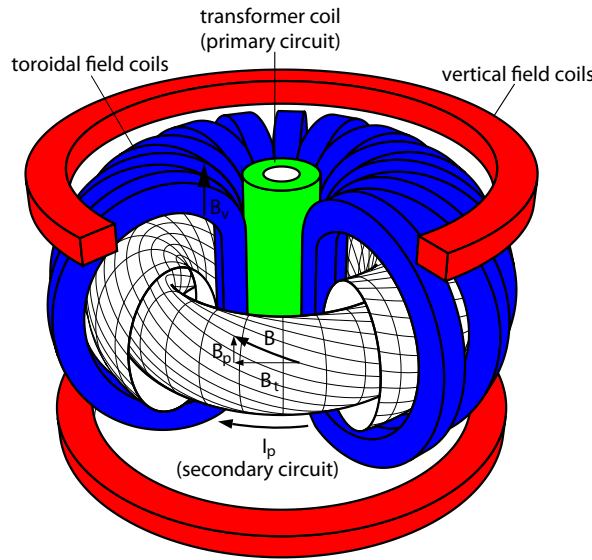


Figure 1.3: The tokamak principle showing the toroidal field, the transformer coils and the vertical field coils ( $\vec{B}_v$ ), all of which are the minimum requirement for stable plasma confinement. (adapted from [1])

expansion of the plasma due to the so-called hoop-force. This force is a consequence of the fact that the plasma parameters and thus pressure are quickly equilibrated along field lines while the area of the flux surfaces at the outboard side is larger than at the inboard side. Additionally, the magnetic pressure gradient given by the poloidal magnetic field gradient acts in the same direction. The vertical field weakens the poloidal magnetic field at the inboard side and strengthens the field at the outboard side, reducing the magnetic pressure gradients. Concomitantly, the vertical magnetic field causes a Lorentz force on the plasma current which prevents the expansion of the plasma. In reality, the setup of coils is even more complex, as a large number of vertical field coils allows also for shaping the plasma and for obtaining special topologies, e.g. the divertor configuration. In figure 1.4 a cross-section of the poloidal field coils of ASDEX<sup>2</sup> Upgrade is presented, a tokamak operated by the Max-Planck Institut für Plasmaphysik in Garching. Along with the coils

<sup>2</sup>Axial Symmetric Divertor EXperiment

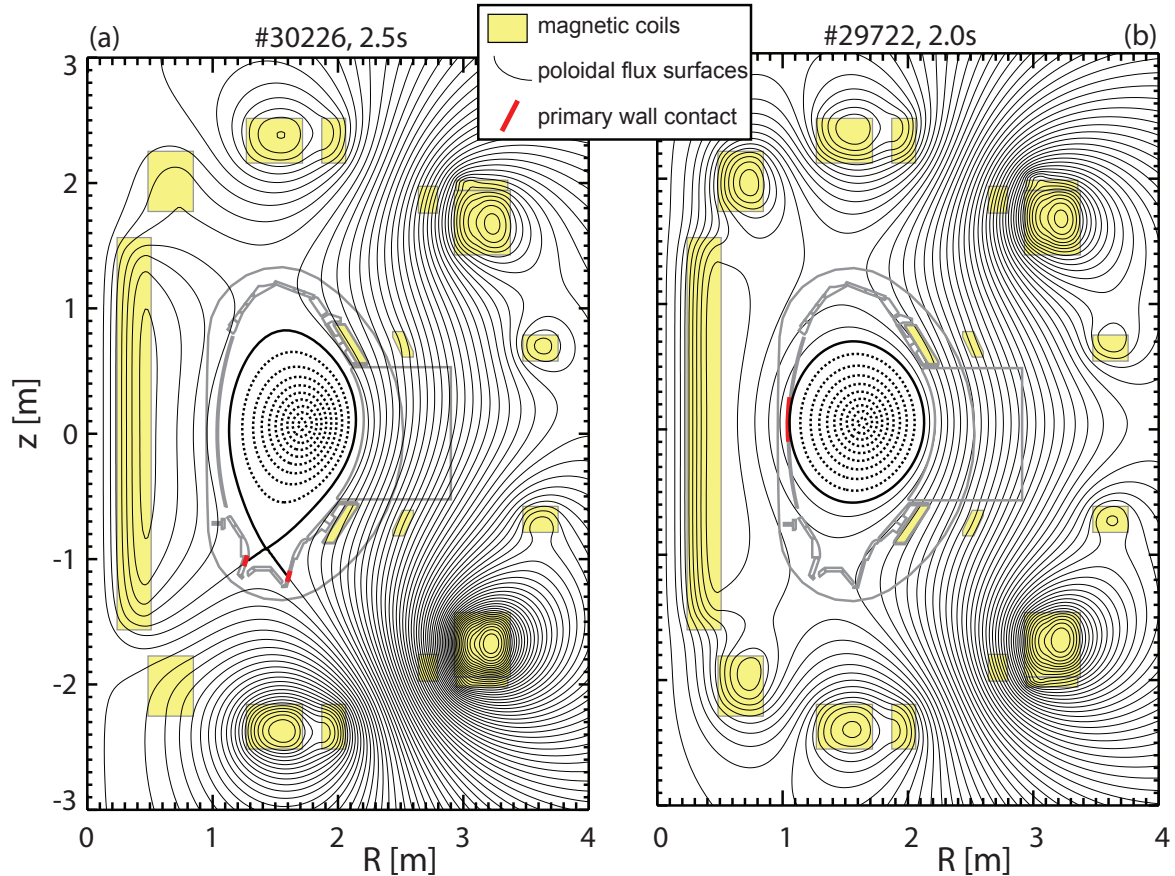


Figure 1.4: (a) A poloidal cross-section of the ASDEX Upgrade vacuum vessel (gray), the poloidal magnetic flux surfaces (thin, black) and the poloidal field coils including the central solenoid, passive and active shaping coils. The closed flux surfaces confining the plasma are presented inside of the vacuum vessel (thick, dashed, black). They are surrounded by the separatrix (thick, solid, black). The magnetic configuration features a divertor at the bottom of the plasma. The regions of the primary wall contact are indicated in red. (b) same for a discharge in the so-called limiter configuration.

also surfaces of constant poloidal flux are presented for discharge #30226 at 2.5 s (divertor configuration) and for discharge #29722 at 2.0 s (limiter configuration). The explanation of divertor and limiter configuration will follow in the next section. The three coils at  $R < 1$  m act as the transformer coils, while the exact distribution of current among the three coils also influences the shape of the plasma. The other coils are either passive or active coils that are used to control the position and shape of the plasma, which exists inside of the plasma vessel (also depicted in figure 1.4) confined by the closed flux surfaces (dashed lines). The volume of the confined plasma is surrounded by the separatrix, i.e. the flux surface separating the confined plasma from the region where parallel transport brings particles and energy to the first wall. As parallel transport is much larger than the

perpendicular one, the radial gradient lengths are of the order of millimeters (e.g. power fall off length in [2, 3]). Due to the efficient parallel loss mechanism all flux surfaces between wall and separatrix are called the scrape-off layer or the region of open field lines. As the magnetic field has no sources due to  $\vec{\nabla} \cdot \vec{B} = 0$  the term ‘open’ refers only to the fact that on these flux surfaces the particles and energy may be lost to the wall.

The flux surface structure is often used to define a normalized plasma radius. In this thesis,  $\rho_{pol}$  is used several times, which is the plasma radius normalized via the poloidal magnetic field dependence (s. equation 1.2, where  $\Psi$  is the poloidal magnetic flux,  $\Psi_{separatrix}$  corresponds to the poloidal flux at the last closed flux surface and  $\Psi_{axis}$  is the poloidal flux at the magnetic axis.).  $\rho_{pol}$  ranges between 0 and 1 in the confined plasma region while values above 1 are also well defined and correspond to the scrape-off layer of the plasma.

$$\rho_{pol}(\Psi) = \sqrt{\frac{\Psi - \Psi_{axis}}{\Psi_{separatrix} - \Psi_{axis}}} \quad (1.2)$$

### 1.2.2 Divertor Concept

The plasma configuration as presented in figure 1.4(a) is elaborate, as the external coils are used to form a separatrix inside of the contours of the first wall. A simpler approach, which requires less external coils, is the so-called limiter configuration (cf. figure 1.4(b)). Historically, the limiter configuration was employed first, however, direct contact of the first wall with the closed flux surfaces leads to a large impurity content of the plasma, as well as high heat loads and particle fluxes onto the first wall. In the 1980s the development of the divertor concept was a breakthrough, because of the beneficial effects for plasma and wall, but also because of the accessibility to the so-called high confinement mode (H-mode, explained in section 3.4.1).

The divertor configuration allows for the separation of the confined plasma from the plasma wall contact. The latter is realized in a region, called the divertor, which is slightly separated from the main plasma. In this volume the density of neutrals, electrons and ions strongly increases, which decreases the local temperatures as also in the scrape-off layer the plasma pressure is typically equilibrated along field lines following the parallel force balance. The temperature and density may vary along the field line as these are determined by transport and sources. Typically this leads to divertor temperatures in the range of 10 eV, while for high divertor densities, temperatures in the range of a few eV are accessible. In figure 1.5 a 2D plot of a the modelling by the computer code EMC3 (cf. [4]) is presented which exemplifies the electron parameters for a typical H-mode discharge in ASDEX Upgrade. In the plasma core, temperatures of several keV are obtained while the whole scrape-off layer features temperatures of a few tens of eV and the divertor approaches 10 eV close to the wall. The electron densities drop from about  $8 \cdot 10^{19} \text{ m}^{-3}$

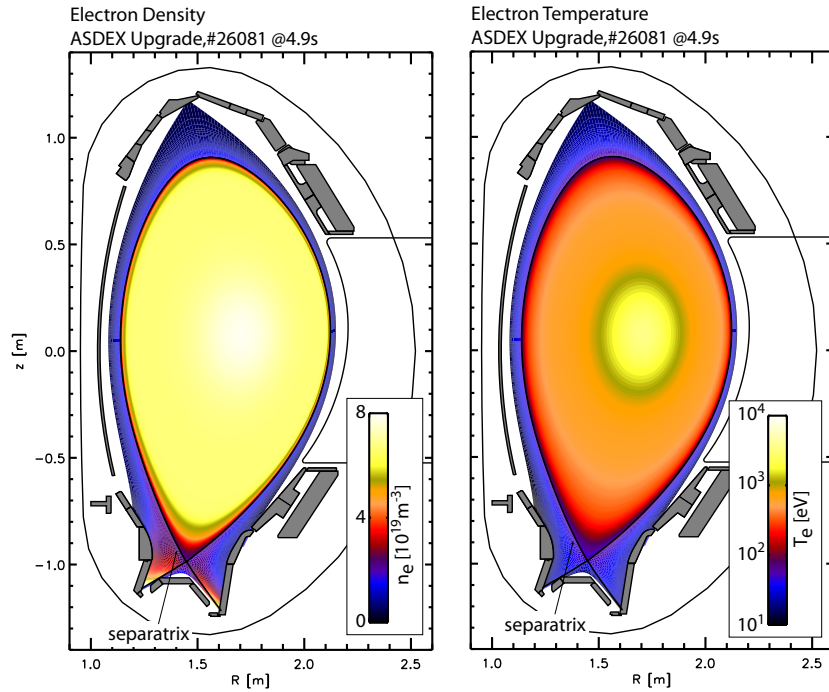


Figure 1.5: 2D distribution of electron density and temperature of the EMC3-modelling (courtesy of T. Lunt) for #26081 at 4.9 s. Note the numerical grid does not fill the entire volume in the vacuum vessel.

in the plasma core to about  $2 \cdot 10^{19} \text{ m}^{-3}$  at the separatrix, while reaching values of about  $8 \cdot 10^{19} \text{ m}^{-3}$  in the divertor close to the wall.

The scrape-off layer acts as a protective layer, such that when impurities are eroded at the wall the impurity level in the confined plasma remains remarkably low. The divertor configuration is thus an important measure when controlling the impurity level of a plasma. As will be explained in section 1.3 impurity control of high-Z elements such as tungsten is a necessity for the successful operation of a fusion plasma and thus, the divertor concept is crucial when using tungsten as a plasma facing material. Due to the fact that this measure was not available in the 1970s, W was then regarded as unusable as a first wall material. Only after the development of the divertor concept did W again become a promising wall material.

In any case, when a fusion reactor constantly produces power in steady state not only the imperfect plasma confinement is of concern for the wall erosion, also some fraction of the produced power will be transported to the first wall. This yields concerns even in divertor configuration, because the power exiting the plasma is transported along the field lines to the divertor and the radial power fall-off length is of the order of a few millimeters, such that high power densities may result at the wall. Additionally, there are other properties that influence the choice of wall material, which will be elaborated

in the following section 1.3.

## 1.3 The Choice of the Wall Material

The wall material must meet several criteria provided by economical, physics and safety considerations. The most important of these aspects are addressed in the following.

### Erosion (Lifetime of the Wall)

The erosion of the wall material in a reactor may be approximately quantified by estimating wall fluxes of neutrals, ions and power. In figure 1.6 sputtering yields, i.e. the ratios of eroded wall atoms per impinging  $D^+$  ion, for several wall candidates are given for an impinging deuterium flux. There is an obvious trend that materials consisting of lighter atoms exhibit a lower sputtering threshold than materials consisting of heavier atoms. This is simply due to the energy transfer during the collisions between individual atoms, which becomes maximal for collision partners of the same mass. This simple consideration needs extension by considering the binding energy of the material which retains the atom below a material dependent threshold energy. For carbon (C), the effects of so-called

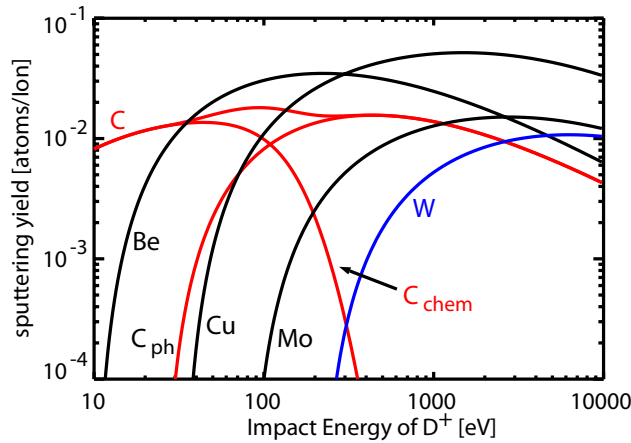


Figure 1.6: The erosion yield of several elements for an impinging  $D^+$  flux. (Adapted from [5] after [6])

chemical erosion (cf. [7]) are included in figure 1.6, which leads to an enhanced sputtering yield even below the threshold energy of physical sputtering. This is given by a lowered binding energy due to the chemical reactions between the C and D atoms. As a result, the expected erosion rates for light elements such as Be and C in a reactor, are estimated to be much too large in order to economically run a fusion reactor. Several cm of material would be eroded per month of operation which would require an exchange of the first wall

material every few months. Such an exchange implies considerable costs for material and down-time of the fusion power plant such that the use of a material with heavier atoms is unavoidable. For heavy elements like W, the typical energy of deuterium ions hitting the first wall in the divertor is below the sputtering threshold, which reduces the erosion rates drastically such that only the erosion by plasma impurities is of importance. Thus, the low-Z impurity content of the plasma dominates the sputtering yield of a W-wall.

### Storage of Fuel (in Particular Tritium)

The particle fluxes onto the first wall cause not only erosion, but also the implantation of the impinging particles which leads to a retention of the fuel particles within the vacuum vessel. Additionally, the eroded plasma facing material can also be re-deposited together with hydrogen. The retained fuel includes tritium, for which the authorities define safety limits specifying the maximum tritium inventory allowed inside of the vacuum vessel. Thus, it is important to keep track of all injected tritium and to minimize the tritium inventory stored in the first wall. The implantation of fuel in the wall can be calculated and is investigated in todays devices, however, complications exist that require consideration:

- For carbon the re-deposition results in amorphous hydrocarbon layers. Due to the large amounts of eroded material, this leads to macroscopic deposits at various locations. Not all of these deposits are accessible by the plasma, as the originally produced hydrocarbons might be neutral and may even bounce off during the wall contact. Such observations are ubiquitous in fusion experiments using C as a first wall material. [8]
- The storage of the fuel inside of a material is influenced by the internal structure of the material, which is changed by the neutron irradiation expected in a fusion reactor.
- The release of the fuel inventory during heating of the material or during particle impact depends on the wall material. Also the diffusion of the fuel particles from the surface layers into the bulk might be important.

One of the most comprehensive studies of the mentioned effects for ITER is provided in [9]. Figure 1.7, which is adapted from [9] depicts the retained tritium in the vacuum vessel versus the length of full power operation in ITER, depending on the various wall material mixes. The design goal of ITER are 1000 discharges at 400 s length. Thus, a pure carbon wall and the original ITER design (C+Be+W) would not meet the design goal. Only removing C from the torus allows for meeting the design goals without employing elaborate (and not yet developed) cleaning schemes. Originally, the use of C in the

divertor was planned, because also high power fluxes are expected for which C would be superior (cf. following section). However, as the effectiveness of the carbon cleaning schemes remains unclear, a solution with a full W divertor was recently chosen by the ITER organization from day one on.

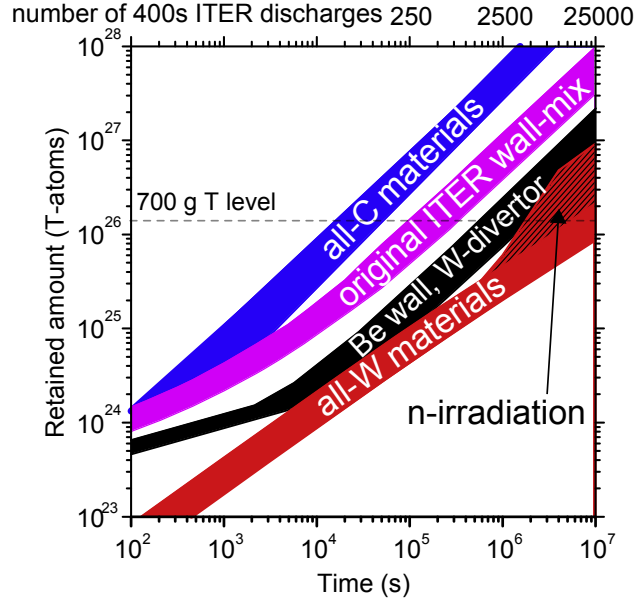


Figure 1.7: Tritium inventory versus discharge/discharge time for different material mixes. The material mixes correspond to an hypothetical all-C ITER (all-C materials), ITER with Be in the main chamber, W in the divertor and C at the strike points (original ITER wall-mix), ITER with Be in the main chamber and a full W divertor (Be wall, W-divertor) and a full-W ITER (all-W materials). The maximum allowed tritium inventory inside of ITER is 700 g. (adapted from [9])

## Heat Resilience

The components at the divertor, specifically at the strike points, i.e. the intersection of separatrix and first wall, needs to be compatible with high heat fluxes in the order of  $10 \text{ MW/m}^2$ . This large number arises due to the small radial power fall-off length, such that all the power exiting the plasma is deposited in a toroidal ring in the divertor with the radial extension of only a few millimeters (e.g. [2]). High power fluxes lead to large surface temperatures depending also on the heat conductivity of the used material. The considered materials for the high heat flux areas in ITER are CFC and bulk W, which both feature high tolerance against heat fluxes. The sublimation point of carbon is below 4000 K and the melting point of W is at 3700 K.

Excursions from the steady-state power load seem to be unavoidable, as the plasma

spontaneously varies the expelled power by small amounts during routine operation (e.g. ELMs, section 3.4.2) or by larger amounts during off-normal events. For graphite such excursions would lead to local sublimation of material, which at least features high effective cooling of the tile by sublimation. Additionally, the shape of the tile is not drastically changed by the sublimation unlike melting, which may lead to droplets and locally protruding melt layers (cf. to [10, 11]). Nevertheless sublimation also leads to a deviation from the optimal tile shape and increased erosion such that unintended excursions from the steady-state power loads must be minimized in any case.

### Mechanical Stability

The aspect of mechanical stability is less directly connected to the use of a specific element, as many complications exist. For instance, CFC has much better mechanical stability than graphite even though consisting of the same element. Similarly, W changes its mechanical and structural properties after the so-called transition from brittle to ductile taking place at a few hundreds degree C. However, if W is heated above approximately 1500K recrystallization happens which may result in a slightly higher temperature for the transition between brittle and ductile. This may influences the stability of the material especially during thermal expansion. New solutions are investigated for W (e.g. using W-fibres to support bulk W [12]) in order to improve its engineering properties.

An additional aspect of the mechanical implications is the electrical conductivity of the tiles, as for changes of the magnetic field at the tile location currents are induced. These currents imply a  $j \times B$ -force on the tile and its mounting structure which is depending on the induced current and thus conductivity. As the conductivity of W is about two orders of magnitude larger than for CFC, special measures, such as castellation of tiles, are necessary to limit the induced currents. A reinforced mounting structure is anyhow necessary, as the specific weight of W is  $19.3 \text{ t/m}^3$  as compared to values in the range of  $2 \text{ t/m}^3$  for the type of CFC typically used as first wall.

### Other Aspects

Additional questions which are addressed when considering the choice of the first wall and which are not further discussed in this work, are:

- What is the change of the material properties under neutron irradiation? How do the properties of the material change, due to displacements and transmutation? What are the activation properties of the material?
- What are the magnetic properties of the material? Will the magnetic field confining the plasma be altered by the perturbation yielded by the dia-, para- and ferro

magnetism of the material?

- What are the properties of mixing materials via migration, when different first wall materials are used at the divertor and at the main chamber?
- Embrittlement via hydrogen and helium in the material

### **Effect of the Wall Material on the Plasma**

When using W at the first wall, the impact of radiative cooling by W is a potential limit for the performance and stability of the fusion plasma such that strategies are important to diagnose and control the W content of the plasma. This caveat was a show stopper for tokamaks in the 1970s (e.g. ORMAK [13] and PLT [14]), which used W as a wall material, while using a limiter configuration (cf. section 1.2.2). Large W-concentrations in the range of one per mille have been observed in the plasma core as non-favourable transport lead to an accumulation of W close to the magnetic axis (cf section 3.5). As a consequence the radiation lead to hollow temperature profiles making fusion relevant plasmas impossible. Only after the development of the divertor configuration (cf. section 1.2.2) in the 1980s the impurity control worked well enough to reconsider W as a wall material (demonstrated in [15]). As the first experiences with W in the limiter machines PLT and ORMAK have been very negative, W has been reconsidered only in the 1990s as a wall material. It may be noted that the divertor configuration provides the possibility of using W as a wall material, which is a remedy to many challenges for the first wall, however, the control of the W-content is even in divertor configuration a goal that requires elaborate strategies. Such possible strategies are described in chapter 3.

Note that Alcator C-Mod [16] has been using molybdenum as a first wall material since 1991 (e.g. [17]) which makes it a pioneer for high-Z wall operation in a divertor tokamak. However, molybdenum is not suited for the usage at a reactor wall due to its activation properties, while the effects of Mo on the plasma are comparable to those of W. Today the experiments ASDEX Upgrade [18] (since 1996, cf. [19, 20] ) and JET [21] (since 2011, cf. [22, 23, 24]) investigate the effects of large first wall fractions made from W on the plasma. Almost all other experiments investigate the properties of W as a first wall material by testing small W surfaces such as single tiles or erosion probes at the boundary of the plasma.

In the future, ITER (cf. [25]) is the most prominent experiment using W as a plasma facing material in the divertor. But also smaller experiments follow the idea of W being a reactor relevant candidate, e.g. WEST (cf. [26]) is planned to operate with a full W wall.

## 1.4 Sources of Impurities

The impurities in fusion plasmas originate from different sources, which influences their behaviour and thus the possibilities of their control.

### Helium

In a reactor plasma DT-fusion takes place and He is produced in the plasma core (equation 1.1). This He must be removed in order to keep the dilution of the fuel low. Ultimately, the He confinement time is considerably longer than the particle confinement of the plasma, because He recycles at the wall, is less efficiently compressed in the divertor due to edge physics effects and depending on the pumps may also be less efficiently pumped than D or T (cf. to [27, 28, 29]). Thus, the global confinement time of He,  $\tau_{He}^*$  is defined (where \* is indicating the consideration of the mentioned additional effects), which is much longer than the energy confinement time. Note that a removal of the thermal He is intended, while the fast He nuclei before thermalization are required to stay in the plasma core until thermalization.

In today's devices, not using DT-fuel, He is either intentionally puffed or originates from the walls, in which it may have been implanted during He glow discharges. The latter are used to condition and clean the walls.

### Unintentionally Produced Impurities (Erosion, Evaporation, Sublimation)

In today's devices most of the impurities originate from the wall (except for special impurity seeding experiments) eroded by the impinging plasma ions (cf. to section 1.3). These ions are accelerated in the plasma sheath, which is an edge layer (thickness of order Debye length) in which the electric potential drops towards the wall. This potential difference is a result of the larger thermal velocities of the electrons, which in equilibrium are repelled from the wall, while ions are accelerated towards the wall in order to maintain ambipolar fluxes to the wall. Thus, the electron temperature is influencing the erosion process via the potential drop in the sheath, while also the ion temperature has an effect on the energies of the incident particle flux. Of course, the incident flux is also an important player, which puts focus on the divertor material as here the largest wall fluxes occur. The potential drop in front of the wall may also be influenced by the effects from ion cyclotron heating (ICRH), as a strong increase of the W-erosion and sputtering yield at the ICRH antennae are observed during ICRH operation [30, 31]. The comparison to the observations from Alcator C-Mod [32, 33], where the erosion is attributed to less local erosion positions, suggests that the details of limiter positions with respect to ICRH antennae influence this effect, which is still subject to investigations.

Additionally, a considerable heat flux arrives at the wall which may lead to melting or sublimation of the wall material. Such events, occasional arcing or even standard conditions lead to dust production in fusion devices, which yields a secondary impurity source. This needs special consideration, because due to the macroscopic size of the dust particles the plasma radiation may considerably rise if such a particle is entering the main plasma (cf. to [34, 35]).

In a reactor device additionally seeded impurities are introduced, which complicates the situations, because they may lead to an enhancement or reduction of erosion, as is explained in section 3.1.

### Intentionally Seeded Impurities

Low-Z impurities have the property that they radiate strongly at low electron temperatures via line radiation, while at high electron temperatures they are fully stripped and only contribute to bremsstrahlung (cf. section 1.5.2). This leads to the possibility to mitigate localized heat fluxes at the plasma edge by radiative cooling, while the confinement of the core plasma is unperturbed. This scheme is investigated in today's devices and it is obligatory for a reactor grade device (cf. to [36]), because the steady-state power fluxes to the wall at least scale with the volume of the plasma, thus with at least  $R^3$ , and the ‘wetted’ surface scales with only  $R$  corresponding to a ring in the divertor with constant width independent of  $R$  (cf. to [2, 3]). It is estimated that about 90-95 % of the power leaving the fusion zone of the plasma core must be radiated inside and outside the confinement region before it arrives at the first wall.

This may be possible, as already today impurity seeding is used to control wall loads. In figure 1.8 a comparison of the power fluxes in the outer divertor from ASDEX Upgrade as measured by IR-thermography is depicted. A strong modulation of the power flux is given by edge localized modes (ELMs). The power flux to the divertor wall in a discharge without impurity seeding (red) is much larger than in a similar discharge with nitrogen seeding (blue). The effect of radiative cooling is obtained for nitrogen concentrations in the range of 1 % in the plasma core. A review on impurity seeding in tokamaks can be found in [36].

## 1.5 The Burn Condition of a Fusion Reactor

In a fusion reactor much more energy shall be gained than is invested in plasma heating. Thus, it is envisaged that a substantial fraction of the plasma heating power will be provided by the fusion process itself: The kinetic energy of the produced  $\alpha$ -particle will heat the surrounding plasma via Coulomb collision, while the produced neutrons will

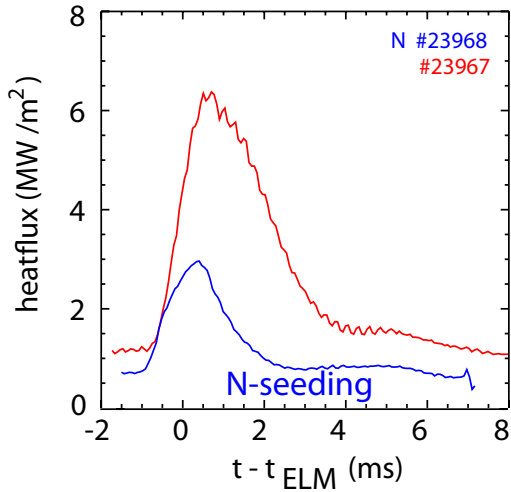


Figure 1.8: For two discharges with 9 MW auxiliary heating the thermography measurements viewing the lower divertor are compared. A strong modulation is given by edge localized modes (ELMs). In red the data of a discharge without impurity seeding is presented, while for the blue data nitrogen was added reaching about 1-2 % in the plasma core. With nitrogen seeding the power load at the outer divertor is strongly reduced. (adapted from [37])

be absorbed outside of the plasma in the breeding blankets and their kinetic energy is harnessed for energy production.

The requirement to provide a major fraction of the plasma heating via  $\alpha$ -particles produced by fusion processes can be approximated by demanding that all of the heating power must be provided by the  $\alpha$ -particles. This simplification allows a burn condition to be derived, at which the plasma provides enough  $\alpha$ -particles to sustain the high temperatures necessary for fusion. Note that in the following the burn condition is discussed in a 0D approach, while the considerations shall apply to the plasma core of a reactor. Details of plasma and impurity transport are not included in detail, however, these may matter and are also subject of the later considerations of this thesis. In the following, the 0D burn condition is derived for a variety of assumptions, i.e. for plasmas without impurities, for plasmas with light and heavy impurities and for plasmas containing light and heavy impurities and He ash. This section is inspired by the comprehensive study in [38].

### 1.5.1 Without Impurities

The burn condition is obtained by considering the power balance between the plasma heating densities and the power loss densities due to transport and radiation in the plasma core. This can be expressed as

$$P_{heating} = P_{radiation} + P_{transport} , \quad (1.3)$$

where  $P_{heating}$  is provided by the kinetic energy  $E_\alpha = 3.5 \text{ MeV}$  of the  $\alpha$  particles produced by the fusion of deuterium and tritium. The densities of these two isotopes for an impurity free plasma is ideally given by half of the electron density  $n_e$ . For such an impurity free plasma the radiation losses ( $P_{radiation}$ ) is given by pure bremsstrahlung, i.e.  $C_{Br} n_e^2 \sqrt{T} g_{ff}$ , where  $T$  is the plasma (electrons and ions) temperature,  $C_{Br}$  a constant and  $g_{ff}$  the free-free Gaunt factor. The transport losses ( $P_{transport}$ ) are simply approximated by a typical energy confinement time  $\tau_E$ , which relates the  $P_{transport}$  to the stored energy densities in the plasma core as given by the kinetic energies of ions and electrons. Thus, equation 1.3, becomes

$$\left(\frac{n_e}{2}\right)^2 \langle\sigma v\rangle E_\alpha = C_{Br} n_e^2 \sqrt{k_B T} g_{ff} + \frac{3k_B T n_e}{\tau_E} \quad (1.4)$$

where  $k_B$  is Boltzmann's constant. A simple transformation gives

$$n_e \tau_E = \frac{3k_B T}{\langle\sigma v\rangle \frac{E_\alpha}{4} - C_{Br} \sqrt{k_B T} g_{ff}} \quad (1.5)$$

providing a condition for  $n_e \tau_E$  at each temperature  $T$ . Note that  $\langle\sigma v\rangle$  has a strong  $T$ -dependence, which defines the temperature range in which the heating by  $\alpha$ -particles is larger than bremsstrahlung and thus, a physical solution, i.e. a positive solution, for  $n_e \tau_E$  exists. As, in practice, the plasma pressure is the limited quantity for the confining apparatus a more natural figure of merit is given by  $n_e T \tau_E$ , which is obtained from equation 1.5 by multiplication with  $T$ .

### 1.5.2 With Impurities

The effect of a plasma impurity  $Z$  ( $Z$  representing an element or its nuclear charge) with charge  $q$  and concentration  $c_Z$  on the burn condition can be separated into the effects on each term in equation 1.3. The presence of impurities dilutes the fuel particles lowering the reaction rate at the same electron density.

$$P_{heating} = \left(\frac{n_e(1 - qc_Z)}{2}\right)^2 \langle\sigma v\rangle E_\alpha \quad (1.6)$$

The multiple charge of the impurity ions increases the bremsstrahlung proportional to the effective ion charge  $Z_{eff}$  of the plasma, which may be calculated via  $Z_{eff} = \frac{\sum_Z \sum_q q^2 n_{q,Z}}{n_e}$ ,

where  $n_{q,Z}$  is the density of charge stage  $q$  of the element  $Z$ . If the impurity nucleus is not fully stripped, recombination and line radiation is emitted which is much stronger than the losses by bremsstrahlung. The plasma radiation is then given by

$$P_{radiation} = C_{Br} Z_{eff} n_e^2 \sqrt{k_B T} g_{ff} + c_Z n_e^2 R_{rec} + c_Z n_e^2 R_{line} , \quad (1.7)$$

where  $R_{rec}$  is the power coefficient for recombination radiation and  $R_{line}$  is the power coefficient for line radiation. The treatment of all radiation losses can be generalized, by using an element specific cooling factor  $L_Z$ . Bremsstrahlung is also included in  $L_Z$ . Thus,

$$P_{radiation} = (1 - qc_Z) n_e^2 L_H + c_Z n_e^2 L_Z \quad (1.8)$$

The dilution of the ion density also leads to corrections to  $P_{transport}$  in equation 1.3 containing the thermal energy of all plasma particles.

$$P_{transport} = \frac{\frac{3}{2} k_B T (n_e + n_D + n_T + c_Z n_e)}{\tau_E} = \frac{\frac{3}{2} k_B T n_e (2 - (q - 1)c_Z)}{\tau_E} \quad (1.9)$$

In the following, specific impurity species are discussed separately, as there are systematic differences in their effect on the burn condition.

### He-Ash

Even for a perfectly clean plasma the production of He is unavoidably connected with the fusion process. Thus, a treatment of He is the minimum requirement for a consistent burn condition. The He content of the plasma is given by a similar balance to that presented for the power. In equilibrium the production of He, as given by the fusion processes, equals the loss of He by transport. The latter may be described by the global He confinement time  $\tau_{He}^*$  (for the explanation of the subscript ‘\*’ cf. to section 1.4), which relates the loss, i.e. the He transport flux, to the He content of the plasma. In equilibrium the production rate equals the losses:

$$\left( \frac{n_e (1 - 2c_{He})}{2} \right)^2 \langle \sigma v \rangle = \frac{n_e c_{He}}{\tau_{He}^*} \quad (1.10)$$

where the dilution of the fuel by He is taken into account via correcting the fuel densities by the concentration  $c_{He}$  weighted by its charge 2. For practical reasons,  $\tau_{He}^*$  is defined via  $\rho^* = \frac{\tau_{He}^*}{\tau_E}$  relating the He confinement to the energy confinement. According to the modifications presented in equations 1.6, 1.8 and 1.9 the burn condition becomes

$$\left( \frac{n_e (1 - 2c_{He})}{2} \right)^2 \langle \sigma v \rangle E_\alpha = (1 - 2c_{He}) n_e^2 L_H + c_{He} n_e^2 L_{He} + \frac{\frac{3}{2} k_B T n_e (2 - c_{He})}{\tau_E} \quad (1.11)$$

Combining equation 1.10 and the definition of  $\rho^*$  allows for the elimination of  $\tau_E$ ,  $\tau_{He}^*$  and  $n_e$  in equations 1.11 resulting in the following cubic equation in  $c_{He}$ , which has, for a specific temperature, 0 to 2 physical solutions for  $c_{He}$ .

$$-4\left(\frac{E_\alpha}{\rho^*} + \frac{3}{2}kT\right)c_{He}^3 + 4\left(\frac{E_\alpha}{\rho^*} + \frac{L_{He} - L_H}{\rho^*\langle\sigma v\rangle} + \frac{9}{2}kT\right)c_{He}^2 + \left(4\frac{L_H}{\rho^*\langle\sigma v\rangle} - \frac{E_\alpha}{\rho^*} - \frac{27}{2}kT\right)c_{He} + 3kT = 0 \quad (1.12)$$

The obtained solutions for  $c_{He}$  may be used in equation 1.11, in order to derive the burn condition for  $n_e T \tau_E$ . The burn condition depends on the value of  $\rho^*$  and for  $\rho^* > 15.7$  no burn condition exists. In all cases, the finite He confinement results in a burn condition that is a closed curve in the  $n_e T \tau_E$  versus  $T$  plane. This is in contrast to the pure DT solution (equation 1.5), which gives a possible burn condition at arbitrarily large values of  $n_e T \tau_E$  (cf. figure 1.12 - described later).

### Low-Z versus High-Z Impurities

The label ‘low-Z impurity’ can be defined in various ways. First the type of radiation from the impurity ions, which is related to the number of bound electrons, shall be considered. Impurities with lower nuclear charge  $Z$  and fewer bound electrons are more easily stripped, such that in a sufficiently hot fusion plasma the impurity radiation is given purely by bremsstrahlung. Using the radiation type as definition, the distinction between low-Z and high-Z depends somewhat on the temperature of the considered plasma. In figure 1.9, the cooling factor  $L_Z$ , taken from [39], and the partial cooling factor considering only bremsstrahlung ( $L_{Z,brems}$ ) are presented for many elements at  $T_e = 3$  keV (blue circles),  $T_e = 10$  keV (orange triangles) and  $T_e = 30$  keV (red squares). With higher nuclear charge all radiation types, i.e.  $L_Z$  and  $L_{Z,brems}$ , increase strongly. The bremsstrahlung  $L_{Z,brems}$  scales with  $q^2$ , where  $q$  is the charge stage of the impurity ions. The values for  $L_{Z,brems}$  are obtained by using the mean charge  $q$  as given in [39] in the Bremsstrahlung formula from [40]. The gaunt factors necessary to evaluate the bremsstrahlung formula are taken from [40]. Even if only the bremsstrahlung was of importance, the  $q$ -dependence leads to an increase of the bremsstrahlung for high-Z elements, as the charge stage  $q$  obtained at high temperatures correlates with the nuclear charge  $Z$ . Only for very large  $Z$ ,  $q$  and  $Z$  may deviate as a few electrons remain bound to in the ionization potential of the highly charged ions/nucleus. Comparing beryllium and tungsten, the bremsstrahlung increases between 2 and 3 orders of magnitude depending on the electron temperature, which governs also the charge stage of the impurities. For impurities that are not fully stripped or have a considerable recombination rate, line radiation and recombination radiation add on top of the bremsstrahlung. This is the case for higher nuclear charges and for lower electron temperatures. In order to have a quantitative criterium for the importance of bremsstrahlung, figure 1.10 is considered. The ratio  $L_Z/L_{Z,brems}$ , as presented

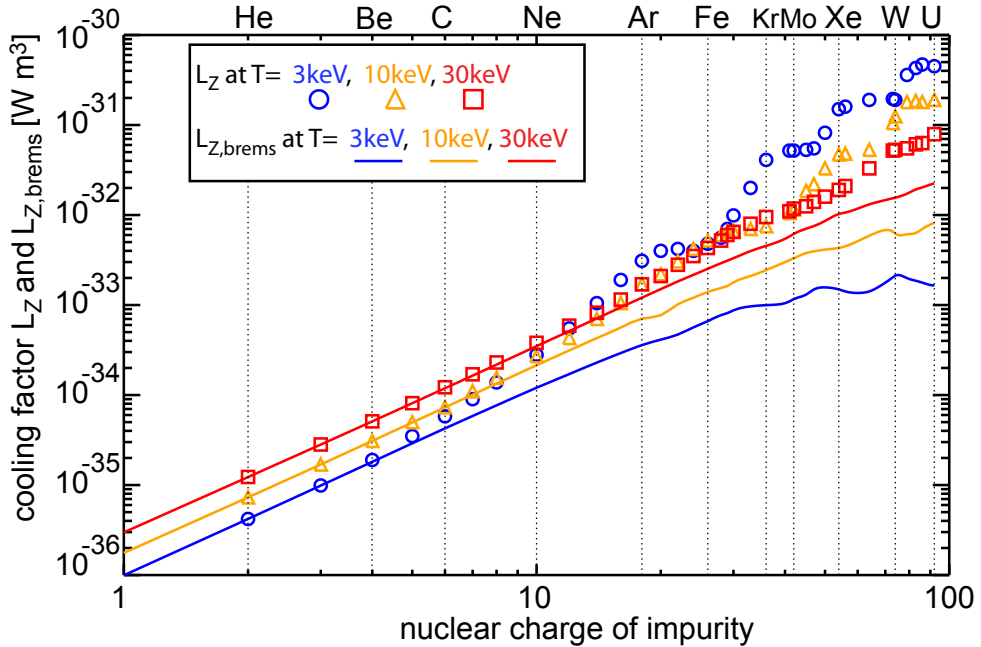


Figure 1.9: The lines give the bremsstrahlung radiation coefficient  $L_{Z,brems}$ , i.e. the portion within the cooling factor  $L_Z$  describing only bremsstrahlung, at 3 keV (blue), 10 keV (orange) and 30 keV (red) plasma temperature for elements with nuclear charge between 1 and 92. The symbols give the total cooling factor at the same plasma temperatures for selected impurities as calculated in [39].

in figure 1.10, delivers a quantitative discriminator for low-Z and high-Z elements. For elements which exhibit a ratio of  $L_Z/L_{Z,brems}$  below 2, the bremsstrahlung is the largest contribution to  $L_Z$ . This definition of ‘low-Z’ versus ‘high-Z’ elements is somewhat flexible depending on the considered electron temperature. The additional contributions from line and recombination radiation are larger than bremsstrahlung for nuclear charges above oxygen ( $Z = 8$ ) at 3 keV, argon ( $Z = 18$ ) at 10 keV and about iron to krypton ( $Z = 26$ - $38$ ) at 30 keV. Note that at 30 keV the line radiation of high-Z elements looks tolerable, however, the bremsstrahlung itself is also very high such that radiative cooling is also an issue at 30 keV (cf. to figure 1.9). In order to acknowledge the temperature dependence of the discrimination between low-Z and high-Z impurities often the term mid-Z is used (cf. to the bottom of figure 1.10).

An alternative way of discriminating between ‘low-Z impurities’ from ‘high-Z impurities’ is provided by their effect on the terms  $P_{heating}$  and  $P_{radiation}$  in the burn condition. In both cases these terms are changed such that the burn condition is more difficult to obtain. For simple considerations, the third term ( $P_{transport}$ ), is usually neglected as the effects are either small or follow trends that can only be understood in the context of a much more complicated model. Including the effects of impurities,  $P_{heating}$  and  $P_{radiation}$  are

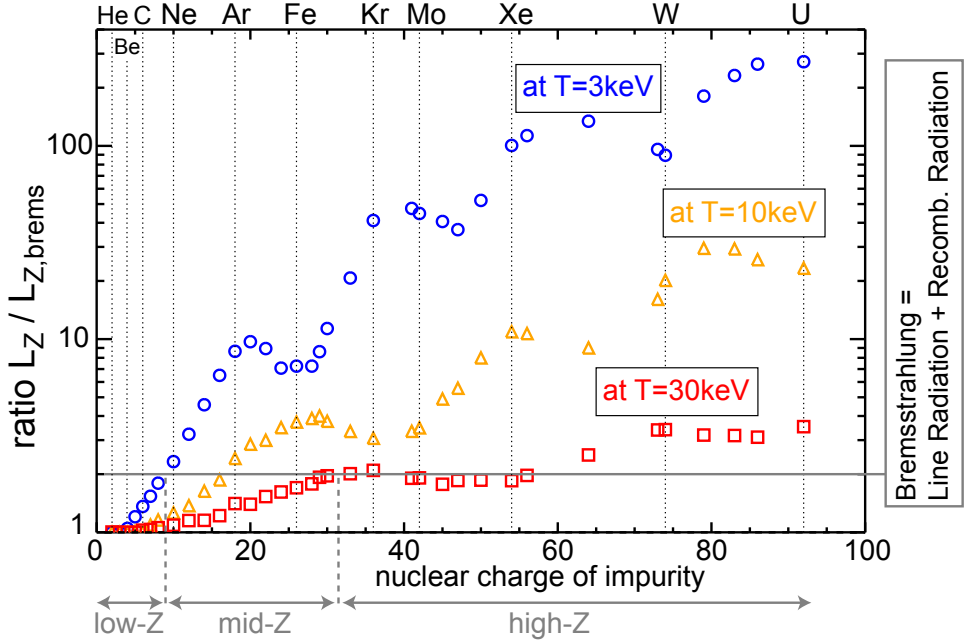


Figure 1.10: For the data in figure 1.9 the ratio of cooling factor over the bremsstrahlung radiation coefficients are presented at the plasma temperatures 3 keV (blue), 10 keV (orange) and 30 keV (red) for selected impurities. A ratio of 2 means that line and recombination radiation matches bremsstrahlung.

changed by  $\Delta P_{heating}$  and  $\Delta P_{radiation}$  as given by

$$\Delta P_{heating} = \left( \frac{n_e(1 - qc_Z)}{2} \right)^2 \langle \sigma v \rangle E_\alpha - \left( \frac{n_e}{2} \right)^2 \langle \sigma v \rangle E_\alpha = \frac{n_e^2}{4} \langle \sigma v \rangle E_\alpha (q^2 c_Z^2 - 2qc_Z) \quad (1.13)$$

and

$$\Delta P_{radiation} = (1 - qc_Z) n_e^2 L_H + c_Z n_e^2 L_Z - n_e^2 L_H = n_e^2 c_Z (L_Z - qL_H) \quad . \quad (1.14)$$

For  $qc_Z \ll 1$  the quadratic term in equation 1.13 can be neglected and we get

$$\left| \frac{\Delta P_{radiation}}{\Delta P_{heating}} \right| = \frac{n_e^2 c_Z (L_Z - qL_H)}{\frac{n_e^2}{4} \langle \sigma v \rangle E_\alpha 2qc_Z} = \frac{(L_Z - qL_H)}{\frac{1}{2} \langle \sigma v \rangle E_\alpha q} \quad (1.15)$$

which is independent of both  $n_e$  and  $c_Z$ . The ratio  $|\Delta P_{radiation}/\Delta P_{heating}|$  is presented in figure 1.11 for a 10 keV and 30 keV plasma. It is increasing for impurities with larger nuclear charge, because of the strong dependence of  $L_Z$  on the charge of the impurity (cf. figure 1.9). In absolute numbers it is smaller than 1 for impurities with nuclear charge below that of neon for 10 keV and iron for 30 keV. Thus, the boundary between low-Z and high-Z impurities again depends on the plasma temperature, and the transition region is again labeled ‘mid-Z impurities’. The values for 3 keV have been omitted, as at 3 keV the

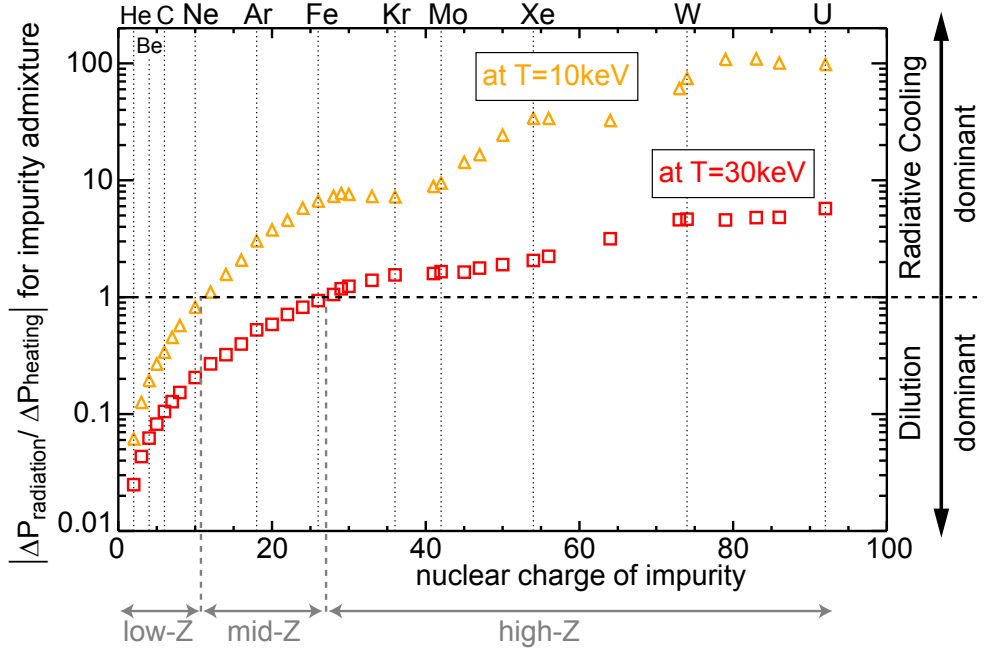


Figure 1.11: For the approximation of small dilutions, i.e.  $qc_Z \ll 1$ , the loss of  $\alpha$ -heating power ( $\Delta P_{heating}$ ) due to dilution is compared to the loss due to radiative cooling ( $\Delta P_{radiation}$ ) when a certain element is introduced to a fusion plasma. For the used approximation the ratio  $\Delta P_{heating}/\Delta P_{radiation}$  is independent of  $n_e$  and  $c_Z$ .

power balance gives no burn condition and thus the evaluation does not make sense. In the following the term ‘low-Z impurity’ is mostly used for He, Be, B, C and N, while the term ‘high-Z’ is mostly used for W and occasionally for Mo. Thus, for these impurities the labels are unambiguously applicable no matter which of the two presented ways of defining ‘low-Z’ and ‘high-Z’ impurities is used.

After examining the terms of the burn condition for various impurities the focus is now put on the impurities that are expected to dominate (wall materials) in ITER [29], the next step fusion experiment, namely beryllium (Be) and tungsten (W). In figure 1.12(a) and (c), the burn curves considering Be and W are depicted. These have been evaluated taking into account a He confinement of  $\tau_{He}^* = 5\tau_E$ , e.g. discussed in [27, 28, 29]. Similar to the evaluation of He concentrations without other impurities (cf. equations 1.10 and 1.11) the He concentration needs to be evaluated first taking additional terms for the the impurity effects into account. The obtained He concentrations are presented in the figures 1.12(b) and (d). With the determined He concentrations the burn curves are evaluated. The burn curves for Be, only deviate considerably from the Be-free plasma when  $c_{Be}$  is at the percent level. For increasing Be-concentrations the burn curves become smaller around an approximately constant center. The burn condition cannot be fulfilled anymore for  $c_{Be} > 0.08$ . For W, the burn curves become clearly different from the W-free case

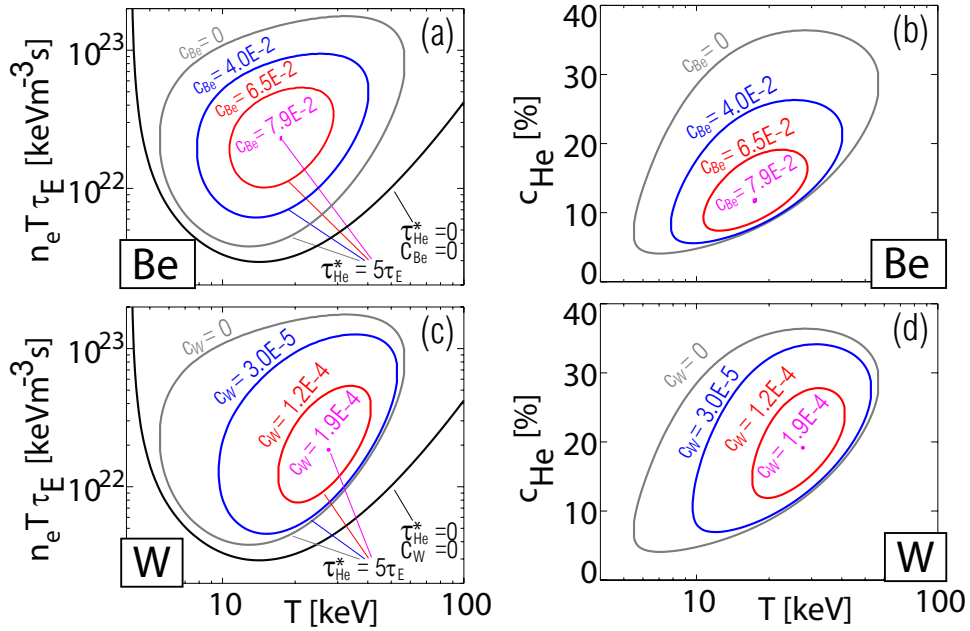


Figure 1.12: (a) Curves indicating the burn condition in the presence of different Be concentrations for the case that  $\tau_{\text{He}}^* = 5\tau_E$  along with the curve for no He and no Be for reference. (b) Equilibrium He concentrations corresponding to burn curves from part (a). (c) Same as (a) for different W concentrations. (d) Equilibrium He concentrations corresponding to burn curves from part (c).

already for  $c_W \approx 10^{-5}$ , while no burn condition exists for  $c_W > 1.9 \cdot 10^{-4}$ . The burn curves are systematically shifted to higher temperatures for increasing W-concentrations, as W radiates more strongly at lower temperatures. The details of these curves depend on the quality of the atomic data that is used to evaluate the cooling factor  $L_W$ . In Publication 1, Publication 2 and Publication 3 (cf. chapter 5 on major publications), atomic data for W is derived and benchmarked. Ultimately it is used in Publication 2 to evaluate the burn curves as presented in figure 1.12(c), but also diagnostics applications (cf. to section 2) are based on that atomic data.

## 1.6 Structure of This Thesis

The results presented in this thesis are mainly concerned with three topics that are crucial for high-Z impurity control and diagnostics in fusion plasmas.

- Publications 1 – 3 (featured in chapter 5) are concerned with the **atomic properties of tungsten ions** in order to obtain the atomic data necessary for predicting radiative losses from the plasma and spectral lines emitted by tungsten. Both are necessary for understanding and modelling the performance of a fusion plasma with

high-Z impurities and to diagnose the high-Z impurity content.

- Publications 4, 5 and 6 improve our understanding of the **impurity transport in the plasma core, at the plasma edge and in the scrape-off layer** in JET and ASDEX Upgrade.
- Publications 6 – 12 focus on **the physics of the plasma edge**, where steep gradients exist in H-mode discharges owing to the existence of a transport barrier for particles and energy. This region is also called the pedestal as it yields the boundary conditions for the core profiles. Due to the fact that future fusion experiments and possibly reactors rely on the enhanced confinement due to that barrier a considerable effort is being put into **understanding the impurity transport at the barrier and the underlying physics of the barrier itself**.

This thesis is structured as follows: In chapter 5 the publications, which form the main part of this thesis, are presented, while the preceding chapters give background information in order to highlight the contributions of the publications to the challenge of building a fusion reactor.

In chapter 2 the impurity diagnostics of the investigated fusion plasmas are described. The diagnostic methods benefit from the atomic data calculated and benchmarked in publications 1-3. They are used to analyze impurity transport (publications 4-6) and the physics of the plasma edge (publications 8-12), which is closely connected to impurity transport. The charge exchange recombination spectroscopy system at ASDEX Upgrade is also described in chapter 2 and in publication 7, as it is important tool used in publications 6 and 8-12.

In chapter 3 the different locations where impurity control may be imposed are considered, describing also the important transport mechanisms. Publication 5 presents knowledge about transport on open field lines and in the plasma edge, while publications 6 and 8-12 focus not only on the impurities, but on the full physics of the plasma edge, i.e. the pedestal. Finally, publications 4 and 5 provide insights on the core transport of tungsten.

In both chapters, i.e. chapters 2 and 3, it is indicated when the publications featured in chapter 5 are present knowledge or give extended information on a topic. In chapter 4 the publications featured in chapter 5 are again brought into the context of the bigger picture described in the previous chapters.



# Chapter 2

## Diagnostic of Impurities in Fusion Plasmas

For understanding and controlling the densities of plasma impurities good diagnostics are necessary. Thus, an introduction to several diagnostic principles is presented first, before the actual control of impurities is considered in chapter 3.

### 2.1 Spectroscopy

A standard method for diagnosing specific impurities inside of a plasma is measuring their characteristic line radiation, which allows for an unambiguous identification of ions of a specific element. Spectroscopy follows a big variety of strategies, which depend on the envisaged deliverable of the diagnostics, i.e. impurity density, influx or fluid velocity of the impurity. The individual application has implications on the wavelength region of interest and the choice of sight line geometry. In this section the applications of spectroscopy for visible light and UV to X-ray spectroscopy are explained and the focus is put on instrumentation and the interpretation of the measurements. We distinguish first between passive and active spectroscopy, while for the latter only charge exchange recombination spectroscopy is addressed.

#### 2.1.1 Passive Spectroscopy

Passive spectroscopy relies on simply collecting the photons that are emitted by the plasma along a line of sight (LOS). Therefore, it is intrinsically non-perturbative. As in the featured publications (cf. chapter 5) all passive spectroscopy is applied to investigations on tungsten (W), the focus in this section is put on W spectroscopy.

### Visible Spectroscopy allows for Influx Determination

Visible spectroscopy makes use of the wavelengths in the range of 400-700 nm. For this wavelength range a wide variety of optics and optical elements exists, which makes visible spectroscopy very flexible. A major advantage of this wavelength range is the existence of optical fibres, which can transmit the light virtually unattenuated for many tens of meters. Therefore, small optical heads may be mounted at hardly accessible locations, while the analysing spectrometer may be located in an easily accessible laboratory. Additionally, spectrometer camera systems can simultaneously analyze a few tens of independent channels, i.e. light from different optical fibres, at comparably low costs. In figure 2.1, an experimental setup from ASDEX Upgrade is presented, which indicates 37 individual lines of sight, provided by 6 independent optical heads. The red circles indicate where the

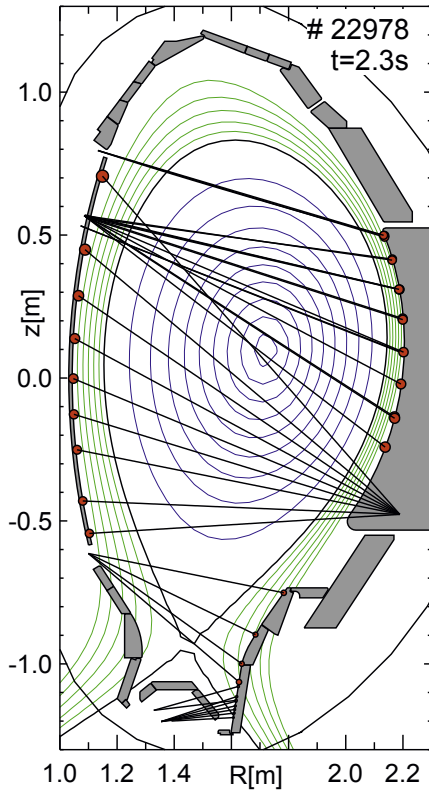


Figure 2.1: Setup for measuring the W-erosion from the first wall in ASDEX Upgrade. The light emission of the spectral line from neutral W is expected at the locations of the red circles. (adapted from [41])

lines of sight intersect the surface of the first wall. In these regions the emission of spectral lines of neutral W is expected. Typically, all spectral lines in the visible range are emitted in the plasma edge and their intensity gives quantitative information about the influx of the impurity. The reasoning behind this statement will be explained in the following

paragraph. Additionally, the emitted light is localized close to the erosion locations such that all erosion locations need to be monitored in order to get global information about the impurity influx. Fortunately, this can be accomplished due to the flexibility of visible spectroscopy.

For the interpretation of the light intensities the so-called S/XB-method (cf. to [42, 43]) is applied. The S/XB-method relies on the fact that the plasma that led to the erosion is also hot enough to immediately excite and ionize the eroded atoms, while recombination may be neglected. If the latter is the case, any ionization flux is equal to the influx of the impurity. As both, the ionization and excitation, happen very locally at the erosion location, the characteristic light of the lowly charged (or neutral) impurity ions/atoms indicates the erosion location and the intensity of the light is proportional to the influx. The latter becomes clear when considering the local emissivity  $\epsilon_{line}$  of a spectral line and the ionization rate density  $\mathcal{S}_{ion}$  (both for a low charge stage  $q = 0, 1, 2, \dots$  of W) given by:

$$\mathcal{S}_{ion,W^{q+}} = n_e n_{W^{q+}} S_{q,q+1} \quad (2.1)$$

$$\epsilon_{line} = n_e n_{W^{q+}} X_{line} B_{line} \quad (2.2)$$

where  $n_{W^{q+}}$  is the local charge stage density (which is usually not known),  $S_{q,q+1}$  is the ionization rate coefficient for ionization of  $W^{q+}$ ,  $X_{line}$  is the excitation rate coefficient into the upper state of the observed spectral transition and  $B_{line}$  is the connected branching ratio for the radiative decay of the observed spectral line. Thus, the ratio  $S_{q,q+1}/(X_{line} B_{line})$  (short S/XB) gives the local ratio of ionizations per photon. As an approximation this is often assumed to be a constant, because the excitation rate coefficient  $X_{line}$  has a similar  $T_e$ -dependence as  $S_{q,q+1}$ , however, for accurate considerations the  $T_e$ -dependence of the ratio S/XB ought to be taken into account. In the experiment, the local values  $\epsilon_{line}$  and  $\mathcal{S}_{ion,W^{q+}}$  are not available, as the spectroscopic measurements are an integral along a line of sight. The S/XB method is applicable if the line of sight is approximately perpendicular to the wall surface. If such a spatial integral is applied, the following expressions result

$$\Gamma_{W^{q+}} = \int_{LOS} n_e n_{W^{q+}} S_{q,q+1} dl \quad (2.3)$$

$$\Gamma_{line} = \int_{LOS} n_e n_{W^{q+}} X_{line} B_{line} dl \quad (2.4)$$

where (for a radial LOS)  $\Gamma_{W^{q+}}$  is the influx of  $W^{q+}$  and  $\Gamma_{line}$  the measured photon flux. Thus, a measurement of  $\Gamma_{line}$ , gives the impurity influx via

$$\Gamma_{W^{q+}} = \Gamma_{line} \frac{\int_{LOS} n_e n_{W^{q+}} S_{q,q+1} dl}{\int_{LOS} n_e n_{W^{q+}} X_{line} B_{line} dl} \quad (2.5)$$

Both the ionization and photon emission take place in a very limited radial region and the integrals may be replaced by the values at an effective radial position in the plasma such that

$$\Gamma_{W^{q+}} = \Gamma_{line} \frac{S_{q,q+1}(T_{e,eff})}{X_{line}(T_{e,eff})B_{line}} \quad (2.6)$$

where  $T_{e,eff}$  is an effective temperature roughly connected to the emission locations. This way the exact radial locations of ionization and emission do not need to be known, which is the obvious advantage of the S/XB-method. Nevertheless, the  $T_e$ -dependence ought to be known for high accuracy measurement. In figure 2.2, this dependence is depicted for the S/XB-value of a spectral line of neutral W at 400.9 nm. The data of many experiments is combined and a fit is applied.

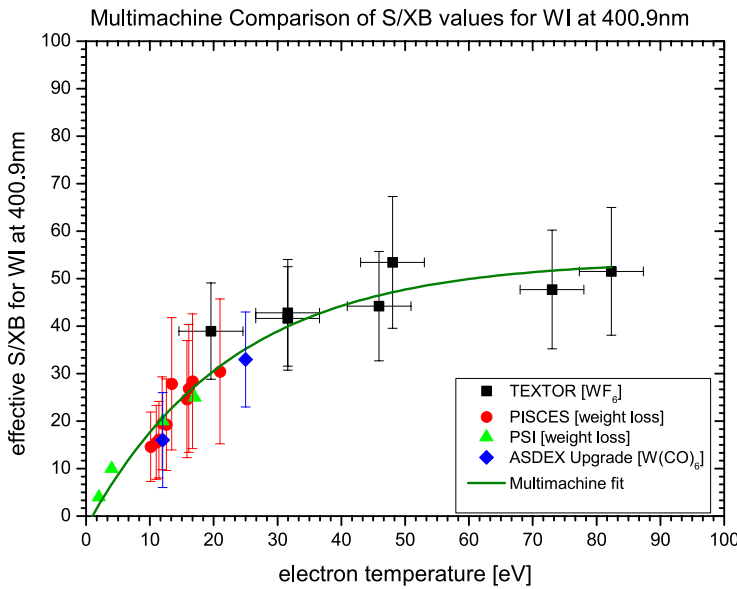


Figure 2.2: S/XB values for the spectral line of neutral W at 400.9nm. Data from different tokamaks and linear machines have been combined and a parametrization of the S/XB curve has been fit. (courtesy of S. Brezinsek (FZ Jülich))

### UV to X-ray Spectroscopy allows for Density Determination

In the wavelength region between 250-400 nm similar experimental setups than for visible wavelength can be applied, if for the optical elements quartz glass or mirrors are used, which both allow efficient transmission or reflection of light at these wavelengths. For shorter wavelengths a completely different scheme is required, because all materials and also air absorb the photons too efficiently. Thus, the spectrometers need to be attached to the vacuum of the plasma vessel. In figure 2.3, a spectrometer for the vacuum UV light and its setup at ASDEX Upgrade is depicted. A large hydraulic mechanism allows for

flexibility in the line of sight on which the spectrometer gathers photons. The depicted

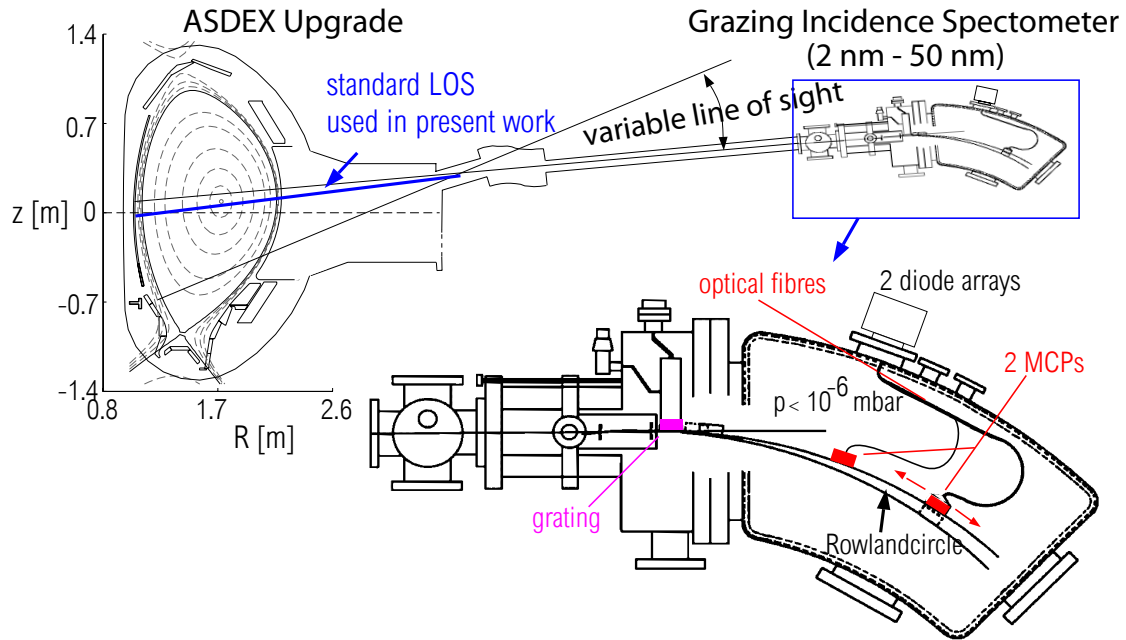


Figure 2.3: The grazing incidence spectrometer at ASDEX Upgrade is attached to the torus vacuum, while the line of sight is flexible. The zoom-in onto the spectrometer shows the grating and detector (micro channel plates, MCPs) positions along the Rowland circle. The MCPs create photo-electrons, multiply these and then accelerate them onto a phosphor producing visible photons by fluorescence. The photons are guided to the cameras via image guides. (adapted from [44])

spectrometer is using a grazing incidence geometry of the grating, i.e. very small angle of incidence. This small angle provides an enhanced reflectivity of the grating, which allows for the measurement of spectral lines down to about 2 nm, while for setups with angles larger than 20 degrees the reflectivity below 30 nm is drastically reduced and measurements below 10 nm are not possible. The photons are detected via the photo-electric effect, where microchannel plates are used to multiply the photo-electrons conserving their spatial distribution. These electrons are accelerated onto a fluorescent phosphor layer in order to produce visible light. This light is transmitted via image guides to a diode array outside the vacuum. The vacuum inside of the spectrometer needs to be better than  $10^{-6}$  mbar not only to avoid photoabsorption, but also because the microchannel plates could be damaged by arcing. As W emits hundreds of strong spectral lines at about 5 nm, the depicted spectrometer is a very sensitive tool for determining the W densities in the electron temperature range of about 1 to 1.8 keV. However, the spectrometer delivers only integrated information along a line of sight and it is necessary to apply models in

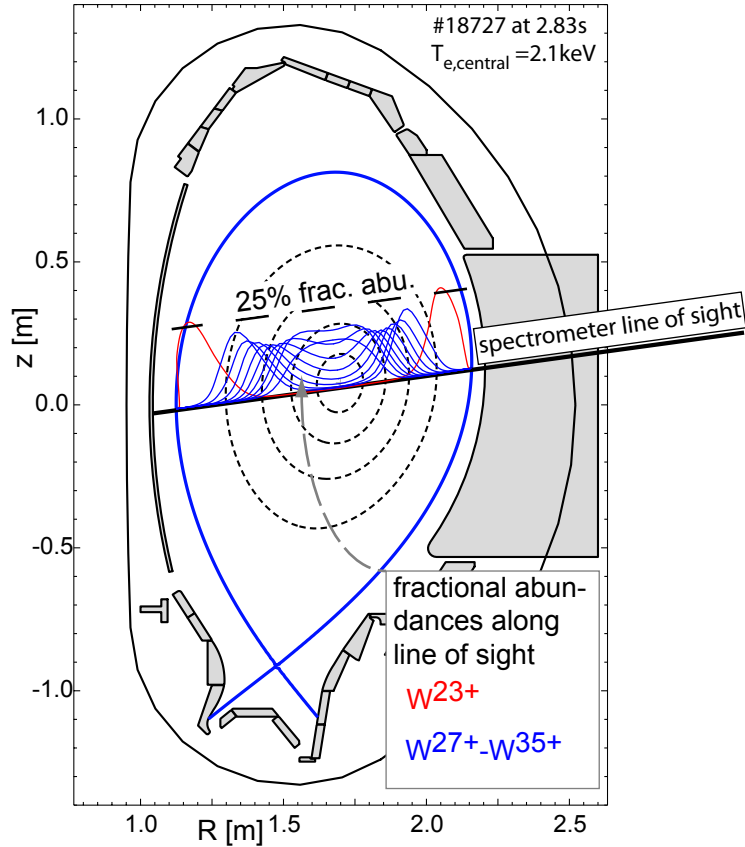


Figure 2.4: Along the line of sight of the spectrometer the fractional abundances of a few ionization charge stages of W are depicted for a central electron temperature  $T_{e,central}$  of 2.1 keV. The dashed line parallel to the line of sight indicates the 25 % level of the fractional abundance. The measured spectra contain a superposition of the emissions from all observed ionization stages. (adapted from publication 3)

order to obtain radial information. In figure 2.4 the fractional abundance of a few ionization stages of W are depicted along the line of sight of the spectrometer. The fractional abundance of a charge stage is its relative density fraction as compared to the density of all W-ions. The emissions that are used to quantify the W-density are emitted by the ionization stages  $W^{27+}$  to  $W^{35+}$ , while  $W^{23+}$  emits spectral lines that might also be of importance for understanding the spectrum of W at 5 nm. Details of this discussion are addressed in publication 1 and 3.

For determining the W-densities, the intensity  $I_W$  of the spectral line needs to be interpreted.  $I_W$  is the integral of the local emissivities along the line of sight (LOS), which is given by

$$I_W = \int_{LOS} n_e n_W f_q \mathcal{PEC}_{line} dl \quad (2.7)$$

where  $n_W$  is the W density and  $f_q$  the fractional abundance of the charge stage  $q$  emitting the spectral line of interest.  $\mathcal{PEC}_{line}$  denotes the so-called photon emissivity coefficient for the spectral line of interest and is equivalent to the previously introduced  $X_{line}B_{line}$  while taking non-zero density effects into account. The integral in equation 2.7 is strongly weighted at the locations where  $f_q$  is close to its maximum. In this small radial region  $n_W$  may be replaced by an effective  $n_W^-$  such that

$$I_W = n_W^- \int_{LOS} n_e f_q \mathcal{PEC}_{line} dl \quad (2.8)$$

$$n_W^- = \frac{\int_{LOS} n_e f_q \mathcal{PEC}_{line} dl}{I_W} \quad (2.9)$$

It may be noted that many spectra of W exhibit spectral features consisting of many unresolvable spectral lines from several ionization stages. These features are called quasicontinua. For interpretation, the intensity of the full spectral feature is determined by the measurement and instead of performing the line of sight integral for single spectral lines (equation 2.8) the integrals for all spectral lines contributing are added up.

### 2.1.2 Charge Exchange Recombination Spectroscopy

In order to obtain localized information about impurities charge exchange recombination spectroscopy (CXRS) (cf. to [45]) is applied at almost all fusion experiments. Usually, a neutral heating or diagnostic beam which is injected into the plasma is observed with an optics that features lines of sight intersecting the beam. The CX process and the emission of photons may be written as



Where D is the donor species (typically deuterium from a heating beam) and  $A^{+q}$  the receiver element A in charge stage  $+q$ . The electron bound to D is transferred during the CX collision onto  $A^{+q}$ . The transfer happens mostly into states with relatively high main quantum numbers and large angular momentum such that even for highly charged impurities visible transitions happen after the electron transfer with a time lag of typically nanoseconds corresponding to the life times of the excited levels. An advantage of this process is given by the fact that a considerable fraction of the emitted photons is emitted in the visible wavelength region, where many lines of sight are easily implemented. In figure 2.5 the lines of sight of several CXRS systems at ASDEX Upgrade are presented.

For W, the single spectral lines are not strong enough to be exploited for diagnostics purposes, due to the many simultaneously existing charge stages and the typically low W content. Still, in the publications 6 through 12 CXRS is an important tool for understanding the plasma transport, which is either directly or indirectly related to W transport.

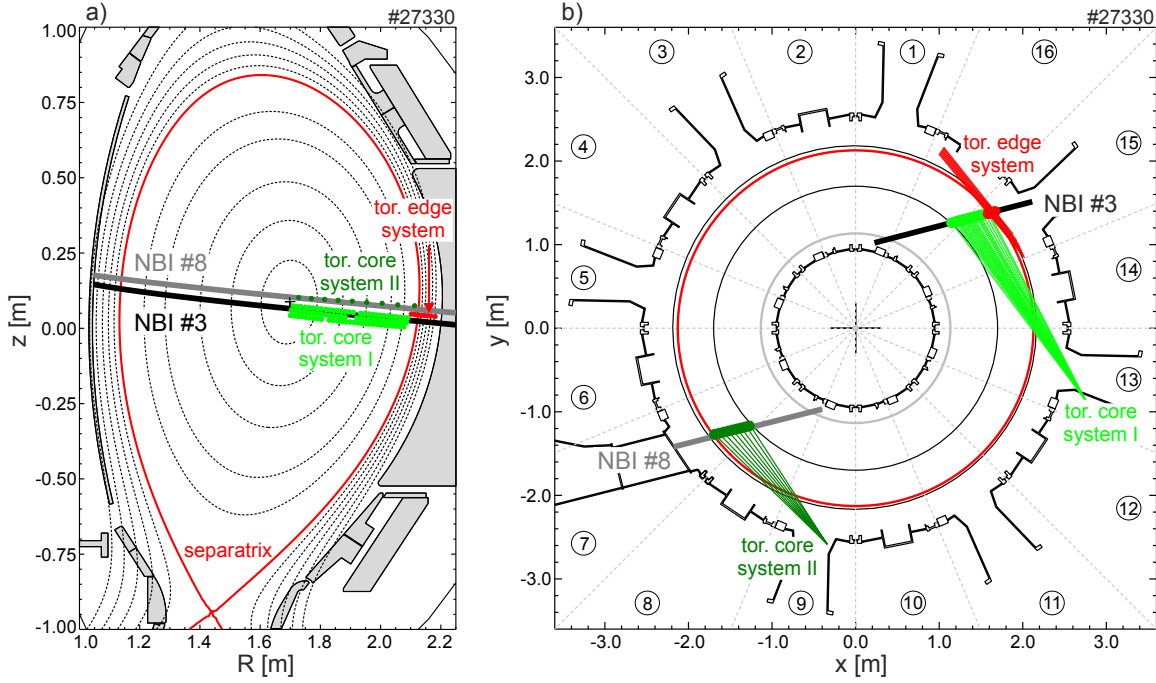


Figure 2.5: (a) The poloidal viewing geometry of the toroidal CXRS systems at ASDEX Upgrade. The CXRS signals originate from locations marked with the small dots, which indicate the intersection of line of sight and beams. (b) The top view of the same lines of sight and the involved beams. In reality the beam has a cross section diameter of about 20-25 cm and the lines of sight extend also beyond the beam. (adapted from publication 7)

In these publications the receiver is mostly a fully stripped low-Z impurity, such as  $C^{6+}$ , which emits CXRS photons as a recombined H-like ion, e.g.  $C^{5+}$  emitting a photon via the transition  $n=8$  to  $n=7$  at 529.059 nm. The spectral line delivers information about the impurity density via the line intensity, the impurity temperature via the Doppler broadening of the spectral line and plasma rotation via the Doppler shift of the spectral line. It should be noted that CXRS is a highly developed tool achieving high accuracies by applying corrections that are explained in more detail in publication 7. It may be noted that the donor may be a beam with energies in the range of 100 keV, but it may be also a localised gas puff. The latter is more flexible, however, a gas puff does not penetrate deeply into the plasma such that only the plasma edge may be investigated via CXRS at a gas puff. Such measurements are crucial for the investigations in publications 11 and 12.

## 2.2 Bolometry

When encountering W as a plasma impurity, a major concern for plasma operation is the radiation caused by W. Thus, a crucial diagnostics is bolometry measuring the total radiation power emitted by the plasma. A comprehensive measurement of the radiation power is obtained by absorbing all photons by a metal foil, e.g. gold or platinum, and determining the temperature change of the absorber. In order to sensitively measure the radiation power, the absorbers are thin foils, which allows for a time resolution in the order of 10 ms. Each foil delivers the radiated power flux on a line of sight. In order to perform a tomography of the radiation many lines of sight are needed.

In figure 2.6(a) a set of bolometer lines of sight from ASDEX Upgrade is presented. Figure 2.6(b) depicts an example for a tomographic reconstruction featuring a typical distribution of radiated power. The tomography using bolometer measurements is challenging because the radiation distribution is quite asymmetric as compared to the flux surfaces. The radiation distribution from the confined plasma, where plasma transport of electrons and impurities along field lines is very efficient, is typically aligned with the flux surfaces. Deviations from that symmetry, which do exist also in the plasma core, have large scales, such as the asymmetry induced by centrifugal forces ([46] and investigations in publication 5) or ion cyclotron heating (cf. to [47]). The radiation from the divertor and the plasma edge is breaking the flux surface alignment of radiation more drastically and additionally, it is a major fraction of the total radiated power. For W diagnostics the radiation in the main plasma is of highest interest. A focus on the main chamber may be accomplished by using only a specific subset of bolometer lines of sight, or by applying band pass filters cutting away the low energetic photons which originate from the plasma edge (cf. next section about soft X-ray cameras).

Nevertheless, the bolometers are an important tool to calibrate all other W-diagnostics via dedicated W injections into the plasma. The injections lead to a clear increase of signal in all W-diagnostics and bolometers. The radiation increase is easily interpreted in terms of a change in W-densities using the cooling factor of W, which has been calculated in publication 4 and was described already in section 1.5.2. Generally, the uncertainties of the cooling factor are considered smallest compared to those of other atomic data, because of averaging effects between different ion stages and for the excitation cross sections within ions. The high credibility of the atomic data is also the underlying reason why the bolometer measurements are considered the best standard for determining the absolute W density. Additionally, the absolute W density is often not directly of interest, as it is the radiative power which is influencing the operational stability and the burn curves of a reactor.

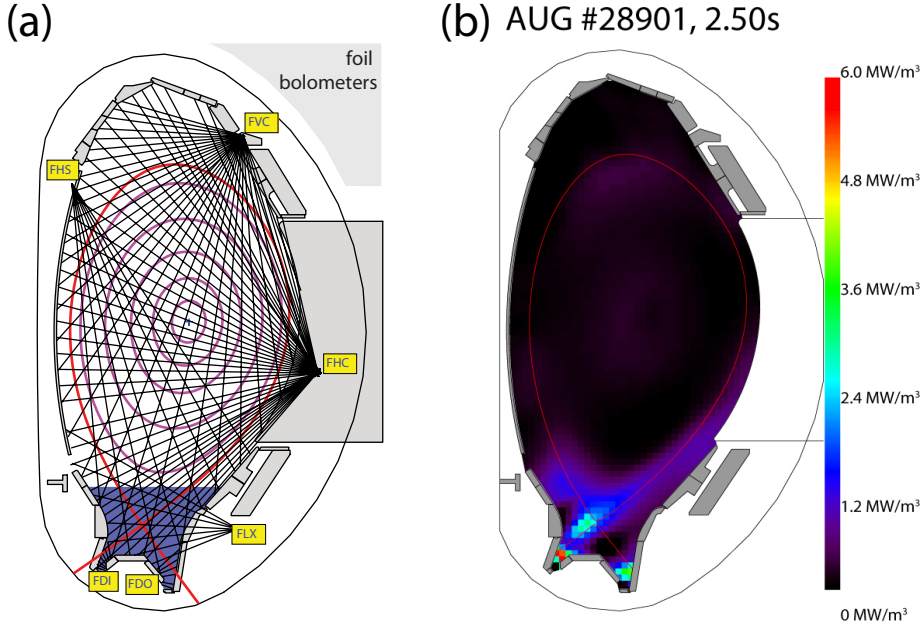


Figure 2.6: (a) Poloidal geometry of the sight lines of the foil bolometry system at ASDEX Upgrade consisting of six cameras. (b) An example tomography demonstrating the large divertor radiation density as compared to the radiation densities in the main chamber. (adapted from [48])

## 2.3 Soft X-ray Cameras

The soft X-ray cameras are pinhole cameras with diode detectors behind Be-filters, which allow only photons above a certain energy threshold to reach the diodes. The high energetic photons create electron-hole pairs within the diode, while for each pair  $E_{pair} \approx 3.62 \text{ eV}$  is required. Thus, the current in the diode  $I_{diode}$  relates to the photon energy  $P$  via

$$I_{diode} = \eta \frac{P}{E_{pair}} , \quad (2.11)$$

where  $\eta$  is the detection efficiency. For the soft X-ray cameras at ASDEX Upgrade a Be-thickness of  $75 \mu\text{m}$  is used which implies a detection threshold of about  $1.5 \text{ keV}$ . For the calculation of the sensitivity of the diode, the simplest approach is assuming that the full diode thickness acts as an absorber for photons and every photo-electron is collected by the read-out process. Thus, for high energetic photons the sensitivity decreases because not the full energy of the photon is deposited in the sensitive layer of the diode. In reality the diode is more complicated featuring passivation layers or metal contacts in front of the sensitive volume and additionally a few photo-electrons are lost due to diffusive processes in the barrier layer of the diode. A comparison of detection

efficiencies is presented in figure 2.7. For the more realistic diode the additional layers in front of the sensitive volume of the diode lead to a shift and an absorption edge in the low energy threshold (comparing black vs. blue curve in figure 2.7), while detection efficiencies for higher energies are changed due to the non-perfect collection of the photo-electrons. For comparison a detector efficiency for a Be filter with a thickness of 20  $\mu\text{m}$  is presented (dashed red curve), which demonstrates that the Be filter acts on the low energy threshold. The usage of a soft X-ray camera system for diagnostics has three advantages:

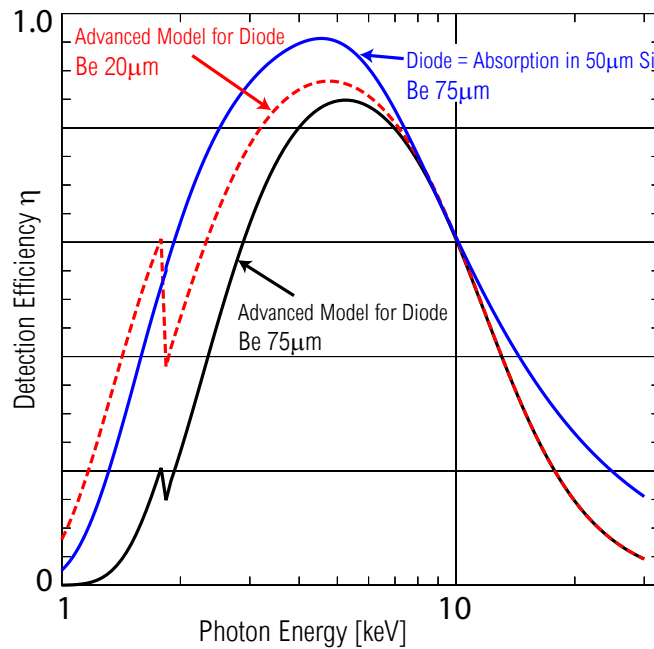


Figure 2.7: Detection efficiencies calculated with different Be-filter thicknesses and models for the diodes. The simplest model (blue curve) multiplies the absorption of a 50  $\mu\text{m}$  thick Si layer with the transmission curve of a Be-filter with 75  $\mu\text{m}$ . The advanced diode model [49] takes also passivation layers and charge diffusion in the diode into account and results for the same Be-filter thickness in the black curve. The red dashed curve is depicted to demonstrate the effect of a thinner Be-filer, i.e. 20  $\mu\text{m}$ .

- A The soft X-ray radiation is emitted from the core of the plasma and thus its interpretation requires only a model for the core of the plasma. Similarly to the spectroscopy in the UV to soft X-ray wavelength range the light emission is related closely to the impurity densities.
- B The geometry of the emissions are mostly flux surface aligned. Deviations from this alignment exist, e.g. by centrifugal forces on heavy impurities (cf. to [46] and investigations in publication 5). Still, the geometry is typically simpler than for

bolometric tomographies. Due to the simple setup a large number of lines of sight can be implemented also allowing for good spatial coverage.

C A high time resolution in the range of several MHz is possible allowing to study also fast phenomena such as magneto-hydrodynamic (MHD) effects such as MHD-modes or Alfvén waves.

For demonstration, figure 2.8(a) depicts the lines of sight of the soft X-ray cameras presently installed in ASDEX Upgrade and figure 2.8(b) shows an example tomography, which features a good alignment with the flux surfaces.

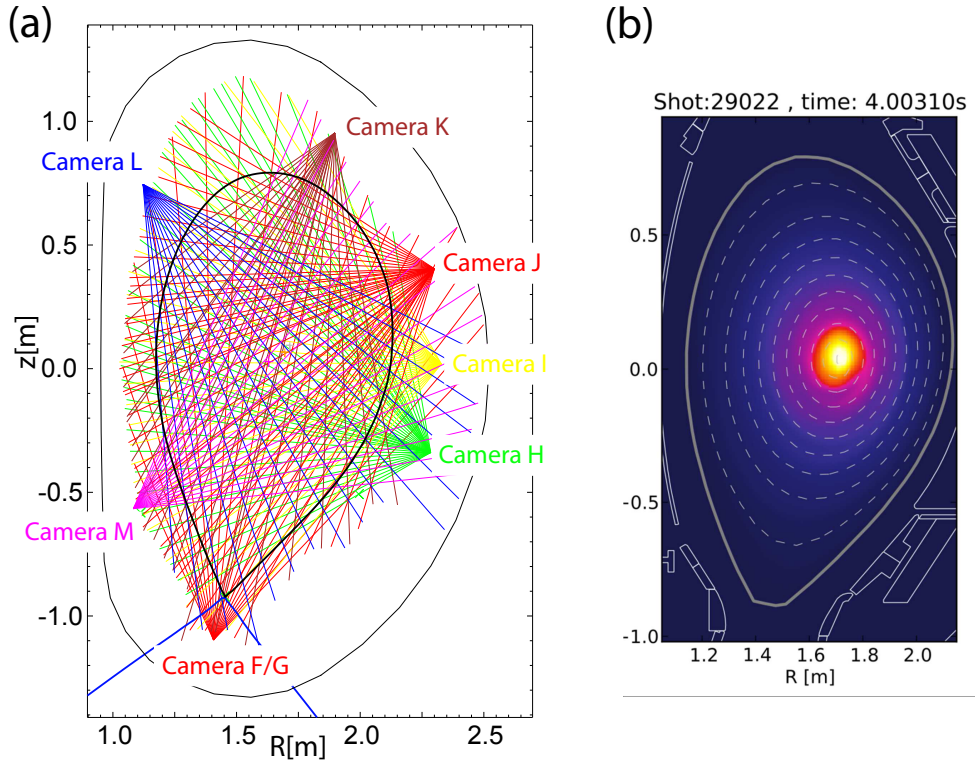


Figure 2.8: (a) Poloidal geometry of the lines of sight of the foil soft X-ray camera system at ASDEX Upgrade consisting of eight cameras. (b) An example tomography demonstrating the sensitivity of the diagnostics to the main chamber radiation, which is typically more symmetric than the total radiation. (courtesy of T. Odstrcil)

In publication 5 the soft X-ray cameras at JET have been used to quantify the W-content in the core plasma, which would not have been possible neither by spectroscopy nor by bolometry due to strong asymmetries on flux surfaces caused by centrifugal forces. The details of the analysis is explained in publication 5. It should be noted that due to the wavelength selective properties of the soft X-ray cameras, the demand on atomic data is much higher than for bolometry. This may also be the reason, why the atomic

data used for the JET soft X-ray cameras required some adhoc corrections in order to be consistent with the bolometers during dedicated W injections. These discrepancies are still subject of ongoing investigations.

## 2.4 Atomic Data for Tungsten Ions

### 2.4.1 What Types of Data are Needed?

#### Ionization Equilibrium

The temperatures in fusion plasmas lead to a large variety of charge stages of W and each ion has a very characteristic spectrum. Thus, a fundamental piece of information is the knowledge of which charge stage of W exists at which radial location. This is basically given by a balance of ionization and recombination processes that may compete with transport processes in the plasma transporting charge stages from cold to hot plasma regions and vice versa. This balance is described using the rate coefficients for ionization ( $S_q$ ) and recombination ( $\alpha_q$ ) of charge stage q. These rate coefficients may carry corrections due to finite density effects. The ionization equilibrium of W may be obtained by solving the following equation system while  $\frac{\partial n_q}{\partial t} = 0$  for all q,

$$\frac{\partial n_q}{\partial t} = -\nabla \Gamma_q + Q_q \quad (2.12)$$

where  $-\nabla \Gamma_q$  is the transport term and  $Q_q$  the source term of the charge stage density  $n_q$  including the ionization and recombination processes to and from neighbouring ionization stages. The source term connects the ion stage q to the neighboring ion stages q-1 and q+1 via ionization and recombination, as can be seen in equation 2.13.

$$\begin{aligned} Q_q = & - (n_e S_q + n_e \alpha_q) \cdot n_q \\ & + n_e S_{q-1} \cdot n_{q-1} \\ & + n_e \alpha_{q+1} \cdot n_{q+1} \end{aligned} \quad (2.13)$$

$$-\nabla \Gamma_q = \frac{1}{r} \frac{\partial}{\partial r} r \left( D_q \cdot \frac{\partial n_q}{\partial r} - v_q \cdot n_q \right) \quad (2.14)$$

Equation 2.14 details the transport term in equation 2.12 for the case that radial transport may be described in terms of diffusion (diffusion coefficient  $D_q$ ) and convection (drift velocity  $v_q$ ). These coefficients are subject to experimental investigations, e.g. Publication 4.

In the case of W the ionization and recombination coefficients predominately govern the so-called fractional abundance of each ionization stage  $q$ , i.e.  $n_q / \sum_{i=0}^Z n_i$ , because the

associated rates are much larger than the changes due to the transport fluxes. Thus, high importance is attributed to the determination of ionization and recombination rates. These have been investigated, benchmarked and corrected as reported in Publication 1. The comparison of the uncorrected data sets to the corrected data set is presented in figure 2.9. Three combinations of ionization and recombination rates are presented, i.e. 'ADPAK+ADPAK' corresponding to ionization and recombination rates from the average ion model [39] and improvements from [50], 'CADW+ADPAK' corresponding to ionization rates from a configuration averaged distorted wave calculation [51] and recombination rates from an average ion model and 'CADW+modif. ADPAK' corresponding to the same data as the 'CADW+ADPAK'-equilibrium instead of the recombination rates which have been modified as described in Publication 1.

Additionally, the atomic data describing the emission of radiation are of interest for each ionization stage in order to model spectra, integrals of spectral regions or the total radiated power. For the calculation of the total radiated power a very rough model might be sufficient, as one is not interested in the exact distribution of power in the spectrum. Thus, no detailed quantum mechanical treatment is necessary. Such an approach was pursued in the average ion model [39], the data of which was presented earlier for the discussions about the impact of impurities on the burn conditions of a fusion plasma. For calculating the spectra of each ion stage more effort is necessary and usually a three step process is applied, which is described in the following. For the results presented in publication 1 through publication 5 these steps have been performed using the Cowan code [52] and FAC [53], while for the last step models from ADAS [54] have been used or extended.

### STEP 1: Structure Calculation

The structure of the ions needs to be evaluated, which means that the wave functions of all levels are determined. In this context, a 'level' corresponds to the finest discrimination between wave functions taking the differences in angular momentum and radial distribution of the wave functions amplitudes into account. For the calculation of the unknown wave functions usually a scheme is used called multiconfiguration Hartree-Fock (MCHF) or - for a fully relativistic treatment - multiconfiguration Dirac-Hartree-Fock (MCDHF), which both model the unknown wave function by a linear combination of basis functions obtained by the multiplication of hydrogenic orbitals. These (because they are hydrogenic) wave functions are well-known. For details confer to [52]. Note, that the calculated structure exhibits as many levels as the number of levels in the basis and the accuracy and the properties of the structure depend strongly on the basis functions used. For example, if the structure for Cu-like W<sup>45+</sup> is calculated by using all levels contained in the configuration 1s<sup>2</sup>2s<sup>2</sup>2p<sup>6</sup>3s<sup>2</sup>3p<sup>6</sup>3d<sup>10</sup>4s<sup>1</sup> as a basis (which are actually just two levels, given

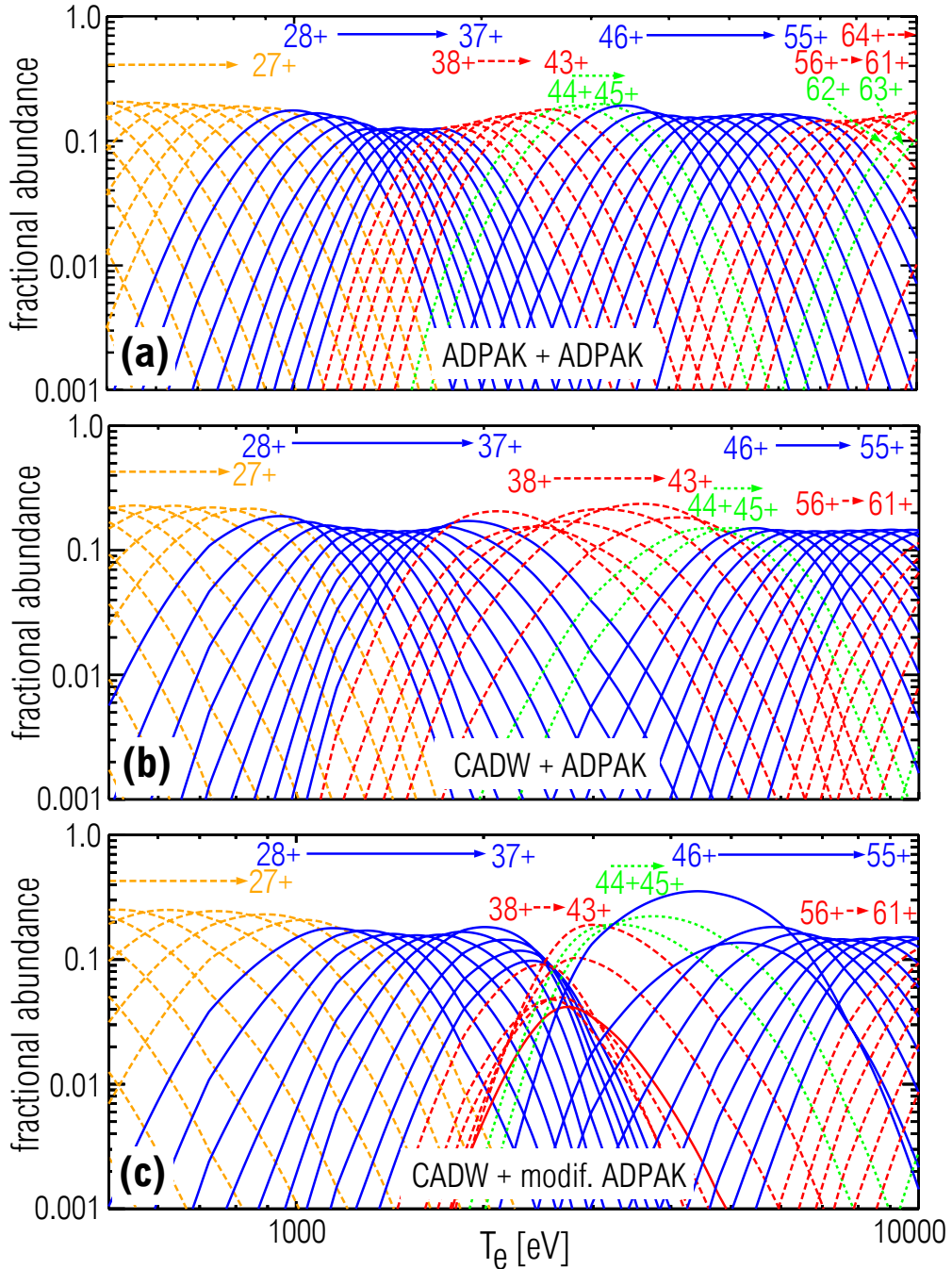


Figure 2.9: (a) Fractional abundances of tungsten ionization stages without transport for zero electron density using ionization and recombination data from [39], i.e. ‘ADPAK’, which were modified according to [50]. The numbers denote the ionization stage, while line styles and colors group ions with the same outermost subshell, e.g. ‘4d’. (b) Same as (a), but ionization rates taken from [51]; (c) Same as (b), while recombination rates have been modified (cf. Publication 1) according to experimental findings. (reprinted from Publication 1)

by the different spin of the electron) only two unknown wave functions will be described. This will not yield a good description of the spectrum, e.g. dipole transitions require a parity change of the involved wave functions. Clearly, a rather large basis is necessary to describe the structure of a W ion well. Note that for a complete description the basis must be infinitely large implying that always a choice has to be made when performing calculations on atomic structure.

Note that when evaluating the wave functions, it is rather the radial part that is evaluated, while the angular part of any wave function follows the same simple algebra known from the hydrogen atom. Often the angular part is described by coupling schemes (e.g. LS-coupling and jj-coupling) in order to better understand how the total angular momentum of a level is obtained. However, for a quantum mechanically correct description only the total angular momentum is of importance and correct, while coupling schemes are approximations that work only for certain subsets of ions and levels.

## STEP 2: Collision Cross-Sections for Electron Impact Excitation

In magnetically confined fusion plasmas the dominant excitation mechanism is usually electron impact excitation, which then leads to spontaneous emission of photons. Thus, in order to predict spectra of the impurity ions the calculation of electron collision cross-sections is necessary. This calculation is computationally challenging, because any two levels of the W ion may be linked via an electron collision, while the cross-section calculation needs to be performed at many energies in order to calculate rates in a thermal plasma. A pre-requisite for the cross-section calculation is the knowledge of the ion structure (cf. Step 1), i.e. the wave functions of each level. These wave functions are then combined with that of the colliding electron in order to quantify the excitation probabilities and thus, cross-sections. For the excitation process there are different approximations, three of which are presented below:

- **Plane-Wave Born** For the so-called plane-wave Born approximation the incoming and outgoing electron are described as plane waves. The difference in the wave vectors corresponds to a plane wave that is combined with the wave functions of each level in order to find the characteristics of the wave functions corresponding to excited levels. This procedure works well at high collision energies, where the wave function of the colliding electron is not strongly perturbed by the target ion. A shortcoming of the plane-wave Born approximation is that the colliding electron is always distinguishable from the bound electrons and thus spin changing transitions are not possible within this scheme. Still, for high-Z elements this shortcoming is less of a limitation as the quantum number ‘Spin’ of a single electron is not a well defined quantum number for highly charged ions.

- **Distorted Wave** For the distorted wave approximation the wave function of the colliding electron is perturbed by a ‘collision potential’ for which different choices exist. The perturbation is relevant at low collision energies, i.e. the excitation energy is comparable to the energy of the incoming projectile. Using the distorted wave approximation allows the cross-section calculations at low collision energies to be improved, while spin changing transitions are possible due to the interaction of the colliding electron with the scattering potential.
- **R-Matrix** For the R-matrix calculation, the space around the target ion is separated into an interaction zone and an outer zone, which can be seen as a matrix in which the interaction zone is embedded. While in the outer zone the colliding electrons behave like plane waves, the interaction zone is treated like a  $N+1$  electron system ( $N$  being the number of bound electrons). In this way resonances of the cross-sections, i.e. of the  $N+1$  electron system can be identified and targeted. This scheme was found to deliver the highest quality data at low collision energies, where resonances are of particular importance.

### STEP 3: Collisional-Radiative Modelling

For typical electron densities in the confined part of fusion plasmas, i.e.  $10^{19} - 2 \cdot 10^{20} \text{ m}^{-3}$ , the zero density approximation, assuming that all excitation is performed from the ground state, is not sufficient, as excited populations especially in metastable states may yield additional excitation channels. Thus, the application of a so-called collisional-radiative model is required, which considers the rate equations for each populated state - reminiscent to the rate equations considered for the ionization equilibrium (equation 2.12 and 2.14). The rate equation for an excited level  $k$  contains sinks due to collisions, i.e. de-excitation and excitation away from the considered level  $k$ , and due to spontaneous emission, described by the associated Einstein-coefficients  $A_{kj}$ , where  $j$  denotes states accessible via photon emission. The sources are given by collisional de-excitation and excitation into the level  $k$  and by cascades from higher levels, i.e. spontaneous emissions connecting to the level  $k$ . It may be noted that the mentioned processes are the absolute minimum for the collisional radiative modelling. Further processes like excitation due to inner-shell ionization or populations following radiative recombination may be added if necessary. However, the time scales of ionization and recombination are typically a few orders of magnitude slower than the time scales for excitation and spontaneous emission such that the rate equations for the populations of levels within each ion stage can be separated from the ionization equilibrium. Generally, the described rate equations within each ion stage give in equilibrium a linear equation system with the size of the number of levels. The population of all  $N$  levels of an ion stage with charge  $q$  may be described by

a population vector  $\vec{P}$  with size  $N$ . The vector  $\vec{P}$  contains the populations  $p_i$  of all levels  $N$  normalized by the total ion density such that  $\sum_{i=0}^N p_i = 1$ . Thus, in equilibrium

$$\mathbf{M}\vec{P} = \vec{P} \Rightarrow (\mathbf{M}-\mathbf{1})\vec{P} = \mathbf{0} \quad (2.15)$$

where the matrix  $\mathbf{M}$  describes the discussed sinks and sources connecting the various levels of the ion. Equation 2.15 can be easily solved for  $\vec{P}$ , which may be used to obtain the emission rates by multiplying the populations with Einstein coefficients.

### 2.4.2 Most Recent Developments and Limitations

Due to the continuous development in computing hardware more complex calculations become feasible year by year. However, the codes performing the calculations must be modernized in order to make use of the changing hardware. Still, W features ion stages with open 4f-shells, which provide tens of thousands of levels and nearly 100 million transitions that contribute to the observed spectra (cf. Publication 3). Additionally, the approaches to calculating the spectra of W ions should be increased in complexity, e.g. number of levels, and quality, e.g. R-matrix for all ion stages. It should also be noted that a consistent treatment of all ion stages would be of importance for a fusion plasma in order to understand the W-spectra as emitted from all locations in the plasma. For the featured publications, the Cowan code [52] was run via the infrastructure provided by the ADAS organization [54]. In detail, the structure (MCHF) and collision cross-sections (plane-wave Born) were calculated using the Cowan code and the CR-model was provided by ADAS. Additionally, the flexible atomic code (FAC, [53]) was run for the very complex ionization stage Sb-like  $W^{23+}$  producing vast amount of structure data (MCHF) and collision cross-sections (distorted wave), while the CR modelling was built along the lines of the ADAS CR-model allowing for a population vector of size larger than 10000. For Ni-like  $W^{46+}$  a comparison with data from an R-matrix calculation is presented in Publication 1.

# Chapter 3

## Control of High-Z Impurities in Fusion Plasmas

For controlling the high-Z impurity content of the plasma the mechanisms of wall erosion and impurity transport need to be understood. In this chapter these points are discussed and possible options of influencing the mechanisms are addressed. The focus is put mainly on W, however, most of the considerations are applicable to other high-Z elements.

### 3.1 Erosion of Tungsten

All W which radiates in the plasma originates from the wall, where it is eroded by physical sputtering. The amount of erosion may be estimated, by quantifying the incident particle fluxes and their energy distribution and then applying the sputtering yields as presented in figure 1.6. The energy distribution is often characterized by the electron temperature, because for high densities and low temperatures the ion temperature is coupled to the electron temperatures and the electron temperature governs the sheath potential that accelerates the positively charged ions onto the first wall. In the experiment the incident deuterium flux  $\Gamma_D$  can be either quantified by determining the recycling flux of deuterium via the S/XB method, or by Langmuir probe measurements which allow for determining the flux by measurement of the ion saturation current. The ratio of W-flux  $\Gamma_W$  and deuterium flux  $\Gamma_D$  or  $\Gamma_{sat}$  is called the effective sputtering yield. In figure 3.1 the measured effective sputtering yield (from several discharges at ASDEX Upgrade) is compared to several theoretical curves derived for a case of a pure deuterium flux and for cases with a deuterium flux containing an admixture of  $C^{4+}$ . The latter is used in the modelling as a placeholder for a low-Z impurity mix. This approximation is applied, because in the experiment it is unclear which impurities in which charge stage contribute locally at the erosion location. Independently of these assumptions figure 3.1 demonstrates that

without impurities the observed sputtering yield (symbols) is too large by several orders of magnitude. A realistic amount of low-Z impurities, i.e. of the order of a percent, brings

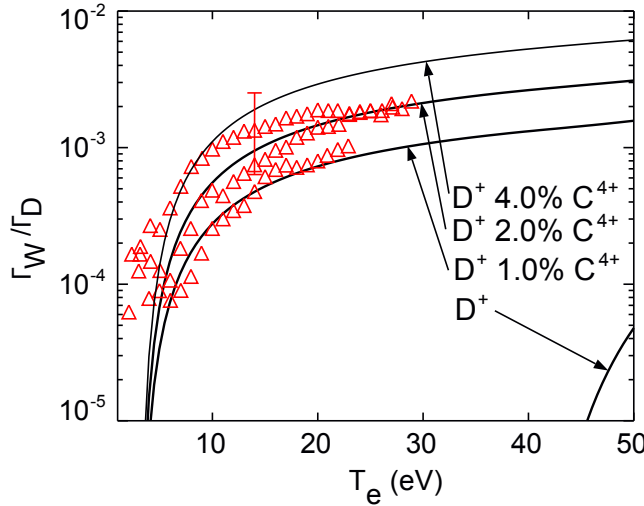


Figure 3.1: The symbols give the effective sputtering yields, i.e. the ratio of W-influx over incident ion flux as measured, for the phases in between edge localized modes in H-mode at ASDEX Upgrade. The solid lines give theoretical sputtering yields for an incident particle flux consisting of pure deuterium and deuterium with an admixture of  $C^{4+}$ , which is thought to emulate the effects of the impurity mix from experiment. (adapted from [41] )

the theoretical sputtering yield in agreement with the experimental data. This implies that low-Z impurities play a key role for the source of high-Z impurities.

Discharges with intentionally puffed nitrogen have been investigated with respect to the observed effective sputtering yields in the divertor of JET [55]. However, the nitrogen puff not only increases the nitrogen density, it also radiatively cools the edge plasma such that the electron temperature in the divertor drops. As a result, the size of the nitrogen puff decreases the electron temperature. This mechanism is documented in figure 3.2 (a), where for different nitrogen puff levels, the intensity of a spectral line emitted by  $N^{2+}$  is varied while also the electron temperature at the plasma wall contact in the divertor is affected. The four depicted nitrogen puff levels lead to a continuous increase of the nitrogen radiation and cooling of the divertor plasma. As a result, the observed effective sputtering yield of W behaves non-linear. For the investigated case, it first increases for increasing nitrogen puff, because the number of sputtering nitrogen ions increases, while the electron temperature decreases only from 25 eV to 20 eV. At higher nitrogen puff rates the effective sputtering yield of W decreases as the electron temperature strongly decreases. The effective sputtering yield of the nitrogen ions and

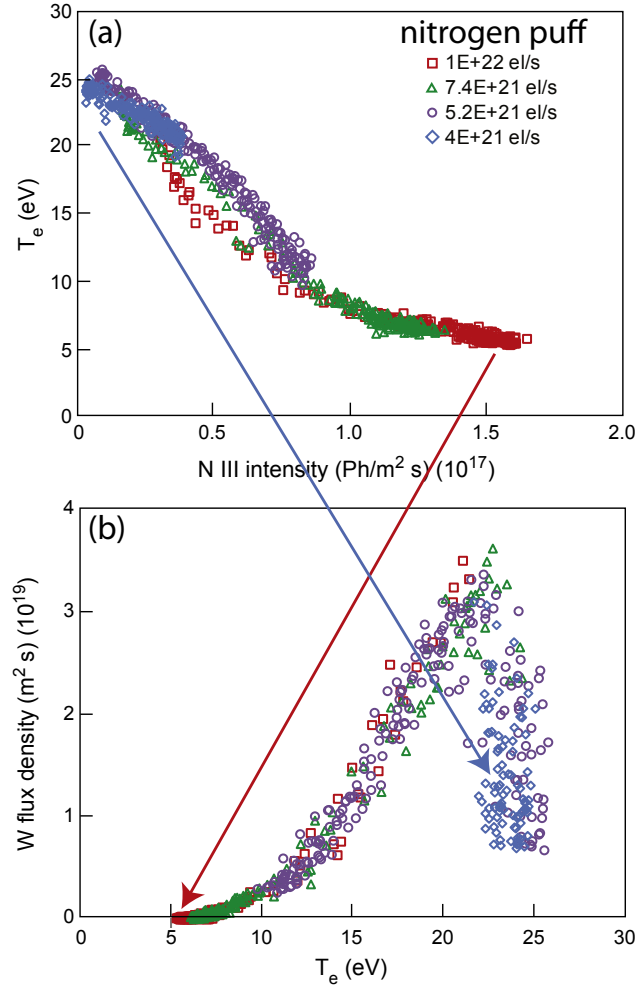


Figure 3.2: (a) The measured correlation between nitrogen radiation (NIII spectral line) and electron temperatures measured by Langmuir probes in the divertor shows a clear trend. The variation is obtained by applying four nitrogen puff levels in L-mode at JET. (b) For the nitrogen puff levels a strong variation of the effective sputtering yield of W is observed. More nitrogen at electron temperatures above 20 eV implies increased W-sputtering and a further increase of nitrogen leads to a cooling of the divertor which ultimately leads to a strong reduction of W-sputtering (adapted from [55] )

thus, the slowly increasing concentration of nitrogen is more than compensated by the decrease of electron temperature.

Thus, impurity seeding not only allows for controlling the power load onto the first wall, it also allows to reduce the total sputtering of W at regions with strong particle fluxes such as the divertor region. Note that the divertor temperature for a reactor has to be in the range of a few eV in order to limit the power flux density at the large particle fluxes. Thus, it is expected that for such conditions also W erosion will be strongly reduced.

## 3.2 Transport of Tungsten on Open Field Lines (Divertor, SOL)

The plasma region in front of the wall is a transition region between the hot confined plasma and a cold plasma contacting the wall, which leads to the erosion of the wall material. The magnetic field lines intersect the wall and particles traveling along field lines are lost to the wall via parallel transport. As this mechanism basically removes the plasma from these flux surfaces, this region is called scrape-off layer (SOL). Due to the fact that finite perpendicular transport is refilling the SOL, there is still plasma, however the power fall off length is of the order of millimeters. For the divertor configuration the field lines close to the separatrix intersect the wall in the divertor such that most of the plasma wall interaction takes place there. At the same time the plasma can reach other areas through perpendicular transport. Vice versa the impurities eroded at the wall may travel towards the confined plasma region via a combination of parallel and perpendicular transport. A schematic illustrating the pathways of eroded W ions in the divertor of JET is presented in figure 3.3. In particular the question is how far and how efficient the eroded W ions travel along the field lines and how efficient radial transport at various poloidal positions brings W to the confined plasma. The efficiency of the latter process determines the flux surface averaged impurity density at the boundary of the confined plasma, i.e. the separatrix, which directly influences the total impurity content in the volume of the confined plasma. However, the transport from the erosion location to the separatrix is difficult to predict or to model, because the plasma flows, the particle recycling patterns and relative importance of perpendicular to parallel transport on the field lines of the SOL remains subject to large uncertainties such that no trustworthy prediction is possible. Note that for JET the divertor W sources are of high interest due to the lack of other W plasma facing components, while for ASDEX Upgrade the impurity sources in the main chamber dominate the W content of the main plasma. This is true even though the W source in the ASDEX Upgrade divertor is larger than that of the main chamber [41, 37], however, the eroded W ions are well retained in the divertor. The modelling uncertainties lead to a stronger emphasis on experimental approaches that simply relate the impurity content of the plasma to the erosion fluxes [57, 17, 58, 59]. This procedure is pursued in publication 5. It provides an effective impurity confinement time integrating over several effects such as the plasma edge transport located already inside the separatrix, the transport within the scrape-off layer but also the so-called prompt deposition of eroded particles. Prompt redeposition can take place when an eroded W particle is ionized soon after the erosion. Due to the magnetic field this leads to a gyration movement which might direct the particle back to the wall (cf. figure 3.4). In detail, the ionization length of particles is characterized by a typical ionization length  $\lambda_{ion}$  and for the

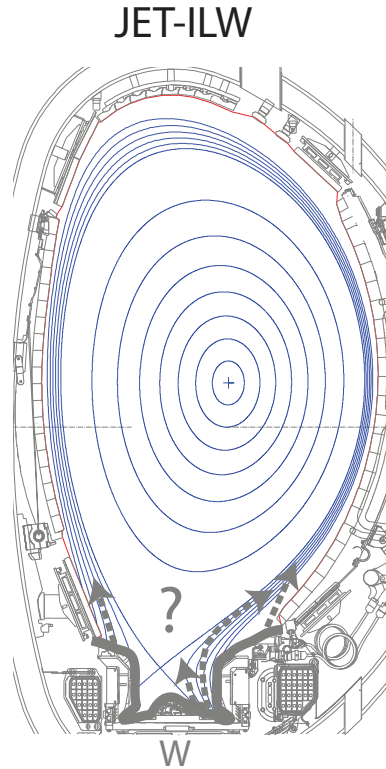


Figure 3.3: Schematic illustrating possible pathways of eroded W from the erosion location to the confined plasma. The details of the transport within the divertor and the scrape off-layer are difficult to model and thus, the exact transport is often ambiguous.

gyration the Larmor radius  $r_{L,W} = \frac{m_W v_\perp}{eB}$  is of importance, where  $m_W$  is the mass of a W ion,  $v_\perp$  its perpendicular velocity,  $e$  its charge and  $B$  the magnetic field strength. If  $\lambda_{ion}$  is comparable or even smaller than  $r_{L,W}$  prompt redeposition is reducing the flux of eroded particles considerably. This is the case for all high-Z elements, because due to their large mass  $r_{L,Z}$  is larger than for low-Z elements, while their loosely bound electrons and low thermal velocities lead to a relatively short  $\lambda_{ion}$ . As a result, the fraction of eroded W ions undergoing prompt redeposition may be close to 100 % in a high density divertor of ITER or a reactor [60, 56]. The latter publications address the problem in much more detail than outlined above, because the geometrical details of the wall surface versus magnetic field line and the velocity distribution of the eroded W are of high importance for the quantification of the prompt redeposition. Additional effects considered are the effects of the plasma sheath and multiple ionization of W.

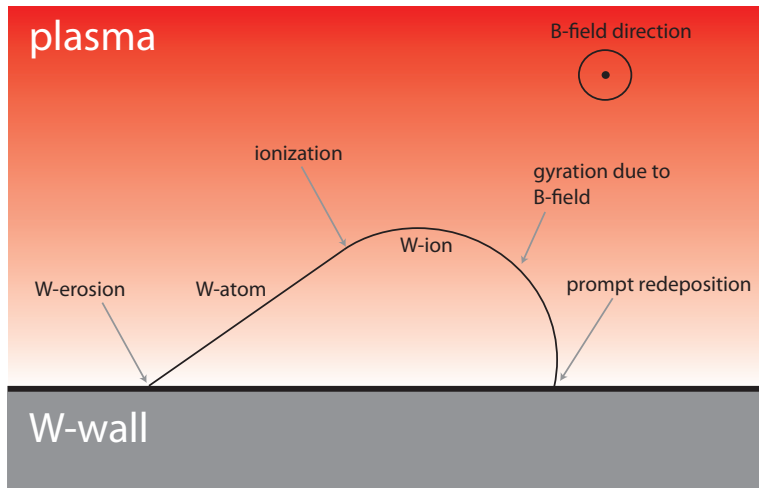


Figure 3.4: The schematic of the prompt redeposition showing the impact of a large Larmor radius versus the ionization length of a neutral W-atom eroded at the wall. For a quantification of the prompt redeposition the velocity distribution of the eroded W-atoms and the exact geometry of the surface versus the magnetic field are important. Note that at high plasma densities the fraction of W-atoms undergoing prompt redeposition is close to 100 % [56].

### 3.3 Transport Processes in the Confined Plasma

#### 3.3.1 Collisional Transport

Collisional transport is the combined effect of classical and neoclassical transport, both is described below. Neoclassical theory actually provides more insights than just transport, it can also be used to investigate the properties of the plasma edge including the poloidal rotation of main ions and impurities, which is closely connected to the radial electric field. The latter are crucial parameters for the plasma edge physics, which is also determining impurity transport, and are investigated by comparison to neoclassical predictions in publications 8-12.

##### Classical Transport

The most obvious mechanism of transport is given by binary collisions between plasma particles. These collisions are able to change the center of the gyration motion, while typical displacements are of the size of the Larmor radius. This type of collisional transport is also called classical transport. It is described here in more detail, because the basic parameter dependencies, which are also found for neoclassical transport, can be simply explained for classical transport. Collisional transport on closed flux surfaces (i.e. classical

and neoclassical transport) and its interplay with other type of transport is of importance when considering impurity control mechanisms, especially at the plasma edge (outer 5% of the radius) and in the plasma core (inner 10% of the radius), as is explained in the following sections and publications 4 and 6. The transport resulting from many binary collisions may be described as a Random-Walk phenomenon, i.e. diffusive transport, in which the typical step size ( $\Delta x$ ) of a particle is described by the Larmor radius  $r_L$  and the time between two steps ( $\Delta t$ ) by the inverse of the collision frequency  $\nu$  which represents the effective frequency until a particle is deflected by an angle of  $90^\circ$ . Thus, the diffusion coefficient may be estimated as  $D = \frac{1}{2} \frac{\Delta x^2}{\Delta t} = \frac{1}{2} r_L^2 \nu$ . Note that if two particles of the same species collide, no particle transport is caused by a Coulomb collision, because the particles are just exchanged. However, energy transfer is possible and thus a heat flux may be associated with the collisions within a species. For particle transport, the collisions between species are important and thus,  $\nu$  has to be chosen for the appropriate collision partners. Note that the diffusive transport in a pure hydrogen plasma is ambipolar. For a constant temperature this is easily seen, because

$$D_e = r_{L,e}^2 \nu_{e,i} = \left( r_{L,i} \sqrt{\frac{m_e}{m_i}} \right)^2 \nu_{i,e} \frac{m_i}{m_e} = D_i \quad . \quad (3.1)$$

When introducing impurities, the friction effects between all species need to be taken into account. Typically, the collisions between impurities and ions dominate the impurity transport due to the largest collision frequency. The collisions also cause directed transport, i.e. convection. This can be understood by considering particle drifts caused by any force  $\vec{F}$ . Generally, a drift velocity

$$\vec{v}_D = \frac{\vec{F} \times \vec{B}}{qeB^2} \quad (3.2)$$

results as can be derived by using the guiding center Ansatz (e.g. [1]). In figure 3.5, a schematic is shown that explains the origin of the convective transport in a pure hydrogen plasma. Electrons and ions gyrate in opposite directions. The diamagnetic drift, i.e.

$$v_{dia} = \frac{\frac{\partial p_{e,i}}{\partial r}}{qen_{e,i}B} \quad (3.3)$$

where  $q$  is the charge stage and  $e$  the elementary charge, is the drift velocity resulting from the force on particles due to a pressure gradient  $\frac{\partial p_{e,i}}{\partial r}$ . This is applicable for each species and causes at a specific location a net velocity of electrons and ions depicted as green and blue arrows in figure 3.5. Obviously there is a friction force on the ion species and electron species which is directed oppositely having the same magnitude. This friction force is perpendicular to the magnetic field lines as is the diamagnetic drift. As a result the particle fluxes  $\Gamma_e = \Gamma_i$ , i.e. they are ambipolar. When introducing impurities

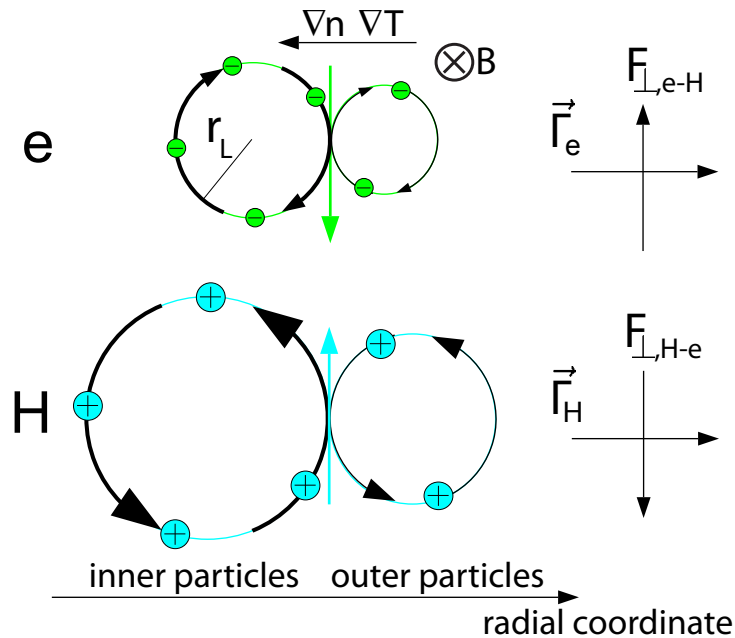


Figure 3.5: Schematic illustrating the diamagnetic velocities of electrons and hydrogen ions. The difference in velocities leads to friction and consequently to radial transport into the same radial direction. (adapted from [1])

the friction between ions and impurities is much larger than between impurities and electrons. For impurities the diamagnetic velocity is directed into the same direction than the diamagnetic velocity of the hydrogen ions, however, due to the charge dependence of  $v_{dia}$  there exists a velocity difference between ions and impurities. This causes a friction force, which is strongly enhanced by the charge of the impurities. In figure 3.6, a schematic of the described situation is depicted. Due to the fact that hydrogen and impurities carry a charge with the same sign, the opposite direction of the friction force translates into a inward convection of impurities and an outward convection of hydrogen.

However, if a radial gradient in temperature exists, the friction force is not strictly proportional to the differences of  $v_{dia}$  due to the  $1/v^2$  decrease of friction at larger relative velocities  $v$ . In the fluid treatment, an extra term  $\propto \nabla T$  related to the  $v$ -dependence of Coulomb friction appears when fully considering the first order changes of the velocity distribution function (cf. to [61]). This term ultimately causes an outward flux of impurities.

A calculation based on a fluid treatment (e.g. [61]) results in a total flux  $\vec{\Gamma}_q$

$$\vec{\Gamma}_q = \frac{r_{L,q}^2 \nu_{q,H}}{2} \left( -\nabla n_q + n_q q \left( \frac{\nabla n}{n} - \frac{1}{2} \frac{\nabla T}{T} \right) \right) \quad (3.4)$$

for a highly charged impurity with charge  $q$  including diffusive and convective components. Note that for this result a simplification has been introduced setting the coefficient in front

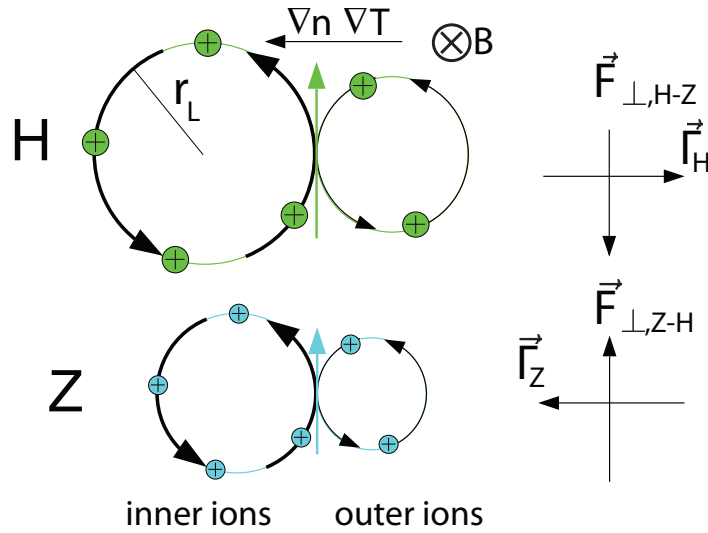


Figure 3.6: Schematic illustrating the diamagnetic velocities of hydrogen ions and impurity ions of an element Z. The difference in velocities leads to friction and consequently to radial transport into opposite directions for hydrogen and impurities. (adapted from [1])

of the normalized temperature gradient to  $\frac{1}{2}$ , which is again generalized below.

### Neoclassical Transport

Classical transport only relies on the gyro motion of particles and is thus applicable to any magnetized plasma. However, when magnetic field lines are bent, e.g. to a torus, an additional effect occurs due to  $\nabla B$ -drifts which also results in a coupling of perpendicular and parallel dynamics. This leads to an increased transport level as compared to classical transport, while the considerations are still based on binary collisions.

Large excursions from flux surfaces are possible for particles with small parallel momentum. When such a particle travels along field lines from the outboard side of a flux surface, i.e. the low (magnetic) field side (LFS), to the inboard side of a flux surface, i.e. the high field side (HFS), the Larmor radius decreases and in order to preserve the magnetic moment of the gyro-motion, which is an adiabatic invariant, the perpendicular velocity ( $v_{\perp}$ ) increases. Due to energy conservation the parallel velocity  $v_{\parallel}$  is decreased. For particles with  $\left.\frac{v_{\parallel}}{v_{\perp}}\right|_{LFS} < \sqrt{\frac{B_{max}}{B_{min}} - 1}$ , where  $B_{max}$  is the maximum magnetic field strength on a flux surface and  $B_{min}$  the minimum, the particle's parallel velocity is reversed and thus it returns along the field side. Actually, it travels not exactly on the same path, because the particle constantly is subject to the  $\nabla B$ -drift (cf. to figure 3.7). A particle which is reflected once, e.g. above the midplane, will also fulfill the reflection condition on the other side of the orbit, e.g. below the midplane, leading to a cyclic particle orbit, such that the particle may be considered trapped. As the poloidal projection of this orbit resembles

the shape of a banana, the orbits are called banana orbits. Such an orbit and its poloidal projection is depicted in figure 3.7. These orbits considerably increase particle and heat

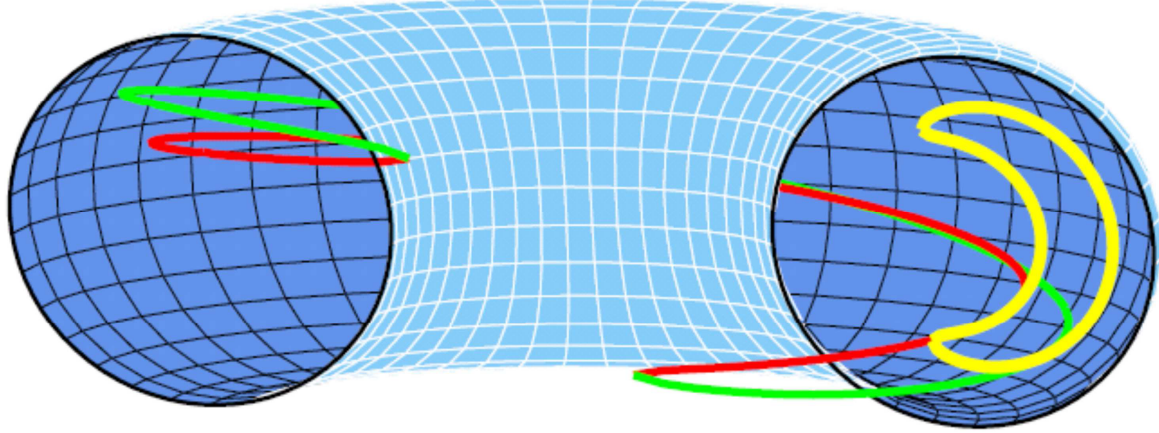


Figure 3.7: Illustration of a 3D banana orbit (green and red) and its poloidal projection (yellow). (adapted from [62])

transport as via collisions any particle may be brought on a banana orbit and particles on banana orbits may be de-trapped. The particles are thus potentially transported in radial direction by up to a banana width. An estimation of the diffusion coefficient due to banana transport, is determined by the banana width the effective collision frequency of trapping and de-trapping and the relative importance of banana orbits with respect to free particles. The resulting diffusion coefficient is for a circular plasma approximated by

$$D_{banana} = r_L^2 \nu \frac{q_{saf}^2}{\epsilon^{\frac{3}{2}}} = \frac{q_{saf}^2}{\epsilon^{\frac{3}{2}}} D_{classic} , \quad (3.5)$$

where  $\epsilon = r/R$  is the inverse aspect ratio of the considered flux surface and  $q_{saf}$  the so-called safety factor. The latter denotes, when following a field line, the number of toroidal turns for one poloidal turn.  $q_{saf}$  is a constant for each flux surface. As  $q_{saf}$  is typically between 1 and 5 and  $\epsilon$  smaller than about 1/3, the diffusion coefficient  $D_{banana}$  is much larger than the diffusion coefficient for classical transport  $D_{classic}$ .

However, for plasma species that are subject to many collisions the full banana width never applies. Such species may be highly charged impurities: Even in a fusion plasma close to the plasma core the W ions do not complete a full banana without collisions that would de-trap them. For most of the plasmas investigated today W ions are in the so-called Pfirsch-Schlüter regime, i.e. where collisions between W and deuterium happen often before the particles can complete their drift motion as given by a collisionless trajectory. Thus, for the ions it is unimportant whether they travel on a banana orbit or on a free orbit. In figure 3.8 both types of drift orbits are depicted demonstrating that at the LFS

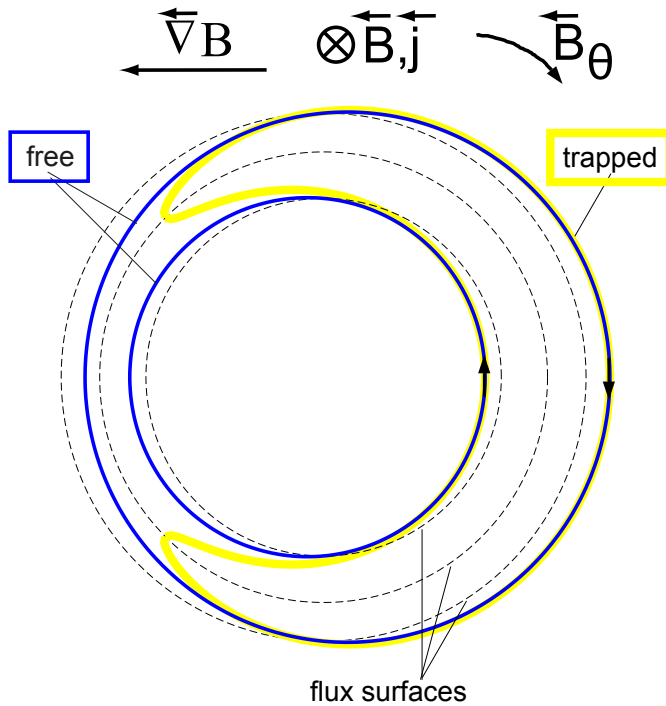


Figure 3.8: Poloidal projections of free drift orbits and trapped orbits of banana particles. (adapted from [62])

a free and a trapped orbit look very similar. Due to the particle drift and the frequent collisions a particle flux between flux surfaces is driven. If radial pressure gradients exist, poloidal asymmetries are obtained due to the drifts. These asymmetries drive transport parallel to magnetic field lines. Thus, this parallel dynamics becomes important due to the drifts. For the diffusion coefficient the importance of the parallel flows is reflected by the appearance of  $q_{saf}$  in the following equation describing the diffusion coefficient for the strongly collisional case

$$D_{PS} = 2q_{saf}^2 r_L^2 \nu = 2q_{saf}^2 D_{classic} . \quad (3.6)$$

The collisionality regime between the low collisionality regime, i.e. the banana regime, and the high collisionality regime, i.e. the Pfirsch-Schlüter regime, is called the plateau regime. It is called such, because here the sum of the  $D_{banana}$  and  $D_{PS}$  weighted with their relative importance is approximately constant forming a plateau in the respective plot of  $D$  versus  $\nu$ .

The effects of neoclassical transport may also be considered in a fluid picture, which then again brings up the importance of diamagnetic flows that drive parallel flows in order to comply with the continuity equation. Similarly to classical transport also convection may be treated by this scheme. Again the diamagnetic drift and the related friction between particles enter into the resulting drift velocity, such that it has a very similar structure

to that of the classical transport. By summing over all contributions due to Coulomb collisions, a general form of the radial impurity flux is obtained.

$$\vec{\Gamma}_q = \sum_{x=classic,banana,PS} D_x \left( -\nabla n_q + n_q q \left[ \frac{\nabla n}{n} - H_x \frac{\nabla T}{T} \right] \right) = -D_{neo} \nabla n_q + v_{neo} n_q \quad (3.7)$$

In all transport regimes, including classical transport, the convection is proportional to the charge of the impurity. The convection term consists of a term into the direction of the density gradient and a term that may point opposite depending on the parameter  $H_x$ , which is determined by plasma parameters, geometry, and the mass ratio between collision partners. As typically the temperature gradient points into the same direction as the density gradient and the parameters  $H_x$  are positive, the effect of temperature screening is also observed for neoclassical transport. The convective part is proportional to the charge of the considered impurity, such that effects due to the neoclassical drifts are strongly enhanced for highly charged species such as W.

Note that in a realistic plasma more than one impurity species is present such that the friction equilibrium between all species is important for the transport fluxes of each species. For the neoclassical transport coefficients evaluated in the featured publications these effects have been taken into account by the usage of NEOART [63, 64, 65], which is a numerical code evaluating the frictional effects between an arbitrary number of impurity species. The underlying physics can be reviewed in [66, 67].

### 3.3.2 Mixing of Collisional and Anomalous Transport

For a major part of the tokamak plasmas the transport is dominated by turbulent transport, but also influences of other transport effects such as MHD modes are observed. All these additional mechanisms are collectively called 'anomalous' transport and the related diffusion coefficient and drift velocity are denoted with  $D_{an}$  and  $v_{an}$ , respectively. The collisional transport is always present and thus features a base level for transport in cases for which the anomalous transport is negligible. Indeed the transport coefficients are thought to linearly add on top of each other such that an impurity flux of the charge stage  $q$  may be described by:

$$\vec{\Gamma}_q = -(D_{neo,q} + D_{an,q}) \nabla n_q + (v_{neo,q} + v_{an,q}) n_q = -D_q \nabla n_q + v_q n_q \quad (3.8)$$

In situations where turbulent transport is important, typically  $D_{neo} \ll D_{an}$  such that neoclassical diffusion may be neglected. Therefore, only for situations when the turbulent transport is suppressed (confer to subsequent sections) or small, neoclassical diffusion becomes important. For cases, where  $D_{an}/v_{neo}$  is large versus the system dimensions neoclassical convection may be neglected, however, this is not generally the case.

For high-Z elements, neoclassical convection is enhanced due to the charge dependence such that the neoclassical transport effects are sometimes visible even though turbulent transport is present. In most recent studies [68, 69], another enhancement of neoclassical transport is identified when plasma rotation causes asymmetries of impurities on a flux surface. The centrifugal force leads to a redistribution of plasma particles along field lines such that heavy particles gather on the outboard side of a flux surface. Therefore, for strongly rotating plasmas the neoclassical transport is identified to be a major player even though turbulent transport is present.

In any case, if neoclassical transport is important the density gradients of high-Z elements tend to become large due to the  $q$ -dependence of transport leading to strongly peaked density profiles of high-Z elements. The latter is easily derived from the transport coefficients: For the equilibrium situation where  $\Gamma_q = 0$  the following relation holds (cf. equation 2.14).

$$\frac{\partial n_q / \partial r}{n_q} = v_q / D_q \quad (3.9)$$

$$\ln(n_q(r_1)) - \ln(n_q(r_0)) = \int_{r_0}^{r_1} v_q / D_q dr \quad (3.10)$$

$$\frac{n_q(r_1)}{n_q(r_0)} = \exp \left[ \int_{r_0}^{r_1} v_q / D_q dr \right] \quad (3.11)$$

In equation 3.9 the relation between the normalized density gradient of a charge stage and the ratio of the respective drift velocity over diffusion coefficient is presented. Equation 3.11 results after integration of this relation between the two radii  $r_1$  and  $r_0$ . It equation enables the investigation of impurity density peaking factors, i.e. the impurity density ratios at two radii. This is especially useful, because typically the measurement of the gradients yields large uncertainties, while the density ratios at two separated radii may be measured with high accuracy. Equation 3.11 is ideal for such a situation, as it translates the detailed  $v$  and  $D$  profiles from modelling into a peaking factor which can be well measured in the experiment.

## 3.4 Plasma Edge and Pedestal

The plasma edge and pedestal (i.e. an edge region with steep gradients) comprises the first few cm inside of the separatrix. As it is explained below, reduced anomalous transport is often observed at the plasma edge such that also steep impurity gradients are possible. Ultimately, the impurity content in the plasma core is influenced by the transport at various locations and figure 3.9 exemplifies how the edge transport may influence the core

W content. The impurity transport at the edge may only be predicted if the physics of

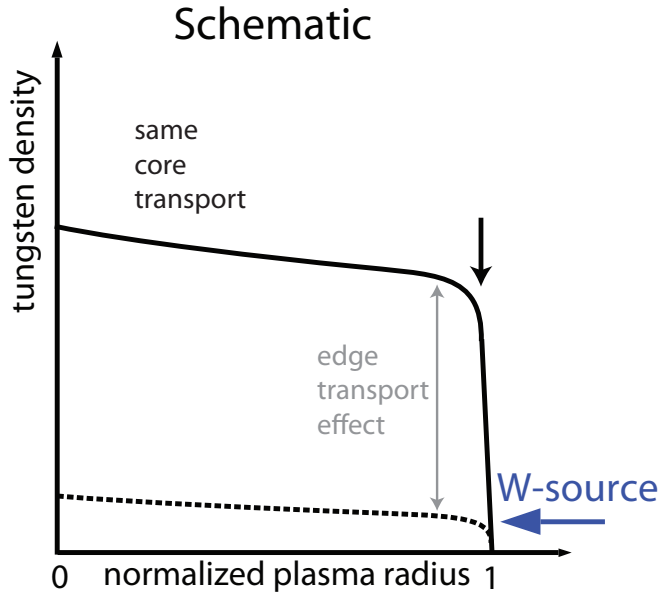


Figure 3.9: Schematic exemplifying the effect of different impurity transport at the plasma edge and its influence on the core density of W.

the background plasma in this region is understood. Thus, a considerable part of this chapter and of the publications listed in chapter 5 concern the physics of the plasma edge.

### 3.4.1 H-mode Regime

The H-mode regime ('H' for 'high confinement') is achieved in divertor tokamaks by applying a heating power larger than a certain threshold. The transition into the H-mode is provided by a formation of a transport barrier at the plasma edge such that plasma turbulence is locally suppressed. In figure 3.10 the evolution of an L-mode (plasma state without transport barrier, 'L' for 'low confinement') into an H-mode is presented. At about 1.416 s, when the neutral beam heating is switched on, the transition takes place and the stored energy starts rising. The Doppler reflectometry diagnostic measures the velocity of plasma layers due to a reflection of a scattered microwave beam at turbulent eddies that move according to the  $E \times B$  velocity caused by a radial electric field  $E_r$ . The eddies are a typical feature of plasma turbulence and they are responsible for transport of particles and heat. The Doppler reflectometry enables the measurement of  $E_r$  and a characterization of the turbulent state of a plasma. As can be seen from the Doppler measurement, the radial electric field increases prior to the L to H transition, and finally, after the transition the intensity of the reflectometry signal strongly decreases. The latter indicates a mitigation or suppression of the turbulence effects as observable by the diagnostics. When keeping

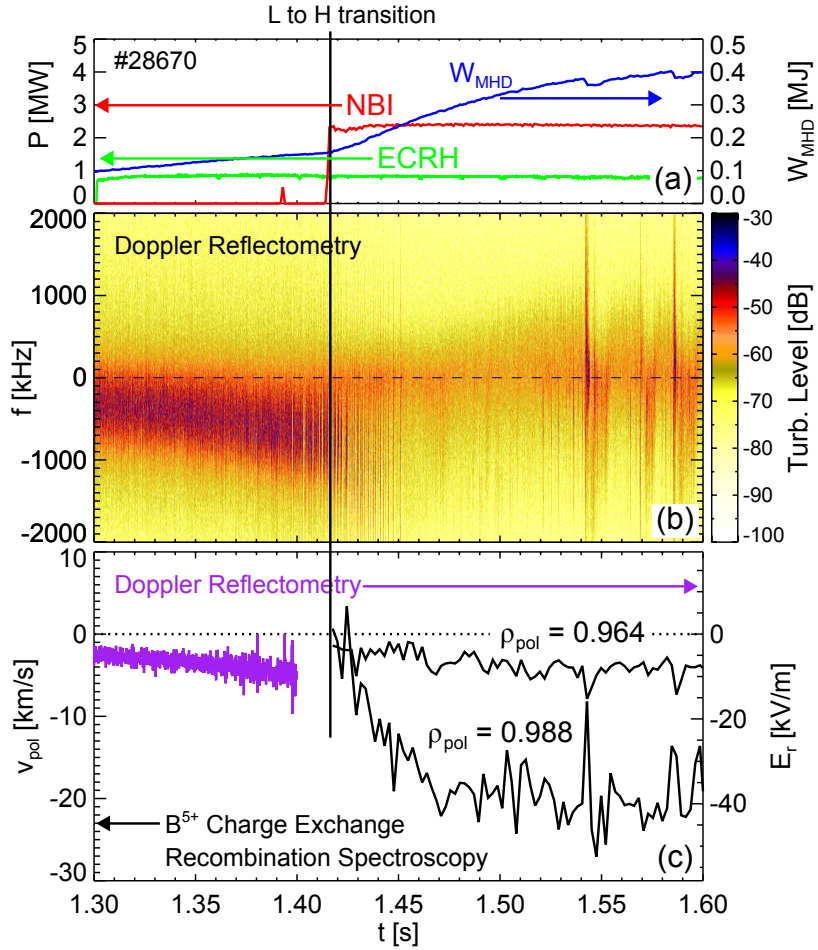


Figure 3.10: (a) Trajectories of electron cyclotron resonance heating (ECRH), heating by neutral beam injection (NBI) and plasma stored energy ( $W_{MHD}$ ); (b) raw data from Doppler reflectometry; (c) Flow velocities as derived from Doppler reflectometry and charge exchange recombination spectroscopy (courtesy of E. Viezzer and T. Happel)

track of the plasma flows by charge exchange spectroscopy (cf. publication 7) a strong shear flow is observed, as following the L to H transition the plasma at  $\rho = 0.964$  moves at a much slower velocity than that at  $\rho = 0.988$ , while the radial distance between the layers is a mere 1.5 cm. This shear flow is thought to tear turbulent eddies apart or to at least damp the activity of turbulent eddies. As a result, the plasma profiles steepen in H-mode, which leads to a larger stored energy and to higher values of density and temperature very close to the separatrix. An example of two sets of electron profiles before and after an H-mode transition is given in figure 3.11. The drastic increase of the edge profiles leads to a so-called pedestal in temperature, density and pressure, which enhances the confinement of the total plasma. As confinement is a vital parameter for the success of a fusion reactor the H-mode regime is an important research field. At the same time the impurity confinement also increases due to the transport barrier, which actually poses a risk for the

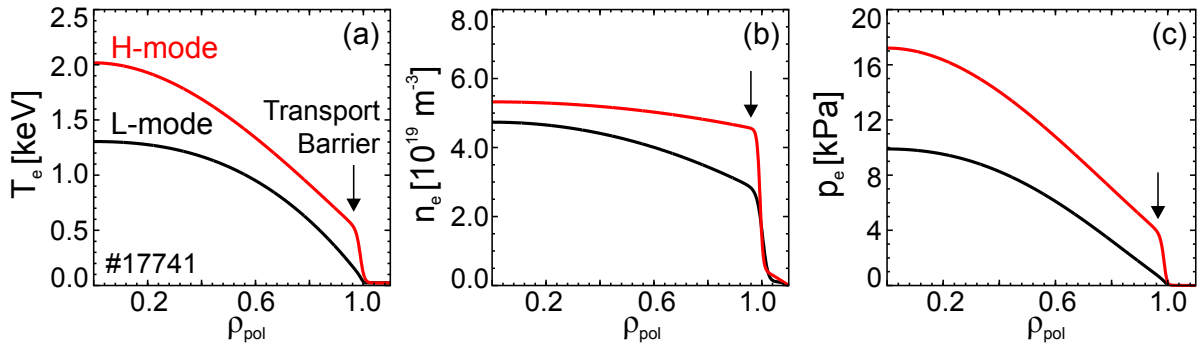


Figure 3.11: (a) Electron temperature fit to data during an L-mode and H-mode phase just before and just after an L to H transition in the ASDEX Upgrade discharge #17741. (b) Same for electron densities. (c) Same for the derived electron pressure. (adapted from [70])

performance of a fusion reactor. The properties of the edge transport barrier and its effect on impurity transport are investigated in Publications 6, 8, 9, 10, 11 and 12. It is found that neoclassical theory describes the H-mode pedestal well, as the radial electric field is self-consistent with the kinetic profiles, while the impurities transport is also neoclassical. Additionally, a correction due to an impurity density asymmetry on the flux surfaces of the pedestal is identified and found to yield a minor correction to standard neoclassical transport. However, a complication to that picture is given by the frequent activity of edge-localized modes (ELMs) described in the next section.

### 3.4.2 ELMs and Their Impact on Impurity Control

The H-mode edge is characterized by steep gradients in the kinetic profiles. In the so-called type-I ELM H-mode, the transport barrier leads to a continuous built-up of densities and temperatures and local current densities such that at the plasma edge a peeling-balloonning instability forms called edge localized mode (ELM). When critical values for the edge pressure and current densities are reached this instability kicks in, expelling particles and energy. Typically, a single ELM can remove a few percent of the total stored energy within about a ms and limiting the pressure gradients at the edge potentially yielding problems for the power load at the first wall. The ELMs not only limit the energy confinement they also expel impurities, an effect which turns out to be very important, because the impurity transport in H-mode without ELMs was found to be neoclassical (cf. publication 6) and thus, is featuring a strong radial inward convection (cf. section 3.3.1) which leads to an unacceptable high impurity content of the plasma. In equilibrium, the expulsion of impurities by ELMs balances the inward convection between ELMs. The latter is also called ELM flushing and it has been shown to be of high importance especially for W

(cf. to [15, 71]). A complication is given by the fact that the ELMs also cause a strongly increased source of impurities at the wall due to them causing an elevated particle and power flux to the plasma facing components. In publication 6 it is attempted to provide a consistent picture of the flushing and source effects of ELMs, which is described in more detail in [72]. However, as there are many unknown parameters the presented modelling is no prove of the concept, it just shows that there are no obvious contradictions.

### 3.5 Impurity Control in the Plasma Core

The transport of high-Z elements in the plasma core exhibits an effect called impurity accumulation, which is an ubiquitous effect in tokamak devices. In fact, it was observed in the first tokamaks that used W as a first wall material in the 1970s [13, 14] and was considered as a showstopper for high-Z elements. The transport close to the magnetic axis may exhibit a strong neoclassical inward convection (pinch) for impurities such that impurity peaking localized in the plasma core is observed (cf. [73, 37, 74]) similar to that presented in figure 3.12. This pinch is of low importance if other transport effects such as

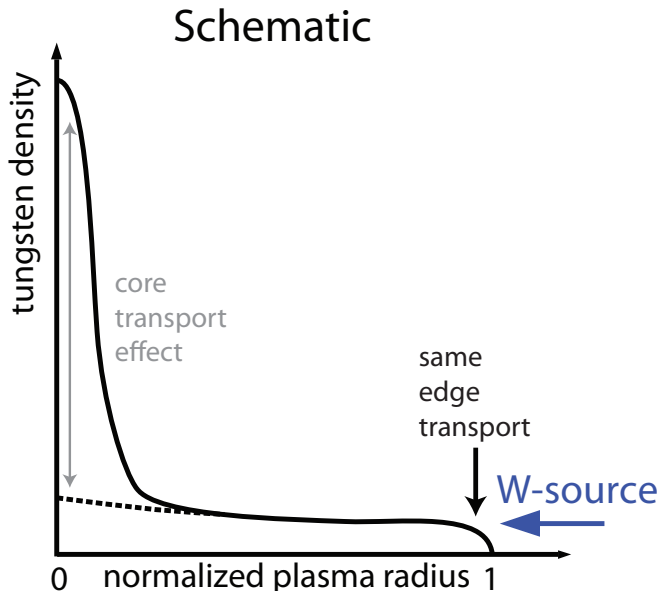


Figure 3.12: Schematic exemplifying the effect of different impurity transport in the plasma core and its influence on the core density of W.

turbulent transport are dominant. However, all kinetic profiles approach a zero derivative at the magnetic axis. As turbulent transport in the regimes ITG (ion temperature gradient mode) and TEM (trapped electron mode) is strongly increasing above a threshold in the normalized gradients, it is clear that in the plasma core turbulent transport becomes less important. If then the density gradients and temperatures of the main ions are

such that a neoclassical pinch for impurities exists, it is very large for W, because of the charge dependence of neoclassical transport (cf. section 3.3.1). Note that there is no threshold for neoclassical transport. Such a transport situation is not easily reversed, because the enhanced W-concentration leads to a reduction of electron temperatures in the plasma core which reduces further turbulent transport and may even enhance the neoclassical pinch. The latter is the case if also ion temperatures are affected which reduces the neoclassical temperature screening. In any case a strategy to avoid or reverse impurity accumulation is the application of core localized heating. In figure 3.13 the core heating is varied via the application of electron and ion cyclotron heating, but also via the usage of neutral particle beams with different injection geometry and thus core heating fractions. The radiation peaking in the plasma core is quantified by two bolometer

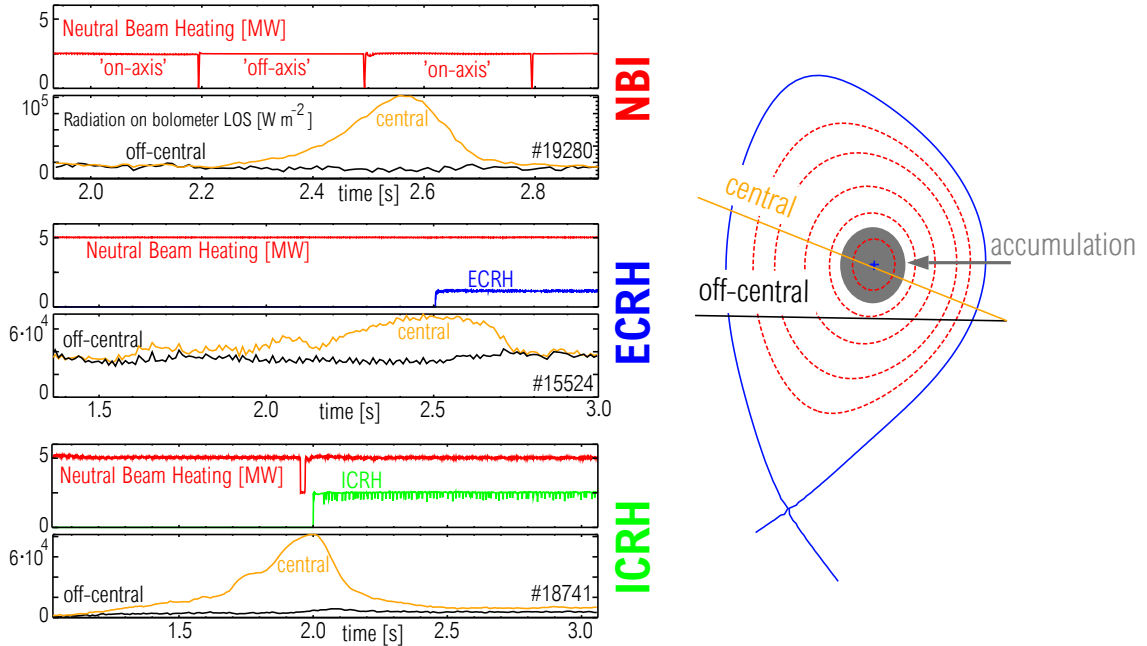


Figure 3.13: The effect of core localized heating on impurity accumulation is shown for neutral beam injection (NBI), electron and ion cyclotron heating (ECRH and ICRH). The impurity accumulation is diagnosed by comparing two bolometer lines of sight with a geometry similar to that shown on the right hand side. The location of the accumulation region is estimated by the shaded area.

channels with a central and off-central line of sight. In all three cases radiation peaking develops spontaneously and a change of heating manages to reverse it. The different time-lag may be explained by the slightly different effects of the heating schemes on the kinetic profiles and by their effect on the transport coefficients. However, a detailed proof that the switching is exactly explained by a switch from neoclassical to turbulent transport is difficult to provide as all the necessary parameters are not measurable to

the required accuracy. In any case, the total impurity transport profiles for a change of heating was directly investigated in [75] for silicon. In figure 3.14, the results of these investigations are presented. It is observed that indeed the measured silicon transport coefficients, i.e. diffusion coefficient and drift velocity, for small central heating are close to neoclassical transport coefficients, while the application of ECRH and ICRH increases the diffusive transport and reduces the inward convection. This is qualitatively expected from the switch of neoclassical to turbulent transport, however, the turbulent transport coefficients could not be accurately calculated. It should be noted that the effective

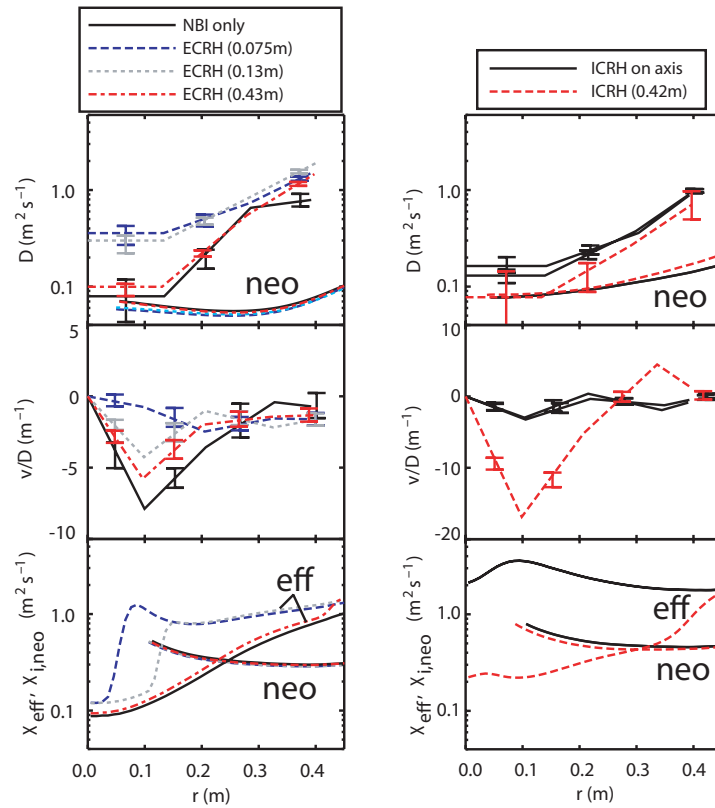


Figure 3.14: The effect of ECRH and ICRH on the silicon transport in the plasma core is investigated. Along with the change of the diffusion coefficient  $D$  also the convection drift velocity  $v$  and the heat diffusivity  $\chi$  is investigated. Calculated neoclassical values are labeled 'neo' while the other curves are measured values.  $\chi_{\text{eff}}$  denotes the effective heat diffusivity derived from the total power flux and the average of ion and electron temperatures. (adapted from [75])

heat diffusivity  $\chi_{\text{eff}}$  is driven by the additional heating and an excess of  $\chi_{\text{eff}}$  versus the neoclassical ion heat diffusivity  $\chi_{i,\text{neo}}$  seems to be directly connected to an increased diffusive transport or at least to a reduced inward convection of silicon with respect to neoclassical transport.

Other candidate mechanisms influencing the impurity accumulation may be MHD activities at the  $q_{sa,f} = 1$  flux surface and possibly an influence of rotation, which is predicted to influence radial transport sensitively for high-Z elements and which may be changed by the heating schemes. The mentioned alternatives are under investigation. In publication 4 (cf. chapter 5) a correlation between central fishbone activity (MHD - fast ion instability) and an outward convection of W is observed, however, an explanation for the observation is still missing.

# Chapter 4

## Summary Bringing the Featured Publications into Context

In order to gain energy from fusing deuterium (D) and tritium (T) nuclei to helium (He), hot plasmas (10-30 keV) with D and T ions are confined by a combination of strong magnetic fields such as those provided by a tokamak configuration. This configuration allows for confining the plasma, however, an economical energy production is only possible when the plasma confinement (thermal insulation) exceeds a certain value, which is challenging to obtain, while at the same time the concentration of the He ash and other impurities are kept at sufficiently low values. The impurities dilute the fuel and can lead to a cooling of the plasma via radiation in the vacuum-ultraviolet (VUV) to X-ray wavelength range, both of which are undesirable effects. This thesis and the featured publications in chapter 5 focus on how the impurities originating from the wall, specifically tungsten, affect the plasma and on the control of these impurities.

**Publication 1** focuses on the spectroscopic diagnostics of tungsten in the main plasma via passive spectroscopy (cf. section 2.1.1). Measurements of the strongest emission lines of tungsten are presented from the VUV to X-ray wavelength region. The measured spectra are compared to modelled ones in order to also benchmark the atomic data (cf. section 2.4), which has been calculated within the same study. The benchmarks result in a reliable basis for the diagnostics of tungsten in present day devices, but also in credible predictions of the spectra in ITER, the next step fusion device. In publication 1, recommendations are also given for the spectral lines best suited for diagnostics. The atomic data provided and investigated in publication 1 are still the basis for the diagnostics of tungsten in today's devices.

**Publication 2** is concerned with the cooling factor  $L_Z$  of tungsten (cf. section 1.5.2), which can be understood as the efficiency of tungsten to emit electro-magnetic radiation, which causes energy losses from the confined plasma. For a wide range of electron tem-

peratures (30 eV to 40 keV), the cooling factor is evaluated by determining the ionization balance (cf. section 2.4.1) and the contribution of line radiation, recombination radiation and bremsstrahlung of each ion. The uncertainties of the atomic data are investigated and the results are compared to earlier calculations of the cooling factor. As a result of these investigations it is found that the cooling factor of tungsten is a robust quantity as older calculations agree with the ones presented in publication 2 within 50% of the new values. Additionally, the uncertainties of the atomic data for the individual ions are mitigated as for a certain temperature several ion stages contribute radiation to the total radiation. Note that more recent evaluations of the cooling factor of tungsten (cf. to [76]) apparently disagree at high temperatures, however, the disagreement is mostly caused by the neglect of bremsstrahlung in [76]. An experimental evaluation of the cooling factor is also performed and agreement to the calculated data is found, however, the uncertainties span about an order of magnitude, such that a direct measurement of the cooling factor seems futile. The newly evaluated cooling factor is used to calculate the so-called burn curves (cf. figure 1.12), i.e. curves that indicate the necessary plasma parameters and confinement quality for a fusion reactor such that the fusion processes keep the temperature of the fusion plasma high enough to sustain fusion, without external heating.

In **publication 3** the emission lines of  $\text{W}^{23+}$  are investigated, because this ion stage is representative of several ionization stages for which the calculation of the atomic data is very challenging due to the complexity of the electronic system, i.e. an open 4f-shell. This publication demonstrates how large a calculation ought to be in order to get spectral emissions that resemble the experimental observations. (cf. section 2.4.2)

Ultimately, the diagnostics of tungsten are just tools for understanding the transport of tungsten in the plasma, which is a pre-requisite for controlling it. For example, a very drastic transport effect of tungsten is observed in the plasma core, where most probably neoclassical transport (cf. section 3.3.1) leads to an accumulation of tungsten in the innermost part of the plasma (cf. section 3.5). This leads to a strong radiative cooling where it is least tolerable and thus, mechanisms are required that help to prevent the accumulation of tungsten in the plasma core.

**Publication 4** addresses this phenomenon at JET and ASDEX Upgrade. At JET a novel interpretation of the measurements from the soft X-ray cameras (cf. section 2.3) helps to diagnose the effect of accumulation. An interpretation of the data with a transport model helped to identify the possible impact of MHD modes on the tungsten transport in the core. This hints in the direction that both MHD modes and turbulence are able to suppress impurity accumulation by mitigating the effects of neoclassical transport (cf. section 3.3.2). The additional transport channel caused by MHD may explain why, up to now, no reliable onset condition could be formulated for impurity accumulation. The presented investigations from ASDEX Upgrade suggest that after the initial onset of

impurity accumulation, it seems to become a run-away effect, even though the background plasma is only slightly changed. Again this implies a big challenge for finding a way of predicting impurity accumulation, as the uncertainties in the measurements of the plasma profiles may be too large to pinpoint the onset condition.

**Publication 5** explains the soft X-ray based diagnostic method at JET used in publication 4. Additionally, the erosion source of tungsten in the divertor of JET measured via the S/XB method (cf. section 2.1.1) is related to the tungsten content of the plasma for a variety of discharges. This allows for the derivation of an effective confinement time of tungsten including the effects of divertor and scrape-off layer transport (cf. section 3.2). It is observed that an elevated deuterium gas puff for fueling the plasma density is able to decrease the tungsten confinement time. Also the plasma confinement and ELM frequency are changed by the gas puff, such that the exact causality of the tungsten reduction cannot be determined. Nevertheless, these observations are qualitatively in line with earlier findings at ASDEX Upgrade.

When investigating impurity accumulation it was found that localized core heating may avoid or even reverse impurity accumulation (cf section 3.5). As transport is determined by the kinetic profiles it is clear that any radiative cooling in the plasma core will have the opposite effect to heating and indeed it is observed that a high tungsten level in the core plasma, e.g. given by large tungsten sources at the edge, leads to a stronger tendency for impurity accumulation. Thus, any reduction of the tungsten flux towards the core, i.e by reduction of the tungsten source or by changes of tungsten edge transport, has a similar effect to plasma heating in the core and thus helps to avoid tungsten accumulation there. Therefore, a large tungsten content in the plasma has two effects: Firstly, it leads to strong radiative losses and secondly, it may change tungsten transport such that strong tungsten accumulation results. The latter not only causes strong radiation but also affects the stability of the plasma and plasma operation. When considering the transport separately at the plasma core and the plasma pedestal, it should not be neglected that the edge transport may influence the core transport.

In **publication 6** the impurity transport at the H-mode pedestal is investigated by employing charge exchange recombination spectroscopy (CXRS). As tungsten cannot be measured with CXRS, helium, carbon, neon and argon transport was investigated in order to extrapolate to tungsten. The impurity transport was analyzed in-between edge localized modes and found to be in agreement with neoclassical values, which means that the diffusion coefficient is strongly reduced in the edge transport barrier, while a charge dependent inward convection exists for impurities. For tungsten this pinch is calculated to be even stronger than the measured ones for He, C, Ne and Ar, such that the tungsten density would peak at the plasma edge by about a factor of 100, while the electron density is enhanced by only about a factor of 2 to 3. In order to investigate the plausibility of

that result, a model is put together that considers neoclassical transport at the plasma edge, but also takes into account the beneficial effect of edge localized modes removing tungsten from the plasma. Additionally, it is included in the model that the edge localized modes cause an additional tungsten sputtering source at the edge, while rough estimates of scrape-off layer transport are employed. The model manages to explain the tungsten core densities in three different discharges with different gas puffing levels leading to different frequencies of edge localized modes. Thus, assuming neoclassical transport at the plasma edge does not lead to contradictions with any observations, however, due to the numerous free parameters in the model this cannot be considered as an independent proof for neoclassical tungsten transport. Note that the transport model for tungsten developed in publication 6 and in [72] is the scientific basis for [77] and influenced the decision of the ITER organization to start with a full tungsten divertor from day one.

In **publication 7** the CXRS systems of ASDEX Upgrade are presented (cf to section 2.1.2), which are essential for all investigations on the plasma edge. Publications 6-12 are concerned with the plasma edge and the investigations could not have been performed without the high quality and high throughput of the ASDEX Upgrade CXRS systems.

In **publication 8** CXRS measurements of plasma rotation at the H-mode edge are reported which shed a surprising light on the physics of the plasma edge. A reversal of the rotation gradient is observed at the plasma edge leading to a considerable rotation at the plasma boundary, where actually breaking of rotation was expected. While publication 8 is a report of this phenomenon it may be considered as the start of a larger investigation effort including a very successful PhD thesis, in order to better understand the rotation physics at the plasma edge.

A crucial parameter correlated with the kinetic profiles at the plasma edge is the radial electric field (cf. to section 3.4.1). It is closely correlated to plasma rotation via the radial force balance. In order to investigate the radial electric field with CXRS, which allows ion temperatures to be measured simultaneously to the electric fields, the CXRS system was further extended by a poloidally viewing head (described in publication 7).

In **publication 9 and 10** the radial electric field at the plasma edge is investigated for H-mode discharges at ASDEX Upgrade. The CXRS measurements performed on fully stripped impurity ions give remarkably good agreement to the neoclassical values of the poloidal plasma rotation. It was also confirmed that the edge transport barrier exists most probably due to a suppression of turbulent transport by a strong sheared  $E \times B$  flow. This was suspected before, and additionally in publication 9 the radius of the largest shearing rate in the  $E \times B$  flows was found to closely match the radius of the steepest pressure gradients. This comparison was possible, because a high-accuracy alignment scheme allowed for uncertainties of less than 5 mm in the radial alignment of the kinetic profiles measured by different diagnostics. The good match of the radial electric field

with the neoclassical values was also investigated in helium plasmas (additionally to the investigations in deuterium plasmas), due to the better diagnostic opportunities on the main ions via CXRS on  $\text{He}^{2+}$ . Again a good match to neoclassical poloidal rotation was found.

However, the agreement to neoclassical theory does not allow for an explanation of the edge rotation feature reported in publication 8, i.e. the reversal of the rotation gradient at the plasma edge leading to strong rotation at the outboard separatrix. A possible mechanism could be provided by deviations from the flow equilibrium on a flux surface as postulated by neoclassical theory. Inspired by recent work at Alcator C-Mod (cf. to [78], [79]) the plasma rotation was investigated not only at the outboard midplane, but also at the inboard midplane. This required some diagnostic development as at ASDEX Upgrade only beam based CXRS was established, while at the inboard side no beam is available. Thus, a CXRS system based on a gas puff valve was built-up, reminiscent of the system at Alcator C-Mod.

In **publications 11 and 12** the measurements of that system were exploited and impurity rotation velocities were compared between the inboard and outboard sides of the plasma. Similar to what was reported in [78], the impurity rotation on a flux surface exhibited clear deviations from the neoclassical expectation, which is based on the continuity equation. In order to resolve contradictions to the continuity equation an excess impurity density at the inboard side of the flux surfaces at the plasma edge was postulated, while also other explanations like a non-zero divergence of radial transport were considered. An effect of the latter could not be excluded, however, a direct measurement of the impurity density (publication 12) helped to confirm an asymmetry of impurity densities, which brings all rotation measurements into agreement with the continuity equation. The direct measurement of the impurity densities support the postulate of an excess impurity density at the inboard side of the plasma. This asymmetry implies an alteration of neoclassical transport, because it is not poloidally symmetric, such that the observed impurity density asymmetry weights the inboard transport more strongly than the outboard transport. An evaluation of this effect within the model showed that a change of the transport coefficients is indeed obtained, however, the changes are in the range of a few tens of percent as compared to a fully symmetric case. Thus, the observations in publication 6, which determined the impurity transport levels at the plasma edge to be neoclassical, for symmetric impurity distributions, would still arrive at the same conclusion (within the uncertainties) even when benchmarking the measurements against the neoclassical theory including the asymmetry. The Z-dependence observed in publication 6 is also an indicator for neoclassical transport, which is preserved also for the case in which impurity asymmetries occur.

In summary, the observations concerning the impurity transport at the edge pedestal

suggest that neoclassical transport including impurity asymmetries is the best model for predictions to future devices. However, edge localized modes must be taken into account as they are an important player for obtaining an equilibrium between the in- and outflux of impurities. Still, predictions for ITER using the assumption of neoclassical transport [80] are very encouraging, as they suggest that the neoclassical edge transport in ITER will be dominated by temperature screening (cf. section 3.3.1), which suppresses the impurity influx from preferentially high-Z elements.

Due to the fact that the transport of impurities is closely connected to the transport of electrons and main ions, the topic of impurity physics requires an understanding of all plasma components. This presents also a weakness for the predictions for future devices, because already the kinetic profiles in these devices are difficult to predict and thus, the neoclassical and turbulent impurity transport coefficients are uncertain. For tungsten a small change of the kinetic profiles implies a large change of the neoclassical transport. At the same time the erosion sources and edge transport of tungsten are also able to change the core transport, which adds further complexity and yields further issues for the predictability of impurity transport.

Future large fusion devices will provide very limited time to do parameter scans searching for impurity control mechanisms. Therefore, for future devices a well characterized knowledge base of impurity control mechanisms is important, while also the realization of the related control tools must be included in the design. Such an anticipatory planning provides the possibility to compensate for inaccuracies of the predictions. Vice versa if special operation modes are developed in order to improve the plasma confinement, the consideration of impurity control must be included, as impurities are one of the possible show-stoppers of a fusion device. A rather encouraging example is provided by the recent transfer of operational experiences from ASDEX Upgrade to JET, such that after a few months of operation at JET using the ITER-like wall, the most important impurity control schemes such as gas puffing, impurity seeding and central wave heating are now successfully applied at both machines keeping the W-content of the plasmas below critical levels.

# Chapter 5

## Major Publications

### 5.1 Publication 1

*Modelling of measured tungsten spectra from ASDEX Upgrade and predictions for ITER*

Plasma Physics and Controlled Fusion 50 (2008) 085016

## Modelling of Measured Tungsten Spectra from ASDEX Upgrade and Predictions for ITER

**T Pütterich<sup>1</sup>, R Neu<sup>1</sup>, R Dux<sup>1</sup>, A D Whiteford<sup>2</sup>, M G O'Mullane<sup>2</sup>, and the ASDEX Upgrade Team<sup>1</sup>**

<sup>1</sup>*Max-Planck-Institut für Plasmaphysik, EURATOM Association, D-85748 Garching, Germany*

<sup>2</sup>*Department of Physics, University of Strathclyde, Glasgow G4 0NG, UK*

**Abstract.** Tungsten (W) has moved into the focus of fusion research as being a main candidate for the plasma facing components (PFC) of ITER and a future fusion reactor. A main ingredient for understanding the influence of W as a plasma impurity and its impact on the plasma is the spatially resolved, spectroscopic diagnosis of W. The focus of the experimental investigations at ASDEX Upgrade is on the most intense emissions of W-ions (about I-like W<sup>21+</sup> to Mn-like W<sup>49+</sup>) in the VUV to soft X-ray region covering the electron temperature range from about 0.5 – 5.0 keV. The relative shape of the fractional abundances of the ionization stages Se-like W<sup>40+</sup> to Ni-like W<sup>46+</sup> and of the bundle of ionization stages between Sn-like W<sup>24+</sup> to Sr-like W<sup>35+</sup> were determined. Calculated fractional abundances using published ionization and recombination rates do not accurately describe the experimental temperature dependence. Adjustments to the recombination rates were calculated to reconcile with the measurements. The spectral features of W at 0.4 – 0.8 nm, around 5 nm, between 12 – 14 nm and between 10 – 30 nm have been recorded and compared to modelling results. The quality of agreement is best for highly charged ionization stages and short wavelengths and decreases for lower charged ionization stages and longer wavelengths. However, in the latter case the predictions manage to reproduce the total emissivity in each considered spectral range and also the rough distribution of emissions versus wavelengths within these spectral ranges. The modelling of the SXR-range at 0.4–0.8 nm looks very similar to the measurement. Further observations of weaker spectral features between 0.6 – 0.7 nm, between 1.8 – 3.5 nm and at 8 nm could be attributed to certain ionization stages. The modelling of W-spectra for ITER predicts emissions of Cr-like W<sup>50+</sup> to about C-like W<sup>68+</sup> at 0.1 – 0.15 nm, 1.8 – 4.0 nm and around 8 nm.

### 1. Introduction

Tungsten is moving back into the focus of spectroscopy for fusion plasmas because it is planned to be used as a plasma facing material in upcoming large tokamaks, such as ITER [1]. As sputtering at the surfaces with plasma contact cannot be avoided completely, tungsten will be an intrinsic impurity in these plasmas. The electron temperatures in ITER will span from below 0.1 keV at the edge up to about 30 keV in the core of the plasma. Many different ionization stages – each with a large number of electrons – will contribute to a measured spectrum because spectroscopic measurements are performed on a line of sight

*Modelling of Measured Tungsten Spectra from ASDEX Upgrade and Predictions for ITER 2*

(LOS) crossing regions of the plasma with various plasma temperatures. Therefore, the measured spectra often contain many spectral lines from several ionization stages forming spectral features. For interpretation, the identification of the spectral emissions is necessary; the process of understanding the spectra must also be accompanied by model calculations using atomic data. This analysis supports the disentangling of the experimental spectra and yields a quantitative understanding of the measurement. However, atomic data for high-Z elements are scarce and elaborate to produce, because of the high computational effort needed to perform calculations for these ions as well as more pronounced relativistic effects. Theoretical data for the ionization equilibrium and the excitation rate coefficients along with the energy level structure and transition probabilities are the basic input to model the emissions of tungsten. Neighbouring ionization stages with similar electron structure emit spectral lines at similar wavelengths. This leads to the spectral features mentioned above, especially, when open d- or f-orbitals are involved. First observations of this phenomenon have been performed in the ORMAK [2] and PLT [3] tokamaks in the 1970s, where the quasicontinuum emission around 5 nm was reported. Further investigations have been performed at the ASDEX Upgrade tokamak [4, 5, 6, 7, 8], which also revealed spectral emissions at electron temperatures above 2 keV in the soft X-ray and the VUV. The ionization equilibrium has been analysed in [4] by using the ADPAK ionization and recombination data from the average ion model [9, 10]. Analysis of the VUV spectrum in EBIT devices were conducted at the Berlin [11], the Lawrence Livermore National Laboratory [12] and National Institute of Standards and Technology [13] EBITs. These and supplementary investigations at ASDEX Upgrade [14] identified the emitting ionization stages of most spectral lines between 4 and 15 nm. This allowed for the analyses presented below which determine the abundance of ionization stages versus electron temperatures (1 – 4.5 keV) for fusion-relevant electron densities. Furthermore, several new spectral features emitted by tungsten are measured at ASDEX Upgrade and investigated by comparison to modelling results. The model is based on atomic data produced by the Cowan code [15] using a plane-wave Born approximation for electron impact excitation. On the experimental side, ASDEX Upgrade is offering tungsten spectra emitted from various plasma discharges, as all plasma facing components (PFCs) have been stepwisely covered with tungsten [16] (starting in 1999 and reaching 100% in 2007). Details of the investigations can be found in [7], however, the calculations used in [7] have been improved and limitations of the code calculations have been overcome, such that for a single ionization stage up to a million transitions can be included. Especially, for the ionization stages with open d- and f-shells this led to an improvement of the modelling results. The paper aims to improve the knowledge about the spectra of tungsten ions, such that features of these spectra can be used for quantitative measurements in a fusion plasma. This effort includes measurements of the ionization equilibrium and the measurement and modelling of spectra to benchmark the quality of atomic data and to increase the understanding of the W spectra. In the next section, the investigations concerning the ionization balance are presented. In section 3, the modelling of spectra is described, while in section 4 the measurements of the brightest spectral features are presented and modelled. In section 5, observations of additional spectral features are presented. Before the summary is given in section 8, an outlook to future

### *Modelling of Measured Tungsten Spectra from ASDEX Upgrade and Predictions for ITER 3*

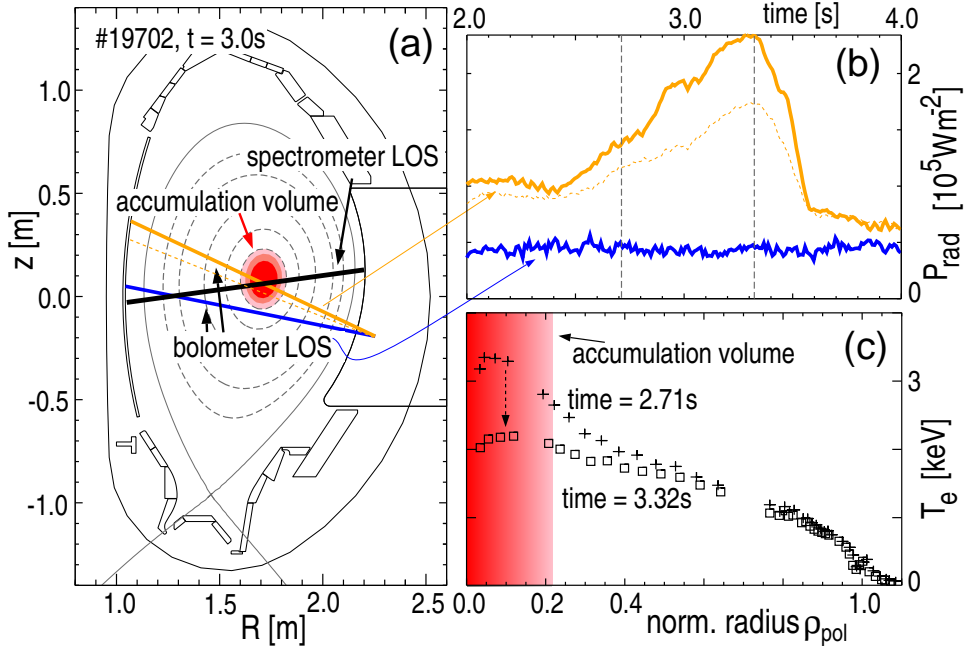
tungsten spectra for JET and ITER is given (section 6) and recommendations on diagnostic lines for fusion plasmas in general are given (section 7).

## 2. The Ionization Equilibrium of Tungsten

For the interpretation of spectral emissions and their modelling, it is necessary to know the abundance of each tungsten ionization stage along the line of sight (LOS) of the measurement. In a fusion plasma, the fractional abundance is determined by the recombination and ionization rates along with the plasma transport. It was found earlier [4] that within a certain plasma radius ( $\rho_{pol} \leq 0.7$ ) plasma transport affects the ionization equilibrium of W only weakly. At these radii, the typical transport times are large in comparison to the equilibration time of the ionization balance. Outside this radius, fast transport events and an increased diffusive transport are observed, which make the interpretation of impurity radiation more challenging. Below, the focus is placed on the central part of the plasma. The ionization equilibrium is calculated by the transport code STRAHL [17, 18] in which typical transport coefficients are used (e.g. [19, 20]). Due to the fact, that ionization and recombination rates for high-Z elements are large compared to transport times, transport plays only a minor role for the ionization equilibrium (within  $\rho_{pol} \leq 0.7$ ). Therefore, no detailed explanation about transport coefficients is provided in the following. Different sets of ionization and recombination rates are discussed and compared to measurements. A large experimental dataset is available from ASDEX Upgrade for various types of plasma discharges. In particular discharges with impurity accumulation are very useful to determine the abundance range of an ionization stage as explained in the following paragraphs. During impurity accumulation, a very small central part of the plasma exhibits tungsten concentrations which are higher than in the rest of the plasma by factors of up to 100 [21, 22]. Line-integrated measurements by bolometers and spectrometers are dominated from the plasma region where accumulation takes place (see figure 1). The electron temperature in this small region as measured by electron cyclotron emissions and Thomson scattering, is spatially about constant in the accumulation volume because the spatial extension of the region is small with respect to gradients in electron temperature. Moreover, the radiative losses lead to a flattening of the electron temperature profile. This allows for taking quasi-local spectra which are associated with a single electron temperature. Conclusions about the fractional abundance of ionization stages can be drawn, because the following two issues are well understood:

Firstly, the intensity of spectral lines emitted by highly-ionized tungsten (i.e. in this work ionization stages above  $\sim W^{20+}$ ) depends strongly on the fractional abundance of the emitting ionization stage, while additional factors are relatively small and can be corrected or neglected at all. For illuminating the latter statement, the emissivity  $\epsilon_{line}$  of a measured spectral line is considered in the following, using  $n_e$  as local electron density,  $n_W$  as local tungsten density,  $f_Z$  as the local fractional abundance of the emitting ionization stage Z and  $PEC_{line}$  as the photon emissivity coefficient of the measured spectral line.

$$\epsilon_{line} = n_e n_W f_Z PEC_{line}(n_e, T_e)$$

*Modelling of Measured Tungsten Spectra from ASDEX Upgrade and Predictions for ITER* 4

**Figure 1.** (a) Setup for the measurements. A magnetic equilibrium with three lines of sight (LOS) of the bolometer system and the LOS of the spectrometer are presented. On flux surfaces the plasma parameters are spatially constant. (b) Time traces for the line-integrated measurements (corresponding to the presented LOS of the bolometer) of total radiated power diagnosing impurity accumulation; (c) Electron temperature profiles for two timepoints (indicated in part (b)) measured during impurity accumulation using the electron cyclotron emission.

The total radiated power density  $\epsilon_{\text{tot}}$  is subject to bolometer measurements and can be written as

$$\epsilon_{\text{tot}} = n_e n_W L_W(n_e, T_e)$$

using  $L_W$  as the cooling factor of tungsten. Thus:

$$f_Z = \frac{\epsilon_{\text{line}}}{n_e n_W PEC_{\text{line}}(n_e, T_e)} = \frac{\epsilon_{\text{line}}}{\epsilon_{\text{tot}}} \frac{L_W(n_e, T_e)}{PEC_{\text{line}}(n_e, T_e)}.$$

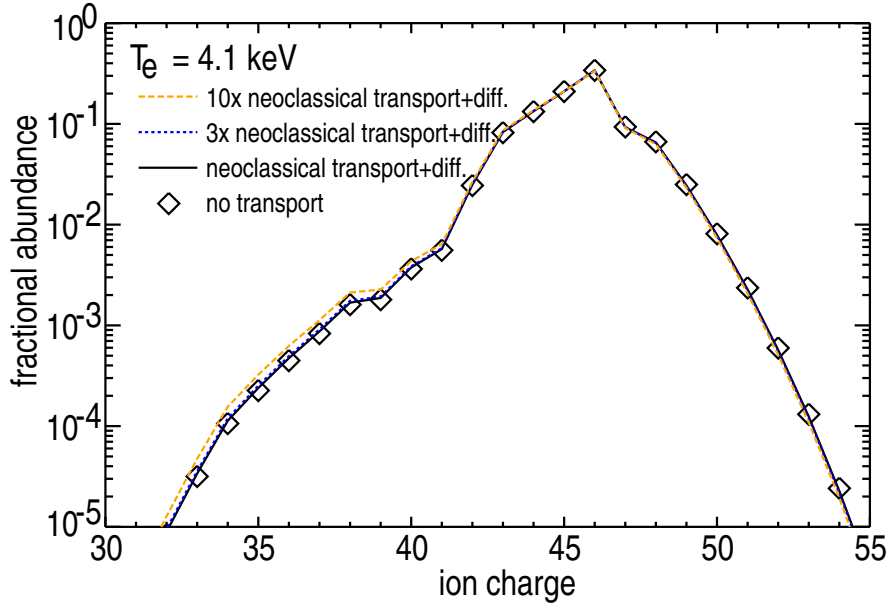
The density dependence of  $L_W(n_e, T_e)$  and  $PEC_{\text{line}}(n_e, T_e)$  for the actual application is small and can be neglected. As pointed out in [14], the relative population of the levels, which decay by emitting the photons, is nearly independent inside the electron temperature range in which the specific ionization stage is abundant. In principle, exceptions to this general rule exist, but in the present section, spectral lines have been used for which it applies. Therefore, the temperature dependence of  $PEC_{\text{line}}(n_e, T_e)$  can also be neglected, while that of  $L_W(n_e, T_e)$  must be taken into account, using the calculated  $L_W$  [9, 10, 23]. The latter corrections are smaller than a factor of 3.

Secondly, the ionization equilibrium inside the accumulation region is very well described without taking transport into account, such that the difference is experimentally not distinguishable. This fact was generally described above, but is treated here specifically

*Modelling of Measured Tungsten Spectra from ASDEX Upgrade and Predictions for ITER* 5

for impurity accumulation in more detail. In figure 2, the fractional abundances inside the accumulation volume for an electron temperature of 4.1 keV (case is taken from experiment) are presented for different transport coefficients and the ionization/recombination rates, which are later identified to describe the experimental data best. The accumulation is assumed to be the result of the neoclassical inward drift. The effects of the latter on the W profile depends on the diffusion coefficient which may be a mixture of neoclassical and anomalous contributions. The neoclassical inward drift has been evaluated from the measured plasma parameters using NEOART [24]. NEOART calculates the collisional transport coefficients for an arbitrary number of impurities including collisions between all components. The code solves the set of linear coupled equations for the parallel ‘velocities’ in arbitrary toroidally symmetric geometry for all collision regimes. The classical fluxes are given by Eqs.(5.9) and (5.10) in [25]. The equations for the banana plateau contribution are equal to that used in [26]. The Pfirsch-Schlüter contribution is calculated from the coupled equations (6.1-2) and (6.14-15) in [25], as described in [27]. The anomalous contributions to the diffusion coefficients have been chosen such that the impurity density profile in the transport model matches the experimentally measured one (central diffusion coefficient:  $0.1 \text{ m}^2/\text{s}$ ). This choice also allows to reproduce the time scale of impurity transport towards the accumulation region within a factor of 2. For these transport coefficients, the ion abundances indicated in figure 2 with the solid line have been evaluated. They do not exhibit any visible difference to the transport-free abundances denoted by the black diamonds. When transport coefficients clearly larger than the neoclassical ones are used and the anomalous diffusion coefficient is increased proportionally in the transport model (3 times larger and 10 times larger transport coefficients (dotted, blue curve and dashed, orange curve)) still no differences are visible for the most abundant ionization stages. Differences for the enhanced transport scenarios occur only for the ionization stages for which the accumulation region is too hot, but for which the increased inward transport leads to an increase of their abundance. However, the effect is only visible, if the amount of the ionization stage, which is abundant in the central plasma is small (about factor 100 below the most abundant stage). Therefore, the measurements in the accumulation region allow to investigate the transport-free situation, in which only the ionization and recombination rates determine the fractional abundance of each ionization stage.

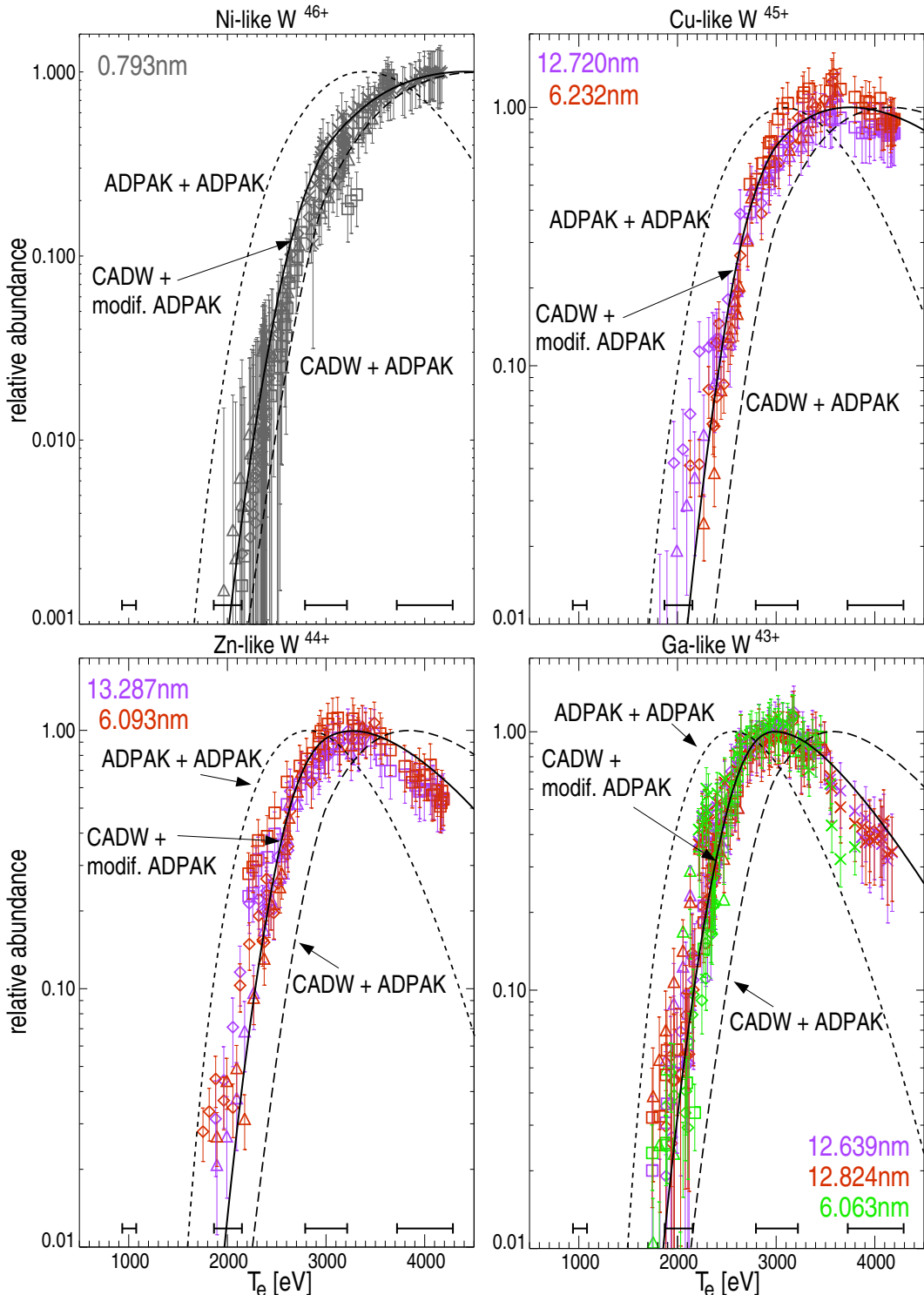
In figure 1(a) the geometrical setup of measurements is presented. The impurity accumulation is diagnosed by bolometer measurements of which three LOS are depicted in the figure. One (thick, solid, orange) of them is observing the central part of the plasma and an other (thick, solid, blue) is slightly off-central. The difference between the measured signal of the two LOS at each timepoint is associated to a localized peak of the radiated power density in the central part of the plasma and is suited to quantify the impurity accumulation. Due to the fact that the plasma parameters are spatially constant along the magnetic flux surfaces, already a measurement on a few LOS covering the central plasma region is sufficient to quantify the magnitude and radial extent of the radiation peaking at each point in time. It may be noted that earlier investigations [19] revealed poloidal asymmetries (deviations of the radiation profile from the magnetic symmetry) for high-Z elements due to centrifugal effects

*Modelling of Measured Tungsten Spectra from ASDEX Upgrade and Predictions for ITER* 6

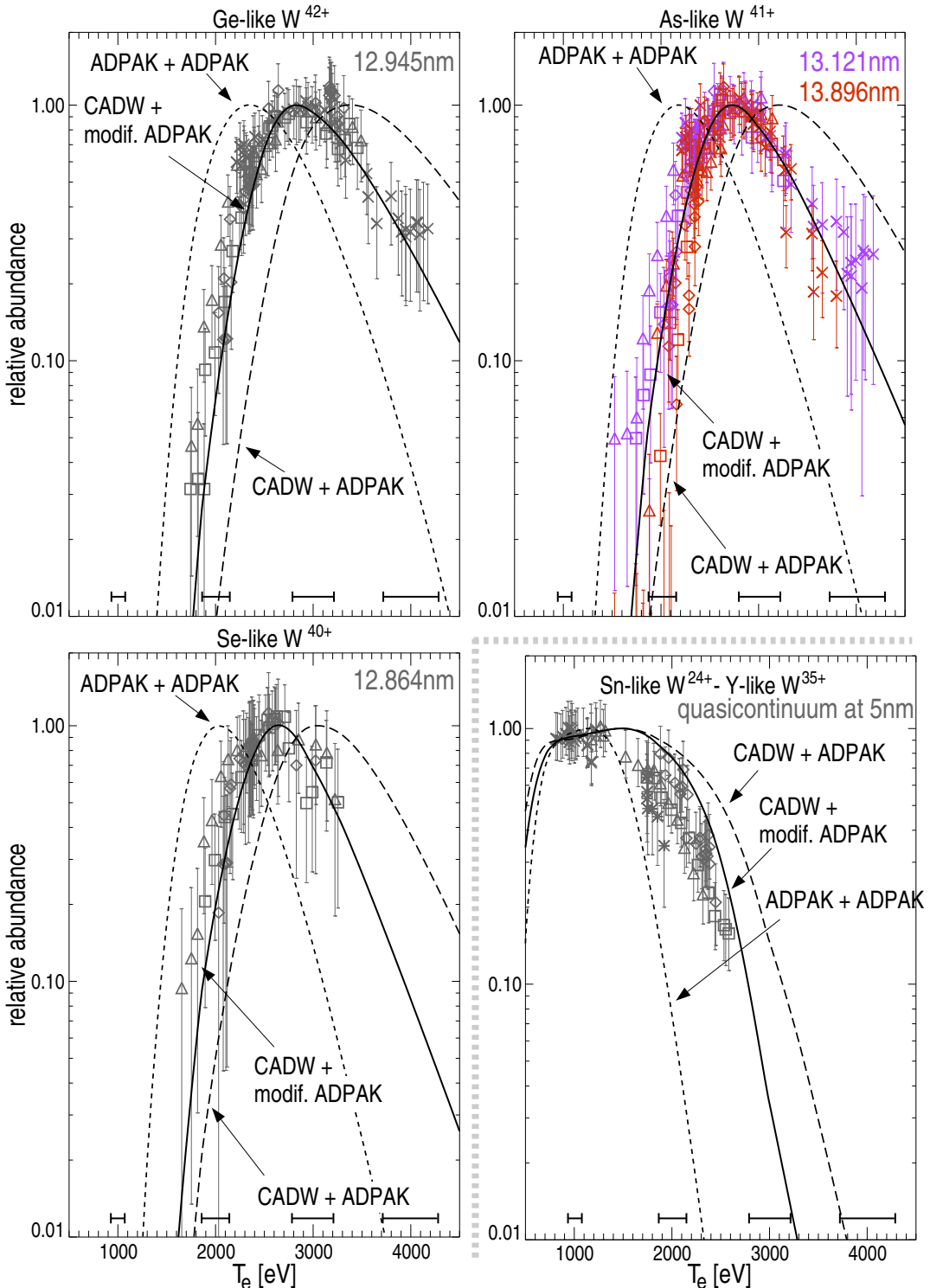
**Figure 2.** Effects of transport on the ion abundances within the accumulation region. Neoclassical inward drifts are evaluated for tungsten using the measured electron profiles. Diffusion due to turbulence is adjusted such that magnitude and time scale of impurity accumulation match the experiment within a factor of 2. A minor effect on the equilibrium is only visible for transport coefficients much larger than predicted for a neoclassical inward drift.

[28]. Such effects only weakly influence the measurements presented here, because all the used LOS are directed almost radially integrating over such asymmetries. Another concern might be the accuracy of the alignment of bolometer LOS compared to the spectrometer LOS. The uncertainty of the magnetic flux surfaces at the plasma center exhibits uncertainties below 2 cm as known from comparison to measurements from soft X-ray cameras. The thin, dashed, orange LOS in figure 1(a) depicts a bolometer LOS, which crosses the plasma center 4 cm below the bolometer LOS which is equivalent to the spectrometer LOS (thick, solid, orange). The corresponding measurement is depicted in figure 1(b) showing that even for an exaggerated spatial deviation of 4 cm the latter result for the realitve shape of  $f(Z)$  is influenced by less than a relative correction of about 30% (keeping in mind, that the quantity, which is entering the results of  $f(Z)$  is the relative behaviour of the radiated power measured on the central LOS (thick, solid, orange) minus the the radiated power on the off-central LOS (thick, solid, blue), see below). The central part of the plasma is also monitored by several spectrometers (e.g. VUV SPRED spectrometer [29], grazing incidence spectrometer [30], scanning Bragg crystal spectrometer [31] and a highly resolving Johann spectrometer [8]). The LOS of a grazing incidence spectrometer is depicted in figure 1(a). The spectral lines from the accumulation region dominate the spectrum, because the corresponding lines emitted outside the plasma center are emitted at regions with a  $\approx 20 - 100$  times lower tungsten concentration. For several phases, the intensities of spectral lines (corresponding to  $\int_{LOS} \epsilon_{line}$ ) have been recorded as a function of time, while the bolometer was used to

## Modelling of Measured Tungsten Spectra from ASDEX Upgrade and Predictions for ITER 7



**Figure 3.** Relative abundances of Ni-like  $W^{46+}$  to Ga-like  $W^{43+}$  derived from theoretical data (lines) and from measurement (symbols). The measurements originate from impurity accumulation phases. Further information in the text.

*Modelling of Measured Tungsten Spectra from ASDEX Upgrade and Predictions for ITER* 8

**Figure 4.** Relative abundances of Ge-like  $W^{42+}$  to Se-like  $W^{40+}$  and the relative behaviour of the compound emissions around 5 nm of Y-like  $W^{35+}$  to Sn-like  $W^{24+}$  derived from theoretical data (lines) and from measurement (symbols). The measurements originate from impurity accumulation phases. Further information in the text.

*Modelling of Measured Tungsten Spectra from ASDEX Upgrade and Predictions for ITER* 9

determine  $\int_{LOS} \epsilon_{tot}$  on an equivalent LOS. The absolute values of the integrals and the absolute values of  $\frac{L_W}{PEC_{line}}$  are not considered here, as the uncertainties in the absolute values might be considerable. However, the relative behaviour of  $\int_{LOS} \epsilon_{line}/\int_{LOS} \epsilon_{tot}$  using corrections for the temperature dependence of  $L_W$  gives the relative behaviour of  $f_Z$  in the accumulation region as the integrands of both integrals are dominated by emissions from that volume. As pointed out above the corrections due to the temperature dependence of  $L_W$  are smaller than factor of 3 owing to a change of the ionization equilibrium and connected to that a change of the radiated power by spectral lines and radiative recombination. The factor of 3 corresponds to the change of  $L_W$  between electron temperatures of 1 keV to 5 keV. The error bars for the relative shape of  $f_Z$  are determined partly by the spectroscopic uncertainties and partly by the estimated uncertainties in determining the correct time behaviour of  $\int_{LOS} \epsilon_{tot}$  and  $L_W$ . For the latter 20 % of the central radiation are assumed. At the same time the electron temperature in the accumulation region is recorded, which allows for monitoring the ionization equilibrium at different electron temperatures. For the whole analysis discharges were chosen which exhibit a continuous behaviour of accumulation and drop in electron temperature, i.e. no sawteeth are observed. For two time points (see vertical lines in figure 1(b)), the electron temperature profiles are plotted in figure 1(c) as measured by electron cyclotron radiation diagnostics. In figure 3 and 4, the measured  $f_Z$  are presented for several ionization stages, while all data points have been normalized (for each spectral line a single factor, for all discharge phases), such that the maximum of the measured curve reaches 1. Within the diagramm of each ionization stage the same symbols correspond to the same occurrence of impurity accumulation, while the colors indicate the spectral line or feature which was interpreted. For the whole analysis, the electron temperature measurement was supplied by the electron cyclotron radiation diagnostics, because it supplies high quality profile measurements. The diagnostics is calibrated each year correcting changes of each channel individually. The changes of calibration factors between two calibrations plus the statistical uncertainties are smaller than 7 % (indicated at the bottom of each diagramm of figures 3 and 4), which is also supported by comparisons to the Thomson scattering diagnostics. For better comparison to the experimental data, the theoretical data derived from three combinations (described below) of ionization and recombination rates have been also normalized to 1 for better comparison to the experimental data. A special case is the fractional abundance derived from the emissivity of the quasicontinuous emission around 5 nm which is emitted by ionization stages around Sn-like W<sup>24+</sup> to Y-like W<sup>35+</sup>. Here, all contributing ionization stages have been added and a weighting according to the predicted brightnesses of the spectral lines (from calculations of atomic data - see next section) of each ionization stage was applied. The experimental data shows the integrated intensity of the quasicontinuum at 5 nm. For the other ionization stages, the following spectral lines have been used (if not specified, uncertainty of the wavelength is 0.005 nm): W<sup>40+</sup>: 12.864 nm; W<sup>41+</sup>: 13.121 nm, 13.896 nm; W<sup>42+</sup>: 12.945 nm; W<sup>43+</sup>: 6.063 nm, 12.639 nm, 12.824 nm; W<sup>44+</sup>: 6.093 nm, 13.287 nm; W<sup>45+</sup>: 6.232 nm, 12.720 nm; W<sup>46+</sup>: 0.793 ± 0.001 nm

For comparison with the experimental data, three combinations of ionization and recombination rates are used. The first makes use of improved [4] ADPAK rates [9]

*Modelling of Measured Tungsten Spectra from ASDEX Upgrade and Predictions for ITER 10*

for ionization and the original ADPAK rates for recombination. In the following figures ‘ADPAK+ADPAK’ is used for labelling the fractional abundances which result from that combination. A second, more elaborate option is available for the ionization rates, which originate from configuration-averaged distorted-wave calculations [32] (CADW). The calculations using them in combination with the recombination data from ADPAK yields the fractional abundances labelled with ‘CADW+ADPAK’. A third data set (labelled ‘CADW+modif. ADPAK’) is derived from the latter combination, while the recombination rates have been scaled by temperature independent factors, such that the best agreement with the experimental data (i.e. the relative abundance versus electron temperature, but also the ion abundance with respect to neighbouring ionization stages as investigated below) is achieved. The factors are given in table 1. The recombination rates of more than the observed ionization stages have been changed, because also the abundance of lower and higher charged ionization stages influence the abundance of the observed ionization stages. The adjustments are done

Recombined Ion	$F_{corr}$	Recombined Ion	$F_{corr}$	Recombined Ion	$F_{corr}$
Xe-like W <sup>20+</sup>	0.97	Mo-like W <sup>32+</sup>	1.62	Zn-like W <sup>44+</sup>	0.47
I-like W <sup>21+</sup>	1.07	Nb-like W <sup>33+</sup>	1.62	Cu-like W <sup>45+</sup>	0.39
Te-like W <sup>22+</sup>	1.17	Zr-like W <sup>34+</sup>	2.25	Ni-like W <sup>46+</sup>	1.78
Sb-like W <sup>23+</sup>	1.27	Y-like W <sup>35+</sup>	2.15	Co-like W <sup>47+</sup>	0.60
Sn-like W <sup>24+</sup>	1.37	Sr-like W <sup>36+</sup>	2.05	Fe-like W <sup>48+</sup>	0.99
In-like W <sup>25+</sup>	1.47	Rb-like W <sup>37+</sup>	1.76	Mn-like W <sup>49+</sup>	0.99
Cd-like W <sup>26+</sup>	1.58	Kr-like W <sup>38+</sup>	1.76	Cr-like W <sup>50+</sup>	0.96
Ag-like W <sup>27+</sup>	1.52	Br-like W <sup>39+</sup>	1.10	V-like W <sup>51+</sup>	0.95
Pd-like W <sup>28+</sup>	1.52	Se-like W <sup>40+</sup>	1.33	Ti-like W <sup>52+</sup>	0.94
Rh-like W <sup>29+</sup>	1.62	As-like W <sup>41+</sup>	0.34	Sc-like W <sup>53+</sup>	0.95
Ru-like W <sup>30+</sup>	1.62	Ge-like W <sup>42+</sup>	0.26	Ca-like W <sup>54+</sup>	0.97
Tc-like W <sup>31+</sup>	1.62	Ga-like W <sup>43+</sup>	0.45	K-like W <sup>55+</sup>	0.98

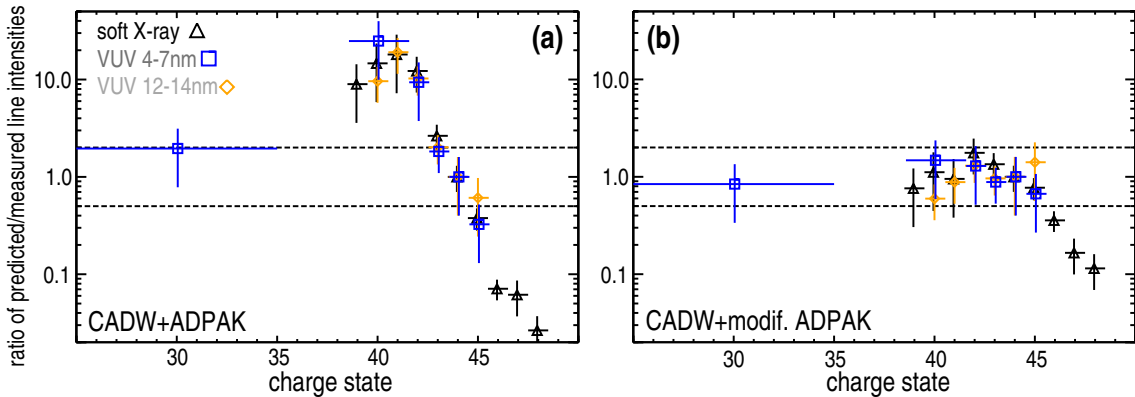
**Table 1.** Correction factor  $F_{corr}$  of the ADPAK recombination rate coefficients which are introduced for improved agreement with the experimental findings (temperature dependence of fractional abundances, relative weight of ionization stages).

to give an indication where the discrepancies are largest and to provide a set of rates, which is in agreement with experiment within the uncertainties. The measurements, however, are only available for most of the ionization stages between Sn-like W<sup>24+</sup> and Ni-like W<sup>46+</sup>. Due to this fact and since the uncertainties of this measurements leave some flexibility, the adjustments are not a unique solution and have been performed by hand. In principle, differences could also originate from recombination rates, which have a different shape versus electron temperature or due to different ionization rates - as the described discrepancies are not understood the choice of correction has no preference. Nevertheless, the investigations provide valuable feedback to fundamental cross section calculations.

Apart from the electron temperature dependence of the fractional abundances of ionization stages, also the absolute values could be investigated by comparing the total brightness of an ensemble of spectral lines of one ionization stage to that of other ionization stages using predictions for their brightness from atomic data. An ensemble of lines is

### Modelling of Measured Tungsten Spectra from ASDEX Upgrade and Predictions for ITER 11

chosen to rely less on the accuracy of the calculated emissivity for a single line. For these investigation, plasma discharges are used which exhibit a flat radial tungsten profile, as can be judged from the radiation profile and a tungsten diagnostics based on calibration discharges – described in [4]. In figures 8, 9 and 11 (discussed in section 4), the used spectral lines for each ionization stage are highlighted by small, black arrows. Some spectral lines have been omitted for this comparison if the identification was unclear or line blending occurred. The details of the atomic data calculations for predicting line intensities will be presented in the next section, however, the impact on the investigations on the ionization stage abundances is discussed here. In detail, the emissions from each ionization stage have been summed up for the soft X-ray region and two VUV regions. For each spectral region, this sum is then divided by the predicted line intensities resulting from a detailed modelling. All ratios are normalized such that the ratio for Zn-like  $W^{44+}$  equals 1. The latter normalization is because the absolute tungsten concentration is a free parameter when looking at the fractional abundances of each ionization stage. In figure 5, the results are presented for the data set ‘CADW+ADPAK’



**Figure 5.** (a) Ratios of predicted to measured line intensities for different wavelength ranges versus ionization stage using the ‘CADW+ADPAK’ ion balance (see figure 6). Several lines of an ionization stage are summed in the model and in the spectrum to reduce the uncertainties that could occur for a single spectral line. (b) Similar data as (a), but using the data set ‘CADW+modif. ADPAK’ which is described in the text. Dashed lines correspond to ‘factor of 2’-margin around 1 introduced to guide the eye.

and the set ‘CADW+modif. ADPAK’ demonstrating that the adjustments applied to the ADPAK recombination rates lead to an improvement also for the absolute values of fractional abundances. Whereas for the ‘ADPAK+CADW’ case, deviations for the ionization stages below Cu-like  $W^{45+}$  (including  $W^{45+}$ ) of up to a factor of 30 are observed, a reduction of that deviation to less than a factor of 2 is achieved with the modified recombination rates. For the ionization states above Ni-like  $W^{46+}$  (including  $W^{46+}$ ) the model underestimates the emissions for the unmodified case by up to a factor of 50 and the modifications reduce this maximum discrepancy to a factor of 10. The discrepancy is smallest for Ni-like  $W^{46+}$  (about factor of 3) and increases for higher charge. These discrepancies could not be corrected by the modification of the recombination rates using energy independent factors without sacrificing the above presented agreement in the relative shape of the abundance shells versus electron

### *Modelling of Measured Tungsten Spectra from ASDEX Upgrade and Predictions for ITER 12*

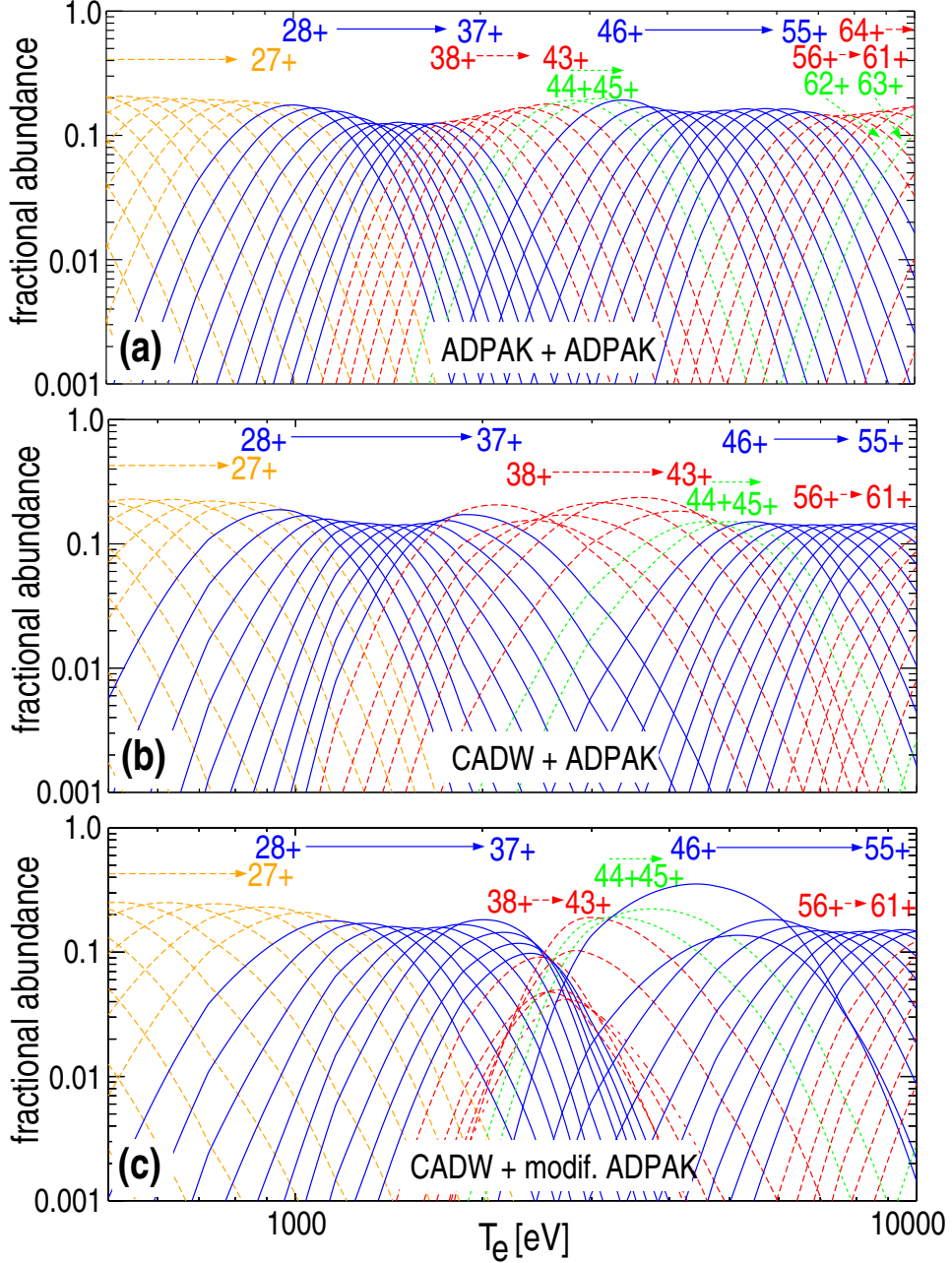
temperature. Possibly, energy dependent corrections are necessary. It should be noted, that weak impurity accumulation with an impurity peaking factor of about 3 might be undetected and cannot be excluded. This would lead to an increased contribution from exactly the ionization stages above Ni-like  $\text{W}^{46+}$ .

In figure 6, a comparison of the resulting ionization equilibria is presented. The two ionization equilibria depicted in figure 6 (b) and (c) exhibit a less continuous behaviour than that of the ‘ADPAK+ADPAK’ data in part (a). This structure corresponds to the more detailed information entering into the ionization rates, while additional structure is added by the adjustments of recombination rates. It may be noted that the combination of absolute and relative information on the fractional abundances also restricts the fractional abundances of ionization stages, for which no direct measurement is available, like Sr-like  $\text{W}^{36+}$  to Kr-like  $\text{W}^{38+}$ . Since the abundances of neighbouring ionization stages is measured to be high, the abundance of these ionization stages is suppressed. This consequence is in agreement with not observing spectral lines emitted by these ionization stages in the VUV region where bright enough lines are predicted by the code calculations. This also gives further support to the modifications to the ADPAK recombination rates, as the unmodified version would predict clearly visible spectral lines in the modelled spectra emitted by these ionization stages. In figure 7, some of the chosen rates are presented.

### 3. The modelling of spectra

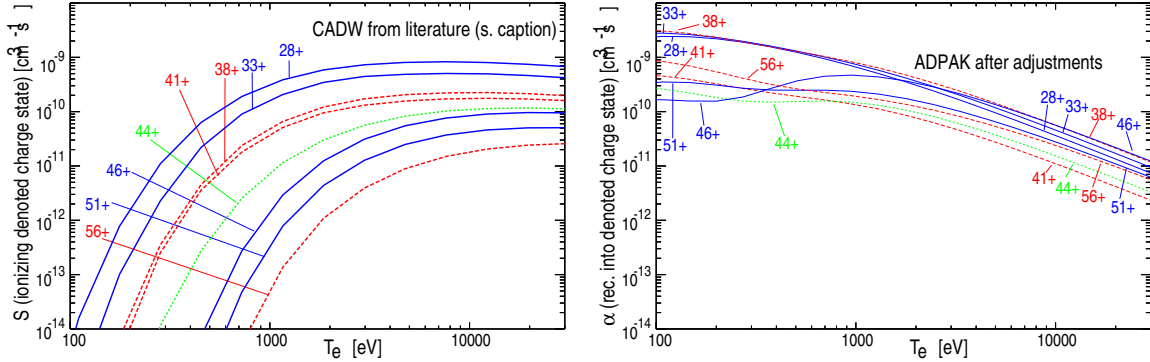
The modelling of the spectra involves several steps. With the Cowan code [15] fundamental properties of the emitting ions have been evaluated. For the ions of interest, energy levels and transition probabilities were calculated. Additionally, cross sections for electron-impact excitation have been targeted with the Cowan code by using the plane wave Born approximation resolving all levels of the target ions. All the data were then fed into a collisional-radiative model to derive emissivities of spectral lines in a plasma for densities of  $10^{18} \text{ m}^{-3}$  –  $10^{20} \text{ m}^{-3}$ . All codes are part of or have been integrated into a program suite provided by the ADAS (Atomic Data and Analysis Structure) Project [33]. Therefore, data originating from the present work will be labelled with ‘ADAS’. For comparison to measurements, these data were then used to produce synthetic spectra in the real geometry. The integration along the LOS of the spectrometer was numerically performed taking measured plasma shapes, plasma parameters, the ionization equilibrium as discussed in the preceding section and estimated transport coefficients into account. The exact values of the latter do not matter within a certain plasma radius as discussed in section 2. For investigations of the atomic data, plasmas which exhibit a flat impurity profile have been chosen. These are identified by the radiation profile and the calibrated tungsten emissions (see [4] for the calibration of tungsten emissions) with an accuracy of about factor 2.

The calculation results of an atomic code depends to a large extent on how accurate the wave functions are determined. Within the code, the wave functions are described using a linear combination of input wave functions (sets of input wave functions are specified by input configurations), such that the accuracy of the description depends on whether the right (or

*Modelling of Measured Tungsten Spectra from ASDEX Upgrade and Predictions for ITER 13*


**Figure 6.** (a) Transport-free fractional abundances of tungsten ionization stages for zero electron density using ADPAK ionization and recombination data from [9], which were modified according to [4]. Numbers denote the ionization stage. Line styles and colors group ions with the same ‘outermost’ subshell; (b) Same as (a), but ionization rates taken from [32]; (c) Same as (b), while recombination rates have been modified (see table 1) according to experimental findings.

large enough) set of input wave functions was chosen for the calculation. As the plane wave Born approximation is a comparably fast method large sets of input configurations could be used. Determining the best choice of input configurations led to extensive testing on ionization

*Modelling of Measured Tungsten Spectra from ASDEX Upgrade and Predictions for ITER 14*


**Figure 7.** Ionization rates  $S$  from [32] and recombination rates  $\alpha$  obtained by modifying ADPAK data for several ionization stages of tungsten. Both data sets are used to obtain the ionization equilibrium labelled ‘CADW+modif.ADPAK’. Colors and line styles correspond to those in figure 6

stages above Cd-like  $W^{26+}$ . For lower charge stages the number of levels were too large to arrive at an unambiguous configuration set. (for lower charges the calculations get very large, see below). For that purpose, the fast plane wave Born approximation is advantageous compared to other calculation methods like distorted-wave or  $R$ -matrix calculations. The results for electron impact cross sections at high electron energies are considered to be of good quality [15], while the more elaborate methods provide better quality at low electron energies. As a drawback, the plane wave Born approximation lacks the possibility of spin changes during an electron collision, which might influence the resulting line strengths. However, this drawback is typically less important for high-Z elements, as the total spin quantum number is not well defined. The plane-wave Born approximation and the distorted wave calculations both lack the possibility of taking resonances in the cross sections at low electron energies into account, which has impact on the excitation rates in a plasma. Unfortunately,  $R$ -matrix calculations, which could handle such effects consume a lot of computing time, such that only certain ionization stages can be targeted today [34, 35]. Another problem occurs for many ionization stages below Sn-like  $W^{24+}$ , as open 4f-shells occur, which leads to thousands of levels for relatively small set of input configurations (e.g. 3401 levels for I-like  $W^{21+}$  with  $4d^{10}4f^6$  and  $4d^94f^7$ ). Even the version of the Cowan code, which was used in this work, could not perform the electron collision calculations with this vast amount of levels. Nevertheless, some of the ions with open 4f-shells could be targeted by the Cowan code.

Bearing the above in mind, the implications for the following modelled spectra are that line intensities of single spectral lines might exhibit larger uncertainties (estimated to be ranging up to factors of about 2-3), but the overall intensity emitted by an ionization stage should be described more accurately, because deviations of calculated excitations cross sections should not be systematic.

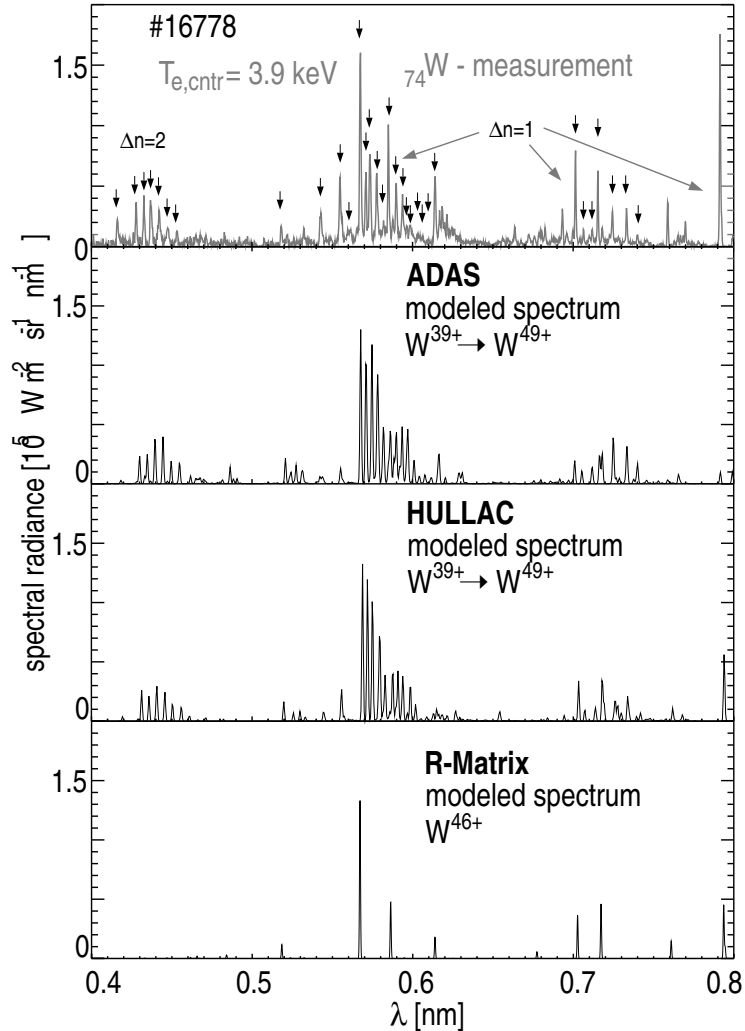
## *Modelling of Measured Tungsten Spectra from ASDEX Upgrade and Predictions for ITER 15*

### **4. Strong Spectral Features of Tungsten**

For diagnostic purposes a good signal to noise ratio is important. Especially in ITER or a reactor, W will be abundant in very small concentrations ( $< 10^{-4}$  for manageable radiative losses) and at the same time a considerable level of Bremsstrahlung and additionally neutron radiation will be abundant contributing to background noise. Therefore, the main focus is placed on strong spectral emissions.

#### *4.1. Spectral feature at 0.4 – 0.8 nm*

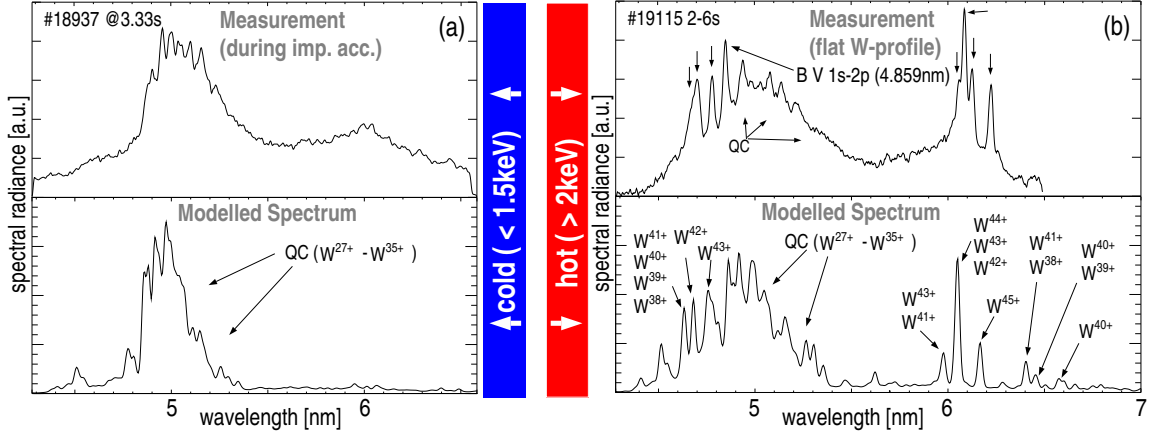
Many spectral lines in this range have been identified earlier by [5, 6, 8]. In the present work, a comparison between the measured and modelled spectra is presented, while for the modelling the emissivity of spectral lines calculated by HULLAC [36] and the Cowan code is used. The ionization stages of Br-like W<sup>39+</sup> to Mn-like W<sup>49+</sup> contribute considerable spectral lines in this range. The emissions of the Ni-like W<sup>46+</sup> are additionally compared using data from a *R*-matrix calculation [34]. Figure 8 presents the measured spectrum together with the modelled ones. The wavelength predictions of all calculations agree better than 0.002 nm. The measured spectrum was obtained in a discharge with a tungsten concentration of about  $2 \cdot 10^{-4}$ , which is obtained by the method explained in [4]. The W concentration profile is flat, while a weak central impurity accumulation with impurity peaking of up to a factor of 3 in a very small central region cannot be excluded within the uncertainties. The comparison is performed by using this concentration in the modelling of all spectra. Most of the lines are modelled within a factor of 2 compared to the measurement. Differences between the models are small. A large difference between modelling and measurement is found at 0.793 nm. The ADAS, HULLAC and *R*-matrix based models are too small by a factor of about 10, 3 and 3, respectively. The HULLAC modelling would be further away than only a factor of 3, if corrections due to excitation following inner-shell-ionization had not been included in the line intensity. In the *R*-matrix case, these contributions are neglected, however, the blending of a magnetic octopole line [37, 34] ([37] a distorted-wave calculation was performed and the data in [34] corresponds to the presented *R*-matrix modelling), is taken into account. In [37] the contribution from this line was more significant than in the modelled spectra in figure 8 possibly because the modelling was done for a monoenergetic electron beam at 4.06 keV, which results in a stronger magnetic octopole line compared to a Maxwellian electron velocity distribution. Even if both mentioned corrections are applied, the modelling cannot match up completely with the measured line intensity. For the modelling with ADAS data the described effects are neglected and additionally, a populating process from a higher (in energy) level identified in [37] is not taken into account. This is, because the plane wave Born approximation cannot be used to calculate the excitation of that higher level, as a spin changing transition is necessary to populate that level. Therefore, it is understood why the result of the ADAS calculations exhibits the largest discrepancies for this particular spectral line. Apart from this transition the Cowan code is a good model of the remaining lines and is therefore well suited to being used to generate spectra at baseline quality in a fast manner.

*Modelling of Measured Tungsten Spectra from ASDEX Upgrade and Predictions for ITER 16*

**Figure 8.** Strong spectral feature emitted by Br-like  $\text{W}^{39+}$  to about Mn-like  $\text{W}^{49+}$  in the soft X-ray range (scanning Bragg crystal spectrometer). The measurement is compared to the modelling based on ADAS data (this work), HULLAC data [36] and *R*-matrix data [34] (only  $\text{W}^{46+}$ ) at a concentration of  $2 \cdot 10^{-4}$ . Small arrows indicate the spectral lines used in section 2 for quantifying fractional abundances of ionization stages.

#### 4.2. Quasicontinuum around 5 nm

In this spectral range the most intense feature emitted from ASDEX Upgrade plasmas is found which has been the focus of earlier investigations [2, 3, 11, 12, 14]. It consists of hundreds of spectral lines emitted by ionization stages from possibly as low charged ions as I-like  $\text{W}^{21+}$  up to about Kr-like  $\text{W}^{38+}$ , while the strongest emissions originate between Ag-like  $\text{W}^{27+}$  to Y-like  $\text{W}^{35+}$ . In figure 9(a), the spectral feature is presented along with the modelled result. A discharge with impurity accumulation is chosen to highlight the emissions at about 1.5 keV electron temperature. The ‘main’ peak at 4.8 nm to about 5.4 nm is observed in the modelling exhibiting some difference in shape. These differences might be a result of the ionization balance, which could not be optimized to such detail. The influence of the

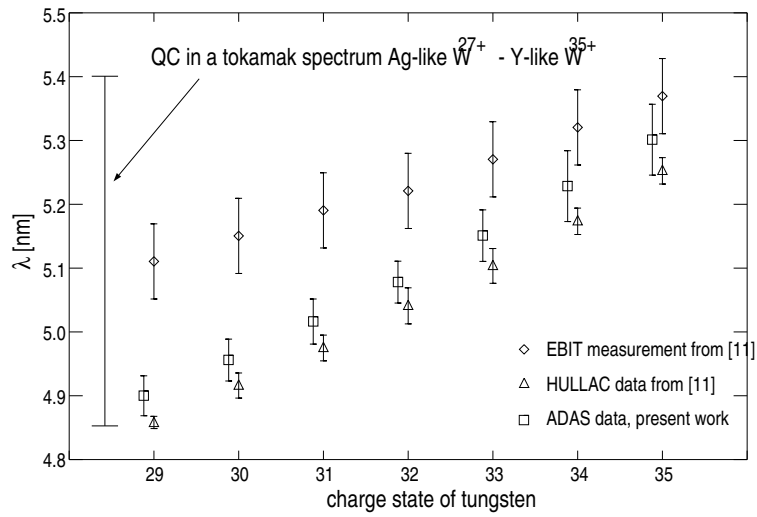
*Modelling of Measured Tungsten Spectra from ASDEX Upgrade and Predictions for ITER 17*


**Figure 9.** (a) Emissions of Ag-like  $W^{27+}$  – Y-like  $W^{35+}$  (grazing incidence spectrometer) during a discharge with impurity accumulation highlighting these ionization stages and modelled spectra using a peaked W-profile. (b) Same spectral range at higher  $T_e$  and flat W-profile, exhibiting additional spectral lines emitted by ionization stages up to  $W^{45+}$  and the corresponding modelling. The emissions depicted in part (a) are still visible because the LOS passes also through colder plasma at the plasma edge. Small arrows indicate the spectral lines used in section 2 for quantifying fractional abundances of ionization stages.

ionization balance is directly influencing the shape of the feature, because each ionization stage between Rh-like  $W^{29+}$  to Y-like  $W^{35+}$  contributes a spectral band consisting of many spectral lines with a width of about 0.15 nm to the quasicontinuum peak. For higher ion charges the emitted band is shifted to longer wavelengths. The compound emissions of all the ionization stages is forming the envelope of the quasicontinuum, which exhibits a width of about 0.5 nm. This systematical dependence has been shown earlier [11, 14]. The wavelengths of the actual modelling agree within 0.05 nm with the calculations from [11] performed by the atomic code HULLAC [36]. However, the wavelengths measured in [11] exhibit discrepancies compared to the calculations. Additionally, the tokamak measurements can not be explained fully as a superposition of the measured spectra in [11]. Figure 10 presents the predicted and measured wavelengths and widths of the spectral feature from [11] and the present work, while the wavelength range of the whole quasicontinuum as measured in ASDEX Upgrade is also indicated. According to the latter, taking the EBIT measurements into account, the emissions between 4.85 nm and 5.05 nm in the tokamak spectrum should originate from Ag-like  $W^{27+}$  and Pd-like  $W^{28+}$ . In the modelling emissions from these ionization stages are found, however, they do not fill the full wavelength range between 4.85 nm and 5.05 nm and a discrepancy remains. It should be noted, that the identification of these ionization stages from the EBIT measurements is not straightforward, as several ionization stages coexist in this energy range. This is the case, because the ionization potentials are separated by only 50 – 70 eV for the ionization stages with several 3d-electrons in the ground state configuration. A further complication might arise, because the modelling also predicts emissions from ionization stages with lower charges than Ag-like  $W^{27+}$  down to I-like  $W^{21+}$  with brightnesses of about the same level than for the above mentioned ionization

### Modelling of Measured Tungsten Spectra from ASDEX Upgrade and Predictions for ITER 18

stages. These predicted emissions are covering the full peak width from 4.8 nm to about 5.4 nm for each ionization stage, but have not been observed in the EBIT investigations. For the tokamak spectra a contribution from these ionization stages seems probable, because the emissions at 5 nm reach their maximum at about 1 keV electron temperature, which can only be explained by a contribution from these lower charged ions or by drastic changes of ionization or recombination rates.



**Figure 10.** Wavelengths and spectral widths (indicated by bars) of the emissions responsible for the quasicontinuous structure around 5 nm from experiment and calculations. The ADAS data points (present work) have been displaced horizontally for better display.

At 5.7 nm to about 6.3 nm a less intense spectral feature is visible in the measurement, which is not seen to the same extent in the modelling. It is unclear, why this is the case, but as these emissions always coexist with the main peak of the quasicontinuum it is apparent that the emitting ionization stages are also in the range between I-like  $W^{21+}$  and Y-like  $W^{35+}$ .

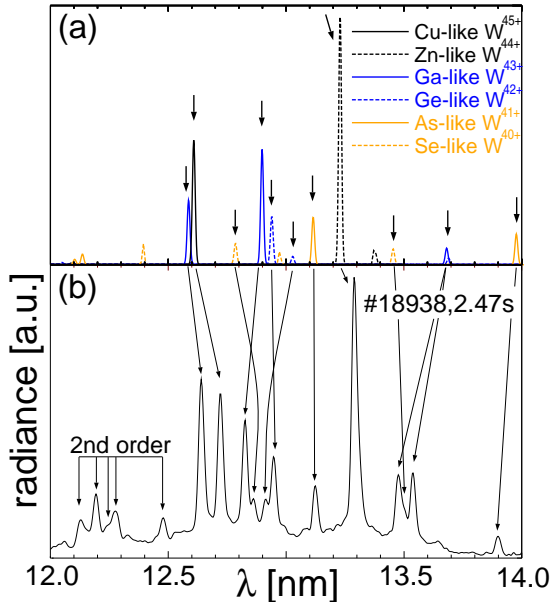
As reported earlier [4, 11, 12, 14] additional spectral lines are emitted by ionization stages of tungsten up to Cu-like  $W^{45+}$  which are superimposed on the quasicontinuous emissions, when the central part of the plasma is hotter than about 2 keV. The quasicontinuum is still visible in the spectra, because the line of sight of the spectrometer is crossing colder parts of the plasma where W-ions with lower charge stages exist. In figure 9(b) this case is presented along with the modelling (note that this spectrum originates from a discharge with a flat W-concentration profile). The intensity of spectral lines and quasicontinuous emissions agree relative to each other within the uncertainties. In agreement with the findings from [14], the structure at 4.7 nm can also be well understood by the modelled data as the Kr-like  $W^{38+}$  to about  $W^{41+}$  exhibit emissions with the right intensity and temperature dependence at this wavelength. It should be noted, that the wavelengths of modelled spectral lines in figure 9 result directly from the Cowan code calculations which is not fully relativistic but uses correction terms in the Hamiltonian, while for table 2 the theoretical wavelengths of many spectral lines have been recalculated by the fully relativistic code GRASP. This was

## Modelling of Measured Tungsten Spectra from ASDEX Upgrade and Predictions for ITER 19

done because in the VUV the discrepancies in wavelength between modelling using the Cowan code and measurement show up clearly being in the range of about 0.1-0.15 nm ( $\Delta\lambda/\lambda \approx 1.5 - 3 \%$ ) unlike for the SXR range where the discrepancies were below 0.002 nm ( $\Delta\lambda/\lambda \approx 0.3 \%$ ). A list of lines, which are well suited for diagnostics is given in table 2. Additional line identifications can be found in [4, 11, 12, 14].

### 4.3. Spectral Lines at 12 – 14 nm

In this wavelength range emissions of Se-like W<sup>40+</sup> to Cu-like W<sup>45+</sup> are observed. In figure 11, a measured and modelled spectrum are compared. The line identification has been



**Figure 11.** (a) Modelled W-emissions around 13 nm. The emissivities of the spectral lines have been evaluated by ADAS calculations, while wavelengths have been corrected with the help of GRASP calculations afterwards. Small arrows indicate the spectral lines used in section 2 for quantifying fractional abundances of ionization stages. (b) Measured W-emissions (grazing incidence spectrometer) around 13 nm. Line identifications can be found in [14, 13].

done in [14]. The wavelengths of the modelled lines are in this case corrected using the structure calculations of GRASP [38], which is a fully relativistic code. GRASP reproduces the wavelengths within a typical accuracy of 0.1 – 0.2 nm in this spectral range, which is better than the Cowan code, which exhibited discrepancies of up to 0.5 nm. For diagnostic of tungsten in a fusion plasma, the spectral lines in this wavelength range are well suited, because several spectral lines are well isolated. However, there are tungsten emissions from plasma temperatures below 1 keV, which might blend with these spectral lines in special cases like described in the next subsection.

### *Modelling of Measured Tungsten Spectra from ASDEX Upgrade and Predictions for ITER 20*

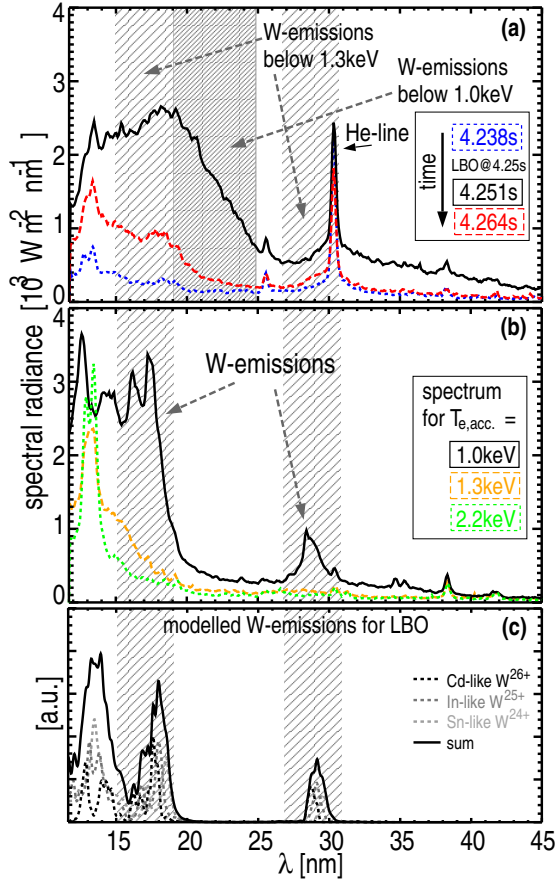
#### 4.4. Quasicontinuum at 10 – 30 nm

At 10 – 30 nm many spectral lines overlap which are emitted from different ionization stages that exist below electron temperatures of about 1.3 keV. Similar to the quasicontinuum around 5 nm, the emissions exhibit a dependence on electron temperature, which allows for deducing the emitting ionization stage. In figure 12(a), the time sequence after a W-injection by laser ablation is presented. Due to the fast rise of the emissions between 10 – 30 nm it is clear that the emitting ionization stages must be located in the plasma edge. A quantitative comparison of the timescales for the emissions between 10 – 30 nm and the emissions around 5 nm revealed that the emitting ionization stages of the first emissions are lower charged than Pd-like  $W^{28+}$ . In figure 12(b) the emissions during impurity accumulation are detected from the central part of the plasma, while the central temperature is slowly dropping below 1.3 keV. Clearly, the emissions around 18 nm originate from the accumulation region possibly from the ionization stages Ag-like  $W^{27+}$  to about Sn-like  $W^{24+}$ . Just below 30 nm additional emissions are observed from the same ionization stages as deduced from the temporal behaviour of the spectral feature. The comparison of figure 12(a) and 12(b) implies that between about 19 nm and 27 nm spectral lines emitted at electron temperatures below 1.0 keV can be found. These lines are not visible for electron temperatures above 1.0 keV (figure 12(b)), while in figure 12(a) the emissions are visible after the laser ablation increased the tungsten density at the plasma edge, i.e. at electron temperatures from about 10 eV to 1000 eV. The presented emissions are distributed over a wide spectral range. They are barely detectable in the spectrum, unless impurity accumulation occurs which cools down the central accumulation region plasma to low enough temperatures, or W is injected into the plasma which increases the W-concentration at the edge drastically.

The modelling results presented in figure 12 support the experimental findings that the strong emissions around 18 nm originate from the ionization stages Cd-like  $W^{26+}$  to Sn-like  $W^{24+}$ , while the unaccounted emissions between 19 nm and 27 nm could be the emissions of Sb-like  $W^{23+}$  to Nd-like  $W^{14+}$ . Modelling is limited to the ionization stages above Sn-like  $W^{24+}$ . The atomic calculations are difficult for lower charged ionization stages, because the ground state of Sn-like  $W^{24+}$  is contained in the configuration  $4d^{10} 4f^4$ , while the most important excited configuration is  $4d^9 4f^5$ , yielding a total of 1985 levels. The emissions between 10 – 30 nm contain contributions from the configurations  $4f^3 5s$ ,  $4f^3 5p$ ,  $4f^3 5d$  and  $4f^3 5f$ , while  $4f^3 5g$  does not strongly influence the emissions in the considered spectral range. Given the boundary conditions of the available code, the calculations for lower charged ions was not possible to the same detail than for Cd-like  $W^{26+}$  to Sn-like  $W^{24+}$ .

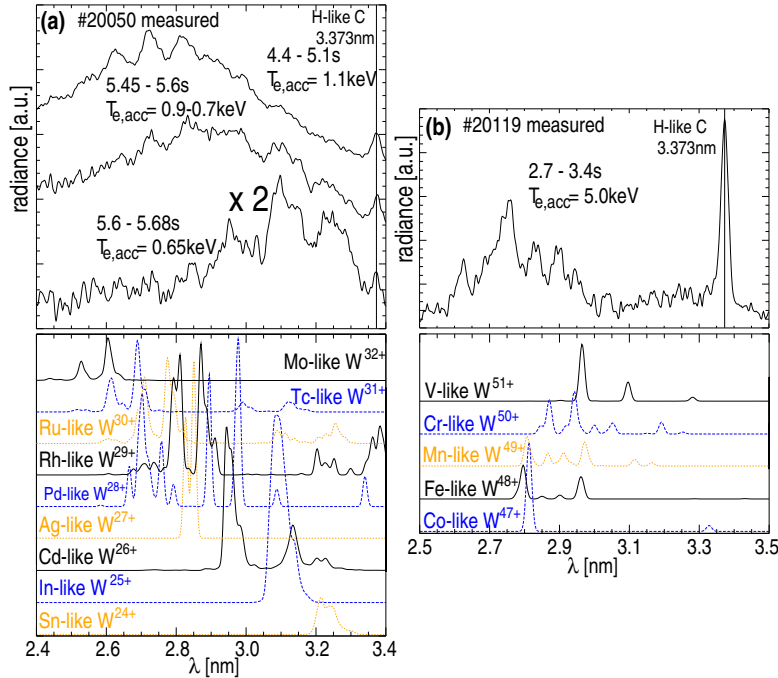
## 5. Additional Observations

In many spectral regions, emissions of tungsten are apparent during impurity accumulation because comparably weak emissions get enhanced by this phenomena, such that the spectral lines rise above the limit of detection. In the following, some of these features are briefly reported. In figure 13(a), a spectral feature is presented, which could be identified in

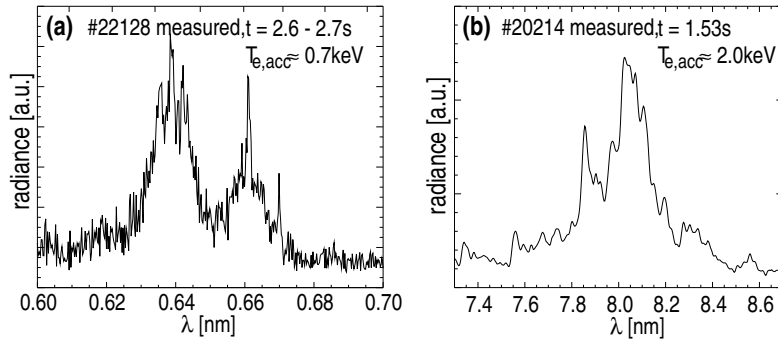
*Modelling of Measured Tungsten Spectra from ASDEX Upgrade and Predictions for ITER 21*


**Figure 12.** (a) Measured W-emissions (SPRED spectrometer) before and after W injection by laser ablation. The short time constant of the emissions demonstrates that the emissions take place at the very plasma edge. (b) Measured W-emissions (SPRED spectrometer) around 18 nm during impurity accumulation, where  $T_e$  in the accumulation region ( $T_{e,acc.}$ ) drops from 2.2 keV to 1.0 keV. (c) Modelled W-emissions during a LBO, for a few ionization stages only, as calculations for lower ionization stages than Sn-like  $W^{24+}$  could not be performed in the necessary detail.

the modelling as being emitted by ionization stages below Mo-like  $W^{32+}$  down to Sn-like  $W^{24+}$ . These emissions have already been reported and analyzed in [3, 39], while their behaviour versus electron temperature is documented in the present work. In figure 13, also the theoretical predictions of ADAS (intensity and wavelength) for each contributing ionization stage are presented, which originate from transitions between the configurations  $4d^{10}4f^n$  and  $4d^94f^n5p/4d^{10}4f^{n-1}5g$  for ionization stages below Ag-like  $W^{27+}$  (inclusive) and between  $4d^n$  and  $4d^{n-1}5p$  for the ionization stages above. For the ionization stages Rh-like  $W^{29+}$  to Tc-like  $W^{31+}$  also contributions from  $4d^n$  to  $4d^{n-1}5s$  are predicted between 2.9 and 3.5 nm. The presented modelling assumes equal abundances of ionization stages. The wavelength-shift of the spectral feature for decreasing electron temperature represents a change of the ionization equilibrium. This direction of the wavelength shift is in agreement with increasing wavelengths of the predicted spectral lines for decreasing ionization stages.

*Modelling of Measured Tungsten Spectra from ASDEX Upgrade and Predictions for ITER 22*

**Figure 13.** (a) Emissions at  $T_e \leq 1.1\text{keV}$  (grazing incidence spectrometer) during impurity accumulation together with ADAS modelling for corresponding ionization stages presented beneath. The measurement at  $T_{e,acc} = 0.65\text{keV}$  was scaled by factor of 2. Each spectrum is shifted on the intensity axis for better visibility.(b) Emissions at  $T_e \approx 5\text{keV}$  (grazing incidence spectrometer) during impurity accumulation together with ADAS modelling presented beneath.



**Figure 14.** (a) Emissions at  $T_e \approx 0.7\text{keV}$  (scanning Bragg crystal spectrometer) during impurity accumulation. (b) Emissions at  $T_e \approx 2\text{keV}$  (grazing incidence spectrometer) during impurity accumulation.

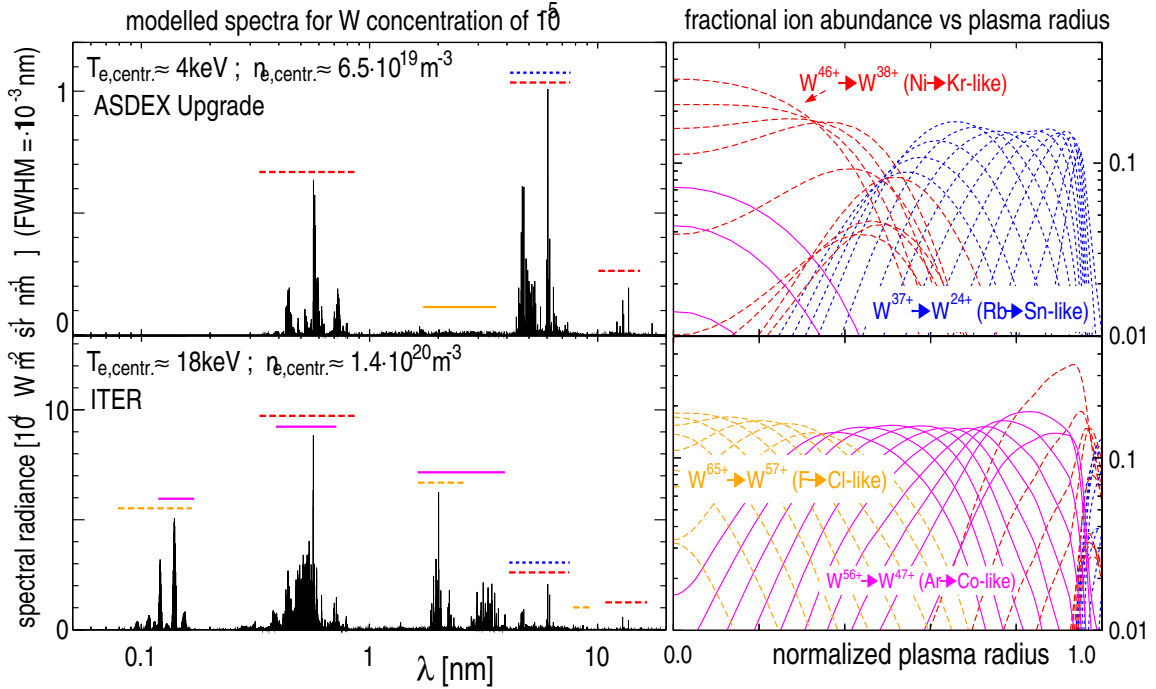
In figure 13 (b), spectral lines of highly charged W are presented, which are observed in the same spectral range. The wavelengths of the modelling do not agree well enough to identify all spectral lines. The configurations, which are responsible for the modelled spectral lines are  $3p^63d^n$  and  $3p^53d^{n+1}$ . These lines being emitted by ionization stages above Ni-like W<sup>46+</sup> prove to be very important for diagnosing W in hot JET plasmas or in ITER, where Ni-like

### *Modelling of Measured Tungsten Spectra from ASDEX Upgrade and Predictions for ITER 23*

$\text{W}^{46+}$  will only exist in the outer half of the plasma (see next section). In figure 14 (a) and (b) two features are depicted, which could not be found in the modelling. From the electron temperature range, in which they have been emitted, conclusions about the emitting ionization stage can be drawn. The emissions in figure 14 (a) are emitted by ionization stages well below Sr-like  $\text{W}^{36+}$  as the electron temperature of 0.7 keV suggests the abundance of I-like  $\text{W}^{21+}$  to about Pd-like  $\text{W}^{28+}$ . The photon energy ( $\geq 1.85$  keV) for the presented emissions is more than the ionization potential (for Sr-like  $\text{W}^{36+}$  the ionization potential is 1.591 keV according to [40]) of the abundant ionization stages. Therefore, this feature is possibly emitted during the process of dielectronic recombination, which is not included in the spectral modelling. Figure 14 (b) depicts W emissions at 8 nm, which are emitted by ionization stages between Sr-like  $\text{W}^{36+}$  and Zn-like  $\text{W}^{44+}$ .

## 6. Predictions for ITER

In figure 15, the modelling predictions for a typical ASDEX Upgrade and ITER plasma are presented. While in the right column the fractional abundances of W ionization stages are depicted, the modelled spectra are presented on the left. In the case of ASDEX Upgrade a H-mode discharge with average performance was chosen (central electron parameters are given in the figure). The ITER case is based on the calculated electron profiles in [41]. A radial viewing geometry at the midplane is used for the modelled spectra. Absolute numbers are given for the spectral brightness. The modelled results of ASDEX Upgrade depicted in figure 15 reproduce the most important spectral features observed in experiment (see above). In ITER, central electron temperatures of 18 keV and above (e.g. advanced scenarios) are envisaged. The current experience with W spectroscopy provides an insight into the outer part of an ITER plasma. An appraisal of the full diagnostic capability of spectroscopic measurements of W relies on models. The predictions are intended to demonstrate the diagnostic needs for such a plasma, while the exact weighting of ionization states and line intensities contain larger uncertainties than the modelling for lower electron temperatures as less experimental background information is available. For plasma transport a rough estimation was used, which is  $0.5 \text{ m}^2/\text{s}$  increasing to  $2 \text{ m}^2/\text{s}$  from the core plasma to the pedestal top for the diffusion coefficient. The drift velocity was adjusted such that a constant W concentration is found inside the pedestal top. The diffusion coefficient and drift velocity are chosen such that their magnitude is comparable with the findings of actual tokamaks. This is an assumption, because there is no precise prediction for ITER and it is beyond the scope of this work to provide detailed transport coefficients. However, for the ionization equilibrium in the confined plasma, the large ionization and recombination rates make plasma transport unimportant compared to low-Z impurities. Apart from the assumptions on the shape of the W concentration profile, the W source was adjusted such that an ITER-relevant W concentration of  $10^{-5}$  is found in the plasma. From mid-radius to the plasma center Cr-like  $\text{W}^{50+}$  to C-like  $\text{W}^{68+}$  or maybe for special discharges even He-like  $\text{W}^{72+}$  might exist in a diagnosable abundance. To allow for a possible extrapolation the ionization equilibrium for electron temperatures between 5 keV and 40 keV is presented in figure 16. In this temperature range,

*Modelling of Measured Tungsten Spectra from ASDEX Upgrade and Predictions for ITER 24*


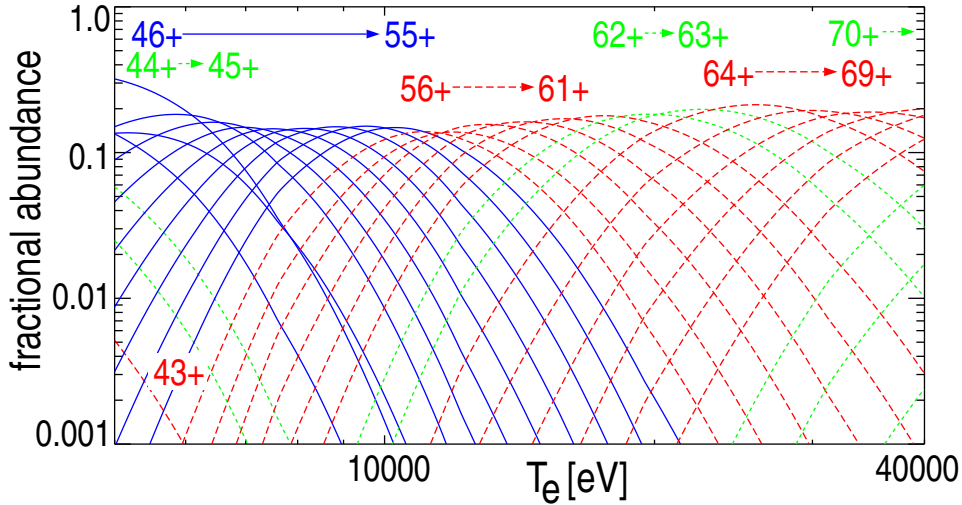
**Figure 15.** Modelling results and predictions for a typical ASDEX Upgrade plasma and the standard ITER scenario. In the left column the predicted spectra are presented. The fractional abundances of ionization stages vs. normalized plasma radius ( $\rho_{pol}$ ) are depicted in the right column. The horizontal lines on the left indicate the emitting ionization stages by the line style and brightness, corresponding to the line style and brightness in the right column.

the adjustments of the ionization equilibrium performed in section 2 do not play a significant role. Hence, the equilibrium probably exhibits deviations from experiments. Already for the upcoming ITER-like wall project [42] at JET, the diagnosis of W at electron temperatures above 6 keV will be of interest which requires the measurement and interpretation of the emissions from ionization stages above Cr-like  $W^{50+}$ .

In detail, the interesting wavelength regions for diagnosing the ionization stages between Co-like  $W^{47+}$  to Ar-like  $W^{56+}$  are the ranges 0.1–0.15 nm, 0.4–0.7 nm and 2.7–4.0 nm. For the ionization stages Cl-like  $W^{57+}$  to  $W^{70+}$  the wavelength ranges 0.1–0.15 nm, 1.8–2.4 nm and the region around 8 nm are of interest. Therefore, it seems that especially the ranges at 0.1–0.15 nm and at 1.8–4.0 nm are capable to provide information about tungsten from mid-radius to the center of the ITER plasma. These findings should be verified and quantified by performing dedicated experiments in fusion plasmas and also in EBIT devices, while the theoretical effort should be focussed on improving the accuracy of the key diagnostic stages.

## 7. Spectral Emissions Suited for Diagnostics

In table 2, an overview on recommended diagnostic lines is given, which have been verified by experiments. This table is not a complete list, but contains promising candidates

*Modelling of Measured Tungsten Spectra from ASDEX Upgrade and Predictions for ITER 25*


**Figure 16.** Transport-free ionization equilibrium for electron temperatures between 5 keV and 40 keV at zero density using ionization rates from [32] and ADPAK recombination rates, which have been modified according to the experimental findings ('CADW+modif. ADPAK', see table 1).

for diagnosing tungsten at various electron temperatures, i.e. different ionization stages. Calculated and measured wavelengths, configurations and terms are given. In cases, where no LS-coupled term contributes a major part of the wavefunction (less than 50%) the J values and the transition probability A is given to identify the transition. To indicate possible problems with line blending the last column was introduced, in which B and BL are denoted for line blending of ionization stages of similar/same charge (B) and considerably lower charge (BL). If an additional '\*' is specified, the line blending is more severe. It may be noted that problems of line blending depend on the specifications of spectrometer hardware – therefore, the given indications may have to be reconsidered for different hardware. In table 3 predictions of spectral lines are listed, which look promising for future diagnostics in JET, ITER or a reactor. For these predictions, also a column is given for anticipated line blending, derived from modelling, which assumed similar hardware than present on ASDEX Upgrade. In that respect, the emissions at 0.1 – 0.15 nm seem to be well suited for central tungsten diagnostics, as emissions from lower charged ions are not blended with the spectral lines.

## 8. Summary

Detailed experimental investigations on W spectra at ASDEX Upgrade along with modelling efforts using fundamental atomic data calculations have been performed to provide more insight in the characteristics of the spectral emissions of W. Recommendations for quantitatively diagnosing tungsten at various electron temperatures in fusion plasmas and an overview of spectral features found in the spectra of tungsten have been presented. Spectroscopic measurements during the transport phenomenon of impurity accumulation

*Modelling of Measured Tungsten Spectra from ASDEX Upgrade and Predictions for ITER 26*

Ion	I.P. (eV)	$\lambda_{calc}$ (nm)	$\lambda_{tok}$ (nm)	transition/configurations	blend.
$\approx W^{14+} - \approx W^{28+}$ (Nd-like – Pd-like)	325.3 – 1132	10-30	10-30	many (cf. text)	B
$\approx W^{21+} - W^{35+}$ (I-like – Sr-like)	594.5 – 1512	4.5-6.5	4.5-6.5	$\leq W^{28+}: 4d^9 4f^{n+1} - 4d^{10} 4f^n$ $> W^{28+}: (4p^6 4d^{n-1} 4f)/(4p^5 4d^{n+1}) - 4p^6 4d^n$	B B
$W^{39+}$ (Br-like)	1883	6.403 (G)	6.457	$4s^2 4p^5 {}^2P_{3/2} - 4s^2 4p^4 4d {}^2F_{5/2}$	BL*
$W^{40+}$ (Se-like)	1941	6.243 (G) 12.786 (G) 13.455 (G)	6.268 12.864 13.487	$4s^2 4p^4 {}^3P_2 - 4s 4p^5 {}^3P_2$ $4s^2 4p^4 {}^3P_2 - 4s^2 4p^4 {}^1D_2$ $4s^2 4p^4 {}^3P_2 - 4s^2 4p^4 {}^3P_1$	BL* B* B*
$W^{41+}$ (As-like)	1995	6.482 (G) 13.106 (G) 13.968 (G)	6.481 13.121 13.896	$4s^2 4p^3 {}^2D_{3/2} - 4s 4p^4 {}^4P_{5/2}$ $4s^2 4p^3 {}^2D_{3/2} - 4s^2 4p^3 {}^2D_{5/2}$ $4s^2 4p^3 {}^2D_{3/2} - 4s^2 4p^3 {}^4S_{3/2}$	BL*
$W^{42+}$ (Ge-like)	2149	0.5818 (C) 0.5823 (C) 0.6010 (C) 4.685 (G) 6.115 (G) 12.940 (G) 13.029 (G) 13.690 (G)	0.583 0.583 0.601 4.718 6.123 12.945 12.912 13.475	$3d^{10} 4s^2 4p^2 {}^3P_0 - 3d^9 4s^2 4p^2 4f J = 1$ ( $A = 2.5 \cdot 10^{14} s^{-1}$ ) $3d^{10} 4s^2 4p^2 {}^3P_0 - 3d^9 4s^2 4p^2 4f J = 1$ ( $A = 1.5 \cdot 10^{14} s^{-1}$ ) $3d^{10} 4s^2 4p^2 {}^3P_0 - 3d^9 4s^2 4p^2 4f J = 1$ ( $A = 1.3 \cdot 10^{14} s^{-1}$ ) $4s^2 4p^2 {}^3P_0 - 4s^2 4p 4d {}^3D_1$ $4s^2 4p^2 {}^3P_0 - 4s 4p^3 {}^3D_1$ $4s^2 4p^2 {}^3P_0 - 4s^2 4p^2 {}^1D_2$ $4s^2 4p^2 {}^3P_1 - 4s 4p^3 {}^3P_2$ $4s^2 4p^2 {}^1D_2 - 4s 4p^3 {}^3P_2$	B B B B*, BL B*, BL B B B
$W^{43+}$ (Ga-like)	2210	0.5798 (G) 0.5801 (G) 0.5988 (G) 0.5989 (G) 4.760 (G) 6.020 (G) 6.119 (G) 12.587 (G) 12.899 (G) 13.682 (G)	0.579 0.579 0.598 0.598 4.791 6.063 6.135 12.639 12.824 13.534	$3d^{10} 4s^2 4p {}^2P_{1/2} - 3d^9 4s^2 4p 4f J = \frac{1}{2}$ ( $A = 3.7 \cdot 10^{14} s^{-1}$ ) $3d^{10} 4s^2 4p {}^2P_{1/2} - 3d^9 4s^2 4p 4f J = \frac{3}{2}$ ( $A = 4.0 \cdot 10^{14} s^{-1}$ ) $3d^{10} 4s^2 4p {}^2P_{1/2} - 3d^9 4s^2 4p 4f J = \frac{3}{2}$ ( $A = 1.3 \cdot 10^{14} s^{-1}$ ) $3d^{10} 4s^2 4p {}^2P_{1/2} - 3d^9 4s^2 4p 4f J = \frac{1}{2}$ ( $A = 1.3 \cdot 10^{14} s^{-1}$ ) $4s^2 4p {}^2P_{1/2} - 4s^2 4d {}^2D_{3/2}$ $4s^2 4p {}^2P_{1/2} - 4s 4p^2 {}^2P_{1/2}$ $4s^2 4p {}^2P_{1/2} - 4s 4p^2 {}^2D_{3/2}$ $4s^2 4p {}^2P_{1/2} - 4s^2 4p {}^2P_{3/2}$ $4s^2 4p {}^2P_{1/2} - 4s 4p^2 {}^4P_{1/2}$ $4s^2 4p {}^2P_{3/2} - 4s 4p^2 {}^2D_{5/2}$	B B B B BL B*, BL B*, BL B
$W^{44+}$ (Zn-like)	2355	0.5749 (G) 0.5938 (G) 6.073 (G) 13.230 (G)	0.575 0.595 6.093 13.287	$3d^{10} 4s^2 {}^1S_0 - 3d^9 4s^2 4f {}^1P_1$ $3d^{10} 4s^2 {}^1S_0 - 3d^9 4s^2 4f {}^3D_1$ $4s^2 {}^1S_0 - 4s 4p {}^1P_1$ $4s^2 {}^1S_0 - 4s 4p {}^3P_1$	B, BL
<i>continued</i>					

*Modelling of Measured Tungsten Spectra from ASDEX Upgrade and Predictions for ITER 27*

Ion	I.P. (eV)	$\lambda_{calc}$ (nm)	$\lambda_{tok}$ (nm)	transition/configurations	blend.
$W^{45+}$ (Cu-like)	2414	0.5721 (G)	0.572	$3d^{10}4s\ ^2S_{1/2} - 3d^94s4f\ ^2P_{1/2}$	B
		0.5725 (G)	0.572	$3d^{10}4s\ ^2S_{1/2} - 3d^94s4f\ J = \frac{1}{2}$ ( $A = 4.1 \cdot 10^{14}s^{-1}$ )	B
		0.5911 (G)	0.591	$3d^{10}4s\ ^2S_{1/2} - 3d^94s4f\ J = \frac{1}{2}$ ( $A = 1.3 \cdot 10^{14}s^{-1}$ )	B
		0.5912 (G)	0.591	$3d^{10}4s\ ^2S_{1/2} - 3d^94s4f\ J = \frac{3}{2}$ ( $A = 1.3 \cdot 10^{14}s^{-1}$ )	B
		0.7268 (G)	0.725	$3d^{10}4s\ ^2S_{1/2} - 3d^94s4p\ ^4D_{1/2}$	B
		0.7273 (G)	0.725	$3d^{10}4s\ ^2S_{1/2} - 3d^94s4p\ J = \frac{3}{2}$ ( $A = 4.7 \cdot 10^{12}s^{-1}$ )	B
		6.217 (G)	6.232	$4s\ ^2S_{1/2} - 4p\ ^2P_{3/2}$	BL
		12.609 (G)	12.720	$4s\ ^2S_{1/2} - 4p\ ^2P_{1/2}$	
$W^{46+}$ (Ni-like)	4057	0.5687 (G)	0.569	$3d^{10}\ ^1S_0 - 3d^94f\ ^1P_1$	
		0.5875 (G)	0.587	$3d^{10}\ ^1S_0 - 3d^94f\ ^3D_1$	
		0.7035 (G)	0.702	$3d^{10}\ ^1S_0 - 3d^94p\ ^1P_1$	
		0.7184 (G)	0.716	$3d^{10}\ ^1S_0 - 3d^94p\ ^3D_1$	
		0.7944 (G)	0.793	$3d^{10}\ ^1S_0 - 3d^94s\ ^1D_2$	
$W^{47+}$ (Co-like)	4180	0.5550 (C)	0.556	$3d^9\ ^2D_{5/2} - 3d^84f\ J = \frac{5}{2}$ ( $A = 2.3 \cdot 10^{14}s^{-1}$ )	B
		0.5553 (C)	0.556	$3d^9\ ^2D_{5/2} - 3d^84f\ J = \frac{7}{2}$ ( $A = 4.2 \cdot 10^{14}s^{-1}$ )	B
$W^{48+}$ (Fe-like)	4309	0.5438 (C)	0.545	$3d^8\ ^3F_4 - 3d^74f\ J = 5$ ( $A = 4.2 \cdot 10^{14}s^{-1}$ )	B
		0.5444 (C)	0.545	$3d^8\ ^3F_4 - 3d^74f\ J = 4$ ( $A = 1.9 \cdot 10^{14}s^{-1}$ )	B
		0.5446 (C)	0.545	$3d^8\ ^3F_4 - 3d^74f\ J = 3$ ( $A = 2.0 \cdot 10^{14}s^{-1}$ )	B

**Table 2.** Experimentally observed spectral lines of W ions recommended for diagnostics of W in a fusion plasma. Ionization potentials (I.P.) are taken from [40]. Theoretical wavelengths originate either from GRASP (G) or from the Cowan code (C). Experimental wavelengths are from ASDEX Upgrade. For wavelengths in the SXR (below 2 nm) the uncertainty is  $\pm 0.001$  nm, while for the wavelengths in the VUV range (above 2 nm) the uncertainties are 0.005 nm. In the last column problems due to blending with other spectral emissions are indicated. ‘B’ or ‘BL’ indicate, that the given line is blended with emissions from ionization stages of similar charge or considerably lower charge, respectively. If line blending is considered to cause difficulties for interpreting the spectral line a ‘\*’ is added.

allowed for a quasi-local measurement. Exploiting this principle, it was possible to determine for the ionization stages Se-like  $W^{40+}$  to  $W^{46+}$  the shape of the fractional abundance vs. electron temperature. The same was possible for the bundle of ionization stages from about Sn-like  $W^{24+}$  to Y-like  $W^{35+}$ . These measurements were compared to theoretical predictions using ionization rates, which result from configuration-averaged distorted wave calculations or from the average ion model, and recombination rates from the average ion model. As none of the theoretical predictions could describe the measurements, ad-hoc correction factors, which are independent of electron temperature, were introduced to correct the recombination rates. As an additional boundary condition, the contributions from the different ionization

*Modelling of Measured Tungsten Spectra from ASDEX Upgrade and Predictions for ITER 28*

Ion	I.P. (eV)	$\lambda_{calc}$ (nm)	transition/configurations	blending
$W^{47+} - W^{55+}$ (Co-like – K-like)	4180– 5348	2.7–4.0 0.4–0.7	$3p^63d^n - 3p^53d^{n+1}$ $3p^63d^n - 3p^63d^{n-1}4f$ and $3p^63d^n - 3p^63d^{n-1}4p$	B*, BL B*, BL* B*, BL*
$W^{52+} - W^{63+}$ (Ti-like – Na-like)	4927– 7130	1.8–2.4	various $\Delta n = 0$ transitions	B*
$W^{57+}$ (Cl-like)	5671	0.13961–0.14003(G)	$2p^63s^23p^5 \ ^2P_{3/2} - 2p^53s^23p^53d J = \frac{1}{2}, \frac{3}{2}, \frac{5}{2}$ (4 transitions with $A \approx 10^{15}s^{-1}$ )	
$W^{58+}$ (S-like)	5803	0.13905–0.13924(G)	$2p^63s^23p^4 J = 2 - 2p^53s^23p^43d J = 1, 2, 3$ (4 transitions with $A \approx 10^{15}s^{-1}$ )	
$W^{59+}$ (P-like)	5936	0.13845–0.13894(G)	$2p^63s^23p^3 J = \frac{3}{2} - 2p^53s^23p^33d J = \frac{1}{2}, \frac{3}{2}, \frac{5}{2}$ (4 transitions with $A \approx 10^{15}s^{-1}$ )	
$W^{60+}$ (Si-like)	6468	0.13810(G)	$2p^63s^23p^2 J = 0 - 2p^53s^23p^23d J = 1$ ( $A = 2.5 \cdot 10^{15}s^{-1}$ )	
$W^{61+}$ (Al-like)	6611	0.13752(G) 0.13755(G) 7.2687(G)	$2p^63s^23p^1 J = \frac{1}{2} - 2p^53s^23p^13d J = \frac{1}{2}$ ( $A = 2.6 \cdot 10^{15}s^{-1}$ ) $2p^63s^23p^1 J = \frac{1}{2} - 2p^53s^23p^13d J = \frac{3}{2}$ ( $A = 2.6 \cdot 10^{15}s^{-1}$ ) $2p^63s^23p^1 J = \frac{1}{2} - 2p^63s^13p^2 J = \frac{1}{2}$ ( $A = 3.5 \cdot 10^{10}s^{-1}$ )	
$W^{62+}$ (Mg-like)	6919	0.13692(G) 8.0019(G)	$2p^63s^2 \ ^1S_0 - 2p^53s^23d \ ^1P_1$ $2p^63s^2 \ ^1S_0 - 2p^63s^13p^1 J = 1$ ( $A = 1.9 \cdot 10^{10}s^{-1}$ )	
$W^{63+}$ (Na-like)	7055	0.13638(G) 0.13643(G) 7.5977(G)	$2p^63s^1 \ ^2S_{1/2} - 2p^53s^13d J = \frac{3}{2}$ ( $A = 2.7 \cdot 10^{15}s^{-1}$ ) $2p^63s^1 \ ^2S_{1/2} - 2p^53s^13d J = \frac{1}{2}$ ( $A = 2.6 \cdot 10^{15}s^{-1}$ ) $2p^63s^1 \ ^2S_{1/2} - 2p^63p^1 \ ^2P_{1/2}$	
$W^{64+}$ (Ne-like)	14760	0.13590(G)	$2p^6 \ ^1S_0 - 2p^53d \ ^1P_1$	
$W^{65+}$ (F-like)	15140	0.13341–0.13433(G)	$2p^5 \ ^2P_{3/2} - 2p^53d J = \frac{1}{2}, \frac{3}{2}, \frac{5}{2}$ (4 transitions with $A \approx 10^{15}s^{-1}$ )	
$W^{66+}$ (O-like)	15520	0.13167(G) 0.13190(G)	$2p^4 \ ^3P_2 - 2p^33d J = 3$ ( $A = 2.2 \cdot 10^{15}s^{-1}$ ) $2p^4 \ ^3P_2 - 2p^33d J = 2$ ( $A = 9.8 \cdot 10^{14}s^{-1}$ )	
$W^{67+}$ (N-like)	15900	0.12989(G)	$2p^3 J = \frac{3}{2} - 2p^23d J = \frac{5}{2}$ ( $A = 1.4 \cdot 10^{15}s^{-1}$ )	

**Table 3.** Predicted spectral lines of tungsten ions. Only lines with high intensities are chosen. For the ionization stages of Co-like  $W^{47+}$  to Ar-like  $W^{+56}$  no clear candidates exist, as line blending is leading to quasicontinuous emissions at 2.7 – 4.0 nm and 0.4 – 0.7 nm. Further explanation see table 2.

*Modelling of Measured Tungsten Spectra from ASDEX Upgrade and Predictions for ITER 29*

stages to the spectral emissions have been taken into account in an absolute manner. For this purpose, the line intensities from the modelled spectra have been compared to the absolute intensity of the measured line intensities for a flat W profile. As a result of the correction factors on the recombination rates, also the absolute emissions of the different ionization stages are described more consistently. Looking at the most intense spectral features of W for the plasmas of ASDEX Upgrade, the focus was placed on the emissions between 0.4 – 0.8 nm, at 5 nm, between 12 – 14 nm and between 10 – 30 nm. For the emissions at 0.4 – 0.8 nm, the lines are emitted by ionization stages between Br-like W<sup>39+</sup> to about Mn-like W<sup>49+</sup>. The modelling in that wavelength range agrees well for the rough distribution of emissions vs. the wavelength. The intensities of single spectral lines are predicted typically with deviations of around factor 2, while the wavelengths are predicted within 0.002 nm. For most of the lines, no larger differences occur between the modelling using atomic data from the Cowan code (plane-wave Born approximation) and that using the atomic data from HULLAC or *R*-matrix calculations. For the most intense spectral line in the range, the line at 0.793 nm, larger differences of up to factor 10 are apparent, which are understood to a large extent. For the emissions at 5 nm, the modelling is more difficult, as here hundreds of spectral lines from ionization stages from Y-like W<sup>35+</sup> down to possibly I-like W<sup>21+</sup> contribute to a spectral feature, which cannot be resolved experimentally. The agreement of modelling is less accurate, as discrepancies in wavelength predictions occur and certain features like a small local maximum at 6 nm of the emissions are not accounted for in the modelling. However, the total spectral radiance of the predictions allowing for wavelength mismatch agree with the observed one within a factor of 2. At higher electron temperatures, additional spectral lines emitted by Br-like W<sup>39+</sup> to Cu-like W<sup>45+</sup> are observed at the same spectral range, which are also seen in the modelling. The spectral lines at 12 – 14 nm emitted by Se-like W<sup>40+</sup> to Cu-like W<sup>45+</sup> are described to a similar quality, as the spectral lines around 5 nm being emitted by the corresponding ionization stages. In the spectral range from 10 – 30 nm, a broad quasicontinuous feature is observed below  $T_e \approx 1.3$  keV. The emitting ionization stages have a lower charge than Pd-like W<sup>28+</sup>. The atomic data calculations could only be performed down to Sn-like W<sup>24+</sup>, because of the large number of coupling possibilities for configurations with more than 4 f-electrons, while excited configurations need to be included additionally, exceeded the capabilities of the code. Further emissions around 3 nm ( $T_e \leq 1.1$  keV and  $T_e \approx 5$  keV), between 0.6 – 0.7 nm ( $T_e \approx 0.7$  keV) and at 8 nm ( $T_e \approx 2$  keV), which are relatively weak, have been experimentally observed, while only the emissions around 3 nm could be found in the modelling. Finally, the atomic data were used to predict the spectral features of W in ITER for a standard scenario, in which a central  $T_e \approx 18$  keV is envisaged. The known emissions will occur at the outer half of the plasma, while new spectral features will be emitted from mid-radius to the plasma center by ionization stages of about Cr-like W<sup>50+</sup> to about C-like W<sup>68+</sup>. Important spectral ranges will be at 0.1 – 0.15 nm and 1.8 – 3.5 nm for ionization stages of about Co-like W<sup>47+</sup> to C-like W<sup>68+</sup>. Predictions of spectral lines around 8 nm for the ionization stages above Cl-like W<sup>57+</sup> are relatively weak, but seem also an interesting alternative. Further investigations in EBITs and tokamaks are needed to confirm these predictions.

*Modelling of Measured Tungsten Spectra from ASDEX Upgrade and Predictions for ITER 30*

## References

- [1] R. Aymar, P. Barabaschi, and Y. Shimomura, *Plasma Physics and Controlled Fusion* **44**, 519 (2002).
- [2] R. Isler, R. Neidigh, and R. Cowan, *Phys. Lett.* **A63**, 295 (1977).
- [3] E. Hinnov and M. Mattioli, *Phys. Lett.* **A66**, 109 (1978).
- [4] K. Asmussen *et al.*, *Nuclear Fusion* **38**, 967 (1998).
- [5] R. Neu, K. B. Fournier, D. Schlögl, and J. Rice, *J. Phys. B: At. Mol. Opt. Phys.* **30**, 5057 (1997).
- [6] R. Neu, K. B. Fournier, D. Bolshukhin, and R. Dux, *Physica Scripta* **T92**, 307 (2001).
- [7] T. Pütterich, Technical Report No. 10/29, IPP Garching, Germany, doctoral thesis at Universität Augsburg, (2006).
- [8] R. Neu, Technical Report No. 10/25, IPP, Garching, Germany (2003).
- [9] D. Post *et al.*, *At. Data Nucl. Data Tables* **20**, 397 (1977).
- [10] D. Post, J. Abdallah, R. Clark, and N. Putvinskaya, *Phys. Plasmas* **2**, 2328 (1995).
- [11] R. Radtke *et al.*, *Phys. Rev. A* **64**, 012720 (2001).
- [12] S. B. Utter, P. Beiersdorfer, and E. Träbert, *Can. J. Phys.* **80**, 1503 (2002).
- [13] Y. Ralchenko *et al.*, *Journal of Physics B: Atomic, Molecular and Optical Physics* **40**, 3861 (2007).
- [14] T. Pütterich *et al.*, *J. Phys. B: At. Mol. Opt. Phys.* **38**, 3071 (2005).
- [15] R. D. Cowan, *The Theory of Atomic Structure and Spectra (Los Alamos Series in Basic and Applied Sciences)* (University of California Press, California, 1981).
- [16] R. Neu *et al.*, *Plasma Physics and Controlled Fusion* **49**, B59 (2007).
- [17] R. Dux, Technical Report No. 10/30, IPP, Garching, Germany (2006).
- [18] K. Behringer, 'Description of the impurity transport code STRAHL', JET-R(87)08, JET Joint Undertaking, Culham (1987).
- [19] R. Dux *et al.*, *Nuclear Fusion* **39**, 1509 (1999).
- [20] R. Dux, Technical Report No. 10/27, IPP, Garching, Germany (2004).
- [21] R. Neu *et al.*, *Journal of Nuclear Materials* **313–316**, 116 (2003).
- [22] R. Dux *et al.*, *Proc. of the 20th IAEA Conference Fusion Energy (CD-Rom), Vilamoura, Portugal, November 2004* (IAEA, Vienna, 2005), Vol. IAEA-CSP-25/CD, pp. IAEA-CN-116/EX/P6-14.
- [23] T. Pütterich *et al.*, to be published
- [24] A. G. Peeters, provided the NEOART code
- [25] S. P. Hirshman and D. J. Sigmar, *Nuclear Fusion* **21**, 1079 (1981).
- [26] W. A. Houlberg, K. C. Shaing, S. P. Hirshman, and M. C. Zarnstorff, *Physics of Plasmas* **4**, 3230 (1997).
- [27] A. G. Peeters, *Physics of Plasmas* **7**, 268 (2000).
- [28] J. Wesson, *Nuclear Fusion* **37**, 577 (1997).
- [29] R. Fonck, A. Ramsey, and R. Yelle, *Applied Optics* **21**, (1982).
- [30] E. Unger, Technical Report No. III/187, IPP, Garching, Germany (1992).
- [31] D. Bolshukhin *et al.*, *Review of Scientific Instruments* **72**, 4115 (2001).
- [32] S. D. Loch *et al.*, *Physical Review A (Atomic, Molecular, and Optical Physics)* **72**, 052716 (2005).
- [33] H. P. Summers, The ADAS User Manual, version 2.6 <http://adas.phys.strath.ac.uk> (2004).
- [34] C. P. Ballance and D. C. Griffin, *Journal of Physics B: Atomic, Molecular and Optical Physics* **39**, 3617 (2006).
- [35] C. P. Ballance and D. C. Griffin, *Journal of Physics B: Atomic, Molecular and Optical Physics* **40**, 247 (2007).
- [36] K. Fournier, *At. Data Nucl. Data Tables* **68**, 1 (1998).
- [37] Y. Ralchenko *et al.*, *Physical Review A (Atomic, Molecular, and Optical Physics)* **74**, 042514 (2006).
- [38] I. P. Grant, C. T. Johnson, F. A. Parpia, and E. P. Plummer, *Comput. Phys. Commun.* **55**, 425 (1989).
- [39] M. Finkenthal *et al.*, *Physics Letters A* **127**, 255 (1988).
- [40] A. Kramida and J. Reader, *At. Data Nucl. Data Tables* **92**, 457 (2006).
- [41] G. N. Pereverzev, C. Angioni, A. G. Peeters, and O. V. Zolotukhin, *Nuclear Fusion* **45**, 221 (2005).
- [42] G. Matthews *et al.*, *Physica Scripta* **T128**, 137 (2007).

## 5.2 Publication 2

*Calculation and experimental test of the cooling factor of tungsten*

Nuclear Fusion 50 (2010) 025012

# Calculation and Experimental Test of the Cooling Factor of Tungsten

**T Pütterich<sup>1</sup>, R Neu<sup>1</sup>, R Dux<sup>1</sup>, A D Whiteford<sup>2</sup>, M G O'Mullane<sup>2</sup>, H P Summers<sup>2</sup> and the ASDEX Upgrade Team<sup>1</sup>**

<sup>1</sup>*Max-Planck-Institut für Plasmaphysik, EURATOM Association, D-85748 Garching, Germany*

<sup>2</sup>*Department of Physics, University of Strathclyde, Glasgow G4 0NG, UK*

**Abstract.** The cooling factor of W is evaluated using state of the art data for line radiation and an ionization balance which has been benchmarked with experiment. For the calculation of line radiation, level-resolved calculations were performed with the Cowan code to obtain the electronic structure and excitation cross sections (plane-wave Born approximation). The data were processed by a collisional radiative model to obtain electron density dependent emissions. These data were then combined with the radiative power derived from recombination rates and Bremsstrahlung to obtain the total cooling factor. The effect of uncertainties in the recombination rates on the cooling factor were studied and were identified to be of secondary importance. The new cooling factor is benchmarked, by comparisons of the line radiation to spectral measurements as well as to a direct measurement of the cooling factor. Additionally, a less detailed calculation using a configuration averaged model was performed. It was used to benchmark the level-resolved calculations and to improve the prediction on radiation power from line radiation for ionization stages which are computationally challenging. The obtained values for the cooling factor validate older predictions from literature. Its ingredients and the absolute value are consistent with the existing experimental results regarding the value itself, the spectral distribution of emissions and the ionization equilibrium. A table of the cooling factor versus electron temperature is provided. Finally, the cooling factor is used to investigate the operational window of a fusion reactor with W as intrinsic impurity. The minimum value of  $nT\tau_E$ , for which a thermonuclear burn is possible, is increased by 20% for a W concentration of  $3.0 \cdot 10^{-5}$  compared to a plasma without any impurities, except for the He ash which is considered in both cases.

## 1. Introduction

Tungsten (W) is well suited as a plasma facing component (PFC) in terms of power handling capability, low erosion yield and low deuterium retention [1, 2]. However, when the W concentration exceeds a certain level in the central part of the plasma the radiative losses limit the plasma operation and performance such that for ITER the central concentration lower than several  $10^{-5}$  is obligatory [3]. This has been found earlier in the ORMAK [4] and PLT [5] tokamaks in which the central W radiation prevented fusion relevant plasma operation due to W concentrations in the range of  $10^{-3}$ . Due to the use of a divertor and other operational precautions the W concentration can be controlled to low enough values

*Calculation and Experimental Test of the Cooling Factor of Tungsten*

2

[6] and fusion relevant operation is possible as demonstrated at ASDEX Upgrade [7, 8]. Still, the radiative cooling by W is a concern and the maximum tolerable W concentration is an important value for ITER and a future fusion reactor. This value, however, is based on calculations of the cooling factor [9, 10] using the average ion model, a model which does not calculate quantummechanical wave functions of the levels in each ion, but uses scale formulas based on a hydrogenic orbital model. In this work, the Cowan code [11] is used for level resolved calculations in order to calculate a cooling factor based on more detailed atomic physics. Such atomic data allow for spectroscopic comparisons in which the spectral contributions to the cooling factor can be benchmarked. The data calculations in this work underwent such a benchmark with experimental spectra, which underlines their credibility. Due to the fact, that the level resolved calculations of cross sections for electron impact excitation are too large and time consuming for ionization states below about Cd-like  $W^{26+}$  the calculations have been supported and extended using a configuration averaged model, which allowed to tackle all ionization states of W. It may be noted that a detailed work on the interplay between configuration averaged and level-resolved calculations for high-Z elements can be found in [12].

## 2. Atomic Data

### 2.1. Ionization Equilibrium

In [13], a detailed analysis of the ionization equilibrium has been performed which compared measured results for Pd-like  $W^{27+}$  to Fe-like  $W^{48+}$  to the predictions derived from different combinations of ionization and recombination rates. The best agreement has been found for a set of ionization rates, which originate from configuration averaged distorted wave (CADW) calculations [14] and recombination rates which originate from the average ion model [9] but have been adjusted by temperature independent factors to match the experimental observations. These adjustments have been performed ad-hoc without a physics explanation to provide a set of ionization and recombination rates that led to an ionization equilibrium as observed in experiment. These adjustments are used also in the present work. In order to check the influence of the ionization equilibrium, a sensitivity study is presented in section 2.5. It should be noted that the ionization rates are evaluated for zero density while the optimization of the ionization equilibrium has been performed in the density range  $5 - 10 \cdot 10^{19} \text{ m}^{-3}$ . Due to the fact that the ionization rates are expected to vary weakly in the reactor relevant density range the ionization balance obtained in [13] is relevant for this range. Concerning the recombination rates, it should be noted that there are rates of higher quality for a few ionization stages (e.g. DR rates of Ni-like W [15], Ar-like W [16] and Ne-like W [17]) available. However, for a compilation of the cooling factor, rates for all ions are needed. A comparison of the rates used in this work to the mentioned rates of higher quality gives agreement within a factor of 2 in the relevant electron temperature ranges.

*Calculation and Experimental Test of the Cooling Factor of Tungsten*

3

*2.2. Radiation due to Recombination and Bremstrahlung*

To provide a consistent set of radiation power with respect to the adjusted recombination rates a rather simple model is chosen to calculate the radiation emitted during the recombination process. When an electron is captured by an ion the radiation energy which is emitted during the recombination and the following cascade equals the ionization potential plus the kinetic energy of the electron minus the kinetic energy gain of the recombined ion. Due to the large difference of ion and electron mass the kinetic energy gain of the recombined ion can be neglected. For simple radiative recombination the involved electron energies are comparably small, while only for dielectronic recombination electron energies up to a maximum of two times the ionization potential play a major role. In the following the radiation emitted during recombination is approximated by  $f_{rec-rad}$  times the ionization potential times the recombination rate. As small electron energies are most important for the recombination rates,  $f_{rec-rad} = 1.2$  is used. For this approximation, an uncertainty of less than 20% is anticipated because it includes the lower limit for  $f_{rec-rad}$ . However, values of  $f_{rec-rad} > 1.4$  are possible. Therefore, the impact of the value of  $f_{rec-rad}$  on the cooling factor is investigated separately in section 2.5. For the major part of the electron temperature range under consideration this contribution to the total cooling factor is small. The contribution of Bremstrahlung is calculated using the formula of [9] and the free-free Gaunt factor of [18].

*2.3. Line Radiation*

In the following two types of calculations, i.e. the level-resolved (LR) and configuration averaged (CA) calculations, are varied and compared. The LR calculation treats each level separately which results in large computations. For certain ionization stages (e.g. stages with open f- or d-orbitals), the computational effort is so large that either the calculation could not be performed (e.g. below Cd-like W<sup>26+</sup>) or the computational effort had to be decreased by allowing for less wave functions (i.e. including less configurations in the calculations) possibly neglecting contributions to the radiated power. In that case the important spectral features might be predicted as observed and benchmarked in [13], but less obvious spectral features could make up this missing power. The CA calculation does not include the details of each level and is less accurate concerning the spectral distribution of radiation. It might also show inaccuracies in the total radiated line power as to some extent the detailed physics of the levels could be important. However, large sets of configurations can be included in the calculations which is the strength of the CA calculations and which allows to tackle the charge stages below Cd-like W<sup>26+</sup>. In the following, there will be references to one LR calculation and two CA calculations (i.e. CA-LR and CA-LARGE). The CA-LR calculation includes for each charge stage the same sets of configurations as the LR calculation. A comparison thus allows to identify differences which occur due to the type of calculations. The CA-LARGE calculation includes a very large set of configurations and a comparison between CA-LR and CA-LARGE gives information about the missing radiation due to the smaller set of configurations used in the LR and CA-LR calculation.

The elaborate LR calculations (cf. [13]) and the CA calculations for each W ion have

*Calculation and Experimental Test of the Cooling Factor of Tungsten*

## 4

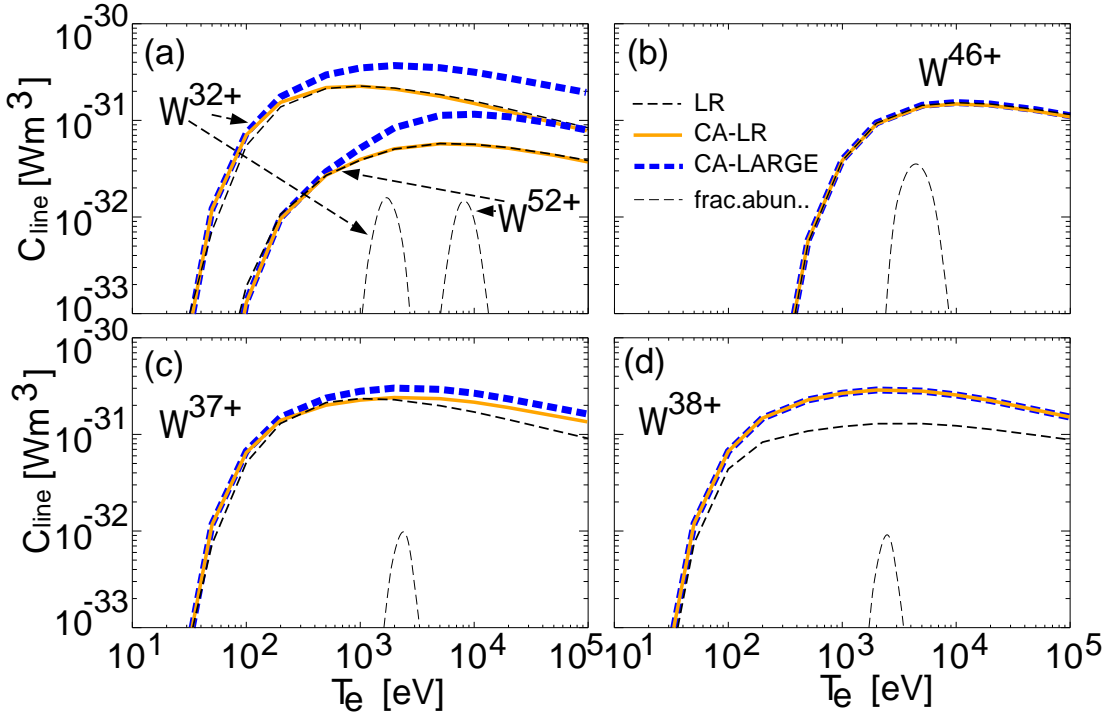
been performed using the Cowan code via the front end and infrastructure provided by the ADAS project [19]. The calculations determined the electronic structure including transition probabilities and the cross sections for electron impact excitation. Electric and magnetic dipole and electric quadrupole transitions have been included in the calculation using the plane-wave Born approximation for the excitation part. A collisional-radiative modelling was then applied to determine the spectra of each ionization stage separately. In the following a density of  $7.5 \cdot 10^{19} \text{ m}^{-3}$  is chosen for all presented plots. A variation in density in the range  $5 - 15 \cdot 10^{19} \text{ m}^{-3}$  has been performed, but does not change the results significantly. This work follows detailed investigations (cf. [13]) about the dominant spectral features emitted by W. In the course of these investigations the ionization balance was adjusted to the experimental findings and LR calulations have been compared to measured spectra and their dependence on electron temperatures (cf. also [20]). In table 1, the input configurations for five ionization stages and calculation methods are given. In figure 1, the corresponding results on the emissivity coefficient for line radiation  $C_{line}$  is given. The power density  $P_q$  for line radiation from a single ionization stage  $q$  with density  $n_q$  is given by  $P_q = n_e \cdot n_q \cdot C_{line}$ . The difference between the three calculation methods (LR, CA-LR, CA-LARGE) varies with the complexity of the targeted ionization stage. For Mo-like W<sup>32+</sup> the level-resolved calculation allowed to include only the seven most important configurations (open 4d-shell), such that the experimentally observed, intense spectral feature around 5 nm is reproduced (cf. [13]). When comparing  $C_{line}$  from the LR-calculation to that from the CA-LR calculation in figure 1(a) a rather good agreement is found, which validates the configuration averaged approach. Even the shape of the two  $C_{line}$  graphs versus  $T_e$  matches well, although the individual energy levels which yield thresholds for the single electron impact excitations are not resolved in the CA calculation. Further emissions in the spectra are not experimentally attributed to this ionization stage, however, it is clear that an inclusion of higher excited configurations is connected to additional emissions. This inclusion is performed by the CA-LARGE calculation, which consequently arrives at larger  $C_{line}$  values as is presented in figure 1(a). The results for Ti-like W<sup>52+</sup> (cf. figure 1(a)) resembles the features for the Mo-like W<sup>32+</sup>. As the LR calculation must already take 770 levels into account (open 3d-shell) an extension of the input configurations is not easily possible. For Rb-like W<sup>37+</sup> (cf. figure 1(c)), already the LR and CA-LR calculations are large enough to include most of the emissions which are calculated by the CA-LARGE calculation. Similarly, the results for Ni-like W<sup>46+</sup> (cf. figure 1(b)) arrive at a very good agreement between LR and CA-LR, while the set of configurations used in the LR calculation is already very large and was not extended in the CA-LARGE calculation. It was possible to choose the set of configurations for the LR calculation so large because the ground state exhibits a closed subshell which translates in a much smaller number of levels for ground configuration (one level) and the excited configurations and thus less computational effort. For a few cases like for Kr-like W<sup>38+</sup> (cf. figure 1(d)) a discrepancy is observed already between the LR and CA-LR calculation. This effect will be discussed below. In figure 2 the three calculation procedures are compared for the ionization stages from Ag-like W<sup>28+</sup> to He-like W<sup>72+</sup>. The  $C_{line}$  graphs for each ionization stage are evaluated at the electron temperature at which the fractional abundance of the respective ionization

*Calculation and Experimental Test of the Cooling Factor of Tungsten*

	LR/CA-LR	CA-LARGE
Mo-like $W^{32+}$	$4d^6, 4d^54f \rightarrow 4d^55f,$ $4p^5 4d^7,$ $\Sigma = 7$	$4d^6, 4d^54f \rightarrow 4d^55g,$ $4p^54d^7 \rightarrow 4p^54d^65g,$ $4s4p^64d^7 \rightarrow 4s4p^64d^65g,$ $3d^94s^24p^64d^7 \rightarrow 3d^94s^24p^64d^65g ; \Sigma = 28$
Rb-like $W^{37+}$	$4p^64d \rightarrow 4p^65f,$ $4p^54d^2 \rightarrow 4p^54d5f,$ $4s4p^64d^2 \rightarrow 4s4p^64d5f,$ $\Sigma = 18$	$4p^64d \rightarrow 4p^65g,$ $4p^54d^2 \rightarrow 4p^54d5g,$ $4s4p^64d^2 \rightarrow 4s4p^64d5g,$ $3d^94s^24p^64d^2 \rightarrow 3d^94s^24p^64d5g ; \Sigma = 28$
Kr-like $W^{38+}$ (no difference)	$4p^6, 4p^54d \rightarrow 4p^55g,$ $4s4p^64d \rightarrow 4s4p^65g,$ $3d^94s^24p^64d \rightarrow 3d^94s^24p^65g,$ $\Sigma = 22$	$4p^6, 4p^54d \rightarrow 4p^55g,$ $4s4p^64d \rightarrow 4s4p^65g,$ $3d^94s^24p^64d \rightarrow 3d^94s^24p^65g,$ $\Sigma = 22$
Ni-like $W^{46+}$ (no difference)	$3d^{10}, 3d^94s \rightarrow 3d^95g,$ $3p^53d^{10}4s \rightarrow 3p^53d^{10}5g,$ $3s3p^63d^{10}4s \rightarrow 3s3p^63d^{10}5g,$ $\Sigma = 28$	$3d^{10}, 3d^94s \rightarrow 3d^95g,$ $3p^53d^{10}4s \rightarrow 3p^53d^{10}5g,$ $3s3p^63d^{10}4s \rightarrow 3s3p^63d^{10}5g,$ $\Sigma = 28$
Ti-like $W^{52+}$	$3d^4, 3d^34s \rightarrow 3d^34f$ $3p^5 3d^5,$ $\Sigma = 6$	$3d^4, 3d^34s \rightarrow 3d^35g,$ $3p^53d^5 \rightarrow 3p^53d^45g,$ $3s3p^63d^5 \rightarrow 3s3p^63d^45g ; \Sigma = 30$

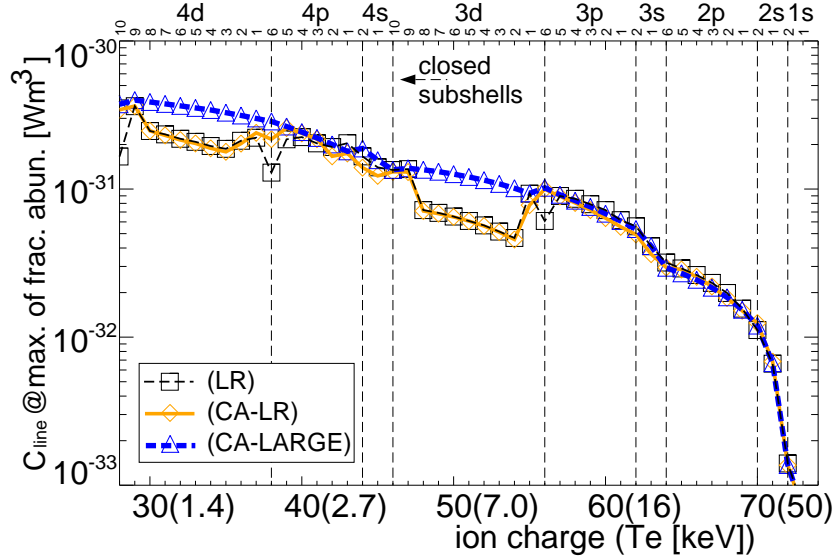
**Table 1.** Used input configurations for the level-resolved (LR) (cf. [13]) and corresponding configuration averaged (CA-LR) calculation and the extended configuration averaged (CA-LARGE) calculation. The arrow in between two configurations indicates that all configurations were included which result from a stepwise propagation of the outermost electron (e.g.  $4s^2 \rightarrow 4s4d$  means  $4s^2, 4s4p, 4s4d$ ).

stage reaches its maximum. Two systematic behaviours get apparent. For ionization stages exhibiting a ground state with more than two and less than eight electrons in a d-shell the LR calculation agrees with the CA-LR calculation, while the CA-LARGE calculation predicts more radiation. The second observation is that for the ionization stages Ag-like  $W^{28+}$ , Kr-like  $W^{38+}$  and Ar-like  $W^{56+}$  discrepancies get apparent between the LR and CA-LR calculations while the CA-LARGE agrees with the latter. The first observation can be understood when looking at the sets of configurations used in the calculations. An open d-shell (with more than two electrons and less than two free holes) offers a considerably larger number of levels such that for the LR calculations only a limited number of configurations have been included. In fact, enough configurations have been included to predict important spectral features as observed in experiment [13], but for predicting the total radiated power additional emissions that are not so obvious in the spectra become important. The fact that the CA-LR calculation agrees with the LR calculation supports the finding that the CA-LR calculation is consistent and numerically stable. The inclusion of further configurations in the CA-LARGE case leading to a higher cooling factor is also consistent. This means that for the determination



**Figure 1.** (colored in online-version) (a) Emissivity coefficient for line radiation  $C_{line}$  arising from different calculation procedures (i.e. level-resolved (LR), configuration averaged with LR configuration set (CA-LR) and configuration averaged with large configuration set (CA-LARGE)) and fractional abundances multiplied by  $10^{-31} \text{ Wm}^3$  (to fit into plot) for Mo-like  $\text{W}^{32+}$  and Ti-like  $\text{W}^{52+}$ . (b) same as (a) for Ni-like  $\text{W}^{46+}$ ; (c) same as (a) for Rb-like  $\text{W}^{37+}$ ; (d) same as (a) for Kr-like  $\text{W}^{38+}$ .

of the cooling factor the CA-LARGE results should be used. For the cases with only one electron or free hole in an open subshell larger sets of configurations could be used in the LR case and the differences between the calculations disappear. The explanation for the second observation is not so straight forward because the discrepancies between the calculations using the same set of configurations hints towards a deficiency of the calculation method. This deficiency is there for the ionization stages Ag-like  $\text{W}^{28+}$  ( $4\text{d}^{10}$ ), Kr-like  $\text{W}^{38+}$  ( $4\text{p}^6$ ) and Ar-like  $\text{W}^{56+}$  ( $3\text{p}^6$ ) with a ground state exhibiting a closed subshell denoted in brackets. However, the ground states of the ionization stages Zn-like  $\text{W}^{44+}$  ( $4\text{s}^2$ ), Ni-like  $\text{W}^{46+}$  ( $3\text{d}^{10}$ ), Mg-like  $\text{W}^{62+}$  ( $3\text{s}^2$ ), Ne-like  $\text{W}^{64+}$  ( $2\text{p}^6$ ), Be-like  ${}^{70+}$  ( $2\text{s}^2$ ) and He-like  $\text{W}^{72+}$  ( $1\text{s}^2$ ) exhibit a closed subshell, too, but do not show a discrepancy between the three calculation methods. A possible explanation to the discrepancy could be the occurrence of configuration mixing, which is not considered for both CA calculations. This effect may play a special role for cases with closed subshells, when the mixing of metastables is concerned but at the same time depends on the details of wave functions. The latter property could explain why the effect is apparent only for a few cases. Since, the described effect is important for only three ionization stages it plays only a small role for the total cooling factor. The associated differences would not be visible within the line thickness of the presented cooling factor below.

*Calculation and Experimental Test of the Cooling Factor of Tungsten*

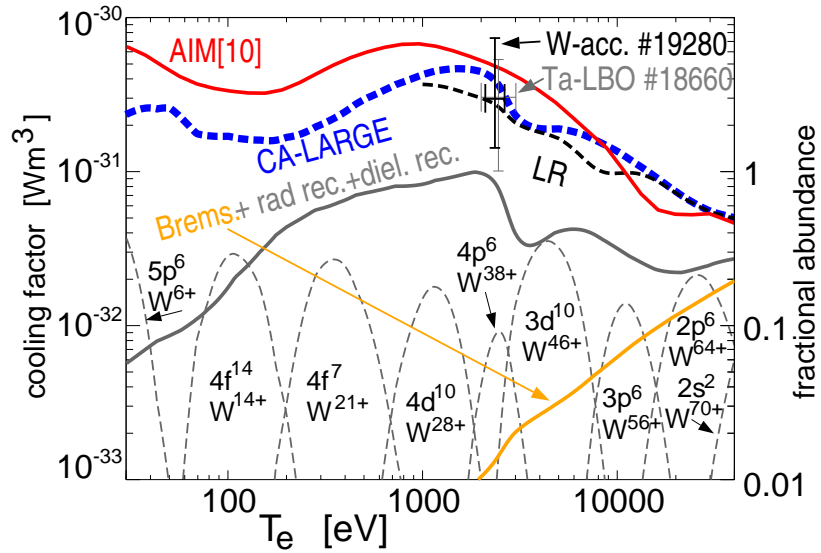
**Figure 2.** (colored in online-version) Line radiation rate coefficients  $C_{line}$  arising from different calculation procedures for the ionization states from Ag-like  $W^{28+}$  through He-like  $W^{72+}$ . The  $C_{line}$  is evaluated at the temperature (given in brackets for a few charge states) at which the maximum fractional abundance of the respective ionization stage occurs.

#### 2.4. Resulting Cooling Factor of Tungsten

In figure 3 all above results were included, while the line radiation was taken from the LR (thin-dashed) and the CA-LARGE (thick-dashed) calculation. The LR calculation is only presented above 1 keV due to the less credible data for line radiation concerning the ionization stages below Ag-like  $W^{28+}$ . The sum of the radiation emitted due to radiative and dielectronic recombination and Bremsstrahlung is presented separately to document their relative contribution, which is mostly minor. The dominant part is the line radiation for electron temperatures of up to about 20 keV. For higher electron temperatures the power from line radiation decreases, while Bremsstrahlung gets more important. Thus, its relative importance increases in this range. For comparison, the results from the average ion model are presented [10], which are in remarkably good agreement. In the range above 1 keV the differences are small and reach at most a factor of 2. In the range which is relevant for the core of a fusion reactor, i.e. for electron temperatures above 10 keV the new data gives an up to factor 1.5 higher cooling rate, which will influence moderately the limit of the maximal tolerable W concentration in a reactor, as will be shown below. Between 30 eV and 1 keV about a factor of 2 less radiation is predicted throughout. Below this temperature range the credibility of the data must be considered uncertain as the calculation of electron impact and the ionic structure data has not been optimized for the lowly charged ions. Anyhow, the cooling factor for the case of negligible transport as presented in figure 3 is not valid at the edge of a fusion plasma (approximately below a few hundred eV, depending on the device). It may be noted that the occurrence of such effects and their implications on the cooling factor have been investigated in [10]. In table 2 the values of the cooling factor  $L_Z$ , the coefficient

## Calculation and Experimental Test of the Cooling Factor of Tungsten

8



**Figure 3.** (colored in online-version) The total cooling factors of W from AIM [10] (red, thick, solid) and those derived from the LR (black, thin, dashed) and CA-LARGE (blue, thick, dashed) calculations are presented. The summed contributions (contained in the total cooling factors from LR and CA-LARGE) due to radiative and dielectronic recombination and by Bremsstrahlung are given as an additional curve (gray, thick, solid). The Bremsstrahlung contribution is also presented separately (orange, thick, solid). The fractional abundances are presented for a few ionization stages. The data points with error bars arise from a comparison of radiation and Bremsstrahlung as explained later in the text.

$C_{r-b}$ , which is the cooling factor excluding line radiation and the mean charge of the W ion are listed as a function of electron temperature. When  $\log L_Z$  is linearly interpolated on the  $\log T_e$  grid the resulting  $L_Z$  curve gives the calculated  $L_Z$  with deviations of less than 3% over the full  $T_e$  range of 30 – 40000 eV.

### 2.5. Sensitivity of Cooling Factor on Recombination Radiation and Rates

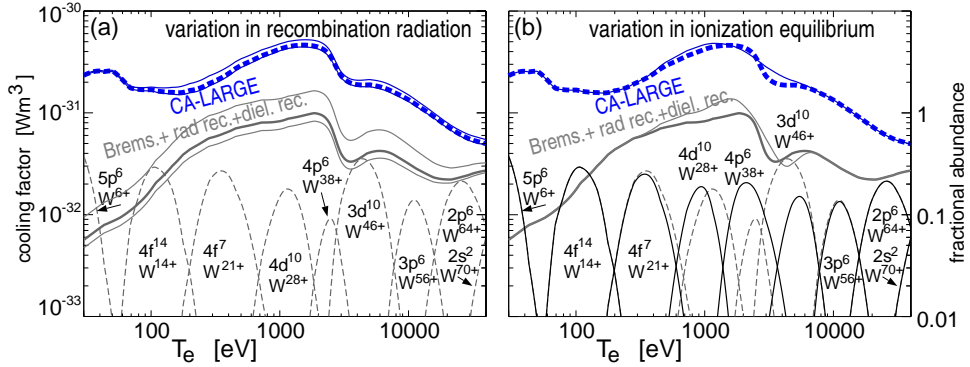
As for the recombination rates ad-hoc adjustments have been made, their impact on the total cooling factor is investigated with special care. Related to these adjustments are also the radiation rates due to recombination which have been connected rigidly to the recombination rates (cf. section 2.2). In figure 4(a) the radiation due to recombination is calculated using different  $f_{rec-rad}$  (cf. section 2.2), i.e.  $f_{rec-rad} = 1$  and  $f_{rec-rad} = 2$  instead of  $f_{rec-rad} = 1.2$ . These two cooling factors (thin lines) are compared to the original cooling factor (thick, dashed). The differences are small compared to the variation in  $f_{rec-rad}$  by a factor of 2, demonstrating the inferior importance of the recombination radiation for the total cooling factor. In figure 4(b) the variations of the cooling factor due to a different ionization equilibrium is presented as a thin curve, while the original cooling factor is included a the thick dashed curve. The alternative ionization equilibrium is obtained by using the original recombination rates from the average ion model without adjustments. The differences in the cooling factor are visible, however, the absolute value is not strongly changed. Structures in

*Calculation and Experimental Test of the Cooling Factor of Tungsten*

9

$T_e$ [eV]	$L_Z$ [Wm <sup>3</sup> ]	$C_{r-b}$ [Wm <sup>3</sup> ]	mean Z
30	2.32E-31	5.65E-33	6.77
40	2.56E-31	7.40E-33	7.95
50	2.55E-31	8.59E-33	9.13
60	2.08E-31	9.69E-33	10.25
70	1.73E-31	1.12E-32	11.46
100	1.67E-31	1.77E-32	13.47
150	1.57E-31	3.11E-32	15.70
200	1.65E-31	4.37E-32	17.71
300	1.99E-31	5.75E-32	20.18
400	2.42E-31	6.54E-32	21.62
500	2.91E-31	7.23E-32	22.81
600	3.23E-31	7.59E-32	23.75
800	3.79E-31	8.05E-32	25.33
1000	4.21E-31	8.28E-32	26.67
1500	4.59E-31	9.36E-32	30.47
2000	4.38E-31	9.76E-32	33.93
2300	3.94E-31	8.76E-32	36.08
2700	2.88E-31	5.65E-32	40.39
3000	2.28E-31	3.96E-32	42.84
3500	1.96E-31	3.32E-32	44.43
4000	1.88E-31	3.47E-32	45.30
5000	1.87E-31	4.08E-32	46.72
6000	1.79E-31	4.23E-32	48.20
7000	1.67E-31	4.09E-32	50.00
10000	1.33E-31	3.17E-32	54.58
12000	1.15E-31	2.75E-32	57.02
15000	9.47E-32	2.38E-32	59.42
20000	7.30E-32	2.22E-32	62.02
25000	6.11E-32	2.32E-32	63.64
30000	5.47E-32	2.48E-32	64.99
40000	4.95E-32	2.71E-32	66.83

**Table 2.** The tabulated cooling factor  $L_Z$  of W, the coefficient  $C_{r-b}$ , which denotes the cooling factor only for radiation due to recombination including Bremsstrahlung and the mean charge of the ionization equilibrium for different electron temperatures.



**Figure 4.** (colored in online-version) Similar to figure 3. (a) The cooling factor of W from CA-LARGE scheme (blue, thick, dashed) is compared to cooling factors using the assumption  $f_{rec-rad} = 1$  and  $f_{rec-rad} = 2$  instead of  $f_{rec-rad} = 1.2$  (cf. section 2.2) (b) The cooling factor of W from CA-LARGE scheme (blue, thick, dashed) is compared to a cooling factor for which only the ionization equilibrium is differently evaluated using the original recombination rates from the average ion model (blue, thin, dashed). The alternative curves for the radiation from recombination and the abundances of ionization stages are shown in thin lines.

the cooling factor curve are smoothed, but there is the tendency that radiative power from one ionization stage is replaced by a similar amount from a neighboring ionization stage. Both investigations exhibit that the calculation of the line radiation is crucial for determining the cooling factor, while the accuracy of the other atomic data has relatively low impact. It should be noted that this is only true for the cooling factor while for spectral investigations the ionization equilibrium has a more profound influence.

### 3. Experimental Data

#### 3.1. Observation of Spectral Features

The atomic data used to calculate the cooling factor of W have the advantage over the data from the average ion model that predictions on spectral signatures can be derived and compared to the experimentally measured ones. This has already been done in [13] where good agreement has been found for this comparison. This comparison was done after adjusting the ionization equilibrium by corrections of the recombination rates such that the experimental evidence was matched for circumstances which allowed to ignore impurity transport. The comparisons of synthetic and measured spectra revealed that in the spectral regions, which contain most of the radiated power, the agreement between modelled and measured emissions is better than a factor of 2 (in VUV) and a factor of 1.5 (in soft X-ray) for electron temperatures of 1-2 keV and 2-5 keV, respectively. The uncertainty of the benchmark is dominated by calibration uncertainties of the VUV and soft X-ray spectrometers. The VUV spectrometer was calibrated via two methods which agreed within the uncertainties. The first method relies on modelling the carbon and boron densities which have been deduced by charge exchange recombination spectroscopy using spectral lines in the visible spectral

*Calculation and Experimental Test of the Cooling Factor of Tungsten*

11

range, which is emitted after the recombination of completely stripped ions interacting with the neutral hydrogen atoms from the neutral beam heating. Such a modelling allows for predicting the H-like and He-like emissions for both elements between 3.3 nm and 6.1 nm. Additionally, a cross calibration with the SPRED spectrometer was performed at 24.3 nm. The latter is an overview spectrometer which has been calibrated via branching ratios to a spectral line observed with visible spectroscopy. Both calibrations have been connected with a typical detector sensitivity curve. The procedure is described in more detail in [21]. The soft X-ray spectrometer was calibrated on the one hand by modelling the emissions of H-like and He-like Ar from 0.37 nm and 0.4 nm and on the other hand by using a large area X-ray source. Emissions for different anodes (Sn ( $L_\alpha$  0.36 nm), Y ( $L_\alpha$  0.64 nm), Al ( $K_\alpha$  0.83 nm)) have been quantified in lab measurements using a semiconductor detector and pulse height analysis, similar to the procedure described in [22]. Detailed EBIT measurements are available in the VUV [23, 24, 25] and in the soft X-ray range [26, 27, 28], which allow for an unambiguous line identification and benchmark for the atomic data (e.g. [20, 13]). The spectral structure of the emissions supports this good agreement, as within the spectral ranges 0.4-0.8 nm, 4-7 nm and 11-14 nm the distribution of spectral lines from experiments is reproduced by the modelling [13]. However, for few single spectral lines larger deviations could be observed (e.g Ni-like W<sup>46+</sup> E2-line at 0.793 nm), which are largely understood after comparing to more detailed calculations on single ionization states. For more details on these comparisons see [13, 29, 30].

Electron temperatures above 5 keV are not easily accessible in todays fusion experiments, but respective spectral lines can be studied in EBIT experiments. Measurements performed at EBITs in the EUV range [31, 32] are consistent with the calculations in terms of dominant spectral lines and detailed benchmarks with the data from the Berlin EBIT in the soft X-ray range yield good agreement [33, 34]. It has been found in [33, 34], that the important spectral features are reproduced by the LR calculations predicting most of the spectral lines within an accuracy of factor of 2, while only a few special spectral lines exhibited larger discrepancies. This yields the same accuracy as found for the tokamak spectra in the range of 0.4-0.8 nm. Taking these results the obtained atomic data exhibit a high credibility. On the other hand, the agreement with the data from AIM calculations [9, 10] validates these older results.

### *3.2. Direct Measurement of the Cooling Factor*

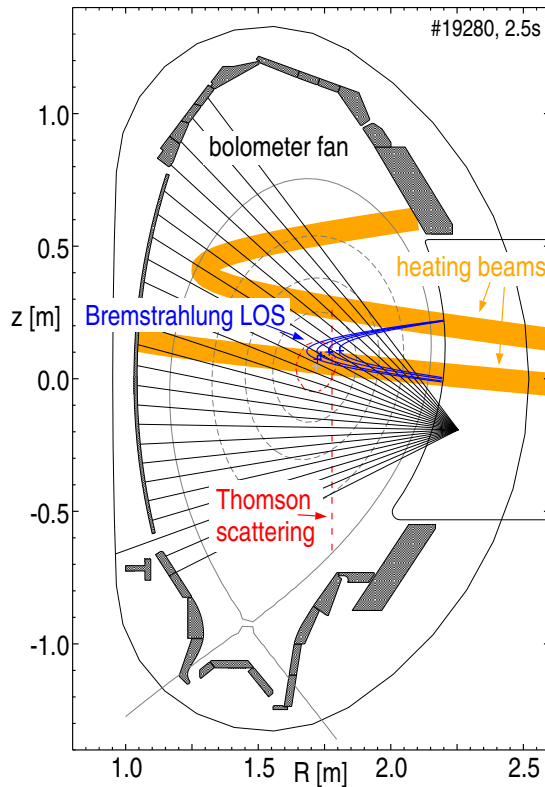
A direct measurement of the cooling factor in a plasma relies on the absolute determination of the W density independent from the total radiation measurement. In principle, a small change of the W concentration leads to an increase in the effective ion charge  $Z_{eff} = \frac{\sum_k n_k Z_k^2}{\sum_k n_k Z_k}$  (where  $n_k$  and  $Z_k$  are the density and charge of the various ion species) which is diagnosed via the Bremsstrahlung intensity. Consequently, the direct measurement of the cooling factor relies on determining a small change of  $Z_{eff}$  due to an increased W concentration and comparing this to the change in radiated power. It is tedious to perform such experiments in a fusion plasma, because a large radiation increase means troublesome operation of the plasma. At ASDEX Upgrade the best experimental data for such an experiment was obtained for a Ta

*Calculation and Experimental Test of the Cooling Factor of Tungsten*

12

(Z=73) injection by laser blow-off. The data point is introduced in figure 3 (gray, thin), because the differences of the cooling factor of Ta and W are expected to be small compared to the uncertainties (cf. [21]). In the following a slightly different approach, which makes use of a peculiar behaviour of a plasma discharge is explained in detail.

At ASDEX Upgrade there are eight different heating beams available, which all inject neutral deuterium into a magnetically confined fusion plasma. The beams inject continuously the neutrals with energies up to 93 keV, such that they penetrate the plasma. The heating of the plasma is performed after the neutrals are ionized and confined by the magnetic field. The heating location is defined by the injection geometry and in detail also by plasma parameters. In figure 5, the geometry of two beams are depicted, one heating the center of a discharge and one pointing away from the center. Additionally, the geometry of a few plasma diagnostics are presented, which are discussed below .



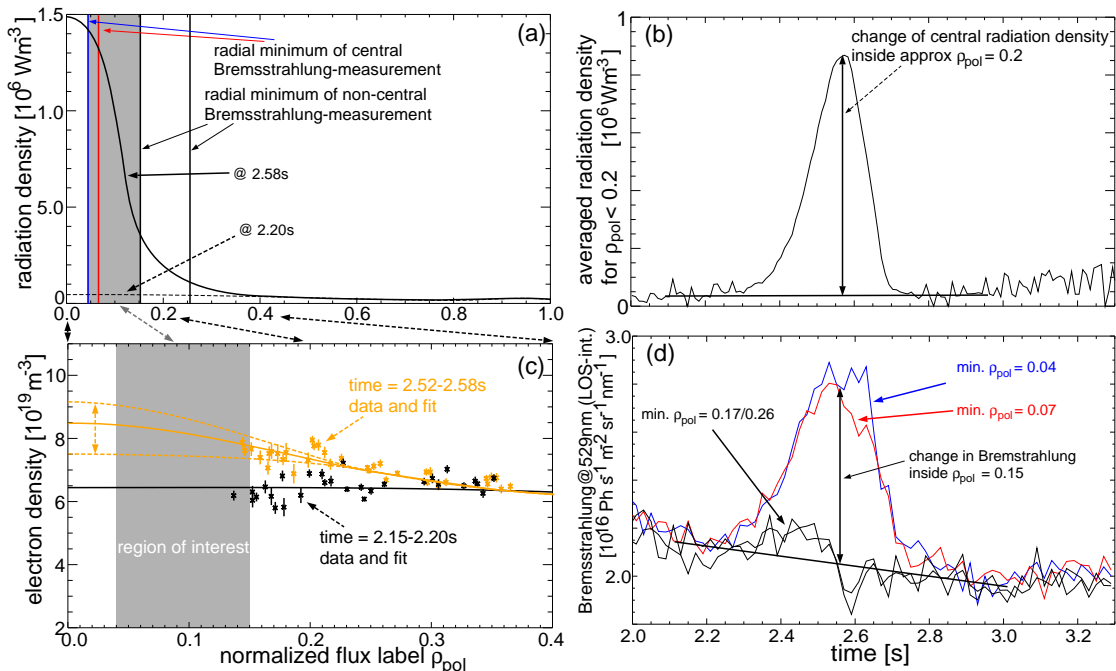
**Figure 5.** (colored in online-version) Geometry of heating beams, lines of sight of the bolometer and Bremsstrahlung measurement and Thomson scattering along with the plasma equilibrium of discharge #19280 at 2.5 s. The curved trajectories result from the projection of tangential LOS and beam lines in the poloidal plane.

In the discharge #19280, the plasma is heated with these neutral deuterium beams. Each of the eight beams is turned on for 500 ms in sequence. The beam which is switched on at 2.0 s is aligned such that the innermost 10-20 cm of the plasma core are not heated, which leads to a small turbulent transport in that region. This decrease in turbulent transport makes the neoclassical transport, i.e. transport based on particle trajectories and collisions, dominant

*Calculation and Experimental Test of the Cooling Factor of Tungsten*

13

[35, 36]. In detail, the neoclassical inward pinch is acting on all impurity species, while its strength is approximately proportional to the charge of the species. This inward drift relies on a gradient of the background deuterium ion density and can be mitigated or reversed by an ion temperature gradient, which is not the case in the actual discharge. The inward pinch leads to so-called impurity accumulation which is dominated by W as can be deduced from the impurity mix available at ASDEX Upgrade. At 2.5 s another beam is turned on heating the plasma core which starts reversing impurity accumulation by increasing the turbulent transport. Figure 6 (a) depicts the radiation profiles derived from the measurements of the



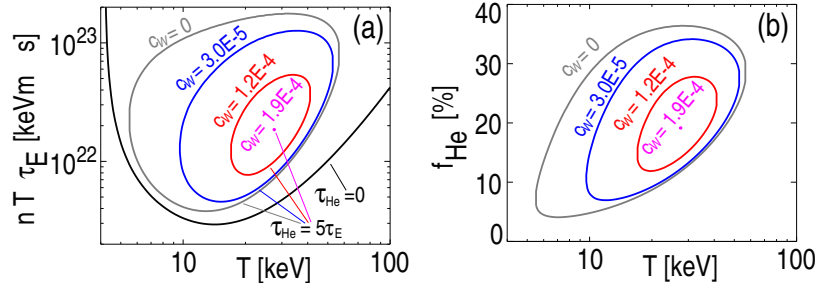
**Figure 6.** (colored in online-version) (a) Deconvoluted radiation profile before and during W-accumulation. Vertical lines denote the minimum radius seen by four lines of sight measuring Bremsstrahlung. (b) Evolution of the radiation density averaged within  $0 < \rho_{pol} < 0.2$ . (c) Electron density measurement (Thomson scattering) and respective fits before and during W-accumulation. (d) Evolution of four (cf. part (a) of this figure) LOS-integrated Bremsstrahlung measurements.

bolometer fan as depicted in figure 5 before and during the accumulation phase and figure 6 (b) documents the evolution of the radiated power density averaged inside  $\rho_{pol} < 0.2$ , i.e. the core region of the plasma with a radius of approximately 7-10 cm. In figure 6 (d) the Bremsstrahlung measurement integrated along a line of sight (LOS) with a toroidal viewing geometry (cf. figure 5) are presented. An increase in Bremsstrahlung is only seen for lines of sight (LOS) which integrate over plasma radiation inside  $\rho_{pol} < 0.15$ . A detailed analysis was performed using the fits to the measured electron densities depicted in 6 (c). The uncertainty of the fit is relatively large because the measurement does not fully cover the core region. However, the shaded region is only about 4 cm wide and the electron density profile cannot change arbitrarily in this region due to constraints from plasma transport considerations. The

fit is a spline function, which is forced to have a zero derivative in the plasma center. The obtained variation in the electron density fit is indicated with the dashed lines. For stronger variations of the electron densities the uncertainties for the cooling factor would increase. The result of this analysis is introduced as a data point in figure 3 (black, thin). As can be seen the value and the error bars are comparable to those from the Ta experiment and both measurements are in agreement with all theoretical curves. It must be noted that some uncertainties have not been included in the error bars of the W-data point. For instance, it is assumed that the change of  $Z_{eff}$  is exclusively caused by W and that the contribution of other ions to the  $Z_{eff}$  of  $2.1 \pm 0.1$  does not vary during the accumulation phase. Therefore, the measurement must be interpreted with care and the main conclusion of the analysis is that the cooling factor is consistent with observations within less than an order of magnitude.

#### 4. Implications on Operation of a Fusion Reactor

The newly obtained cooling factor is used to assess the influence of W as an impurity in a future reactor on the condition for the thermonuclear burn. The ignition condition is derived from the heating of the plasma by  $\alpha$ -particles from DT-fusion, which must compensate the energy losses of the plasma due to transport and radiation. For this balance the energy confinement time  $\tau_E$  is used to describe the losses by transport, while radiation losses are treated using the cooling factor as obtained in this work. Helium is included in the condition as it is naturally produced by the fusion process and then dilutes the fuel. To describe the fact that He is less efficiently pumped from the plasma than the fuel, a He confinement time  $\tau_{He} = 5\tau_E$  is used which reflects the predictions in [37]. For the different values of temperatures  $T$  the burn equilibrium will occur at different values of  $nT\tau_E$ , where  $n$  is the density. The additional impurities might lead to the disappearance of a burn condition for all  $T$  due to dilution and radiation. For W the effect of radiation is much more important than the dilution due to the large cooling factor. The discussed scheme corresponds to case 4 in section 3 of [38] where more details about the evaluation of the burn conditions are given and in which the impurity radiation is separately included in the considerations. In [3] the evaluation of the burn condition has been performed in the same manner, but with the data from the AIM. In figure



**Figure 7.** (colored in online-version) (a) Ignition curves in the presence of different W concentrations for the case that  $\tau_{He} = 5\tau_E$  along with the curve for no He and no W for reference. (b) Equilibrium He concentrations corresponding to burn curves from part (a).

*Calculation and Experimental Test of the Cooling Factor of Tungsten*

15

7(a), the curves are shown which represent conditions for which ignition appears. The curve without He is presented for reference only and will not be discussed below. For the curves with He, the corresponding He concentration curves are presented in figure 7(b). For a W concentration of  $3.0 \cdot 10^{-5}$ , the minimum  $nT\tau_E$  is 20% larger than the value for no W, which is  $3.8 \cdot 10^{21} \text{ keV m}^{-3} \text{ s}$  and its minimum is found at  $T = 15.2 \text{ keV}$ , instead of  $T = 12.8 \text{ keV}$  for the case without W. The respective He-concentrations are approximately 8% and 6%. When comparing these values to the results using the AIM data, the corresponding change of  $nT\tau_E$  by 20% is observed for a W concentration of  $4.5 \cdot 10^{-5}$ , as the cooling factor based on the AIM data is lower in the respective temperature range. The burn condition is not anymore achievable for W concentrations above  $1.9 \cdot 10^{-4}$  using the new cooling factor, while the cooling factor from the AIM calculation gives an upper limit of  $2.3 \cdot 10^{-4}$ . However, it should be noted that in a reactor other impurities will be abundant additionally to W which implies that a realistic limit for the maximum W concentration is in the range of several  $10^{-5}$ .

## 5. Summary

This work follows up work [13] on the modelling of dominant spectral features in the W spectrum. In the course of this earlier work the ionization equilibrium was matched to experiment in the electron temperature range 1-5 keV by adjustments of the recombination rates. These findings were used in the actual work to calculate the cooling factor of W. The line radiation has been evaluated by calculations on atomic/ionic structures and excitation rates using the plane-wave Born approximation. All calculations have been performed with the Cowan code using the infrastructure and collisional-radiative modelling of the ADAS project. Level-resolved calculations have been compared to less elaborate configuration averaged calculations in order to extend the involved number of configurations entering the calculations and also to extend the calculations to ions with a lower charge than Ag-like W<sup>28+</sup>. The results of the different calculation approaches could be understood qualitatively and the best suited data to enter the cooling factor originated from the configuration averaged calculation with a very large set of input configurations. The total radiated power predicted by level-resolved calculations, which reproduce the dominant spectral features observed in experiment, is matched within a few percent by the configuration averaged calculation scheme using the same set of input configurations. For a few exceptions, i.e. three ionization states with closed subshells, differences between the two calculation methods as large as 50% in line radiation are observed, but play only an insignificant role for the total cooling factor. The radiated power during recombination (i.e. radiative and dielectronic recombination) is predicted by taking the recombination rate and assuming that 1.2 times the ionization potential is radiated in the course of recombination. This approach is chosen, to obtain data consistent to the recombination rates which have been adjusted to experimental observations. However, details of the recombination radiation are not important since line radiation is the dominant radiation source for the plasma parameters considered here. A study was performed to ensure that uncertainties in the recombination rates and the connected radiation have only minor influence on the cooling factor. Additionally, the Bremsstrahlung is taken into account. The

resulting cooling factor is given in tabulated form. Its value at approx. 2.3 keV is measured in experiment by comparing the total radiation to the Bremsstrahlung during a special phase of a plasma discharge in ASDEX Upgrade. The measurement agrees with the calculation, however, the uncertainties of the measurement are nearly one order of magnitude. When comparing the actual cooling factor to that derived from the average ion model (AIM), about a factor of 2 less radiation is predicted below 1 keV, while the differences decrease for higher electron temperatures. Both cooling factors are quite similar above 6 keV, while the newly evaluated cooling factor slightly exceeds the cooling factor from the AIM above electron temperatures of approx. 10 keV. Therefore, the predictions of the maximum tolerable tungsten concentration for a fusion reactor, which prior to this work were based on the AIM, are reduced only slightly by about 20-35%.

## References

- [1] N. Noda, V. Philipps, and R. Neu, Journal of Nuclear Materials **241–243**, 227 (1997).
- [2] R. Neu, Physica Scripta **T123**, 33 (2006).
- [3] R. Neu *et al.*, Fusion Engineering and Design **65**, 367 (2003).
- [4] R. Isler, R. Neidigh, and R. Cowan, Phys. Lett. **A63**, 295 (1977).
- [5] E. Hinnov and M. Mattioli, Phys. Lett. **A66**, 109 (1978).
- [6] R. Neu *et al.*, Nuclear Fusion **45**, 209 (2005).
- [7] R. Neu *et al.*, Plasma Physics and Controlled Fusion **49**, B59 (2007).
- [8] A. C. C. Sips and O. Gruber, for the ASDEX Upgrade Team, Plasma Physics and Controlled Fusion **50**, 124028 (2008).
- [9] D. Post *et al.*, At. Data Nucl. Data Tables **20**, 397 (1977).
- [10] D. Post, J. Abdallah, R. Clark, and N. Putvinskaya, Phys. Plasmas **2**, 2328 (1995).
- [11] R. D. Cowan, *The Theory of Atomic Structure and Spectra (Los Alamos Series in Basic and Applied Sciences)* (University of California Press, California, 1981).
- [12] A. Foster, doctoral thesis at Department of Physics, University of Strathclyde, Glasgow, UK (2008)-  
[http://adas.phys.strath.ac.uk/theses/foster\\_thesis.pdf](http://adas.phys.strath.ac.uk/theses/foster_thesis.pdf)
- [13] T. Pütterich *et al.*, Plasma Physics and Controlled Fusion **50**, 085016 (2008).
- [14] S. D. Loch *et al.*, Physical Review A (Atomic, Molecular, and Optical Physics) **72**, 052716 (2005).
- [15] E. Behar, R. Doron, P. Mandelbaum, and J. L. Schwob, Phys. Rev. A **58**, 2115 (1998).
- [16] A. Peleg, E. Behar, P. Mandelbaum, and J. L. Schwob, Phys. Rev. A **57**, 3493 (1998).
- [17] E. Behar, P. Mandelbaum, and J. L. Schwob, Phys. Rev. A **59**, 2787 (1999).
- [18] W. J. Karzas and R. Latter, Astrophysical Journal — Supplement Series **6**, 167 (1961).
- [19] H. P. Summers, The ADAS User Manual, version 2.6 <http://adas.phys.strath.ac.uk> (2004).
- [20] T. Pütterich *et al.*, J. Phys. B: At. Mol. Opt. Phys. **38**, 3071 (2005).
- [21] T. Pütterich, Technical Report No. 10/29, IPP Garching, Germany, doctoral thesis at Universität Augsburg.
- [22] R. Neu *et al.*, Review of Scientific Instruments **67**, 1829 (1996).
- [23] R. Radtke *et al.*, Phys. Rev. A **64**, 012720 (2001).
- [24] Y. Ralchenko *et al.*, Journal of Physics B: Atomic, Molecular and Optical Physics **40**, 3861 (2007).
- [25] S. B. Utter, P. Beiersdorfer, and E. Träbert, Can. J. Phys. **80**, 1503 (2002).
- [26] R. Radtke, C. Biedermann, P. Mandelbaum, and J. L. Schwob, in *HCI 2006: 13th International Conference on the Physics of Highly Charged Ions*, Vol. 58 of *J. Phys. Conf. Ser.*, edited by R. McCullough *et al.* (IOP, Bristol, England, 2007), pp. 113–116.
- [27] P. Neill *et al.*, Can. J. Phys. **82**, 931 (2004).
- [28] Y. Ralchenko *et al.*, Physical Review A (Atomic, Molecular, and Optical Physics) **74**, 042514 (2006).

*Calculation and Experimental Test of the Cooling Factor of Tungsten* 17

- [29] C. P. Ballance and D. C. Griffin, Journal of Physics B: Atomic, Molecular and Optical Physics **39**, 3617 (2006).
- [30] Y. Ralchenko, Journal of Physics B: Atomic, Molecular and Optical Physics **40**, F175 (2007).
- [31] Y. Ralchenko *et al.*, J. Phys. B-At. Mol. Opt. Phys. **41**, 021003 (2008).
- [32] U. Feldman, J. E. Seely, E. Landi, and Y. Ralchenko, Nucl. Fusion **48**, 045004 (2008).
- [33] C. Biedermann, R. Radtke, R. Seidel, and T. Pütterich, Physica Scripta **T134**, 014026 (2009).
- [34] R. Neu *et al.*, in *Highly Charged Ions*, edited by R. Hutton *et al.* (CRC Press, London, England, 2010), to be published.
- [35] R. Dux *et al.*, Plasma Physics and Controlled Fusion **45**, 1815 (2003).
- [36] R. Dux, Fusion Science and Technology **44**, 708 (2003).
- [37] D. Campbell, Phys. Plasm. **8**, 2041 (2000).
- [38] D. Reiter, G. H. Wolf, and H. Kever, Nuclear Fusion **30**, 2141 (1990).

### **5.3 Publication 3**

*The extreme ultraviolet emissions of W<sup>23+</sup>(4f5)*

AIP Conf. Proc. 1545, 132 (2013)

# The Extreme Ultraviolet Emissions of W<sup>23+</sup> (4f<sup>5</sup>)

**T Pütterich†, V. Jonauskas‡, R Neu†, R Dux† and ASDEX Upgrade Team**

† Max–Planck–Institut für Plasmaphysik, EURATOM Association, D–85748 Garching, Germany

‡ Institute of Theoretical Physics and Astronomy of Vilnius University, A Goštauto, LT01108 Vilnius, Lithuania

**Abstract.** In order to comply with the special challenges (open 4*f*-shell, configuration mixing) of simulating the spectrum of W<sup>23+</sup> an extensive atomic model was implemented using the flexible atomic code (FAC). In detail, the basis functions from 11 configurations were used to model about 12000 levels, which give rise to roughly 60 million transitions including nearly 6 million electric and magnetic dipole transitions. A collisional radiative model has been put together which could handle the size of the input data. The modelled spectra (4–40 nm) show low sensitivity on the electron density, which validates the comparison of EBIT and tokamak spectra. The emissions between 4 and 7 nm are discussed in the context of the observations at fusion plasmas. In this range, the influence of W<sup>23+</sup> is limited due to the small contribution to the measurement - however, elements of the presented modelling might explain the second, not understood spectral feature at 6 nm. Further details of the spectra are only briefly discussed as a close comparison to experimental data requires also models for the neighbouring ionisation stages. Additionally, the importance of configuration mixing becomes apparent motivating further investigations on neighbouring ionisation stages with similarly complex models.

## 1. Introduction

Tungsten is moving back into the focus of spectroscopy for fusion plasmas because it is used in present day tokamaks [1] as a plasma facing material in preparation of future reactor relevant devices, such as ITER [2]. There are basically two rationales why tungsten is a candidate for future fusion devices. First, it features tolerable erosion [3] such that the first wall of the reactor withstands for several years the impinging ion fluxes. Second, the retention of fuel inside of the reactor chamber is comparably small [4] and thus compatible with safety requirements. If used as plasma facing material, tungsten will be an intrinsic impurity in these plasmas as sputtering at the plasma wetted surfaces cannot be avoided. The electron temperatures of the confined plasma will span from 0.1 keV at the very edge up to 25 keV in the core. While the spectrum for tungsten ions with charges above Pd-like W<sup>28+</sup> (ground state 4d<sup>10</sup>) have been subject to many theoretical and experimental investigations at fusion plasmas and electron beam ion traps (EBITs) (cf. overview in Ref. [5]), the ionisation stages with lower

*The Extreme Ultraviolet Emissions of W<sup>23+</sup> (4f<sup>5</sup>)*

2

charge have been covered in less detail. The reason for this is the high complexity of the spectrum which is accompanied by large computational efforts for the calculation of atomic data for these ionisation stages, which exhibit an open 4f-shell leading to numerous coupling possibilities for the 4f-electrons. When considering excited states, an important group of excited levels originates from the promotion of a 4d electron to the 4f shell, which multiplies the coupling possibilities by approximately a factor of 10. Additionally, configuration interaction and mixing plays an important role for high-Z elements. Thus, the individual wave functions are described best by including several configurations as basis function sets. As a consequence the calculations inevitably need to be huge including tens of thousands of levels and tens of millions of transitions. In the experiment, a separate consideration of ionisation stages is challenging, because the ionisation potentials of neighbouring ionisation stages are separated by only a few tens of electron volts such that even EBITs cannot prepare a single ionisation stage, further complicating the identification of spectral emissions.

In this work Sb-like W<sup>23+</sup> has been tackled using the flexible atomic code (FAC) [6], while the collisional-radiative model from the ADAS project [7] was extended to be able to handle the huge input files. The spectrum of Sb-like W<sup>23+</sup> is modelled in the VUV range 4-7 nm and 10-40 nm, because these wavelength ranges exhibit the strongest emissions and some experimental data are available for comparison. The range 7-10 nm neither exhibits considerable spectral radiance in the modelled spectra nor in the measurements.

The emissions in the wavelength range 4-7 nm have been investigated in detail at EBITs [8, 9], fusion experiments [10–18] as well as in purely theoretical studies [19, 20]. Up to now the spectral feature at 5 nm observed at tokamaks has been attributed to the emissions of Ag-like W<sup>27+</sup> to Y-like W<sup>35+</sup>, as lower charged ions do not exhibit a considerable abundance in the hot plasmas. Nevertheless, the suspicion is that more lowly charged ionisation stages contribute to the line of sight integrated spectra. In the present work we evaluate the importance of this contribution.

For the wavelength range 10-40 nm investigations have been performed on the spectral lines of W-ions with charges higher than W<sup>38+</sup> [12–14, 21], but investigations on the emissions from ions with charges lower than W<sup>28+</sup> are scarce [8, 14, 16] and open questions remain.

It should be noted that the previous investigations on the ionisation stages with an open 4f-shell are performed by tackling only a few configurations [15, 16, 20] or by applying configuration averaged calculations, which do not allow for configuration interaction. Both simplifications are known to produce unreliable predictions of the spectra for high-Z elements. In the present work, we present a calculation that includes about 12000 levels and considers roughly 60 million transitions. Due to the size of the calculation we were not able to model all ions featuring an open 4f shell, but we could elucidate the properties of the spectral emissions for one ionisation stage.

*The Extreme Ultraviolet Emissions of W<sup>23+</sup> (4f<sup>5</sup>)*

3

**2. Calculation of Structure and Effective Collision Strengths**

The energy levels, electric dipole and magnetic dipole transition probabilities and electron-impact excitation collision strengths in the distorted-wave approximation for the W<sup>23+</sup> ion were obtained using FAC [6]. It realizes the Dirac-Fock-Slater approach. In the course of the calculation the configuration mixing coefficients and energy levels result from the diagonalization of the Dirac-Coulomb-Breit Hamiltonian matrix. Vacuum polarization and self energy (known as Lamb shift) treated in screened hydrogenic approximation are included in the Hamiltonian matrix.

Figure 1 shows the diagram for energy levels used in the calculations. The present study included levels originating from the 4f<sup>5</sup>, 4f<sup>4</sup>5s, 4f<sup>4</sup>5p, 4f<sup>4</sup>5d, 4f<sup>4</sup>5f, 4f<sup>3</sup>5s<sup>2</sup>, 4f<sup>3</sup>5s5p, 4f<sup>3</sup>5p<sup>2</sup>, 4f<sup>3</sup>5s5d, 4d<sup>9</sup>4f<sup>6</sup>, 4d<sup>9</sup>4f<sup>5</sup>5s configurations. The choice of configurations is based on the highest energy level of the 4d<sup>9</sup>4f<sup>6</sup> configuration which is taken as the energy of reference. All configurations which have energy levels lower than the reference one are included in the collisional radiative modelling. The difference of the highest energy level of the 4d<sup>9</sup>4f<sup>6</sup> configuration and the energy of the ground level is equal to 306 eV (4 nm), i.e. the lowest limit of the shortest wavelength range (4-7 nm) studied in the present work. Because the levels of the 4f<sup>3</sup>5p<sup>2</sup>, 4d<sup>9</sup>4f<sup>5</sup>5s, 4f<sup>4</sup>5f and 4f<sup>3</sup>5s5d configurations overlap with the levels of the 4d<sup>9</sup>4f<sup>6</sup> configuration they were included in our modelling. However, those configurations are of odd parity and mixing with 4d<sup>9</sup>4f<sup>6</sup> configuration does not take place.

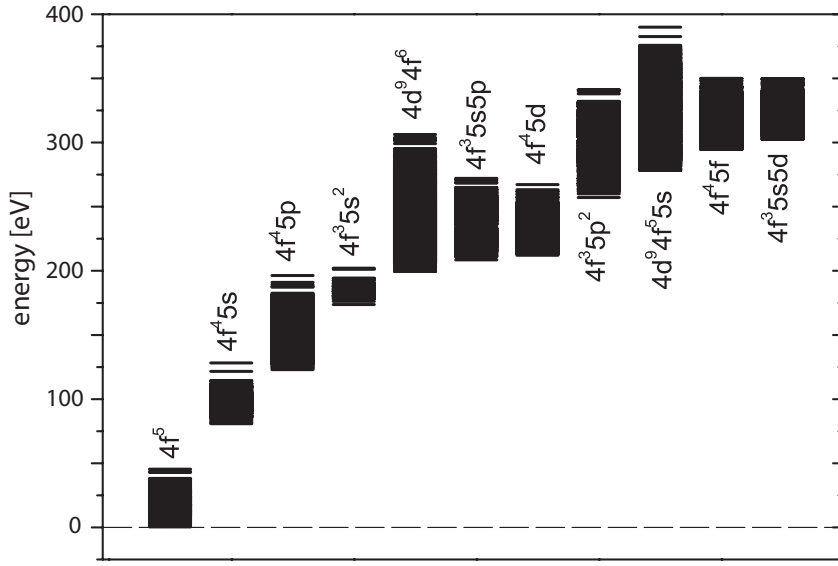
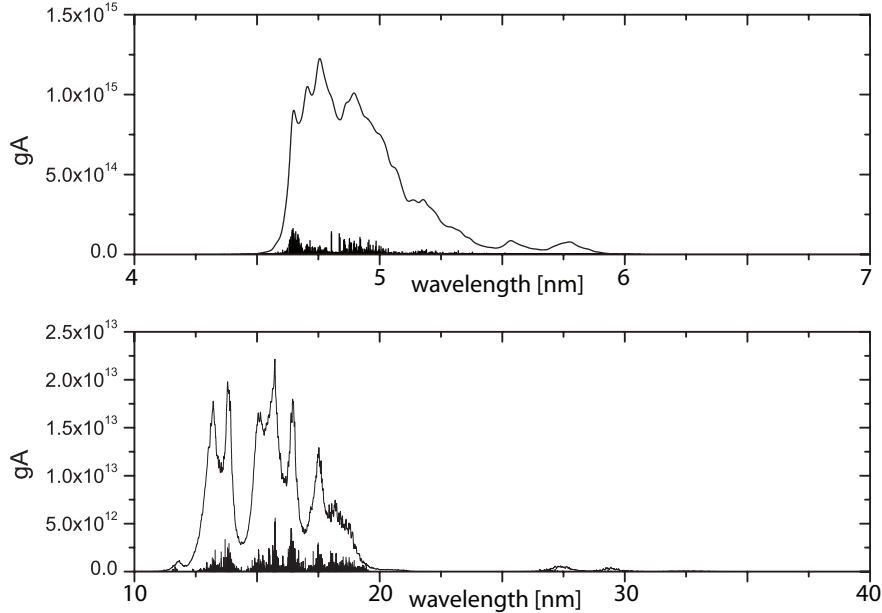
The study did not take into account the 4d<sup>9</sup>4f<sup>5</sup>5p configuration of even parity which is closest in energy to the employed configurations. This configuration has 10934 levels and the inclusion of it would approximately double the number of transitions to be calculated. As well, many other configurations of the even parity overlap with the 4d<sup>9</sup>4f<sup>5</sup>5p configuration and mixing among the states of those configurations would have to be taken into account. Due to this, the rate matrix would drastically increase and the calculations would become even more challenging which is the main reason why the present work omits those configurations.

Figure 2 features the  $gA$  values for electric dipole transitions in the range 4-7 nm and 10-40 nm - the spectral region in-between (7-10 nm) exhibits no considerable emissions. The first interval corresponds to the transitions from the 4d<sup>9</sup>4f<sup>6</sup>, 4f<sup>3</sup>5s5p, 4f<sup>4</sup>5d configurations to the one containing the ground state and transitions from four configurations of odd parity with the largest energies (4f<sup>3</sup>5p<sup>2</sup>, 4d<sup>9</sup>4f<sup>5</sup>5s, 4f<sup>4</sup>5f, 4f<sup>3</sup>5s5d) to the 4f<sup>4</sup>5s configuration. However, the transitions from the 4f<sup>3</sup>5s5p configuration to the ground configuration are not allowed in the single configuration approximation because those configurations propagate two electrons. The mixing of the former configuration with the 4f<sup>4</sup>5d configuration which in addition interacts with the 4d<sup>9</sup>4f<sup>6</sup> configuration opens additional decay channels for the 4f<sup>3</sup>5s5p configuration. In a similar way, transitions from the 4f<sup>3</sup>5p<sup>2</sup> to the 4f<sup>4</sup>5s configuration will not take place if configuration interaction is not included in the calculations.

Practically all configurations contribute to the second range of wavelengths. The

*The Extreme Ultraviolet Emissions of W<sup>23+</sup> (4f<sup>5</sup>)*

4

**Figure 1.** Energy levels of the first eleven configurations for W<sup>23+</sup>.**Figure 2.**  $gA$  distributions for transitions in W<sup>23+</sup> (bars). Lines correspond to convolved  $gA$  with a 0.01 nm wide Gaussian. Note the different scales.

total number of electric and magnetic dipole transitions in that range is equal to 4843954 compared to the 610671 transitions in the first wavelength range. However, the latter transitions are much weaker. The sum of the dipole transition probabilities is about one order of magnitude smaller for the range 10-40 nm than for transitions in the range 4-7 nm.

*The Extreme Ultraviolet Emissions of W<sup>23+</sup> (4f<sup>5</sup>)*

5

### 3. Collisional-Radiative Modelling

The mere size of the calculation results of FAC makes it challenging to process them in a collisional-radiative model (CRM), which was developed by the ADAS project [7] and is not optimized for computational speed. The baseline capabilities of this CRM were isolated and a basic CRM optimized for speed was set up, as described below. It takes into account the excitation and de-excitation by electron impact and the spontaneous decay. The individual populations are described in a population vector  $\vec{N}$  which has the size of the total number of considered levels. The population matrix  $\bar{P}$  is now arranged such that the multiplication  $\bar{P}\vec{N}$  gives the rate of change of  $\vec{N}$ , i.e.  $d\vec{N}/dt$ . Thus, the equilibrium  $d\vec{N}/dt = 0$  is found for a population vector for which  $(\bar{E} + \bar{P})\vec{N} = \vec{N}$ , where  $\bar{E}$  is the identity matrix. The solution of this equation is not a unique vector, as additional solutions can be produced by multiplying  $\vec{N}$  with a constant, i.e. the total W-density is a free parameter. Therefore, the normalization  $\sum_k p_k = 1$  is introduced where  $p_k$  is the population fraction in the level  $k$ .

This system of equations is solved for various combinations of electron temperature and density using the iterative biconjugate gradient method (cf. 'linbcg' in chapter 2.7 in Ref. [22]) as well as LU decomposition. Both procedures lead to the same result within the numerical accuracy. The final result is the emissivity normalized by electron and impurity ion density for each spectral line, which is called photon emissivity coefficient (PEC) and is obtained by multiplication of the relative population with the respective A-value (cf. equation below). Thus the emissivity  $\epsilon_{ij}$  of a spectral line emitted by the decay of level  $i$  into level  $j$  is given by:

$$\epsilon_{ij} = n_e n_{W^{23+}} p_i A_{ij} = n_e n_{W^{23+}} \text{PEC}_{ij}$$

where  $n_e$  is the electron density,  $n_{W^{23+}}$  the density of W<sup>23+</sup> and  $\text{PEC}_{ij}$  is the PEC for the transition between the levels  $i$  and  $j$ .

### 4. Comparison with Experimental Data

#### 4.1. EUV emissions in the range 4-7 nm

In the following, the basic structure of the spectral emissions of W<sup>23+</sup> and its density dependence are investigated in order to judge the degree of correspondence between spectra from EBITs and fusion plasmas. Furthermore the importance of the W<sup>23+</sup> emissions in a typical spectrum from a fusion plasma, i.e. a line of sight integrated measurement across the full cross section of a plasma, will be analyzed.

In this wavelength range an intense spectral feature has been observed in various fusion experiments [10–18]. However, detailed comparisons between tokamak and EBIT spectra [13] reveal that a considerable fraction of the emissions observed in fusion experiments for  $T_e < 2$  keV cannot be brought into accordance neither with the EBIT observations [8] nor with modelling [14]. In figure 3, modelled spectra are presented for the electron densities  $10^{17}$  and  $10^{20} \text{ m}^{-3}$  corresponding to typical EBIT densities

*The Extreme Ultraviolet Emissions of W<sup>23+</sup> (4f<sup>5</sup>)*

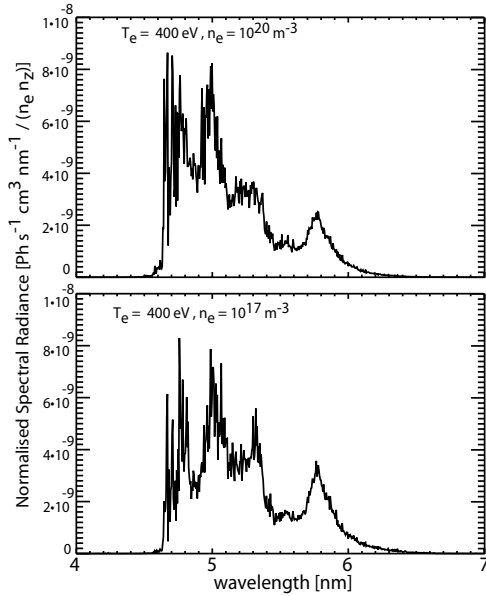
6

and tokamak densities, respectively. In both cases the electron velocity distribution is Maxwellian corresponding to 400 eV (close to maximum abundance of W<sup>23+</sup>). As can be judged from the figure, the effect of electron density on the spectral emissions is rather moderate, which further motivates comparisons between EBIT and tokamak spectra.

In figure 4, the measurements of the Berlin EBIT (cf. Refs. [8, 13]) are compared to a spectrum from the tokamak ASDEX Upgrade. The latter spectrum was measured for a plasma with central plasma temperature of 2.1 keV and is presented alongside its modelling considering the ionisation stages W<sup>27+</sup>-W<sup>35+</sup> (blue) and W<sup>23+</sup> (red) separately. All three curves have the same scale and can be compared to each other. The blue model curve reproduces the observed intensity of the tokamak spectrum if integrated over wavelength, but lacks the detailed spectral shape (for more details see [13, 14]). The EBIT investigations [8] for the ionisation stages from Ag-like W<sup>27+</sup> to Y-like W<sup>35+</sup> (cf. spectra in figure 4 with beam energies between 0.87 and 1.52 keV, note that for a beam energy of 1.52 keV W<sup>36+</sup> may be produced, but the spectrum exhibits contributions from lower charged ionisation stages) found good agreement with the calculated atomic data which were based on the transitions between the configurations 4p<sup>6</sup>4d<sup>n-1</sup>4f-4p<sup>6</sup>4d<sup>n</sup> (e.g. [8]) and 4p<sup>5</sup>4d<sup>n+1</sup>-4p<sup>6</sup>4d<sup>n</sup> and configuration interaction was found to play a crucial role. However, the tokamak spectrum, which is a superposition of the emissions of all ionisation states that exist along a line of sight, exhibit additional emissions at 6 nm (cf. bottom figure 4). One suspicion is that the additional radiation at 6 nm observed in fusion plasmas is caused by ionisation stages more lowly charged than Pd-like W<sup>28+</sup>. The EBIT measurements in Ref. [8] with beam energies below 0.87 keV suggest that these ionisation stages exhibit emission lines in the respective wavelength range, while the structure of the EBIT spectra for these ionisation stages does not reproduce the observations from ASDEX Upgrade (cf. figure 4, bottom). The EBIT measurements for beam energies below 0.87 keV exhibit a rather smooth emission shape versus wavelength, while the modelling in the present work exhibits two clear structures for both modelled densities, i.e. one between 4.6 and 5.5 nm and the other at about 5.8 nm (cf. figure 3). The structure at 5.8 nm has a full width half maximum of about 0.2 nm. It is unclear, why the EBIT measurements are less structured than the modelling. A possible explanation could be that in the EBIT spectra more than one ionisation stage contributes and while the individual ionisation stages might exhibit quite structured emissions the superposition of all the emissions look smooth. This effect is known for the tokamak spectrum, where even more charge stages contribute. Note that in none of the EBIT spectra there is an indication for a maximum at 6 nm. An alternative explanation for both observations could be additional processes, such as dielectronic recombination, which have not been included in the calculations and contribute more or less significantly to the tokamak spectrum. Further investigations on the ionisation stages around W<sup>23+</sup> in similar detail are needed to clarify this question. As mentioned above the model sees no significant change of the spectrum for a change of the density. This means that spectral structures of W<sup>23+</sup> as observed in EBIT measurements should look very similar to those observed in spectra from fusion plasmas.

*The Extreme Ultraviolet Emissions of W<sup>23+</sup> (4f<sup>5</sup>)*

7



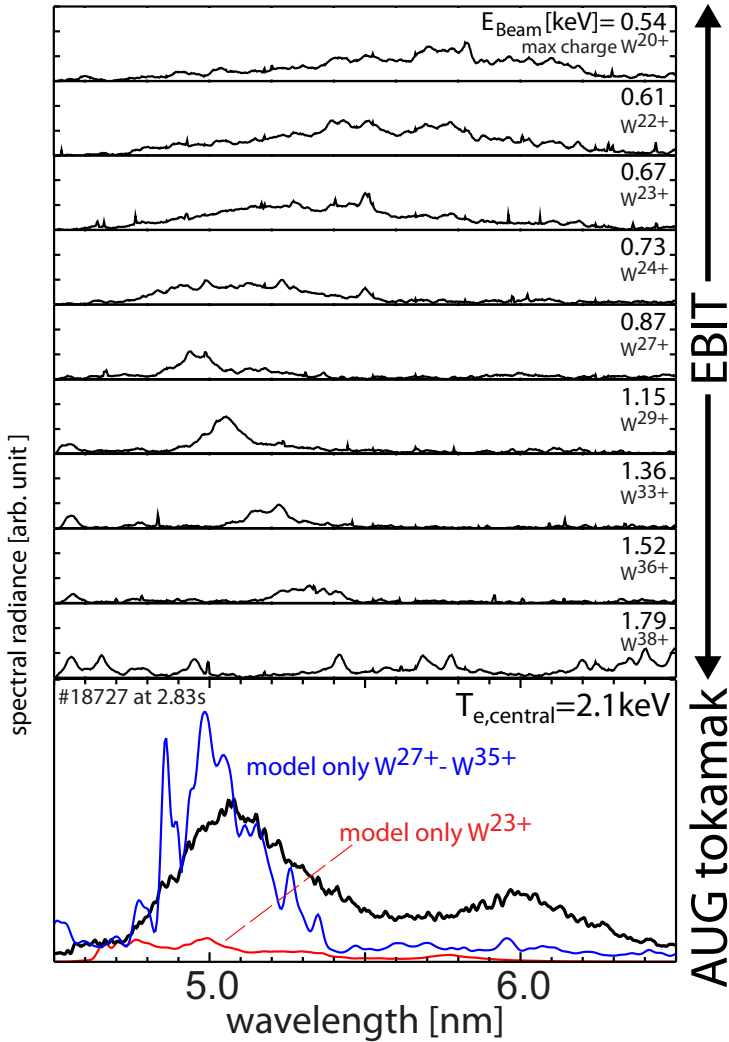
**Figure 3.** Modelled spectrum for W<sup>23+</sup> at two densities,  $10^{17}$  and  $10^{20} \text{ m}^{-3}$ , for an electron temperature of 400 eV (close to the maximum abundance of W<sup>23+</sup> (cf. figure 6 in [14])). The individual lines are broadened using the assumption that the electron and ion temperatures are equal. In the experiment the broadening by the instrument functions is dominant since the instrumental broadening is reported to be 0.02–0.025 nm [8, 14], while at 400 eV the Doppler broadening is less than 0.0006 nm at 5 nm.

In order to illustrate the contributions of the various ionisation stages, the fractional abundances of the relevant ionisation stages along the spectrometer’s line of sight are indicated in figure 5. The fractional abundances were calculated using atomic data as derived in [14]. It should be noted that the underlying recombination rates from the average ion model (radiative + dielectronic recombination) [24, 25] have been adjusted as described in Ref. [14] such that the experimentally determined fractional abundances for several ionization stages are reproduced. No other available dataset could reproduce the experimental findings. In figure 5, W<sup>23+</sup> only exists in a layer at the plasma edge and its contribution in the measured tokamak spectrum of figure 4 (red) is small, but comparable to that of one of the ionization stages of W<sup>27+</sup> – W<sup>35+</sup>. However, for lower charged ionisation stages the layer in which these lower charge stages exist in the plasma is even thinner and the absolute densities at the edge are smaller. Thus, it is hard to imagine that the local maximum around 6 nm results from emissions by W<sup>14+</sup> to W<sup>27+</sup>, i.e. ionisation stages with an open 4f-shell.

Nevertheless, the modelled data exhibits two distinct structures - one between 4.6 and 5.5 nm and one around 5.8 nm (better visible in figure 3). As the previous modelling efforts (W<sup>27+</sup>–W<sup>35+</sup>) for the same spectral range did not reproduce the structure of two local maxima it is worthwhile to look into the transitions that give rise to the second maximum. From earlier modellings (cf. Ref. [14]) it is derived that the transitions

*The Extreme Ultraviolet Emissions of W<sup>23+</sup> (4f<sup>5</sup>)*

8

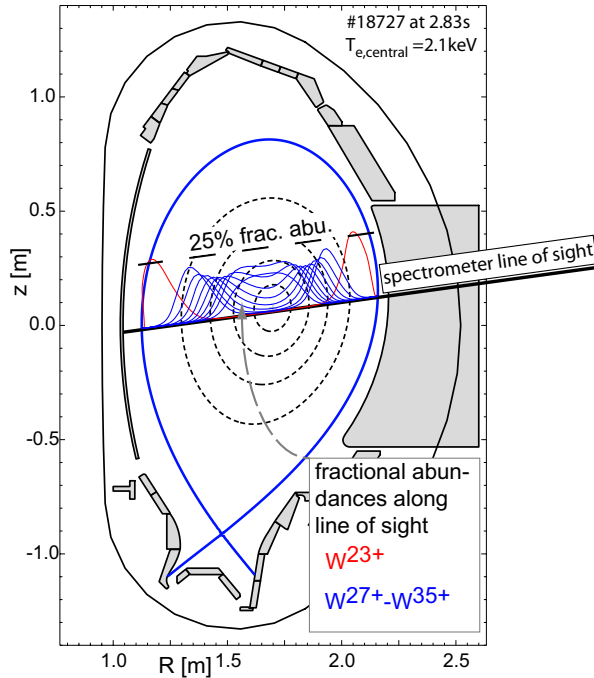


**Figure 4.** A few spectra from EBIT investigations [8] are compared to a spectrum from the tokamak ASDEX Upgrade and modelled spectra corresponding to the tokamak spectrum. The modelled spectrum for W<sup>23+</sup> (red) and the modelled spectrum for W<sup>27+</sup> to W<sup>35+</sup> (blue) are shown on the same scale as the measurement. For the EBIT spectra the applied beam energy and the maximum obtainable charge stages (single impact ionisation) are stated using ionisation potentials from Ref. [23].

of the type 4p<sup>6</sup>4d<sup>9</sup>4f<sup>n+1</sup>-4d<sup>10</sup>4f<sup>n</sup> play a crucial role for these low energy/temperature emissions in this wavelength range 4.6 and 5.5 nm. For the present modelling of W<sup>23+</sup> the emissions between 4.6 and 5.5 nm correspond mainly to transitions of the type 4d<sup>9</sup>4f<sup>6</sup>-4d<sup>10</sup>4f<sup>5</sup>, while many configurations are involved in the transitions between 5.7 and 5.9 nm. In descending importance the following transitions contribute to the emissions in the range 5.7 to 5.9 nm (the first type of transition contributes about 10 times more intensity than the last): 4f<sup>4</sup>5d-4f<sup>5</sup> - 4d<sup>9</sup>4f<sup>6</sup>-4d<sup>10</sup>4f<sup>5</sup> - 4f<sup>3</sup>5s5p-4f<sup>5</sup> - 4f<sup>4</sup>5f-4f<sup>4</sup>5s - 4d<sup>9</sup>4f<sup>5</sup>5s-4d<sup>10</sup>4f<sup>4</sup>5s and 4f<sup>3</sup>5s5d-4f<sup>4</sup>5s. As a conclusion this means that in order to reproduce the local emission maximum at 5.8 nm a large amount of configurations need to be included

*The Extreme Ultraviolet Emissions of W<sup>23+</sup> (4f<sup>5</sup>)*

9



**Figure 5.** Geometry of the tokamak measurement yielding the spectrum in figure 4. The fractional abundances (from model in [14]) along the spectrometer line of sight are indicated by the blue ( $W^{27+} - W^{35+}$ ) and red ( $W^{23+}$ ) lines above the line of sight of the spectrometer.

in the calculation. Considering that this might have been missed out on the modelling efforts for the ionisation stages Ag-like  $W^{27+}$  up to Y-like  $W^{35+}$  these should be revised in order to possibly reproduce the emission maximum at 6 nm as observed in the tokamak spectra.

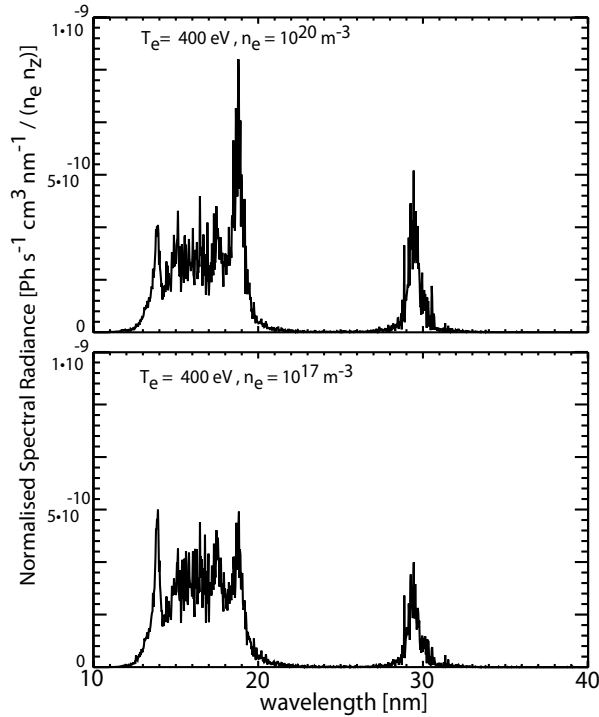
It should be noted that the identification of contributing configurations does not mean that the calculation result is the same if only these configurations are included as basis function sets. The not mentioned configurations may influence the result significantly, an effect which is attributed to configuration mixing and non-linear behaviour of collisional radiative models.

#### 4.2. EUV emissions in the range 10-40 nm

In Ref. [14], it has been found that the spectral emissions in the wavelength range 10-40 nm originate from the edge plasma region with electron temperatures below about 1 keV. For this temperature range the ionisation stages of W up to about Pd-like  $W^{28+}$  exist in relevant abundances. From the modelling of  $W^{24+}$  to  $W^{26+}$  in Ref. [14], which was performed with a limited set of configurations, it was concluded that the W-emissions between 20 and 28 nm must originate from even more lowly charged ionisation stages. In figure 6 the modelled spectra of  $W^{23+}$  are presented for the two electron densities  $10^{17}$  and  $10^{20} \text{ m}^{-3}$  in this wavelength range. Both cases are similar to a degree

*The Extreme Ultraviolet Emissions of W<sup>23+</sup> (4f<sup>5</sup>)*

10



**Figure 6.** Modelled spectrum for W<sup>23+</sup> at two densities, 10<sup>17</sup> and 10<sup>20</sup> m<sup>-3</sup>. Please note the different scale as compared to figure 3.

that again the application of EBIT findings for the interpretation of tokamak spectra seems sensible. In the calculations the emissions in the range 10-20 nm are provided by transitions of the type 4f<sup>4</sup>5s-4f<sup>5</sup> – 4f<sup>4</sup>5p-4f<sup>4</sup>5s – 4f<sup>4</sup>5d-4f<sup>4</sup>5p and 4d<sup>9</sup>4f<sup>6</sup>-4d<sup>10</sup>4f<sup>4</sup>5p. In the range 28 to 32 nm transitions of the type 4f<sup>4</sup>5p-4f<sup>4</sup>5s are dominant. In Ref. [14], the modelled emissions of W<sup>24+</sup> to W<sup>26+</sup> correspond to the configurations 4d<sup>10</sup>4f<sup>n-1</sup>5p-4d<sup>10</sup>4f<sup>n-1</sup>5s. In the present calculations the corresponding emissions in W<sup>23+</sup> are also identified as important, however, additional transitions from other configurations are found to also emit considerable number of photons in this wavelength range.

## 5. Summary and Conclusion

An extensive atomic model for W<sup>23+</sup> has been implemented using the flexible atomic code (FAC). The approximately 12000 levels have been modelled using basis functions from 11 configurations. The spectral contributions from 6 million electric and magnetic dipole transitions have been considered. Furthermore, the collision cross sections for electron impact have been evaluated for roughly 60 million transitions using the distorted wave approximation. This input data was then processed with a baseline collisional radiative model that considers electron impact excitation and de-excitation as well as radiative decays by electric and magnetic dipole transitions. The resulting spectra show only a weak dependence on electron density which suggests that also for W<sup>23+</sup> the

*The Extreme Ultraviolet Emissions of W<sup>23+</sup> (4f<sup>5</sup>)*

11

spectra from EBIT devices can be used to interpret the spectra from fusion devices in order to identify the emitting ionisation stages responsible for observed spectral features. The modelled spectra exhibit strong emissions at 5 nm, which can also be reproduced by much simpler atomic models (cf. earlier work). However, for the first time the modelling provides a possible explanation of the second maximum in the spectrum at about 6 nm: while the modelled spectra exhibit this second maximum at 5.8 nm it is speculated that the spectra of higher charged ionisation stages when modelled with the same amount of detail might exhibit a similar maximum at longer wavelengths.

Additional emissions are found between 10 and 35 nm. Again simpler models have also reproduced emissions in this spectral range, however, the more complicated model (present work) demonstrates that configuration interaction and mixing is crucial. Therefore it is suggested that all the ions between W<sup>14+</sup> and W<sup>35+</sup> ought to be approached in similar detail as described in the present work. As computing power increases also a re-evaluation of the W<sup>23+</sup> spectra should be undertaken by including the 4d<sup>9</sup>4f<sup>5</sup>5p configuration and by extending the optical transitions to those of quadrupole and possibly octupole type.

### Acknowledgement

This research was partly funded by European Social Fund under the Global Grant Measure (No.: VP1-3.1-SMM-07-K-02-015)

### References

- [1] R. Neu *et al.*, Plasma Phys. Control. Fusion **53**, 124040 (2011).
- [2] R. Pitts *et al.*, J. Nucl. Mater. **415**, S957 (2011).
- [3] H. Bolt *et al.*, J. Nucl. Mater. **329-333**, 66 (2004).
- [4] J. Roth *et al.*, J. Nucl. Mater. **390-391**, 1 (2009).
- [5] A. Kramida, Can. J. Phys. **89**, 551 (2011).
- [6] M. Gu, Astrophys. J. **582**, 1241 (2003).
- [7] H. P. Summers, The ADAS User Manual, version 2.6 <http://adas.phys.strath.ac.uk> (2004).
- [8] R. Radtke *et al.*, Phys. Rev. A **64**, 012720 (2001).
- [9] S. Utter, P. Beiersdorfer, and E. Trabert, Can. J. Phys. **80**, 1503 (2002).
- [10] R. Isler, R. Neidigh, and R. Cowan, Phys. Lett. **A63**, 295 (1977).
- [11] E. Hinnov and M. Mattioli, Phys. Lett. **A66**, 109 (1978).
- [12] K. Asmussen *et al.*, Nucl. Fusion **38**, 967 (1998).
- [13] T. Pütterich *et al.*, J. Phys. B: At. Mol. Opt. Phys. **38**, 3071 (2005).
- [14] T. Pütterich *et al.*, Plasma Phys. Control. Fusion **50**, 085016 (2008).
- [15] C. S. Harte *et al.*, J. Phys. B: At., Mol. Opt. Phys. **43**, 205004 (2010).
- [16] C. Suzuki *et al.*, J. Phys. B: At., Mol. Opt. Phys. **44**, 175004 (2011).
- [17] Y. A. Podpaly *et al.*, Can. J. Phys. **89**, 591 (2011).
- [18] O. Meyer *et al.*, J. Nucl. Mater. accepted (2013).
- [19] V. Jonauskas, S. Kucas, and R. Karazija, J. Phys. B: At., Mol. Opt. Phys. **40**, 2179 (2007).
- [20] D. Kilbane, J. Phys. B: At., Mol. Opt. Phys. **44**, 165006 (2011).
- [21] Y. Ralchenko *et al.*, J. Phys. B: At., Mol. Opt. Phys. **40**, 3861 (2007).

*The Extreme Ultraviolet Emissions of W<sup>23+</sup> (4f<sup>5</sup>)* 12

- [22] W. H. Press, S. A. Teukolsky, W. T. Vetterling, and B. P. Flannery, *Numerical recipes in C (2nd ed.): the art of scientific computing* (Cambridge University Press, New York, NY, USA, 1992).
- [23] A. Kramida and J. Reader, At. Data Nucl. Data Tables **92**, 457 (2006).
- [24] D. Post *et al.*, At. Data Nucl. Data Tables **20**, 397 (1977).
- [25] D. Post, J. Abdallah, R. Clark, and N. Putvinskaya, Phys. Plasmas **2**, 2328 (1995).

## 5.4 Publication 4

*Observations on the W-transport in the core plasma of JET and ASDEX Upgrade*

Plasma Physics and Controlled Fusion 55 (2013) 124036

## Observations on the W-transport in the Core Plasma of JET and ASDEX Upgrade

T. Pütterich<sup>1</sup>, R. Dux<sup>1</sup>, R. Neu<sup>1,2</sup>, M. Bernert<sup>1</sup>,  
M.N.A. Beurskens<sup>3</sup>, V. Bobkov<sup>1</sup>, S. Brezinsek<sup>4</sup>, C. Challis<sup>3</sup>,  
J.W. Coenen<sup>4</sup>, I. Coffey<sup>5</sup>, A. Czarnecka<sup>6</sup>, C. Giroud<sup>3</sup>,  
P. Jacquet<sup>3</sup>, E. Joffrin<sup>7</sup>, A. Kallenbach<sup>1</sup>, M. Lehnen<sup>4</sup>,  
E. Lerche<sup>8</sup>, E. de la Luna<sup>9</sup>, S. Marsen<sup>10</sup>, G. Matthews<sup>3</sup>,  
M.-L. Mayoral<sup>2,3</sup>, R.M. McDermott<sup>1</sup>, A. Meigs<sup>3</sup>, J. Mlynar<sup>11</sup>,  
M. Sertoli<sup>1</sup>, G. van Rooij<sup>12</sup>, the ASDEX Upgrade Team and  
JET EFDA Contributors<sup>†</sup>

JET-EFDA, Culham Science Centre, Abingdon, OX14 3DB, UK

<sup>1</sup>Max-Planck-Institut für Plasmaphysik, EURATOM Assoc., 85748 Garching, Germany

<sup>2</sup>EFDA CSU, Boltzmannstr. 2, 85748 Garching, Germany

<sup>3</sup>EURATOM CCFE Fusion Assoc., Culham Science Centre, Abingdon, Oxon OX14 3DB, UK

<sup>4</sup>Institute of Energy- and Climate Research, Forschungszentrum Jülich, Association EURATOM-FZJ, Germany

<sup>5</sup>Queen's University Belfast, University Road, Belfast BT7 1NN, Northern Ireland, UK

<sup>6</sup>EURATOM Assoc., Inst Plasma Phys & Laser Microfus, PL-01497 Warsaw, Poland

<sup>7</sup>CEA, Assoc. EURATOM-CEA, IRFM, Cadarache 13108 Saint Paul Lez Durance, France

<sup>8</sup>Association EURATOM-Etat Belge, ERM-KMS, Brussels, Belgium

<sup>9</sup>EURATOM CIEMAT Assoc., Lab Nucl Fus, Madrid, Spain

<sup>10</sup>Max-Planck-Institut für Plasmaphysik, EURATOM Assoc., D-17491 Greifswald, Germany

<sup>11</sup>Association Euratom-IPP.CR, Institute of Plasma Physics AS CR, 18200 Prague, Czech Rep.

<sup>12</sup>DIFFER, Assoc. EURATOM-FOM, 3430BE Nieuwegein, Netherlands

**Abstract.** The W-transport in the core plasma of JET is investigated experimentally by deriving the W-concentration profiles from the modelling of the signals of the soft X-ray cameras. For the case of pure neutral beam heating W accumulates in the core ( $r/a < 0.3$ ) approaching W-concentrations of  $10^{-3}$  in between the sawtooth crashes, which flatten the W-profile to a concentration of about  $3 \cdot 10^{-5}$ . When central ICRH heating is additionally applied the core W-concentration decays in phases that exhibit a changed mode activity, while also the electron temperature increases and the density profile becomes less peaked. The immediate correlation between the change of MHD and the removal of W from the plasma core supports the hypothesis that the change of the MHD activity is the underlying cause for the change of transport. Furthermore, a discharge from ASDEX Upgrade is investigated. In this case the plasma profiles exhibit small changes only, while the most prominent change occurs in the W-content of the confined plasma caused by the reduction of the fueling deuterium gas puff. Concomitantly, the W-concentration profiles in the core plasma  $r/a < 0.2$  steepen up reminiscent to the well-known connection between central radiation and transport during cases with strong, established W-accumulation, while in the present analysis such a causality between the two during the onset of W-accumulation could not be pinned down. Both case studies exemplify that small changes of the core parameters of a plasma may influence the W-transport in the plasma core drastically.

<sup>†</sup> See the Appendix of F. Romanelli et al., Proceedings of the 24th IAEA Fusion Energy Conference 2012, San Diego, US

*Observations on the W-transport in the Core Plasma of JET and ASDEX Upgrade* 2

## 1. Introduction

In ASDEX Upgrade (AUG) and JET tungsten (W) is used as a plasma facing material (cf. Ref. [1] for AUG and Ref.[2] for JET), because it will be used in ITER and it is a promising candidate material for a fusion reactor. While at AUG a stepwise approach to replacing the graphite wall tiles by W-coated ones was pursued from 1999-2007, the ITER-like wall (ILW) at JET consisting of Be (main chamber) and W (divertor) plasma facing components (PFCs) was implemented during one single vent in 2010/2011. A crucial task for plasma operation (cf. Ref. [3]) is the control of the W-concentration in the confined plasma, as W may lead to unacceptable radiative cooling for concentrations above  $\approx 10^{-4}$ .

A high W-content is also an issue for the stability of a plasma as plasma operation becomes more difficult when W-transport leads to a strong increase of the W-content. An extreme case of a transport phenomenon is core localized impurity accumulation. The latter is a well-known effect observed already in the limiter tokamaks PLT and ORMAK which were both operated with high-Z limiters (cf. Ref. [4, 5]). At ASDEX Upgrade and JET the operation with W PFCs is possible since the divertor concept helps to drastically reduce the W-content of the plasma [6]. However, core localized impurity accumulation is still observed in discharges where in the plasma core neoclassical transport dominates the impurity transport [7]. This happens naturally, because the profiles of density and temperature have only small gradients in the plasma core. As turbulent transport requires a threshold in the gradients of the kinetic profiles there is always a small region in the core where neoclassical transport for the impurity ions may be important, as has been shown for Ne, Ar, Kr and Xe in Ref. [8]. Neoclassical transport in the core may lead to steep impurity gradients that cause strong local radiative cooling. The easiest way of preventing impurity accumulation has been shown to be central heating by electron cyclotron resonance heating (ECRH), ion cyclotron resonance heating (ICRH) or neutral beam heating [9]. The effectiveness of this approach has been attributed to an increased turbulence level, rendering the neoclassical transport less important. The analyses of impurity transport (Si, Ar and Ni) for cases with central heating compared to cases without central heating in AUG [9, 10] and JET [11, 12] give larger diffusion coefficients and a reduction or even reversal of the convective velocity (cf. Ref.[9, 10]). In the next section a recently developed diagnostic method [13], which provides W-concentration profiles by modelling the soft X-ray emissions, is exploited in order to investigate further the transport of W in the core plasma of JET-ILW. Note that the actual work is the first at JET that focuses on W. As there is a strong Z-dependence of neoclassical transport, the uncertainties of the evaluated neoclassical transport coefficients for W receive special attention. An analysis of a discharge at ASDEX Upgrade is used to emphasize the large effect on W-transport for small changes of the plasma profiles.

In section 2 a detailed analysis of the W-transport in the core of JET discharges is presented, which emphasizes the importance of MHD for the central W-transport.

*Observations on the W-transport in the Core Plasma of JET and ASDEX Upgrade* 3

In section 3 the correlation of W-transport and W-radiation is presented and discussed and finally, section 4 summarizes the results.

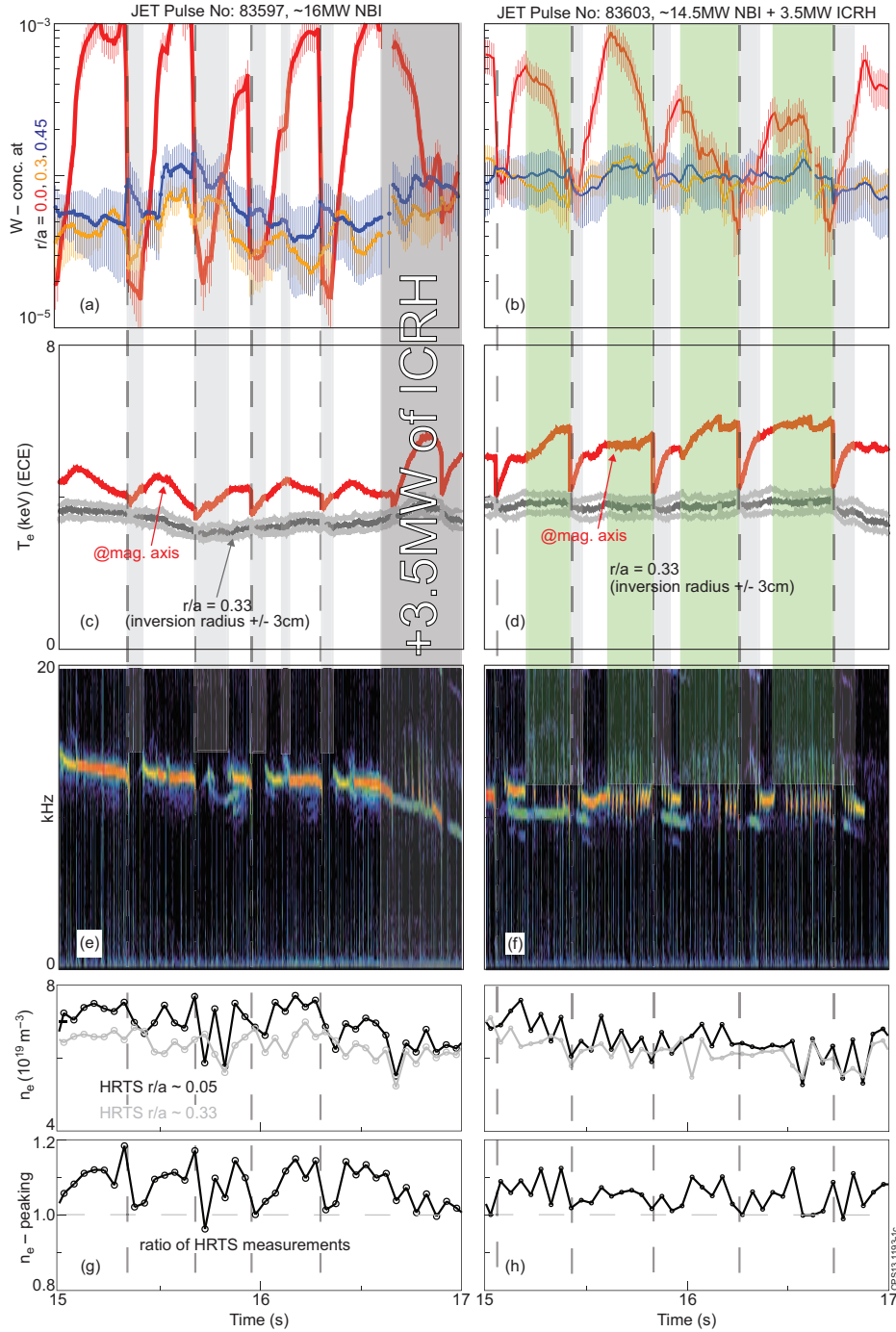
## 2. Core Transport of Tungsten investigated in JET

### 2.1. Experiment and Observations

The soft X-ray cameras at JET-ILW are used to derive the profiles of W-concentration and poloidal asymmetries due to centrifugal forces. The details of the diagnostics are described in [13]. The basic assumption that allows the determination of the W-concentration is that the low-Z impurities give rise to Bremsstrahlung, while the only other radiator is W, i.e. the radiation from Ni is negligible. The rotation velocity as derived from the poloidal in-out asymmetry provides a consistency check of that assumption. For the same rotation velocity the in-out asymmetry for W is larger than for Ni. For the measured asymmetries the derived rotation velocities for W match those measured by charge exchange recombination spectroscopy, while those derived for the assumption that Ni is the main radiator would be about a factor of two too large. Generally, this observations holds in agreement to the spectroscopic observation that Ni contributes only a minor fraction < 10% even for plasmas with the highest Ni concentrations. As adjustments of the atomic data describing the soft X-ray emissions for W have been explained in Ref.[13] the physical meaning of the results may be considered preliminary, however, future corrections of the data will not change the main thrust of this paper as most of the conclusions rely on large changes of the soft X-ray emissions, outside of the uncertainties of the adjustments.

Two discharges with a plasma current of 2 MA performed at a magnetic field of 2.7 T are compared in the following. The first discharge (pulse 83597) features  $\approx 16$  MW of neutral beam injection (NBI) at a central density of about  $7 \cdot 10^{19} \text{ m}^{-3}$ . The second, pulse 83603, is heated with 14.5MW of NBI and an additional 3.5 MW of central ICRH. The central density is about  $6.5 \cdot 10^{19} \text{ m}^{-3}$ . The slight difference in density appears even though the deuterium gas fueling is equal for both discharges, i.e.  $10^{22} \text{ D/s}$ .

In Fig.1(a) and (b) the W-concentrations at  $r/a=0.0, 0.3$  and  $0.45$  are depicted for both pulses. For 83597 (pure NBI), the core W-concentration at  $r/a=0.0$  shows large excursions compared to the values at  $r/a=0.3$  and  $0.45$ . At these outer radii, the only excursion is provided by a W-event at about 15.5s, which increases the W-concentration from about  $3 \cdot 10^{-5}$  to  $10^{-4}$ . The central W-concentration varies between these values and about  $10^{-3}$ . In Fig.1(c) and (d) the electron temperature measurements from electron cyclotron emission (ECE) channels close to the magnetic axis and close to the sawtooth inversion radius ( $r/a \approx 0.33$ ) are presented. Using these signals as indicators of the sawtooth crashes a qualitative difference between the two discharges becomes apparent. For 83597 (pure NBI), the excursions of the W-concentration are aligned to the sawtooth crashes such that the sawtooth crash results in a flat or slightly hollow W-profile, while in the phases between the sawtooth crashes the W-concentration increases

*Observations on the W-transport in the Core Plasma of JET and ASDEX Upgrade* 4

**Figure 1.** (a) and (b) Evolution of the W-concentrations at three radii for 83597 and 83603; (c) and (d) Electron temperatures close to the magnetic axis and close to the sawtooth inversion radius for 83597 and 83603; (e) and (f) Spectrogram of a magnetic coil located at the outer midplane for 83597 and 83603; (g) and (h) Electron densities close to the magnetic axis and close to the sawtooth inversion radius and their ratios for 83597 and 83603;

monotonically, slowly leveling off towards the end of the sawtooth cycle. For 83603

*Observations on the W-transport in the Core Plasma of JET and ASDEX Upgrade* 5

(NBI+ICRH), the W-concentration at  $r/a=0.3$  and  $r/a=0.45$  are slightly higher than in 83597 quantitatively consistent with the increase of the radiated power (by approx. 2 MW) from the main plasma as compared to 83597. In 83603, the increasing and decreasing phases of the central W-concentrations (at  $r/a=0.0$ ) are not governed by the sawtooth cycle only. After a sawtooth crash, the W-concentration profile is flat, however, there are phases with decreasing W-concentration in between the sawteeth crashes. The interpretation of that observation is quite challenging and an attempt will be presented in the discussion section below. As an additional observation, the MHD behaviour as shown in Fig.1(e) and (f) seems to be quite different for the two pulses. For 83597 (pure NBI), a regular (1:1) mode is active during the the sawteeth cycle, while only a few perturbations of that mode activity are visible (cf. gray, transparent areas in Fig.1(a),(c) and (e)), e.g. one at 16.12 s. However, most of these special phases appear right after the sawtooth crash were density and temperature gradients are reduced, which could be the underlying reason for both, the changed transport and the changed mode activity: Right after the sawtooth crashes the mode activity is weaker and the inward transport of W pauses for about 50 to 100 ms. For 83603 (NBI+ICRH), these phases also appear after the sawtooth crashes (cf. gray, transparent areas in Fig.1(b), (d) and (f)). Apart from these, more perturbations of the MHD activity (e.g. fishbones or jumps of the frequency of the (1:1) mode) show up regularly during the sawtooth cycle (cf. green, transparent areas in Fig.1(b), (d) and (f)) and correlate with the phases in which the W-concentration in the core decreases. Simultaneously, these phases also exhibit higher electron temperatures, which could also be a cause of changed transport. In Fig.1 (g) and (h) the evolution of the electron densities in the plasma core and at the sawtooth inversion radius is shown for both discharges. Also depicted is their ratio to better diagnose the peaking of the electron density profiles. In 83597, there is a clear evolution from non-peaked to peaked within the sawtooth cycle, while in 83603 there seems to be a considerable scatter overlayed. In both cases the density ratio (core density / density at sawtooth inversion radius) is on average larger than one, thus we deal with peaked density profiles in the plasma core, while a consideration of uncertainties, as performed in the discussion section, may be crucial. The statistical uncertainties of the presented density measurements are smaller than 6 % through-out, while the propagated uncerctainties of the peaking are between 8 % and 9 % through-out.

## 2.2. Modelling and Discussion

In this discussion we address the following three questions:

- Is the increase of the W-concentration after a sawtooth crash in 83597 consistent with neoclassical transport or is an additional effect required?
- How strongly different is the transport in 83603?
- Is the change in MHD activity responsible for the removal of W from the plasma core in 83603?

*Observations on the W-transport in the Core Plasma of JET and ASDEX Upgrade* 6

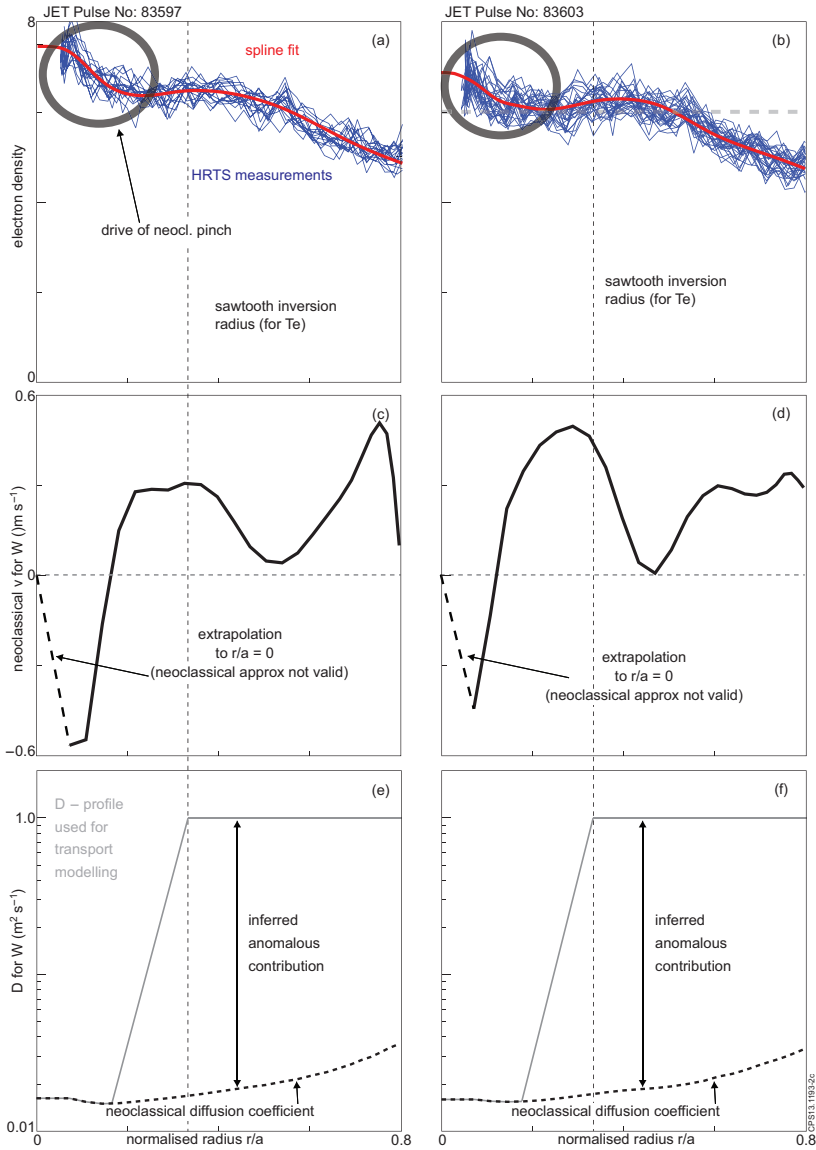
In order to estimate the neoclassical W-transport in the plasma core a close look at the ion density and temperature profiles is necessary. The gradients of the background ions (deuterium) lead to an inward impurity convection, while the gradients in ion temperature lead to an outward convection. It should be noted that we do not attempt to do a detailed accounting of the neoclassical transport, as the uncertainties in the required measurements have a considerable effect on the neoclassical transport coefficients. The effect of these uncertainties on the W-transport is discussed below. Anyhow, the uncertainties in the electron density measurements are comparable to the change of density within a sawtooth cycle, as can be understood by looking at the time traces in Fig.1 (g) and (h). While the more regular behaviour in 83597 allows to identify a rough evolution of densities within a sawtooth cycle, it is harder to see a consistent evolution of the electron densities in 83603. For 83597, the density peaking is decreased by the sawtooth crashes and rebuilds during the sawtooth cycle. When several sawtooth cycles are taken into account, there seems to be a short phase of about 50-100ms after the sawtooth crash, where the density peaking is not reestablished or very slowly reestablished, followed by a 50-100ms phase in which the peaking is reestablished and after which the peaking saturates. Note that this is a non-negligible fraction of the sawtooth cycles, which lasts for 300-450 ms. As we plan to estimate the typical time scales of neoclassical transport we evaluate the average electron density profile including only measurements from the second half of the sawtooth cycle in which the density peaking seems to saturate. This choice neglects time-dependences and is expected to give a slightly stronger inward pinch than applies on average. For 83603, a consistent picture of the density evolution is not observed, which could mean that there is no evolution after the sawtooth crash, hence there is no peaking, or the evolution is slightly smaller than the statistical scatter of the data. In order to get at least a profile that gives us the average peaking of the densities, all time points are included in the determination of an electron density profile.

In Fig.2 the electron density profiles for the pulses 83597 and 83603 are depicted. In order to estimate the neoclassical inward convection for W, the described choice of profiles were included in the fit. For the ion temperature in the plasma core no measurement is available for large fractions of the first campaign JET with the ITER-like wall (JET-ILW). Therefore, the electron temperature measurement are used instead. At the considered high electron densities the experience of earlier campaigns at JET is suggesting that the electron temperature should be almost equal to the ion temperature, while the underlying reason for that is the fact that the typical energy exchange time is more than an order of magnitude shorter than the typical transport time. For 83603 strong localized core electron heating is provided by the ICRH, therefore, the electron temperature are considered as an upper limit for the ion temperature. In order to make this discussion for 83603 less complex, we use, for further considerations, only one temperature profile within the phase of the sawtooth cycle, i.e. the one featuring the highest central temperatures ( $\approx 6$  keV) and thus the largest outward-directed contribution for the neoclassical convection. Note that we do

*Observations on the W-transport in the Core Plasma of JET and ASDEX Upgrade* 7

not attempt to do a time-dependent modelling, i.e. the transport coefficients and kinetic profiles are fixed in time (unless indicated), as the purpose of the modelling is to check the rough magnitude of the transport coefficients required to describe the observed transport phenomena. The electron temperatures measurements at the center and at the sawtooth inversion radius are presented in Fig.1 (c) and (d). The effect of impurities on the neoclassical transport coefficients is taken into account by NEOART and requires the input of impurity densities. NEOART [14, 15] calculates the collisional transport coefficients for an arbitrary number of impurities including collisions between them. The code solves the set of linear coupled equations for the parallel velocities in arbitrary toroidally symmetric geometry for all collision regimes. The classical fluxes are given by Eqs.(5.9) and (5.10) in [16]. The equations for the banana-plateau contribution are that in [17]. The Pfirsch-Schlüter contribution is calculated from the coupled equations (6.1-2) and (6.14-15) in [16], as described in [18]. The presented calculation do not take impurity asymmetries into account, which is known to alter the neoclassical transport coefficients (e.g. [19]). It should be noted that asymmetries based on centrifugal forces become less important close to the axis, while the nature of the presented analysis is that of an estimate of neoclassical transport. In the following we assume constant impurity concentration profiles ( $1.5\% c_{Be}$  and  $10^{-4} c_W$ ). Both values are in the right ball park according to the data from the visible Bremsstrahlung (Be) and the soft X-ray cameras (W). Using the presented electron density profiles, the electron temperatures as measured by electron cyclotron emissions and the mentioned assumptions on impurity densities the neoclassical diffusion coefficients for W, as evaluated by NEOART, are around  $0.015\text{m}^2\text{s}^{-1}$  for both cases (cf. Fig.2(e)and (f)). The profiles of the drift velocities for W are shown in Fig.2 (c) and (d). In both cases the most central transport is directed inward giving rise to accumulation, while at about  $r/a \approx 0.15$  the drift velocity reverses and is directed outward. The outward convection is only partly due to the temperature gradients, as a bump in the density profiles between  $r/a \approx 0.25$  and  $r/a \approx 0.55$  gives rise to flat (83597) or slightly hollow (83603) density profile at  $r/a \approx 0.2$ . It is unclear if this bump is an artefact. Even though only an estimate of the neoclassical transport coefficients is attempted, we are concerned about the possible impact of such artefacts and additional complications such as the impact of gradients in the density of low-Z impurity densities which have been neglected for this analysis. These uncertainties are discussed below where also other caveats of the analysis are investigated.

For the transport modelling performed with STRAHL [14] using the atomic data derived in [20], the neoclassical transport is combined with anomalous transport, which is in the present analysis assumed ad hoc according to the results of earlier investigations on impurity transport and according to the typical impurity confinement time (s. below). In [21, 8] typical values for diffusion coefficients are found to be within the order of magnitude of  $1\text{m}^2\text{s}^{-1}$ , while for cases without central heating the plasma core may exhibit neoclassical transport coefficients for impurities. As in the present work the impurity peaking inside of  $r/a=0.3$  is investigated the exact value of the anomalous diffusion coefficient outside of  $r/a=0.3$  is of no importance. It is only able to influence

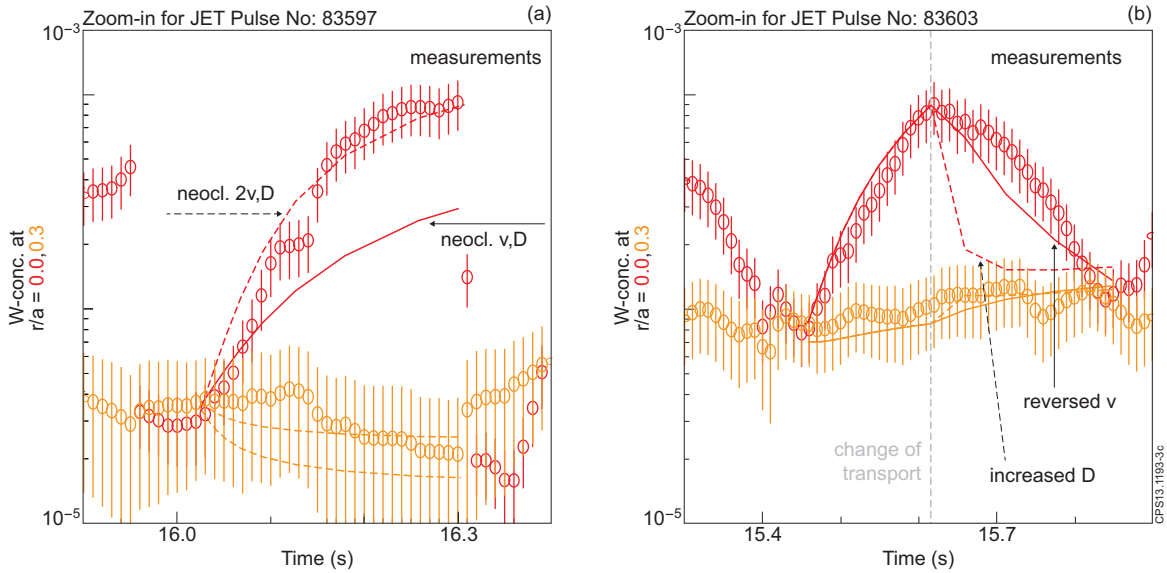
*Observations on the W-transport in the Core Plasma of JET and ASDEX Upgrade* 8

**Figure 2.** (a) Density profiles as measured by HRTS during the 2nd half of the sawtooth cycles in 83597 - data (blue), spline fit (red); (b) All density profiles as measured by HRTS during the time interval 15.0 to 16.5s in 83603 - data (blue), spline fit (red); (c) Drift Velocity for W as derived from NEOART using  $n_e$ -profiles of part (a) and  $T_i = T_e$  at the corresponding time points; (d) Drift Velocity for W as derived from NEOART using  $n_e$ -profiles of part (b) and  $T_i = T_e$  at the end of the sawtooth cycles; (e) W-Diffusion coefficient D as used in the transport modelling and neoclassical D as derived from NEOART using  $n_e$ -profiles of part (a) and  $T_i = T_e$  at the corresponding time points; (f) W-Diffusion coefficient D as used in the transport modelling and neoclassical D as derived from NEOART using  $n_e$ -profiles of part (a) and  $T_i = T_e$  at the corresponding time points;

the absolute W-concentration at  $r/a=0.3$ , which is considered a free parameter in the present study, because it can be as well influenced by the edge source and screening of

*Observations on the W-transport in the Core Plasma of JET and ASDEX Upgrade* 9

the plasma, both of which are not subject of the investigations. In fact the anomalous diffusion coefficient was varied by a factor of 4 in order to confirm the insensitivity of the core analysis to the anomalous transport outside of  $r/a=0.3$ .



**Figure 3.** (a) Zoom-in to one sawtooth cycle in 83597; The measured W-concentrations (symbols) at  $r/a = 0.0$  (red) and  $r/a=0.3$  (orange) are compared to modelled ones using  $v_{neo}$  and  $D_{neo}$  from neoclassical theory (solid lines) and using the  $v = 2 \cdot v_{neo}$  and  $D=D_{neo}$ . (b) Zoom-in to one sawtooth cycle in 83603; The measured W-concentrations (symbols) at  $r/a = 0.0$  (red) and  $r/a=0.3$  (orange) are compared to modelled ones using  $v$  and  $D$ , which are within a factor of 2 of the neoclassical coefficients up to about 15.6 s. From 15.6 s the decay of the central W-concentration is modelled by a reversed convection (solid lines) or by an increased diffusion coefficient (dashed line).

The transition of the anomalous diffusion coefficient towards low, neoclassical values determines in which radial region the drift velocity has the biggest impact on the impurity profile. As we observe a strong W-peaking in the core only, we designed that transition region accordingly (cf. depicted diffusion coefficients in Fig.2(e) and (f)). All these adjustments are done with the aim to check the magnitude of the convective velocity and the diffusion coefficient in the region where the W-peaking is observed by comparing the time evolution of the measurements with that of the model. As mentioned above the level of the anomalous diffusion coefficients have been chosen such that approximately the impurity confinement time (few 100 ms) from experiment is reproduced and at the same time the core transport stays at the neoclassical level, while the additional W-confinement due to the W-accumulation in the plasma core was not taken into consideration for matching impurity confinement time and level of anomalous diffusion.

Indeed, the discussed increase of the W-concentrations in the plasma core of pulse 83597 can be described (cf. Fig.3(a)) with transport coefficients reasonably close to

*Observations on the W-transport in the Core Plasma of JET and ASDEX Upgrade* 10

the depicted (cf. Fig.2(c) and (e)) transport coefficients. In Fig.3(a) the results of two simulations are presented; one using exactly the transport coefficients as shown in (cf. Fig.2(c) and (e)) and one using twice the presented inward convection. The measured W-concentrations suggest that the real transport features time averaged drift velocities close to the latter coefficients. Considering the cavats, i.e. the uncertainties in the electron density profile measurements and the fact that the modelling is not time-dependent and that corrections of the neoclassical model due to centrifugal asymmetries are not taken into account, the level of agreement is surprisingly good and there is no obvious contradiction to the assumption that neoclassical transport as the main driver for the observations.

For 83603, the measurements within a sawtooth cycle cannot be described by the depicted transport coefficients, as especially the innermost part of the neoclassical transport  $r/a < 0.2$  always produces a peaked profile in the core. Note that this direction of the neoclassical drift velocity is still inward even though the temperature profile featuring the highest temperatures during the sawtooth cycle are taken into account, such that the neoclassical inward convection is even stronger for most time points of the sawtooth cycle. This suggests that a change of the diffusive transport or an additional outward convection must apply in 83603, which cannot be explained by neoclassical theory. In order to document this finding the sawtooth cycle between 15.4 s and 15.8 s is modelled (cf. Fig.3(b)), while a change of transport coefficient is necessary at about 15.6 s. The increase of the W-concentration at  $r/a < 0.2$  up to 15.6 s requires similar W-coefficients than for the sawtooth cycle in 83597, in detail, the core diffusion coefficient is  $0.016 \text{ m}^2\text{s}^{-1}$  while the convective velocity requires scaling by a factor of 2.15 such that it peaks at  $-0.95 \text{ ms}^{-1}$ . At 15.6 s the transport coefficients are changed in two different ways such that at the end of the sawtooth cycle roughly flat W-profiles result. First, the diffusion coefficient is increased to  $0.5 \text{ m}^2\text{s}^{-1}$  in the full region  $r/a < 0.3$  and the dashed lines result in Fig.3(b). These model results feature a very steep decay of the W-concentration at  $r/a = 0.0$  which then slowly approaches the flat W-profile. Second, the transport is changed in the model such that the inward convection velocity is changed from  $-0.95 \text{ ms}^{-1}$  to an outward convection of  $0.2 \text{ ms}^{-1}$  in the full region  $r/a < 0.3$  while the low diffusion coefficient of  $0.016 \text{ m}^2\text{s}^{-1}$  is maintained. These model results are shown by the solid model curves in Fig.3(b). Comparing the model curves to the data, the second model assumption seems to fit better to the data, however, if the transport coefficients are time-dependent in experiment also an increased diffusion coefficient could reproduce the measurement. In this context it is interesting to note that the neoclassical and turbulent transport is mostly governed by the kinetic profiles, which stay roughly constant between 15.55 s and 15.75 s. The modelling clearly shows that a change of transport coefficients within a sawtooth cycle is necessary to obtain a match between the measurements and the modelling. It is not clear whether the transport coefficients are constantly changing after 15.6 s, or whether there is a simple switch of transport at 15.6 s.

*Observations on the W-transport in the Core Plasma of JET and ASDEX Upgrade* 11

Both types of transport change could be caused by a change of turbulence in the plasma core or due to changed MHD activity. It is worthwhile noting that in each sawtooth cycle in 83603 the reversal of transport (i.e. from inward to outward) appears at slightly different times and combinations of central electron temperatures and densities (cf. Fig.1). The fact, that the phases with decreasing W-concentrations correlate clearly and immediately with the change in MHD activity without time lag suggests that the MHD activity could be the underlying reason for the change of the W-content, which in terms of transport coefficients may be identified as a larger anomalous diffusion coefficient or an outward drift velocity (e.g. [10, 22, 23]). The MHD activity is probably closely connected to the application of ICRH, as for example fishbone activity is known to be driven by fast particles, which may be provided by ICRH. Alternatively, the strong increase of the temperatures decreases the slowing down time of all fast particles, which leads to higher densities of fast particles, which in turn could trigger the fishbones. In [24] a similar observation is reported, as fishbones are observed to reduce the core emissivity of the soft X-ray range, which is attributed to a reduction of the core iron-density. The exact mechanism of the changed MHD activity is not subject of this study, however, it is strongly recommended to understand in more detail the mechanisms of how MHD-modes can interact with impurity transport. There are clear signs, e.g. [22, 23, 8], that not only fishbones have impact on impurity transport, but also regular (1,1)-modes. Such a future study is highly complex, because it not only has to include the mode dynamics, but also at least neoclassical impurity transport, which is very difficult to combine, as the measurements of the kinetic profiles need to be mapped onto the mode structure, which quickly rotates. Even the time-dependent treatment of the parallel redistribution of W may be a vital ingredient for perpendicular transport effects.

An alternative interpretation of the observations would be necessary, if the density peaking is much smaller than the measurements suggest (cf. discussion of caveats below). For this case no established reason for the W-accumulation in the plasma core exists, but from the obvious correlation between MHD and transport one could also conclude that the regular (1,1)-mode, which is always present during the phases which features inward transport of W, is actually causing this transport. It should be noted that such a hypothesis has several implications: There would be no clear explanation for the underlying physics of such an effect, as typically the mode activity is interpreted to cause strong, non-directional, radial transport of energy and particles. However, a change in mode-activity has been connected above and in work before (e.g. [23]) to a possible outward convection, which also cannot be described by this standard view. One should also note, that the time-scales of the increase in central W-concentrations is not compatible with  $v$  and  $D$  being both much larger than the neoclassical values (derived from the measured density peaking), thus, a directional mode transport would by coincident result in transport of the same order of magnitude. Simulations using much larger  $v$  and  $D$  values suggest that the diffusion coefficient must be clearly smaller than  $0.15 \text{ m}^2\text{s}^{-1}$  during the phases with increasing W-concentrations, while the respective  $v$

*Observations on the W-transport in the Core Plasma of JET and ASDEX Upgrade* 12

is about proportional to D. The importance of the modes cannot be excluded for the present analysis, however considering earlier high-quality work (e.g. [8]) there are clearly cases where the (1,1)-modes in the core do not play a big role for impurity transport, as it was found that neoclassical transport coefficients in the plasma core of ASDEX Upgrade apply and also exhibit a Z-dependence corresponding to that from neoclassical theory. Additionally, for the present investigation the sawtooth inversion radius, which is an indicator for the  $q=1$  surface, is at about  $r/a=0.33$  in 83597 and 83603, which is clearly outside of the accumulation region. Still, considering the uncertainties of the actual analysis and the incomplete understanding of interaction between modes and heavy impurities this alternative explanation can not be excluded.

### *2.3. Caveats*

First, the derivation of the W-concentration profile from the soft X-ray cameras may be in doubt, because adjustments and recalibrations were necessary in order to use the soft X-ray cameras as a W-diagnostics. The adjustments can also be seen as a calibration procedure in order to arrive in a specific calibration discharge (without high-Z radiators) at a good description of the continuum background radiation and in a different calibration discharge at W-concentration profiles that are consistent with bolometry and spectrometer diagnostics. The mentioned adjustments are described in more detail in Ref.[13], and for the actual discharge a consistency check is in order. As the peaking of the W-concentration is the main interest of the actual work, the question is investigated whether the diagnostic introduces a bias for the peaking and whether the considerable peaking of the W-concentration is plausible. One expectation from sawtooth crashes is that they roughly flatten all profiles, including the impurity density profiles. When comparing the W-concentrations at  $r/a=0.0$  to the W-concentration at  $r/a=0.3$  and  $r/a=0.45$ , the sawtooth crash indeed flatten the profiles and in a few cases even provide slightly hollow profiles (slightly outside of the error bars), which gives a hint that there might be additional uncertainties not fully captured in the error bar. On the other hand, for 83597 an impurity peaking which approaches a W-concentration of  $10^{-3}$  just before the sawtooth is observed, which is consistent to the drop of signal in a central, horizontal chord of the bolometer system. The chord misses slightly the center of the plasma and it should be noted that due to the coarse coverage of the bolometer the neighboring chords do not detect the core localized accumulation region. The total radiated power flux on that central chords drops by  $55 \text{ kW m}^{-2}$  at the sawtooth crash. Assuming that the path length through the volume with the increased W-concentration is roughly 0.1 m (as can be derived from the signal distribution on the soft X-ray diagnostics) the average power density in the accumulation region attributed to W before the crash is thus  $550 \text{ kW m}^{-3}$ , which corresponds to a change of the W-concentration of roughly  $5 \cdot 10^{-4}$  using the cooling factor from Ref. [25]. This is roughly a factor of two smaller than derived by the soft X-ray analysis, which reflects the fact that this estimate gives the average W-concentration in the accumulation region and additionally it could be

*Observations on the W-transport in the Core Plasma of JET and ASDEX Upgrade* 13

caused by the fact that the bolometer chord misses the magnetic axis by a few cm.

Second, the evaluation of the neoclassical transport coefficients for 83597 was performed taking the rough impurity densities into account, however, the influence of the impurity density profile was ignored. This was necessary, because the exact profile is unknown. Assuming that the transport is indeed neoclassical one can estimate how peaked the low-Z impurity could be. The ratio  $v/D$  describes the equilibrium impurity density profile, as in equilibrium the normalized gradient of the impurity density  $n_Z$  is given by the local ratio  $v_Z/D_Z$ . Thus, the central density peaking of an impurity Z, which may be characterized by the ratio of the impurity density at  $r/a=0.0$   $n_Z(0.0)$  over the impurity density at  $r/a=0.3$   $n_Z(0.3)$ , is given by

$$\frac{n_Z(0.0)}{n_Z(0.3)} = \exp\left(\int_{r@r/a=0.3}^{r@r/a=0.0} v_Z/D_Z dr\right)$$

, where r is the radial coordinate on which also the definition of v and D is performed. Using the obtained v and D profiles, the W-peaking in equilibrium would be about a factor of 120. As  $v_Z/D_Z$  scales to first order with the charge of the impurities, the expected  $v_Z/D_Z$  for Be, the main low-Z impurity in JET-ILW, is about a factor of 10 smaller in the plasma core. This means for the equilibrium peaking of Be that it is only a factor of 1.6. The main effect of the impurity gradients on the neoclassical transport of higher-Z elements is the reduction of the deuterium gradients, as has been shown in [26]. Thus, the relevant effect on  $v_W/D_W$  is that the deuterium gradients are reduced by less than 3.6%, as the Be-concentration peaks towards the plasma core from 1.5% to less than 2.4%. The value 2.4% is not reached, because the sawtooth crash appears before the equilibrium is reached. Thus, the estimate makes clear that the low-Z impurity gradients do not matter for the investigated discharges compared to other uncertainties.

Third, the electron density peaking in the plasma core is of similar magnitude than the density bump at mid radius, which is possibly an artefact. Still, the core localized electron density peaking is thought to be the underlying reason for the strong peaking of W-concentrations in 83597 and 83603. In 83597, the peaking is clearly real, as it features an evolution which is nicely aligned with the sawtooth cycles, however, one may wonder about the magnitude of the peaking. In 83603, the evolution is less clearly aligned with the sawtooth cycle, as is the W-concentration profile - Both suggests there is an additional effect at play, which is exactly the claim of the above discussion section. Namely the MHD activity is postulated to be important. Note that even though the density measurement is of comparably high quality, the small uncertainties affect the model results drastically, because due to the strong Z-dependence of neoclassical transport small changes in the gradient of the normalized ion densities are amplified. For an impurity charge q, the local ratio of v/D is proportional to q. For W a typical charge state in the plasma core is q=40-50. The sensitivity of the W-transport on small changes of the background profiles is also visible in the following example from ASDEX Upgrade presented in the next section.

*Observations on the W-transport in the Core Plasma of JET and ASDEX Upgrade* 14

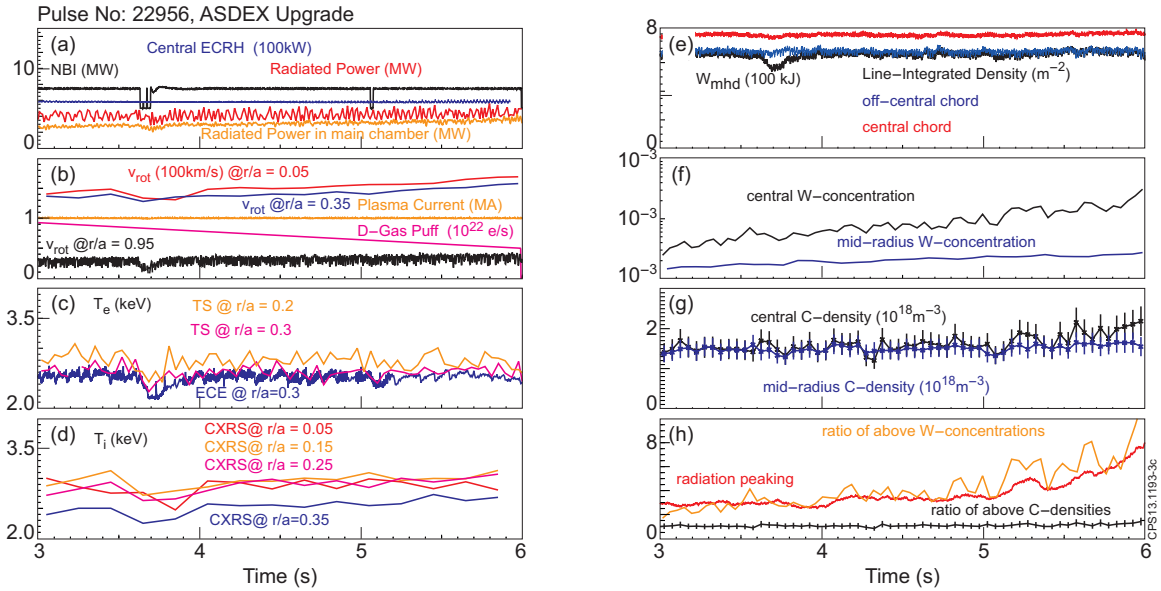
### 3. Sensitivity of Core Transport of Tungsten Investigated in ASDEX Upgrade

#### 3.1. Experiment and Observations

Fig.4 shows time traces from an AUG discharge in which all parameters are kept as constant as possible from 3 to 6 s. The only parameter that is varied is the deuterium gas puff, which is ramped down continuously (cf. Fig.4(b)). The applied heating power is 7.5 MW of NBI and 600 kW of central ECRH (cf. Fig.4(a)). The radiated power including the divertor radiation changes from about 4 MW to 4.5 MW, while the radiated power in the main chamber increases from about 2.75 MW to 3.75 MW (cf. Fig.4(a)), which is roughly consistent with the change of the mid-radius W-concentration from  $1.5 \cdot 10^{-5}$  to  $3.0 \cdot 10^{-5}$  (cf. Fig.4(f)). The individual measurements of the W-concentrations are based on two different spectral emissions. The W-concentration which is attributed to mid-radius corresponds to the spectral feature at about 5 nm emitted by ion stages between  $W^{27+}$  and  $W^{35+}$ , while the central W-concentration measurement is derived from a spectral line emitted by Ni-like  $W^{46+}$  at 0.793 nm. The details of the diagnostic principle can be found in Refs. [27, 20]. Note that the bolometry cannot separate the effect of ELMs, which usually increases the bolometer signals compared to the values in between ELMs as can be derived by comparisons to fast diode measurements. The electron temperatures (cf. Fig.4(c)) and densities (cf. Fig.4(e)) do not change within the scatter of the data. This is true for the individual chords of the interferometer, and thus also for their ratio. Also, the electron temperatures close to the plasma core ( $r/a \approx 0.2$ ) do not change. While more central measurements of the electron temperatures are not available, it is worthwhile to also consider the ion temperatures as measured by charge-exchange recombination spectroscopy (CXRS) (cf. Fig.4(e)). In order to reduce the scatter of the data the measurements have been smoothed over 4 data points (i.e. 200 ms). The ion temperature measurement at  $r/a=0.35$  indicates a slight increase, while in the plasma core the profile is comparably flat and from  $\approx 5.3$  s in the discharge the difference between the core  $T_i$ -measurement ( $r/a=0.05$ ) and the measurement at  $r/a=0.35$  becomes slightly smaller indicating a reduction of the gradients. All these changes are small and are only visible after the data is smoothed, consistently no change in the stored energy derived from magnetics ( $W_{mhd}$ ) is observed (cf. Fig.4(e)). The plasma rotation as measured by CXRS is also documented in Fig.4(b) and it is increasing steadily from 3 to 6 s by about 20 %, while the whole profile seems to grow consistently by about the same factor.

At about 4.8 s, an increase of W-peaking is observed (from about factor of 3 up to about a factor of 8-10, as can be derived from the ratio of the core localized W-measurement compared to the W-measurement that corresponds to about mid-radius. In agreement to that observation, the radiation peaking increases starting at the same time (cf. Fig.4(h)). The depicted radiation ratio attributes the excess signal of a central bolometer chord to a region in the plasma core that has a diameter of about 10 cm. For considering the low-Z impurities, carbon (C) is investigated by CXRS and

*Observations on the W-transport in the Core Plasma of JET and ASDEX Upgrade* 15



**Figure 4.** Time traces for discharge #22956 in ASDEX Upgrade. (a) Power from neutral beam injection (NBI), central electron cyclotron resonance heating (ECRH) and radiated power; (b) plasma current and deuterium gas puff for fueling; (c) Electron temperatures from Thomson scattering (TS) and electron cyclotron emission (ECE); (d) Ion temperatures (averaged over 200 ms) from charge-exchange recombination spectroscopy (CXRS); (e) Plasma stored energy (black) and line-integrated densities as measured by the DCN interferometer on a central (red) and off-central (blue) chord; (f) W-concentrations derived from spectroscopy corresponding to ion stages at mid radius and in the plasma core; (g) C-densities at mid radius and in the plasma core derived from CXRS; (h) ratio of the above W-concentrations, ratio of the above C-densities and ratio of the radiation density in the plasma core over bulk radiation density derived from bolometer chords assuming that accumulation occurs in a central region with a diameter of about 10 cm;

an interpretative code that allows for determining the C-densities from the CXRS-intensities is applied. The mid-radius C-density is changing by about 10 % from 3 to 6 s, and at about 4.8 s a slight C-peaking (up to factor of 1.4) is visible. In view of the discussion in the above sections, it should be noted that a regular (1,1)-mode exists in between sawtooth activity, very similar to the modes observed in 83597. The activity of that mode is not changing for the full time interval considered.

### 3.2. Discussion

It is a common observation (e.g. [28]) that decreasing the deuterium gas puff leads to an increase of the W-content of the plasma, as the W-screening and the W-sources at the edge are both influenced into that direction (e.g. [29, 30]). Thus, the decreasing gas puff causes the W-content at mid-radius to slowly rise. In the investigated discharge it is empirically found that the core transport also changes as can be seen by the increasing core W-concentration, which increases by a larger factor than the W-concentration

*Observations on the W-transport in the Core Plasma of JET and ASDEX Upgrade* 16

at mid-radius (cf. Fig.4(e) and (f)). This effect becomes more enhanced and is well visible from 5 s onwards. It seems only parameters in the plasma core may change, while outside the only clear changes are the W-concentrations and the radiation. The interpretation of the observation is that due to the change in gas puff the edge source of W is increased which affects the radiation losses in the whole volume of the confined plasma. The radiation losses may be interpreted as negative heating power, thus, they lead to a decrease of electron temperature and its gradient. Unfortunately, the central application of ECRH prevents a central ECE measurement and the TS observation does not cover the very core of the plasma, but via heat transfer between electron and ions this effect is visible on the ion temperature which slowly and mildly decreases after 5.0 s relative to the value at  $r/a=0.35$ .

This decrease might also be so small, because the local radiation within  $r/a=0.2$  leads to losses of about 100kW at about 5s in the discharge, while 600kW of ECRH and a few 100kW of NBI heating are deposited in the same volume. In order to understand the correlation of temperature gradients and heat flux it is necessary to quantitatively understand the turbulent state and onset thresholds for different types of turbulence. From the obtained measurements the exact causality is difficult to derive, as any effect, even the strongest one, i.e. radiation, will influence transport via the kinetic profiles which hardly change. Additionally, also rotation which is exhibiting a 20 % change may influence the core transport (cf. [31]), while typically the effect of rotation is considered small, it may become important in a situation where all changes in the plasma are small. However, it is worthwhile noting that turbulent transport is known to have a threshold in the temperature profiles, which makes a connection between temperature gradients and a strong transport change most plausible. However, the transport change takes place close to the magnetic axis (inside of  $r/a=0.2$ ), where a high-quality analysis of turbulent transport is not possible due to the sensitivity of the transport codes on details of the kinetic profiles, while the measurements in the plasma core yield typically considerable uncertainties or are sparse. Note that a small change of the temperatures may affect the transport drastically, which again emphasizes the challenge to quantitatively predict and detect the conditions that lead to W-accumulation. As the transport change shows up very clearly for W and much weaker for C, a Z-scaling as observed for neoclassical transport seems to apply, which puts also an explanation in favour that describes a transition towards neoclassical transport. It should be noted that, after W-accumulation is established (not investigated here) flat or even hollow temperature profiles are observed and a change in transport (e.g. [32]) supporting the transport causing the accumulation is a well accepted fact.

Support of this transport mechanism is also provided by earlier investigations which documented a clear correlation between heating and transport as the core transport could be influenced by localized heating [9]. In fact, it is rather the findings of other work (also [32]) that documented the importance of core radiation also for the onset of W-accumulation. The actual work demonstrates that the onset of W-accumulation relies on tiny changes within the confined plasma suggesting that these are encountering

*Observations on the W-transport in the Core Plasma of JET and ASDEX Upgrade* 17

a threshold at which the W-transport turns instable. Note that the change of transport happens even though the radiated power is clearly much smaller than the core localized heating power giving rise to the speculation that other parameters are also playing a role.

#### 4. Summary and Conclusions

The core transport in type-I ELMy H-modes has been investigated for JET plasmas with a plasma current of 2 MA, toroidal field of 2.7 T, a fueling gas puff of  $10^{22} \text{ m}^{-3}$  and about 16MW/14.5MW of beam heating. One plasma with central ICRH has been compared to a plasma without central ICRH. The plasma without ICRH yields a strong increase of the W-concentration from about  $3 \cdot 10^{-5}$  up to  $10^{-3}$  within  $r/a = 0.3$  during a sawtooth cycle and the sawtooth crash results in an approximately flat W-concentration profile. However, the uncertainties affect the neoclassical transport coefficients considerably, because small uncertainties in the electron measurements translate into big uncertainties for the neoclassical transport coefficients due to the strong charge dependence of the latter. When adding central ICRH the W-content of the plasma at  $r/a=0.45$  and  $r/a=0.3$  increases to about  $10^{-4}$  and the central excursions of the W-concentrations become much smaller. For the same discharge the transport in between sawtooth crashes has phases which feature transport roughly consistent with neoclassical theory, but also has phases with outward transport clearly not consistent with neoclassical theory. The outward transport is best explained by an increased diffusive transport ( $\approx 0.5 \text{ m}^2 \text{s}^{-1}$ ) or a temporary outward convection ( $\approx 0.2 \text{ ms}^{-1}$ ). Due to the immediate correlation between a change of transport and a change of MHD activity (from regular (1,1)-mode to fishbones) the underlying reason for the different transport is attributed to the mode activity rather than to effects from turbulent transport or neoclassical transport. A slow change of the transport coefficients within the sawtooth cycle is also an option, still the start of the change correlates with the change in MHD.

From ASDEX Upgrade a discharge is presented in order to shed light on mechanisms that trigger W-accumulation in the core. In the discharge the heating, electron density and electron temperatures stay constant within the experimental uncertainties, while the fueling gas puff is slowly reduced. This causes a rise of the net W-influx at the edge of the confined plasma which is observed via a rise of the W-concentration at mid radius by a factor of about 2. The monitoring of the C-impurity reveals that its density at mid-radius rises only slightly and less obvious by about 10%. At a certain time point the W-transport changes producing steeper W-concentration gradients in the plasma core, while the low-Z impurities show also weak signs of peaking, which suggests that there is a Z-dependence of transport. During this time interval the core localized ion temperature measurement seems to be less peaked in agreement with the idea that a flattening of temperature profiles goes along with less anomalous transport, while the neoclassical transport could give rise to a Z-dependent inward transport. The changes are most obvious in the W-concentration and connected radiated power, and

*Observations on the W-transport in the Core Plasma of JET and ASDEX Upgrade* 18

the W-peaking, while all other changes are close to the detection limit. The change of core transport is ultimately achieved by the change of the plasma edge, while the plasma outside of  $r/a=0.2$  is hardly affected at all. However, the exact causality is hard to disentangle. The most obvious change is the increasing W-concentration which may lead to a decrease in core electron temperatures, which is only visible via the ion temperature changes and which seems to be rather subtle. Possibly this causes the change of W-transport leading to the W-peaking, however there are other subtle changes happening in the plasma profiles such as rotation. As an obvious conclusion the onset of W-accumulation is identified as a process that is hard to predict, because a well stable plasma is turned into an unstable plasma, while the changes in plasma profiles are subtle.

In conclusion, the W-transport in the plasma core has been investigated and the limitations of the interpretation for both analyses exist mainly due to the fact that small changes of plasma profiles result in a large effect of the W-transport. While the driving mechanisms may be identified in today's devices, still the quantitative understanding of the transport effects are limited, e.g. for predicting the necessary mode activity to prevent W-accumulation in the core and the interaction between mode activity, turbulent transport and neoclassical transport. This also limits the predictive capabilities for future plasmas, as the prediction of the background profiles for future devices is mainly based on scaling laws.

### Acknowledgement

This work was supported by EURATOM and carried out within the framework of the European Fusion Development Agreement. The views and opinions expressed herein do not necessarily reflect those of the European Commission.

### References

- [1] R. Neu *et al.*, Physica Scripta **T138**, 014038 (6pp) (2009).
- [2] G. F. Mathews *et al.*, Journal of Nuclear Materials **438**, S2 (2013).
- [3] A. Kallenbach *et al.*, Plasma Physics and Controlled Fusion **47**, B207 (2005).
- [4] R. Isler, R. Neidigh, and R. Cowan, Phys. Lett. **A63**, 295 (1977).
- [5] E. Hinnov and M. Mattioli, Phys. Lett. **A66**, 109 (1978).
- [6] R. Neu *et al.*, Nuclear Fusion **45**, 209 (2005).
- [7] R. Neu *et al.*, Journal of Nuclear Materials **313–316**, 116 (2003).
- [8] R. Dux *et al.*, Nuclear Fusion **39**, 1509 (1999).
- [9] R. Dux *et al.*, Plasma Physics and Controlled Fusion **45**, 1815 (2003).
- [10] M. Sertoli *et al.*, Plasma Physics and Controlled Fusion **53**, 035024 (2011).
- [11] M. Puiatti *et al.*, PHYSICS OF PLASMAS **13**, (2006).
- [12] M. Valisa *et al.*, NUCLEAR FUSION **51**, (2011).
- [13] T. Pütterich *et al.*, Proc. of the 24rd IAEA Fusion Energy Conference, San Diego, USA (IAEA, Vienna, 2012), Vol. IAEA-CN-197, pp. EX-P3.15.
- [14] R. Dux, Technical Report No. 10/30, IPP, Garching, Germany.
- [15] A. G. Peeters, provided the NEOART code, 1998.

*Observations on the W-transport in the Core Plasma of JET and ASDEX Upgrade 19*

- [16] S. P. Hirshman and D. J. Sigmar, Nuclear Fusion **21**, 1079 (1981).
- [17] W. A. Houlberg, K. C. Shaing, S. P. Hirshman, and M. C. Zarnstorff, Physics of Plasmas **4**, 3230 (1997).
- [18] A. G. Peeters, Physics of Plasmas **7**, 268 (2000).
- [19] T. Fulop and P. Helander, Physics of Plasmas **8**, 3305 (2001).
- [20] T. Pütterich *et al.*, Plasma Physics and Controlled Fusion **50**, 085016 (2008).
- [21] C. Giroud *et al.*, Nuclear Fusion **47**, 313 (2007).
- [22] J. Stober *et al.*, in *Europhysics Conference Abstracts (CD-ROM, Proc. of the 34th EPS Conference on Plasma Physics, Warsaw, 2007)*, Vol. 31F, pp. P-5.138.
- [23] M. Sertoli *et al.*, in *Europhysics Conference Abstracts (CD-ROM, Proc. of the 38th EPS Conference on Plasma Physics, Strasbourg, France, 2011)*, Vol. 35G of *ECA*, P-5.116.
- [24] S. Günter *et al.*, Nuclear Fusion **39**, 1535 (1999).
- [25] T. Pütterich *et al.*, Nuclear Fusion **50**, 025012 (9pp) (2010).
- [26] R. Dux, Technical Report No. 10/27, IPP, Garching, Germany.
- [27] R. Neu *et al.*, in *Handbook for Highly Charged Ion Spectroscopic Research*, edited by Y. Zou and R. Hutton (CRC Press, Boca Raton, FL, 2011), pp. 239–266.
- [28] A. Kallenbach *et al.*, Nuclear Fusion **49**, 045007 (2009).
- [29] R. Dux, A. Janzer, T. Pütterich, and ASDEX Upgrade Team, Nuclear Fusion **51**, 053002 (2011).
- [30] T. Pütterich *et al.*, Journal of Nuclear Materials **415**, S334 (2011).
- [31] C. Angioni, F. J. Casson, C. Veth, and A. G. Peeters, Physics of Plasmas **19**, 122311 (2012).
- [32] M. Z. Tokar *et al.*, Nuclear Fusion **37**, 1691 (1997).

## 5.5 Publication 5 - (not refereed)

*Tungsten Screening and Impurity Control in JET*

Proc. 24rd IAEA Fusion Energy Conf. (San Diego, CA) (Vi-

enna: IAEA) vol IAEA-CN-197, EXP3.15(2012)

not refereed

[http://www-naweb.iaea.org/napc/physics/FEC/FEC2012/papers/193\\_EXP315.pdf](http://www-naweb.iaea.org/napc/physics/FEC/FEC2012/papers/193_EXP315.pdf)

## Tungsten Screening and Impurity Control in JET

**T. Pütterich<sup>1</sup>, R Dux<sup>1</sup>, M.N.A. Beurskens<sup>2</sup>, V. Bobkov<sup>1</sup>, S. Brezinsek<sup>3</sup>, J. Bucalossi<sup>4</sup>, J.W. Coenen<sup>3</sup>, I. Coffey<sup>5</sup>, A. Czarnecka<sup>6</sup>, C. Giroud<sup>2</sup>, E. Joffrin<sup>4</sup>, K.D. Lawson<sup>2</sup>, M. Lehnen<sup>3</sup>, E. de la Luna<sup>7</sup>, J. Mailloux<sup>2</sup>, S. Marsen<sup>8</sup>, M.-L. Mayoral<sup>2</sup>, A Meigs<sup>2</sup>, R. Neu<sup>1</sup>, F. Rimini<sup>2</sup>, M. Sertoli<sup>1</sup>, M. Stamp<sup>2</sup>, G. van Rooij<sup>9</sup> and JET EFDA Contributors\***

JET-EFDA, Culham Science Centre, Abingdon, OX14 3DB, UK

<sup>1</sup>Max-Planck-Institut für Plasmaphysik, EURATOM Assoc., 85748 Garching, Germany

<sup>2</sup>EURATOM CCFE Fusion Assoc., Culham Science Centre, Abingdon, Oxon OX14 3DB, UK

<sup>3</sup>Institute of Energy- and Climate Research, Forschungszentrum Jülich, Association EURATOM-FZJ, Germany

<sup>4</sup>CEA, Assoc. EURATOM-CEA, IRFM, Cadarache 13108 Saint Paul Lez Durance, France

<sup>5</sup>Queen's University Belfast, University Road, Belfast BT7 1NN, Northern Ireland, UK

<sup>6</sup>EURATOM Assoc., Inst Plasma Phys & Laser Microfus, PL-01497 Warsaw, Poland

<sup>7</sup>EURATOM CIEMAT Assoc., Lab Nucl Fus, Madrid, Spain

<sup>8</sup>Max-Planck-Institut für Plasmaphysik, EURATOM Assoc., D-17491 Greifswald, Germany

<sup>9</sup>DIFFER, Assoc. EURATOM-FOM, 3430BE Nieuwegein, Netherlands

e-mail: Thomas.Puetterich@ipp.mpg.de

**Abstract** The impact of tungsten on stability and confinement of plasma discharges is studied in JET featuring the ITER-like wall. A W-diagnostic combining the soft X-ray cameras and a VUV spectrometer was used to analyze the balance between heating and radiative cooling in the core plasma. In a typical example discharge featuring impurity accumulation, the core W radiation is quantified. It is strong enough to affect the  $T_e$ -profiles. The flattening of the  $T_e$ -profile is thought to cause a further reduction of turbulent transport including a turbulent outward pinch. In this situation the neoclassical inward pinch is provided with more weight, which leads to further accumulation of W. Smaller deuterium gas puff levels which lead to low ELM frequencies allow for a more efficient penetration of eroded W into the main plasma. For low gas puff conditions, also W-erosion and electron density peaking foster impurity accumulation which ought to be mitigated by a medium sized gas puff in the range of  $1\text{--}2 \times 10^{22}$  electrons/s.

### 1. Introduction

In a fusion reactor, a central tungsten (W) concentration of only  $3 \times 10^{-5}$  increases the minimum triple product for ignition  $nT\tau_E$  by 20% and at  $1.9 \times 10^{-4}$  the ignition condition can not be reached [1]. Tungsten is used as a plasma facing component in today's experiments, e.g. ASDEX Upgrade [2] and JET [3], and one objective is to quantify the mechanisms that determine the W-concentration in the plasma, when using W as a first wall material. While a stepwise transition at ASDEX Upgrade allowed to document the relative importance of various components for a full W device JET's ITER-like wall was implemented during one shut down allowing an easier comparison with the previous carbon plasma facing components (PFCs). The PFCs resemble the wall mix of ITER featuring W in the divertor and Beryllium (Be) in the main chamber. Now the most abundant impurity originating from the walls in JET is beryllium and the carbon concentrations have been reduced by factors of 10-20 which results in levels of 0.05 % [4]. In JET, the Be dominates the low-Z impurity mix and thus the W erosion [5,6]. In ASDEX Upgrade, W has been observed to be well screened by the divertor plasma, see for example [7,8], and is thus thought to play also a minor role in the main plasma of JET and ITER. The W-screening in the divertor of JET is investigated and quantified in the present work. Unexpectedly, W eventually affects the main plasma for the ITER-like wall experiments at JET. The properties of these effects are investigated and characterized. To this end details of a specific discharge featuring impurity accumulation are analyzed. This allows for understanding the

\*See the Appendix of F. Romanelli et al., Proceedings of the 24th IAEA Fusion Energy Conference 2012, San Diego, US

processes that lead to and govern impurity accumulation, which is the biggest concern when dealing with W. At the same time a comprehensive database of pulses has been built which enables the testing of these findings. Due to space limitations the latter will be presented elsewhere.

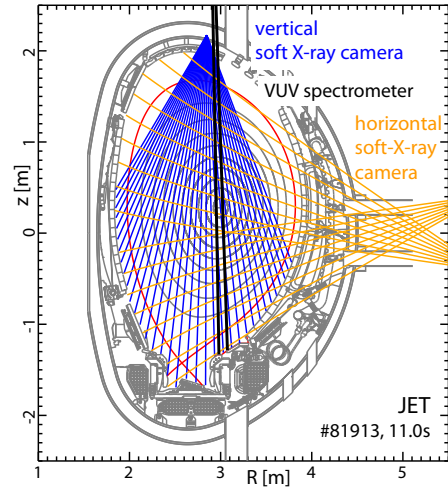
## 2. Quantitative Diagnosis of the W-density

Two approaches are chosen to provide a quantitative measure for the W-content in the core plasma. In Fig.1 soft X-ray (SXR) cameras and a VUV spectrometer are depicted. The first approach makes use of the spectrometer which is set to 5nm where a strong spectral feature of the W-ions  $W^{27+}$  to  $W^{35+}$  is emitted (cf. [9]). This spectral feature, also called 'quasicontinuum', is emitted at electron temperatures between about 0.8-1.8 keV. Its intensity is interpreted by taking the geometry, and electron density and temperature profiles into account and combining those with the atomic data of W as presented in [9]. In order to provide robust absolute numbers for the W-concentration a recalibration of the procedure is performed for radiation events that are known to be caused by W only. Such radiation events can be intentional laser ablations, but also natural events for which other radiators could be excluded by survey spectroscopy. For these events the total radiated power is connected to an absolute W-concentration via the cooling factor of W (cf. [1]), which is a robust number independently of the evaluation method used. The spectrometer provides W-concentrations that are valid only in a limited radial range, where the ambient  $T_e$  allows the emission.

Poloidal asymmetries, especially in-out asymmetries, might lead to an underestimation of the W-concentration. However, spectroscopy provides a direct method to determine the W-concentration independently of other radiators in the plasma.

The second approach is using the SXR cameras to determine the W-concentrations. The large number of lines of sight allows determining a 2D radiation profile and poloidal asymmetries can easily be handled. However, it is not unambiguous what species in the plasma are responsible for the radiation in the soft X-ray range. Additionally, the atomic data that is necessary for the interpretation yield systematic uncertainties. As a result we needed to apply correction factors to come to a consistent picture with total radiated power and spectrometer measurements.

While the spectrometer data is not explained in the present work (for that cf. [9,10]), the SXR data interpretation is described in this paragraph. In a first approach, several discharges with a low content of W and other soft X-ray radiators have been analyzed. In these discharges the electron density and temperature measurements from high resolution Thomson scattering (HRTS) and LIDAR have been used to predict the local SXR emissivities due to Bremsstrahlung. The lines-of-sight integrals are then performed using their geometry and a magnetic equilibrium from EFIT. In order to simulate the resulting signal of the vertical and horizontal camera the corresponding beryllium filter thicknesses of 250 and 350 microns are taken into account, while for the response of the diodes the model of [11] has been implemented. Unfortunately, a simple assumption of  $Z_{eff} = 1$  already predicts higher signals than measured.

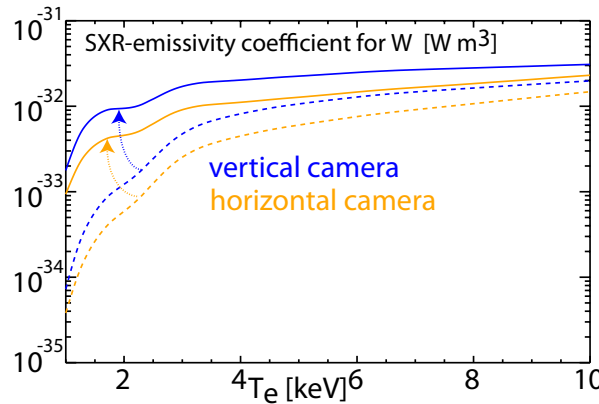


*FIG. 1: Diagnostic setup for determining the W-concentration and its poloidal asymmetry. The sight lines of soft X-ray cameras (blue and orange) and of a spectrometer (black) are featured together with the magnetic equilibrium of #81913 at 11.0 s.*

Thus, it is assumed that the absolute calibration of the SXR signals requires a correction factor of unknown origin. When using a realistic  $Z_{eff}$ -value (typically between 1 and 1.5, flat profile assumed), as derived from line-of-sight-integrated Bremsstrahlung measurements in the visible range, correction factors of 2.8 and 2.5 are derived for the vertical and horizontal camera, respectively.

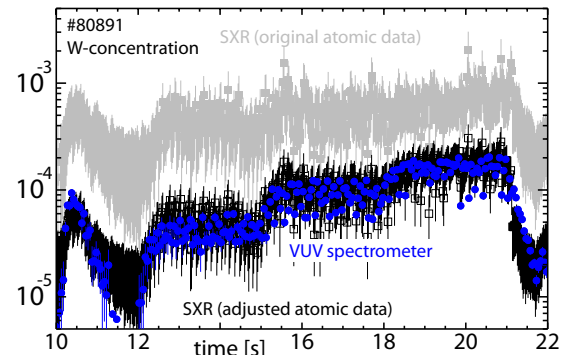
As a second step the discharge #80891 has been analyzed which features W-concentrations between  $5 \times 10^{-5}$  to  $2 \times 10^{-4}$  and flat W-concentration profiles, as measured by spectroscopy and bolometry. In #80891 only ICRH heating is used leading to low plasma rotation and the soft X-ray radiation is observed to be poloidally symmetric. In order to derive absolute W-concentrations from the SXR camera signals the Bremsstrahlung contribution due to low-Z ions is subtracted and the excess radiation is attributed to W.

This excess radiation is then interpreted using the atomic data as derived in [9,1] while the Be filters and diode responses are taken into account. On top of line radiation and radiative recombination a rough model for dielectronic recombination is included. The model attributes to each dielectronic recombination process a photon with an average energy of half the ionization potential. When taking this dataset into account a discrepancy is found between the W-concentrations derived from the spectrometer (blue) and SXR cameras (grey) (cf. Fig.2). The discrepancy is larger for the phases with lower plasma temperature.



**FIG. 3:** The soft X-ray emissivity coefficients for W derived for the vertical and horizontal SXR-cameras. The data entering the analysis (solid lines) contain adjustments to the original data (dashed lines).

energy dependent correction factor has been used to adjust the atomic data. The original and adjusted data are presented in Fig.3. When using the adjusted dataset the derived W-concentrations (black) in Fig.2 agree well with the spectrometer values and the W-concentration profiles are flatter, while with the original dataset they have been hollow. It should be noted that there are un-



**FIG. 2:** Comparison of the W-concentration measurements derived from the spectrometer measurements (blue) and the soft X-ray cameras (grey, black). The evaluation of the grey data uses the original atomic data, while the black data makes use of the presented adjustments.

The presented error bars are obtained by propagating a 10%-uncertainty of the measured electron densities and temperatures.

This 10%-level is thought to capture the typical differences between different electron density and temperature diagnostics. The discrepancy fits to the fact, that the description of the atomic data at the low energy cut-off of the Be-filter is most probably not correct. When considering the modeled spectra in [9], an energy cut off at about 0.5 nm leaves only very small spectral lines of W-ions with charges larger than 38+ within the sensitivity window of the SXR cameras. Thus, unconsidered emissions from higher-n transitions or radiation from dielectronic recombination may change the emissions noticeably. An en-

certainties for the case that the  $Z_{eff}$ -value exhibits strong radial variations as for the subtraction of the Bremsstrahlung background a radially constant  $Z_{eff}$  is used. For the chosen discharge #80891 the measured signals in the core are much larger than the predicted Bremsstrahlung, such that the uncertainties attributed to  $Z_{eff}$  are negligible. Thus, the correction factor determined here is used through-out the interpretation of the SXR camera signals.

### 3. Effects of W on Discharge Evolution

In the 2011/2012 campaigns effects of W on the main plasma have been observed that influence the stability of a plasma discharge especially for beam heated discharges. In Fig.4 time traces of selected parameters in such a discharge are presented. The discharge with  $I_p = 2.0$  MA has been performed at a magnetic field of  $2.1\text{ T}$  yielding a  $q_{95} = 3.3$ . The ELM-frequency of the type-I ELM My H-mode was about 10-15 Hz. From 9.0 s on the deuterium gas puff is lowered to  $5 \times 10^{-21}\text{ m}^{-3}$ . Up to 11.5 s the diamagnetic energy ( $W_{dia}$ ) does not considerably change, while the radiated power in the main chamber ( $P_{rad}$ ) constantly increases. A steep increase of  $P_{rad}$  is observed after 11.5 s affecting ( $W_{dia}$ ) of the plasma. From 9.0 s to 11.5 s, the core electron temper-

ature ( $T_e$ ) as measured by electron cyclotron emission (ECE) keeps falling while the edge values stay constant (cf. Fig. 4(b)). During the same period the electron density ( $n_e$ ) (cf. Fig. 4(c)), as measured by HRTS, keeps rising in the plasma core and the edge values stay constant, which implies that the density starts peaking. Only after 11.5 s the core  $T_e$  collapses drastically. These observations are also reflected in the evolution of the confinement H98-factor (cf. Fig. 4(d)), which is 0.85 during the flattop and drops at the end of the flattop. As the line-averaged  $Z_{eff} \approx 1.2$  and does not change much during the radiation rise a medium to high-Z element must be the responsible for it. However, the W-concentration ( $c_W$ ) as measured by the spectrometer stays constant through out. In order to estimate the radiated power due to W, the W-concentration, which is locally measured at a certain radial range, is assumed to apply for the full plasma volume - this estimate is depicted in Fig. 4(a) and labeled 'est. W-rad'. The W-radiation seems to be negligible during all phases of the discharge and thus seems to indicate that W may not be responsible for the rise of the main chamber radiation. However, the spectrometer line of sight is vertical (cf. Fig. 1) and may be missing parts of the W emissions because of poloidal asymmetries that arise from centrifugal forces. A further complication is that the W emissions seen by VUV spectrometer yield information from a limited radial region only. Indeed, the vertical SXR camera shows clear signs of poloidal asymmetries when looking at the line-of-sight-integrated raw signals. Thus, as described in section 2 a 2D deconvolution of the radiation attributed to W was performed, allowing for poloidal asymmetries which are consistent with the Wesson-formula [12]. The W-density on a flux surface is thus described by

$$n_W(r_{norm}, R) = n_{W,0}(r_{norm}) e^{\lambda(r_{norm})(R^2 - R_0^2(r_{norm}))},$$

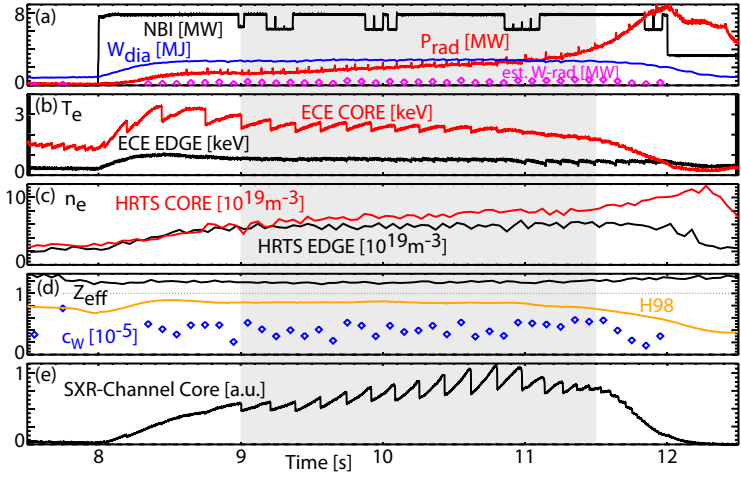


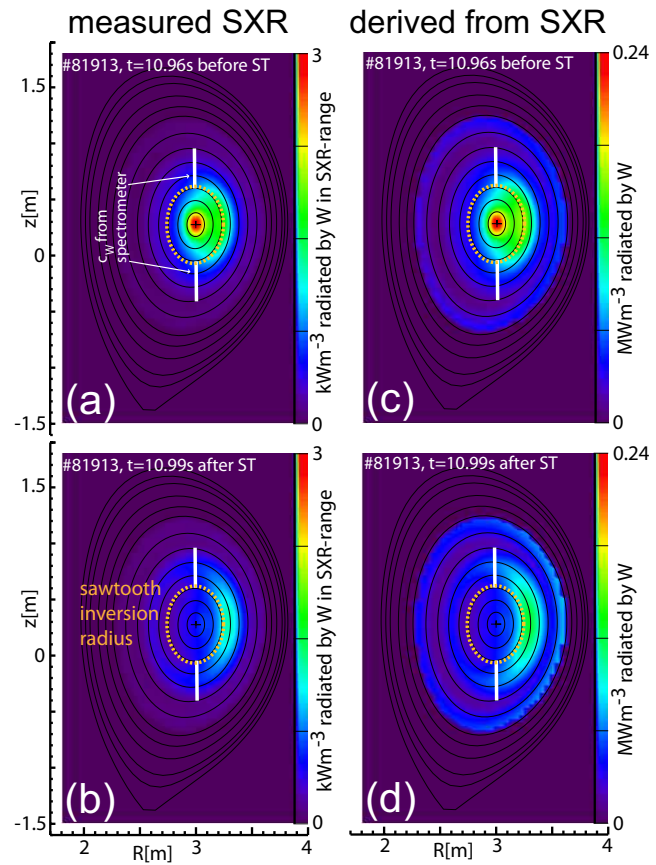
FIG. 4: Time traces of selected parameters for #81913. Further information is in the text.

where  $R$  is the large radius and  $n_{W,0}(r_{norm})$  is the W-density on the flux surface labeled  $r_{norm}$  at the large radius  $R_0(r_{norm})$ .  $\lambda(r_{norm})$  contains the dependence on the rotational frequency of the plasma. For the case that all plasma species have the same temperature it is given by:

$$\lambda(r_{norm}) = (1 - 0.5Z_W \frac{m_D}{m_W}) \frac{m_W \omega^2}{2T_W}$$

When the SXR analysis is applied to #81913 the strong asymmetries in measurements of the vertical SXR camera are translated into local poloidal asymmetries. The measured data is well described by the deconvolutions presented in Fig.5(a) and (b). The asymmetries show up most clearly just outside of the sawtooth inversion radius. If the radiation is purely caused by W, a rotation velocity of about 80km/s is required to explain the poloidal asymmetry. The measurements of charge-exchange recombination spectroscopy are consistent with that. As Ni is a candidate impurity for causing SXR radiation, the Ni levels have been checked by additional spectroscopic measurements (cf. [13]) and a major contribution of Ni can be excluded. Additionally, if we assume the SXR radiator was Ni, the required rotation velocity needed to be about a factor of 2 higher. Thus, we assume that all of the SXR signal originates from W, which allows for the calculation of the local W-concentrations using an ionization equilibrium neglecting transport. The latter assumption has been proven to be reasonable for W (e.g. [14]). From the W-concentration the total, local radiated power densities due to W are derived using its cooling factor [1]. These power densities are presented in Fig.5(c) and (d).

Please note that the radiation ring at the edge of the evaluation region might be an artefact yielded by larger uncertainties of the evaluation at plasma radii where the SXR-emissions are close to the Bremsstrahlungs-level. The 2D structure of the emissions inside of that ring are real and make apparent, why the spectrometer measurements underestimate the W-content of the core plasma. The measurement location of the spectrometer is indicated by white bars in Fig.5 and do not radially or poloidally coincide with the regions exhibiting the strongest W-emissions. The strong localized peaking itself is no big surprise, as this is very characteristic for so-called impurity accumulation. We note that the term impurity accumulation is used ambiguously and that in the present work we always refer to core localized impurity accumulation. In [15,16] it has been found that impurity accumulation occurs when turbulent transport in the plasma core is weak, and the collisional transport



*FIG. 5: (a)+(b): 2D deconvolutions of the SXR signals before (a) and after (b) a sawtooth (ST). Bremsstrahlung contributions of low-Z elements have been subtracted. The white lines indicate the region of the W-concentration measurement based on the VUV spectrometer; (c)+(d): calculated total radiated power densities using the W-densities derived from (a) and (b).*

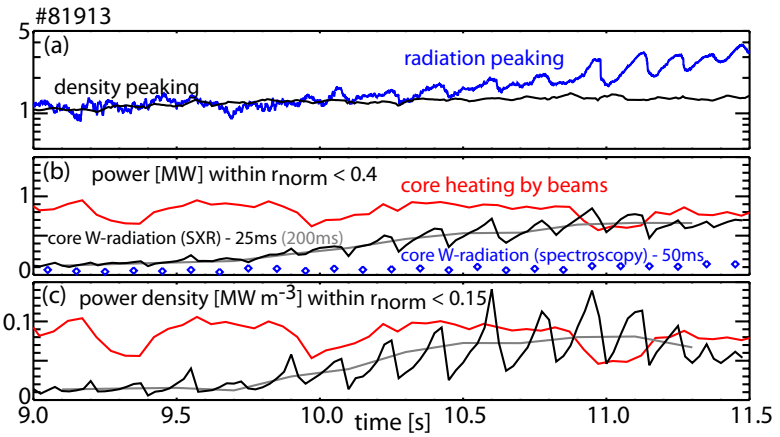
and (d). Please note that the radiation ring at the edge of the evaluation region might be an artefact yielded by larger uncertainties of the evaluation at plasma radii where the SXR-emissions are close to the Bremsstrahlungs-level. The 2D structure of the emissions inside of that ring are real and make apparent, why the spectrometer measurements underestimate the W-content of the core plasma. The measurement location of the spectrometer is indicated by white bars in Fig.5 and do not radially or poloidally coincide with the regions exhibiting the strongest W-emissions. The strong localized peaking itself is no big surprise, as this is very characteristic for so-called impurity accumulation. We note that the term impurity accumulation is used ambiguously and that in the present work we always refer to core localized impurity accumulation. In [15,16] it has been found that impurity accumulation occurs when turbulent transport in the plasma core is weak, and the collisional transport

becomes more important. The cleaning effect of large turbulent core transport is not only based on diffusive effects, but also supported by a turbulent outward pinch for the impurities. Both turbulent effects require steep temperature gradients [17,16,18]. When the temperature gradients are weak neoclassical transport becomes important. If a gradient in the deuterium density exists, the neoclassical inward pinch arises for the impurities.

In #81913, the occurrence of impurity accumulation is consistent with the development of density peaking. In order to judge on the power fluxes inside the plasma a closer look into the radiation/heating balance of the core plasma of #81913 is necessary. Considerable radiative cooling is able to decrease the core  $T_e$  and will flatten the gradients in  $T_e$ , which causes a decrease of turbulent transport (e.g. [19]) and starts a feedback loop of transport and radiation.

Thus, the SXR analysis is applied to the full time sequence using 25 ms and 200 ms time intervals in which the signals are averaged. The obtained 2D radiation profiles similar to those in Fig.5(c) and (d) are used to derive the total radiated power due to W in the core plasma. In Fig.6 the evolution of relevant core parameters are depicted. While the density peaking (cf. Fig.6 (a)) develops gradually and becomes maximal already at about 10.5 s, the radiation peaking is almost

constant up to about 10.0 s and then starts rising until the end of the heating phase. The density peaking reaches values of 1.5 (i.e. the ratio of core ( $r_{norm} = 0$ ) and pedestal-top densities) and the radiation peaking (derived from comparing two bolometer lines of sight) rises to values of 4 and keeps rising after 11.5 s. It should be noted that the radiation peaking is very localized in the core as the peaking happens within about  $r_{norm} = 0.4$ . The W-radiation in the core (cf. Fig.6(b)) is at negligible levels at 9.0 s and starts rising at about 9.75 s consistently with the diagnosed radiation peaking. When comparing the NBI heating power within  $r_{norm} < 0.4$  to the radiated power attributed to W via the SXR camera analysis, they become comparable only after 10.0 s. The reason for the change in transport might be localized even more centrally. At the plasma volume within  $r_{norm} < 0.15$ , the radiation power density is strongly modulated by sawteeth already at 9.5 s. At the end of the sawtooth cycle the radiation density is about a third of the heating power density - thus an impact on the  $T_e$ -profiles and turbulence seems possible. This evolution is consistent with the general observation that impurity accumulation starts in the plasma core, where gradients approach zero close to the magnetic axis. Clearly, this observation suggests that central impurity accumulation may be avoided by more localized core heating or a smaller level of W-concentration [20]. Both mechanisms have been reported before at ASDEX Upgrade [17,16,20] or JET [18]. ICRF heating at JET provides core localized heating and thus is a good candidate for controlling the impurity accumulation. This has been demonstrated in earlier campaigns (e.g. [18]), and the present work suggests that it also works for controlling W-accumulation.



*FIG. 6: (a) time traces for density (black) and radiation (red) peaking; (b) heating and radiation power within  $r_{norm} < 0.4$ ; (c) heating and radiation power densities within  $r_{norm} < 0.15$*

#### 4. Screening of W

The erosion of W is localized in the divertor, where the ion flux is largest and during ELMs a considerable fraction of the W-erosion occurs [5,6]. For the inter-ELM phase the electron temperature has been found to be a controlling factor of the erosion process in the divertor, while impurities are always the sputtering species [5,6]. The erosion is quantified by spectroscopic measurements on lines of sight observing the W-surfaces. The W-flux is deduced from the photon fluxes using the S/XB-method [21]. The ratio of the total W-content and total W-flux gives the effective W-confinement time  $\tau_W$ . It is a figure of merit, which allows to quantify the efficiency of an eroded atom to enter the plasma bulk. Thus,  $\tau_W$  integrates the prompt deposition, the screening mechanisms in divertor and scrape-off layer, pedestal transport and partly core transport in a single number. In [22,23] the edge transport and erosion has been modeled, and edge-localized modes (ELMs) have been identified to play a major role for control of impurities.

More frequent ELMs have been observed to provide cleaner main plasmas, as impurities are flushed by the ELMs, while in between the ELMs they experience an inward pinch at the pedestal. In the present work deuterium gas puffing is used to increase the ELM frequency of discharges with low and high triangularity (low  $\delta$  and high  $\delta$ ) shapes. In Fig.7(a)  $\tau_W$  versus the ELM-frequency is depicted for 2.0 MA plasmas performed at 2.2 T. The data points exhibit a considerable scatter, but the expected trend of higher  $\tau_W$  at lower ELM-frequency is visible. No clear separation between the low and high triangularity is observed, which could be related to the scatter. In Fig.7(b)  $\tau_W$  versus the deuterium gas rate is presented. For lower gas puff  $\tau_W$  is systematically higher. In Fig.7(c) a clear relation between  $\tau_W$  and the energy confinement time  $\tau_E$  becomes apparent. Note that the zero on the  $\tau_E$ -axis is suppressed. The W-screening is strongly enhanced for a moderate confinement degradation. Looking in more detail, the lower confinement either correlates to higher ELM-frequencies or higher deuterium gas puff levels. It should be noted that  $\tau_W$  only provides information about the screening of W, however, the W-concentration is determined also by the source of W. The latter is a complicated function of power transported to the divertor, particle fluxes and impurity densities. For our limited data set the W-source is small for high gas puff rates and high ELM frequencies.

These findings support the strategy to operate at a non-zero gas puff level and an elevated ELM-frequency (e.g. ELM-pacemaking), while the slightly reduced confinement of the plasma [24] may be enhanced by additional means. This might be nitrogen seeding [25] or the exploitation of an enhanced confinement due to a favorable  $\beta$ -dependence [26]. The latter is observed for discharges at finite gas puffing levels when the highest beam heating powers are applied.

#### 5. Summary

The impact of tungsten eroded in the divertor on stability and confinement of plasma discharges is studied in JET featuring the ITER-like wall. A localized quantification of W has been developed by a combination of measurements from soft X-ray cameras and a

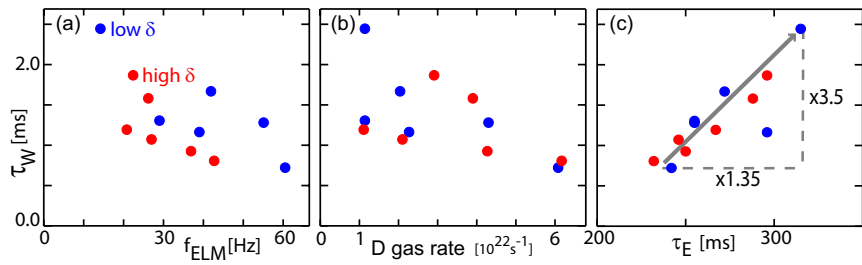


FIG. 7: (a) W-confinement time ( $\tau_W$ ) versus ELM-frequency ( $f_{ELM}$ ) (b)  $\tau_W$  versus deuterium gas rate (c)  $\tau_W$  versus energy confinement time  $\tau_E$ , factors of 3.5 in  $\tau_W$  and 1.35 in  $\tau_E$  are indicated; note the suppressed zero.

VUV spectrometer. The soft X-ray cameras allow for a detailed accounting of core radiation and poloidal asymmetries. The latter are explained by parallel transport in the presence of centrifugal forces using rotation velocities consistent with charge-exchange recombination spectroscopy. Beam heated discharges are observed to develop central impurity accumulation for cases in which the central power balance is considerably influenced by W-radiation. In pulse #81913, which is representative for most of the impurity accumulation cases, it could be shown that the impurity accumulation starts by radiation peaking in the very core, locally flattening the  $T_e$ -profiles which in turn provides less turbulent transport and giving more weight to the neoclassical inward pinch. The importance of the radiation/heating balance directly implies that the stability against impurity accumulation can be improved by more core localized heating or by a lower W-impurity level. A study of the W confinement time ( $\tau_W$ ) is presented in order to identify the parameters that allow to operate at low W levels.  $\tau_W$  is found to be a factor 100-500 smaller than the energy confinement time indicating the efficient screening by the divertor. At low levels of deuterium gas puff, which coincides with low ELM frequencies,  $\tau_W$  are systematically higher. At the same time strong density peaking is observed at low gas puff levels consistently with the collisionallity scaling of density peaking [26]. All the described effects sum up and provide an unfavorable situation at zero gas puff. Thus, a recommendation of the present work is to operate with minimum gas puff levels of about  $1-2 \times 10^{22}$  electrons/s and use additional core heating means like ion cyclotron heating in order to maintain a stable core balance between heating and radiation.

### References

- [1] PÜTTERICH, T. et al., Nuclear Fusion **50** (2010) 025012 (9pp).
- [2] NEU, R. et al., Physica Scripta **T138** (2009) 014038 (6pp).
- [3] MATHEWS, G. F. et al., Journal of Nuclear Materials (2012), submitted.
- [4] BREZINSEK, S. et al., Journal of Nuclear Materials (2012), submitted.
- [5] VAN ROOIJ, G. J. et al., Journal of Nuclear Materials (2012), submitted.
- [6] DUX, R. et al., Journal of Nuclear Materials **390-391** (2009) 858.
- [7] GEIER, A. et al., Plasma Physics and Controlled Fusion **44** (2002) 2091.
- [8] THOMA, A. et al., Plasma Physics and Controlled Fusion **39** (1997) 1487.
- [9] PÜTTERICH, T. et al., Plasma Physics and Controlled Fusion **50** (2008) 085016.
- [10] NEU, R. et al., *Importance of Tungsten Spectroscopy to the Success of ITER*, CRC Press, Boca Raton, FL, USA, 2011.
- [11] ANTON, M. et al., Review of Scientific Instruments **66** (1995) 3762.
- [12] WESSON, J. A., Nuclear Fusion **37** (1997) 577.
- [13] CZARNECKA, A. et al., Plasma Physics and Controlled Fusion **53** (2011) 035009.
- [14] ASMUSSEN, K. et al., Nuclear Fusion **38** (1998) 967.
- [15] DUX, R. et al., Journal of Nuclear Materials **313-316** (2003) 1150.
- [16] DUX, R. et al., Plasma Physics and Controlled Fusion **45** (2003) 1815.
- [17] SERTOLI, M. et al., Plasma Physics and Controlled Fusion **53** (2011) 035024.
- [18] PUIATTI, M. et al., PHYSICS OF PLASMAS **13** (2006).
- [19] RYTER, F. et al., Nuclear Fusion **43** (2003) 1396.
- [20] NEU, R. et al., Nuclear Fusion **45** (2005) 209.
- [21] COENEN, J. W. et al., EPS Stockholm (2012), P1.036.
- [22] PÜTTERICH, T. et al., Journal of Nuclear Materials **415** (2011) S334.
- [23] DUX, R. et al., Nuclear Fusion **51** (2011) 053002.
- [24] JOFFRIN, E. et al., 2012, this conference.
- [25] GIROUD, C. et al., 2012, this conference.
- [26] BEURSKENS, M. N. A. et al., 2012, this conference.

### 6. Acknowledgement

This work was supported by EURATOM and carried out within the framework of the European Fusion Development Agreement. The views and opinions expressed herein do not necessarily reflect those of the European Commission.

## 5.6 Publication 6

*ELM flushing and impurity transport in the H-mode edge barrier in ASDEX Upgrade*

Journal of Nuclear Materials 415 (2011) S334

# ELM flushing and Impurity Transport in the H-mode Edge Barrier in ASDEX Upgrade

**T. Pütterich, R. Dux, M.A. Janzer, R.M. McDermott and the ASDEX Upgrade Team**

*Max-Planck-Institut für Plasmaphysik, EURATOM Association, D-85748 Garching, Germany*

**Abstract.** Density profiles of  $\text{He}^{2+}$ ,  $\text{C}^{6+}$ ,  $\text{Ne}^{10+}$  and  $\text{Ar}^{16+}$  are measured at ASDEX Upgrade with high temporal (1.9 ms) and radial resolution ( $> 3 \text{ mm}$ ) using CXRS. This allows the transport coefficients at the edge transport barrier to be analyzed in between type-I ELMs during H-mode. All measurements resemble the neoclassical transport coefficients, which means that the diffusion coefficient ranges from 0.15–0.35  $\text{m}^2/\text{s}$  and the maximum of the inward convection velocity is Z-dependent increasing from 15 m/s ( $\text{He}^{2+}$ ) to 90 m/s ( $\text{Ar}^{16+}$ ). These results are combined into a simplified transport-erosion model for W which calculates the neoclassical transport coefficients self-consistently while taking several impurity species into account. The model also calculates erosion fluxes at the wall, prompt redeposition of W and loss terms due to parallel flows in the scrape-off layer. While several free parameters exist in the model, it demonstrates that a quantitative consistency between the measured erosion fluxes of W and the observed W concentration inside the plasma is obtainable.

## 1. Introduction

In H-mode plasmas the turbulent transport of energy and particles is strongly suppressed in a thin radial region at the edge of the confined plasma. The width of this edge transport barrier (ETB) is rather small (for ASDEX Upgrade  $< 2 \text{ cm}$ ) with large radial gradients for  $T_e$ ,  $T_i$  and  $n_e$ . In ELMy H-modes, edge-localized modes (ELMs) occur which make the steep gradients of temperature and density collapse for a few 100 microseconds. These recover again in the following milliseconds until the next ELM occurs. The transport details of this barrier determine how well the plasma confines energy enhancing its performance and how well it confines impurities and He ash which, in general, reduce the performance of a fusion plasma. The small spatial extent of the barrier and the fast change due to ELMs requires a diagnostic with good spatial and temporal resolution. In this work special focus is put on tungsten (W) as a plasma impurity. However, as a direct determination of the W-transport profile was not possible, a Z-dependent measurement has been performed, which is used to predict the W-transport by extrapolation. The edge charge exchange system at ASDEX Upgrade [1] was utilized for this, as it has a spatial resolution of up to 3 mm and is able to operate with a temporal resolution of 1.9 ms enabling the actual pedestal investigations.

## *ELM flushing and Impurity Transport in the H-mode Edge Barrier in ASDEX Upgrade* 2

The ETB is only one player controlling the impurity content of the plasma. Other influences are the time-dependent impurity sources at the first wall or the transport across and within the scrape-off layer (SOL). Both is influenced by the ELMs ejecting energy and particles from the plasma while the tens of milliseconds long phase between the ELMs does exhibit a considerably smaller erosion at the first wall and densities/temperatures in the SOL. The ultimate goal is to predict the impurity content of the confined plasma and thus an integral part is to quantitatively connect impurity erosion fluxes to the pedestal-top densities. A model is presented, which delivers this connection while including many experimentally observed details. It should be noted that the model is relatively simple and contains free parameters, which are chosen within a credible range to fit the measurements.

## **2. Impurity Transport at the ETB**

### *2.1. Determination of Transport Coefficients*

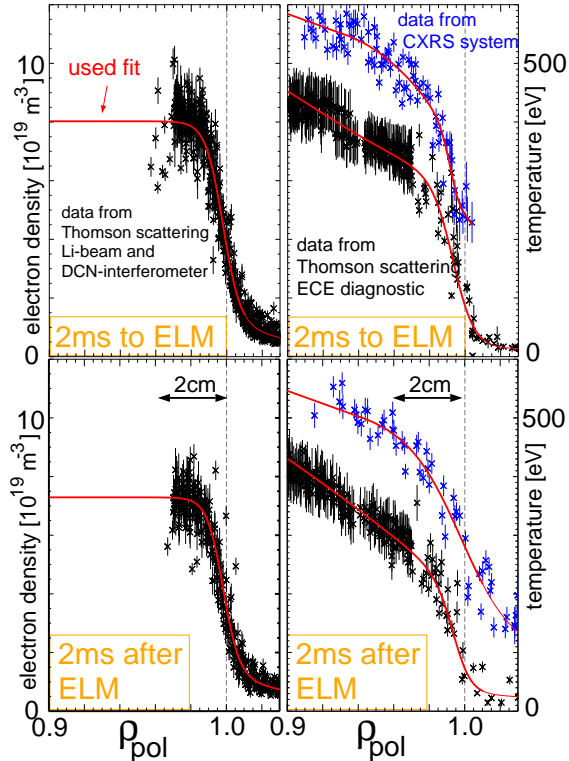
The impurity transport for He, C, Ne and Ar is measured by comparing the measured density profiles of specific ions from these impurities to a variety of results from a transport model, which are obtained by varying the diffusion coefficient and convection velocity at the ETB. In the following the details of the measurements are described and then the transport model is explained.

The edge CXRS system at ASDEX Upgrade covers the plasma edge at the outboard midplane with up to 8 different lines of sight (LOS) that are radially spaced by approximately 0.9 cm. In order to fully resolve the steep gradients in impurity densities the plasma is swept by 2 cm in a 300 ms long phase during flattop. Along with the local CX-brightness the local ion temperature ( $T_i$ ) and toroidal rotation can be derived from the Doppler broadening and shift of the corresponding spectral line. The impurity density is calculated from the brightness of the spectral line using the local beam density of the 60 keV heating beam and the reaction rate data from ADAS [2]. The plasma sweep allows also for good radial coverage by the Thomson scattering system, which measures the electron temperature ( $T_e$ ) and density profiles ( $n_e$ ). The electron density is measured additionally by utilizing the beam emission of a neutral Lithium beam penetrating the plasma edge. Inside the pedestal-top electron cyclotron emission is used to determine the core  $T_e$ . Interferometer measurements, which give line integrated densities, are used to restrict the electron density profiles at the pedestal-top. The uncertainty of the separatrix position from magnetic reconstruction can be minimized with the help of the steep  $T_e$ -profiles by setting  $T_{e,sep} = 85$  eV (typically 80-120 eV at ASDEX Upgrade), a mandatory condition set by the parallel heat transport and power balance [3]. The  $n_e$ -profiles from the Li-beam are then aligned to the measurements of the Thomson scattering. The CX-data are then aligned such that the steep  $T_i$ -gradient region coincides with that of the  $T_i$ -measurement (cf. figure 1). This process can be done within an accuracy of 2-3 mm.

As a first step, the transport model is applied to the measurements of the  $C^{6+}$  density. In that case the data quality allowed for taking the evolution of several profiles within an ELM-cycle into account. In figure 1, the edge  $T_i$ -,  $T_e$ - and  $n_e$ -profiles are presented for two

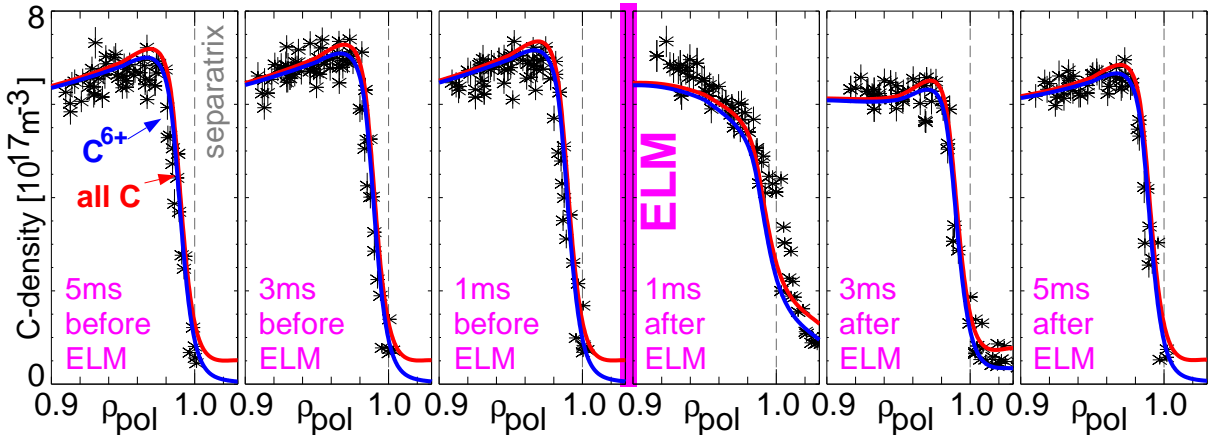
*ELM flushing and Impurity Transport in the H-mode Edge Barrier in ASDEX Upgrade* 3

time points relative to an ELM in discharge #22273. The parameters of the discharge are  $I_p = 1$  MA,  $B_t = -2.5$  T,  $q_{95} = 4.5$ ,  $P_{aux} = 2.5$  MW,  $n_e/n_{GW} = 0.65$  and the ELM frequency is about 60 Hz. The spacing between  $\rho_{pol} = 0.98$  and 1.00 corresponds to about 1 cm radial distance at the outer midplane of ASDEX Upgrade.



**Figure 1.** Temperature and density profiles before and after an ELM as measured during the analyzed discharge phase of #22273.

The evolution of the  $C^{6+}$  density profiles (cf. figure 2) was modeled with the impurity transport code STRAHL [4, 5], which takes into account ionization and recombination rates [2] and calculates time-dependently the densities of all ionization stages along the plasma radius in a flux surface averaged manner. The local ionization and recombination rates are evaluated by taking the measured, time-dependent, electron profiles into account. The impurity transport is treated using D and v profiles. The model simulates ELM cycles until the C-density arrives at a quasi-equilibrium just modulated by the ELMs, while a constant carbon (neutral C) influx is assumed. In the model, the effects of an ELM are imitated by increasing D ( $10 \text{ m}^2/\text{s}$ ) for  $200\mu\text{s}$  in the pedestal region, while the transport in-between ELMs is the subject of this investigation. For this the transport coefficients are assumed to be constant during the inter-ELM phase. This assumption is not far-fetched as the neoclassical transport coefficients do not vary strongly during the inter-ELM phase as will be shown later. It is known from earlier reports (e.g. [6]) that just inside the H-mode ETB there exists a region with relatively high turbulent (diffusive) transport (of the order of  $1 \text{ m}^2/\text{s}$ ). For discharge #22273, a slightly hollow  $C^{6+}$  density profile is found inside  $\rho_{pol} = 0.96$ . The model is adjusted for this by assuming a moderate outward pinch of  $1.0 \text{ m/s}$  in this inner region. As the model aims to find

*ELM flushing and Impurity Transport in the H-mode Edge Barrier in ASDEX Upgrade* 4


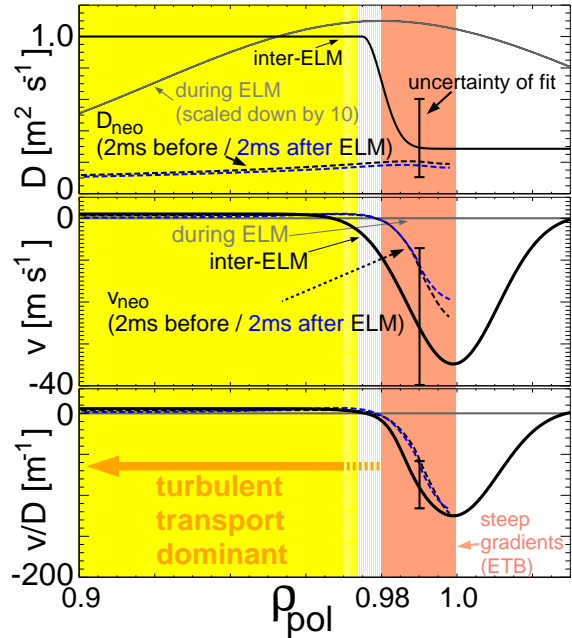
**Figure 2.** Result of an ELM-synchronized data analysis from #22273. A measured time sequence of the  $C^{6+}$  density (symbols) around a single ELM is presented along with the transport model results for the  $C^{6+}$  density (blue lines) and the total C density (red lines).

the transport coefficients in the ETB itself these adjustments do not matter.

In figure 2, the results for the best fit of  $v$  and  $D$  are presented. The agreement between data and model is quite good except for the phase 1 ms after the ELM. This time includes light from the dynamic ELM effects such as filaments. These effects are not included in the impurity model and therefore, the discrepancies are not surprising. It is astonishing that the steep gradients at the ETB are nearly fully restored within about 5 ms after the ELM crash. These steep gradients in the  $C^{6+}$  density which persist until the occurrence of the ELM, can only be modeled by including an inward drift. Local ratios of  $v/D$  at  $\rho_{pol} = 0.99$  are found to be  $-90 \pm 30 \text{ m}^{-1}$  nearly independent of all other model assumptions. For the radial location of these steep gradients the absolute values of  $v$  matter and, thus, can be derived. This is done by a least square fit for which the algorithm adjusts  $D$  and  $v$  in the barrier region, while the value of  $D$  is assumed to drop in a small radial region to a constant value and the  $v$ -profile is represented by a Gaussian curve centered at the separatrix. The value of  $D$  and the maximum of the Gaussian used to describe  $v$  are subject to the fit. In order to determine  $v$  and  $D$  only the relative shape of the  $C^{6+}$  density profile between  $\rho_{pol} = 0.96$  and  $\rho_{pol} = 1.01$  and its evolution was considered. The best agreement (s. model curves in figure 2) is found for the transport coefficients depicted in figure 3 (black, solid). Evaluating the uncertainties of the fit-parameters, the diffusion coefficient is found to be in the range  $0.1\text{-}0.6 \text{ m}^2/\text{s}$  at  $\rho_{pol} = 0.99$ , where  $v$  is between 7-40 m/s. The transport coefficients in the ETB (compared at  $\rho_{pol} = 0.99$ ) are in agreement with neoclassical predictions for impurity transport ( $D_{neo}$  and  $v_{neo}$ ) taken from the code NEOART [5, 7]. NEOART calculates the collisional transport coefficients for an arbitrary number of impurities including collisions between them. The code solves the set of linear coupled equations for the parallel velocities in arbitrary toroidally symmetric geometry for all collision regimes. The classical fluxes are given by Eqs.(5.9) and (5.10) in [8]. The equations for the banana-plateau contribution are that in [9]. The Pfirsch-Schlüter contribution is calculated from the coupled equations (6.1-2) and (6.14-15) in [8], as described in [10]. It may be noted, that the neoclassical prediction for  $D$  exhibits different shape as

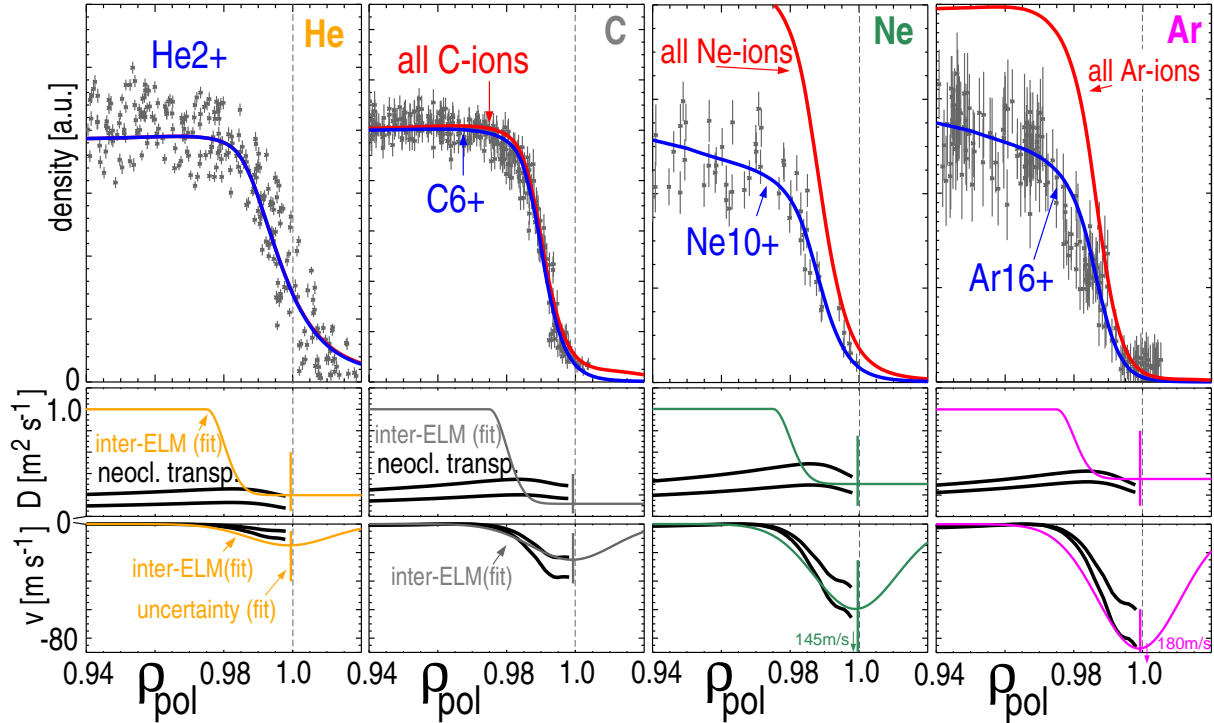
*ELM flushing and Impurity Transport in the H-mode Edge Barrier in ASDEX Upgrade* 5

a function of  $\rho_{pol}$  than the used model function, but the latter is supposed to take also the turbulent transport occurring at  $\rho_{pol} < 0.97$  into account.



**Figure 3.** The transport coefficients for C, as obtained by the presented analysis, are compared to neoclassical transport coefficients. Due to the additional turbulent transport inside of  $\rho_{pol} = 0.97$  the comparison is only relevant in the ETB region.

For revealing the Z-dependence of D and v in the ETB, a discharge very similar to #22273 was performed repeatedly and in each a different impurity density profile (intrinsic He<sup>2+</sup> and C<sup>6+</sup>, puffed Ne<sup>10+</sup> and Ar<sup>16+</sup>) was measured. The puff of Ne and Ar was designed such that for a phase of 600 ms an approximately constant pedestal-top density of the impurity was achieved. Due to the scatter in the data for Ne and Ar, the inter-ELM edge density profiles could not be analyzed time-dependently as was done for C<sup>6+</sup> in discharge #22273. However, it was found for the carbon density profile in #22273 that it is nearly constant throughout a large fraction of the ELM cycle. Therefore, the measured data points from the inter-ELM phase (5 ms after the ELM to 2 ms before the ELM) are accumulated and taken into account for the least square fit. Still, a separation of v and D is possible as the radius at which a specific ionization stage exists depends on the absolute value of v. In figure 4, these measurements are presented along with the model curves which result from the inter ELM transport profiles as shown at the bottom of the figure. There, the neoclassical prediction is also depicted. The two presented neoclassical profiles represent the results for the two background profiles just after and just before the ELM as presented in figure 1. Included in the prediction is also the influence of the concentrations of He, C and O as measured by CXRS or survey spectrometers. The neoclassical curves deliver good agreement in the pedestal region, while the uncertainties in the individual v and D values (colored bars just inside separatrix) are considerable. The uncertainties in the v/D values are smaller. For higher charged impurities a stronger inward pinch is necessary to explain the observed impurity density data, which is

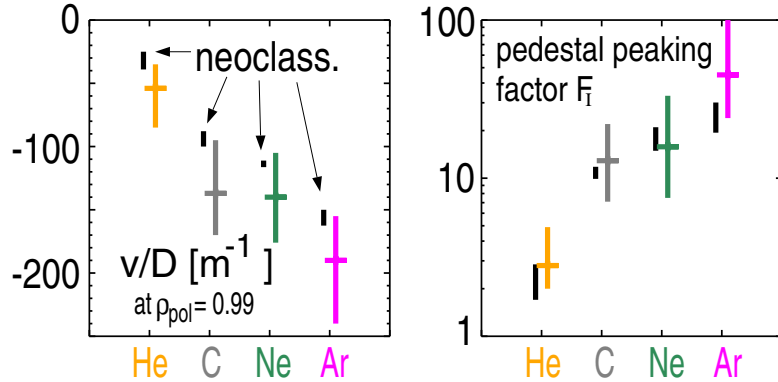
*ELM flushing and Impurity Transport in the H-mode Edge Barrier in ASDEX Upgrade* 6


**Figure 4.** top: Impurity ion densities (symbols), i.e. for  $\text{He}^{2+}$ ,  $\text{C}^{6+}$ ,  $\text{Ne}^{10+}$  and  $\text{Ar}^{16+}$ , as measured during the inter-ELM phase are presented along with the best fit of modeled profiles for the specific ions (blue) and the total impurity densities (red); bottom: The underlying transport coefficients are presented and compared to the neoclassical coefficients.

exactly what neoclassical theory predicts. The fit results for  $v/D$  evaluated at  $\rho_{pol} = 0.99$  are presented in figure 5, along with the pedestal peaking factor  $F_I$ . The latter contains the integrated effects of pedestal transport, i.e. here between separatrix and  $\rho_{pol} = 0.97$ , and it is defined as  $F_I = \frac{n_I(\rho_{pol}=0.97)}{n_I(\rho_{pol}=1.0)} = \exp\left[\int_{\rho_{pol}=1.0}^{\rho_{pol}=0.97} \frac{v}{D} dr\right]$ , where  $n_I$  is the impurity density. This expression is accurate only for a real equilibrium without a source term. Nevertheless, it shall be used here as a figure of merit. For comparison, the neoclassical values for  $v/D$  and the pedestal peaking factor  $F_I$  are also presented and within the uncertainties agreement is found.

## 2.2. Discussion

The results indicate that turbulent transport is of negligible importance for the impurities at the edge transport barrier and thus, transport arrives at the neoclassical level. This is in agreement with the results of earlier investigations from ASDEX Upgrade [6], ASDEX [11], C-Mod [12], DIII-D [13] and JET [14], all of which lacked the charge stage resolved information and were performed for only single impurities. A clear sign of neoclassical transport is also that the inward pinch follows the neoclassical scaling as it is stronger for higher charged impurities. This leads to the conclusion that each impurity has a different gradient at the ETB. The transport parameters depend slightly on the local impurity mix, as the neoclassical transport for one impurity species is the result of its friction with the background ions and the

*ELM flushing and Impurity Transport in the H-mode Edge Barrier in ASDEX Upgrade* 7

**Figure 5.** The resulting ratios  $v/D$  and the pedestal peaking factors  $F_I$  (orange, gray, green and magenta) are compared to neoclassical values (black).

various other impurities. For W, which exhibits charge states of about 15-25 at the ETB, the largest ratios of  $v/D$  apply. This means that for a given pedestal in  $T_e$ ,  $T_i$  and  $n_e$  the impurity transport can be predicted. However, the physics that determines the background profiles is not explained by the recent measurements.

It should be noted that neoclassical theory breaks down for deuterium at the pedestal, but stays valid for the impurity species. There are two reasons for this: On the one hand the banana widths are smaller for impurities and additionally, the banana and plateau contributions for the impurity transport are negligible at the radii in question. Thus, only Pfirsch-Schlüter (PS) Transport is of importance.

### 3. Connecting ETB-Transport and Wall-Erosion

The measurements described in section 2 call for an integrated modeling approach, in which several impurities are taken into account to predict the transport of W. In this section a simplified model is described, which allows for connecting the pedestal-top W density to the erosion fluxes at the first wall. Such a model involves free parameters that can be adjusted within credible ranges to obtain a match between the model results and the measurements. In order to keep the number of free parameters small, the complicated processes at the plasma edge were targeted with a 1.5D impurity transport code. Simplifications were introduced not only to reduce the 3D geometry but also to handle complex systems like the SOL with only a few parameters. A more complex model would need to be filled with more assumptions, i.e. free parameters. Thus, the model is an attempt to demonstrate how the various processes might combine. In fact, the model gives a possible explanation for a peculiar feature observed for the W confinement time, which will be described below.

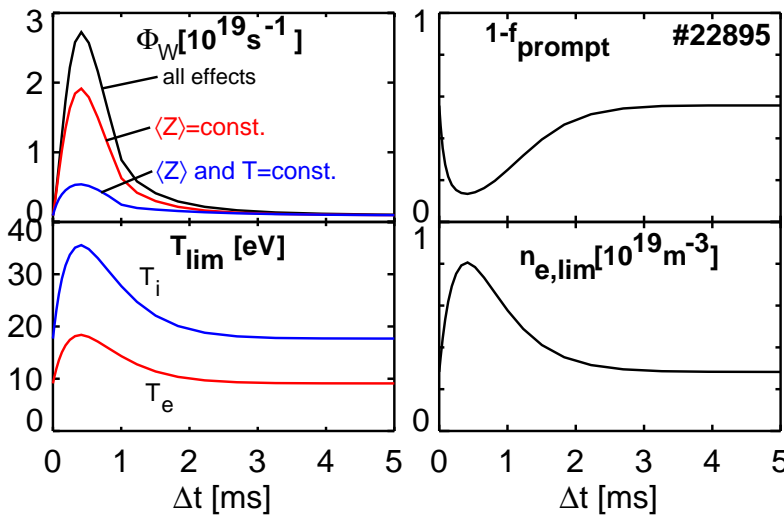
In the actual model C, O and W are modeled simultaneously and the transport coefficients for each species are determined dynamically in the ETB, depending on the local impurity densities. For W, also the erosion flux from the first wall is dependent on the impurity mix of the plasma which contacts the first wall as W erosion is almost exclusively done by light impurities. When the ELM brings impurities to the wall, the pedestal-top densities

## *ELM flushing and Impurity Transport in the H-mode Edge Barrier in ASDEX Upgrade* 8

of the impurities influence the wall sputtering. This gives the gross erosion of W, which can be compared to the spectroscopic measurement. Part of the eroded material is promptly redeposited and the rest enters the plasma in the SOL. Here, the radial transport competes with the parallel losses. When the impurity ions enter the confined plasma, the measured transport coefficients apply closing the loop.

### *3.1. Erosion and Prompt Re-deposition*

The erosion fluxes of W are measured in the experiment at numerous locations and with high time-resolution [15] and a variation of the erosion is observed within an ELM cycle as the ELM is responsible for a major part of the erosion [15]. It was demonstrated before [15] that the outboard limiters are by far the most important W source for the confined plasma. In the model this is reflected by the choice that only 1/3 of the total low-Z impurity losses were considered for the W production at the outboard limiters. In the model, the transport coefficients, the impurity densities and the temperatures at the first wall define the gross erosion of W. The sputtering yield [16] for normal incidence, which is a function of impurity mass and energy, is used. The energy at the surface is approximated by  $E = k_B(2T_i + 3ZT_e)$ , where the second term describes the acceleration in the sheath, which depends on the ion charge. The ionization stage distribution varies during an ELM cycle, when higher charged ions are swept out from the ETB and hit the limiter. An example of the temporal evolution



**Figure 6.** Temporal evolution of the tungsten influx and the fraction of not promptly redeposited W during an ELM cycle. The used values for  $T_e$ ,  $T_i$  and  $n_e$  at the limiters are shown in the lower graphs.

of the W influx is given in the upper left graph of figure 6, which gives results from the modeling of a phase with 100 Hz ELM frequency in discharge #22895. The blue curve shows the influx change due to the increased losses of C, O, and W without considering the changes in the sputtering yield. For the red curve, only the temperature change at constant charge distribution is considered, while the black curve is calculated taking all effects into account.

*ELM flushing and Impurity Transport in the H-mode Edge Barrier in ASDEX Upgrade* 9

The sputtering is very sensitive to the temperatures at the limiters. As these temperatures are not known to the necessary accuracy, the temperatures were adjusted (using  $T_i = 2T_e$ ) such that the measured W influx during the inter-ELM phase and during the ELM was reproduced. Thus, the erosion model can't give much insight for itself, it just allows to close the loop between the confinement of light impurities and the W erosion.

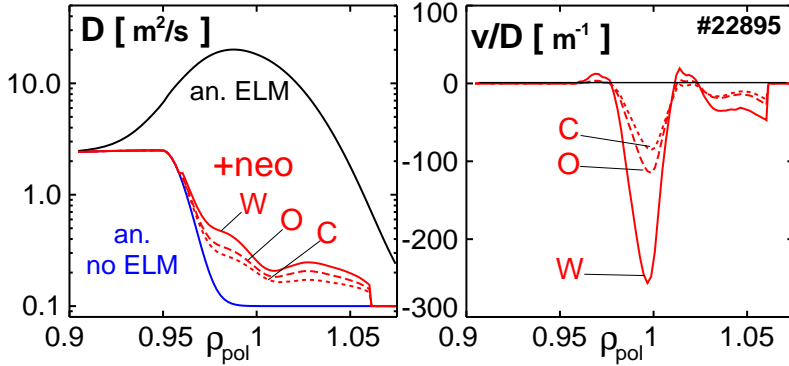
From the energy of the incident impurity a mean neutral velocity for the sputtered W is calculated assuming a Thompson [17] distribution. The ionization length of W is of the order of the Larmor radius of the ionized W and a fraction  $f_{prompt}$  of ionized W returns to the surface on the first travel along the Larmor radius. This prompt redeposition effect is calculated for the sputtering by each ion species using a  $\cos \theta$  angular velocity distribution of the sputtered W. In figure 6, the upper right graph shows the part of the ionized W that is not promptly redeposited, where the toroidal field was  $B_t = 2.5 T$ . During the ELM, the rise of  $n_e$  and  $T_e$  leads to shorter ionization lengths and thus enhanced prompt redeposition.

### 3.2. Parallel Losses in the SOL

In the SOL, the parallel transport towards the divertor or to the limiting elements in the main chamber is described by volumetric losses with a loss frequency that is given by the parallel connection length between the surface elements ( $L_{\parallel}$ ) and the mean flow velocity of the deuterium ions:  $\nu_{\parallel} = (2M/L_{\parallel})\sqrt{k_B(3T_i + T_e)/m_D}$ , where the Mach number  $M$  was set to 0.1 for the presented results. At a certain radius in the SOL, the main chamber limiters are introduced into the code by switching the connection length from 50 m to 1 m. The neutral impurities start with a prescribed influx rate at this limiter position. They have a constant radial velocity  $v_0$  and their density decays radially according to the rate  $\nu_{ion} = n_e \langle \sigma_{ion} v_e \rangle$  for ionization:  $n_0(r) = n_0(r_{lim})(r_{lim}/r)\exp[-\int(\nu_{ion}/v_0)dr]$ .

### 3.3. Radial Transport of Impurities

For the radial transport, which is mainly collisional, the light impurities and W are included in the calculation from the SOL, across the ETB up to the pedestal-top. As has been described above, neoclassical transport is found to be applicable at the ETB. The calculation of the transport is also extended to the SOL, while only the PS transport is taken into account as the contributions from the banana and plateau regime are negligible. The diffusion coefficient due to collisions increases with increasing low-Z impurity concentration. Furthermore, the low-Z impurities lead to a dilution of the deuterium ions. Thus, the  $n_D$  profile has a decreasing gradient with increasing low-Z concentration in the ETB and the PS inward pinch of W decreases. The resulting transport coefficients of the radial transport model are depicted in figure 7, which is again for discharge #22895. In the phase between ELMs, the anomalous diffusion coefficient (blue curve) was reduced in the ETB to a very low value of  $0.1 \text{ m}^2/\text{s}$ . The collisional values from classical and PS transport are larger and exhibit the highest values for W. The total value of the drift parameter  $v/D$  in this phase are shown on the right, where W has the strongest inward drift as it exhibits the highest charge at the ETB. The mean charge at poloidal flux label  $\rho_{pol} = 0.99$  is 5.6 for C, 7.4 for O and 16 for W. An ELM is induced

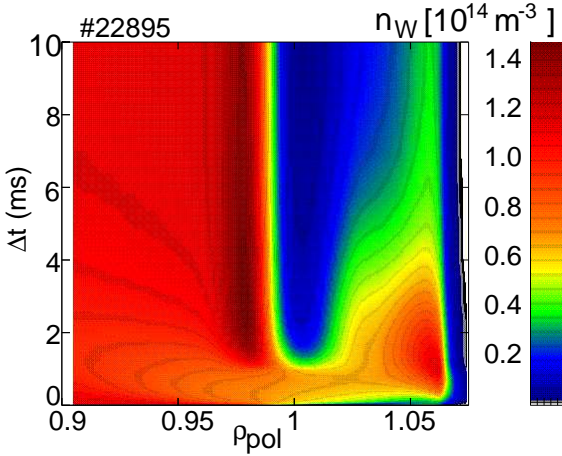
*ELM flushing and Impurity Transport in the H-mode Edge Barrier in ASDEX Upgrade* 10


**Figure 7.** Profiles of diffusion coefficient and drift parameter for the modeling of discharge #22895.

by a sudden switch-on of a large diffusion coefficient in the edge (black curve), which decays linearly within 1 ms.

### 3.4. Model Results and Discussion

The resulting evolution of the total W density during an ELM cycle of discharge #22895 is shown in figure 8. The cycle has been repeated up to quasi-equilibrium, i.e. the density



**Figure 8.** Modeled evolution of the total W density during one ELM cycle.

profile at the end and at the beginning of the ELM cycle are equal. The W density gradient around the separatrix is strongly degraded during the ELM and the increasing source from the limiter, which is at  $\rho_{\text{pol}} = 1.063$ , leads to a density rise in the outer SOL. After the ELM, the source decreases and a strong density gradient forms in the ETB. The ratio of the W density at  $\rho_{\text{pol}} = 0.9$  to the value at  $\rho_{\text{pol}} = 1$  is 22 at the end of the cycle and 7.2, when taking the temporal average during an ELM cycle. For a similar discharge #22901, which had 10 times less deuterium fueling and an ELM frequency of about 50 Hz, the respective density ratios were 51 and 17.

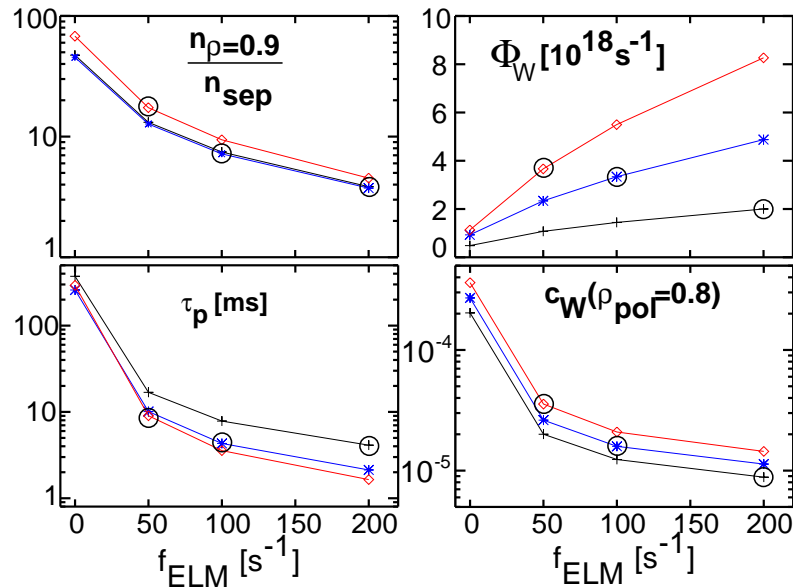
*ELM flushing and Impurity Transport in the H-mode Edge Barrier in ASDEX Upgrade* 11

Three discharge phases with different deuterium puff levels  $\Phi_D$  and ELM frequencies were modeled #22898:  $\Phi_D = 1.5 \cdot 10^{22} \text{ s}^{-1}$ ,  $f_{ELM} \approx 200 \text{ Hz}$ , #22895:  $\Phi_D = 10^{22} \text{ s}^{-1}$ ,  $f_{ELM} \approx 100 \text{ Hz}$ , and #22901:  $\Phi_D = 10^{21} \text{ s}^{-1}$ ,  $f_{ELM} \approx 50 \text{ Hz}$ . Time-dependent profiles of  $T_e$ ,  $T_i$  and  $n_e$  were fitted for equal time delays relative to the ELM start using the data from a 500 ms long period.

The carbon influx level was chosen to match the measured C concentration at  $\rho_{pol} = 0.95$  which was 0.9% for #22898, 1.2% for #22895, and 2.1% for #22901. The oxygen influx was set to 1/4 of the carbon influx.

The plasma temperatures in front of the limiters were adjusted to match the W erosion flux and the used inter-ELM and ELM values for  $T_e$  at the limiter were 8.4 eV/12 eV for #22898, 10 eV/20 eV for #22895, and 12 eV/35 eV for #22901. All of these values are consistent with typical temperatures from measurements (e.g. [18]).

The transport model was solved for three artificial scans of the ELM frequency with  $f_{ELM} = 0, 50, 100, \text{ and } 200 \text{ Hz}$  using one of the three settings at a time for the background profiles, limiter temperatures and low-Z fluxes. Figure 9 shows a number of key quantities for



**Figure 9.** Calculated edge density ratio, source rate, particle confinement time and W concentration for a scan of the ELM frequency. Different colors correspond to the use of the edge  $T_{e^-}$ ,  $T_i$  and  $n_e$ -profiles from the discharges #22898 (black, 200 Hz, coldest at limiter), #22895 (blue, 100 Hz) and #22901 (red, 50 Hz, hottest at limiter). Circles correspond to the experimental values for the three discharges. All quantities are temporal averages of one ELM cycle.

these scans. Black curves are for the settings of #22898 (200 Hz, coldest at limiter), blue for #22895 (100 Hz), and red for #22901 (50 Hz, hottest at limiter). The black circles surround the points for which the limiter temperatures, ELM sizes, and influx values were adjusted to the measurement. The upper left box shows the strong decrease of the W density peaking with increasing ELM frequency, which can reach values on the order of 100 for the artificial zero ELM case. The plasma with the lowest puff level has the highest peaking factors. The particle

*ELM flushing and Impurity Transport in the H-mode Edge Barrier in ASDEX Upgrade* 12

confinement time  $\tau_p$  of W (lower left box) is calculated with the total number of W ions in the confined region  $N_W$  and the total source  $\Phi_W$ . It decreases strongly with the ELM frequency. A hotter SOL leads to higher losses in the SOL which explains that  $\tau_p$  for the medium sized gas puff is below the value of the highest puff case. In the upper right box, the increase of the erosion source with  $f_{ELM}$  is due to the linear picture without taking the change of the ELM size and the lower inter-ELM temperatures into account. The encircled points reflect the measured behavior. Nevertheless, the rise of the source is not strong enough to beat the change in  $\tau_p$  and the W concentration  $c_W$  (relative to  $n_e$ ) at  $\rho_{pol} = 0.8$  decreases on each of the linear curves, as shown in the lower right box. Even though the model reproduces the experimental values of  $c_W$  within 10 %, we consider the model only to be a consistent description based on many ad hoc assumptions, which need further detailed experimental investigations.

It should be noted that free parameters exist in the model, which were chosen within credible ranges to obtain a good match between measurements and model. These parameters are:

- the SOL and limiter temperatures, which influence parallel losses in the SOL and erosion at the limiter
- the parallel Mach number, which influences parallel losses in the SOL
- the level of turbulent, radial transport in the SOL
- the length and impact of an ELM

Furthermore, following simplifications have been assumed:

- the 3D structure of the SOL is replaced by simple volume losses with characteristic loss times
- the radial transport is modeled with diffusion and convection
- the ELM is modeled as an increased radial diffusion for impurities at the plasma edge and SOL
- the erosion model is idealized and simplified, resulting in a Thompson distribution for the eroded W atoms
- the prompt re-deposition of W does not consider electric fields and surface roughness

However, the strength of the model is the connection between erosion and confined plasma, while leaving not an arbitrary amount of freedom for the free parameters: The impurities influence the radial transport coefficients and erosion. The SOL and limiter temperatures are connected via an exponential that connects to the measured separatrix temperatures. The limiter temperatures are given by the measured W erosion fluxes. The Mach number of 0.1 in the SOL is fixed for all modeled cases. The mechanisms described in the model offer also an explanation for the fact that with increasing ELM frequency the particle confinement first decreases and then increases again for even higher ELM frequencies.

*ELM flushing and Impurity Transport in the H-mode Edge Barrier in ASDEX Upgrade* 13

#### 4. Summary and Outlook

At ASDEX Upgrade, the 1D transport coefficients for impurities in the edge transport barrier (ETB) have been measured for  $\text{He}^{2+}$ ,  $\text{C}^{6+}$ ,  $\text{Ne}^{10+}$  and  $\text{Ar}^{16+}$  during the inter-ELM phase in type-I ELM My H-mode. This was accomplished by modeling the impurity densities as measured by the edge CXRS system with the impurity transport code STRAHL. The values of v/D at the ETB are restricted by the measurements with small uncertainties. Even the individual values of v and D can be determined, however, with larger uncertainties. The transport coefficients are found to be neoclassical in absolute value and the neoclassical Z-dependence, i.e. an increasing inward pinch for higher charged impurities, is observed.

Independently from these measurements, a model was developed which for W relates the ETB transport, the erosion fluxes at the wall and the transport across the scrape-off layer to each other. This approach is seen to be especially worthwhile for W, as its transport at the ETB is dependent on the other impurities and its erosion at the wall is a result of impurity sputtering. The model incorporates some free parameters that were used to match the experimentally observed W concentrations within 10 %. The free parameters were chosen within credible ranges which suggests that the model captures the important physics of the processes involved. Still, the model can only be considered as a guideline for investigations until the inherent assumptions can be experimentally validated. It should be noted, that the pedestal in the density of the background deuterium ions is not explained or understood by the actual work, but it is the main drive of the described transport processes at the ETB.

#### References

- [1] T. Pütterich *et al.*, Physical Review Letters **102**, 025001 (2009).
- [2] H. P. Summers, The ADAS User Manual, version 2.6 <http://adas.phys.strath.ac.uk> (2004).
- [3] J. Neuhauser *et al.*, Plasma Physics and Controlled Fusion **44**, 855 (2002).
- [4] K. Behringer, 'Description of the impurity transport code STRAHL', JET-R(87)08, JET Joint Undertaking, Culham (1987).
- [5] R. Dux, Technical Report No. 10/30, IPP, Garching, Germany.
- [6] R. Dux, Fusion Science and Technology **44**, 708 (2003).
- [7] A. G. Peeters, provided the NEOART code, 1998.
- [8] S. P. Hirshman and D. J. Sigmar, Nuclear Fusion **21**, 1079 (1981).
- [9] W. A. Houlberg, K. C. Shaing, S. P. Hirshman, and M. C. Zarnstorff, Physics of Plasmas **4**, 3230 (1997).
- [10] A. G. Peeters, Physics of Plasmas **7**, 268 (2000).
- [11] ASDEX Team, Nuclear Fusion **29**, 1959 (1989).
- [12] T. S. Pedersen *et al.*, Nuclear Fusion **40**, 1795 (2000).
- [13] M. E. Perry *et al.*, Nuclear Fusion **31**, 1859 (1991).
- [14] D. Pasini *et al.*, Plasma Physics and Controlled Fusion **34**, 677 (1992).
- [15] R. Dux *et al.*, Journal of Nuclear Materials **390-391**, 858 (2009).
- [16] W. Eckstein, C. García-Rosales, J. Roth, and W. Ottenberger, Technical Report No. IPP 9/82, Max-Planck Institut für Plasmaphysik, Garching, Germany.
- [17] M. W. Thompson, Phil. Mag. **18**, 377 (1968).
- [18] M. Kočan *et al.*, PSI 2010, San Diego, submitted to J. Nucl. Mater. (2010).

## 5.7 Publication 7

*High-resolution charge exchange measurements at ASDEX Upgrade*

Review of Scientific Instruments 83, 103501 (2012)

High-resolution CXRS at ASDEX Upgrade

**High-resolution charge exchange measurements at ASDEX Upgrade**

E. Viezzer,<sup>1</sup> T. Pütterich,<sup>1</sup> R. Dux,<sup>1</sup> R. M. McDermott,<sup>1</sup> and the ASDEX Upgrade Team<sup>1, a)</sup>

*Max-Planck-Institut für Plasmaphysik, EURATOM Association, Boltzmannstr. 2,  
85748 Garching, Germany*

( Dated: 17 January 2014)

The charge exchange recombination spectroscopy (CXRS) diagnostics at ASDEX Upgrade (AUG) have been upgraded and extended to provide high-resolution measurements of impurity ion temperature, density and rotation profiles. The existing core toroidal CXRS diagnostic has been refurbished to increase the level of signal, thus enabling shorter exposure times down to 3.5 ms. Additional lines of sight provide more detailed profiles and enable simultaneous measurements of multiple impurities. In addition, a new CXRS system has been installed which allows for the measurement of poloidal impurity ion rotation in the plasma edge with high temporal (1.9 ms) and spatial resolution (down to 5 mm). A new wavelength correction method has been implemented to perform in-situ wavelength calibrations on a shot-to-shot basis. Absolute measurements of the poloidal impurity ion rotation with uncertainties smaller than 1.5 km/s have been obtained. Comparison of all the CXRS measurements provides a consistency check of the diagnostics and good agreement has been found for all of the CXRS systems.

---

<sup>a)</sup>For authors' list see A. Kallenbach et al., Nucl. Fusion **51** 094012 (2011)

## High-resolution CXRS at ASDEX Upgrade

### I. INTRODUCTION

The most common method to measure the rotation in a tokamak plasma is active charge exchange recombination spectroscopy (CXRS)<sup>1</sup>. The light emitted due to charge exchange (CX) reactions between fully ionized impurity ions and injected neutral atoms yields localized information on impurity ion temperature and velocity from the Doppler widths and Doppler shifts of the measured spectra. Impurity densities are obtained from the line intensities of the measured spectra. For the next generation fusion experiment ITER<sup>2</sup>, CXRS will play a crucial role for measuring the density of the fusion ash He<sup>2+</sup>.

At ASDEX Upgrade (AUG)<sup>3</sup>, toroidal CXRS systems viewing the core and the edge<sup>4</sup> of the plasma provide temporally and radially resolved CXRS profiles. Recently, the core toroidal CXRS diagnostic was upgraded to obtain more detailed radial profiles and a higher level of signal enabling shorter integration times. In addition, the edge toroidal view of the CXRS systems has been supplemented with a poloidal view. Along with a consistency check of ion temperature and impurity ion density, the diagnostic enables the measurement of the poloidal impurity ion rotation. Thus, it provides the missing measurements for deriving the radial electric field from the radial force balance equation<sup>5</sup>. Furthermore, the combination of toroidal and poloidal views allows the determination of full plasma rotation profiles both parallel and perpendicular to the magnetic field lines.

This paper is organized as follows: In section II the upgrades of the toroidal CXRS diagnostics at AUG are described. The setup of the new poloidal system, along with example profiles in H-mode<sup>6</sup> plasmas, is presented in section III. The radial plasma sweep technique, which is applied to improve measurements at the plasma edge, is described in section IV. Wavelength corrections as well as corrections due to the CX cross-section and Zeeman effects are discussed in section V. A summary of the paper is given in section VI.

### II. UPGRADE OF TOROIDAL CXRS AT AUG

At AUG CXRS measurements are routinely made to provide temporally and spatially resolved profiles of impurity ion toroidal rotation, temperature and density. The core CXRS systems on AUG view two different (toroidally separated) heating beams, see figure 1. One of the core systems has recently been upgraded to increase the number of lines of sight (LOS)

## High-resolution CXRS at ASDEX Upgrade

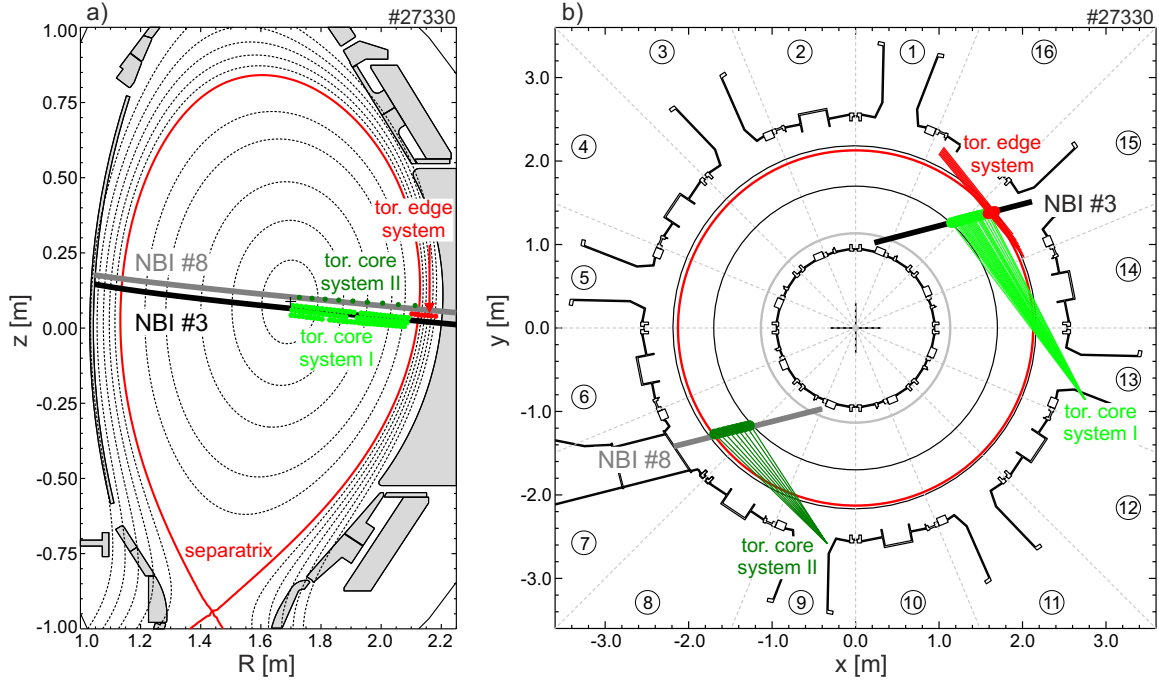


FIG. 1. a) Poloidal cross-section of AUG showing the collection regions of all toroidal CXRS diagnostics, b) top down view of AUG vessel showing the lines of sight of the toroidal CXRS systems. The indicated beam lines do not correspond to the actual width of the beams ( $\sim 25$  cm).

and the level of signal, thus enabling measurements at shorter integration and repetition times. The diagnostic uses an optical head which is mounted at sector 13 outside of the vessel. The optical setup has been redesigned to install additional LOS, thus allowing more detailed radial CXRS profiles to be measured. The optical head is equipped with 91 high-temperature fibers (diameter of  $400\ \mu\text{m}$ ) divided into three vertically displaced rows ( $\sim 30$  fibers/row, see figure 1a)), which are focused on the center of the neutral beam injection (NBI) source #3 (sector 15) using a Nikon  $f/1.8$  objective lens and an in-vessel Al mirror (coated with  $\text{MgF}_2$ ). Where the views intersect the beam the three rows are vertically separated by only 1.6 cm, which is considerably smaller than the size of the heating beam ( $\sim 25$  cm). Each row of fibers covers a radial range extending from the magnetic axis ( $\sim 1.65$  m) to the top of the pedestal ( $\sim 2.15$  m) with a spot size in the focal plane of 1.5 cm and a radial resolution of  $\pm 2\text{-}2.5$  cm. The three rows are dedicated to separate diagnostics, with the top row used for CXRS measurements, the central row for beam emission spectroscopy (BES)<sup>7</sup>, and the bottom row for fast-ion  $D_\alpha$  (FIDA) measurements<sup>8</sup>. The BES measurements enable the evaluation of the

### High-resolution CXRS at ASDEX Upgrade

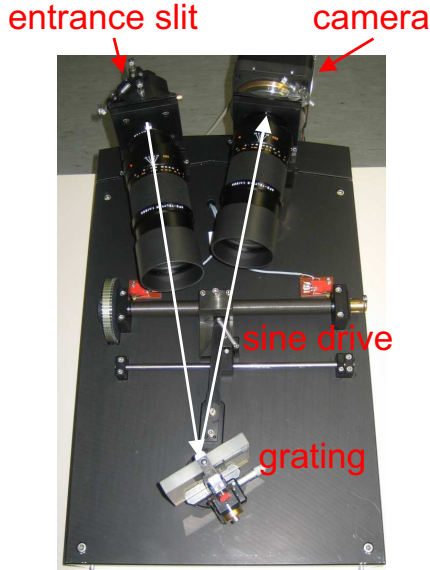


FIG. 2. Setup of a lens-based Czerny-Turner like spectrometer: The fibers, which guide the collected light from the torus to the spectrometer, are stacked vertically along the entrance slit. After passing through the entrance slit the light is collimated, then dispersed by a 2400 grooves/mm grating and then focused onto the camera. The sine drive enables to move the central wavelength of the spectrometer.

beam neutral density along LOS virtually identical to those used for CXRS, thus providing a cross-check on the beam densities evaluated with attenuation codes and improving the accuracy of impurity density profiles calculated from CXRS intensities.

The CX emission collected along the LOS is transmitted to a high throughput  $f/4$  Czerny-Turner like spectrometer, which utilizes a variable width entrance slit, two objective lenses (Leica APO-ELMARIT-R), and a movable grating with 2400 grooves/mm (see figure 2). The spectrometer is coupled to a new Princeton Instruments ProEM, back-illuminated, frame-transfer charge coupled device (CCD) camera with on-chip multiplication gain<sup>9</sup>. This allows for low light applications and improves the measurement capability in the plasma core. The camera features a  $512 \times 512$   $16 \mu\text{m}$  pixel chip which, when coupled with the spectrometer, enables a 13.1 nm spectral range at a central wavelength of 494.5 nm. The entrance slit to the spectrometer is typically set to  $100 \mu\text{m}$ , but can be adjusted to any value between 0 and  $400 \mu\text{m}$ . For a slit width of  $100 \mu\text{m}$  and a central wavelength of 494.5 nm the instrumental width of the system is of the order 0.067 to 0.074 nm (slight variations of the different

### High-resolution CXRS at ASDEX Upgrade

spectrometer channels arise due to imperfections of the entrance slit). The shape of the instrument functions for the slit widths used ( $\leq 100 \mu\text{m}$ ) is well described by a Gaussian function. Hence, the deconvolution can be performed analytically in the fitting process and the measured width of the spectrum has contributions from the instrumental width and the Doppler width. The collimating lens at the entrance slit has a focal length of 280 mm, while the focusing lens has a focal length of 180 mm. This choice of lenses introduces a de-magnification factor of 1.56 and enables the light from 25 fibers, which are stacked vertically along the entrance slit, to be imaged concurrently on the camera. Compared to a conventional Czerny-Turner spectrometer the main advantages of using the optical layout of a lens-based Czerny-Turner like spectrometer are the good imaging properties of the system at high aperture (no astigmatism) and at the same time, the simultaneous measurement of many channels.

The ability to move the central wavelength of the spectrometer enables the system to make CX measurements of different impurity species. The system typically utilizes either the  $\text{B}^{5+}$  ( $n = 7 \rightarrow 6$ ) CX line at 494.467 nm or the  $\text{C}^{6+}$  ( $n = 8 \rightarrow 7$ ) line at 529.059 nm. However, it has also been used for He, N, Ne and Ar. Typically, the core toroidal CXRS system runs with an exposure time of 10 ms, but it can be operated down to 3.5 ms allowing for intrinsic rotation measurements through the use of short beam blips<sup>10</sup>. The new upgrades enable now more detailed studies of toroidal momentum transport<sup>11,12</sup>, impurity transport<sup>10</sup> and MHD instabilities.

The second core CXRS system is equipped with an in-vessel optical head located in sector 9 (see figure 1b)) which views the NBI source #8 (sector 7). This system has 10 LOS evenly distributed between the magnetic axis and the top of the pedestal. The LOS of this system are not as tangential to the magnetic flux surfaces as those in sector 13 and thus have poorer radial resolution ( $\pm 5 - 6 \text{ cm}$ ). Fibers with a diameter of  $400 \mu\text{m}$  guide the collected light from this system to a conventional  $f/6.5$  Czerny-Turner spectrometer which employs a movable grating with 2400 grooves/mm and two mirrors with a focal length of 500 mm. The entrance slit is adjustable, but is typically set to  $100 \mu\text{m}$  and therefore the instrumental widths of the channels are ranging between 0.038 and 0.058 nm (at a central wavelength of 494.5 nm). The measured spectra are analyzed by a Princeton Instruments MicroMax camera, which has a back-illuminated CCD chip with  $512 \times 512 13 \mu\text{m}$  pixels allowing for a spectral range of 3.5 nm at a central wavelength of 494.5 nm. The CCD camera is operated

## High-resolution CXRS at ASDEX Upgrade

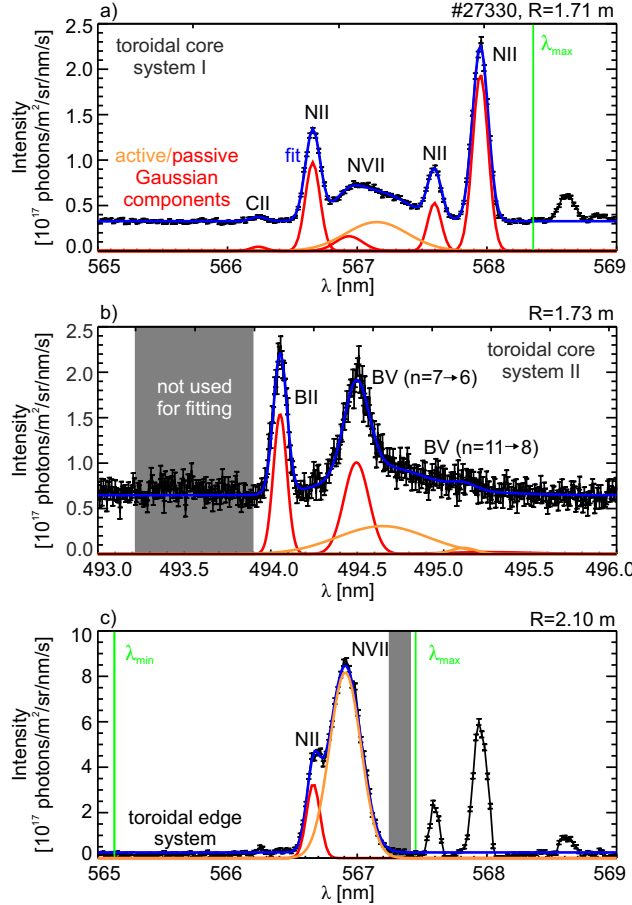


FIG. 3. Example spectra of toroidal CXRS diagnostics: a)  $N^{7+}$  spectrum of core system I, b)  $B^{5+}$  spectrum of core system II, c)  $N^{7+}$  spectrum of edge system. The areas highlighted in gray as well as those larger (smaller) than  $\lambda_{max}$  ( $\lambda_{min}$ ) are not used for fitting the spectra.

in frame-transfer mode. Binning the CCD chip to 9 regions of interest allows for a temporal resolution of 7.5 ms. However, the diagnostic is typically set to 20 ms due to the signal to noise ratio. The poor signal to noise ratio arises from the degraded in-vessel optics. For experiments in which the NBI source #8 is not utilized the spectrometer is equipped with extra LOS from the optical head of the toroidal core CXRS system I. This enables the measurement of two different impurity species on the same beam and a cross-check on intensity and wavelength calibrations when imaging the same impurity. Figure 3a) and b) show typical spectra obtained with the core toroidal CXRS systems. The fit to the spectrum is shown in blue, while the Gaussian components are plotted in orange (active lines) and red (passive lines). In this discharge, the toroidal core system I measured the  $N^{7+}$  ( $n = 9 \rightarrow 8$ ,

### High-resolution CXRS at ASDEX Upgrade

$\lambda=566.937$  nm) spectral line. The spectra are fitted with 6 Gaussians; one Gaussian for the active  $N^{7+}$  line, one for its passive component, 3 Gaussians accounting for 3 nearby passive  $N^{1+}$  lines at 566.663, 567.602 and 567.956 nm and one Gaussian for a passive  $C^{1+}$  line at 566.246 nm<sup>13</sup>. A discrimination between electron impact excitation and charge exchange with thermal neutral deuterium<sup>14</sup> is not applied for the passive component as it is typically small compared to the active CX line. In this discharge the spectrometer of the core CXRS system II utilized LOS from the core CXRS system I (i.e. viewing NBI source #3 (see figure 1)) and measured the  $B^{5+}$  spectral line. The measured spectra are fitted with 5 Gaussians; one accounting for the active  $B^{5+}$  ( $n = 7 \rightarrow 6$ ) line at 494.467 nm, one for the active  $B^{5+}$  component ( $n = 11 \rightarrow 8$ ) at 495.087 nm, two for their passive components and one Gaussian to fit the passive  $B^{1+}$  line at 494.038 nm.

Independently, the toroidal edge CXRS diagnostic has also been upgraded to increase the intensity level. The system has been equipped with a new spectrometer and a new CCD camera (identical to those used by the core system I) enabling 25 LOS to be imaged on the chip simultaneously with a repetition time of 2.65 ms. Shorter exposure times are obtained by using less LOS and binning the CCD chip to fewer regions of interest. For the edge diagnostic, the entrance slit to the spectrometer is typically set to 50  $\mu\text{m}$ . For this slit width the instrumental width of the spectrometer channels is in the range of 0.031 to 0.036 nm (at a central wavelength of 494.5 nm). The toroidal edge system uses an in-vessel  $f/4$  optical head which images the plasma edge at the outer midplane onto 8 LOS. The LOS are separated by about 1 cm and each LOS is equipped with 3 optical fibers (with a diameter of 400  $\mu\text{m}$ ) to improve the signal. At the outer midplane ( $R = 2.15$  m) the toroidal curvature of the plasma across the width of the heating beam ( $\sim 25$  cm) is significant. For this reason a separate Al mirror coated with MgF<sub>2</sub> was used for each LOS (see figure 4) to optimize the radial resolution down to 3 mm, which is obtained when a radial sweep of the plasma (see section IV) is performed. Without this sweep, the radial resolution is given by the channel spacing, i.e.  $\sim 1$  cm. In the plasma edge of AUG ( $T = 500$  eV,  $B = 2$  T), the typical Larmor radii of impurity species are of the order  $\sim 1$  mm and thus, smaller than the radial resolution.

An example spectrum of the toroidal edge CXRS diagnostic is shown in figure 3c). Here, the edge system was set to the  $N^{7+}$  spectral line. The  $N^{7+}$  spectra are typically fitted with 2 Gaussians, one accounting for the active  $N^{7+}$  line and one for a nearby  $N^{1+}$  line. For the

### High-resolution CXRS at ASDEX Upgrade

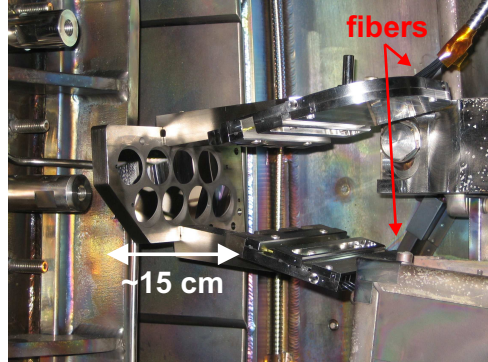


FIG. 4. In-vessel view of the optical head dedicated to toroidal edge CXRS measurements: For each LOS a separate mirror is used to optimize the radial resolution of the system down to 3 mm.

edge system the passive  $N^{6+}$  component is negligible as it is very small compared to the active CX line. Note the difference in scale when comparing the intensities between the core and edge systems, which reflects mainly the attenuation of the beam density. At the plasma edge the intensity of the active line is  $2.5 \cdot 10^{17}$  photons/m<sup>2</sup>/sr/s while the full width at half maximum (FWHM) is 0.25 nm (corresponding to an ion temperature of  $T_i = 0.56$  keV) and the absolute wavelength shift of the spectral line is 0.03 nm (equal to a rotation of  $v_{rot} = 15.6$  km/s). In the core the signal is much lower due to the attenuation of the neutral beam. For the spectrum shown in figure 3a) the intensity of the active line is  $1.9 \cdot 10^{16}$  photons/m<sup>2</sup>/sr/s, the FWHM of the spectral line is 0.54 nm ( $T_i = 2.17$  keV) while the wavelength shift is 0.19 nm ( $v_{rot} = 103.9$  km/s).

The toroidal edge CXRS diagnostic typically images 20 channels enabling a time resolution of 2.2 ms. One channel is always dedicated to a wavelength calibration measurement. This channel is connected to a neon lamp which provides a wavelength calibration on a shot-to-shot basis (see section V A). It should be noted that the requirements for temporal and spatial resolution at the plasma edge are considerably more demanding due to the fast transport phenomena and steep gradients. This is one basic reason why special attention is necessary for the plasma edge measurements. The edge profiles may be combined with those measured in the core to obtain full radial profiles, i.e. from the magnetic axis out to the separatrix. Figure 5 shows example profiles of toroidal rotation,  $v_{tor}$ , and ion temperature,  $T_i$ , for one time point. The profiles are plotted against the normalized poloidal flux coordinate  $\rho_{pol}$ . The data points resulting from the fits in figure 3 are highlighted in gray. In

High-resolution CXRS at ASDEX Upgrade

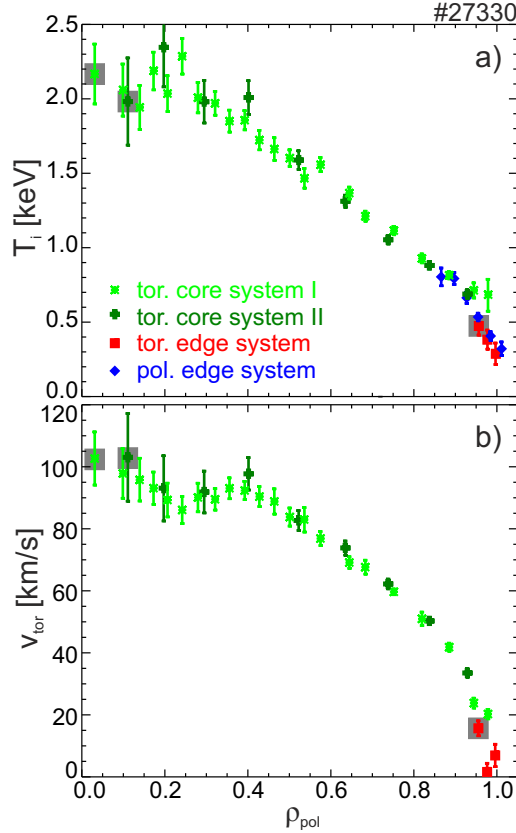


FIG. 5. a) Ion temperature,  $T_i$ , profile obtained from toroidal systems and new poloidal CXRS diagnostic (see section III), b) toroidal rotation,  $v_{\text{tor}}$ , profile. The data points marked in gray result from the fits to the measured spectra shown in figure 3.

addition, the ion temperature profile measured by the new poloidal CXRS diagnostic (see section III) is shown in the upper plot of figure 5. Good agreement in  $T_i$  and  $v_{\text{tor}}$  is obtained for all CXRS systems.

### III. POLOIDAL EDGE CXRS DIAGNOSTIC AT AUG

A newly installed edge poloidal CXRS system also utilizing beam 3 in sector 15 enables the measurement of poloidal impurity ion rotation profiles. The diagnostic has been designed to obtain high spatial resolution (down to 5 mm) measurements of the plasma edge at AUG. The system features an  $f/2.5$  optics mounted inside the vessel and employs one lens with a focal length of 40 mm. Note that the radial resolution had to be compromised (by 2 mm compared

### High-resolution CXRS at ASDEX Upgrade

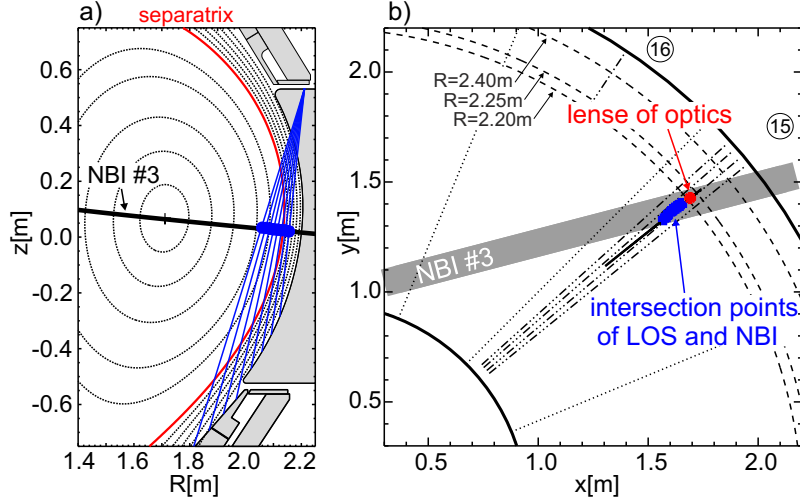


FIG. 6. a) Poloidal cross-section of AUG indicating the location of the poloidal LOS, b) top down view of sector 15. Note that the beam line does not correspond to the actual size of the beam.

to the toroidal edge system) due to spatial restrictions inside the vessel. The optical head has 8 LOS which view the plasma edge. Each LOS is comprised of two fibers to enhance the signal. In the focal plane the radial distance between two adjacent LOS is 1.25 cm while the spot size is 5 mm. The in-vessel optical head has been aligned such that the 8 LOS view the edge pedestal in a poloidal plane and to ensure that no toroidal rotation component is picked up. Figure 6 shows an overview of the viewing geometry of the new system. In figure 6a) a poloidal cross-section of AUG is shown along with the LOS of the poloidal diagnostic and the path of the neutral beam. Figure 6b) shows the focal points of the poloidal system with respect to the path of the neutral beam in a toroidal cross-section. The collected light is transmitted to a high-throughput  $f/4$  Czerny-Turner like spectrometer, which is similar to the spectrometer used for the edge toroidal system. It employs two objective lenses with a focal length of 280 mm. Thus, the light from 15 fibers can be imaged simultaneously. The entrance slit of the spectrometer is typically set to a width of 50  $\mu m$ . At this slit width and at a central wavelength of 494.5 nm the instrumental width of the system is between 0.023 to 0.027 nm depending on the spectrometer channel. The collected photons are imaged onto a frame-transfer back-illuminated CCD camera (Princeton Instruments PhotonMax, 512×512 16  $\mu m$  pixels) capable of an electron multiplication readout. The CCD chip, coupled with the spectrometer, allows for a spectral range of 8.2 nm at a central wavelength of 494.5 nm.

## High-resolution CXRS at ASDEX Upgrade

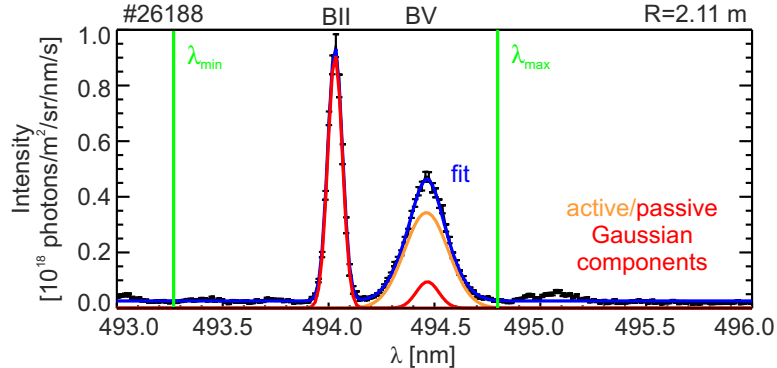


FIG. 7. Example spectrum of the  $B^{5+}$  CX line measured with the poloidal edge CXRS system. The spectrum is fitted with three Gaussians (one accounting for the active  $B^{5+}$  line, one for the passive component and one for the passive  $B^{1+}$  line); fit in blue, Gaussian components in orange (active line) and red (passive lines); the green lines mark the wavelength range used for the fit.

The spectra from 12 out of 16 fibers, which are connected to the optical head, are routinely measured with a repetition time down to 1.9 ms, while 2 channels of the spectrometer are connected to a neon lamp to provide a wavelength calibration measurement (see section V A). The poloidal system is typically set to 2.2 ms to obtain concurrent measurements with the toroidal edge CXRS diagnostic. Figure 7 shows an example spectrum of the  $B^{5+}$  spectral line along with the fit which includes a background and a passive CX component ( $B^{4+}$ ,  $n = 7 \rightarrow 6$ ). The spectrum is fitted with 3 Gaussians; one accounting for the active  $B^{5+}$  line, one for the passive component and one Gaussian for a nearby passive  $B^{1+}$  line at a rest wavelength of 494.038 nm. The lines marked in green in figure 7 show the wavelength range used in the fitting procedure.

Figure 8 shows poloidal rotation, temperature and density profiles of the  $B^{5+}$  spectral line measured during the inter-ELM (Edge Localized Mode<sup>15</sup>) phase of an H-mode plasma. In this discharge a magnetic field on-axis of -2.5 T, plasma current of 1 MA, NBI heating of 5 MW and electron cyclotron resonance heating of 0.8 MW were applied. Note that the sign convention in this paper is as follows: The toroidal magnetic field  $B_\phi$  is negative (i.e. clockwise viewed from above), the poloidal magnetic field  $B_\theta$  is positive (i.e. pointing downward at the outboard midplane), the plasma current and NBI are in the positive toroidal direction (i.e. counter-clockwise viewed from above). Using this convention, the ion diamagnetic drift direction is positive.

## High-resolution CXRS at ASDEX Upgrade

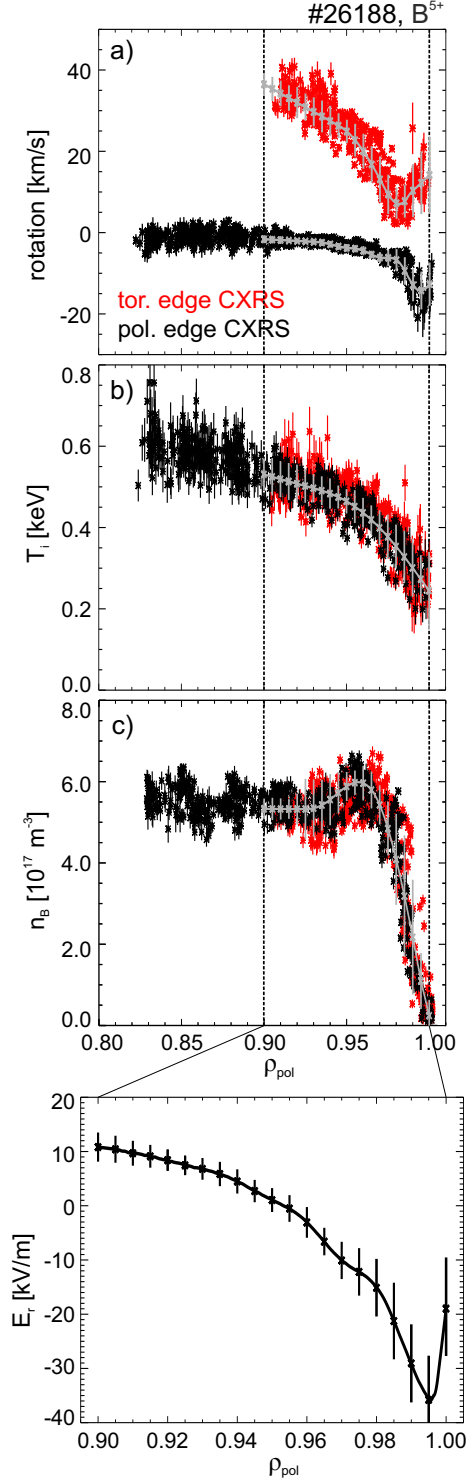


FIG. 8. CX measurements in H-mode: a) poloidal and toroidal rotation, b) ion temperature, c)  $B^{5+}$  density; the measurements obtained from the poloidal diagnostic are illustrated in black, while data from the toroidal system are shown in red. In d) the resulting  $E_r$  profile is shown.

### High-resolution CXRS at ASDEX Upgrade

The profiles illustrated in figure 8 are ELM-synchronized, i.e. data acquired during the occurrence of an ELM has been excluded. ELMs cause transient changes to the emission of the spectral line and to the resulting CX profiles and thus, should be removed. Data obtained with the poloidal optical head are shown in black, while the measurements in red result from the toroidal edge system. Furthermore, the radial plasma sweep technique (see section IV) was applied to obtain full radial profiles of the edge transport barrier (ETB)<sup>6</sup> region. Note that the profiles shown in figure 8 correspond to averaged profiles using data from the whole plasma scan, while the fits to the data are shown in gray. Impurity ion density and temperature profiles show a clear H-mode pedestal. The poloidal impurity ion rotation velocity is very low towards the plasma core, while inside the ETB a strongly sheared rotation in the electron diamagnetic direction is observed consistent with measurements on other devices, such as DIII-D<sup>16–18</sup>, Alcator C-Mod<sup>19</sup>, JET<sup>20–22</sup>, TFTR<sup>23</sup>, TEXTOR<sup>24</sup>, MAST<sup>25</sup>, NSTX<sup>26</sup> and LHD<sup>27</sup>.

Combining the poloidal and toroidal measurements enables the determination of the radial electric field,  $E_r$ , using the radial force balance equation<sup>5</sup>. In figure 8d) the resulting  $E_r$  profile is shown. Note that the CX profiles have been aligned relative to the separatrix position and to the electron temperature,  $T_e$ , and density,  $n_e$ , measurements (see section IV).

## IV. RADIAL PLASMA SWEEP TECHNIQUE TO IMPROVE EDGE CXRS MEASUREMENTS

To obtain the best radial resolution of the edge CXRS measurements and hence, detailed edge profiles a radial sweep of the plasma edge through the LOS of the diagnostic is performed. Typically, the plasma position is moved by 2 cm in about 800 ms during a steady-state portion of the discharge. The radial scan also allows the refinement of the relative sensitivity calibration of different LOS of the edge CXRS diagnostics as slight differences in the calibration show up as discontinuities in the intensity profiles, after mapping the measurements onto the plasma coordinate system  $\rho_{pol}$ . Furthermore, this technique enables the alignment of the toroidal and poloidal edge systems via the ion temperature and intensity profiles. In figure 9a–d) several plasma parameters from an H-mode<sup>6</sup> discharge, which includes a radial plasma sweep, are shown. The time period highlighted in yellow

### High-resolution CXRS at ASDEX Upgrade

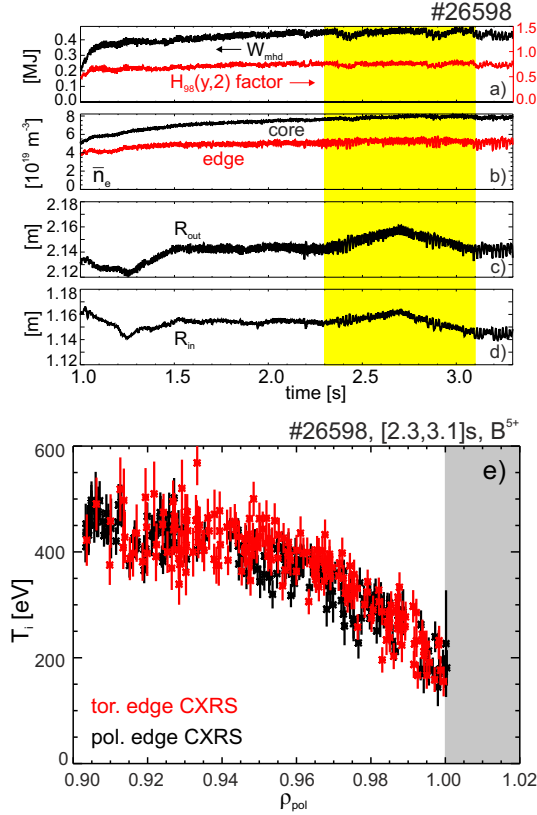


FIG. 9. Plasma parameters from an H-mode discharge that includes a radial plasma sweep: a) plasma stored energy  $W_{mhd}$  (black) and H/L scaling factor  $H_{98}(y,2)$  with respect to the ITER confinement scaling<sup>34</sup> (red), b) line averaged electron density in the plasma core (black) and edge (red), c) radial plasma position at outer midplane, d) radial plasma position at inner midplane, e) ion temperature profile plotted against the normalized poloidal flux coordinate  $\rho_{pol}$  obtained during the radial plasma scan highlighted in yellow.

contains the radial scan of the plasma. This technique enables complete, very detailed edge CXRS profiles, such as the ion temperature (see figure 9e)). Note that the  $T_i$  profile is ELM-synchronized (i.e. data acquired during an ELM have been excluded). All the data measured during a radial plasma sweep are combined to one averaged profile. Care has been taken to reduce uncertainties due to the magnetic equilibrium and to optimize the radial profile alignment<sup>28</sup> (see e.g. figure 2 of ref.<sup>4</sup>). The  $T_e$  profile measured by Thomson scattering<sup>29</sup> and the electron cyclotron emission (ECE) diagnostic<sup>30</sup> is shifted such that  $T_e \approx 100$  eV at the separatrix. This condition arises from power balance and parallel heat transport stud-

### High-resolution CXRS at ASDEX Upgrade

ies using a 1-D heat conduction model<sup>31</sup>. The  $n_e$  measurements obtained with the lithium beam diagnostic<sup>32,33</sup> are aligned to the profiles measured by Thomson scattering, which has identical measurement volumes for both  $n_e$  and  $T_e$ . The  $T_i$  profile is then aligned relative to the  $T_e$  profile such that the steep gradient regions overlap each other. The accuracy of the relative profile alignment is 2 – 3 mm, while the shifts applied for the profiles are within the radial resolution of each diagnostic.

In the scrape-off-layer (SOL, highlighted in gray in figure 9e)) the fit results have been omitted. In this region the fractional abundance of fully stripped impurity ions is very small, while additional background emissions disturb the fitting procedure. Therefore, the fitted CX line does not provide information on the actual impurity properties.

## V. CORRECTIONS TO EDGE CXRS MEASUREMENTS

At the plasma edge both the toroidal and poloidal rotation velocities are quite low and therefore, very accurate knowledge of the wavelength calibration is needed. For this purpose several wavelength corrections have been documented for the edge CXRS diagnostics and are presented in the next subsection. Furthermore, there are atomic physics effects to the spectra, which can give spurious temperature and rotation measurements if they are not properly taken into account. These include the CX cross-section effect, which will be discussed in subsection V B, and the gyro-motion effect, which is described in subsection V C. Corrections due to the Zeeman effect are discussed in subsection V D.

### A. Wavelength corrections

The small rotation velocity of the impurity ions at the plasma edge requires a very accurate wavelength correction, since systematical uncertainties in the rotation would arise from any error in the wavelength calibration. The optical fibers are stacked vertically in front of the entrance slit of the spectrometer. However, the images of these fibers are not vertically aligned on the CCD chip, rather they appear in a curve, which is well described by a parabola. This curvature arises due to the vertical angle of off-axis point sources to the optical axis and is described in detail in ref.<sup>35</sup>. However, small displacements of the input fibers from a perfectly vertical arrangement lead to small deviations from the

### High-resolution CXRS at ASDEX Upgrade

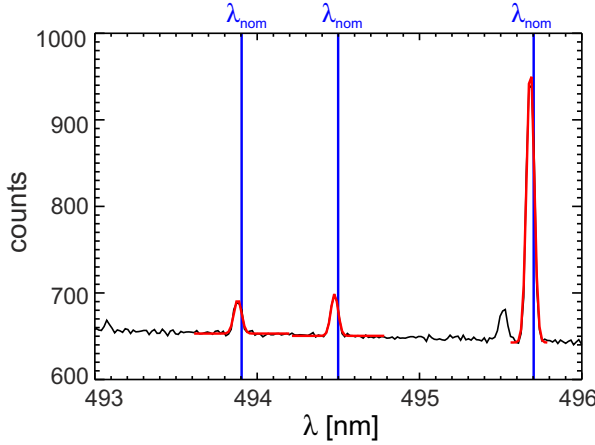


FIG. 10. Example neon spectrum acquired during a discharge, the poloidal edge CXRS diagnostic was set to the  $B^{5+}$  wavelength.

parabola formula. The deviation from the parabolic image of a straight entrance slit of each spectrometer channel has been determined at several different wavelengths using Hg and Ne calibration lamps and is taken into account in the analysis of the CX measurements.

For the  $B^{5+}$  line, the wavelength shift associated with a rotation velocity of 1 km/s is 1.65 pm. On this scale a systematic change in the Doppler shift may even arise from changes in the air pressure and temperature<sup>26</sup>. Therefore, an additional wavelength calibration is performed on a shot-to-shot basis. Two channels of the spectrometer dedicated to poloidal CX measurements (one channel for the spectrometer of the toroidal edge system) are switched to a neon lamp which allows a neon spectrum to be measured in every discharge. From these spectra, the apparent systematic shift is calculated and the 'true' poloidal rotation velocity is evaluated. This method allows the determination of the wavelength calibration quite accurately with uncertainties smaller than 1 km/s. Figure 10 shows an example spectrum of the neon lamp acquired during a discharge. The sum of 200 spectra collected at the end of the discharge is used for the calibration. In the vicinity of the  $B^{5+}$  wavelength three well-known neon lines are fitted. The lines, marked in blue in figure 10, represent the nominal value of the neon lines at 493.904, 494.499 and 495.703 nm. The spectral lines are each fitted using one Gaussian. The average of the difference between the central wavelength and the theoretical wavelength of the three neon lines is then used to calculate the apparent systematic shift. In this discharge, the shift of the neon lines is 0.023, 0.022 and 0.021 nm corresponding to velocities of 13.9, 13.3 and 12.7 km/s, respectively. Note that this shift is

### High-resolution CXRS at ASDEX Upgrade

mainly given by the mechanical uncertainties of the sine drive, which controls the position of the grating.

A similar wavelength calibration method is used for the core CXRS systems. However, these are not performed on a shot-to-shot basis and are typically only accurate to  $\pm 2\text{-}3 \text{ km/s}$ .

### B. Charge exchange cross-section effect

Due to the energy-dependent CX cross-sections several atomic physics effects arise when measuring CX emission. The main effect is that an apparent wavelength shift, which is not associated with the Doppler motion of the parent ion distribution, can be observed in the measured spectra<sup>36</sup>. Ions moving towards/away from the beam sample different regions

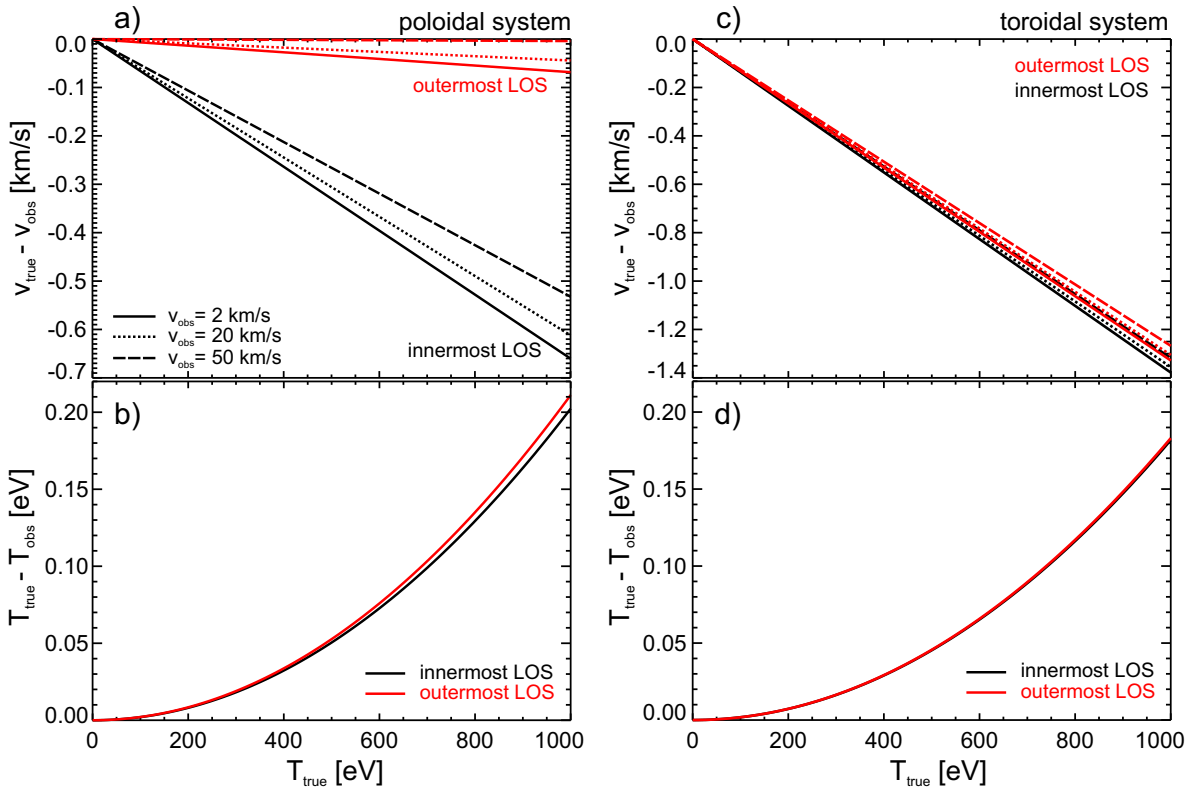


FIG. 11. Cross-section effects on measured  $\text{B}^{5+}$  CX spectra for a 60 keV deuterium beam: a) difference of true and observed velocities,  $v_{true} - v_{obs}$ , for poloidal system, b) corrections to observed temperatures,  $T_{obs}$ , with respect to the true temperature,  $T_{true}$ , for the poloidal diagnostics, c)  $v_{true} - v_{obs}$  for toroidal optical head, d)  $T_{true} - T_{obs}$  for toroidal system.

### High-resolution CXRS at ASDEX Upgrade

of the energy-dependent CX cross-sections and thus, have a higher/lower probability to undergo CX. This leads to an enhancement of the observed line intensity on one side of the spectrum, while the other side is reduced. Hence, the spectra are distorted and result in an apparent line broadening and shift not associated with the true ion temperature and velocity. The apparent line shift is due to the first derivative of the cross-section while the apparent line broadening arises due to its second derivative. The cross-section effects on the measured CX spectra have been simulated for the geometry of the edge systems and for a 60 keV deuterium beam (first, second and third beam energy components) using the approach of von Hellermann et al<sup>36</sup>. The LOS have a nearly perpendicular view and are aligned in a poloidal (see figure 6) and toroidal (see figure 1) plane, respectively. Figure 11a) and b) show the corrections to the observed temperatures,  $T_{obs}$ , and velocities,  $v_{obs}$ , with respect to the true temperature,  $T_{true}$ , and velocity,  $v_{true}$ , for  $B^{5+}$  for the inner- and the outermost LOS

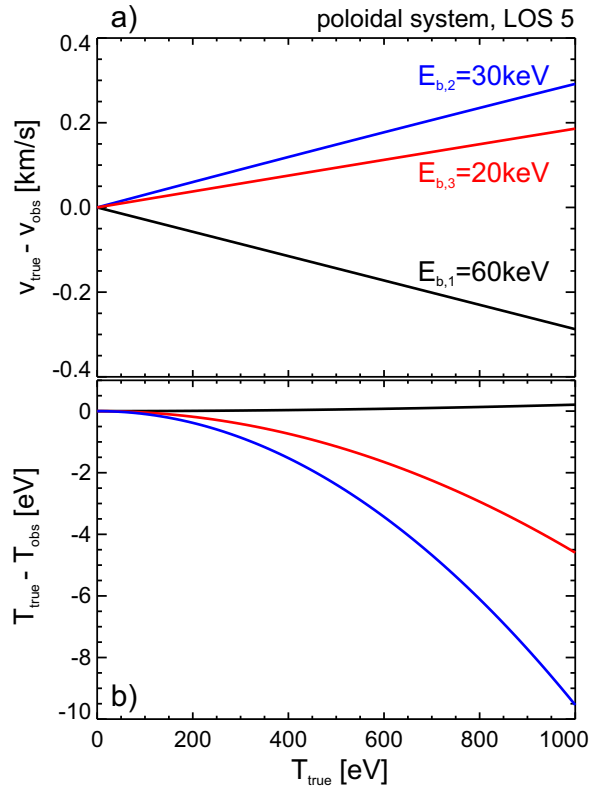


FIG. 12. Cross-section effects in  $B^{5+}$  CX spectra for first, second and third energy component of a 60 keV deuterium beam: a) difference of true and observed velocities, b) corrections to observed temperatures.

### High-resolution CXRS at ASDEX Upgrade

of the poloidal optical head, while figure 11c) and d) show the corrections for the toroidal edge system. The corrections are well within the error bars of the measurements. Even for an edge rotation of 50 km/s the correction due to the energy-dependent CX cross-section is less than 1.5 km/s for the toroidal system and less than 0.7 km/s for the poloidal system. In the considered temperature range at the plasma edge (200 – 500 eV) the temperature corrections are between 0.01 to 0.05 eV.

Figure 12 shows the corrections for the first, second and third beam energy components of a 60 keV deuterium beam. Both the velocity and temperature corrections of the second and third beam energy components change sign, while the temperature corrections are an order of magnitude higher compared to the correction of the first beam energy component. Note, however, that the first beam energy component contributes about 90% to the total CX emission, while the contributions of the second and third component are of the order 8% and 2%, respectively (taking into account the effective CX emission rate and the beam energy population densities,  $E_0 : E_0/2 : E_0/3 = 65\% : 25\% : 10\%$ ).

The results obtained from these calculations indicate that for the observed temperature and velocity ranges the cross-section effects on the measured spectra are negligible and hence, they are not included in the analysis.

### C. Gyro-motion effect

In addition to the CX cross-section effect described above, the effect of the gyro-motion of the impurity ion along with the finite lifetime of the observed state<sup>37</sup> can become important when measuring in the plane of the gyro-orbit. An apparent vertical velocity arises as the ion rotates  $\omega\tau$  before emitting a photon, with  $\omega$  the ion gyro-frequency and  $\tau$  the lifetime of the excited state of the transition. The gyro-orbit finite-lifetime effect scales with ion temperature and magnetic field strength. At the plasma edge the ion temperature is low, hence, the correction due to the gyro-orbit effect becomes less important. A correction for the gyro-orbit motion during the finite lifetime of the excited state has been calculated for the geometry of the new poloidal system using the analytic expressions derived by Solomon et al<sup>18</sup> and performing a LOS-integration<sup>38</sup>. For a typical magnetic field of 2 T at the low-field side of AUG, the gyro-frequency of  $B^{4+}$  is of the order  $7 \cdot 10^7$  Hz. The typical lifetime for the  $B^{4+}$  ( $n = 7 \rightarrow 6$ ) transition is on the timescale of ns, similar to the lifetime of

### High-resolution CXRS at ASDEX Upgrade

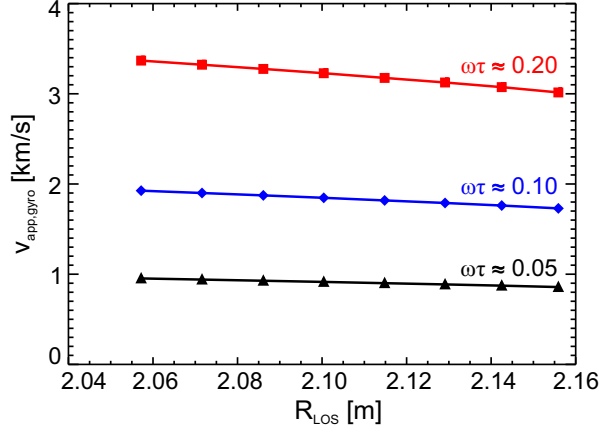


FIG. 13. Apparent velocity,  $v_{app,gyro}$ , for  $B^{5+}$  as a function of the major radius of the LOS,  $R_{LOS}$ , of the poloidal system arising due to the gyro-motion effect for different values of  $\omega\tau$  and an observed velocity of  $v_{obs}=20$  km/s.

$C^{5+}$  ( $n = 8 \rightarrow 7$ ). The Einstein coefficients for  $B^{4+}$  and  $C^{5+}$  have been calculated using the Cowan code<sup>39</sup> (as provided by the Atomic Data Analysis Structure ADAS<sup>40</sup>), which are in agreement with those derived from Wiese et al.<sup>41</sup> (deviations are smaller than  $0.04 \cdot 10^8$  s<sup>-1</sup>). Calculating the vacuum radiative lifetime of both  $B^{4+}$  and  $C^{5+}$  yields similar values, i.e. 0.638 ns for  $B^{4+}$  and 0.552 ns for  $C^{5+}$ , in good agreement with the vacuum radiative lifetime used in ref.<sup>37</sup>. Using a collisional-radiative model and allowing radiative decay from higher  $n$  levels<sup>37</sup> an effective lifetime for  $C^{5+}$  was estimated as 0.7 ns. Measurements on TFTR revealed an effective lifetime of 1.1 ns for the  $C^{5+}$  transition<sup>37</sup>, while on DIII-D the experimentally derived lifetime was 1.7 ns<sup>18</sup>. For parameters at AUG and considering the  $B^{4+}$  transition these lifetimes translate to  $\omega\tau \approx 0.05$ ,  $\omega\tau \approx 0.08$  and  $\omega\tau \approx 0.12$ , respectively. A sensitivity study of increasing lifetimes has been performed and the results are shown in figure 13. The combined effect due to both the gyro-orbit motion and the CX cross-sections (section VB) is shown in figure 14, which illustrates the apparent velocity for  $B^{5+}$  as a function of the major radius of the LOS. For increasing values of  $\omega\tau$  the apparent velocity appears to be higher for lower ion temperatures due to competing corrections arising from the CX cross-section and gyro-motion effect. For  $\omega\tau=0$  the remaining effect is due to the energy-dependent CX cross-sections as discussed in section VB (see figure 11).

The combined CX cross-section and gyro-motion effect has been simulated for real impurity ion temperature and poloidal rotation profiles, as shown in figure 8. For this case only the

## High-resolution CXRS at ASDEX Upgrade

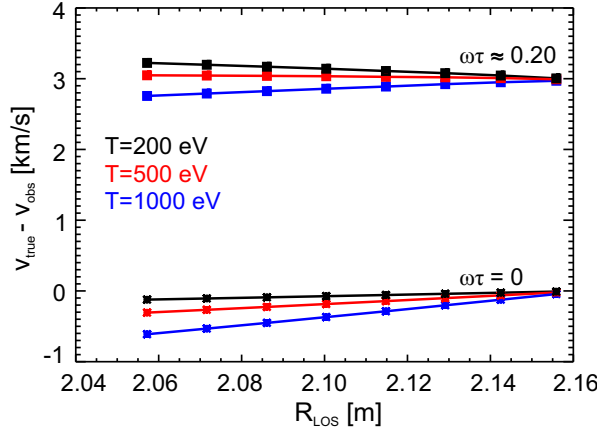


FIG. 14. Combined CX cross-section and gyro-motion effect for poloidal edge CXRS system: corrections for  $B^{5+}$  as a function of the major radius of the LOS,  $R_{LOS}$ , for two different values of  $\omega\tau$  and for different ion temperatures. The curves are shown for an observed velocity of  $v_{obs}=20$  km/s. Note that for the case  $\omega\tau=0$  (i.e. no gyro-motion effect) the impact of the energy dependence of the CX cross-sections is shown separately (as in figure 11).

first beam energy component has been considered. The effect of varying the lifetime of the  $B^{4+}$  transition is shown in figure 15. Note that the theoretically and experimentally derived lifetimes<sup>18,37</sup> discussed above have been used for the simulations. In H-mode the poloidal

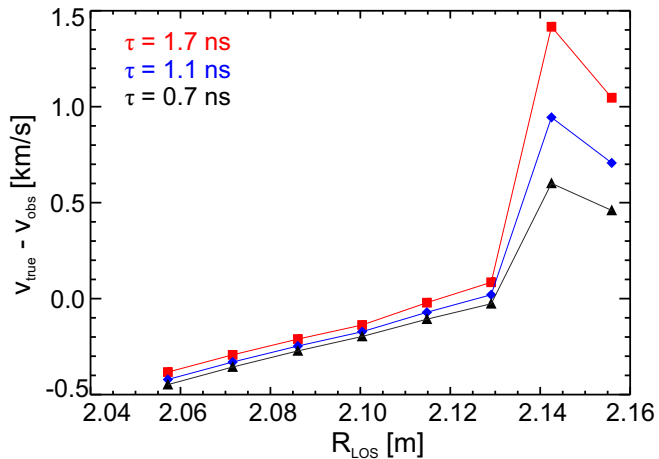


FIG. 15. Calculations for a real AUG case using measured impurity ion temperature and poloidal rotation profiles (as shown in figure 8): corrections for  $B^{5+}$  as a function of the major radius of the LOS,  $R_{LOS}$ , for different values of the lifetime  $\tau$ .

## High-resolution CXRS at ASDEX Upgrade

rotation increases by an order of magnitude inside the ETB and competing corrections due to the CX cross-section and gyro-motion effect result in the profile shown in figure 15. The calculations presented in this section show that for the observed temperature and rotation ranges the corrections due to CX cross-section and gyro-motion effects on the measured spectra are small. The magnitude of the correction depends on the value of  $\omega\tau$ , which itself is uncertain within a factor of 2. Therefore, the corrections are not included in the analysis. Due to the atomic physics effects an additional uncertainty of  $\pm 0.5$  km/s arises for the poloidal rotation measurements, yielding a total uncertainty of  $\pm 1.5$  km/s.

### D. Correction due to Zeeman splitting

Due to the presence of a magnetic field in tokamak plasmas the Zeeman effect needs to be taken into account. Each Zeeman component is a Gaussian itself with a Doppler width which represents the true ion temperature. When all of the components are added up a line-shape which is nearly Gaussian is produced. However, the width of this Gaussian overestimates the ion temperature<sup>1,42</sup>. Several methods are employed to account for the Zeeman splitting in CX spectra. Note that the total Zeeman pattern includes both the Zeeman and the fine structure contributions, i.e. the fine structure is also taken into account in the fitting process. At AUG, correction factors calculated as a function of the apparent ion temperature<sup>43</sup> are used to account for the Zeeman broadening, assuming that the total line shape of the measured spectra is Gaussian. This assumption is valid at high temperatures and low magnetic fields,

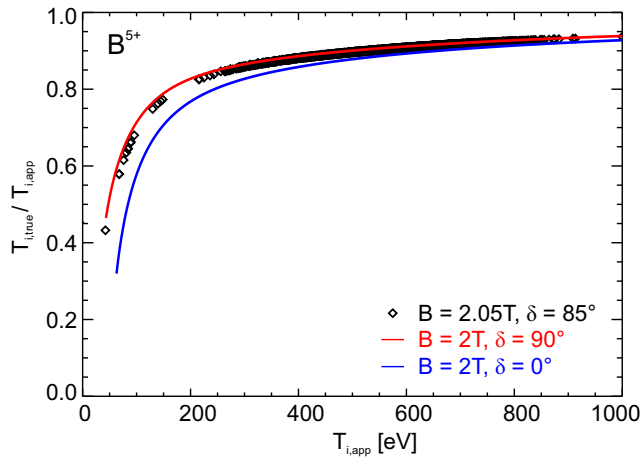


FIG. 16. Correction factor  $T_{i,true}/T_{i,app}$  for  $B^{5+}$  to account for Zeeman splitting in CX spectra.

### High-resolution CXRS at ASDEX Upgrade

i.e. where the Doppler broadening is dominant compared to the Zeeman splitting. The Zeeman components are calculated assuming fully mixed populations of the  $l$ -states ( $l$  being the orbital angular momentum quantum number). This assumption is valid in the ETB of AUG using an empirical formula<sup>44</sup> for determining the critical plasma density at which a given transition is fully mixed. For the  $B^{5+}$  transition, a critical density of  $1.3 \cdot 10^{19} \text{ m}^{-3}$  is obtained which is lower than typical densities at the plasma edge of AUG indicating that the  $l$ -levels are fully mixed. Each component of the Zeeman pattern is convolved with a Gaussian which corresponds to the Doppler broadening at the real ion temperature. The resulting feature is well described by a single Gaussian with an apparent ion temperature  $T_{i,app}$ . Figure 16 shows the dependence of the correction factor for  $B^{5+}$  on the apparent ion temperature calculated for the LOS of the poloidal optical head (almost perpendicular view to the magnetic field) and a magnetic field of about 2 T. The solid lines in blue and red show the theoretical curves calculated for  $B = 2 \text{ T}$  and an angle of  $0^\circ$  and  $90^\circ$ , respectively. The true ion temperature  $T_{i,true}$  is obtained by multiplying the measured apparent temperature with the correction factor. This procedure is performed for all of the CXRS diagnostics.

## VI. SUMMARY

The CXRS diagnostics at AUG have been upgraded and extended to provide impurity ion temperature, density and velocity profiles with increased temporal and radial resolution. The main core toroidal system and the edge toroidal system have been equipped with a new CCD camera and a new spectrometer enabling the measurement of 25 channels simultaneously. Additional lines of sight have been installed for the core toroidal system to provide detailed radial profiles ( $\approx 2 \text{ cm}$  resolution) with high temporal resolution down to 3.5 ms. The edge toroidal system has a radial resolution of down to 3 mm and a temporal resolution of 2.2 ms. Combining the measurements at the plasma core and at the edge allows full radial profiles to be obtained. The simultaneous measurement of impurity ion temperature, density and rotation velocity allows the cross-calibration of the different CXRS diagnostics. Good agreement is found between all systems. In addition, a new poloidal CXRS system has been installed which enables spatially (down to 5 mm) and temporally (1.9 ms) resolved measurements of poloidal impurity ion rotation. Care has been taken to determine the wavelength calibrations with quite high accuracy. Deviations from the parabolic image of

### High-resolution CXRS at ASDEX Upgrade

a straight entrance slit, which would lead to an apparent velocity, have been quantified by measurements on spectral lamps. To minimize systematic uncertainties of the edge rotation measurements an additional wavelength correction is performed on a shot-to-shot basis. This method allows the determination of the wavelength calibration with uncertainties smaller than 1 km/s. Due to the atomic physics effects in the CX spectra additional uncertainties of  $\pm 0.5$  km/s arise for the poloidal rotation measurements. Complementing the toroidal edge system with a poloidal view provides full edge rotation profiles at AUG, i.e. parallel and perpendicular to the magnetic field. To obtain detailed radial profiles of the edge transport barrier the radial plasma sweep technique is applied, thus enabling the alignment of the measurements of both edge CXRS diagnostics. Moreover, the measurements of the new poloidal edge system now enable the determination of the radial electric field from CXRS measurements at AUG needed for investigating the physics of the L-H transition.

### ACKNOWLEDGMENTS

This work was supported by the State Government of Bavaria through the 'Bayerisches Konjunkturpaket II'. The hardware upgrades for the toroidal core system I were funded in part by the EFDA 2009 Workprogram WP09-TGS-02/02.

### REFERENCES

- <sup>1</sup>R. J. Fonck, D. S. Darrow and K. P. Jaehnig. Determination of plasma-ion velocity distribution via charge-exchange recombination spectroscopy. *Phys. Rev. A*, 29(6):3288, 1984.
- <sup>2</sup>M. Shimada et al. M. Shimada, D.J. Campbell, V. Mukhovatov, M. Fujiwara, N. Kirneva, K. Lackner, M. Nagami, V.D. Pustovitov, N. Uckan, J. Wesley, N. Asakura, A.E. Costley, A.J.H. Donné, E.J. Doyle, A. Fasoli, C. Gormezano, Y. Gribov, O. Gruber, T.C. Hender, W. Houlberg, S. Ide, Y. Kamada, A. Leonard, B. Lipschultz, A. Loarte, K. Miyamoto, V. Mukhovatov, T.H. Osborne, A. Polevoi and A.C.C. Sips. Chapter 1: Overview and summary. *Nuclear Fusion*, 47:S1, 2007.
- <sup>3</sup>A. Herrmann, O. Gruber. Special Issue on ASDEX Upgrade. *Fusion Science and Technology*, 44(3), 2003.

### High-resolution CXRS at ASDEX Upgrade

- <sup>4</sup>T. Pütterich, E. Wolfrum, R. Dux, C. F. Maggi and ASDEX Upgrade Team. Evidence for Strong Inversed Shear of Toroidal Rotation at the Edge-Transport Barrier in ASDEX Upgrade. *Phys. Rev. Lett.*, 102:025001, 2009.
- <sup>5</sup>K. Ida. Experimental studies of the physical mechanism determining the radial electric field and its radial structure in a toroidal plasma. *Plasma Phys. Control. Fusion*, 40:1429, 1998.
- <sup>6</sup>F. Wagner, G. Becker, K. Behringer, D. Campbell, A. Eberhagen, W. Engelhardt, G. Fussmann, O. Gehre, J. Gernhardt, G. v. Gierke, G. Haas, M. Huang, F. Karger, M. Keilhacker, O. Klüber, M. Kornherr, K. Lackner, G. Lisitano, G. G. Lister, H. M. Mayer, D. Meisel, E. R. MüLLER, H. Murmann, H. Niedermeyer, W. Poschenrieder, H. Rapp, H. Röhr, F. Schneider, G. Siller, E. Speth, A. äbler, K. H. Steuer, G. Venus, O. Vollmer, Z. Yü. Regime of Improved Confinement and High Beta in Neutral-Beam-Heated Divertor Discharges of the ASDEX Tokamak. *Phys. Rev. Lett.*, 49(19):1408, 1982.
- <sup>7</sup>R. Dux, B. Geiger, R. M. McDermott, T. Pütterich, E. Viezzler and ASDEX Upgrade team. *Impurity density determination using charge exchange and beam emission spectroscopy at ASDEX Upgrade*. Conf. Proceedings of the 38<sup>th</sup> EPS Conference on Plasma Physics, ECA Vol. 35G, P1.056, Strasbourg, 2011.
- <sup>8</sup>B. Geiger, M. Garcia-Muñoz, W. W. Heidbrink, R. M. McDermott, G. Tardini, R. Dux, R. Fischer, V. Igochine and the ASDEX Upgrade Team. Fast-ion D-alpha measurements at ASDEX Upgrade. *Plasma Phys. Control. Fusion*, 53:065010, 2011.
- <sup>9</sup>Princeton Instruments <http://www.princetoninstruments.com>.
- <sup>10</sup>R. M. McDermott, C. Angioni, R. Dux, E. Fable, T. Pütterich, F. Ryter, A. Salmi, T. Tala, G. Tardini, E. Viezzler and the ASDEX Upgrade Team. Core momentum and particle transport studies in the ASDEX Upgrade tokamak. *Plasma Phys. Control. Fusion*, 53:124013, 2011.
- <sup>11</sup>C. Angioni, R. M. McDermott, E. Fable, R. Fischer, T. Pütterich, F. Ryter, G. Tardini and the ASDEX Upgrade Team. Gyrokinetic modelling of electron and boron density profiles of H-mode plasmas in ASDEX Upgrade. *Nucl. Fusion*, 51:023006, 2011.
- <sup>12</sup>C. Angioni, R. M. McDermott, F. J. Casson, E. Fable, A. Bottino, R. Dux, R. Fischer, Y. Podoba, T. Pütterich, F. Ryter, E. Viezzler and ASDEX Upgrade Team. Intrinsic Toroidal Rotation, Density Peaking, and Turbulence Regimes in the Core of Tokamak Plasmas. *Phys. Rev. Lett.*, 107:215003, 2011.

### High-resolution CXRS at ASDEX Upgrade

- <sup>13</sup>NIST Atomic Spectra Database. [http://physics.nist.gov/PhysRefData/ASD/lines\\_form.html](http://physics.nist.gov/PhysRefData/ASD/lines_form.html)
- <sup>14</sup>E. Viezzer, T. Pütterich, R. Dux, A. Kallenbach and the ASDEX Upgrade Team. Investigation of passive edge emission in charge exchange spectra at the ASDEX Upgrade tokamak. *Plasma Phys. Control. Fusion*, 53:035002, 2011.
- <sup>15</sup>H. Zohm. Edge localized modes (ELMs). *Plasma Phys. Control. Fusion*, 38:105, 1996.
- <sup>16</sup>J. Kim, K. H. Burrell, P. Gohil, R. J. Groebner, Y.-B. Kim, H. E. St. John, R. P. Seraydarian and M. R. Wade. Rotation characteristics of main ions and impurity ions in H-mode tokamak plasma. *Phys. Rev. Lett.*, 72(14):2199, 1994.
- <sup>17</sup>K. H. Burrell, D. H. Kaplan, P. Gohil, D. G. Nilson, R. J. Groebner, D. M. Thomas. Improved charge coupled device detectors for the edge charge exchange spectroscopy system on the DIII-D tokamak. *Rev. Sci. Instrum.*, 72(1):1028, 2001.
- <sup>18</sup>W. M. Solomon, K. H. Burrell, P. Gohil, R. J. Groebner, L. R. Baylor. Extraction of poloidal velocity from charge exchange recombination spectroscopy measurements. *Rev. Sci. Instrum.*, 75(10):3481, 2004.
- <sup>19</sup>R. M. McDermott, B. Lipschultz, J. W. Hughes, P. J. Catto, A. E. Hubbard, I. H. Hutchinson, R. S. Granetz, M. Greenwald, B. LaBombard, K. Marr, M. L. Reinke, J. E. Rice, D. Whyte, and Alcator C-Mod Team. Edge radial electric field structure and its connections to H-mode confinement in Alcator C-Mod plasmas. *Phys. Plasmas*, 16:056103, 2009.
- <sup>20</sup>N. Hawkes, D. V. Bartlett, D. J. Campbell, N. Deliyanakis, R. M. Giannella, P. J. Lomas, N. J. Peacock, L. Porte, A. Rookes and P. R. Thomas. Evolution of edge radial electric field at the L to H transition in JET. *Plasma Phys. Control. Fusion*, 38(8):1261, 1996.
- <sup>21</sup>K. Cromb  , Y. Andrew, I. Coffey, P. De Vries, C. Giroud, N. C. Hawkes, E. Joffrin, D. C. McDonald, A. Murari, J. Ongena, F. Sattin, M. Valisa, K. D. Zastrow and EFDA-JET contributors. *Improved measurements of impurity ion poloidal rotation velocity in JET*. Conf. Proceedings of the 30<sup>th</sup> EPS Conference on Contr. Fusion and Plasma Physics, ECA Vol. 27A, P-1.55, St. Petersburg, 2003.
- <sup>22</sup>Y. Andrew, N. C. Hawkes, K. Cromb   and JET EFDA contributors. Improved charge exchange spectroscopy on the Joint European Torus for ion temperature and rotation velocity profiles. *Rev. Sci. Instrum.*, 77:10E913, 2006.
- <sup>23</sup>R. E. Bell, F. M. Levinton, S. H. Batha, E. J. Synakowski and M. C. Zarnstorff. Poloidal Rotation in TFTR Reversed Shear Plasmas. *Phys. Rev. Lett.*, 81(7):1429, 1998.

### High-resolution CXRS at ASDEX Upgrade

- <sup>24</sup>C. Busch. Volume 50 of 'Schriften des Forschungszentrums Juelich', Energy Technology edition, ISBN 3-89336-433-1, Forschungszentrum Juelich GmbH, 2006.
- <sup>25</sup>A. R. Field, J. McCone, N. J. Conway, M. Dunstan, S. Newton and M. Wisse. Comparison of measured poloidal rotation in MAST spherical tokamak plasmas with neo-classical predictions. *Plasma Phys. Control. Fusion*, 51:105002, 2009.
- <sup>26</sup>R. E. Bell, R. Andre, S. M. Kaye, R. A. Kolesnikov, B. P. LeBlanc, G. Rewoldt, W. X. Wang and S. A. Sabbagh. Comparison of poloidal velocity measurements to neoclassical theory on the National Spherical Torus Experiment. *Phys. Plasmas*, 17:082507, 2010.
- <sup>27</sup>K. Ida, S. Kado and Y. Liang. Measurements of poloidal rotation velocity using charge exchange spectroscopy in a large helical device. *Rev. Sci. Instrum.*, 71(6):2360, 2000.
- <sup>28</sup>E. Wolfrum, R. Fischer, B. Langer, T. Pütterich, G. D. Conway, D. P. Coster, R. Dux, J.C. Fuchs, M. Gemisic Adamov, N. Hicks, L. D. Horton, C. Konz, B. Kurzan, K. Lackner, C. F. Maggi, P. J. McCarthy, M. Reich, J. Schweinzer, W. Suttrop, C. Tröster and ASDEX Upgrade Team. *Pedestal Studies at ASDEX Upgrade*. Conf. Proceedings of the 22<sup>nd</sup> IAEA Fusion Energy Conference, EX/P3-7, Geneva, 2008.
- <sup>29</sup>B. Kurzan, H. D. Murmann. Edge and core Thomson scattering systems and their calibration on the ASDEX Upgrade tokamak. *Rev. Sci. Instrum.*, 82:103501, 2011.
- <sup>30</sup>W. Suttrop. *Practical Limitations to Plasma Edge Electron Temperature Measurements by Radiometry of Electron Cyclotron Emission*. IPP Report 1/306, Max-Planck-Institute for Plasma Physics, Garching, Germany, 1997.
- <sup>31</sup>J. Neuhauser, D. Coster, H. U. Fahrbach, J. C. Fuchs, G. Haas, A. Herrmann, L. Horton, M. Jakobi, A. Kallenbach, M. Laux, J. W. Kim, B. Kurzan, H. W. Müller, H. Murmann, R. Neu, V. Rohde, W. Sandmann, W. Suttrop, E. Wolfrum and the ASDEX Upgrade Team. Transport into and across the scrape-off layer in the ASDEX Upgrade divertor tokamak. *Plasma Phys. Control. Fusion*, 44:855, 2002.
- <sup>32</sup>R. Fischer, E. Wolfrum, J. Schweinzer and the ASDEX Upgrade Team. Probabilistic lithium beam data analysis. *Plasma Phys. Control. Fusion*, 50:085009, 2008.
- <sup>33</sup>M. Willensdorfer, E. Wolfrum, R. Fischer, J. Schweinzer, M. Sertoli, B. Sieglin, G. Veres, F. Aumayr and the ASDEX Upgrade Team. Improved chopping of a lithium beam for plasma edge diagnostic at ASDEX Upgrade. *Rev. Sci. Instrum.*, 83:023501, 2012.
- <sup>34</sup>ITER Physics Expert Group on Confinement and Transport, ITER Physics Expert Group on Confinement Modelling and Database and ITER Physics Basis Editors. Chapter 2:

## High-resolution CXRS at ASDEX Upgrade

- Plasma confinement and transport. *Nucl. Fusion*, 39:2175, 1999.
- <sup>35</sup>R. E. Bell. Exploiting a transmission grating spectrometer. *Rev. Sci. Instrum.*, 75(10):4158, 2004.
- <sup>36</sup>M. von Hellermann, P. Breger, J. Frieling, R. K\"{u}nig, W. Mandl, A. Maas and H. P. Summers. Analytical approximation of cross-section effects on charge exchange spectra observed in hot fusion plasmas. *Plasma Phys. Control. Fusion*, 37:71, 1995.
- <sup>37</sup>R. E. Bell and E. J. Synakowski. New understanding of poloidal rotation measurements in a tokamak plasma. *AIP Conf. Proc.* 547, 547:39, 2000.
- <sup>38</sup>K. Cromb\'{e}. Spectroscopic studies of Impurity Ion Dynamics on the JET and TEXTOR Tokamaks. *PhD thesis, ISBN 90-8578-033-0, Ghent University, available at <http://hdl.handle.net/1854/5551>*, 2006.
- <sup>39</sup>R. D. Cowan. The Theory of Atomic Structure and Spectra. *University of California Press, ISBN 9780520038219*, 1981.
- <sup>40</sup>H. P. Summers. ADAS User Manual 2.6, *available at <http://www.adas.ac.uk/manual.php>*, 2004.
- <sup>41</sup>W. L. Wiese, M. W. Smith and B. M. Glennon. Atomic Transition Probabilities, Volume I Hydrogen Through Neon, A Critical Data Compilation, NSRDS-NBS 4. *National Standard Reference Data Series, National Bureau of Standards 4, U. S. Government Printing Office, Washington, D. C.*, 1966.
- <sup>42</sup>A. Blom and C. Jup\'{e}n. Parametrization of the Zeeman effect for hydrogen-like spectra in high-temperature plasmas. *Plasma Phys. Control. Fusion*, 44:1229, 2002.
- <sup>43</sup>J. D. Hey, Y. T. Lie, D. Rusb\"{u}ldt, E. Hintz. *Spectroscopic Measurements of Ion Temperatures in the Boundary Layer of TEXTOR and their Interpretation*. Conf. Proceedings of the 20<sup>th</sup> EPS Conference on Contr. Fusion and Plasma Physics, ECA Vol. 17C/III, p. 1111, Lisbon, 1993.
- <sup>44</sup>D. H. Sampson. On statistical equilibrium among the sublevels of hydrogenic atoms and ions. *J. Phys. B: At. Mol. Phys.* , 10:749, 1977.

## 5.8 Publication 8

*Evidence for Strong Inversed Shear of Toroidal Rotation at the Edge-Transport Barrier in the ASDEX Upgrade*  
Physical Review Letter 102, 025001 (2009)

## Evidence for Strong Inversed Shear of Toroidal Rotation at the Edge Transport Barrier in ASDEX Upgrade

T Pütterich,\* E. Wolfrum, R. Dux, C.F. Maggi, and ASDEX Upgrade Team  
*Max-Planck-Institut für Plasmaphysik, EURATOM Association, D-85748 Garching, Germany*

The toroidal rotation of H-mode plasmas in ASDEX Upgrade is studied in the outermost 5 cm of the confined plasma. The projection of the rotation velocity along the line of sight (approx. toroidal) is measured using charge exchange recombination spectroscopy, with a radial resolution of up to 3 mm and a temporal resolution of 1.9 ms. The full toroidal rotation profile exhibits considerable rotation in the plasma center, where the neutral beam heating injects toroidal momentum in co-direction (i.e. direction of plasma current). Towards the plasma edge up to the last 1-2 cm of the plasma radius the rotation decreases. About 1 cm inside the last closed flux surface the rotation exhibits a local minimum. From there, the rotation in co-direction increases towards the last closed flux surface. The increase is in the range of 10 – 20 km/s. It is observed for  $D^+$ ,  $He^{2+}$ ,  $B^{5+}$ , and  $C^{6+}$ . The measurements are fast enough to distinguish between time frames with and without edge localized modes (ELM). The described rotation feature at the edge is not visible during an ELM crash and is probably connected to the occurrence of steep gradients in this plasma region. The quality of the measurements allows to unambiguously identify and localize this feature providing valuable input for modelling the plasma edge.

### INTRODUCTION

In H-mode fusion plasmas [1], an edge transport barrier (ETB) [1] is found leading to steep gradients in the plasma parameters at the last few cm of the magnetically confined plasma. The ETB is disturbed frequently by edge localized modes (ELMs, here: type-I), which are characterised by bursts of particles and energy being expelled from the plasma edge. In ASDEX Upgrade [2] the duration of an ELM is in the range of a millisecond, while the time between ELMs can be as long as tens of milliseconds. The width of the ETB region and the gradients cannot be predicted by a model using first principles. Nevertheless, the performance of ITER and a future fusion reactor is very sensitive to the densities and temperatures at the top of the edge pedestal. It is widely assumed that the occurrence of a sheared plasma flow perpendicular to the magnetic field suppresses turbulence and thus leads to reduced transport, i.e the ETB. The persistence of the ETB can be understood by the existence of a self-consistent radial electric field maintaining a sheared  $E \times B$  flow, while being produced by the gradients and the plasma flow. An open issue still is the influence of the toroidal rotation profile on the ETB and the H-mode transition and vice versa the effects of the H-mode edge on the toroidal rotation (e.g. [3]). Measurements focusing on the pedestal need to provide high radial resolution ( $< 1$  cm) and fast temporal resolution ( $\approx 1$  ms) due to the frequent occurrence of ELMs. Diagnostic systems capable of measuring highly resolved edge profiles are scarce. Additionally, the rotation measurements need to be spatially related to electron temperature and density measurements to enable a comprehensive localization of the last closed flux surface (LCFS) relative to the rotation measurements.

### EXPERIMENT

The viewing geometry of the edge charge exchange recombination spectroscopy (CXRS, [4]) system at ASDEX Up-

grade is adjusted to high spatial resolution. The f/4 optics gathers the light, which is transmitted by 400  $\mu$ m optical fibres and analyzed by a f/4 spectrometer employing commercial objective lenses with a focal length of 280 mm and a grating with 2400 grooves/mm. The dispersed light is detected by a CCD camera with electron multiplication readout allowing for a pixel rate of 10 MHz at acceptable readout noise. The light from eight radial positions at the outboard midplane (separated by  $\approx 1$  cm) is analyzed by the spectrometer with a repetition time of 1.9 ms. The evaluation of spectral lines emitted following a charge exchange (CX) reaction is used to obtain local information about the impurity ion temperature  $T_i$  and toroidal rotation  $v_{tor}$ , which are evaluated by Doppler broadening and line shift. The systematical uncertainties of the rotation measurements originate from uncertainties in the wavelength calibration of the spectra. These have been thoroughly quantified by measurements on calibration lamps and the analysis of intrinsic impurity lines. The absolute rotation velocities are uncertain by 5 km/s, while the relative uncertainties between different LOS are less than 1-2 km/s. Statistical uncertainties are indicated in the following figures using vertical, symmetric error bars. The radial resolution of the setup is determined by the size of the plasma volume (diameter of 4 mm) which is imaged onto the optical fibres. Additionally, the measurements are smeared by  $\approx 5$  mm due to the fact, that the plasma is curved within the beam width of 0.2 m. However, for emissions, which exhibit a strong radial gradient in intensity, the spatial resolution is strongly enhanced, reaching for the presented cases values down to 3 mm. With this new diagnostic, plasma discharges in H-mode have been studied, while the fast temporal resolution was used to analyse the development of the measured quantities within an ELM cycle. To obtain best data, the plasma discharges were horizontally swept by 2 cm, such that the plasma was not disturbed while the edge of the plasma moved through the view of the described LOS. The measured spectra are then analysed by a spectral line fit. Measurements have been obtained for  $C^{6+}$ ,  $B^{5+}$ ,  $He^{2+}$  and  $D^+$  using the CX spectral lines at 529.059 nm

(8-7), 494.497 nm (7-6), 467.857 nm (4-3) and 656.103 nm (3-2), respectively. In the following, data are presented which result from a fit with two Gaussians taking the contribution of passive line emissions into account, while for the comparison between different species beam modulation was applied, i.e. the heating beam, which is used for the CX measurement, is switched on and off while another beam is switched off and on to compensate the total heating power. Using this latter method the background emissions are subtracted and a single Gauss fit can be used to obtain the parameters of the CX emission.

## RESULTS

Figure 1 depicts the fit results, i.e. the CX-line intensity,  $T_i$  and  $v_{tor}$  for an H-mode discharge (#22273) with type-I ELMs. In this discharge, one neutral beam source ( $P_{NBI} = 2.5$  MW), electron cyclotron heating ( $P_{ECH} = 1.4$  MW) and ohmic heating ( $P_{OH} = 0.4$  MW) was used to obtain H-mode at a line integrated electron density  $n_e$  of about  $8 \cdot 10^{19} \text{ m}^{-3}$ , plasma current  $I_p$  of 1 MA and a magnetic field  $B_t$  of 2.4 T resulting in an ELM-frequency of about 65 Hz. The temporal resolution of 1.9 ms allows to synchronize the data to the occurrence of an ELM. In figure 1 four columns are presented labelled with ‘-7 ms’, ‘-1 ms’, ‘+1 ms’ and ‘+5 ms’ which represent light  $\pm 1.45$  ms around these time points. The labels denote the relative time distance to the following/preceding ELM. The plasma radius of the measurement location is determined by a numerical integration along the LOS which determines the CX emission intensity in the observed plasma volumes. The alignment to the  $n_e$  and  $T_e$  profiles and the magnetic measurements is discussed below. The effects of the ELM can be studied for all quantities, but will play a minor role for this work. For the  $v_{tor}$ -profile, a feature is visible in between ELMs. The  $v_{tor}$ -profile exhibits a local minimum at 1 cm inside the LCFS. On the last centimeter of the confined plasma  $v_{tor}$  increases by about 10-20 km/s reaching about 25 km/s at the LCFS. This feature is visible during the whole ELM cycle only interrupted for about 2-3 ms by the ELM. The behaviour during the ELMs cannot be judged by the measurements, because the exposure time of 1.9 ms is too long. Still, it is remarkable, that in figure 1 no data points indicate the dip in rotation velocity for the time labelled ‘+1 ms’. In all other frames the dip is clearly visible and also for the time frame ‘+3 ms’ (omitted in figure 1) a dip is visible.

For all studied plasma discharges in H-mode, this rotation feature is visible to some extent, while in L-mode it has not been observed. The optimized radial alignment is presented in figure 2. The uncertainty of the separatrix position from magnetic reconstruction can be greatly reduced with the help of the steep  $T_e$ -profiles. By setting  $T_e$  at the separatrix to  $\approx 100$  eV, a mandatory condition set by the parallel heat transport and power balance [5] is satisfied. The  $n_e$ -profiles from the Li-beam are then aligned to the measurements of the Thomson scattering, as for the latter diagnostic the mea-

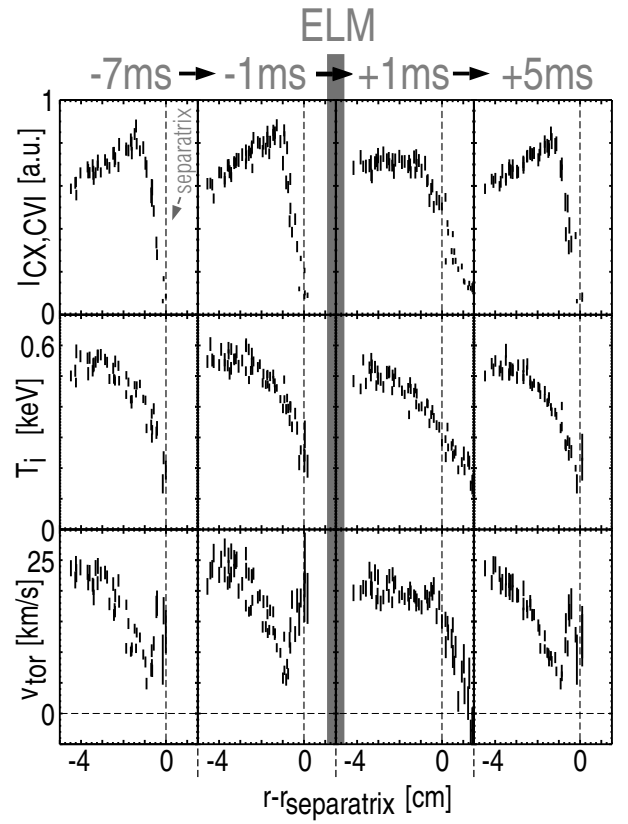


FIG. 1: Measurements derived from the active CX-component between beam neutrals and fully-stripped C. The data were obtained from a 300 ms long phase in which the plasma was horizontally swept by 2 cm. The intensity of the CX-component ( $|I_{CX,CVI}|$ ),  $T_i$  and the  $v_{tor}$  (positive is in co-direction) of the plasma are depicted in different phases of an ELM-cycle.

surement volumes are identical for electron temperatures and densities. The CX-data are then aligned with an accuracy of about 2-3 mm, such that the steep  $T_i$ -gradient region coincides with that of the  $T_e$ -measurement (see figure 2). The necessary corrections are typically smaller than 5 mm. With all profiles aligned it is easily visible that the inversion of the rotation shear is located directly at the region with steep gradients in the  $n_e$ ,  $T_e$ - and  $T_i$ -gradients.

Taking the depicted plasma parameters into account, it is derived that the collisionality of C is above the Pfirsch-Schlüter limit, that of He is about at the limit, while that of deuterium (D) is below. This poses a motivation to investigate the feature in  $v_{tor}$  for different impurities and D. Such measurements have been performed in the discharges for which data are presented in figure 3. The upper measurements in figure 3 ( $D^+$ ,  $B^{5+}$ ) originate from discharges with  $I_p = 1.1$  MA,  $B_t = 2.75$  T,  $n_e = 7.8 \cdot 10^{19} \text{ m}^{-3}$ ,  $P_{NBI} = 2.5$  MW and  $P_{ECH} = 0.75$  MW. The discharge parameters of the lower measurements in figure 3 ( $He^{2+}$ ,  $B^{5+}$ ,  $C^{6+}$ ) are  $I_p = 1$  MA,  $B_t = 2.5$  T,  $n_e = 7.5 \cdot 10^{19} \text{ m}^{-3}$ ,  $P_{NBI} = 5$  MW and  $P_{ECH} = 0.6$  MW. All measurements originate from time points not dis-

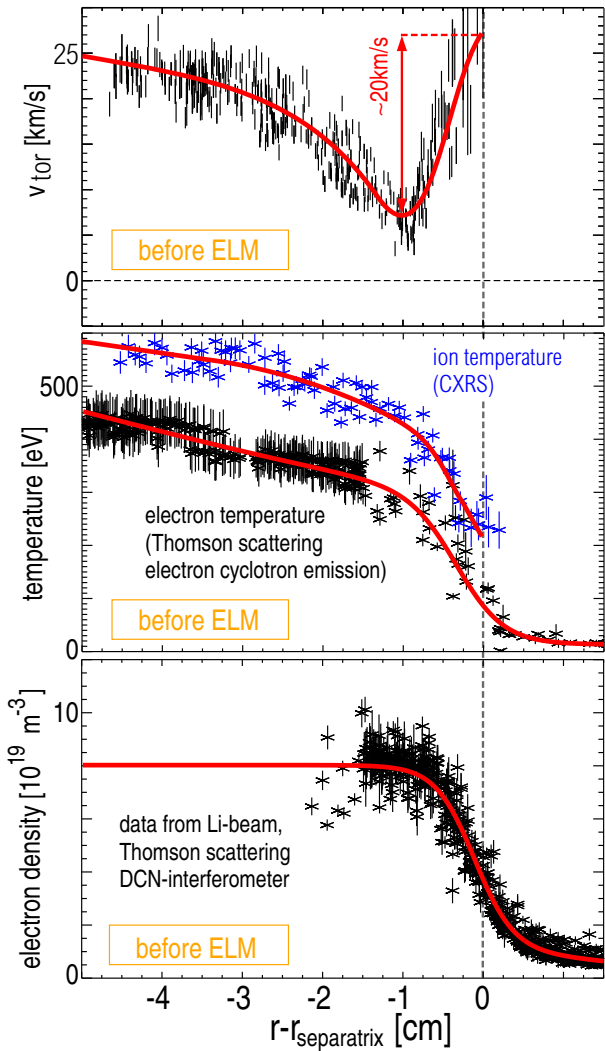


FIG. 2: Measurements of  $v_{\text{tor}}$  (positive is in co-direction) in discharge #22273 (H-mode) overlaying all data from 10 ms before the ELM up to the ELM. Below  $T_i$ ,  $T_e$  and  $n_e$  profiles are depicted for corresponding times. The alignment of the profiles with respect to the separatrix is described in the text. The lines are introduced to guide the eye.

turbed by ELMs. The measurements on C exhibit larger error bars, because the C concentration for the discharge series has been below 0.2% due to a recent boronization. However, from the experience in various other discharges it is observed that there is no significant difference between the rotation velocities of  $B^{5+}$  and  $C^{6+}$ . It must be noted, that for D and He the beam halo and plume [4] effect have not been corrected for. Both effects lead to a smoothening of steep gradients in the measured rotation. While the plume effect of He is estimated to play no major role in the measurements, the halo effect for D is estimated to mix the measurement on a radial scale of about 10-20 mm depending on the local plasma parameters. This estimation is based on how far a neutral cloud (born by CX with the beam) would expand until being ionized by the

electrons.

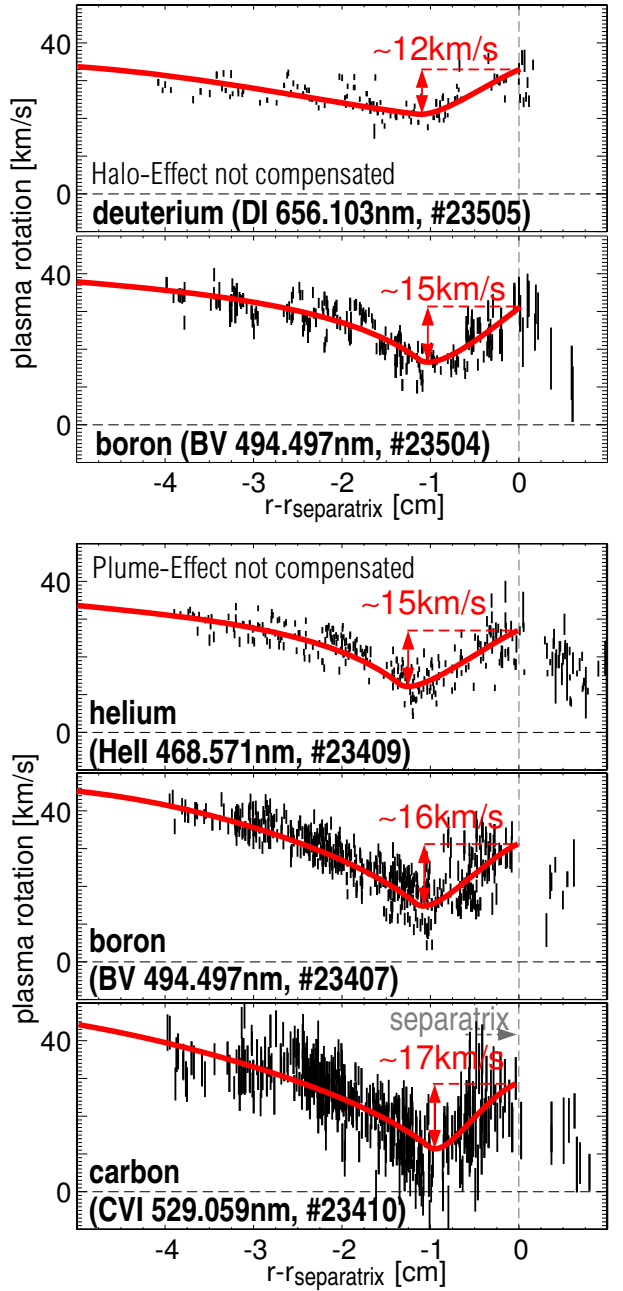


FIG. 3: Measured  $v_{\text{tor}}$  of different species for similar discharges. The measurements of D and He have not been corrected for the halo and plume effect. The latter lead to an apparent flattening of gradients in  $v_{\text{tor}}$ .

## DISCUSSION

The measurements have been thoroughly verified by comparisons of evaluation methods and by measurements using different impurities, hence spectral regions. From the DIII-D

tokamak measurements are presented in [6] which indicate a similar feature at the plasma edge, however, it is not discussed nor verified and the exact alignment to the  $n_e$ ,  $T_e$  profiles and the resolution of the feature are not performed in [6]. An exact knowledge of the separatrix position is of high importance for validating and aligning the measurements with respect to other diagnostics and for narrowing down possible explanations. Various effects which could lead to a rotation feature as described above are discussed in the following. The perpendicular velocity which is fixed via the radial force balance including diamagnetic velocity and  $E \times B$  flow can influence the  $v_{tor}$  measurement via 2 effects. Firstly, the projection of the perpendicular velocity onto the LOS gives a positive and negative contribution for the diamagnetic drift and the (negative) electric field, respectively. These contributions are only about 1/8 to about 1/10 of the perpendicular velocity depending on the exact geometry of the magnetic field at the edge. Secondly, the perpendicular rotation is not divergence free and a parallel flow (Pfirsch-Schlüter) is necessary to provide zero divergence - a strict boundary condition - for the plasma flow. Taking this contributions into account the resulting effect and all of the separate contributions influence the  $v_{tor}$  measurement by less than 5 km/s for the measured plasma parameter profiles and typical electric fields, like measured in [7, 8]. None of the effects can explain the observations. It should be noted that the measurements of the electric field are independent of the feature in  $v_{tor}$  [8]. Differences of the rotation velocity for different species could be expected from neoclassical effects. These have been evaluated by the code NEOART [9]. NEOART calculates the collisional transport coefficients for an arbitrary number of impurities including collisions between all components. The code solves the set of linear coupled equations for the parallel ‘velocities’ in arbitrary toroidally symmetric geometry for all collision regimes. The classical fluxes are given by Eqs.(5.9) and (5.10) in [10]. The equations for the banana plateau contribution are equal to that used in [11]. The Pfirsch-Schlüter contribution is calculated from the coupled equations (6.1-2) and (6.14-15) in [10], as described in [12]. From the code the differences in rotation between D and the impurities are predicted for the measured input profiles of  $n_e$ ,  $T_e$ ,  $T_i$  and impurity concentrations, which were estimated using typical values. The resulting differences are in the range of 2 km/s and cannot be resolved experimentally. It must be noted that approaching the separatrix the neoclassical approximation breaks down, because the poloidal gyroradius gets comparable to the gradients in the plasma parameters.

In experiment, plasma flows pointing in co-direction have been observed in the scrape-off layer (SOL) of ASDEX Upgrade exhibiting Mach numbers of about 0.6 just outside the LCFS [13]. This corresponds to  $\approx 40$  km/s at  $T_e = T_i = 50$  eV. Due to viscous forces such rotation in the SOL could yield a boundary condition to the rotation of the plasma inside the separatrix, while the electric field gradient and rota-

tion would adjust self-consistently. Into the same direction hints the fact, that the banana width of thermal D is at the separatrix about 8 mm wide, which corresponds about to the width of the feature in  $v_{tor}$ . This calls for detailed fluid simulations taking viscosity and drift velocities (also in the SOL) self-consistently into account. In [14], this has been done and similar structures as observed have been obtained from modelling. It should be noted that in the SOL there is a positive, radial electric field outside the LCFS providing a perpendicular plasma rotation with a toroidal projection in the co-direction. The magnitude of this projection is too small to contribute directly to the measurement, but its correlated Pfirsch Schlüter flow is suspected to be responsible for the SOL flows.

Independently, the measured rotational profiles yield a challenge to momentum transport analysis, because the local minimum of the plasma rotation can only be explained by a local sink for toroidal momentum or by a radial pinch velocity profile which changes sign at the position of the minimum. The existence of a local sink could hold also the key for explaining the spontaneous rotation of plasmas [3], in which no momentum is injected by beam heating. The possibility of a local sink for toroidal momentum by effects of fast ions on banana orbits has been investigated by codes which determine the beam deposition and follow the beam ions until they are thermalized using the plasma parameters of figure 2 and realistic contours of the plasma facing components. However, the momentum transfer of the fast ions was at all radii in co-direction exhibiting no sign of a momentum sink.

- 
- \* Electronic address: Thomas.Puetterich@ipp.mpg.de
- [1] F. Wagner *et al.*, Phys. Rev. Lett. **49**, 1408 (1982).
  - [2] A. Herrmann and O. Gruber, Fusion Science and Technology **44**, 569 (2003).
  - [3] J. Rice *et al.*, Nuclear Fusion **47**, 1618 (2007).
  - [4] R. J. Fonck, D. S. Darrow, and K. P. Jaehnig, Physical Review A **29**, 3288 (1984).
  - [5] J. Neuhauser *et al.*, Plasma Physics and Controlled Fusion **44**, 855 (2002).
  - [6] J. S. deGrassie *et al.*, Physics of Plasmas **14**, 056115 (2007).
  - [7] J. Schirmer *et al.*, Nuclear Fusion **46**, S780 (2006).
  - [8] G. D. Conway *et al.*, *8th International Reflectometry Workshop* (IRW8, St. Petersburg, 2007).
  - [9] A. G. Peeters, provided the NEOART code, 1998.
  - [10] S. P. Hirshman and D. J. Sigmar, Nuclear Fusion **21**, 1079 (1981).
  - [11] W. A. Houlberg, K. C. Shaing, S. P. Hirshman, and M. C. Zarnstorff, Physics of Plasmas **4**, 3230 (1997).
  - [12] A. G. Peeters, Physics of Plasmas **7**, 268 (2000).
  - [13] H. W. Müller *et al.*, Journal of Nuclear Materials **337–365**, 605 (2007).
  - [14] V. Rozhansky *et al.*, Plasma Physics and Controlled Fusion **48**, 1425 (2006).

## 5.9 Publication 9

*High-accuracy characterization of the edge radial electric field at ASDEX Upgrade*

Nuclear Fusion 53 (2013) 053005

## High-accuracy characterization of the edge radial electric field at ASDEX Upgrade

E. Viezzer<sup>1</sup>, T. Pütterich<sup>1</sup>, G. D. Conway<sup>1</sup>, R. Dux<sup>1</sup>,  
 T. Happel<sup>1</sup>, J. C. Fuchs<sup>1</sup>, R. M. McDermott<sup>1</sup>, F. Ryter<sup>1</sup>,  
 B. Sieglin<sup>1</sup>, W. Suttrop<sup>1</sup>, M. Willensdorfer<sup>2</sup>, E. Wolfrum<sup>1</sup> and  
 the ASDEX Upgrade Team<sup>1</sup>

<sup>1</sup>*Max-Planck-Institut für Plasmaphysik, EURATOM Association, Boltzmannstr. 2,  
 85748 Garching, Germany*

<sup>2</sup>*Institut für Angewandte Physik, Technische Universität Wien, Association  
 EURATOM-ÖAW, 1040 Vienna, Austria*

**Abstract.** The installation of a new poloidal charge exchange recombination spectroscopy (CXRS) diagnostic at ASDEX Upgrade (AUG) has enabled the determination of the radial electric field,  $E_r$ , using the radial force balance of impurity ions.  $E_r$  has been derived from charge exchange (CX) spectra measured on different impurity species, such as  $\text{He}^{2+}$ ,  $\text{B}^{5+}$ ,  $\text{C}^{6+}$  and  $\text{Ne}^{10+}$ . The resulting  $E_r$  profiles are found to be identical within the uncertainties regardless of the impurity species used, thus, demonstrating the validity of the diagnostic technique. The  $E_r$  profile has been compared to the main ion pressure gradient term, which is found to be the dominant contribution at the plasma edge, thus, supporting that the  $E_r$  well is created by the main ion species. The  $E_r$  profile has been measured in different confinement regimes including L-, I- and H-mode. The depth of the  $E_r$  well and the magnitude of the  $E_r$  shear are correlated with the ion pressure at the pedestal top. The temporal evolution of the measured CX profiles and the resulting  $E_r$  have been studied during an ELM cycle. At the ELM crash, the  $E_r$  minimum is less deep resulting in a reduction of the  $\mathbf{E} \times \mathbf{B}$  shear. Within 2 ms after the ELM crash, the edge kinetic profiles have nearly recovered and the  $E_r$  well is observed to recover simultaneously. In high density type-I ELM mitigated H-mode plasmas, obtained via externally applied magnetic perturbations with toroidal mode number  $n = 2$ , no clear effect on  $E_r$  due to the magnetic perturbations has been observed.

### 1. Introduction

The main baseline scenario for ITER is the H-mode [1], which is characterized by high energy and particle confinement times. H-mode plasmas exhibit an edge transport barrier (ETB) which causes a reduced level of heat and particle transport perpendicular to the magnetic field. The most accepted explanation for the ETB is the existence of a strong shear in plasma flow perpendicular to the magnetic field caused by the radial electric field  $E_r$ . This  $\mathbf{E} \times \mathbf{B}$  velocity shear is thought to be fundamental for edge turbulence suppression [2] thus, aiding the formation of the ETB and leading to the

L-H transition. However, the origin and development of  $E_r$  is still not fully understood although the existence of an  $E_r$  well at the plasma edge is ubiquitous to toroidal magnetic confinement devices such as ASDEX Upgrade [3, 4], DIII-D [5], Alcator C-Mod [6], JET [7], JT-60U [8], TFTR [9], TEXTOR [10], MAST [11], NSTX [12], LHD [13], W7-AS [14], TJ-II [15] and RFX [16]. In order to get a better understanding of the  $\mathbf{E} \times \mathbf{B}$  shear and its connection to the transition from L- to H-mode detailed measurements of  $E_r$  are highly desirable. The most commonly used tool to evaluate  $E_r$  is active charge exchange recombination spectroscopy (CXRS) [17]. At ASDEX Upgrade (AUG), a new high-resolution poloidal CXRS diagnostic utilizing one of the heating beams has been recently installed [18]. The measurements from this system, together with the data from the toroidal edge CXRS diagnostic [19, 18], enables the determination of  $E_r$  using the radial force balance equation, which holds locally for any plasma ion species  $\alpha$ :

$$E_r = \frac{1}{n_\alpha Z_\alpha e} \frac{\partial p_\alpha}{\partial r} + v_{\perp,\alpha} B \quad (1)$$

$$= \frac{1}{n_\alpha Z_\alpha e} \frac{\partial p_\alpha}{\partial r} - v_{\theta,\alpha} B_\phi + v_{\phi,\alpha} B_\theta. \quad (2)$$

Here,  $n_\alpha$  is the density,  $Z_\alpha$  the charge state,  $e$  the elementary charge,  $\frac{\partial p_\alpha}{\partial r}$  the radial pressure gradient of the species and  $v_{\perp,\alpha}$  the species velocity perpendicular to the magnetic field  $B$ . Using the relation  $\mathbf{e}_\perp = -\frac{B_\phi}{B}\mathbf{e}_\theta + \frac{B_\theta}{B}\mathbf{e}_\phi$ , where  $\mathbf{e}_\theta$  and  $\mathbf{e}_\phi$  are the unit vectors in the poloidal and toroidal directions, equation (1) transforms to equation (2). Here,  $v_{\theta,\alpha}$  and  $v_{\phi,\alpha}$  correspond to the poloidal and toroidal rotation velocities of the species, while  $B_\phi$  and  $B_\theta$  denote the toroidal and poloidal magnetic field. The radial force balance relates the lowest-order flow ( $v_{\theta,\alpha}$  and  $v_{\phi,\alpha}$ ) on a magnetic surface to the local  $\mathbf{E} \times \mathbf{B}$  velocity, i.e. the radial electric field, and to the diamagnetic flow (pressure gradient) [20].

The main advantage of deriving  $E_r$  from charge exchange (CX) measurements is the high accuracy in the spatial localization of the measurements. The measured active CX signal is localized in the volume where the lines of sight (LOS) of the CXRS diagnostics intersect the path of the neutral beam particles. Furthermore, a high-accuracy alignment with respect to the edge kinetic profiles is possible, because the temperature  $T_\alpha$  of the ion species  $\alpha$  is part of the CXRS measurements and thus, is rigidly connected to the  $E_r$  profile. Note that  $T_\alpha \approx T_i$ ,  $T_i$  being the main ion temperature, since the energy equilibration time between impurities and main ions is short (several  $\mu\text{s}$ ) compared to local transport time scales ( $\sim 1$  ms) (see appendix). Thus, this quantity is denoted as the ion temperature  $T_i$  throughout the paper.

The high temporal resolution of both edge CXRS diagnostics (2.2 ms) enables the study of the  $E_r$  profile during an ELM (edge-localized mode) [21] cycle. ELMs cause energy losses that lead to large heat and particle loads on the divertor targets, which are high enough to provoke damage and rapid erosion of these targets [22]. For ITER the control or even the full suppression of ELMs is mandatory, while the pedestal top pressure, which affects the global energy confinement through stiff temperatures [23], should not be strongly reduced. One ELM mitigation technique is realized by applying

*High-accuracy characterization of  $E_r$  at AUG*

3

non-axisymmetric magnetic perturbations (MPs) to the plasma edge [24, 25]. In this paper, the influence of MPs on the  $E_r$  profile is presented and the profile with and without the application of MPs is compared.

This paper reports on  $E_r$  profiles derived from CXRS measurements at the plasma edge of AUG. In section 2 a general description on the evaluation of  $E_r$  is provided. CXRS measurements on different impurity species allow the diagnostic technique to be validated and to test whether the  $E_r$  profile is consistently determined. The consistency check is presented in section 3 along with a comparison to Doppler reflectometry measurements. Section 4 discusses the interdependency of  $E_r$  and the main ion pressure gradient term.  $E_r$  profiles measured in different confinement regimes are presented in section 5 and a correlation between the depth of the  $E_r$  well and the pedestal top ion pressure and plasma energy confinement is discussed. The evolution of  $E_r$  during an ELM cycle is described in section 6. The effect of externally applied magnetic perturbations (with toroidal mode number  $n = 2$ ) on the  $E_r$  profile is presented in section 7. Section 8 gives a summary of the findings and discusses the main results.

## 2. Derivation of $E_r$ from CXRS measurements

For an accurate evaluation of  $E_r$  via the radial force balance equation (1), the poloidal and toroidal magnetic fields as well as temperature, density and poloidal and toroidal flow velocity of the observed species are required. The toroidal and poloidal magnetic field are determined from the equilibrium reconstruction of the plasma using CLISTE [26]. The edge CXRS diagnostics provide all of the remaining quantities [17] needed to evaluate  $E_r$ . The ion temperature is determined from the Doppler width, the rotation velocity from the Doppler shift and the impurity density from the spectral radiance of the active CX line. The observed spectral line is usually fitted with 2 Gaussians, one for the active CX component and one for the passive component [18, 27]. The following sign convention is used in this paper:  $\phi$  is counter-clockwise viewed from above and  $\theta$  points vertically downward at the outer midplane. Hence, poloidal rotation velocities, which are vertically upward at the low-field side, are negative (electron diamagnetic direction). In the standard magnetic configuration of AUG  $B_\phi$  is negative and  $B_\theta$  is positive. The plasma current,  $I_p$ , and the neutral beam injection (NBI) are pointing into the positive toroidal direction.

Figure 1 shows example temperature, density and rotation profiles of  $B^{5+}$  ( $n = 7 \rightarrow 6$ ,  $\lambda = 494.467$  nm) obtained with the edge CXRS diagnostics in a type-I ELMy H-mode with  $B_\phi$  on-axis of  $-2.5$  T,  $I_p$  of 1 MA, 5 MW of NBI, 0.8 MW of electron cyclotron resonance heating (ECRH) and a central line-averaged density of  $8 \times 10^{19} \text{ m}^{-3}$ . Good agreement is obtained for the ion temperature and  $B^{5+}$  density profiles. The profiles are ELM-synchronized meaning that the data measured during the occurrence of an ELM crash are excluded. Only measurements 2.2 ms before the onset of an ELM (which corresponds to the time resolution of the edge CXRS diagnostics) are selected if not stated otherwise. To obtain full edge profiles

## High-accuracy characterization of $E_r$ at AUG

a radial plasma sweep [18] of 2 cm is performed during a time window of 800 ms. Note that the measurements in the scrape-off layer (highlighted in gray in figure 1) are omitted as in this region the impurity ion density along with the active CXRS signal drops rapidly and additional background emissions disturb the active spectra making active CXRS measurements unreliable.

To evaluate  $E_r$  each characteristic CXRS profile ( $T_i$ ,  $n_\alpha$ ,  $v_{\theta,\alpha}$  and  $v_{\phi,\alpha}$ ) is fit with a spline function. The resulting fits are then used for the determination of  $E_r$ . Note that usually the  $T_i$  and  $n_\alpha$  profiles measured by the toroidal system are used in the fitting procedure since the toroidal diagnostic has a higher radial resolution (3 mm [19] compared to 5 mm [18] for the poloidal system), which enables the gradients in the profiles to be determined to higher accuracy. In the considered discharge (#26598) data for  $\rho_{pol} < 0.94$  from the poloidal system have also been used for fitting  $T_i$  and  $n_\alpha$ .

In order to reduce uncertainties due to the magnetic equilibrium and to optimize the radial profile alignment [28] the following procedure is performed: the measurements obtained with the toroidal and poloidal system are aligned via the  $T_i$  and  $n_\alpha$  profile. The relative alignment of the CXRS systems is of minor importance for the positioning of  $E_r$ , as in the plasma edge the evaluation of  $E_r$  is dominated by the poloidal impurity ion rotation contribution (see figure 2). While the radial resolutions of the diagnostics are 3 mm and 5 mm, respectively, the alignment is possible to a higher accuracy due to the steepness of the gradients, which are well resolved by the measurements. To align the CXRS profiles relative to the electron profiles it is assumed that the position of the steepest gradients in  $T_i$  coincide with those in the electron temperature,  $T_e$ , measured by the electron cyclotron emission (ECE) [29] and Thomson scattering (TS) [30] systems. While this assumption is not relying on fundamental physics, a highly reproducible radial alignment is found. The plasmas analyzed in the present work are in the collisionality regime that is found to provide a sufficient coupling between the electrons and ions such that  $T_e$  is approximately  $T_i$  [31]. This is also supported by comparing the thermal equilibration times to the local transport time (see appendix). As the separatrix position

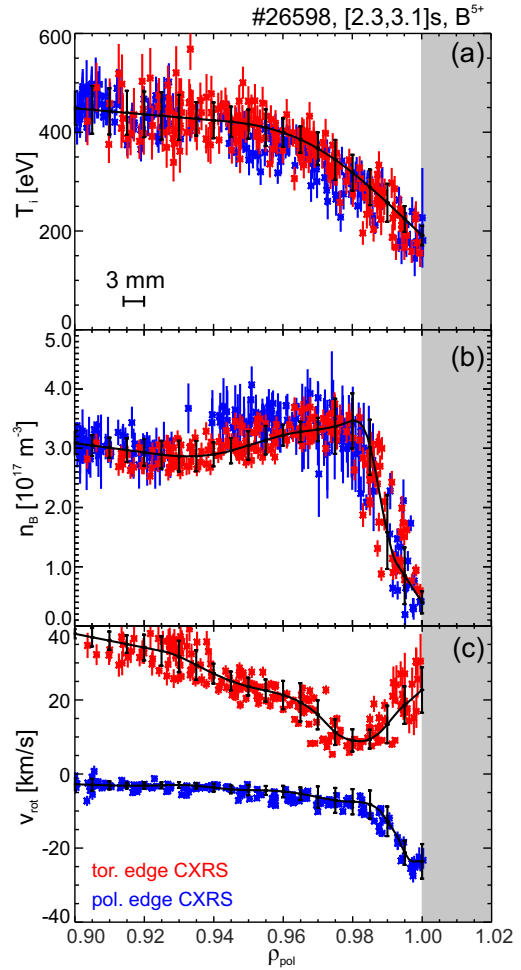


Figure 1: CX profiles obtained from measurements on  $B^{5+}$  in H-mode: (a) ion temperature, (b)  $B^{5+}$  density, (c) toroidal and poloidal rotation velocity.

*High-accuracy characterization of  $E_r$  at AUG*

## 5

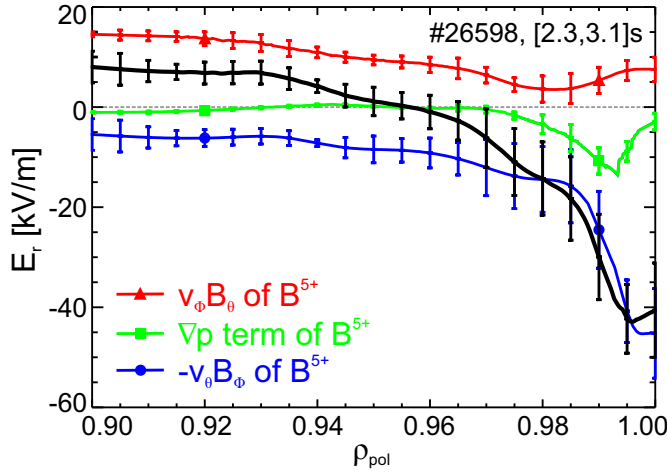


Figure 2: Radial electric field profile derived from CX measurements on  $B^{5+}$ :  $E_r$  in black, toroidal rotation contribution in red, pressure gradient term in green and poloidal rotation contribution in blue.

is rigidly connected to the  $T_e$  profile via a power balance and parallel heat transport argument [32], also the relative alignment to the separatrix position is performed. To minimize the uncertainty of the separatrix position from the magnetic reconstruction, the required  $T_e$  value at the separatrix is  $\approx 100$  eV consistent with studies using a 1-D heat conduction model [32]. The  $T_i$  profile is then aligned relative to the  $T_e$  profile (and thus, relative to the separatrix) such that the steep gradient regions match each other. The accuracy of this relative profile alignment is estimated to 2 – 3 mm as  $T_e$  is closely connected to the separatrix position. The alignment of the profiles is simultaneously performed with respect to the electron density,  $n_e$ , profile as the TS system has identical measurement volumes for both  $n_e$  and  $T_e$ . The  $n_e$  measurements from TS are complemented by those obtained with the lithium beam (LIB) diagnostic [33, 34], which are shifted such that they match those of TS, and the interferometry system [35]. The latter is used to constrain the electron density at the pedestal top. The various diagnostics measure in different sectors of the tokamak vessel and the profiles are aligned radially assuming a toroidally symmetric equilibrium. Note that the shifts applied for the profiles are within the radial resolution of each diagnostic. This method enables the determination of the position of  $E_r$  relative to the electron profiles and to the separatrix position with an accuracy of 2 – 3 mm (indicated by a horizontal error bar in figure 1(a)).

Figure 2 shows the  $E_r$  profile deduced from the profiles of  $B^{5+}$  in figure 1 in black. In the ETB a negative  $E_r$  well, a narrow, localized minimum close to the separatrix, is found. Towards the plasma core, the magnitude of  $E_r$  decreases and changes sign (i.e. becomes positive). The error bars shown in figure 2 are calculated via Gaussian error propagation using the standard deviation of the measured data in a small radial interval ( $\pm 0.005$  in  $\rho_{pol}$ , which is of the order of the radial resolution of the diagnostics). In figure 2 the individual terms in the radial force balance equation (1) are colour-

## High-accuracy characterization of $E_r$ at AUG

## 6

coded: the pressure gradient term (green), the toroidal rotation term (red) and the poloidal rotation term (blue). In the radial force balance of impurity ions the poloidal rotation term is the main contribution for the evaluation of the  $E_r$  well. Towards the plasma core  $E_r$  is dominated by the toroidal rotation velocity.

### 3. Validation of the $E_r$ measurements

#### 3.1. Comparison of different impurity ions

Performing CX measurements on different impurity species allows the validation of the diagnostics and a consistency check of  $E_r$  to be obtained since  $E_r$  must be the same for all impurities [36]. Thus, all analyses must arrive at the same  $E_r$  profile regardless of the impurity species used. For this purpose the discharge described in section 2 was repeated to obtain CX measurements on  $\text{He}^{2+}$  ( $n = 4 \rightarrow 3$ ,  $\lambda = 468.571$  nm) and  $\text{C}^{6+}$  ( $n = 8 \rightarrow 7$ ,  $\lambda = 529.059$  nm). The resulting  $E_r$  profiles are shown in figure 3(a). Within the uncertainties, good agreement between the three different impurity species is obtained, not only in the minimum of the  $E_r$  well, but also in the profile shape towards the plasma core. In a separate discharge a neon puff was included to cross-check the  $E_r$  profile with a fourth species. Due to the spectral range covered by the edge CXRS diagnostics (12.19 nm for the toroidal system and 7.84 nm for the poloidal system at a central wavelength of  $\lambda = 527.5$  nm), simultaneous measurement of both  $\text{C}^{6+}$  and  $\text{Ne}^{10+}$  ( $n = 11 \rightarrow 10$ ,  $\lambda = 524.897$  nm) is possible. The resulting  $E_r$  profiles are shown in figure 3(b). The  $E_r$  profile is reproducible within the uncertainties regardless of the trace impurity used for the analysis.

For all impurity species analyzed in H-mode plasmas, the poloidal rotation contribution is dominant in the radial force balance. In figure 4 the individual impurity ion contributions at the radial position of the  $E_r$  minimum are plotted against the minimum of the  $E_r$  well. Note that for the Ne-seeded phase the  $\text{C}^{6+}$  contributions

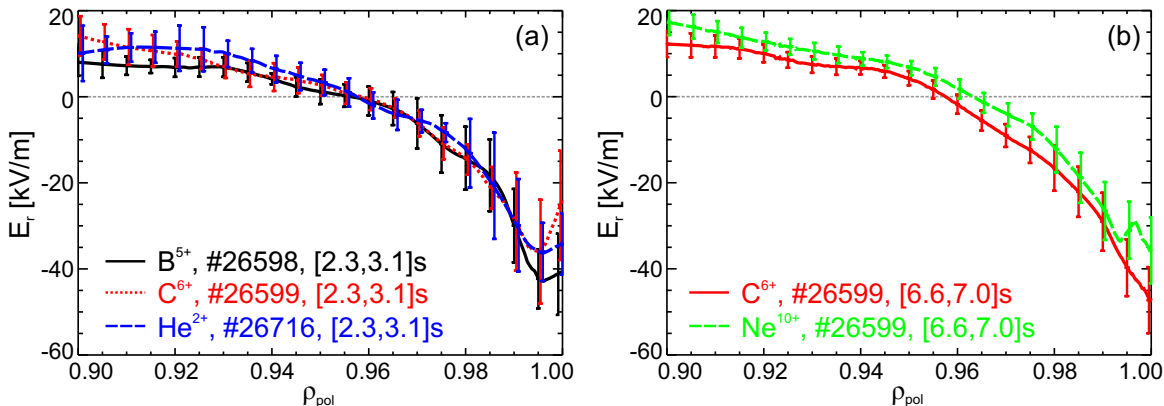


Figure 3: Radial electric field profile determined from CX measurements on different impurity species: (a)  $\text{B}^{5+}$  in black,  $\text{C}^{6+}$  in red (dotted line),  $\text{He}^{2+}$  in blue (dashed line), (b)  $\text{C}^{6+}$  in red and  $\text{Ne}^{10+}$  in green (dashed line) during the Ne-seeded phase.

*High-accuracy characterization of  $E_r$  at AUG*

7

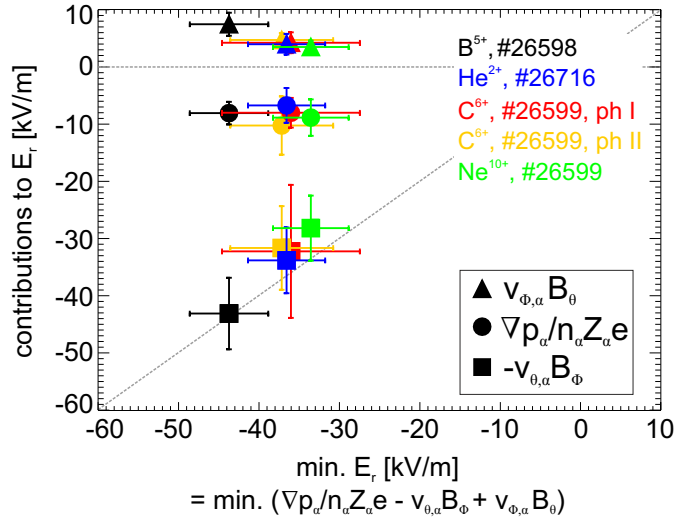


Figure 4: Individual impurity ion contributions for the evaluation of  $E_r$  versus minimum of  $E_r$  in H-mode: for impurity ions the poloidal rotation term is the main player in the evaluation of  $E_r$ . The label ‘ $C^{6+}$ , #26599, ph I’ corresponds to the non-seeded phase and ‘ $C^{6+}$ , #26599, ph II’ to the Ne-seeded phase.

correspond to the position of the minimum of  $E_r$  derived from the  $Ne^{10+}$  measurements, as no clear minimum is visible for  $C^{6+}$ . For all impurities, the toroidal rotation term and the pressure gradient term have almost the same value in absolute magnitude and cancel each other, while the poloidal impurity ion rotation term is the dominant contribution for the evaluation of the depth of the  $E_r$  well. This also indicates that the poloidal rotation is at neoclassical levels [37, 38].

### 3.2. Comparison to Doppler reflectometry measurements

The  $E_r$  profile derived from the CXRS measurements has been compared to Doppler reflectometry (DR) measurements. In contrast to CXRS, which measures the impurity particle velocity and makes use of the radial force balance equation to evaluate  $E_r$ , the DR diagnostic measures the perpendicular fluid velocity of the electron density fluctuations which can be related to the local  $\mathbf{E} \times \mathbf{B}$  velocity. The DR technique [39] is based on the backscattering of an oblique microwave beam with respect to the cut-off layer normal. The spectrum of the backscattered microwave is Doppler shifted by  $\omega_D = \mathbf{u} \cdot \mathbf{k}$  and gives information on the velocity of the plasma fluctuations,  $\mathbf{u}$ , and on its wavenumber  $\mathbf{k}$ . By aligning the reflectometer perpendicular to the magnetic field such that the antenna is only sensitive to the perpendicular wavenumber, the Doppler shift results in  $\omega_D = u_\perp k_\perp$ , where  $u_\perp$  is the perpendicular velocity of the electron density fluctuations and  $k_\perp$  their perpendicular wavenumber. With knowledge of the perpendicular wavenumber,  $u_\perp$  is determined directly from the measured Doppler shift  $\omega_D$ . The perpendicular velocity corresponds to the sum of the  $\mathbf{E} \times \mathbf{B}$  velocity of the plasma ( $v_{\mathbf{E} \times \mathbf{B}}$ ) and the phase velocity of the density fluctuations ( $v_{ph}$ ),  $u_\perp = v_{\mathbf{E} \times \mathbf{B}}$

*High-accuracy characterization of  $E_r$  at AUG*

8

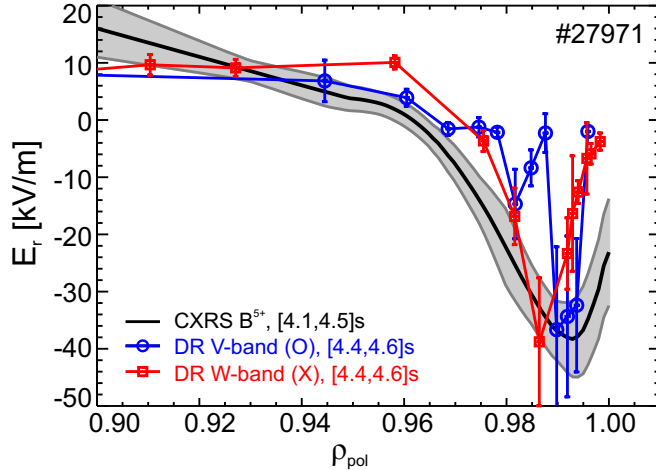


Figure 5: Radial electric field profile derived from CXRS and DR measurements.

$+ v_{ph}$ . Usually,  $v_{ph}$  is assumed to be negligible: an assumption that is supported by comparative measurements performed at multiple devices e.g. W7-AS [40], TJ-II [41], DIII-D [42] and AUG in the plasma core [4]. Hence,  $E_r$  is given by  $E_r = u_\perp B$ . At AUG two DR diagnostics are installed, a dual channel V-band (50 – 75 GHz) system [43] and a W-band (75 – 110 GHz) system [44, 45] with steppable launching frequencies (O-mode and X-mode polarization).

In order to compare the  $E_r$  profiles dedicated discharges have been conducted. The experiment presented was performed in H-mode with  $B_\phi = -2.3$  T,  $I_p = 0.8$  MA, 2.5 MW NBI, 1.7 MW ECRH and a central line-averaged density of  $5.7 \times 10^{19} \text{ m}^{-3}$ . A radial plasma sweep was included to provide detailed edge CXRS profiles. The plasma density was regulated such that both Doppler systems could resolve the edge pedestal. Figure 5 shows the  $E_r$  profile derived from CXRS measurements on  $B^{5+}$  in black and the profile obtained with DR in blue (V-band, O-mode polarization) and red (W-band, X-mode polarization). While for the CXRS measurements the radial resolution is increased by performing a radial plasma sweep, the DR profiles result from frequency sweeps over a time period of 200 ms. During these sweeps the plasma was in a steady-state phase. Good agreement is found for the depth of the  $E_r$  well and its radial position is consistent within the uncertainties of the diagnostics. The differences in the width of the  $E_r$  well result in different levels of  $E_r$  shear and might be explained by the radial resolution of each system. While the DR diagnostics rely on the local density profile to determine the exact measurement location, the CXRS measurements are fixed in real space. In addition, the location of the DR measurements might be sensitive to fluctuations of the edge density profile, which could explain the non-monotonic appearance of the  $E_r$  profiles from DR (i.e. at  $\rho_{pol} \sim 0.985$   $E_r$  decreases to almost 0 and then increases again). These fluctuations might affect the propagation of the electromagnetic wave and thus, the measurement location might be shifted from the actual position. Small changes in the local density profile can affect the radial localization of the  $E_r$  profile. The radial resolution of the DR systems depends on the density gradient, the frequency and the

*High-accuracy characterization of  $E_r$  at AUG*

polarization. For the AUG DR diagnostics the radial resolution is of the order  $\lesssim 0.01$  in  $\rho_{pol}$ , while for the edge CXRS systems it is approximately 0.006. Further comparative measurements are needed to quantify the difference in the  $E_r$  shear.

In the following the  $E_r$  profile derived from CXRS is presented in detail as it is intrinsically aligned to the  $T_i$  profile. The alignment to the kinetic electron profiles and to the separatrix position is performed straightforward, thus, enabling an accurate comparison to the gradients of the main ion species.

#### 4. Comparison of $E_r$ and the main ion pressure gradient term

The radial electric field is supposed to be driven by the main ions, typically deuterium at AUG, and not by the impurities. However, measurements of the main ion population using CXRS are difficult to interpret due to large background emissions and the beam halo [17]. Usually, CXRS measurements are performed on impurity ions as the diagnostic method is easily applicable. Since  $E_r$  is the same for every species, the profile derived from the impurity ions allows information on the main ion species to be obtained indirectly. For this purpose, an estimate of the pressure gradient term of deuterium is calculated using the assumption of quasi-neutrality and two assumptions on the ion density profile: (i) constant dilution,  $n_i \propto n_e$  ( $n_i$  being the ion density and  $n_e$  the electron density), leading to

$$\frac{\nabla p_i}{n_i} = \frac{\nabla(n_i T_i)}{n_i} = \frac{C \nabla n_e}{C n_e} T_i + \nabla T_i = \frac{\nabla n_e}{n_e} T_i + \nabla T_i \quad (3)$$

and (ii) radially varying dilution with  $n_i = n_e(1 - \sum_\alpha Z_\alpha c_\alpha)$ ,  $c_\alpha$  being the radially dependent concentration of the impurity species  $\alpha$ . The  $n_i$  profile has been calculated using the boron and carbon concentrations as measured with CXRS in subsequent discharges. The radial concentration of boron (carbon) changes from 0.2 % to 0.5 % (0.4 % to 0.6 %) over the pedestal region.

Figure 6(a) depicts the  $E_r$  profile in black obtained from CXRS on  $B^{5+}$ , while the pressure gradient term of deuterium is shown in red. Here,  $T_i$  is used from the CXRS measurement, while  $n_e$  is taken from measurements with TS, the LIB diagnostic and the interferometry system. Note that the  $T_i$  and  $n_e$  profiles have been aligned relative to each other as described in section 2. The modification of the main ion pressure gradient term due to a non-constant dilution (see blue dashed line in figure 6(a)) is found to be small (the maximum difference is less than 1.5 kV/m).

The pressure gradient term of deuterium is very similar to  $E_r$  indicating that for the main ions the pressure gradient term is the main contribution in the radial force balance. From this comparison an estimate of the perpendicular flow velocity of the main ions,  $v_{\perp,i}$ , can be calculated via a rearrangement of equation (1):

$$\Rightarrow v_{\perp,i} = \frac{1}{B} \left( E_r - \frac{1}{e} \left( \frac{\nabla n_i}{n_i} T_i + \nabla T_i \right) \right) \quad (4)$$

In figure 6(b) the calculated main ion flow velocity perpendicular to the magnetic field is shown. The perpendicular main ion flow is positive, i.e. in the ion diamagnetic drift

High-accuracy characterization of  $E_r$  at AUG

10

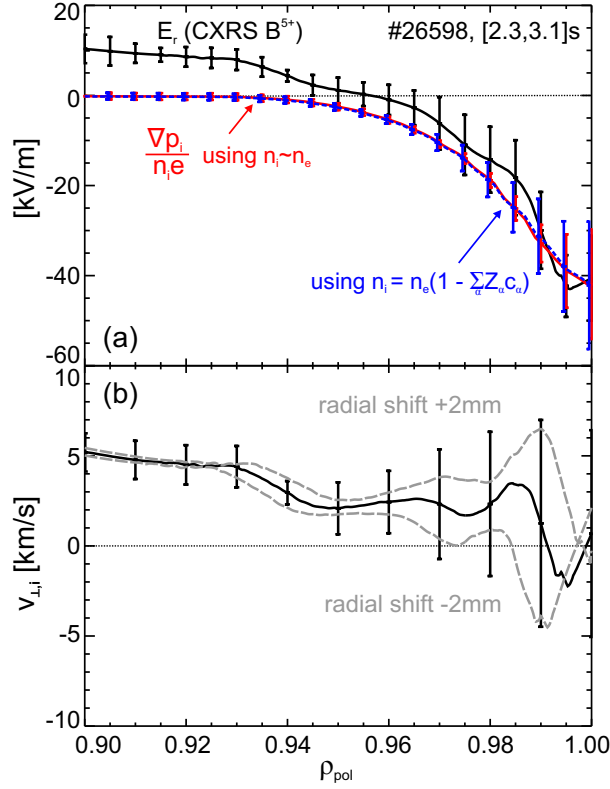


Figure 6: (a) Comparison of  $E_r$  (black curve) to an estimate of the main ion pressure gradient term assuming constant dilution (red curve) and correcting for the effect of impurities (blue dashed line), (b) derived perpendicular main ion velocity. The dashed lines in the lower panel show the effect of a relative shift between electron and ion profiles by  $\pm 2$  mm.

direction. Note that  $v_{\perp,i}$  is small in magnitude. Within an uncertainty of 5 km/s, it approaches  $v_{\perp,i} = 0$  inside the ETB, similar to results obtained at Alcator C-Mod [6]. The dashed lines in figure 6(b) show the effect of a radial shift of  $\pm 2$  mm between  $n_e$  and  $T_i$  measurements.

Helium plasmas provide the opportunity to obtain direct information on the main ion species by using CXRS on He<sup>2+</sup>. These measurements have been performed in an H-mode discharge with  $B_\phi = -2.5$  T,  $I_p = 1.0$  MA, 0.5 MW ECRH, 9.2 MW deuterium NBI heating and a central line-averaged density of  $1.1 \times 10^{20}$  m<sup>-3</sup>. At the plasma edge  $E_r$  is found to be dominated by the pressure gradient term of He<sup>2+</sup> while the Lorentz force term is small and approaches zero close to the separatrix (see figure 7(a)). In the analysis the plume effect is not taken into account, however, the contribution of the helium plume is expected to be small at the plasma edge [17]. This is also confirmed by independent density measurements using the LIB, TS and interferometry diagnostics: as expected, the helium density is found to be half the electron density and the gradients match, i.e.  $\nabla n_i = \nabla n_e / 2$ . Figure 7(b) shows the measured helium density profile, along with a fit (red line) and a fit to the electron density profile (blue dashed line). The fit

High-accuracy characterization of  $E_r$  at AUG

11

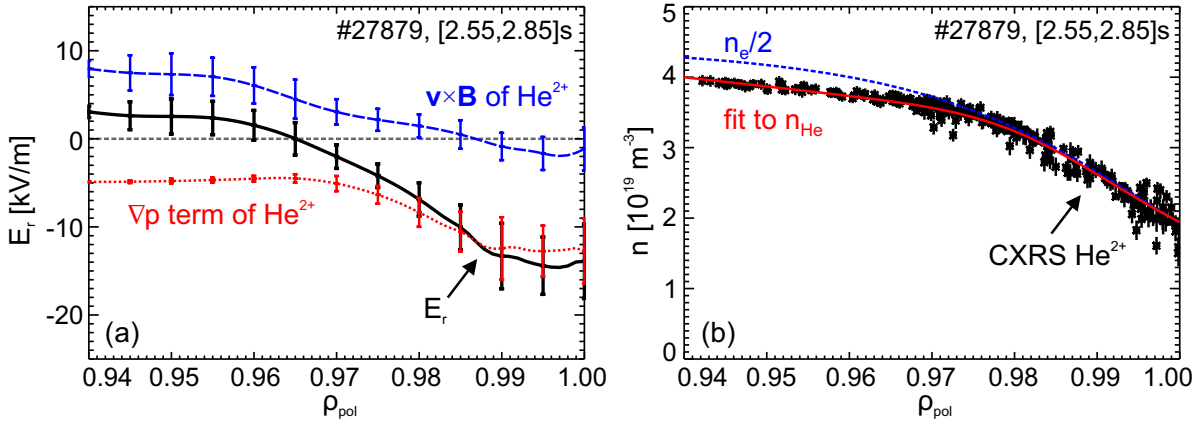


Figure 7: CXRS measurements in a helium plasma: (a)  $E_r$  profile in black, pressure gradient term of  $\text{He}^{2+}$  in red (dotted line) and  $v \times B$  term of  $\text{He}^{2+}$  in blue (dashed line), (b) measured helium density profile in black, fit in red and fit to electron density profile in blue (dashed line). The fit to  $n_e$  is scaled by a factor of 2.

to  $n_e$  has been scaled by a factor of 2.

These results are in agreement with neoclassical theory [20] which predicts that to zeroth order, and in case of small toroidal rotation velocities, the edge radial electric field is balanced by the ion pressure gradient normalized to the ion density [46]. Quantitative comparisons between measurements and neoclassical codes are beyond the scope of this paper and will be presented in a subsequent publication. Investigations on this subject have been performed in [47], which concludes that in H-mode the depth of the edge radial electric field is well described by neoclassical theory.

## 5. $E_r$ profiles in different confinement regimes

Previous work on several devices has demonstrated a connection between edge  $E_r$  profiles and global plasma energy confinement [48, 49, 50, 4, 6, 51]. This connection has also been examined in AUG discharges using the data from the new edge CXRS systems. In order to explore this over the widest range of plasma parameters possible,  $E_r$  profiles have been collected from many different types of discharges including L-, I-, H- and improved H-mode plasmas. Figure 8(a) shows the  $E_r$  profile obtained in an L-mode deuterium plasma with  $B_\phi$  on axis of -2.5 T,  $I_p$  of 1 MA and 1 MW NBI heating. The CX measurements were performed on  $\text{He}^{2+}$ . In L-mode the radial electric field is small in magnitude and exhibits weak gradients. In this confinement regime both impurity ion velocity components are important for the evaluation of  $E_r$ , while the pressure gradient term of the impurity ion is almost negligible (cf. figure 8(a)). I-mode plasmas [52], originally referred to as ‘improved L-mode’ at ASDEX Upgrade [53], are characterized by similar energy confinement times as the H-mode, however, the particle confinement is near L-mode levels. In the I-mode regime (see figure 8(b)) the depth of the  $E_r$  well is found to be intermediate between L- and H-mode and dominated

High-accuracy characterization of  $E_r$  at AUG

12

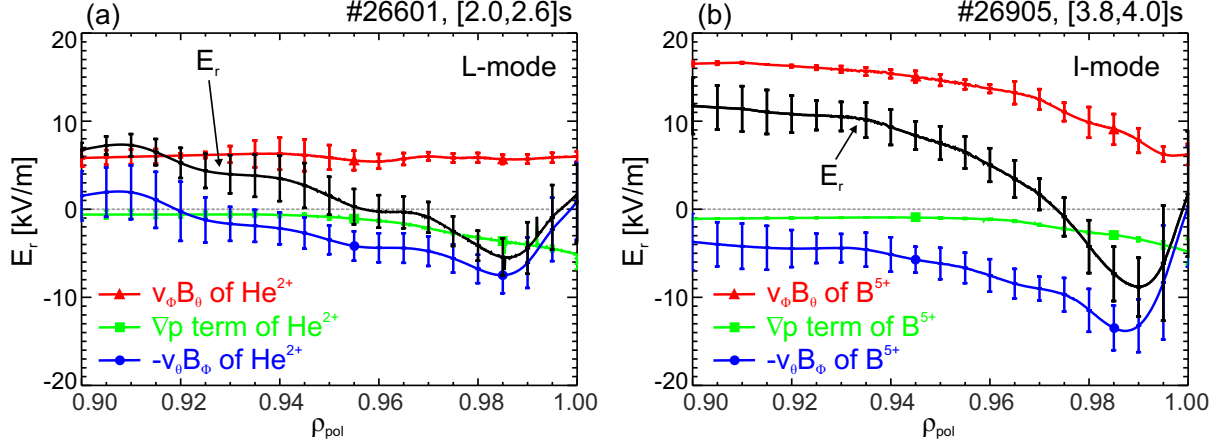


Figure 8: Radial electric field profile in (a) L-mode and (b) I-mode.

by the poloidal impurity ion rotation contribution. The radial electric field has also been studied in improved H-mode discharges with nitrogen ( $N_2$ ) seeding. At AUG an improved confinement has been observed when using nitrogen as a low-Z radiator to protect the divertor [55]. In these plasmas the CX measurements are performed on a nitrogen line, i.e.  $N^{7+}$  ( $n = 9 \rightarrow 8$ ) at  $\lambda = 566.937$  nm. Figure 9(a) shows the resulting  $E_r$  profiles obtained in two phases with different NBI and ECRH power.  $N_2$  seeding was applied throughout the whole discharge and an increase in the pedestal top pressure is concomitant with an increase in the energy confinement (moving from phase I to phase II). The  $E_r$  well is observed to deepen with higher pedestal top pressures.

The effect of increasing the NBI heating was studied in the improved H-mode

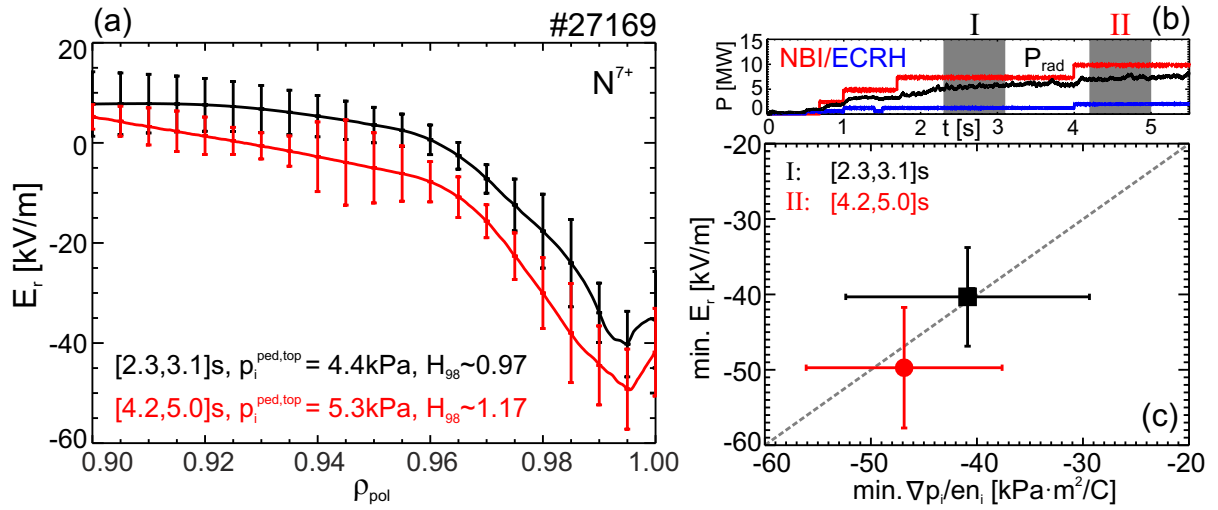


Figure 9: (a) Radial electric field profiles obtained in an improved H-mode discharge with different pedestal top ion pressures  $p_i^{ped,top}$  (at  $\rho_{pol} = 0.97$ ) and thus, different H/L scaling factors  $H_{98}(y,2)$  [54], (b) time trace of NBI, ECRH and radiation power ( $P_{rad}$ ), (c) minimum of  $E_r$  versus minimum of main ion pressure gradient term.

*High-accuracy characterization of  $E_r$  at AUG*

13

discharge and two different phases with 7.5 and 10 MW NBI (see figure 9(b)) were analyzed. Increasing the momentum has no observable effect on the relation between the radial electric field and the pressure gradient term of the main ions at the plasma edge (cf. figure 9(c)). Note that for the calculation of the main ion pressure gradient term, the dilution due to N<sub>2</sub>-seeding was taken into account. This result supports that in H-mode  $E_r$  assumes a value such that the  $E_r$  well is in balance with the gradients in the main ion species and the perpendicular flow of the main ions vanishes at the plasma edge.

Combining the results obtained in L-, I-, H-mode and improved H-mode plasmas shows that the minimum of  $E_r$  is correlated with the ion pressure at the pedestal top  $p_i^{ped,top}$  ( $\rho_{pol} = 0.97$ ). Figure 10(a) shows the minimum of  $E_r$  as a function of  $p_i^{ped,top}$ . As the gradient of the edge pedestal pressure is strongly correlated with the value at the pedestal top [31],  $p_i^{ped,top}$  is a good approximation of the ion pressure gradient at the  $E_r$  minimum. Data obtained in impurity seeded H-modes (including the improved H-mode discharge) are marked in gray in figure 10. A general trend is observed that for higher pedestal top pressures the  $E_r$  well is deeper, further confirming that  $E_r$  corresponds to the main ion pressure gradient term. Figure 10(b) shows the interdependence of the energy confinement factor  $H_{98}(y,2)$  with respect to the ITER confinement scaling [54] and  $p_i^{ped,top}$ . The energy confinement increases for higher pedestal top ion pressures as a result of stiff  $T_i$  profiles. In figure 11(a) the minimum of  $E_r$  is plotted against the

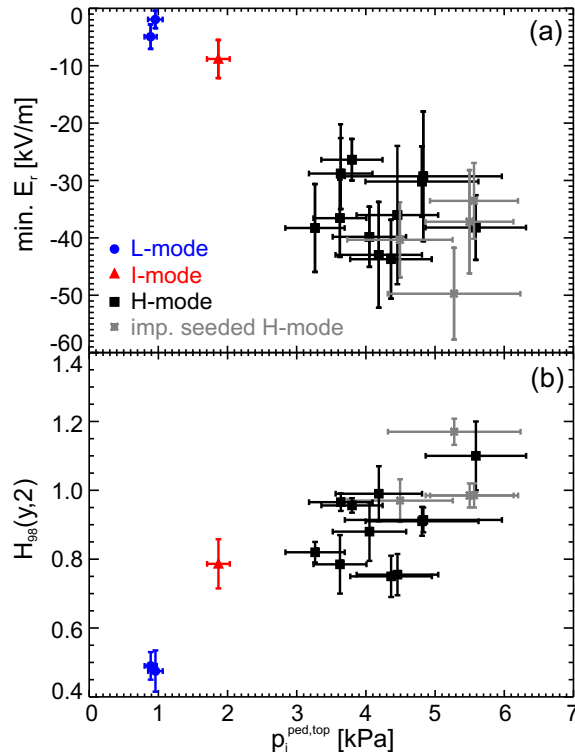


Figure 10: (a) Depth of  $E_r$  well as a function of pedestal top ion pressure  $p_i^{ped,top}$  (at  $\rho_{pol} = 0.97$ ), (b) energy confinement factor  $H_{98}(y,2)$  versus  $p_i^{ped,top}$ .

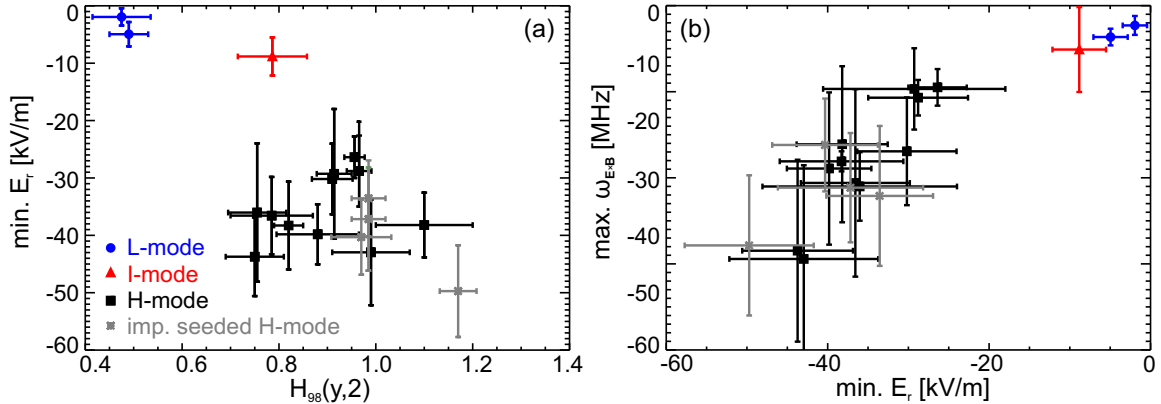


Figure 11: (a) Depth of  $E_r$  well as a function of the energy confinement factor  $H_{98}(y,2)$ , (b) maximum  $\mathbf{E} \times \mathbf{B}$  shearing rate versus  $E_r$  minimum.

global energy confinement factor  $H_{98}(y,2)$ . Moving from L- to I- to H-mode the  $E_r$  well deepens and the energy confinement of the plasma increases. However, within the H-mode the scatter is substantial and no direct correlation between the depth of the  $E_r$  well and  $H_{98}(y,2)$  is found. The observation of deep  $E_r$  wells at lower energy confinement factors ( $\sim 0.75$ ) is consistent with higher pedestal top pressures at lower  $H_{98}(y,2)$  (cf. figure 10(b)). Since the maximum  $\mathbf{E} \times \mathbf{B}$  shearing rate (defined as  $\omega_{E \times B} = \frac{r}{q} \frac{\partial}{\partial r} (\frac{q}{r} \frac{E_r}{B})$  [56]) is strongly correlated to the  $E_r$  minimum (see figure 11(b)),  $\omega_{E \times B}$  and the energy confinement factor have a similar relationship as the minimum of  $E_r$  and  $H_{98}(y,2)$ .

Within the framework of turbulence reduction theory through  $\mathbf{E} \times \mathbf{B}$  shear [2], the following picture develops from these measurements: for constant  $E_r$  well widths [57, 6], deeper  $E_r$  wells have higher  $E_r$  shearing rates which increase the efficiency of turbulence reduction when moving from L- to H-mode. This leads to higher pedestal top pressures, which is correlated to the global plasma confinement. Hence, also the magnitude of the  $E_r$  shear is correlated to the energy confinement and increases from L- to H-mode [58]. Figure 12 shows (a) the  $E_r$  profiles and (b) the calculated  $E_r$  shear obtained in the different confinement regimes. In the L- and I-mode regime the shear is weak (smaller than in H-mode) and comparable to the width of the turbulence spectrum ( $\sim 100 - 200$  kHz at the plasma edge [59]), while in the ETB of the H-mode the  $E_r$  shearing rate reaches values of up to 3 MHz. It is worth noticing that in H-mode the maximum shear coincides with the maximum ion pressure gradient,  $\nabla p_i$  (see figure 12(c)), calculated using the  $n_e$  profile, giving confidence that the radial alignment of the gradients and  $E_r$  is very accurate for the present work. Note also that the maximum in the  $E_r$  shearing rate, or alternatively the steepest  $\nabla p_i$ , lies in the inner part of the  $E_r$  well, indicating that the negative shear region might be the important region for turbulence suppression consistent with previous results [60, 61, 4].

For the transition into H-mode it remains unclear whether there is a threshold of eddy size reduction leading to reduced turbulence and transport or a continual reduction of transport as the shearing rate increases.

*High-accuracy characterization of  $E_r$  at AUG*

15

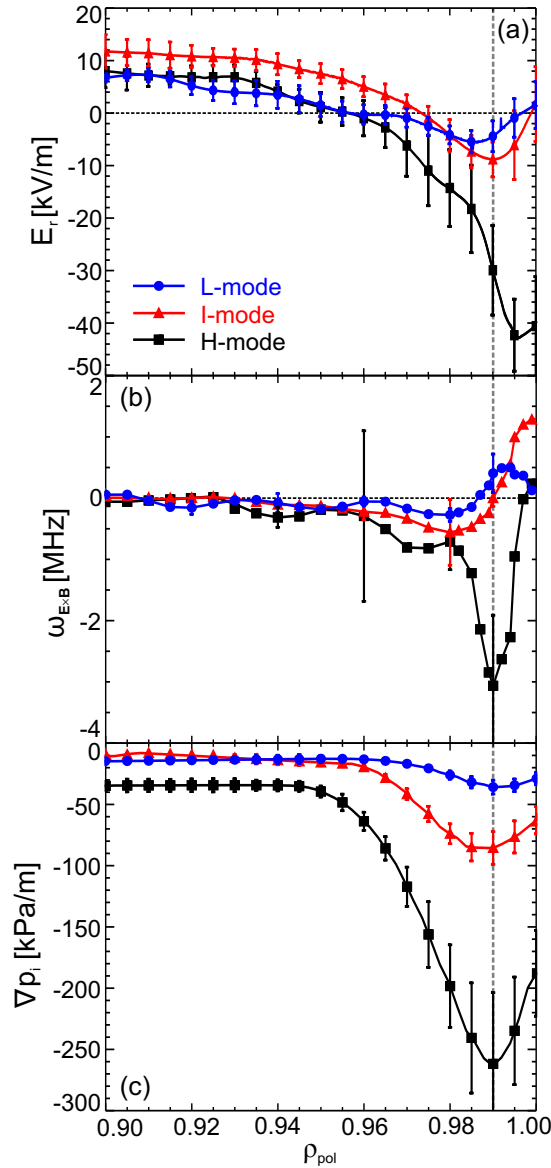


Figure 12: (a)  $E_r$  in L-, I- and H-mode and (b) resulting  $E_r$  shear. For better clarity the uncertainties are only shown for distinct radial positions. (c) Main ion pressure gradient,  $\nabla p_i$ , in different confinement regimes.

## 6. Temporal evolution of $E_r$ during an ELM cycle

Due to the occurrence of edge-localized modes (ELMs) the steep edge gradients of H-modes flatten transiently during each event. The temporal resolution of the edge CXRS diagnostics (2.2 ms) at AUG enables a synchronization of the data with respect to the onset of an ELM. Thus, the behaviour of the radial electric field during the ELM crash can be analyzed in detail. To this end, the data from a set of reproducible type-I ELM cycles measured in a time window of 700 ms, during which the plasma was radially moved through the views of the LOS to obtain complete edge profiles, has been sorted

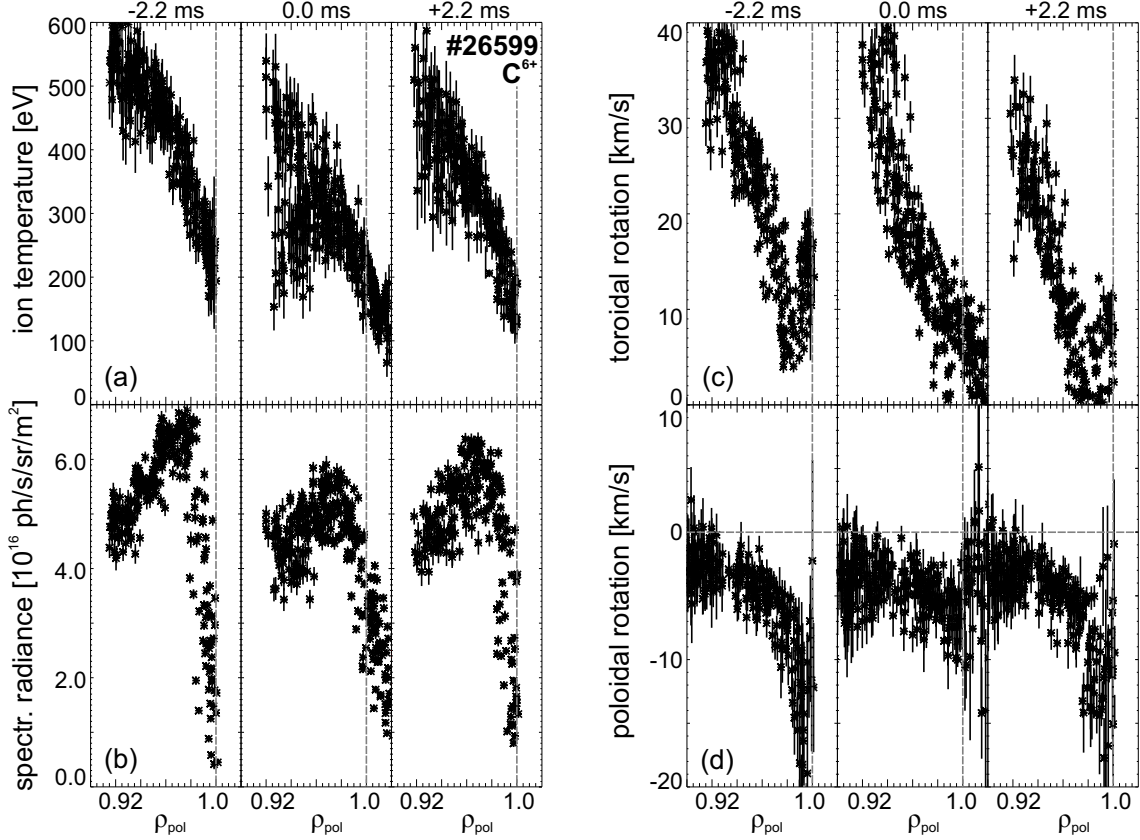


Figure 13: Evolution of CXRS measurements at different time points during an ELM cycle: (a)  $T_i$ , (b) spectral radiance of the active CX line, (c) toroidal rotation and (d) poloidal rotation. The labels ‘-2.2 ms’, ‘0.0 ms’ and ‘+2.2 ms’ denote the relative time to the closest ELM. The profiles originate from a time window of 700 ms in which the plasma was radially moved through the views of the LOS. The vertical dashed line in each subfigure indicates the separatrix position.

and mapped onto a time grid relative to the time of the closest ELM. The discharge is identical to the one discussed in section 2. The ELM frequency was constant at  $\sim 80$  Hz. Figure 13 shows the (a)  $T_i$ , (b) spectral radiance of the active CX line, (c) toroidal rotation and (d) poloidal rotation velocity profiles measured on  $C^{6+}$  during the ELM cycle. The labels ‘-2.2 ms’, ‘0.0 ms’ and ‘+2.2 ms’ of figure 13 denote the relative time to the closest ELM at which the measurements were taken. Before the ELM  $T_i$  and the CX line intensity exhibit a strong gradient at the edge, while the toroidal rotation has a minimum localized at the pedestal top. The feature in the toroidal rotation profile has been reported in [19] and is further investigated in [37, 62]. The poloidal rotation on the other hand exhibits a local minimum close to the separatrix. During the ELM (labeled with ‘0.0 ms’ in figure 13) the steep gradients flatten and the dips in both the toroidal and poloidal rotation vanish. Note that the integration time of the edge CXRS systems might be too long to quantitatively judge the behaviour of the impurity ion profiles, but the qualitative behaviour can be described. During the inter-ELM phase the signal

High-accuracy characterization of  $E_r$  at AUG

17

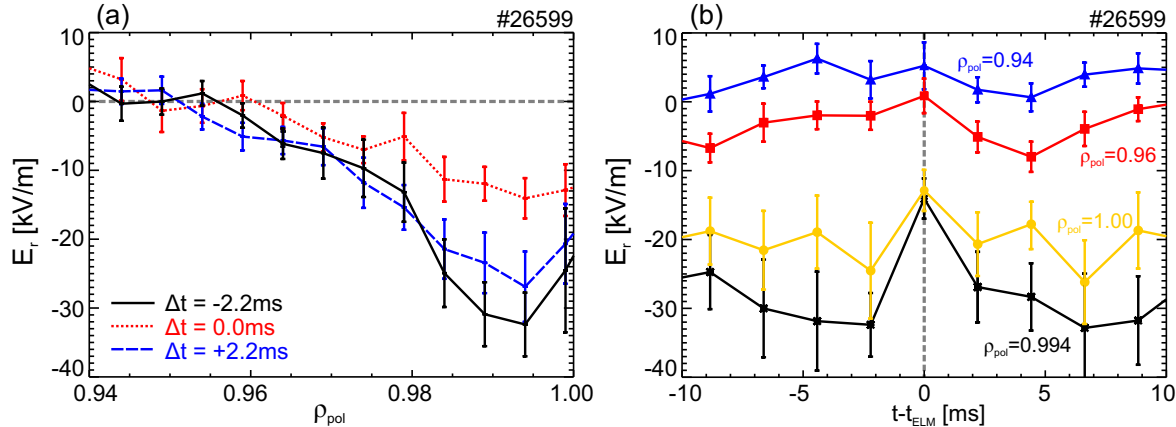


Figure 14: (a) Radial electric field profiles before, during and after an ELM, (b)  $E_r$  at distinct radial positions during an ELM cycle.

in the scrape-off layer is not sufficient to analyze the CXRS spectral line, but when the ELM occurs the signal increases, indicating that the impurities are expelled, and the fits are trustworthy. The profiles start to recover and the typical pedestal structure is visible again already 2.2 ms after the ELM in agreement with experimental studies performed at DIII-D [63] and consistent with time scales of the electron profiles observed at AUG [64].

Figure 14(a) shows the resulting  $E_r$  profiles. The radial electric field is the deepest shortly before the ELM (black profile), while during the ELM crash the profile decreases in the ETB by up to a factor of 3 (red dotted profile), consistent with DR measurements [65]. The collapse of  $E_r$  results in a reduction of the  $E_r$  shear across the whole ETB. The destruction of the  $E_r$  shear layer at the ELM crash has also been observed in MAST using fast CXRS measurements with a time resolution of 200  $\mu\text{s}$  [66]. Shortly after the ELM (+2.2 ms, blue dashed profile in figure 14(a)) the profile recovers and the  $E_r$  well reforms, reaching its initial depth 4 – 6 ms after the ELM event (cf. figure 14(b)), consistent with time scales observed at DIII-D [63]. Figure 14(b) shows the temporal evolution of  $E_r$  at different radial locations. Further inside the plasma  $E_r$  is almost not affected with only slight modifications during the ELM crash, while in the ETB the  $E_r$  well is strongly reduced. Note that the  $E_r$  well might even vanish for a brief time period that is too short to be detected by the diagnostics.

Figure 15 shows the contributions of the individual terms of the radial force balance equation to the  $E_r$  well during the ELM cycle. Throughout the entire ELM cycle the poloidal rotation term of the impurity ions is the dominant contribution for the evaluation of the  $E_r$  well. The temporal evolution of the main ion pressure gradient term is shown in yellow (triangles) in figure 15. The agreement in both the magnitude and evolution is remarkably good and shows that already  $\sim 2$  ms after the ELM crash both the  $p_i$  gradient and the  $E_r$  well are recovering. It should be noted that the main ion pressure gradient term has been calculated using the  $n_e$  profile from an identical discharge (#26716), as the edge  $n_e$  measurements were not available for the considered

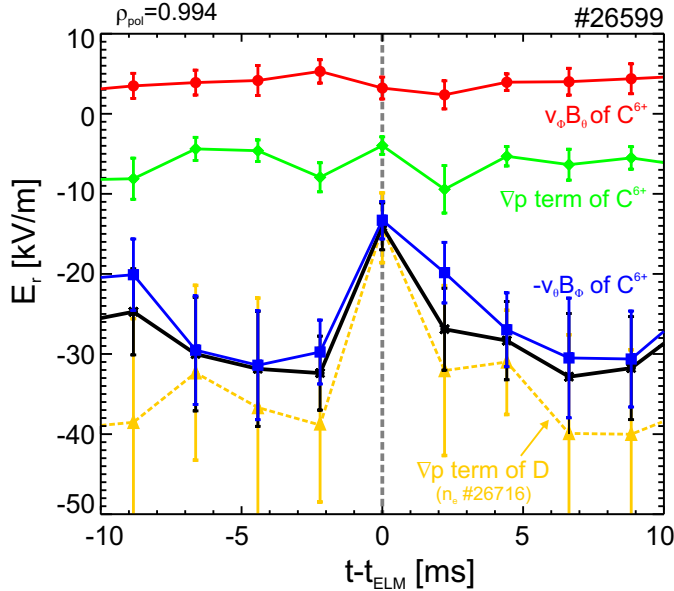


Figure 15: Individual impurity ion terms for the evaluation of  $E_r$  (red circles, green diamonds and blue squares) and main ion pressure gradient term (yellow triangles) at  $\rho_{pol} = 0.994$  during an ELM cycle.

discharge.

## 7. Effect of magnetic perturbations on $E_r$

For the experimental campaign 2011, the AUG tokamak was equipped with the first set of in-vessel saddle coils which consisted of two rows of coils above and below the midplane [67]. Each row had four coils at different toroidal positions. The coils were used to apply non-axisymmetric magnetic perturbations (MPs) to the plasma in order to suppress type-I ELMs. In H-mode plasmas with externally applied MPs (toroidal mode number  $n = 2$ ) ELM mitigation was observed above a critical edge density [68], corresponding typically to a fractional Greenwald density of  $n_{e,ped}/n_{GW} \sim 0.65$ ,  $n_{e,ped}$  being the pedestal electron density and  $n_{GW}$  the Greenwald density [69]. So far, ELM mitigation has been observed in plasmas with different shape, different heating mixes, different levels of heating power [70] and with MPs that are both resonant and non-resonant with the edge  $q$  profile [68].

The experiment presented here was carried out specifically to test if there is an observable effect on the  $E_r$  profile due to the MPs. The discharge was designed with four phases (see figure 16), the first one without MPs, followed by a phase with MPs but without ELM mitigation. In the third phase (MPs on) the density was increased and ELM mitigation was achieved and in the last phase, the MPs were switched off. The discharge was performed in H-mode with  $B_\phi = -2.4$  T,  $I_p = 1$  MA, NBI heating of 7.6 MW and ECRH ranging between 1.5 and 2.2 MW. The safety factor at the surface that encloses 95% magnetic flux,  $q_{95}$ , was ranging between 4.05 and 4.35 throughout

*High-accuracy characterization of  $E_r$  at AUG*

19

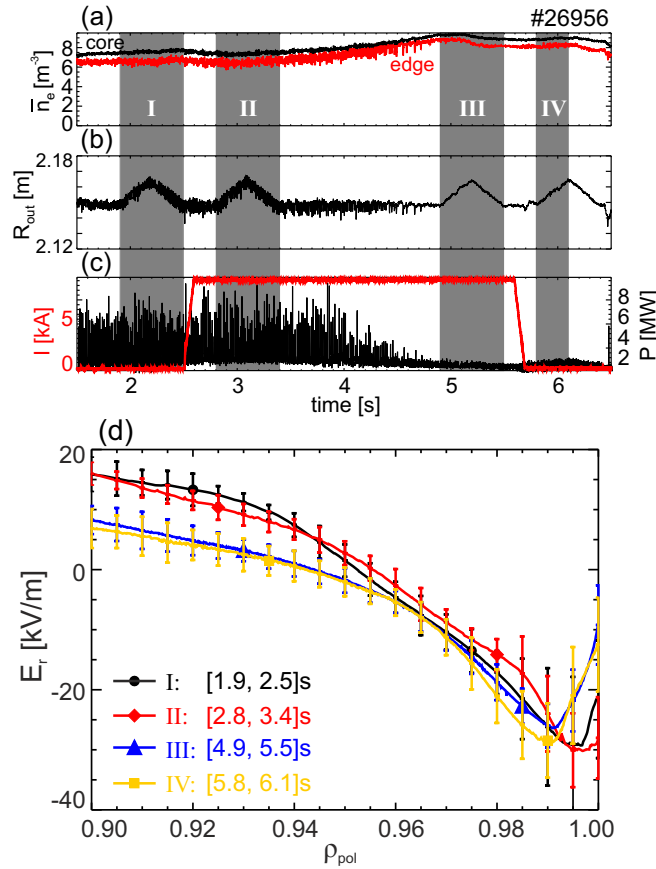


Figure 16: (a) Line-averaged density in the plasma core (black) and edge (red), (b) radial plasma position at outer midplane  $R_{out}$ , (c) ELM monitoring signal in the divertor (black) and current of MP coils (red), (d) radial electric field profiles corresponding to the different phases during the discharge (marked in gray in (a)-(c)). No obvious effect on  $E_r$  is observed due to the MP coils.

the different phases of the discharge. The  $n = 2$ , odd configuration (odd corresponding to the opposite parity of upper and lower MP coils) was used. Figure 16(a) shows the time trace of the line-averaged electron density from a central LOS and an edge LOS of the interferometry system. The radial plasma position at the outer midplane (see figure 16(b)) was scanned several times to obtain detailed edge profiles in each phase. In figure 16(c) the current of the MP coils and an ELM-monitoring signal in the divertor are plotted. At a line-averaged edge density of  $6.5 \times 10^{19}$  m<sup>-3</sup> the application of the MP coils has no effect on the ELMs. However, as soon as a critical edge density is achieved (cf. phase III) the type-I ELMs disappear. From the CXRS measurements in each radial sweep,  $E_r$  profiles were obtained by measuring the B<sup>5+</sup> CX line (see figure 16(d)). For phase I and II the inter-ELM  $E_r$  profile is shown. In general, the  $E_r$  profile does not exhibit any significant change due to the MPs. Moving from phase I to II and switching on the MP coils has no effect on the ELMs and no change in  $E_r$  is observed. As the plasma density increases (moving from phase II to III) the type-I ELMs disappear.

However, the  $E_r$  well (see blue curve of figure 16(d)) is not affected and stays constant also when the coils are switched off. Comparing the  $E_r$  profile of phases II and III, the minimum of the  $E_r$  well appears to be slightly shifted inwards. This shift corresponds to about 2 mm in real space and is just within the error bars. Towards the plasma core the radial electric field decreases by  $\sim 8$  kV/m (at  $\rho_{pol} = 0.9$ ). Note that this reduction and the radial shift are mainly attributed to the increase in the gas puff level and hence, plasma density. In the last phase the density stays at the same level and the MP coils are switched off. Here, the type-I ELMs do not return, however, small high-frequent ELMs ( $\sim 200$  Hz) appear. Note that the radial electric field shows again no response.

These results suggest that in the plasmas studied so far (H-modes at high density) the edge radial electric field is not affected by externally applied MPs. The fact that  $E_r$  remains unaffected may be explained by the shielding of the plasma, i.e. the MP is not fully penetrating into the pedestal. Similar observations were reported from DIII-D in H-mode plasmas with resonant MPs in the  $n = 3$  configuration with odd parity and  $q_{95} = 3.8$  [71]. Here, the  $E_r$  minimum remained unchanged while in the scrape-off layer  $E_r$  increased. At TEXTOR an effect of resonant MPs on  $E_r$  has been observed [72], resulting in a maximum increase of  $E_r$  by 9 kV/m with respect to a reference discharge without MPs. This is attributed to the penetration of open field lines into the confined plasma. Preliminary AUG results in low density L-mode plasmas [73] show that the edge radial electric field is affected by the MPs, i.e. the  $E_r$  well is reduced.

In the 2011 opening, the installation of the in-vessel saddle coils system at AUG was completed, thus enabling operation with MPs up to  $n=4$ . Further experiments will be performed to study the effect of the MPs from the completed set of coils on the  $E_r$  profile.

## 8. Discussion and Summary

Extending the AUG edge CXRS system with a poloidal view enabled the determination of  $E_r$  from CX measurements using the radial force balance equation for impurity ions. The edge  $E_r$  profile is derived from CX measurements on  $\text{He}^{2+}$ ,  $\text{B}^{5+}$ ,  $\text{C}^{6+}$  and  $\text{Ne}^{10+}$  and is found to be identical within the uncertainties regardless of the impurity species used for the analysis. This demonstrates the validity of the diagnostic technique and provides a consistency check of  $E_r$ . In the radial force balance of impurity ions, the poloidal rotation term is the dominant contribution for the evaluation of the  $E_r$  well consistent with measurements on other tokamaks. However, for the main ions, which are supposed to drive  $E_r$ , the pressure gradient term is the dominant contribution in the edge transport barrier (ETB). An estimate of the perpendicular deuterium velocity has been calculated using the main ion pressure gradient term and the  $E_r$  profile derived from CXRS. For  $\rho_{pol} > 0.95$ , i.e. the pedestal, the results suggest that  $v_{\perp,i}$  is 0 with uncertainties less than 5 km/s, in agreement with observations on Alcator C-Mod [6]. This is confirmed by direct measurements of the main ion temperature, density and rotation velocities in helium plasmas, which show that at the plasma edge  $E_r$  is

*High-accuracy characterization of  $E_r$  at AUG*

21

determined by the pressure gradient term of the main ions. These results support that the  $E_r$  well behaves as expected from neoclassical theory.

The  $E_r$  profile has been measured in different confinement regimes. In L-mode,  $E_r$  is small in magnitude and exhibits little shear, while in the ETB of the H-mode a strong, negative  $E_r$  well and a localized minimum close to the separatrix ( $\rho_{pol} > 0.99$ ) is found, consistent with observations in other fusion devices. The steepest gradients of the ion and electron profiles, i.e. the pedestal, are in the inner, negative shear region of the  $E_r$  well. In I-mode plasmas, the minimum of the  $E_r$  well is intermediate between L- and H-mode. A correlation between the depth of the  $E_r$  well, or the magnitude of the  $E_r$  shear respectively, and the ion pressure at the pedestal top is observed, in keeping with the main ion pressure gradient term being the dominant contribution to  $E_r$ .

The time resolution of the edge CXRS diagnostics (2.2 ms) allows the study of the temporal evolution of  $E_r$  during an ELM cycle. At the ELM crash the  $E_r$  minimum decreases leading to a reduction of the  $\mathbf{E} \times \mathbf{B}$  shear layer. Shortly after the ELM, the profile recovers and the  $E_r$  well reforms reaching its initial value 4 – 6 ms after the ELM. A comparison to the main ion pressure gradient term suggests that the ion pressure gradient and the  $E_r$  well recover on similar time scales.

In high density type-I ELM-mitigated H-mode plasmas, obtained via externally applied magnetic perturbations with toroidal mode number  $n = 2$ , no obvious effect on the  $E_r$  profile is visible.

The CXRS data presented in this paper are consistent with reductions in energy transport due to the suppression of turbulence. However, the self-consistent evolution of the  $E_r$  profile, pedestal shape, edge turbulence and transport reduction and improvement in plasma confinement is not completely elucidated due to the lack of clear definition of our understanding. The fact that the maximum  $\mathbf{E} \times \mathbf{B}$  shearing rate coincides with the steepest ion pressure gradient and is localized in the inner part of the  $E_r$  well suggests that the negative shear region might be the important region for turbulence reduction within the  $\mathbf{E} \times \mathbf{B}$  shear model [2]. The results discussed in this paper underline that the ion channel plays a key role in the interdependency between  $\mathbf{E} \times \mathbf{B}$  shearing, turbulence and transport reduction.

## 9. Acknowledgments

The first author would like to thank E. Fable and U. Stroth for very fruitful discussions. M. Willensdorfer is a fellow of the Friedrich Schiedel Foundation for Energy Technology.

## Appendix

In order to justify the approximation of  $T_i \approx T_\alpha$ , the equilibration times are compared to typical transport time scales at the plasma edge. Here, the particle transport time is defined as  $\tau_{tr} = L_{n_e}^2 / D$ , where  $L_{n_e}$  is the electron density scale length and  $D$  the local diffusion coefficient. The thermal equilibration time between two different species

is determined using the definition in [74]:

$$\tau_{\alpha\beta} = \frac{1}{1.8 \times 10^{-19}} \frac{(m_\alpha T_\beta + m_\beta T_\alpha)^{3/2}}{\sqrt{m_\alpha m_\beta} (Z_\alpha Z_\beta)^2 n_\beta \ln \Lambda} \quad (1)$$

where  $m_\alpha$ ,  $m_\beta$  are the masses in g,  $T_\alpha$ ,  $T_\beta$  the temperatures in eV and  $Z_\alpha$ ,  $Z_\beta$  the charge states of the particle species  $\alpha$  and  $\beta$ ,  $n_\beta$  is the density of species  $\beta$  in  $\text{cm}^{-3}$  and  $\ln \Lambda$  the Coulomb logarithm.

Figure 1 shows the local transport time scales in black for different diffusion coefficients ( $D = 0.1 \text{ m}^2/\text{s}$  (dashed dotted line),  $D = 0.2 \text{ m}^2/\text{s}$  (solid line) and  $D = 1 \text{ m}^2/\text{s}$  (dashed line)). The values for the diffusion coefficients are taken from [75]. The thermal equilibration time between electrons and ions,  $\tau_{ei}$ , is shown in red, while the time needed for a  $\text{B}^{5+}$  impurity to thermally equilibrate to the electrons,  $\tau_{ae}$ , and to the main ions (deuterium),  $\tau_{ai}$ , is shown in blue and green. At the plasma edge, the equilibration time between impurities and main ions is much shorter than the local transport time scale and thus,  $T_i \approx T_\alpha$ . The thermal equilibration time between impurities and electrons and electrons and ions is also faster than the local particle transport time. Only at the very plasma edge, close to the separatrix, the ions and electrons can decouple resulting in different ion and electron temperatures (with  $T_i$  usually being larger near the separatrix). Depending on the diffusion coefficient, also the impurities and electrons can decouple close to the separatrix. However, even in case of decoupling at the very edge, it is assumed that the position of the steepest gradients in  $T_i$  and  $T_e$  is the same since the transport barrier is build up in both the ion and electron channels.

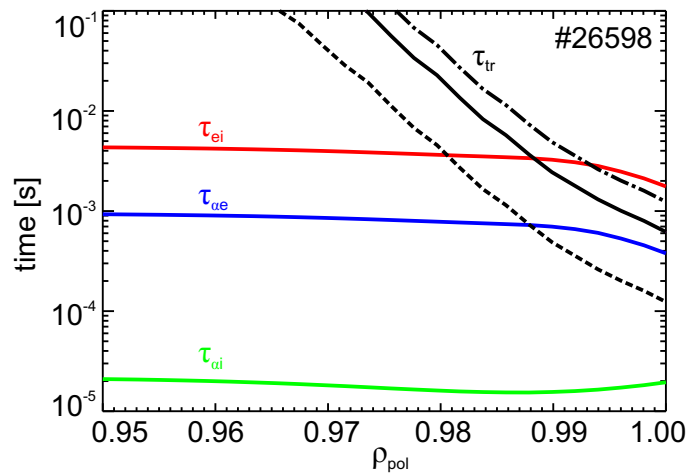


Figure 1: Typical time scales at the plasma edge of an H-mode discharge: transport time  $\tau_{tr}$  in black, thermal equilibration time between electrons and ions ( $\tau_{ei}$ ) in red, between  $\text{B}^{5+}$  and electrons ( $\tau_{ae}$ ) in blue and  $\text{B}^{5+}$  and ions ( $\tau_{ai}$ ) in green. The local transport time scales have been evaluated using different diffusion coefficients ( $D = 0.1 \text{ m}^2/\text{s}$  (dashed dotted line),  $D = 0.2 \text{ m}^2/\text{s}$  (solid line) and  $D = 1 \text{ m}^2/\text{s}$  (dashed line)).

*High-accuracy characterization of  $E_r$  at AUG*

23

## References

- [1] F. Wagner *et al.* *Phys. Rev. Lett.*, 49(19):1408, 1982.
- [2] H. Biglari *et al.* *Phys. Fluids B*, 2(1):1, 1990.
- [3] H. Meister *et al.* *Nucl. Fusion*, 41(11):1633, 2001.
- [4] J. Schirmer *et al.* *Nucl. Fusion*, 46:S780–S791, 2006.
- [5] K. H. Burrell *et al.* *Plasma Phys. Control. Fusion*, 31:10, 1989.
- [6] R. M. McDermott *et al.* *Phys. Plasmas*, 16:056103, 2009.
- [7] Y. Andrew *et al.* *Eur. Phys. Lett.*, 83:15003, 2008.
- [8] K. Kamiya *et al.* *Nucl. Fusion*, 51:053009, 2011.
- [9] R. E. Bell *et al.* *Phys. Rev. Lett.*, 81(7):1429, 1998.
- [10] J. W. Coenen *et al.* *J. Phys. B: At. Mol. Opt. Phys.*, 43:144015, 2010.
- [11] H. Meyer *et al.* *Jour. of Phys.: Conference Series*, 123:012005, 2008.
- [12] R. E. Bell *et al.* *Phys. Plasmas*, 17:082507, 2010.
- [13] K. Ida *et al.* *Rev. Sci. Instrum.*, 71(6):2360, 2000.
- [14] R. Brakel *et al.* *Plasma Phys. Control. Fusion*, 39:B273–B286, 1997.
- [15] T. Happel *et al.* *Phys. Plasmas*, 18:102302, 2011.
- [16] V. Antoni *et al.* *Phys. Rev. Lett.*, 79:24, 1997.
- [17] R. J. Fonck *et al.* *Phys. Rev. A*, 29(6):3288, 1984.
- [18] E. Viezzzer *et al.* *Rev. Sci. Instrum.*, 83:103501, 2012.
- [19] T. Pütterich *et al.* *Phys. Rev. Lett.*, 102(025001), 2009.
- [20] F. L. Hinton and R. D. Hazeltine. *Rev. Mod. Physics*, 48(2), 1976.
- [21] H. Zohm. *Plasma Phys. Control. Fusion*, 38(2):105, 1996.
- [22] G. Federici *et al.* *Plasma Phys. Control. Fusion*, 45:1523, 2003.
- [23] F. Ryter *et al.* *Plasma Phys. Control. Fusion*, 43(A323), 2001.
- [24] T. C. Hender *et al.* *Nucl. Fusion*, 32:2091, 1992.
- [25] T. E. Evans *et al.* *Phys. Rev. Lett.*, 92:235003, 2004.
- [26] W. Schneider *et al.* *Fusion Engineering and Design*, 48:127, 2000.
- [27] E. Viezzzer *et al.* *Plasma Phys. Control. Fusion*, 53:035002, 2011.
- [28] E. Wolfrum *et al.* *Fusion Energy 2008 (Proc. 22<sup>nd</sup> Int. Conf. Geneva, Switzerland, 2008)* (Vienna: IAEA) CD-ROM file EX/P3-7, <http://www-naeweb.iaea.org/napc/physics/FEC/FEC2008/html/index.htm>.
- [29] W. Suttrop. *Practical Limitations to Plasma Edge Electron Temperature Measurements by Radiometry of Electron Cyclotron Emission*. IPP Report 1/306, Max-Planck-Institute for Plasma Physics, Garching, Germany, 1997.
- [30] B. Kurzan *et al.* *Rev. Sci. Instrum.*, 82:103501, 2011.
- [31] P. A. Schneider *et al.* Analysis of Temperature and Density Pedestal in a Multi-machine Database. *submitted to Nucl. Fusion (January 2013)*.
- [32] J. Neuhauser *et al.* *Plasma Phys. Control. Fusion*, 44:855, 2002.
- [33] R. Fischer *et al.* *Plasma Phys. Control. Fusion*, 50:085009, 2008.
- [34] M. Willensdorfer *et al.* *Rev. Sci. Instrum.*, 83:023501, 2012.
- [35] A. Mlynek *et al.* *Rev. Sci. Instrum.*, 81:033507, 2010.
- [36] J. Kim *et al.* *Phys. Rev. Lett.*, 72(14):2199, 1994.
- [37] K. D. Marr *et al.* *Plasma Phys. Control. Fusion*, 52(055010), 2010.
- [38] G. Kagan *et al.* *Plasma Phys. Control. Fusion*, 53(025008), 2011.
- [39] M. Hirsch *et al.* *Plasma Phys. Control. Fusion*, 43:1641, 2001.
- [40] M. Hirsch *et al.* *Plasma Phys. Control. Fusion*, 48:S155, 2006.
- [41] T. Estrada *et al.* *Plasma Phys. Control. Fusion*, 51:124015, 2009.
- [42] G. R. McKee *et al.* *Phys. Plasmas*, 7:1870, 2000.
- [43] G. D. Conway *et al.* *Plasma Phys. Control. Fusion*, 46:951, 2004.
- [44] C. Tröster. *Development of a flexible Doppler reflectometry system and its application to turbulence*

<i>High-accuracy characterization of <math>E_r</math> at AUG</i>	24
--	----

- characterization in the ASDEX Upgrade tokamak.* PhD thesis, Ludwig-Maximilians-Universität München, 2008.
- [45] T. Happel *et al.* Design of a New Doppler Reflectometer Frontend for the ASDEX Upgrade Tokamak. *Proc. 10<sup>th</sup> International Reflectometry Workshop*, <http://www.igi.cnr.it/irw10/proceedings/HappelT.pdf>, 2011.
  - [46] U. Stroth *et al.* *Plasma Phys. Control. Fusion*, 53:024006, 2011.
  - [47] B. Wieland. *Investigations on radial electric fields in the edge transport barrier of H-mode discharges.* PhD thesis, Technische Universität München, 2011.
  - [48] K. Itoh and S.-I. Itoh. *Plasma Phys. Control. Fusion*, 38:1, 1996.
  - [49] K. H. Burrell. *Phys. Plasmas*, 4(5):1499, 1997.
  - [50] K. Ida. *Plasma Phys. Control. Fusion*, 40:1429, 1998.
  - [51] G. D. Conway *et al.* *Fusion Energy 2010 (Proc. 23<sup>rd</sup> Int. Conf. Daejeon, Republic of Korea, 2010)* (Vienna: IAEA) CD-ROM file EX/1-1, <http://www-naweb.iaea.org/napc/physics/FEC/FEC2010/index.htm>.
  - [52] D. G. Whyte *et al.* *Nucl. Fusion*, 50(105005), 2010.
  - [53] F. Ryter *et al.* *Plasma Phys. Control. Fusion*, 40:725, 1998.
  - [54] ITER Physics Expert Group on Confinement and Transport and Confinement Modelling and Database, ITER Physics Basis Editors. *Nucl. Fusion*, 39:2175, 1999.
  - [55] O. Gruber *et al.* *Nucl. Fusion*, 49(115014), 2009.
  - [56] T. S. Hahm and K. H. Burrell. *Phys. Plasmas*, 2(5):1648, 1995.
  - [57] P. Gohil *et al.* *Nucl. Fusion*, 38(1):93, 1998.
  - [58] P. Sauter *et al.* *Nucl. Fusion*, 52:012001, 2012.
  - [59] G. D. Conway *et al.* *Plasma Phys. Control. Fusion*, 44:451, 2002.
  - [60] R. A. Moyer *et al.* *Phys. Plasmas*, 2(6):2397, 1995.
  - [61] K. H. Burrell *et al.* *Phys. Plasmas*, 6(12):4418, 1999.
  - [62] T. Pütterich *et al.* *Nucl. Fusion*, 52:083013, 2012.
  - [63] M. R. Wade *et al.* *Phys. Plasmas*, 12:056120, 2005.
  - [64] A. Burckhart *et al.* *Plasma Phys. Control. Fusion*, 52:105010, 2010.
  - [65] G. D. Conway *et al.* *Plasma Fus. Research*, 5(S2005), 2010.
  - [66] H. Meyer *et al.* *Nucl. Fusion*, 51(113011), 2011.
  - [67] W. Suttrop *et al.* *Fusion Eng. Design*, 84(290), 2009.
  - [68] W. Suttrop *et al.* *Phys. Rev. Lett.*, 106(225004), 2011.
  - [69] M. Greenwald *et al.* *Nucl. Fusion*, 28:2199, 1988.
  - [70] W. Suttrop *et al.* *Plasma Phys. Control. Fusion*, 53:124014, 2011.
  - [71] R. A. Moyer *et al.* *Phys. Plasmas*, 12:056119, 2005.
  - [72] J. W. Coenen *et al.* *Nucl. Fusion*, 51(063030), 2011.
  - [73] M. Kočan *et al.* Far-reaching Impact of Intermittent Transport across the Scrape-off Layer: Latest Results from ASDEX Upgrade. *submitted to Nucl. Fusion (January 2013)*.
  - [74] J. D. Huba. *NRL Plasma Formulary*. Naval Research Laboratory, available at <http://wwwppd.nrl.navy.mil/nrlformulary/>, 2007.
  - [75] T. Pütterich *et al.* *J. Nucl. Mater.*, 415(1):S334–S339, 2011.

## 5.10 Publication 10

*Evidence for the neoclassical nature of the radial electric field  
in the edge transport barrier of ASDEX Upgrade*

Nuclear Fusion 54 (2014) 012003

# Evidence for the neoclassical nature of the radial electric field in the edge transport barrier of ASDEX Upgrade

**E. Viezzer, T. Pütterich, C. Angioni, A. Bergmann, R. Dux, E. Fable, R. M. McDermott, U. Stroth, E. Wolfrum and the ASDEX Upgrade Team**

*Max-Planck-Institut für Plasmaphysik, EURATOM Association, Boltzmannstr. 2, 85748 Garching, Germany*

**Abstract.** Experiments have been performed on ASDEX Upgrade to clarify the nature of the radial electric field,  $E_r$ , in the edge transport barrier of tokamak plasmas. Highly resolved radial profiles of  $E_r$  have been diagnosed spectroscopically through the radial force balance of impurity ions. We show that in the fully developed, highly collisional edge pedestal the nature of the radial electric field is neoclassical. This requires, in particular, that the main ion poloidal rotation is at neoclassical levels. Both main ion and impurity ion poloidal rotation profiles have been measured in deuterium, hydrogen and helium plasmas with main ion pedestal top collisionalities,  $\nu_{*,i}$ , between 1.2 and 12. These profiles have been compared to a hierarchy of neoclassical models (from a conventional description to a comprehensive model including finite orbit width effects). They are found, in all cases, to be in good agreement demonstrating that inside the edge transport barrier the  $E_r$  well is sustained by the gradients of the main ion species.

## 1. Introduction

After the discovery of the high confinement mode (H-mode) on the ASDEX tokamak [1] sheared  $\mathbf{E} \times \mathbf{B}$  plasma flow was identified as a key component for the suppression of turbulent transport and the formation of transport barriers [2]. At the onset of the H-mode, the edge turbulence level is significantly reduced and a steep edge pressure gradient  $\nabla p$  develops which is responsible for the improved H-mode confinement. This pressure gradient as well as the concomitant turbulence stabilization are sustained throughout the H-mode by the presence of a sheared plasma flow perpendicular to the magnetic field caused by a local radial electric field,  $E_r$ . Therefore, the size and the nature of  $E_r$  and the accompanying flow have been the subject of intense research for several decades [3, 4]. One obvious source for  $E_r$  is non-ambipolar transport [5], which also provides the possibility of bifurcation phenomena [6]. The flows parallel and perpendicular to the helical magnetic field lines are the physically relevant parameters and are related to  $E_r$  via  $v_\perp = \mathbf{E} \times \mathbf{B} / B^2 - \nabla p \times \mathbf{B} / qnB^2$  and  $v_\parallel = v_\theta B / B_\theta + RB_\phi(E_r -$

*Neoclassical Nature of  $E_r$  in the ETB of ASDEX Upgrade*

2

$\nabla p/qn)/B$  [7] (charge  $q$ , density  $n$ , local major radius  $R$ , poloidal and toroidal magnetic field  $B_\theta$  and  $B_\phi$ ). In axisymmetric geometry, for a particular poloidal flow, an arbitrary combination of perpendicular and parallel flows can be prescribed since  $E_r$  is a degree of freedom of the system. This is the reason why neoclassical transport in tokamak plasmas is often considered as intrinsically ambipolar [7]. In a tokamak, however, toroidal flows are damped by field inhomogeneities (ripple) and neutral gas friction, and must also comply with momentum conservation. Therefore, the toroidal flows are constrained as well and especially close to the separatrix, where the H-mode transport barrier develops, also in a tokamak a well defined value for the ambipolar radial electric field,  $E_r^{\text{amb}}$ , can be expected [8].

Due to the importance of the electric field for the H-mode,  $E_r$  measurements have already been compared to neoclassical theory but the overall picture is not yet conclusive. Early studies on the edge plasma of the DIII-D tokamak found a disagreement between experimental and neoclassical poloidal rotation in low collisionality plasmas [9]; here the measured main ion poloidal rotation deviated by one order of magnitude from the neoclassical prediction. In dedicated studies of the L-H transition, the evolution of  $E_r$  was decoupled from that of the ion pressure gradient [10]. The core electric field was studied in many experiments and confinement regimes including internal transport barriers. In many cases very large discrepancies between experiment and theory were found [11–14]. In other cases the poloidal flow measurements agreed with neoclassical theory within the experimental uncertainties [15–22]. These measurements have been performed on impurity ions and in the plasma core (except for the work at Alcator C-Mod [17, 18] which was focussed at the plasma edge). Simulation results at LHD [23, 24] showed that in low collisional, high electron temperature plasmas the nonlocal effects arising from the radial drift of helically trapped particles can become important and the finite orbit width effect for electrons need to be taken into account when operating in this regime.

Based on detailed spectroscopic measurements of the plasma flows in ASDEX Upgrade (AUG), this letter presents for the first time direct evidence that neoclassical theory can account for the main features of the radial electric field in the highly collisional edge pedestal of tokamak plasmas. In case of a negligibly small toroidal flow, which is shown to be a good approximation in the pedestal region of AUG, neoclassical theory yields the simple expression  $E_r^{\text{amb}} \approx \nabla p_i/en_i$ , where  $E_r$  is mainly determined by the ion pressure gradient (elementary charge  $e$ , ion density  $n_i$ ). This relation corresponds to the cancellation of the poloidal components of the ion diamagnetic and  $\mathbf{E} \times \mathbf{B}$  drifts up to small neoclassical correction terms. Combining the  $E_r$  data with measurements of the edge kinetic profiles, it is shown that the  $\mathbf{E} \times \mathbf{B}$  velocity and the ion diamagnetic drift balance each other in the edge pedestal.

High quality edge poloidal rotation data of impurities have been measured in deuterium and hydrogen plasmas, and, for the first time, of main ions in helium plasmas at AUG and show consistency with neoclassical theory. This demonstrates the validity of this picture and the applicability of the simple approximation of  $E_r^{\text{amb}}$ .

## 2. Experiment

The most common method to measure the rotation of the plasma is active charge exchange recombination spectroscopy (CXRS) [25]. A combination of poloidal and toroidal views allows for a direct evaluation of  $E_r$  using the radial force balance equation. In general, poloidal flow measurements are challenging due to their relatively small magnitude. At AUG the poloidal rotation velocity is measured using active CXRS on a heating beam [26]. Due to the energy dependence of the CX cross-sections several atomic physics effects [27] may arise when measuring CX emission and can give spurious temperature and rotation measurements. The effect of the gyro-motion of the impurity along with the finite lifetime of the excited state of the transition [28, 29] can become important when measuring in the plane of the gyro-orbit, i.e. in the poloidal direction. The corrections arising from the atomic physics effects have been calculated for the geometry of the poloidal CXRS system and are found to be small [26]. For the main ion poloidal rotation measurements in helium plasmas that are presented in the following the maximum correction due to the atomic physics effects is 0.2 km/s which is well within the experimental uncertainties. The corrections have been calculated using a lifetime of 2 ns for the  $\text{He}^+$  ( $n = 4 \rightarrow 3$ ) transition. This value has been determined from the Einstein coefficients calculated using the Cowan code [30]. To reduce systematical uncertainties in the rotation measurements the wavelength calibration is performed on a shot-to-shot basis using a neon lamp [26]. This enables a quite accurate determination of the wavelength calibration with uncertainties smaller than 1 km/s.

Recent AUG results [31] have shown that using the radial force balance of impurity ions the CXRS measurements yield the same edge  $E_r$  profile independent of the trace impurity used for the evaluation. Comparing the  $E_r$  profile to the gradients of the main ion species allows us to obtain information on the perpendicular main ion flow indirectly. This is done in figure 1 which shows the perpendicular velocity of the main ions (red) and electrons (blue), the  $\mathbf{E} \times \mathbf{B}$  velocity (black) and the ion diamagnetic drift velocity (multiplied by -1, green) measured in an H-mode plasma. Combining all measurements of the edge kinetic profiles, one can provide experimental evidence that, perpendicular to the magnetic field, the ion fluid is almost at rest (below 5 km/s) in the lab frame, while the magnitude of both the  $\mathbf{E} \times \mathbf{B}$  and diamagnetic flow is up to 22 km/s in the edge pedestal.

If the toroidal rotation is small at the plasma edge, the balance between the ion diamagnetic and  $\mathbf{E} \times \mathbf{B}$  flows indicates that the poloidal rotation velocity of the main ions,  $v_{\theta,i}$ , may be approximately neoclassical. In the following, we present the first measurements of  $v_{\theta,i}$  in the edge transport barrier of AUG and compare the measured profile to neoclassical calculations.

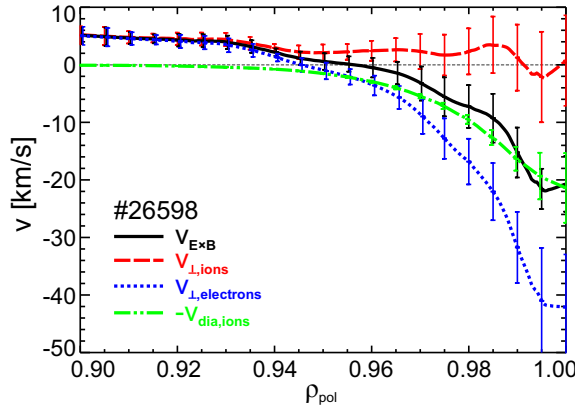


Figure 1:  $\mathbf{E} \times \mathbf{B}$  velocity (black), perpendicular velocity of main ions (red) and electrons (blue) and main ion diamagnetic fluid velocity (multiplied by -1, green) measured in an H-mode discharge with a toroidal magnetic field on-axis of  $B_\phi = -2.5$  T, plasma current of  $I_p = 1$  MA, 5 MW of neutral beam injection (NBI), 0.8 MW of electron cyclotron resonance heating (ECRH) and a central line-averaged density of  $8 \times 10^{19} \text{ m}^{-3}$ . The normalized poloidal flux label is defined as  $\rho_{pol} = \sqrt{(\Psi - \Psi_a)/(\Psi_s - \Psi_a)}$  with  $\Psi_a$  and  $\Psi_s$  being the poloidal flux at the magnetic axis and at the separatrix, respectively.

### 3. Main ion and impurity ion poloidal rotation measurements and comparison to neoclassical models

In order to quantify whether the main ion poloidal rotation is neoclassical, we measured  $v_{\theta,i}$  directly in helium plasmas which provide the opportunity to obtain information on the main ion species via CXRS on  $\text{He}^{2+}$  ( $n = 4 \rightarrow 3$ ,  $\lambda = 468.571$  nm). For the application to deuterium, which is usually the main ion species at AUG, background emissions and the beam halo prevent a simple interpretation of the spectra.

Figure 2 shows the measured main ion (a) temperature, (b) density, (c) toroidal and (d) poloidal rotation velocity profiles along with spline fits in black. In the presented discharge the main ion collisionality  $\nu_{*,\text{He}}$  at the pedestal top ( $\rho_{pol} = 0.97$ ) is  $\sim 12$ , i.e. deep in the Pfirsch-Schlüter regime ( $\nu_* > \epsilon^{-3/2}$  with  $\epsilon$  being the inverse aspect ratio). The collisionality is defined as the effective collision frequency normalized to the trapped particle bounce frequency,  $\nu_* = \nu_{\text{eff}}/\omega_b$  [32, 33]. In the data analysis the plume effect [25] has not been taken into account. The helium plume is caused by  $\text{He}^+$  ions, excited via electron impact (or ion impact), which gyrate along the magnetic field lines and thus, lead to polluting emission in the spectrum. However, at the plasma edge the contribution of the helium plume is expected to be small [25], which is supported by independent electron density measurements: the helium density is half the electron density and the edge gradients are well matched, i.e.  $\nabla n_{\text{He}} = \nabla n_e/2$ , (see figure 2(b)). The sign convention used in this paper is as follows: poloidal rotation velocities, which are vertically upward at the low-field side, are negative, i.e. in the electron diamagnetic drift direction. In the standard magnetic configuration of AUG  $B_\phi$  is negative (clockwise

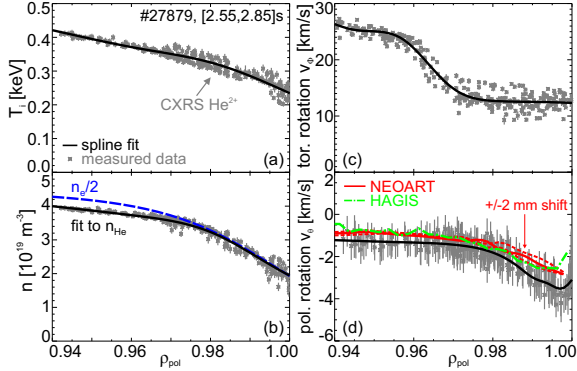
Neoclassical Nature of  $E_r$  in the ETB of ASDEX Upgrade

Figure 2: Main ion CXRS measurements in a helium plasma: (a) temperature, (b) density, (c) toroidal and (d) poloidal rotation velocity. The fit to the measured data is shown in black. In (d) the neoclassical prediction of the main ion poloidal rotation obtained with NEOART and HAGIS is shown in red and green (dashed-dotted line). The data were measured in an H-mode plasma with  $B_\phi = -2.5$  T,  $I_p = 1$  MA, 0.5 MW ECRH, 9.2 MW deuterium NBI heating and a central line-averaged density of  $1.1 \times 10^{20} \text{ m}^{-3}$ .

viewed from above) and  $B_\theta$  is positive (pointing downward at the outer midplane).  $I_p$  and the NBI are pointing into the positive toroidal direction (counter-clockwise viewed from above).

The main ion poloidal rotation is 1–3 km/s (of the order of  $\lesssim 0.03$  of the thermal velocity) and is in agreement with the neoclassical prediction obtained with the neoclassical code NEOART [34] shown in red in figure 2(d). NEOART incorporates a fluid model based on the calculation of collisional transport coefficients for a given number of impurities and includes collisions between all species. The code solves a set of linearly coupled equations for the parallel velocities in an arbitrary toroidally symmetric geometry and calculates neoclassical transport parameters for all collisionality regimes. The consistency between the neoclassical calculation and the experiment shows that the main ion poloidal rotation is driven predominantly by the ion temperature gradient [35]. The red dashed lines in figure 2(d) show the effect of a radial shift of  $\pm 2$  mm between the ion and electron profiles which are used as input for the neoclassical simulations. The green dashed-dotted line shows the neoclassical poloidal rotation profile as calculated with the HAGIS code [36, 37]. HAGIS is a kinetic particle code with a Monte-Carlo pitch angle collision model that simulates a three-species plasma and includes the effects due to finite orbit sizes. The good agreement between the measurement and both neoclassical predictions also demonstrates that in these plasmas the orbit-squeezing effect [38] is negligible.

Compared to the helium plasmas performed at DIII-D, where the ion collisionality at the plasma edge varied from 0.1 to 0.3 [9], the main ion collisionality in our experiment is two orders of magnitude higher. This might explain the opposite direction of the main ion poloidal rotation velocity measured at AUG and DIII-D. At DIII-D  $v_{\theta,i}$  was positive, i.e. in the ion diamagnetic drift direction, and reached values of up to 40 km/s in the plasma edge, which was far off from the neoclassical estimate ( $v_{\theta,i} \approx 0\text{--}2$  km/s). In the

*Neoclassical Nature of  $E_r$  in the ETB of ASDEX Upgrade*

## 6

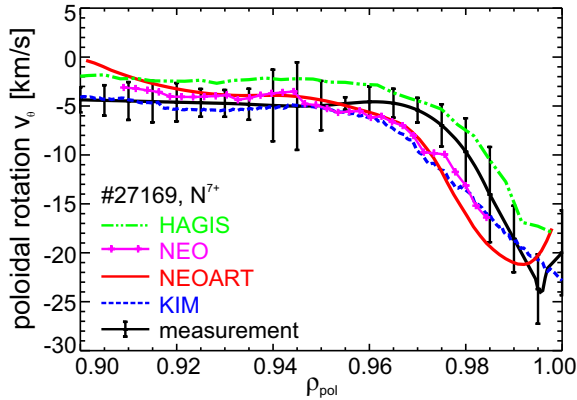


Figure 3: Impurity ion poloidal rotation velocity measured on  $N^{7+}$  in a D plasma, along with the conventional neoclassical prediction [35] in blue (dotted line) and the simulated profile using NEOART (red, solid line), NEO (magenta, crosses) and HAGIS (green, dashed-dotted line). The measurements were obtained in an H-mode plasma with  $B_\phi = -2.5$  T,  $I_p = 1$  MA, 2 MW ECRH, 10 MW NBI and a central line-averaged density of  $8.1 \times 10^{19} \text{ m}^{-3}$ .

neoclassical treatment,  $v_{\theta,i}$  is strongly dependent on the edge ion parameters. Depending on the ion collisionality the main ion poloidal rotation can be in the electron or in the ion diamagnetic drift direction, or be close to zero. The experiments at DIII-D indicate that in the low collisionality regime the neoclassical prediction might not be sufficient to characterize the measured profile. This was also reported in recent DIII-D experiments using indirect measurements of  $v_{\theta,i}$  [39]. The presented data based on CXRS on  $\text{He}^{2+}$  show that in the Pfirsch-Schlüter regime  $v_{\theta,i}$  is well described by neoclassical theory. The comparative analysis has been extended to several different impurities and to a hierarchy of models which describe neoclassical transport theory, i.e. from a conventional neoclassical model [35] to a more comprehensive description, such as that allowed by the HAGIS code, that includes finite orbit width effects. In an H-mode discharge performed in deuterium the poloidal impurity rotation velocity was measured on the  $N^{7+}$  ( $n = 9 \rightarrow 8$ ) spectral line at  $\lambda = 566.937$  nm and compared to conventional neoclassical predictions based on the analytic model by Kim et al. [35]. Here, the calculation is based on a fluid model with simple viscosity coefficients derived using the Hirshman and Sigmar moment approach [40]. Figure 3 shows the spline fit to the measured poloidal rotation data in black, and in blue (dotted line) the neoclassical prediction using the analytic model [35]. In addition, the neoclassical profiles obtained with the numerical codes NEOART, NEO [41] and HAGIS are shown in red (solid line), magenta (crosses) and green (dashed-dotted line). NEO is a drift-kinetic code that uses a  $\delta f$  expansion of the fundamental drift-kinetic Poisson equations and a first-principles approach to calculate the neoclassical transport coefficients directly from the solution of the distribution function  $f$ . As shown in figure 3 all of the models agree reasonably well and are consistent with the measured profile. This also demonstrates that kinetic effects,

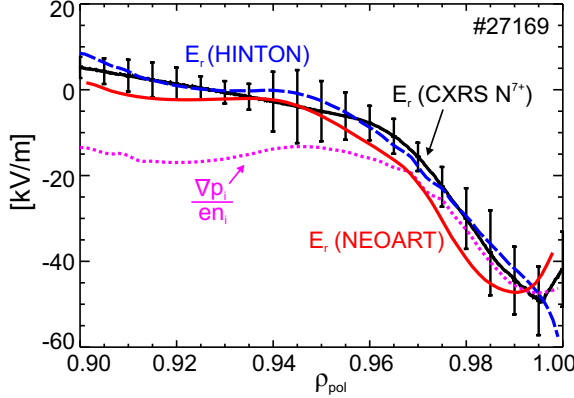


Figure 4:  $E_r$  profile as measured with CXRS in black, estimate of  $\nabla p_i/en_i$  in magenta (dotted line),  $E_r$  calculated using the Hinton-Hazeltine formulation [7] in blue (dashed line) and from NEOART (red, solid line).

which are included in HAGIS, play only a minor role in the plasmas considered here. It should be noted that at the very plasma edge the gradient scale length approaches that of the poloidal ion gyroradius ( $\sim 1$  cm for a D ion at the top of the pedestal), thus breaking the order assumed in the theory and the neoclassical approximation is less valid in this region. In this plasma, the main ion collisionality  $\nu_{*,D}$  is in the banana regime ( $\nu_{*,D} < 1$ ) for  $\rho_{pol} < 0.96$  and approaches the plateau regime ( $1 < \nu_{*,D} < \epsilon^{-3/2}$ ) at  $\rho_{pol} \approx 0.96$ , while the impurity collisionality  $\nu_{*,N}$  is deep in the Pfirsch-Schlüter regime. In the edge transport barrier of helium (as presented above) and deuterium plasmas [42], the toroidal main ion flow is observed to be small (of the order of 0.05–0.2 of the thermal velocity). Thus, the agreement between the measured poloidal rotation and the neoclassical simulations also indicates that the edge radial electric field behaves as expected from neoclassical theory.

Figure 4 shows the  $E_r$  profile derived from the CXRS measurements in black and an estimate of the main ion pressure gradient term  $\nabla p_i/en_i$  in magenta (dotted line). In the edge pedestal ( $\rho_{pol} > 0.97$ ) the  $E_r$  profile matches  $\nabla p_i/en_i$ . The profile shown in blue has been calculated using the Hinton-Hazeltine formulation [7] of  $E_r$ , while in red the profile calculated using NEOART is shown. The Hinton-Hazeltine formulation has been derived for large aspect ratio ( $R/a \gg 1$ , with  $a$  being the minor radius), assuming that the poloidal Larmor radius is smaller than the equilibrium scale lengths and using the weak-coupling approximation, i.e. neglecting the effects of electron-ion collisions on the ion species, [7]. At the plasma edge the poloidal rotation velocity is at neoclassical levels and, for small toroidal rotation velocities, the radial electric field is well described by the simple approximation of  $\nabla p_i/en_i$ .

For a further validation of this result different impurity species, including  $\text{He}^{2+}$ ,  $\text{B}^{5+}$ ,  $\text{C}^{6+}$  and  $\text{N}^{7+}$  measured in deuterium and hydrogen plasmas, have been analyzed. Figure 5 shows the minimum of the poloidal rotation velocity measured in the edge transport barrier plotted against the minimum of the neoclassical profile as simulated

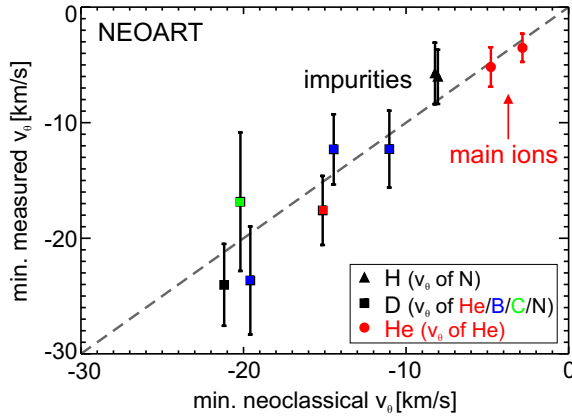


Figure 5: Minimum of measured poloidal rotation velocity versus minimum of neoclassical profile for various species including  $\text{He}^{2+}$ ,  $\text{B}^{5+}$ ,  $\text{C}^{6+}$  and  $\text{N}^{7+}$  (impurities are highlighted in black, main ions in red) in H-mode plasmas with different main ion species (H, D and He).

with NEOART of both impurities (black/coloured squares correspond to D plasmas, black triangles to H plasmas) and main ions (red circles) as measured in He plasmas. In these plasmas, the main ion collisionality at the pedestal top ( $\rho_{pol} = 0.97$ ) varied from 1.2 (plateau regime) to 12 (Pfirsch-Schlüter regime). In H-mode, both the sign and the magnitude of the neoclassical poloidal rotation are consistent with the measurement. Since friction between main ions and impurities is the dominant term in the impurity parallel momentum balance, the poloidal impurity rotation is mainly determined by the main ion pressure and temperature gradient scale lengths, while the contribution from the impurity pressure gradient scale length is small as it is scaled by  $Z_i/Z_\alpha$  [35] ( $Z$  being the charge state of the main ion  $i$  and the impurity  $\alpha$ , respectively).

#### 4. Summary and Conclusions

Measurements of the edge radial electric field and the poloidal rotation of both main ions (in helium plasmas) and impurities (obtained in deuterium and hydrogen plasmas) have been compared to neoclassical theory. The experiments provide evidence that in the fully developed, highly collisional edge transport barrier of an H-mode the radial electric field is neoclassical. This is closely connected to the finding that the main ion poloidal rotation is at neoclassical levels. These results are also in keeping with the poloidal impurity rotation term typically being the dominant contribution for the evaluation of the depth of the  $E_r$  well. In H-modes with pedestal top collisionalities ranging from the plateau to the Pfirsch-Schlüter regime, the measured poloidal rotation of both main ions and impurities are found to be consistent with neoclassical predictions; both the sign and the magnitude of the experimental and simulated profiles are in quantitative agreement. These results show that in the established H-mode the driving mechanism for the main ion poloidal rotation at the plasma edge is given by the ion temperature

gradient (viscous damping). This implies that corrections to the main ion poloidal flow due to parallel flows (friction) or turbulence are negligible in the plasma regimes considered here.

The measurements presented here give hints on the nature of the main ion transport in the edge transport barrier and are in line with the impurity particle transport being neoclassical [43]. The mechanism responsible for damping the toroidal rotation velocity to small values at the plasma edge remains an open issue [44] and requires a more detailed understanding of the toroidal momentum transport in the edge pedestal region which is the subject of future work.

## References

- [1] F. Wagner *et al.* *Phys. Rev. Lett.*, 49(19):1408, 1982.
- [2] H. Biglari *et al.* *Phys. Fluids B*, 2:1, 1990.
- [3] K. H. Burrell. *Phys. Plasmas*, 4(5):1499, 1997.
- [4] K. Ida. *Plasma Phys. Control. Fusion*, 40:1429, 1998.
- [5] J. D. Callen *et al.* *Phys. Plasmas*, 17(056113), 2010.
- [6] S.-I. Itoh and K. Itoh. *Phys. Rev. Lett.*, 60(22):2276, 1988.
- [7] F. L. Hinton and R. D. Hazeltine. *Rev. Mod. Physics*, 48(2), 1976.
- [8] U. Stroth *et al.* *Plasma Phys. Control. Fusion*, 53:024006, 2011.
- [9] J. Kim *et al.* *Phys. Rev. Lett.*, 72(14):2199, 1994.
- [10] R. A. Moyer *et al.* *Phys. Plasmas*, 12:056119, 2005.
- [11] R. E. Bell *et al.* *Phys. Rev. Lett.*, 81(7):1429, 1998.
- [12] K. Cromb   *et al.* *Phys. Rev. Lett.*, 95(155003), 2005.
- [13] T. Tala *et al.* *Nucl. Fusion*, 47:1012, 2007.
- [14] W. M. Solomon *et al.* *Phys. Plasmas*, 13(056116), 2006.
- [15] H. Meister *et al.* *Nucl. Fusion*, 41(11):1633, 2001.
- [16] J. H. F. Severo *et al.* *Nucl. Fusion*, 43:1047, 2003.
- [17] K. D. Marr *et al.* *Plasma Phys. Control. Fusion*, 52(055010), 2010.
- [18] G. Kagan *et al.* *Plasma Phys. Control. Fusion*, 53(025008), 2011.
- [19] A. R. Field *et al.* *Plasma Phys. Control. Fusion*, 51(105002), 2009.
- [20] R. E. Bell *et al.* *Phys. Plasmas*, 17:082507, 2010.
- [21] A. Bortolon *et al.* *Nucl. Fusion*, 53:023002, 2013.
- [22] J. Ar  valo *et al.* *Nucl. Fusion*, 53:023003, 2013.
- [23] S. Matsuoka *et al.* *Phys. Plasmas*, 18:032511, 2011.
- [24] S. Satake *et al.* *Comp. Phys. Comm.*, 181:1069, 2010.
- [25] R.J. Fonck *et al.* *Phys. Rev. A*, 29(6):3288, 1984.
- [26] E. Viezzner *et al.* *Rev. Sci. Instrum.*, 83:103501, 2012.
- [27] M. von Hellermann *et al.* *Plasma Phys. Control. Fusion*, 37:71, 1995.
- [28] R. E. Bell and E. J. Synakowski. *AIP Conf. Proc.* 547, 547:39, 2000.
- [29] W. M. Solomon *et al.* *Rev. Sci. Instrum.*, 75(10):3481, 2004.
- [30] R. D. Cowan. *The Theory of Atomic Structure and Spectra*. University of California Press, 1981.
- [31] E. Viezzner *et al.* *Nucl. Fusion*, 53(053005), 2013.
- [32] P. Helander and D. J. Sigmar. *Collisional Transport in Magnetized Plasmas*. 1<sup>st</sup> edition, ISBN 0-521-80798 -0, Cambridge University Press, Cambridge, 2002.
- [33] H. E. Mynick. *Phys. Plasmas*, 13:058102, 2006.
- [34] A. G. Peeters *et al.* *Phys. Plasmas*, 7(1):268, 2000.
- [35] Y. B. Kim *et al.* *Phys. Fluids B*, 3(8):2050, 1991.
- [36] S. D. Pinches *et al.* *Comp. Phys. Commun.*, 111:133, 1998.

*Neoclassical Nature of  $E_r$  in the ETB of ASDEX Upgrade* 10

- [37] A. Bergmann *et al.* *Phys. Plasmas*, 8:5192, 2001.
- [38] F. L. Hinton *et al.* *Phys. Rev. Lett.*, 72(8):1216, 1994.
- [39] B. A. Grierson *et al.* *Nucl. Fusion*, 53:063010, 2013.
- [40] S. P. Hirshman and D. J. Sigmar. *Nucl. Fusion*, 21(9):1079, 1981.
- [41] E. A. Belli *et al.* *Plasma Phys. Control. Fusion*, 50:095010, 2008.
- [42] T. Pütterich *et al.* *Phys. Rev. Lett.*, 102(025001), 2009.
- [43] T. Pütterich *et al.* *J. Nucl. Mater.*, 415(1):S334–S339, 2011.
- [44] A. G. Peeters *et al.* *Nucl. Fusion*, 51:094027, 2011.

## 5.11 Publication 11

*Poloidal asymmetry of parallel rotation measured in ASDEX Upgrade*

Nuclear Fusion 52 (2012) 083013

# Poloidal Asymmetry of Parallel Rotation Measured in ASDEX Upgrade

**T Pütterich, E Viezzer, R Dux, RM McDermott and the ASDEX Upgrade Team**

Max-Planck-Institut für Plasmaphysik, EURATOM Association, Boltzmannstraße 2,  
D-85748 Garching, Germany

**Abstract.** The parallel flows in the H-mode edge of ASDEX Upgrade are investigated. Beam-based charge-exchange recombination spectroscopy (CXRS) provides the toroidal and poloidal impurity flow velocities at the outboard midplane, while a deuterium-puff based CXRS measurement provides the toroidal impurity flow velocities at the inboard midplane. In order to more easily compare these measurements to fundamental boundary conditions, a basic overview of flows on a flux surface is presented. The boundary conditions are given by the continuity equation and mean that the flow velocities on a flux surface must have a specific structure in order to provide zero divergence. At first, poloidal impurity density asymmetries and radial transport are neglected. Inside of the pedestal-top of the electron density profile the measurements agree with the postulated flow structure, while they do not agree at the pedestal itself. Here, an extension of the theoretical scheme, which allows for a poloidal impurity density asymmetry, suggests that the measured flow velocities could be explained by an excess impurity density at the inboard midplane. In detail, the inboard impurity density is postulated to be at the separatrix up to a factor of 6.5 higher than impurity density at the outboard midplane. Near the pedestal-top of the electron density, this asymmetry disappears. Radial transport is considered as an explanation for that asymmetry. A conclusive disentanglement of the driving mechanisms requires further investigation.

## 1. Introduction

The flows in the plasma edge of a tokamak fusion plasma have a complicated structure and at the same time they are an important ingredient of the physics that rules the transport at the plasma edge. For instance, the shear of the plasma flows perpendicular to the magnetic field lines is closely connected to an edge transport barrier in high confinement discharges (H-modes) [1]. The corresponding steep gradients in densities and temperatures are self-consistent with the flows and thus the radial electric field. However, the parallel flows are little investigated. One basic boundary condition, which they have to meet is given by the continuity equation, which for steady state describes the total flow  $\vec{v}$ , by  $\vec{\nabla} \cdot (n\vec{v}) = 0$ , where  $n$  is the particle density. If radial transport is assumed to be poloidally symmetric, i.e. divergence-free, the perpendicular velocity is closely connected to the parallel velocity via the above equation.

When investigating the H-mode edge at ASDEX Upgrade [2], the measurements from charge exchange recombination spectroscopy (CXRS) gave unexpected rotation profiles in between the occurrence of two edge-localized modes (ELMs). A local minimum in the parallel flow at the radius of the electron density pedestal-top was observed. In Ref. [3] and in the present work, these profiles are presented. Since high-viscosity and strong magnetic braking of the plasma is expected only at the separatrix, the local minimum in the rotation is quite puzzling. Instead of postulating complicated transport or torque profiles, it is attempted to explain these profiles by shedding light on the poloidal asymmetry of the parallel flows. The measurements in Ref. [3] are performed on the outboard midplane and it is possible that they are not representative of the full flux surface. Such poloidal asymmetries are evaluated in the present work by applying the continuity equation to the flow measurements on a flux surface. This work is closely connected to the work in Ref. [4] performed at Alcator C-Mod. This paper is organized as follows: In section 2, the basics of the flow structure on an isolated flux surface are presented. In section 3 the extent to which this structure is visible in experiment and how the diagnostic measurements can be compared to the theoretical scheme are described. In section 4 the diagnostics are introduced in more detail. In section 5 the experiment and the results are presented, while in section 6 they are discussed and compared to the expected flow structure as described in section 3. In section 7, the discussion is extended to a scheme in which the impurity densities are not constant on each flux surface. Finally, in section 8 the effects of radial transport and its non-zero divergence are discussed. Section 9 is the summary.

## 2. Flow Structure on a Flux Surface

The following considerations are basic and have been presented in review papers (e.g. Ref. [5]). The equations are rewritten and reconsidered in this work, to clarify exactly to which terms the experimental data is compared.

The general continuity equation requires that the 3D flow velocity exhibits zero divergence. In detail, it is required that  $\vec{\nabla} \cdot (n_\alpha \vec{v}_\alpha) = 0$ , where  $n_\alpha$  is the density of a species  $\alpha$  and  $\vec{v}_\alpha$  its flow velocity. When the divergence of radial flows is negligible compared to the fluxes within a flux surface, the 2D flows on a flux surface must be divergence free. In sections 2 to 7, the radial divergence of flows is assumed to be zero and the structure of the 2D flows on a flux surface are investigated, while the perpendicular flow velocities are obtained by the radial force balance.

The radial force balance (Eq. 1) for an ion species  $\alpha$  relates the local velocity  $\vec{v}_\alpha$  to the local magnetic field  $\vec{B}$ , electric field  $\vec{E}$  and the diamagnetic term  $-\frac{\vec{\nabla} p_\alpha}{Z_\alpha e n_\alpha}$ , where  $p_\alpha$  is the pressure,  $Z_\alpha$  the charge,  $n_\alpha$  the density of the species  $\alpha$  and  $e$  the elementary charge. The radial force balance is given by

$$0 = \vec{E} - \frac{\vec{\nabla} p_\alpha}{Z_\alpha e n_\alpha} + \vec{v}_\alpha \times \vec{B} \Rightarrow v_{\perp,\alpha} = \left( E_r - \frac{1}{Z_\alpha e n_\alpha} \frac{\partial p_\alpha}{\partial r} \right) \frac{1}{B} \quad (1)$$

where  $r$  is the radial coordinate,  $E_r$  the radial electric field,  $v_{\perp,\alpha}$  the velocity component

*Poloidal Asymmetry of Parallel Rotation Measured in ASDEX Upgrade*

perpendicular within the flux surface to  $\vec{B}$  and  $B\vec{e}_{\parallel} = \vec{B}$ , where  $\vec{e}_{\parallel}$  is the unity vector along a magnetic field line. The two contributions to  $v_{\perp,\alpha}$  are the  $\vec{E} \times \vec{B}$  velocity and the diamagnetic drift velocity. It should be noted that  $v_{\perp,\alpha}$  is different for the inner (high field side, HFS) and outer (low field side, LFS) midplane, which is the basic reason for non-zero divergence of  $v_{\perp,\alpha}$  on a flux surface. This is compensated for by the parallel Pfirsch-Schlüter flows, a derivation of which is presented in the following. Equation 1 may be rewritten as

$$\begin{aligned} v_{\perp,\alpha} \vec{e}_{\perp} &= -\frac{\vec{\nabla}\Phi \times \vec{B}}{B^2} - \frac{1}{Z_{\alpha}en_{\alpha}} \frac{\vec{\nabla}p_{\alpha} \times \vec{B}}{B^2} \\ &= -\left(\frac{\partial\Phi}{\partial\Psi} + \frac{1}{Z_{\alpha}en_{\alpha}} \frac{\partial p_{\alpha}}{\partial\Psi}\right) \frac{\vec{\nabla}\Psi \times \vec{B}}{B^2} = -\omega_{\alpha}(\Psi) \frac{\vec{\nabla}\Psi \times \vec{B}}{B^2} \end{aligned} \quad (2)$$

with  $\omega_{\alpha}(\Psi) = \frac{\partial\Phi}{\partial\Psi} + \frac{1}{Z_{\alpha}en_{\alpha}} \frac{\partial p_{\alpha}}{\partial\Psi}$ , where  $\Phi$  is the electrostatic potential,  $\Psi$  is the poloidal magnetic flux and  $\vec{e}_{\perp}$  is the local unity vector tangential to the flux surface and perpendicular to the magnetic field line. The last equation assumes  $\Phi$ ,  $n_{\alpha}$  and  $p_{\alpha}$  to be constant on the flux surface such that  $\omega_{\alpha}$  is a pure flux function. Note that  $\omega_{\alpha}(\Psi)$  is identified below as the angular frequency of a toroidal rigid body rotation. Using the equality  $\frac{\vec{\nabla}\Psi \times \vec{B}}{B^2} = \frac{RB_p}{B} \vec{e}_{\perp}$  valid for axisymmetric systems, where  $B_p$  is the poloidal magnetic field component and  $R$  is the local major radius, Eq. 2 becomes:

$$v_{\perp,\alpha} \vec{e}_{\perp} = -\omega_{\alpha}(\Psi) \frac{RB_p}{B} \vec{e}_{\perp} \quad (3)$$

This can be further manipulated using relations between the unity vectors for the toroidal ( $\vec{e}_t$ ), poloidal ( $\vec{e}_p$ ), parallel ( $\vec{e}_{\parallel}$ ) and perpendicular ( $\vec{e}_{\perp}$ ) directions, while the same indices on  $B$  indicate the corresponding components of the magnetic field. Note that the unity vector along the plasma radius  $\vec{e}_r$ ,  $\vec{e}_{\parallel}$  and  $\vec{e}_{\perp}$  are chosen such that they form a right-handed system. The equalities  $\vec{e}_{\perp} = \frac{B_t}{B} \vec{e}_p - \frac{B_p}{B} \vec{e}_t$  and  $\vec{e}_p = \frac{B_p}{B} \vec{e}_{\parallel} + \frac{B_t}{B} \vec{e}_{\perp}$ , may be combined to give  $\vec{e}_{\perp} = \frac{B_t}{B_p} \vec{e}_{\parallel} - \frac{B}{B_p} \vec{e}_t$ , which converts Eq. 3 into following form:

$$v_{\perp,\alpha} \vec{e}_{\perp} = \omega_{\alpha}(\Psi) \left( R\vec{e}_t - \frac{RB_t}{B} \vec{e}_{\parallel} \right) \quad (4)$$

While not demonstrated here, it is known that  $v_{\perp,\alpha} \vec{e}_{\perp}$  is not divergence-free. It is clear that the term  $\propto R\vec{e}_t$  (rigid rotation) is divergence-free and thus is not responsible for the non-zero divergence of  $v_{\perp,\alpha} \vec{e}_{\perp}$ . However, the parallel term does lead to a non-zero divergence and thus requires a parallel flow with the same structure to compensate. Therefore, the parallel flows are described by

$$v_{\parallel,\alpha} \vec{e}_{\parallel} = \omega_{\alpha}(\Psi) \frac{RB_t}{B} \vec{e}_{\parallel} + CB\vec{e}_{\parallel} \quad (5)$$

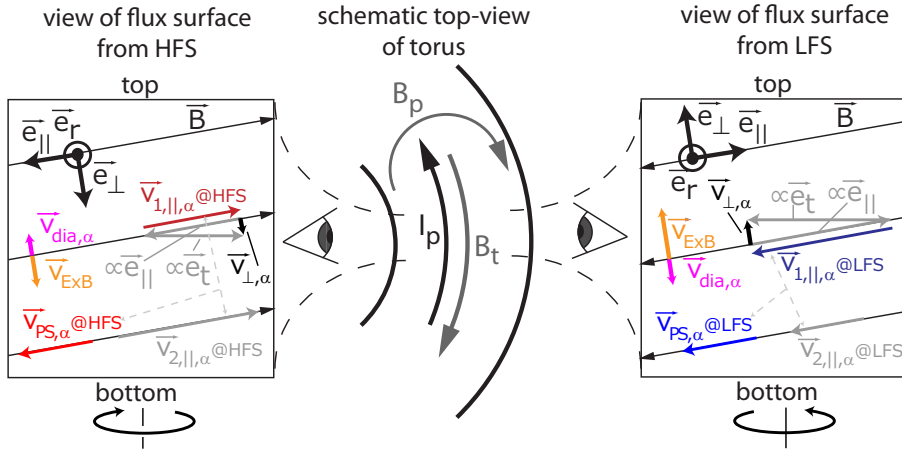
where  $C$  is an undetermined constant allowing for a degree of freedom. A schematic visualization of the terms is presented in Fig. 1. The first term in Eq. 5 (in Fig. 1 labelled  $\vec{v}_{1,\parallel,\alpha}$ ) compensates for the non-zero divergence of the perpendicular velocity  $v_{\perp,\alpha}$  and the second term describes an additional degree of freedom, as any parallel flow that is  $\propto B$  is

## Poloidal Asymmetry of Parallel Rotation Measured in ASDEX Upgrade

divergence free due to  $\vec{\nabla} \cdot \vec{B} = 0$ . For  $C = \frac{\hat{u}_\alpha}{\langle B^2 \rangle} - \omega_\alpha(\Psi) \frac{RB_t}{\langle B^2 \rangle}$ , Eq. 5 may be rewritten in the following way

$$v_{\parallel,\alpha} \vec{e}_\parallel = \omega_\alpha(\Psi) RB_t \left[ \frac{1}{B} - \frac{B}{\langle B^2 \rangle} \right] \vec{e}_\parallel + \hat{u}_\alpha \frac{B}{\langle B^2 \rangle} \vec{e}_\parallel \quad (6)$$

where  $\langle B^2 \rangle$  is the flux surface average of  $B^2$  and  $\hat{u}_\alpha$  a constant. This has the advantage that  $\langle \vec{v}_{\parallel,\alpha} \vec{B} \rangle = \hat{u}_\alpha$ , which is of interest for radial transport considerations. In the following the first term in Eq. 6 is referred to as the Pfirsch-Schlüter flows. This term is labelled  $\vec{v}_{PS,\alpha}$  in Fig. 1 resulting from  $\vec{v}_{1,\parallel,\alpha} + \vec{v}_{2,\parallel,\alpha}$ , where  $\vec{v}_{2,\parallel,\alpha} = -\omega_\alpha(\Psi) RB_t \frac{B}{\langle B^2 \rangle} \vec{e}_\parallel$ .



**Figure 1.** Directions of the various vectors for a typical case in ASDEX Upgrade on a flux surface at about  $\rho_{pol} = 0.975$ . The perpendicular velocity  $\vec{v}_{\perp,\alpha}$  of a species  $\alpha$  is shown as the sum of the diamagnetic velocity  $\vec{v}_{dia}$  and  $\vec{v}_{ExB}$  at the HFS and LFS. The  $\vec{v}_{\perp,\alpha}$  is also represented by a sum of a toroidal and parallel vector (cf. Eq. 4). The compensating parallel term  $\vec{v}_{1,\parallel,\alpha}$  is added to a term  $\propto \vec{B}$ , which is labelled  $\vec{v}_{2,\parallel,\alpha}$  to obtain the Pfirsch-Schlüter flow  $\vec{v}_{PS,\alpha}$  (cf. first term in Eq. 6). With respect to  $\vec{B}$ ,  $\vec{v}_{PS,\alpha}$  at the HFS has the opposite direction from  $\vec{v}_{PS,\alpha}$  at the LFS. Please note that the length of the vectors is not exactly up to scale.

Eqs. 4 and 5 may be combined to form one equation for  $\vec{v}_\alpha$ . This leads to a general form, which is used in Ref. [4] to investigate the flow structure on a flux surface and separates the total flow into a rigid body rotation characterized by the angular frequency  $\omega_\alpha$  and a parallel flow.

$$\vec{v}_\alpha = \omega_\alpha(\Psi) R \vec{e}_t + C B \vec{e}_\parallel \quad (7)$$

Equation 7, can also be used to investigate the effect of a poloidal impurity density ( $n_\alpha$ ) variation on a flux surface. A poloidal redistribution is only provided by the second term in Eq. 7 and thus only this part of the flow is affected by a poloidal impurity density variation. As the particle flux is  $\propto n_\alpha$  the second term needs to be  $\propto 1/n_\alpha$  in order to maintain the divergence-free structure. This was described in Ref. [4] and will be used later in this work. However, it should be noted that a poloidal change of the density will also influence the poloidal structure of the diamagnetic term in the radial force balance. Such a change could

mean that the poloidal flow of the species or possibly even the electrostatic potential may have poloidal dependencies that are not expected.

It should also be noted that in the above the divergence of the radial transport was considered negligible. If the divergence of the radial flow is considerable, then it must be included in the continuity equation and the equations above require an additional term. For sections 2 to 7, the radial transport and its divergence is ignored.

### 3. Observation of the Flow Structure

In the previous section, the cancellation of the parallel terms in Eq. 4 and Eq. 5 might give the impression that this structure, which is poloidally asymmetric, is not observable in experiment. However, in Eq. 4 the toroidal rotation closely matches the parallel term such that the perpendicular flow  $v_{\perp,\alpha} \vec{e}_{\perp}$  is obtained. The projection onto the LOS of  $v_{\perp,\alpha} \vec{e}_{\perp}$  is very small (s. below). At the same time, the parallel Pfirsch-Schlüter flow structure (Eq. 5) has no compensating term attached and thus is visible. If we compare numbers for the actual geometry of the diagnostics, the angle between magnetic field lines and the lines of sight (LOS) for the toroidal views is smaller than 10 degrees for all of the cases considered in this work. The maximum values in the perpendicular rotation, are in the range of 20 km/s, thus the projection on the (approximately) toroidal LOS ( $< \sin 10^\circ$ ) is smaller than 3.5 km/s. The parallel flow, for which the Pfirsch-Schlüter flow compensates, is expected to be in the range of 20-30 km/s at the outer midplane and its projection onto the LOS ( $> \cos 10^\circ$ ) is virtually the full flow. As 20-30 km/s are much larger than the upper bound for the observed perpendicular flow (3.5 km/s), the Pfirsch-Schlüter flows dominate the toroidal flow measurement in comparison to the perpendicular flows.

For a direct comparison between theory and experiment, we can use the equality  $\frac{\partial r}{\partial \Psi} = \frac{1}{RB_p}$  in order to rewrite the product of  $\omega_\alpha$  and  $RB_t$  (cf. first term on the right side in Eq. 6):

$$\omega_\alpha RB_t = \left( -E_r + \frac{1}{Z_\alpha e n_\alpha} \frac{\partial p_\alpha}{\partial r} \right) \frac{B_t}{B_p} \quad (8)$$

Due to the fact that  $\omega_\alpha$  and  $RB_t$  are constants on a flux surface the corresponding terms in Eq. 6 may be evaluated at the LFS and are valid for the full flux surface. Therefore, it is valid to rewrite Eq. 6 as

$$\begin{aligned} v_{\parallel,\alpha}(B) &= \left( -E_{r,LFS} + \frac{1}{Z_\alpha e n_\alpha} \frac{\partial p_\alpha}{\partial r} \Big|_{LFS} \right) \frac{B_{t,LFS}}{B_{p,LFS}} \left( \frac{1}{B} - \frac{B}{\langle B^2 \rangle} \right) + \hat{u}_\alpha \frac{B}{\langle B^2 \rangle} \\ &= v_{PS,\alpha} + \hat{u}_\alpha \frac{B}{\langle B^2 \rangle} \end{aligned} \quad (9)$$

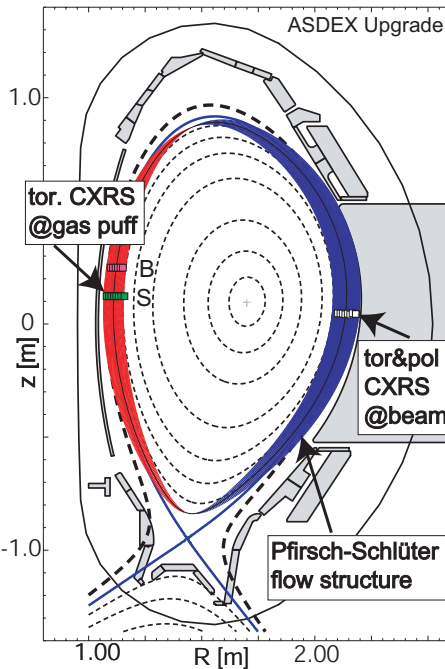
where  $B_{t,LFS}$ ,  $B_{p,LFS}$ ,  $E_{r,LFS}$  and  $\frac{\partial p_\alpha}{\partial r} \Big|_{LFS}$  denote the toroidal and poloidal magnetic field, the radial electric field and pressure gradient of the particle species  $\alpha$  at one location on the LFS. This means that for the interpretation of the experimental data, the LFS measurements and the information about the magnetic equilibrium (from magnetic equilibrium reconstruction) can be used to obtain the Pfirsch-Schlüter flows  $v_{PS,\alpha}$  on the full

## Poloidal Asymmetry of Parallel Rotation Measured in ASDEX Upgrade

6

flux surface. Note that Eq. 9 is an implicit Definition for  $v_{PS,\alpha}$  and exactly corresponds to  $v_{PS,\alpha}$  that was introduced earlier, e.g. in Fig. 1.

In Fig. 2 the structure of the Pfirsch-Schlüter flow for a real geometry at the radius  $\rho_{pol} = 0.975$  is indicated for the condition  $-E_r + \frac{1}{Z_\alpha e n_\alpha} \frac{\partial p_\alpha}{\partial r} > 0$  kV/m. This condition refers to the typical situation inside of the separatrix, where the radial electric field is negative and the absolute value is larger than the diamagnetic term of the impurities, which is also negative. Blue (red) regions indicate flows directed out of (into) the plane of the paper. The thickness of the region indicates the absolute size of the flow. It should be noted that the Pfirsch-Schlüter flows are a property of a flux surface, and thus the values of  $E_r$  and the diamagnetic term of the species  $\alpha$  at the considered radius are of importance. In Fig. 2, the measurement locations



**Figure 2.** Structure of Pfirsch-Schlüter flows at  $\rho_{pol} = 0.975$  for  $-E_r + \frac{1}{Z_\alpha e n_\alpha} \frac{\partial p_\alpha}{\partial r} > 0$  kV/m and diagnostic locations for the beam and gas puff based CXRS systems.

of the toroidal and poloidal (newly installed) rotation at the LFS are indicated along with the newly installed diagnostics for toroidal rotation at the HFS. The locations are well suited to see effects of Pfirsch-Schlüter flows.

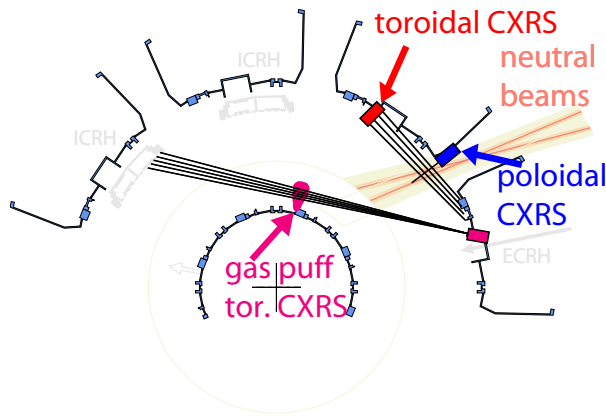
In order to compare the flows as evaluated in Eq. 9 to the measurements, we evaluate  $v_{PS,\alpha}$  in Eq. 9 from the experimental data at the LFS. We then use Eq. 9 to determine the constant  $\hat{u}_\alpha$ , as we know  $v_{PS,\alpha}$  from the LFS measurements and we know  $v_{\parallel,\alpha}$  at the LFS, which is to good accuracy equal to our measured toroidal velocity at the LFS (denoted as  $v_{\parallel,\alpha,LFS}^{exp}$  in the following). After that we have all of the necessary ingredients to predict the parallel flow at the measurement locations on the HFS. Thus we are able to test the prediction by comparing to the measurement at the HFS (denoted as  $v_{\parallel,\alpha,HFS}^{exp}$  in the following). It should be noted that this procedure is equivalent to testing Eq. 7 with all three flow measurement (i.e. both toroidal and one poloidal flow measurement). The equivalence is maybe unclear,

*Poloidal Asymmetry of Parallel Rotation Measured in ASDEX Upgrade*

because for the test of Eq. 7 only flow measurements are required, while for the evaluation of the Pfirsch-Schlüter flows  $E_r$  and the diamagnetic term is required. However, if  $E_r$  is evaluated from the radial force balance of species  $\alpha$ ,  $E_r$  contains exactly the diamagnetic term, which is subtracted for the evaluation of the Pfirsch-Schlüter flows. In that case, Eq. 9 may be evaluated by knowing only the three flow measurements and the two procedures (i.e. exploiting Eq. 7 or Eq. 9) are also equivalent in terms of uncertainties. Note, that in this work Eq. 9 is also analyzed using the diamagnetic term of deuterium, while the flow measurements from impurities are used. This comparison is only possible using Eq. 9 and the uncertainties of the diamagnetic terms of the impurity species and of deuterium enter.

#### 4. Flow Diagnostic at HFS and LFS

For the investigated discharges, the LFS and HFS rotation at the plasma edge are recorded with 2-4 ms time resolution. The rotation measurements at the LFS are performed via CXRS at a heating beam [6]. At the HFS, a D gas puff is applied which leads to CX reactions between the penetrating D gas cloud and the plasma impurities. With this method, information about rotation is obtained only in the outermost plasma region into which the neutrals penetrate, i.e a few cm. A top-view of the edge diagnostics is provided by Fig. 3. Please note that the 'S' and 'B' LOS, which are visible in the poloidal view (Fig. 2), are exactly overlaid in the top-view. For the CXRS reaction between the thermal deuterium gas cloud and the fully



**Figure 3.** Top-view of the beam and gas puff based CXRS systems for the diagnosis of the LFS and HFS plasma edge. 'B' and 'S' stand for background and signal LOS, which are described in the text.

stripped impurity ions, the dominant electron donor is the population of the  $n=2$  state in atomic deuterium. The cross section at thermal energies has only a weak energy dependence and thus the temperature dependence of the effective reaction rate coefficient is weak. Therefore, the Doppler shift of the CX spectral lines allows the direct determination of the impurity flow, while corrections due to cross section effects (cf. e.g. Ref. [7]) are negligible. However, the CX spectral line (active signal) is blended with passive emissions and special effort is required to isolate the active signal. Two toroidal arrays of LOS have been implemented at the

HFS. One is looking directly at the gas puff and gathers the photons from the CX reactions (these LOS are labeled with 'S', for signal, in Fig. 2) along with background photons that are emitted at the plasma edge elsewhere on the paths of the LOS. The LOS of the second array run parallel to those, but miss the gas cloud (labeled 'B', for background, in Fig. 2) and thus provide equivalent spectra but without the CX signal such that the background signal in the active spectra (measured on the 'S' set of LOS) can be subtracted off. For the HFS measurement, a diagnostic gas puff is applied at a time of interest. A few milliseconds before the gas puff, the calibrations of the 'B' channels are refined, i.e. relative calibration factors are obtained with respect to the corresponding 'S' channels. During the gas puff the spectra from the 'B' channels are subtracted from those on the 'S' channels using the previously obtained calibration refinement. In order to provide good diagnostic coverage of the plasma edge, the plasma is swept by 2 cm such that the edge pedestal is slowly moved through the view of the LOS (cf. Ref. [6]).

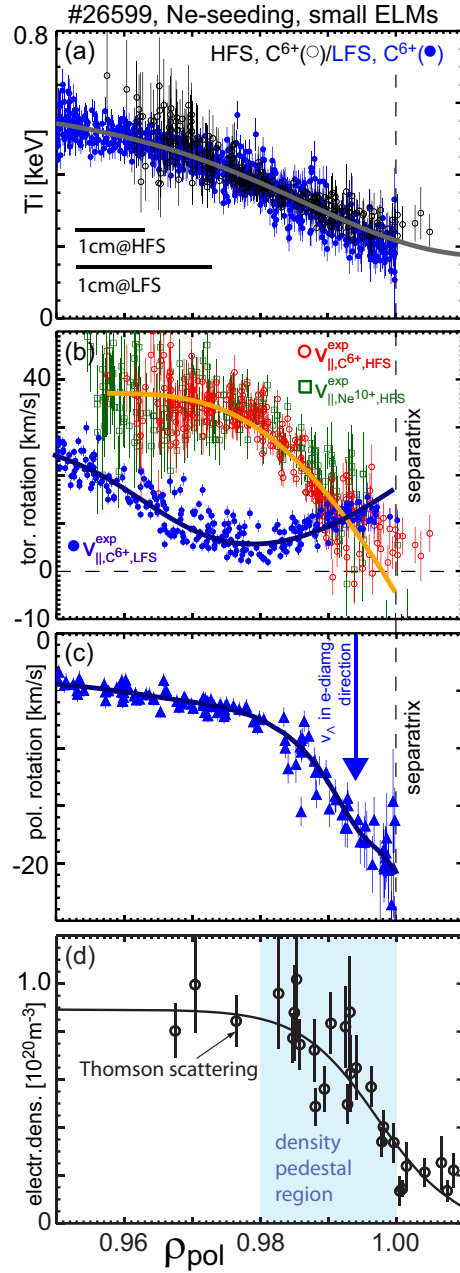
It should be noted that in the following the flow measurements from the LFS and HFS ( $v_{\parallel,\alpha,LFS}^{exp}$  and  $v_{\parallel,\alpha,HFS}^{exp}$ ) are denoted as toroidal rotation. However, the differences between parallel and toroidal velocities are very small due to the field line geometry. This systematic difference is typically smaller than the error bars which represent only the statistical uncertainty and hence, have been neglected. The wavelength calibration is obtained by inter-shot measurements using a Ne lamp and is better than 1 km/s.

## 5. Experiment

The data from two discharge phases are presented in the following. In the first discharge, Ne-seeding leads to improved confinement and fast small ELMs [8], while in the other case a type-I ELMy H-mode [9] is investigated. Both plasma discharges are performed with a toroidal magnetic field of 2.5 T, a plasma current of 1 MA ( $q_{95} \approx 4.5$ ), neutral beam heating of 5 MW, an additional 1.5 MW of ECRH and a density of approx.  $8 \cdot 10^{19} \text{ m}^{-3}$ . The H98(y,2)-confinement-factor is 1.05 for the Ne-seeded case and 0.85 for the type-I ELMy H-mode.

At the LFS, the poloidal and toroidal CXRS measurements are used to obtain a profile of  $E_r$ . The alignment of the toroidal and poloidal CXRS data at the LFS is performed by a comparison of the  $T_i$ -profiles. The position of the separatrix is found by aligning the CXRS data to the electron temperature profiles for which the separatrix position is known from power balance analyses. The procedure is described in Refs. [10, 11, 12].

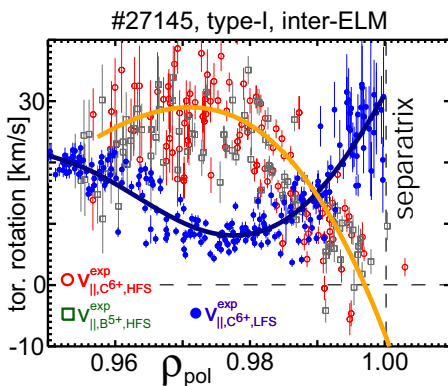
The HFS flow measurements  $v_{\parallel,\alpha,HFS}^{exp}$  are aligned to the LFS flow measurements  $v_{\parallel,\alpha,LFS}^{exp}$  (thus also to the  $E_r$  data) using the  $T_i$ -profiles. The accuracy of the process is estimated to be better than 2–3 mm. In Fig. 4(a), an alignment of the HFS  $T_i$ -profile with respect to the LFS  $T_i$ -profile is presented. In Fig. 4(b), the toroidal rotation profiles for the same discharge are shown. As mentioned earlier the ELMs in this discharge are small, high-frequency perturbations, which have little effect on the edge plasma. The spectra obtained during an ELM crash have been removed from the analysis. The Ne-seeding allows the rotation of  $\text{Ne}^{10+}$  and  $\text{C}^{6+}$  to be derived from the same spectrum (CX-lines at 524.897 nm (Ne) and 529.059 nm (C)). The profile described by the red data (C) agrees within the uncertainties with

*Poloidal Asymmetry of Parallel Rotation Measured in ASDEX Upgrade*

**Figure 4.** (a) HFS/LFS measurements of  $T_i$  to accomplish the alignment of the rotation profiles. (b) Toroidal/parallel rotation at HFS/LFS. (c) Poloidal rotation of  $C^{6+}$  as measured via an independent, poloidal viewing geometry. (d) The electron density as measured by Thomson scattering is provided as an independent identification of the density pedestal region. The lines are spline fits to the data.

that obtained from the green data (Ne) and both data sets exhibit an asymmetric behavior with respect to the toroidal rotation measured at the LFS. For the latter, only  $C^{6+}$  data is presented for clarity; the Ne LFS data also agrees within the uncertainties of the measurements (cf. [3]). In Fig. 4(c), the poloidal rotation profile for  $C^{6+}$  is depicted, which is important for the considerations on the Pfirsch-Schlüter flows. Please note that a strong poloidal rotation for the

impurities is observed, as  $E_r$  is governed by the main ions, i.e. deuterium, while the impurities have to fulfill their species-specific radial force balance. As the diamagnetic term of the impurities is much smaller than that for deuterium, a considerable perpendicular velocity and thus a strong poloidal velocity is required, while the poloidal velocity of deuterium may be quite small. A similar comparison of the parallel flow velocities is presented in Fig. 5, for the inter-ELM phase of a type-I ELM My H-mode. The presented data originate from the second



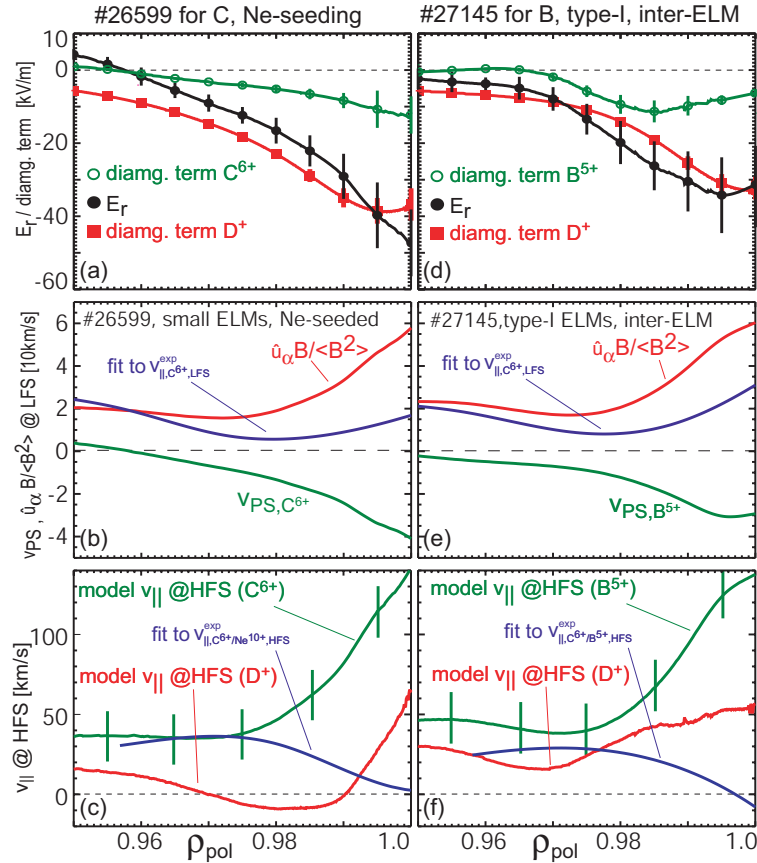
**Figure 5.** Toroidal/parallel rotation at HFS/LFS for  $C^{6+}$  in #27148 and toroidal/parallel rotation at HFS for  $B^{5+}$  in #27145.

half of the ELM cycle, excluding the ELM crash. The discharge was repeated to obtain data for  $B^{5+}$  (494.467 nm) and for  $C^{6+}$ . The shapes of the edge rotation profiles of the type-I and the Ne-seeding cases are similar. For the latter, the difference between the LFS and HFS rotation at about  $\rho_{pol} = 0.975$  is larger by about 10 km/s than for the type-I case. For both cases, the LFS rotation increases and the HFS rotation decreases towards the separatrix, such that they cross inside of the separatrix. These basic observations are valid even if the profiles are shifted within the uncertainties of 2–3 mm.

## 6. Comparison of Experimental Flows with the Pfirsch-Schlüter Prediction

In the following, the question of whether or not the observed flow velocities are consistent with a divergence free flow structure on a flux surface will be addressed. This comparison is the most important result of the present work. For this, the  $E_r$  measurement, i.e. the toroidal and poloidal rotation measurement, performed at the LFS are used. For the Ne-seeding case,  $E_r$  (black) is presented in Fig. 6(a). In Fig. 6(b) the Pfirsch-Schlüter-term  $v_{PS,\alpha}$  and the  $\hat{u}_\alpha$  term at the LFS as derived from the measurements are presented. In order to predict  $v_{||,\alpha}$  (cf. Eq. 9) at the HFS, the measured parallel flow  $v_{||,\alpha,LFS}^{exp}$  at the LFS is compared to  $v_{||,\alpha}$  at the LFS from Eq. 9 and the difference is attributed to  $\hat{u}_\alpha \frac{B_{LFS}}{\langle B^2 \rangle}$ , which determines the constant  $\hat{u}_\alpha$ . Thus  $\hat{u}_\alpha \frac{B}{\langle B^2 \rangle}$  at the HFS is known using the local  $B$ . This allows for the evaluation of  $v_{||,\alpha}$  at the HFS (Eq. 9). In Fig. 6(c), the predicted HFS rotation profile (green) is plotted and compared to the measurement  $v_{||,C^{6+}/Ne^{10+},HFS}^{exp}$  (i.e. the spline fit (blue) to the experimental data), which corresponds to that in Fig. 4(b). The green error bars indicate the propagated

## Poloidal Asymmetry of Parallel Rotation Measured in ASDEX Upgrade



**Figure 6.** (a)  $E_r$  and diamagnetic terms of  $D^+$ ,  $C^{6+}$  for #26599. (b) The two terms in Eq. 9 are presented as evaluated at the LFS measurement position.  $v_{PS}$  (green) is determined from  $E_r$  and diamagnetic term (cf part (a)),  $\hat{u}_\alpha$  (red) is determined such that the measurement (blue) is obtained by Eq. 9. (c) The fit to the measurements  $v_{||,C^{6+}/Ne^{10+},HFS}^{exp}$  (blue) is compared to  $v_{||}$  evaluated by Eq.9 at the HFS (green). The red curve corresponds to the model curve, when  $v_{PS}$  is evaluated with the diamagnetic term of deuterium. Further explanation is in the text. The parts (d),(e) and(f) are the corresponding figures for discharge #27145.

error due to an uncertainty of  $\pm 5$  km/s in  $v_{||,C^{6+}/Ne^{10+},LFS}^{exp}$  (at the LFS). The uncertainty  $\pm 5$  km/s corresponds approx. to the scatter of the data around the spline fit. The measurement agrees with the prediction up to a radius of about  $\rho_{pol} = 0.98$ . Outside of  $\rho_{pol} = 0.98$  strong discrepancies in the values of the flow velocity and also in its radial gradient appear. While the measured, parallel flow velocity decreases towards the separatrix the prediction increases. At the separatrix the parallel flow velocity is measured to be about 0 km/s, while the prediction is in the range of 70 km/s. For the inter-ELM phase in the type-I ELM case (Fig. 6(d), 6(e) and 6(f)) similar observations are made. Due to the lower scatter in the data, the Ne-seeding case is better suited to argue about the HFS flows, however, as the type-I ELM My H-mode is a more common scenario it is presented along with the Ne-seeding data. When looking at Fig. 6, a consistent match of the LFS and HFS velocities would only be possible, if at the pedestal region  $E_r$  was more closely matched by the diamagnetic term and, as a consequence, the calculated  $v_{PS,\alpha}$  would be closer to 0; this is the case for deuterium.

Thus the idea is to investigate the following hypothesis: The parallel flows of the impurities are more strongly influenced by the parallel deuterium flow than neoclassical theory accounts for. This might lead to a non-zero divergence of the impurities. The latter implies a systematic, poloidal density variation, a poloidally asymmetric radial transport (i.e. radial transport with non-zero divergence) or both. Note that this hypothesis would be in disagreement with the neoclassical picture, where the impurity flows exhibit no divergence and the difference in the Pfirsch-Schlüter flows is closely connected to neoclassical radial transport. However, indications that the impurities are dragged along in the parallel deuterium flows have been observed in Ref. [3]. If this hypothesis holds, the measured parallel impurity flows would give us the parallel deuterium flows and we can test, whether the deuterium flows agree with Eq. 9, i.e. are divergence-free. In order to test the hypothesis, we evaluate  $v_{PS,\alpha}$  for deuterium using Eq. 9, under the assumption that the LFS flows of deuterium and impurity flows are equal. For deuterium the match between  $E_r$  and the diamagnetic term (cf. Fig. 6(a)) is very close and, thus the agreement of the HFS flow prediction (red in Fig. 6(c)) and the measurement  $v_{||,C^{6+}/Ne^{10+},HFS}^{exp}$  (performed on the impurity) is indeed slightly better between  $\rho_{pol} = 0.98$  and the separatrix. However, the description is still not satisfactory and does not seem to catch all of the important physics.

On top of that, inside of  $\rho_{pol} = 0.98$  the measurement of the  $C^{6+}/Ne^{10+}$ -flows at the HFS are clearly different from the expectations for D flows. For the type-I ELM case (cf. Fig. 6(f)) the measured flows are not described by the calculated parallel flows, too. Both studied cases show that the D-flow and the Ne/C/B-flows are different, which also means that there should be a difference between the flows of the various impurities. This difference is estimated to be relatively small compared to the scatter in the measurement and, therefore, it is not visible. Future investigations will try to better quantify that difference.

The discrepancy of the flow prediction and the measured flows suggests that one of the assumptions made for deriving Eq. 9 is violated. The assumptions are that the divergence of radial transport is negligible compared to parallel transport and that the impurity density is constant on a flux surface. In principle, there is a close interconnection between the two, because the divergence of radial transport will most probably influence the poloidal asymmetry of the impurity density and the flow structure on a flux surface. For negligible divergence of the radial transport, an impurity density asymmetry is sufficient to alter the flow structure. For that case the impurity flux density, i.e. the flow velocities times the local impurity density, need to be divergence free, as demanded by the continuity equation.

## 7. Interpretation of the Discrepancies as an Impurity Density Asymmetry

In this section we assume that the divergence of radial transport ( $n_\alpha v_r \vec{e}_r$ ) is negligible and we derive a density asymmetry which, in combination with our measured flows, results in a divergence-free situation on each flux surface. We follow the concept presented in Ref. [4] to derive that asymmetry, which means that we alter Eq. 7 to accommodate a poloidal impurity density variation. As the toroidal term in Eq. 7 does not poloidally redistribute the particles,

*Poloidal Asymmetry of Parallel Rotation Measured in ASDEX Upgrade*

13

we need to introduce the impurity asymmetry only in the second term. We get

$$\vec{v}_\alpha = \omega_\alpha(\Psi) R \vec{e}_t + \frac{\tilde{C}}{n_\alpha} B \vec{e}_\parallel \quad (10)$$

The first part in Eq. 10 corresponds to the toroidal component of the perpendicular velocity. Thus using the local field line inclination angle at the LFS  $\delta_{LFS}$  the expression may be replaced by  $\frac{v_{\perp,\alpha,LFS}^{exp}}{\sin \delta_{LFS}} \frac{R}{R_{LFS}}$ , where  $v_{\perp,\alpha,LFS}^{exp}$  is the perpendicular velocity at the LFS, which is determined mostly by the poloidal velocity, and  $R_{LFS}$  is the large radius at the same position on the LFS. The term  $\frac{R}{R_{LFS}}$  is necessary, to maintain the validity of the replacement expression for the full flux surface. The simplification that the toroidal and the parallel direction are indistinguishable for the used viewing geometries at LFS and HFS has two consequences. First, the measured (toroidally) projections of  $\vec{v}_\alpha$  at LFS and HFS, i.e.  $v_{\parallel,\alpha,LFS}^{exp}$  and  $v_{\parallel,\alpha,HFS}^{exp}$ , are not sensitive to the perpendicular nor to the poloidal part of  $\vec{v}_\alpha$ . Second, the measurement  $v_{\parallel,\alpha,LFS}^{exp}$  at the LFS, may be compared to

$$v_{\parallel,\alpha} \approx \frac{v_{\perp,\alpha,LFS}^{exp}}{\sin \delta_{LFS}} \frac{R}{R_{LFS}} + \frac{\tilde{C}}{n_\alpha} B, \quad (11)$$

(corresponding to Eq. 10) when evaluated at the LFS. Note that the toroidal viewing geometry cannot distinguish between the first and second term in Eq. 11, but the additional poloidal rotation measurement at the LFS allows for the determination of  $v_{\perp,\alpha,LFS}^{exp}$  and thus of the first term. Note that on the right hand side the first term ought to be multiplied by  $\cos \epsilon_1$  and the second term by  $\cos \epsilon_2$ , where  $\epsilon_1$  is the angle between LOS and  $\vec{e}_t$  and  $\epsilon_2$  is the angle between the LOS and  $\vec{e}_\parallel$ . This has been omitted for simplicity and the introduced error is negligible, because the cosine of both angles is greater than 0.98.

The second term on the right hand side of Eq. 11 (i.e.  $\frac{\tilde{C}}{n_\alpha} B$ ) is determined by setting  $v_{\parallel,\alpha} = v_{\parallel,\alpha,LFS}^{exp}$ . Thus it is equal to the difference between the measurement of  $v_{\parallel,\alpha,LFS}^{exp}$ , and  $\frac{v_{\perp,\alpha,LFS}^{exp}}{\sin \delta_{LFS}}$ . In order to obtain  $v_{\parallel,\alpha}$  on the full flux surface, this term must be scaled with  $\frac{B}{B_{LFS}}$  and  $\frac{n_{\alpha,LFS}}{n_\alpha}$ , where  $n_{\alpha,LFS}$  is the impurity density at the LFS position. Thus  $\tilde{C} = \frac{n_{\alpha,LFS}}{B_{LFS}} \left[ v_{\parallel,\alpha,LFS}^{exp} - \frac{v_{\perp,\alpha,LFS}^{exp}}{\sin \delta_{LFS}} \right]$ . Using the considerations above, Eq. 11 may be rewritten to give

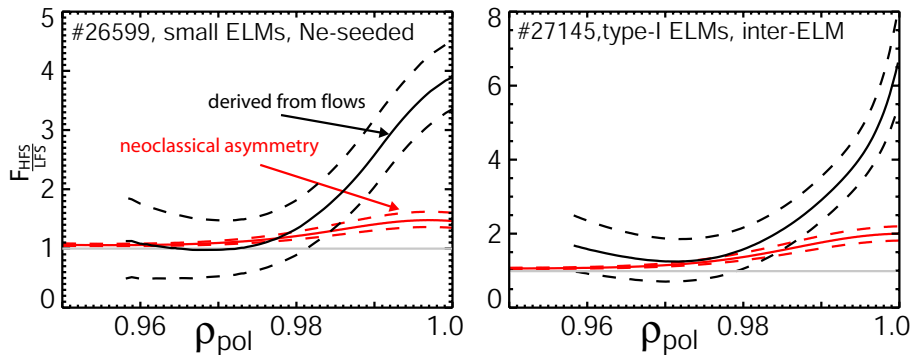
$$v_{\parallel,\alpha,HFS}^{exp} \approx \frac{v_{\perp,\alpha,LFS}^{exp}}{\sin \delta_{LFS}} \frac{R_{HFS}}{R_{LFS}} + \frac{1}{F_{HFS}^{\frac{n_{\alpha,HFS}}{n_{\alpha,LFS}}}} \left[ v_{\parallel,\alpha,LFS}^{exp} - \frac{v_{\perp,\alpha,LFS}^{exp}}{\sin \delta_{LFS}} \right] \frac{B_{HFS}}{B_{LFS}} \quad (12)$$

where  $F_{HFS}^{\frac{n_{\alpha,HFS}}{n_{\alpha,LFS}}} = \frac{n_{\alpha,HFS}}{n_{\alpha,LFS}}$  is the impurity asymmetry factor between the LFS and HFS impurity density. Thus  $F_{HFS}^{\frac{n_{\alpha,HFS}}{n_{\alpha,LFS}}}$  may be determined by:

$$F_{HFS}^{\frac{n_{\alpha,HFS}}{n_{\alpha,LFS}}} \approx \frac{\left[ v_{\parallel,\alpha,LFS}^{exp} - \frac{v_{\perp,\alpha,LFS}^{exp}}{\sin \delta_{LFS}} \right] \frac{B_{HFS}}{B_{LFS}}}{v_{\parallel,\alpha,HFS}^{exp} - \frac{v_{\perp,\alpha,LFS}^{exp}}{\sin \delta_{LFS}} \frac{R_{HFS}}{R_{LFS}}} \quad (13)$$

The evaluation of Eq. 13 is presented in Fig. 7 for both investigated discharges. The discrepancies between the predicted and measured toroidal velocities on the HFS (cf. Fig. 6) translate into impurity density asymmetries factors of 3.9 and 6.5 at the separatrix. For the

presented impurity asymmetries a perfect match of all measured flow velocities is obtained. Inside of the pedestal-top (of the electron density), the observed velocities do not require a density asymmetry and the presented curves approach 1. The dashed lines indicate the error interval due to an uncertainty of 5 km/s in the toroidal velocity measurements and 1 km/s in the poloidal velocity measurements. We consider the postulated asymmetry in impurity density quite large and thus emphasize that an independent test of that result is necessary.



**Figure 7.** The postulated impurity density asymmetries, as derived from the flow measurements on LFS and HFS (black), is compared to the asymmetry as derived in Ref. [4] using the neoclassical scheme from Ref. [13] (red). The dashed lines indicate the uncertainty intervals.

In Ref. [4], it was found that the impurity density asymmetry cannot be described by a neoclassical scheme (cf. Ref. [13]), which allows for impurity asymmetries in regions with strong gradients in ion densities and ion temperatures. The same result is found for the analyzed discharges in the present work. Using the same scheme as in Refs. [4, 13], the experimental gradient lengths of ion densities (derived from the measured electron density profiles) and ion temperatures are used to evaluate the neoclassical asymmetry. The result is presented in red in Fig. 7. The uncertainty in the red curve is obtained by assuming a 40 % uncertainty in the ratio of the ion density and ion temperature gradient lengths. The largest neoclassical asymmetries are found close to the separatrix, but they are less than a factor of two for both cases.

Independently of that finding, a clear correlation between the magnitude of impurity asymmetry and the magnitude of poloidal velocity of the impurities is found in Ref. [4]. In the present work, the magnitude of the density asymmetry correlates with the distance to the separatrix, which is equivalent with the magnitude of the poloidal rotation (cf. Fig. 4(c)).

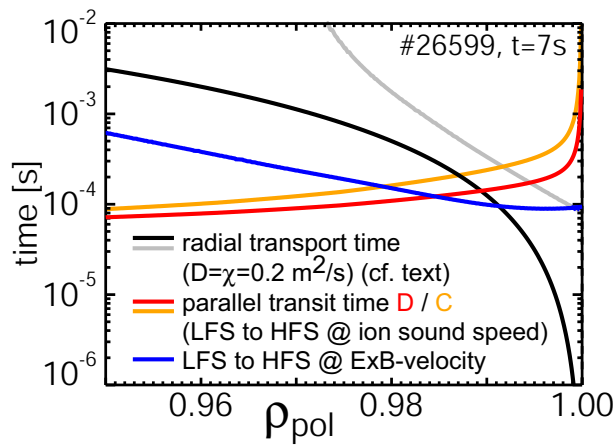
A quantitative evaluation of the impurity densities at LFS and HFS by CXRS is desireable acting as an independent confirmation of the large asymmetry postulated from the flow measurements. However, this requires a quite accurate, quantitative model for the penetration and excitation of the gas puff, which is not available at present. Further investigations into that direction are planned.

## 8. Considerations on Radial Transport and Its Divergence

All considerations in this chapter investigate the possibility of a non-negligible influence of poloidal asymmetric transport, i.e. radial transport with a considerable divergence of  $n_\alpha v_r \vec{e}_r$ , where  $v_r$  is the radial flow velocity.

### 8.1. Time Scales

In Fig. 8, typical time scales of the processes that might influence the flow equilibrium on a flux surface are presented versus normalized radius. For the following considerations the Ne-needed case was chosen. The processes for which the time scales are estimated are radial transport, redistribution on a flux surface along the field lines with ion sound speed and redistribution on a flux surface perpendicular to the field lines according to the perpendicular flows. The idea of the comparison is that radial transport could interfere with the flow equilibrium on a flux surface, by transporting impurities from an erosion location to the flux surface of interest. This would mean that the divergence of  $n_\alpha v_r \vec{e}_r$  is non-zero and could explain the flow structure, a poloidal asymmetry in the impurity density or both. The parallel flows on a flux surface will try to equilibrate these asymmetries and if they manage, the divergence of the radial transport might be considered small with respect to the parallel flows, which is the assumption that we used to derive the 2D flow structure in section 2. The role of the perpendicular velocity is not quite clear, as on the one hand it provides a poloidal redistribution but on the other hand it drives up-down asymmetries that lead to the parallel Pfirsch-Schlüter flows. This ambiguity will be discussed below.



**Figure 8.** Comparison of radial, poloidal and parallel time scales. For radial regions where the parallel time scales are short compared to radial time scales the flows within a flux surface are expected to form a divergence free, 2D flow equilibrium. For radii greater than  $\rho_{pol} = 0.98$  the assumption is not quite valid.

For the radial transport, the time scale is assessed in two ways: For radial particle transport, the typical time scale  $\tau_{r,n}$ , may be estimated by  $\tau_{r,n} = L_\alpha^2 / D$  (grey), where  $L_\alpha$  is the gradient length of the impurity density ( $\frac{1}{L_\alpha} = \frac{\partial n_\alpha}{\partial r} \frac{1}{n_\alpha}$ ) and  $D$  is the local diffusion coefficient.

In Ref. [12] the radial transport of impurities on AUG has been investigated and for carbon  $D \approx 0.2 \text{ m}^2/\text{s}$  was found in agreement with neoclassical values. Thus  $D = 0.2 \text{ m}^2/\text{s}$  is used here. For simplicity, we ignore the inward convection, which is also determined in Ref. [12].

The time scale for the radial momentum transport is not as easily calculated, because gradient lengths are not well defined for rotation velocities. At the same time it is known that  $E_r$  is strongly changing within a few millimeters around the separatrix, as a few millimeters inside of the separatrix  $E_r$  exhibits a global minimum at negative values for  $E_r$ , while in the SOL  $E_r$  is positive. In order to accommodate these boundary condition for the estimate, a diffusion process is assumed for the momentum transport (using  $\chi = D$ ,  $\chi$  being the momentum diffusivity), where instead of  $L_\alpha$  the distance to the separatrix ( $\Delta x$ ) is used. The associated typical time scale is denoted as  $\tau_{r,p} = \Delta x^2 / \chi$  (black). For the parallel time scale, the connection length along the magnetic field lines between LFS and HFS is evaluated and divided by the ion sound speed. The latter is evaluated for both D (red) and for C (orange). The differences, however, are small, because for the impurity a correction due to the drag of electrons is included, which accelerates the impurities ions. For the perpendicular time scale (blue), the poloidal connection length via a flux surface between HFS and LFS is calculated (i.e. of the order 2.0 m) and divided by the  $E \times B$  velocity.

When approaching the separatrix (i.e. outside of  $\rho_{pol} = 0.98$ ), the time scale of radial transport to/from the SOL (black, grey) becomes comparable to the parallel transit time of D and the C ions. The radial density transport (grey,  $\tau_{r,n}$ ) is estimated to be slower than the momentum transport (black,  $\tau_{r,p}$ ), which might be an artefact of the way the time scales were estimated. Regardless, both estimates indicate that in the pedestal region radial transport is comparable to parallel redistribution and poloidal asymmetries of particle and momentum sources might be carried to these radial positions. Thus it is understandable that the flow structure described by Eq. 9 is violated outside of  $\rho_{pol} = 0.98$  as particle and/or momentum transport from neighboring flux surfaces might become relevant via radial transport. This could either transport poloidal asymmetries to the flux surface of interest or influence the flow structure via a non-zero divergence. The importance of radial transport outside of  $\rho_{pol} = 0.98$  is also acknowledged in Refs. [14, 15], where an influence of the scrape-off layer flows on the pedestal flows via viscosity is postulated. The respective B2 modeling in Refs. [14, 15] exhibits similar structures of parallel flows as measured in Ref. [3].

Additionally, the perpendicular velocity is large at the pedestal such that the drift time from LFS to HFS (blue) becomes comparable or even faster than the radial (black, grey) and the parallel transport time (red, orange). For a steady state situation this might not be important, because an equilibrium will form including consistent  $E_r$  and Pfirsch-Schlüter flows. However, in combination with radial transport and density asymmetries the obtained effect is rather unclear.

## 8.2. Non-Zero Divergence due to Poloidally Asymmetric Radial Transport of Impurities

Poloidal Asymmetries in transport (i.e. particle fluxes) exist naturally in turbulent and collisional transport models. At the plasma edge, these asymmetries could lead to density

*Poloidal Asymmetry of Parallel Rotation Measured in ASDEX Upgrade*

17

asymmetries because of the comparable time scales of radial and parallel transport. These effects could be taken account of in the presented equations by including a source and a sink term of the particle fluxes on a flux surface, which corresponds to the transport asymmetries.

Even for poloidally symmetric radial flow velocities, the particle fluxes could be asymmetric, if there are poloidally asymmetric recycling/erosion pattern of Deuterium and Impurities. These patterns could be propagated towards the confinement region of the plasma via radial transport, if parallel transport is sufficiently small.

In order to disentangle these possibilities more information, e.g. a poloidally resolved impurity density measurement, is required.

### *8.3. Non-Zero Divergence due to an Ionization Source*

A poloidally localized ionization source, like the ionization source at the X-point region just inside of the separatrix leads to a non-zero divergence of the flows on the flux surface. Such a source leads to a parallel flow that redistributes particles on a flux surface, while the particles are also transported radially. An X-point ionization source could support a flow that for the used geometry is in co-direction on the LFS and in counter-direction on the HFS.

The following rough estimate assumes that the impurity content of the plasma is maintained by an impurity source at the edge. The magnitude of the source is quantified by assuming that the impurity confinement time is equal to the energy confinement time. It is assumed that 50% of the particles enter the plasma at the X-point and that 50% of these particles are transported along field lines to the upper half of the plasma. Even if that X-point source is a pure deuterium source the impurities will see effects of these flows via friction, which will lead to asymmetries in the impurity density.

The estimate results in parallel flow velocities of several tens of km/s. However, the details of such flows depend not only on the total X-point source, but also on the radial shape of that X-point source and on the poloidal structure of the radial transport in the main plasma. Thus the estimate only motivates further investigations and cannot be considered meaningful for quantitatively understanding the observations.

## **9. Summary**

The flow structure in the H-mode edge of ASDEX Upgrade has been investigated. Three independent measurements allowed for the investigation of the flows on the flux surfaces from the separatrix to the pedestal-top. At the outboard midplane, i.e. low-field side (LFS), charge-exchange recombination spectroscopy (CXRS) measurements were performed on a heating beam and provided parallel and poloidal impurity flow velocities. At the inboard midplane, i.e. high-field side (HFS), a CXRS measurement has been installed, which relies on the interaction of a localized D gas puff and the impurities of the plasma. This diagnostic provides the parallel impurity flow velocities at the inboard midplane. The measurements have been performed in a Ne-seeded phase, in which the edge localized modes (ELMs) cause negligible perturbations and in the inter-ELM phase of a type-I ELM H-mode. The

*Poloidal Asymmetry of Parallel Rotation Measured in ASDEX Upgrade* 18

results/conclusions from both cases are similar. The parallel flows at the LFS and HFS have strongly antisymmetric features. The parallel flow at the LFS exhibits a local minimum at the pedestal-top of the electron density, while at the HFS a local maximum is observed at approximately the same normalized radius. At this radius the HFS flows are larger than the LFS flows. From the pedestal-top towards the separatrix the LFS flow increases, while the HFS flow decreases, such that they become equal between the pedestal-top and the separatrix. At the separatrix, the LFS flow is larger than the HFS flow by a few tens of km/s.

The measurements are compared to a basic model of divergence-free flows on each flux surface. This theory neglects impurity density variations on a flux surface and the divergence of radial transport. The measurements are found to be consistent with the model inside of the pedestal-top of the electron density, i.e. inside of  $\rho_{pol} = 0.98$ . However, at the pedestal itself it is inconsistent. Both is considered the main result of the present work. Further considerations are explored to identify which of the assumptions might be inapplicable at the pedestal.

First, the theoretical scheme is extended to allow for a poloidal asymmetry in the impurity density. This allowed a consistent description of the measurement, but requires a factor of 3.9/6.5 (Ne-seeded/type-I ELM) higher densities at the HFS compared to the LFS at the separatrix. This postulated factor decreases for flux surfaces closer to the pedestal-top and is equal to about 1 (i.e. no asymmetry) at the pedestal-top. Due to the impressive magnitude of the asymmetry at the pedestal an independent confirmation by quantitative CXRS is desireable and planned.

Second, the importance of radial transport and its divergence is investigated. When approaching the separatrix, the time scale of radial transport becomes comparable to the time scales of transport connecting different locations on the same flux surface. This is the case for parallel transport, where particles can equilibrate perturbations with ion sound speed, as well as for perpendicular  $E \times B$  convection. It is concluded that an asymmetric source of impurities could be the reason for an impurity density asymmetry and, thus for the observed flow structure. Independently, an asymmetric deuterium source or radial momentum transport could also lead to a similar result. For this mechanism it is in question whether the impurities exhibit a X-point source or whether the X-point ionization source of deuterium drives deuterium flows which drag impurities along. Both mechanisms will result in impurity density asymmetries. Further investigations are needed to fully understand the observed flow velocities.

## References

- [1] F. Wagner, ASDEX team, and NI team, *Basic Physical Processes of Toroidal Fusion Plasmas* (PUBLISHER, Varenna, 1985), Vol. I, pp. 65–85, eUR 10418 EN.
- [2] A. Herrmann and O. Gruber, *Fusion Science and Technology* **44**, 569 (2003).
- [3] T. Pütterich *et al.*, *Physical Review Letters* **102**, 025001 (2009).
- [4] K. D. Marr *et al.*, *Plasma Physics and Controlled Fusion* **52**, 055010 (2010).
- [5] S. P. Hirshman and D. J. Sigmar, *Nuclear Fusion* **21**, 1079 (1981).
- [6] E. Viezzer *et al.*, in *Europhysics Conference Abstracts (CD-ROM, Proc. of the 39th EPS Conference on Plasma Physics, Stockholm, Sweden, 2012)*, Vol. 36F of *ECA*, edited by S. Ratynskaya, L. Blomberg, and A. Fasoli (European Physical Society, Geneva, 2012), p. O5.118.

*Poloidal Asymmetry of Parallel Rotation Measured in ASDEX Upgrade* 19

- [7] R. J. Fonck, D. S. Darrow, and K. P. Jaehnig, Physical Review A **29**, 3288 (1984).
- [8] J. Schweinzer *et al.*, Nuclear Fusion **51**, 113003 (2011).
- [9] W. Suttrop, Plasma Physics and Controlled Fusion **42**, A1 (2000).
- [10] E. Wolfrum *et al.*, Plasma Physics and Controlled Fusion **51**, 124057 (9pp) (2009).
- [11] J. Neuhauser *et al.*, Plasma Physics and Controlled Fusion **44**, 855 (2002).
- [12] T. Pütterich *et al.*, Journal of Nuclear Materials **415**, S334 (2011).
- [13] T. Fulop and P. Helander, Physics of Plasmas **8**, 3305 (2001).
- [14] V. Rozhansky *et al.*, Journal of Nuclear Materials **415**, S593 (2011).
- [15] V. Rozhansky *et al.*, Journal of Nuclear Materials **363–365**, 664 (2007).

## 5.12 Publication 12

*Rotation and density asymmetries in the presence of large poloidal impurity flows in the edge pedestal*

Plasma Physics and Controlled Fusion 55 (2013) 124037

## Rotation and density asymmetries in the presence of large poloidal impurity flows in the edge pedestal

E. Viezzer<sup>1</sup>, T. Pütterich<sup>1</sup>, E. Fable<sup>1</sup>, A. Bergmann<sup>1</sup>, R. Dux<sup>1</sup>, R. M. McDermott<sup>1</sup>, R. M. Churchill<sup>2</sup>, M. G. Dunne<sup>3</sup> and the ASDEX Upgrade Team

<sup>1</sup>*Max-Planck-Institut für Plasmaphysik, EURATOM Association, Boltzmannstr. 2, 85748 Garching, Germany*

<sup>2</sup>*MIT Plasma Science and Fusion Center, Cambridge, USA*

<sup>3</sup>*Department of Physics, University College Cork, Association Euratom-DCU, Cork, Ireland*

**Abstract.** Novel flow rotation measurements based on charge exchange recombination spectroscopy at the inboard midplane of the ASDEX Upgrade tokamak reveal the existence of an asymmetric flow structure at the H-mode edge, which is shown to arise due to a poloidal impurity density asymmetry. A quantitative evaluation of the impurity density at the inboard side demonstrates that the impurities redistribute along the flux surface, resulting in a poloidal dependency of the impurity density. The poloidal and toroidal impurity flows measured at the high-field side (HFS) and low-field side (LFS) are compared to theoretical predictions based on the parallel momentum balance which includes friction, inertia, the pressure and the electric force. Both a fluid and a kinetic approach are used showing good agreement between each other. The measured impurity flow structure is described by the model quantitatively when a finite poloidal main ion flow of  $\sim 2$  km/s arises, which is in keeping with the standard neoclassical prediction. The interplay of all terms, in particular the inclusion of the impurity inertia term, is important to reproduce the observed flow structure and results in an impurity accumulation at the HFS. The existence of a poloidal impurity density asymmetry in the edge transport barrier slightly reduces the drift parameter  $v/D$ , however, the experimental value is consistent with standard neoclassical theory. This demonstrates that despite the asymmetry in the impurity density, the impurity particle transport is at the neoclassical level.

### 1. Introduction

The interplay between macroscopic flows and transport is of crucial importance to the understanding of plasma confinement and stability. In tokamaks, transport is observed to be dominated by anomalous effects [1], however, there is growing evidence that under certain conditions the ion transport can be explained by neoclassical theory. In the edge transport barrier of H-mode plasmas, where turbulent transport is strongly reduced, the ion heat transport level and the impurity particle transport have been observed to be near neoclassical values [2].

*Rotation and density asymmetries in the presence of large poloidal impurity flows* 2

The poloidal rotation velocity is of particular interest for its role in two phenomena: parallel viscous momentum transport and the shear-flow turbulence-suppression feedback loop, which is responsible for access to the H-mode operation regime. In standard neoclassical theory, the poloidal rotation is coupled to poloidal density asymmetries via particle and momentum conservation. Such poloidal asymmetries can be generated by, amongst others, neoclassical effects [3] or a poloidal variation of the impurity source location [4, 5]. Previous studies have shown that friction between main ions and impurities, which arises due to steep temperature and density gradients, might be one possible mechanism that gives rise to a poloidal impurity density asymmetry [6, 7, 8]. Rigid toroidal plasma rotation has also been considered as one possible player [9, 10, 11]; here, the centrifugal force leads to an impurity accumulation at the outboard side. In addition, in-out asymmetries in the plasma core can arise when ion cyclotron radio frequency heating is applied [12, 13], which can generate an outward convection of the impurities [14, 15].

Poloidal impurity density asymmetries have been observed in the plasma core [12, 16, 17, 18] as well as at the edge [19, 20, 21]. Especially for the edge transport barrier with its steep temperature and density gradients the dominating mechanism responsible for the existence of an asymmetric impurity density profile is ambiguous and a quantitative interpretation has so far not been provided.

Here, the question of what causes the flow structure (and in turn the structure of the impurity particle density) in the edge pedestal of a confined tokamak plasma is addressed. In this paper we present the first measurements of poloidal and toroidal impurity ion rotation velocities at the high-field side (HFS) and low-field side (LFS) of the ASDEX Upgrade (AUG) tokamak. The flow structure is measured using active charge exchange recombination spectroscopy (CXRS) [22] and compared to theoretical predictions based on the parallel momentum balance equation, which includes inertia, friction, the pressure and electric force [23]. The simulations are performed using a fluid model [23] and the drift-kinetic particle code HAGIS [24, 25, 26]. Both the poloidal and toroidal impurity flows and the poloidal impurity density asymmetry are well described by the theoretical predictions and, for the first time, the observed flow structure is reproduced quantitatively. The main drive for the impurity density asymmetry is given by the friction force, while towards the last closed flux surface the poloidal centrifugal term also gives a substantial contribution.

This paper is structured as follows: section 2 describes the measurement technique and presents H-mode edge rotation profiles measured at the HFS and LFS. In section 3 the evaluation of the impurity density at the HFS is presented. Section 4 discusses the comparison of the experimental data to the theoretical predictions and to kinetic simulations. In section 5 the impact of the findings presented with respect to impurity transport are assessed and a summary and conclusions are given in section 6.

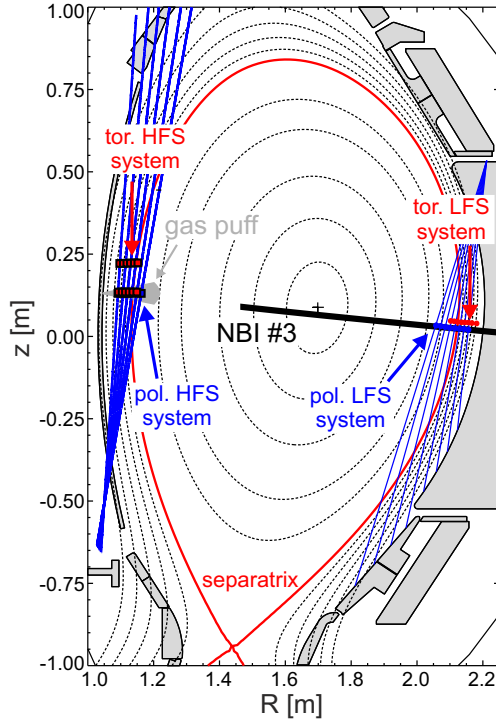


Figure 1: Poloidal cross-section of AUG indicating the measurement locations of the edge CXRS diagnostics.

## 2. Rotation measurements at the inboard and outboard midplane of AUG

At ASDEX Upgrade (AUG) the edge rotation velocities of impurity ions are measured at the low-field side (LFS) and high-field side (HFS) with four independent diagnostics. The LFS system is based on charge exchange recombination spectroscopy (CXRS) at a neutral beam [27] and consists of a toroidal and a poloidal view (see figure 1). The HFS diagnostics utilize a diagnostic D gas puff, and collect light that is emitted after the impurity species undergoes a charge exchange (CX) reaction with a thermal D particle. Using the gas puff technique [28, 29], CXRS measurements are obtained only in the outermost region of the confined plasma since the neutral density, and thus the CX signal, drops rapidly due to the low energy of the injected thermal D atoms. The HFS array consists of a toroidal [20] and a poloidal view (see figure 1) and each view is equipped with two  $f/4$  optical heads to allow for background subtraction (see [28] for details on the experimental setup).

The HFS measurements combined with the data obtained from the LFS diagnostics enable localized CXRS measurements at two different poloidal locations on a flux surface. At the plasma edge the rotation velocities are low and, therefore, accurate knowledge of the wavelength calibration is needed. The wavelength calibration is performed on a shot-to-shot basis using a neon lamp [27]. This method allows the determination of the wavelength calibration quite accurately with uncertainties of the order of  $\sim 1$  km/s.

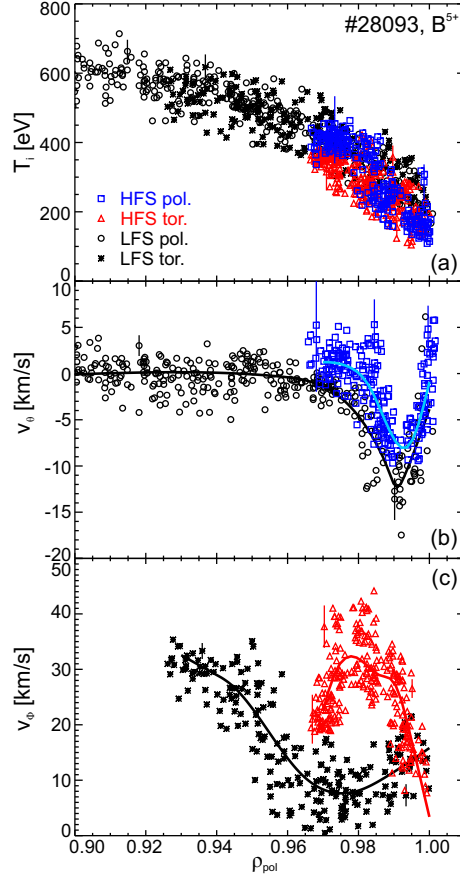


Figure 2: CXRS measurements at the HFS and LFS: (a)  $T_i$ , (b) poloidal rotation and (c) toroidal rotation of  $B^{5+}$ . Data obtained with the LFS systems are shown in black, while measurements from the HFS systems are shown in blue (poloidal view) and red (toroidal view). For better clarity the uncertainties of the measurements are shown at distinct radial positions.

Figure 2 shows example profiles of the ion temperature ( $T_i$ ), poloidal and toroidal impurity rotation velocities ( $v_{\theta,\alpha}$  and  $v_{\phi,\alpha}$ ) obtained at the LFS and HFS. Toroidal rotation velocities, that are counter-clockwise as viewed from above, are positive, while poloidal rotation velocities, that are vertically upward at the LFS, are negative (electron diamagnetic drift direction). The profiles were measured on  $B^{5+}$  ( $n = 7 \rightarrow 6$ ,  $\lambda = 494.467$  nm) in an H-mode discharge with a toroidal magnetic field on-axis of -2.5 T, plasma current of 1 MA, 5 MW of neutral beam injection (NBI) heating and 1.5 MW electron cyclotron resonance heating. In this discharge the main ion collisionality at the pedestal top was approximately 2, i.e. in the plateau regime, while the impurities are deep in the Pfirsch-Schlüter regime. In the standard magnetic configuration of AUG  $B_\phi$  is negative (clockwise viewed from above) and  $B_\theta$  is positive (pointing downward at the outer midplane). The plasma current and the NBI are pointing into the positive toroidal direction, i.e. counter-clockwise viewed from above. The toroidal rotation velocities shown in figure 2(c) are co-current.

*Rotation and density asymmetries in the presence of large poloidal impurity flows* 5

To obtain detailed radial CXRS profiles of both the HFS and LFS the plasma is radially moved through the views of the LOS [27] during a steady state phase of the discharge. First, the plasma is moved over 700 ms towards the outer wall to measure complete LFS profiles and then towards the inner wall to obtain full radial HFS profiles. Shortly before the plasma is moved towards the inner wall the diagnostic gas puff is switched on. At the LFS, the alignment of the toroidal and poloidal CXRS measurements with respect to the separatrix position is performed via the  $T_i$  and impurity density ( $n_\alpha$ ) profiles to reduce uncertainties due to the magnetic equilibrium [30]. The HFS measurements are then aligned relative to the LFS measurements via the  $T_i$  profile assuming that  $T_i$  is constant along the flux surface [7]. The accuracy of the relative profile alignment is estimated to be 2–3 mm [30].

After aligning the HFS profiles with respect to the LFS profiles, the following flow structure is observed: Inside the ETB the poloidal impurity flow exhibits a strongly sheared rotation in the electron diamagnetic drift direction both at the LFS and HFS with the minimum in  $v_{\theta,\alpha}$  approximately at the same radial position. The HFS poloidal rotation velocity is about a factor of 1.5–2 lower than at the LFS. The toroidal rotation velocity is co-current at both the LFS and HFS, however, the profile exhibits an asymmetric structure [20]. At the LFS the toroidal rotation velocity exhibits a minimum located around the pedestal top [31], while at the HFS the profile shows the opposite behaviour and exhibits a maximum at this position (cf. figure 2(c)). Towards the separatrix the toroidal flow at the LFS increases, while it decreases at the HFS.

Both the toroidal flow asymmetry and the difference in magnitude of the poloidal flow might be explained by an excess of impurity density at the HFS, as postulated in [19, 20] and observed in Alcator C-Mod [21]. A poloidal impurity density asymmetry can be inferred based on the neoclassical formalism for the total flow on a flux surface [19, 20]. Allowing for a poloidal dependence of the impurity density, the lowest order divergence-free flow of a species  $\alpha$  on a flux surface is characterized by [32, 33]:

$$\mathbf{v}_\alpha = \omega_\alpha(\Psi) R \mathbf{e}_\phi + \frac{k_\alpha(\Psi)}{n_\alpha} B \mathbf{e}_\parallel \quad (1)$$

where  $\omega_\alpha(\Psi)$  and  $k_\alpha(\Psi)$  are flux functions,  $\Psi$  is the poloidal magnetic flux,  $R$  the local major radius,  $\mathbf{e}_\phi$  and  $\mathbf{e}_\parallel$  the unit vectors in the toroidal and parallel direction,  $n_\alpha$  the impurity density and  $B$  the magnetic field. The divergence-free flow on a flux surface is a composite of the rigid body rotation (first term on the right-hand side of equation (1)) and the parallel flow. Assuming that the impurity density is a flux function,  $k_\alpha(\Psi)$  would result in  $k_\alpha(\Psi) = \frac{v_{\theta,\alpha}}{B_\theta}$  and thus,  $v_{\theta,\alpha}$  is expected to scale with  $B_\theta$ , which is higher at the HFS. Figure 2(b) shows that this dependence is violated since the HFS poloidal rotation is smaller than at the LFS.

Figure 3 shows the measured parallel and poloidal velocity at the HFS (solid black lines). The differences between parallel and toroidal flows are small due to the geometry of the magnetic field lines. However, these differences are taken into account in the following and the measured parallel (and poloidal) impurity flows are compared to the theoretical predictions. The red, dashed lines in figure 3 show the expected parallel and poloidal

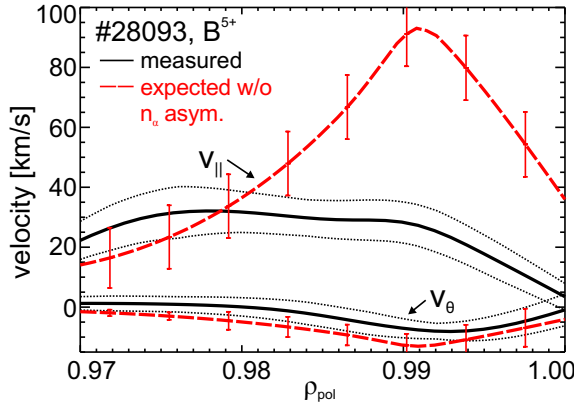


Figure 3: Parallel and poloidal velocities at the HFS: the measured profiles are shown in black while the expected profiles without the existence of an impurity density asymmetry are shown in red (dashed lines). The dotted black lines indicate the uncertainties in the measurement.

impurity flows if no impurity density asymmetry existed. These profiles have been evaluated from the measured LFS profiles using equation (1), assuming that the impurity density is constant on a flux surface. As shown in figure 3 the expected velocities are up to a factor of  $\sim 4$  ( $\sim 2$ ) too high for the parallel (poloidal) flow. This indicates that a poloidal impurity density asymmetry is present in the edge transport barrier. If a poloidal impurity density asymmetry exists [19, 20] the condition of divergence-free flows can be fulfilled.

### 3. Analysis of HFS impurity density and comparison to the LFS

#### 3.1. Direct evaluation of the impurity density from the measured Balmer spectral radiance

For usual CXRS applications the impurity density is evaluated from the measured radiance of the CX signal observed by the line of sight (LOS) combined with knowledge of the neutral density profile and the charge exchange cross-sections. For thermal neutrals the radiance (in photons/sr/m<sup>2</sup>/s) is given by:

$$L_{CX}^{ph}(\lambda) = \frac{1}{4\pi} \int_{LOS} \sum_{n=1}^{n_{max}} n_\alpha n_{D,n} \langle \sigma_n v \rangle_{eff,\lambda} dl \quad (2)$$

where  $n_\alpha$  is the density of the impurity  $\alpha$ ,  $n_{D,n}$  the neutral density with main quantum number  $n$  and  $\langle \sigma_n v \rangle_{eff,\lambda}$  the effective CX rate coefficient, which is derived from the Atomic Data Analysis Structure (ADAS) database [34].  $\langle \rangle$  indicates the Maxwellian average over the cross-section  $\sigma$  and the relative velocity  $v$  between the reaction partners, i.e.  $v = |\mathbf{v}_{D,n} - \mathbf{v}_\alpha|$  with  $\mathbf{v}_{D,n}$  being the velocity of the neutral and  $\mathbf{v}_\alpha$  the velocity of the impurity. Here, the integration is along the LOS and the contributions from all states of the deuterium neutrals (ground and excited states) are summed up.

*Rotation and density asymmetries in the presence of large poloidal impurity flows* 7

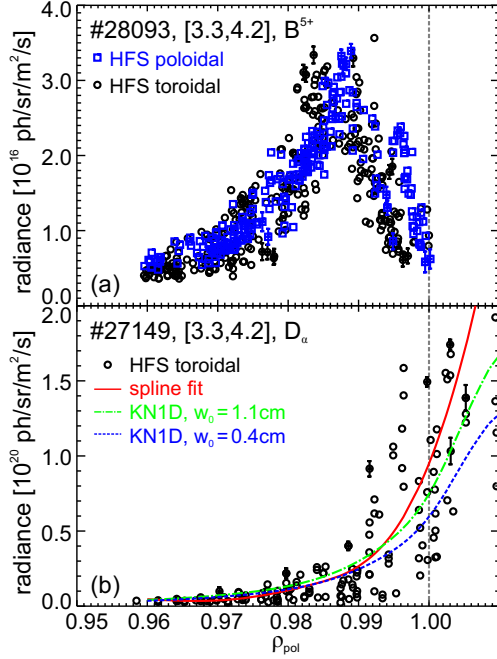


Figure 4: Measured spectral radiance of (a)  $B^{5+}$  and (b)  $D_\alpha$ . Note the difference in magnitude when comparing the absolute values. In (b) the radiance profiles as simulated with KN1D are shown in green (dashed-dotted line) and blue (dashed line).

For charge exchange with thermal neutrals the dominant contribution is given by thermal neutral D in the  $n = 2$  excited state [28, 35]. At low collision energies and considering the  $B^{5+}$  transition, the CX cross-section for D in  $n = 1$  ( $n = 3$ ) is six (four) orders of magnitude smaller than for D in  $n = 2$  [28]. Hence, assuming that the impurity density is constant in the volume where the LOS crosses the gas puff, the impurity density  $n_\alpha$  can be evaluated as follows:

$$L_{CX}^{ph}(\lambda) = \frac{1}{4\pi} n_\alpha \langle \sigma_{n=2} v \rangle_{eff,\lambda} \int_{LOS} n_{D,n=2} dl \quad (3)$$

$$= \frac{1}{4\pi} n_\alpha \langle \sigma_{n=2} v \rangle_{eff,\lambda} \frac{f_{n=2}}{f_{n=3}} \frac{1}{A_{32}} \int_{LOS} \varepsilon_{32} dl \quad (4)$$

$$\Rightarrow n_\alpha = \frac{A_{32}}{\langle \sigma_{n=2} v \rangle_{eff,\lambda}} \frac{f_{n=3}}{f_{n=2}} \frac{L_{CX}^{ph}}{L_{32}} \quad (5)$$

Here,  $A_{32}$  is the Einstein coefficient for the Balmer ( $n = 3 \rightarrow 2$ ) transition,  $f_{n=2}$  and  $f_{n=3}$  the fractional abundances of thermal neutral D in the  $n = 2$  and  $n = 3$  excited states, and  $L_{32}$  the line-integrated emissivity of the  $D_\alpha$  spectral line. Hence, the impurity density can be derived from the measured spectral radiance of the CX line and the  $D_\alpha$  spectral line. Figure 4 shows (a) the measured spectral radiance of  $B^{5+}$  as measured with the poloidal and toroidal HFS system and (b) the  $D_\alpha$  radiance measured in a discharge that is identical to the one described in section 2. Here, only data from the toroidal HFS view is shown as the poloidal system was not yet available. In addition, the spectral radiance derived from the neutral emissivity as simulated with KN1D (see

*Rotation and density asymmetries in the presence of large poloidal impurity flows* 8

next subsection) is shown in figure 4(b).

### 3.2. Calculation of $n_\alpha$ from simulated neutral density profiles

The impurity density can also be evaluated from modelling of the gas puff penetration. The neutral density profiles have been simulated with the 1D in space and 2D in velocity kinetic transport model KN1D [36]. The code uses a slab-like spatial geometry and calculates the distribution functions of neutral atomic and molecular deuterium using a method of successive collision generations with specified input plasma parameters. The molecular neutral pressure at the wall, which is used as input for KN1D, is derived from the manometer measurement of the gas reservoir during the D<sub>2</sub> injection. To obtain the actual D<sub>2</sub> injection rate from the manometer measurement a conversion factor is applied that has been evaluated from a dedicated two chamber experiment [37]. From this injection rate the molecular neutral pressure is calculated taking a cross-sectional area of the gas puff cloud into account, i.e. the molecular neutral pressure is scaled such that the resulting neutral densities fit approximately to the profile derived from the D <sub>$\alpha$</sub>  measurement.

In [28] the shape and the particle density of the gas puff cloud was studied in detail using OSM-EIRENE simulations. It was found that the shape of the gas puff stays approximately the same despite different plasma conditions. The shape of the gas puff is well described by a diverging Gaussian beam [28],  $n_D(R, x) = n_{D,0}(R) \exp(-(x/w(R))^2)$ , where  $x$  is along the line of sight,  $n_{D,0}(R)$  is the nominal neutral density along the center of the gas puff and  $w(R) = w_0 + d(R) \tan(\theta/2)$  the width of the Gaussian. Here,  $w_0$  corresponds to an apparent beam width at the gas puff location (if the shape of the gas puff resembled a truncated cone),  $d(R)$  is the distance to the gas puff location, and  $\theta$  the opening angle of the gas puff [28]. Due to the very similar setup of the gas valve at C-Mod and AUG (horizontal injection), the same opening angle of  $\theta \approx 46^\circ$  is used for the simulated profiles. However, the value for  $w_0$  might change depending on the distance between the measurement volume (as seen by the lines of sight of the diagnostics) and the location of the gas puff. At AUG, the distance between the gas puff location and the separatrix is typically  $\sim 6$  cm. For the KN1D simulations presented here,  $w_0 = 0.4$  cm was used which corresponds to the inner diameter of the gas valve. For a comparison, the value stated in [28],  $w_0 = 1.1$  cm, was used as well. It should be noted, however, that the choice of  $w_0$  does not have a significant impact on the shape of the resulting impurity density profile, but rather on the absolute magnitude (see figure 5).

From the neutral density  $n_{D,0}$  profiles as simulated with KN1D the impurity density at the HFS is derived by taking the geometry of the gas puff into account. Figure 5 shows the impurity density profile at the LFS in black and colour-coded at the HFS. The profile at the LFS has been evaluated including the effect due to the beam halo [38, 39], which is produced by charge transfer from beam neutrals to deuterium ions. The red HFS profile corresponds to the evaluation using the measured Balmer spectral radiance and the profiles shown in blue and green correspond to the simulated  $n_D$  profiles

*Rotation and density asymmetries in the presence of large poloidal impurity flows* 9

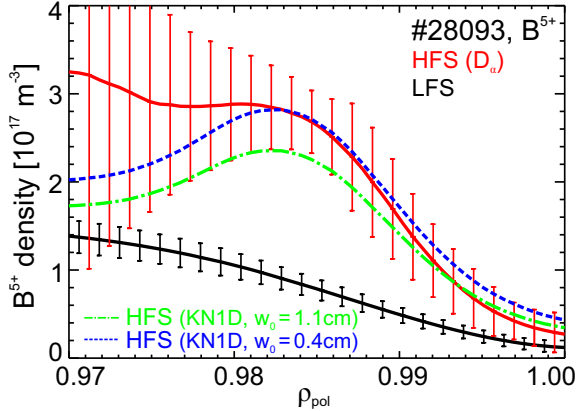


Figure 5:  $B^{5+}$  density at the LFS (black) and HFS (colour-coded): The red profile has been evaluated using the measured radiance of the Balmer spectral line, while the profiles calculated using the neutral density profiles simulated with KN1D are shown in blue ( $w_0 = 0.4$  cm, dashed line) and green ( $w_0 = 1.1$  cm, dashed-dotted line).

with  $w_0 = 0.4$  cm and  $w_0 = 1.1$  cm, respectively. As shown in figure 5 the impurity density is asymmetric on a flux surface, with an impurity accumulation at the HFS. Comparing the HFS impurity density profile as derived from the  $D_\alpha$  spectral line to the one evaluated using the KN1D simulation shows a relatively good agreement for the region with a negative radial gradient. Further inwards ( $\rho_{pol} < 0.98$ ), the shape deviates. Note, however, that towards the plasma core the uncertainties in the HFS measurements increase due to the limited penetration of the gas puff neutrals. In addition, since KN1D is a 1D code and 3D effects might affect the total shape of the neutral density (and thus, the resulting  $n_\alpha$  profile), the KN1D simulation also has uncertainties in the input values. In the region with the maximum asymmetry (see also figure 8) both methods fit reasonably well with one another.

Based on these measurements there is direct evidence that the impurity density is asymmetric on the flux surfaces. Thus, the total flow on a flux surface is described by equation (1) where the parallel flow (second term on the right-hand side of equation (1)) depends on the impurity density which has poloidal variations along the flux surface. In the next section, the possible mechanism that could generate a poloidal impurity density asymmetry inside the edge transport barrier, which in turn affects the flow structure on the flux surfaces, is presented.

#### 4. Comparison to theoretical predictions

The measurements of the rotation velocities at both the LFS and HFS enable a detailed study of the flow structure at the edge of a tokamak plasma. In particular, the measured rotation velocities at two different points along the poloidal arc allow for a comparison to calculations based on neoclassical theory [23]. The poloidal impurity distribution is determined by the parallel momentum balance equation which includes inertia, both

*Rotation and density asymmetries in the presence of large poloidal impurity flows* 10

the pressure and electric drive and friction [23]:

$$\mathbf{B} \cdot \nabla \left[ \frac{k_\alpha^2 B^2}{2n_\alpha^2} - \frac{R^2 \omega_\alpha^2}{2} + v_{th,\alpha}^2 \left( \log(n_\alpha) + \frac{Z_\alpha \tilde{\Phi}}{T_\alpha} \right) \right] + \nu_{\alpha i} B (u_{\parallel,\alpha} - u_{\parallel,i} + \Delta Q_{\parallel}) = 0. \quad (6)$$

Here,  $\mathbf{B}$  is the magnetic field,  $k_\alpha$  is a flux function,  $n_\alpha$  is the density of the impurity species  $\alpha$ ,  $R$  is the local major radius,  $\omega_\alpha$  is the rigid rotation velocity defined as  $\omega_\alpha = \frac{1}{RB_\theta}(E_r - \nabla p_\alpha/(n_\alpha Z_\alpha e))$  where  $E_r$  is the radial electric field and  $\nabla p_\alpha$  the radial impurity pressure gradient.  $v_{th,\alpha}$  is the thermal velocity, i.e.  $v_{th,\alpha} = \sqrt{T_\alpha/m_\alpha}$  with  $T_\alpha$  being the species temperature and  $m_\alpha$  the species mass,  $Z_\alpha$  is the charge of the impurity species,  $\tilde{\Phi}$  is the poloidally varying potential where the perturbation is small compared to the equilibrium potential.  $\nu_{\alpha i}$  is the collision frequency between the impurities and the main ions,  $u_{\parallel,\alpha}$  and  $u_{\parallel,i}$  are the parallel velocities of the impurity and the main ion species, respectively, and  $\Delta Q_{\parallel}$  is the parallel heat flow differential between main ions and impurities, which is proportional to the ion temperature gradient. The terms of equation (6) (from left to right) correspond to the poloidal centrifugal force, the toroidal centrifugal force, the pressure and electric force and the friction force.

The impurity species is assumed to be a trace impurity with  $Z_\alpha n_\alpha \ll n_i$ , where  $n_i$  is the main ion density [23]. Furthermore, it is assumed that  $T_\alpha \approx T_i$ ,  $T_i$  being the main ion temperature, since the time needed for an impurity to equilibrate to the main ions is short compared to local transport time scales [30]. For the fluid model the measured ion temperature, electron density, impurity density and the poloidal and toroidal impurity rotation velocity profiles measured at the LFS are used as input. Using the fluid approach, it has been shown through analytic and numerical simulations [23] that the observed flow structure arises due to the interplay between all forces. The friction force plays a dominant role, however, towards the separatrix, where the poloidal impurity rotation reaches its maximum and becomes supersonic (i.e. the Mach number associated with  $v_{\theta,\alpha} B / B_\theta$  approaches one), the poloidal centrifugal force gives a significant contribution.

In addition, a kinetic approach was used and the experimental data were compared to simulations performed with the drift-kinetic particle code HAGIS [24]. This also enables a comparison between the conventional fluid model and the more comprehensive, kinetic description provided by HAGIS that includes the effects due to finite orbit sizes. The extended version of HAGIS includes a Monte-Carlo pitch angle collision model [25] that enables the calculation of neoclassical transport based on a  $\delta f$  method. Here, the unperturbed distribution function  $f_0$  is a Maxwellian with constant density and temperature on a flux surface, while the perturbed part of the distribution function,  $\delta f$ , is represented by marker particles which are followed along their orbits and the collisions are modelled by a Monte-Carlo procedure. Simulations of plasmas with a single trace impurity were performed with HAGIS that uses the measured LFS electron density and temperature, ion temperature, impurity ion density and the radial electric field ( $E_r$ ) profile as input.

In the following, the flow structure resulting from the formulation presented in [23] is

*Rotation and density asymmetries in the presence of large poloidal impurity flows* 11

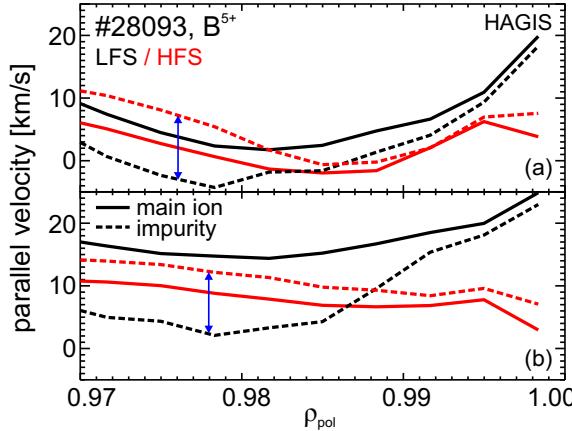


Figure 6: HAGIS simulations of the parallel velocities of the main ions (solid line) and impurities (dashed line) at the LFS in black and HFS in red: (a) using the measured  $E_r$  profile at the LFS as evaluated from the radial force balance of  $B^{5+}$  and  $\nu_{\alpha i}$  calculated using  $n_i = n_e$ , (b) using a decreased collision frequency and an  $E_r$  profile that has been modified within the experimental uncertainties such that the resulting parallel impurity flow at the LFS is similar to the measured profile.

compared to simulations performed with HAGIS [26] and to experimental measurements. First the main ion dynamics is simulated with HAGIS and the resulting profiles (rigid body rotation of the main ions  $\omega_i$  and main ion poloidal rotation  $v_{\theta,i}$ ) are used as input for both models. Then the impurity dynamics is simulated and the resulting flow profiles of both the fluid and the kinetic model are compared to each other.

The HAGIS simulations were performed with an input  $E_r$  that is derived from the CXRS measurements using the radial force balance of  $B^{5+}$ . The resulting parallel velocities for the main ions (solid line) and  $B^{5+}$  impurities (dashed line) at the LFS (black) and HFS (red) are shown in figure 6(a). Note that the LFS parallel velocity of  $B^{5+}$  is too low compared to the actual measured values. An additional simulation was performed with HAGIS in which the input  $E_r$  was slightly modified (within the experimental uncertainties) and the collision frequency between impurities and main ions,  $\nu_{\alpha i}$ , was decreased by a factor of 1.5 compared to the nominal collision frequency, that is evaluated using  $n_i = n_e$  ( $n_i$  and  $n_e$  being the main ion and electron density, respectively), such that the resulting LFS parallel impurity flow is similar to the measured value. For the nominal collision frequency (see figure 6(a)) the friction force dominates close to the separatrix ( $\rho_{pol} > 0.985$ ) and tends to push the impurity parallel flow towards the main ion parallel flow. For a comparison, the parallel flows of both impurities and main ions at the LFS and HFS are shown in figure 6(b) for the case with a slightly modified  $E_r$  and collision frequency. Note that in both cases the LFS parallel flow of the main ions (solid lines) is higher than at the HFS, contrary to the parallel impurity flows (dashed lines). This implies that the impurities are dragged by the main ions, however, parallel impurity dynamics can emerge depending on the interplay between the forces in the parallel momentum balance.

## Rotation and density asymmetries in the presence of large poloidal impurity flows 12

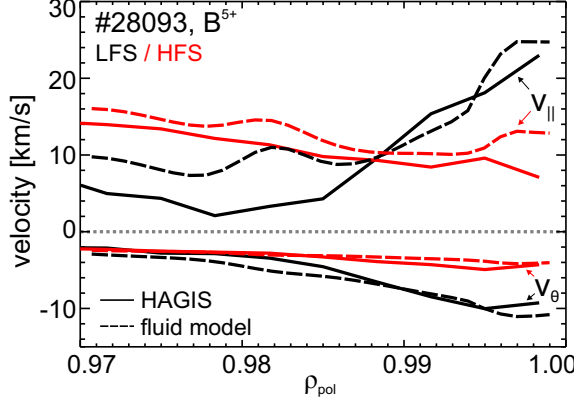


Figure 7: Comparison between HAGIS (solid lines) and fluid model (dashed lines): simulated parallel and poloidal flows at the LFS (black) and HFS (red).

Figure 7 shows a comparison of the simulated flow profiles resulting from the fluid and the kinetic approach when the same input parameters are applied. In this case, the main ion parameters ( $\omega_i$  and  $v_{\theta,i}$ ) as simulated with HAGIS are used as input and the impurity dynamics is then modelled. Good agreement is obtained between both models demonstrating a consistency between the fluid and the kinetic model.

Figure 8 shows the asymmetry factor, defined as the ratio of the HFS and LFS impurity density  $n_{\alpha}^{\text{HFS}}/n_{\alpha}^{\text{LFS}}$ , as evaluated using the measured profiles in black, using KN1D in blue (dotted line) and green (dashed-dotted line), and resulting from the simulations using the fluid approach (red, solid line) and HAGIS (purple, dashed line). For better clarity the uncertainties are shown only at distinct radial positions. Within the experimental uncertainties, the simulated asymmetry factors agree qualitatively with the measured one. The maximum of the asymmetry factor is approximately at the same position where the poloidal impurity flow is maximal and becomes super-sonic, in qualitative

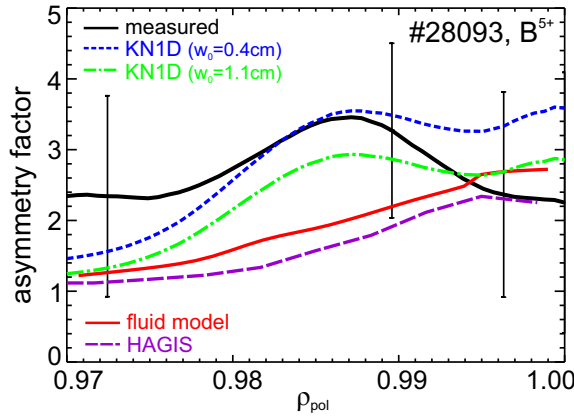


Figure 8: Asymmetry factors resulting from the measured data of  $B^{5+}$  and  $D_{\alpha}$  (black), derived from KN1D (blue and green), from the fluid approach (red) and from HAGIS (purple). For better clarity the uncertainties are shown at distinct radial positions.

*Rotation and density asymmetries in the presence of large poloidal impurity flows* 13

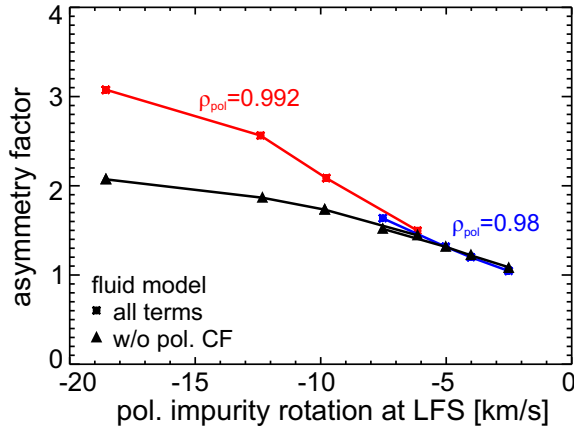


Figure 9: Asymmetry factor versus LFS poloidal impurity rotation velocity.

agreement with [19]. Figure 9 shows the simulated asymmetry factor as a function of the poloidal impurity rotation velocity at the LFS at two radial positions ( $\rho_{pol} = 0.98$  and  $0.992$ ). For higher poloidal impurity flows the asymmetry factor increases and the contribution arising from the poloidal centrifugal force becomes more important.

Compared to the measurement, the separation of the parallel impurity flows and the difference in magnitude of the poloidal flows are modelled qualitatively. However, the difference between the measured HFS and the LFS parallel impurity flows is a factor of  $\sim 2$  larger than in the simulations. To obtain the large separation in the parallel impurity flow as observed in the experiment, a parameter scan in the rigid main ion rotation velocity  $\omega_i$  was performed, while the impurity flows measured at the LFS were used as input [23]. The measured impurity flows are reconstructed quantitatively when  $\omega_i < 0$  and a finite poloidal main ion flow of  $\sim 2$  km/s emerges. The condition  $\omega_i < 0$  means that  $E_r$  is larger than  $\nabla p_i / en_i$ , but only larger by maximal 2–3 kV/m. Note that though the main ion pressure gradient term is the dominant contribution to  $E_r$  [30, 40] such a small difference is well within the experimental uncertainties. The main ion parallel flow at the HFS is now higher than at the LFS, i.e. contrary to the situation in figure 6. Due to friction the impurities tend to follow the main ions. Near the separatrix the poloidal centrifugal term increases (due to an increasing  $v_{\theta,\alpha}$ ) and contributes to the total shape of the parallel impurity flows (see figure 10). Figure 10 shows a comparison between the measured and simulated parallel impurity flows, where the blue curve represents the modelled profile when the poloidal centrifugal term is neglected. This shows that the poloidal centrifugal force arising from the poloidal impurity flow can have a significant contribution in the parallel force balance.

The fact that a poloidal main ion flow of  $\sim 2$  km/s is needed to explain the measured parallel impurity flows is consistent with neoclassical theory. Figure 11 shows the poloidal main ion flow as derived from the fluid model and in comparison the calculated profiles using the neoclassical code NEOART [41]. NEOART calculates the collisional transport coefficients, which represent the sum of a classical, a Pfirsch-Schlüter and a banana plateau term [41, 42], for a given number of impurities and includes collisions

## Rotation and density asymmetries in the presence of large poloidal impurity flows 14

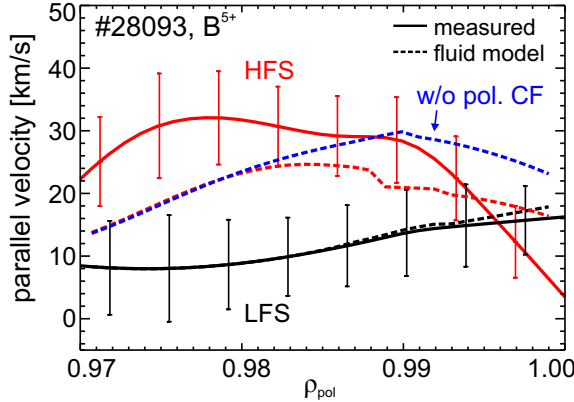


Figure 10: Comparison of the measured and simulated parallel impurity velocities at the LFS and HFS: Here the impact of the poloidal centrifugal force on the resulting flow structure is visible close to the separatrix.

between all species. The red profile of figure 11 shows the calculated poloidal rotation profile of the main ions when boron is used as the only trace impurity. The neoclassical prediction shown in blue includes boron, carbon, helium, oxygen and tungsten as impurity species, resulting in an effective charge of  $Z_{\text{eff}} \approx 1.6$  at the pedestal top which is typical for an H-mode plasma at AUG [43]. Simulating a multi-species plasma shows that  $v_{\theta,i}$  increases from  $\sim 1$  to  $\sim 2$  km/s. The error bars on the blue profile resemble the uncertainty in the measured  $T_i$  profile.

The results presented here show that in the edge transport barrier the impurity density is not a flux function and accumulates at the HFS, mainly due to the friction force. However, also the non-linear inertial term emerging from the poloidal impurity flow can become important, especially in the region where the poloidal Mach number approaches unity, i.e. close to the separatrix [23]. The fact that the impurity density has a poloidal

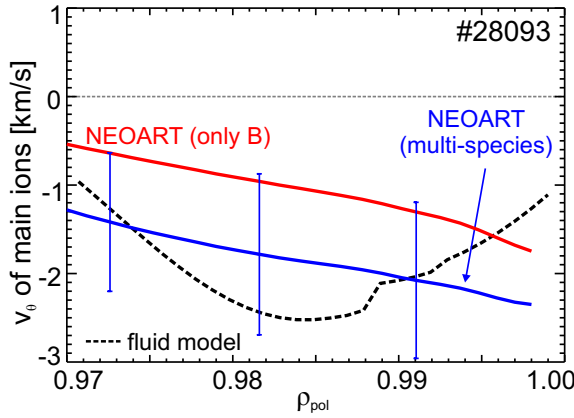


Figure 11: Simulated poloidal rotation of the main ions derived from the fluid model in black (dashed line) and NEOART (red and blue, solid lines). The effect of the presence of multiple impurity species in the plasma ( $Z_{\text{eff}} \approx 1.6$ ) is shown in blue.

*Rotation and density asymmetries in the presence of large poloidal impurity flows* 15

dependence has an impact on the total flow on a flux surface and is responsible for the features of both the toroidal (parallel) and poloidal flows, as observed in experiment.

## 5. Impact on impurity transport

Previous studies on the impurity transport in the edge transport barrier of AUG [2] showed that the experimentally determined radial diffusion coefficients,  $D$ , and convective velocities,  $v$ , of light impurities such as  $\text{He}^{2+}$ ,  $\text{C}^{6+}$ ,  $\text{Ne}^{10+}$  and  $\text{Ar}^{16+}$  are well described by neoclassical transport coefficients. Impurity transport analyses based on the evaluation of soft X-ray radiation [44, 45] also showed that the transport coefficients of Ne and F are at the neoclassical level at the plasma edge. All these studies assumed a constant impurity density on the flux surfaces and the question arises whether a poloidal impurity density asymmetry has an effect on the particle transport.

Due to the redistribution of the impurities along the poloidal arc the friction between main ions and impurities is reduced and thus, the neoclassical particle flux has a non-linear dependence on the temperature and density gradients [46, 6, 7]. If the gradients are sufficiently steep the neoclassical flux can significantly decrease, however, the classical flux increases such that the total flux continues to increase [46].

The neoclassical drift parameter has a  $Z$ -dependence, i.e. it increases with the local charge of the impurity, since the drift velocity is proportional to the diffusion coefficient multiplied by the ratio of the charge numbers between impurity and main ion. We determined the effect of the impurity density asymmetry on the neoclassical transport, in particular the  $Z$  dependence of the drift parameter  $v/D$ , with simulations using HAGIS for different impurity species. The drift velocity  $v$  and the diffusion coefficient  $D$ , which are determined by the relation  $\Gamma = -Ddn/dr + nv$ , with  $\Gamma$  being the flux surface averaged radial particle flux, are obtained from pairs of simulations with different initial impurity density gradients. In the pedestal region, the values of  $v/D$  obtained in the stationary state of the simulation are rather inaccurate, since  $D$  is very small. Therefore values

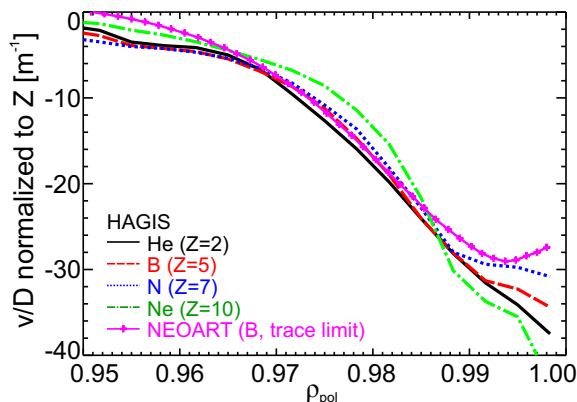


Figure 12: Drift parameter  $v/D$  divided by the charge number  $Z$  for different impurity species ( $\text{He}^{2+}$ ,  $\text{B}^{5+}$ ,  $\text{N}^{7+}$  and  $\text{Ne}^{10+}$ ) simulated using HAGIS and NEOART.

## Rotation and density asymmetries in the presence of large poloidal impurity flows 16

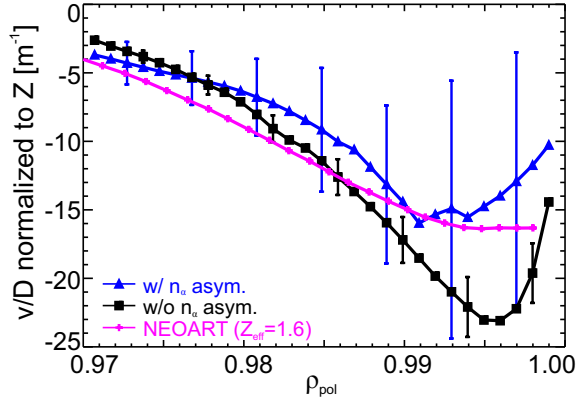


Figure 13: Drift parameter  $v/D$  normalized to the charge state  $Z = 5$  for B simulated with NEOART (magenta crosses), using  $Z_{\text{eff}} \approx 1.6$ , and evaluated from the measurement assuming no impurity density asymmetry (black squares) and including the poloidal dependence of the impurity density (blue triangles).

for  $v/D$  were obtained for the early transient phase of the simulation, after the density asymmetry has evolved. Figure 12 shows the radial profiles of  $v/D$  divided by the charge number  $Z$  for the impurity species  $\text{He}^{2+}$ ,  $\text{B}^{5+}$ ,  $\text{N}^{7+}$  and  $\text{Ne}^{10+}$ . Despite the presence of an impurity density asymmetry, the parameter  $v/D$  is proportional to the charge number  $Z$ . This scaling is the same as in the standard neoclassical theory, represented by the simulation obtained with NEOART (magenta line in figure 12) for one trace impurity (boron). NEOART does not account for the existence of a poloidal impurity density asymmetry and hence, the good agreement between the simulated profiles indicates that the asymmetric impurity density profile does not have a big impact on the drift parameter  $v/D$ .

Using NEOART, the effect of including multiple impurity species ( $Z_{\text{eff}} \approx 1.6$ , as described above) on  $v/D$  can be simulated. As shown in figure 13, the drift parameter decreases due to the presence of multiple impurities in the plasma. Comparing this profile to the  $v/D$  from the experimental profiles shows good quantitative agreement inside the error bars of the experiment. The drift parameters are evaluated using  $v/D = d(\ln\langle n_\alpha \rangle)/dr_{vol}$ , where  $\langle n_\alpha \rangle$  is the flux surface averaged impurity density profile and  $r_{vol}$  the normalized volume flux radius. Here, the black profile has been calculated assuming that the impurity density is constant on a flux surface. The blue profile is evaluated using the flux surface averaged impurity density that accounts for the poloidal dependence of the  $\text{B}^{5+}$  density as simulated with the fluid model.

The presence of a poloidal impurity density asymmetry in the edge transport barrier has an impact on the flux surface averaged density and slightly reduces  $v/D$ . However, the resulting  $v/D$  is consistent with the standard neoclassical prediction (shown in magenta in figure 13), in good agreement with [2]. This indicates that despite a poloidal rearrangement of the impurities in the edge pedestal, the impurity particle transport is at the neoclassical level.

*Rotation and density asymmetries in the presence of large poloidal impurity flows* 17

## 6. Summary and Conclusions

The poloidal flow structure is measured in the edge transport barrier of AUG. Four independent measurements at the outboard and inboard midplane reveal the existence of an asymmetric flow pattern along the flux surface. Inside the edge transport barrier the poloidal impurity flow is strongly sheared in the electron diamagnetic drift direction both at the LFS and HFS. However, the HFS poloidal rotation velocity is about a factor of 1.5-2 lower than at the LFS thus, breaking the expected proportionality between the poloidal flow and the poloidal magnetic field. The toroidal rotation velocity is co-current at both the LFS and HFS, however, the profile exhibits an asymmetric structure. Both the toroidal flow asymmetry and the discrepancy in magnitude of the poloidal flow are explained by an excess of impurity density at the HFS following the postulate of divergence-free flows on a flux surface [19, 20]. The HFS impurity density profile has been evaluated directly from measurements of the Balmer spectral line and from modelling of the gas puff penetration using the code KN1D. Using both evaluation methods the impurity density at the HFS is found to be up to a factor of 3 higher than at the LFS, demonstrating that in the edge pedestal the impurity density is asymmetric on a flux surface.

Comparison to theoretical predictions [23] based on the parallel momentum balance that includes the poloidal and toroidal centrifugal forces arising due to inertia, the pressure drive, the electric force and the friction force reveals the nature of the parallel impurity dynamics. Here, a fluid model [23] and a drift-kinetic approach using HAGIS [26] have been applied and good agreement between the simulated flows is obtained.

The rearrangement of the impurities along the flux surfaces arises due to the interplay of all terms in the parallel force balance with the friction force playing an important role. However, the inclusion of the poloidal centrifugal force, which has been neglected in previous studies, gives additional contributions especially close to the separatrix where the poloidal impurity flow approaches its maximum. The measured flow structure is reproduced quantitatively by the theoretical prediction when a poloidal main ion flow of  $\sim 2$  km/s emerges in the fluid model, which is in agreement with standard neoclassical calculations. Hence, using the measured impurity flows allows information on the poloidal rotation of the main ions to be obtained indirectly.

Comparing the measured drift parameter evaluated from the flux surfaced averaged impurity density to the neoclassical simulation shows quantitative agreement. This demonstrates that despite the existence of a poloidal impurity density asymmetry the impurity particle transport is neoclassical, consistent with previous studies [2].

In summary, the key features of the experimental data including the shape of the rotation profiles, the poloidal impurity density asymmetry as well as the drift parameter are in line with neoclassical theory.

*Rotation and density asymmetries in the presence of large poloidal impurity flows* 18

### Acknowledgements

The first author would like to thank L. Aho-Mantila, M. Bernert and V. Rohde for very fruitful discussions.

### References

- [1] J. D. Callen *et al.* *Phys. Plasmas*, 17:056113, 2010.
- [2] T. Pütterich *et al.* *J. Nucl. Mater.*, 415(1):S334–S339, 2011.
- [3] W. M. Stacey and D. R. Jackson. *Phys. Fluids B*, 5:1828, 1993.
- [4] B. LaBombard and B. Lipschultz. *Nucl. Fusion*, 27:81, 1987.
- [5] W. M. Stacey. *Nucl. Fusion*, 27:1213, 1987.
- [6] T. Fülöp and P. Helander. *Phys. Plasmas*, 6:3066, 1999.
- [7] T. Fülöp and P. Helander. *Phys. Plasmas*, 8:3305, 2001.
- [8] M. Landreman *et al.* *Phys. Plasmas*, 18:092507, 2011.
- [9] J. A. Wesson. *Nucl. Fusion*, 37:577, 1997.
- [10] A. G. Peeters *et al.* *Phys. Plasmas*, 16:042310, 2009.
- [11] F. J. Casson *et al.* *Phys. Plasmas*, 17:102305, 2010.
- [12] L. C. Ingesson *et al.* *Plasma Phys. Control. Fusion*, 42:161, 2000.
- [13] Ye O. Kazakov *et al.* *Plasma Phys. Control. Fusion*, 54:105010, 2012.
- [14] T. Fülöp and S. Moradi. *Phys. Plasmas*, 18:030703, 2011.
- [15] S. Moradi *et al.* *Plasma Phys. Control. Fusion*, 53:115008, 2011.
- [16] M. L. Reinke *et al.* *Plasma Phys. Control. Fusion*, 54:045004, 2012.
- [17] T. Pütterich *et al.*, I2.106, this conference. *Plasma Phys. Control. Fusion (submitted)*.
- [18] J. Arevalo *et al.* Conf. Proceedings of the 40<sup>th</sup> EPS Conference on Plasma Physics, O4.101, <http://ocs.ciemat.es/EPS2013PAP/pdf/04.101.pdf>, Espoo, 2013.
- [19] K. D. Marr *et al.* *Plasma Phys. Control. Fusion*, 52:055010, 2010.
- [20] T. Pütterich *et al.* *Nucl. Fusion*, 52:083013, 2012.
- [21] R. M. Churchill *et al.* *US-EU Joint Transport Task Force Workshop, Santa Rosa, California*, 2013.
- [22] R. J. Fonck *et al.* *Phys. Rev. A*, 29(6):3288, 1984.
- [23] E. Fable *et al.* (*to be submitted*), 2013.
- [24] S. D. Pinches *et al.* *Comp. Phys. Commun.*, 111:133, 1998.
- [25] A. Bergmann *et al.* *Phys. Plasmas*, 8:5192, 2001.
- [26] A. Bergmann *et al.* (*to be submitted*), 2013.
- [27] E. Viezzer *et al.* *Rev. Sci. Instrum.*, 83:103501, 2012.
- [28] R. M. Churchill *et al.* *Rev. Sci. Instrum.* (*accepted for publication*), 2013.
- [29] T. W. Morgan *et al.* Conf. Proceedings of the 37<sup>th</sup> EPS Conference on Plasma Physics, ECA Vol. 34A, P5.122, <http://ocs.ciemat.es/EPS2010PAP/pdf/P5.122.pdf>, Dublin, 2010.
- [30] E. Viezzer *et al.* *Nucl. Fusion*, 53:053005, 2013.
- [31] T. Pütterich *et al.* *Phys. Rev. Lett.*, 102:025001, 2009.
- [32] F. L. Hinton and R. D. Hazeltine. *Rev. Mod. Physics*, 48(2), 1976.
- [33] S. P. Hirshman and D. J. Sigmar. *Nucl. Fusion*, 21(9):1079, 1981.
- [34] H. P. Summers. *ADAS User Manual 2.6*. <http://www.adas.ac.uk/manual.php>, 2004.
- [35] E. Viezzer *et al.* *Plasma Phys. Control. Fusion*, 53:035002, 2011.
- [36] B. LaBombard. *KN1D User Manual*. [http://www.psfc.mit.edu/~labombard/KN1D\\_Source\\_Info.html](http://www.psfc.mit.edu/~labombard/KN1D_Source_Info.html), 2001.
- [37] L. Aho-Mantila *et al.* *Nucl. Fusion*, 52:103007, 2012.
- [38] R. Dux *et al.* Conf. Proceedings of the 39<sup>th</sup> EPS Conference on Plasma Physics, P2.049, Stockholm (Sweden), 2012.

*Rotation and density asymmetries in the presence of large poloidal impurity flows* 19

- [39] B. Geiger *et al.* *Plasma Phys. Control. Fusion*, 53:065010, 2011.
- [40] R. M. McDermott *et al.* *Phys. Plasmas*, 16:056103, 2009.
- [41] A. G. Peeters *et al.* *Phys. Plasmas*, 7(1):268, 2000.
- [42] R. Dux and A. G. Peeters. *Nucl. Fusion*, 40(10):1721, 2000.
- [43] S. K. Rathgeber *et al.* *Plasma Phys. Control. Fusion*, 52:095008, 2010.
- [44] T. Sunn Pedersen *et al.* *Nucl. Fusion*, 40:1795, 2000.
- [45] R. Dux. *Fus. Sci. Technol.*, 44:708, 2003.
- [46] P. Helander. *Phys. Plasmas*, 5:3999, 1998.



# Bibliography

- [1] H. Zohm, R. Dux, and R. Neu, Plasmaphysik II , Einführung in die Fusionsforschung, Skript zur Vorlesung, Ludwig-Maximilians Universität München, SS 2013 URL [http://www.physik.uni-muenchen.de/lehre/vorlesungen/sose\\_13/A\\_PlasmaphysikII/vorlesung/index.html](http://www.physik.uni-muenchen.de/lehre/vorlesungen/sose_13/A_PlasmaphysikII/vorlesung/index.html), 2013.
- [2] T. Eich, B. Sieglin, A. Scarabosio, W. Fundamenski, R. J. Goldston, et al., Phys. Rev. Lett. **107**, 215001 (Nov 2011).
- [3] T. Eich, A. Leonard, R. Pitts, W. Fundamenski, R. Goldston, et al., Nuclear Fusion **53**(9), 093031 (2013).
- [4] T. Lunt, Y. Feng, K. Krieger, A. Kallenbach, R. Neu, et al., Journal of Nuclear Materials **415**, S505–S508 (2011).
- [5] R. Dux, Impurity Transport in Tokamak Plasmas, Technical Report 10/27, IPP, Garching, Germany, Sept. 2004.
- [6] W. Eckstein, C. García-Rosales, J. Roth, and W. Ottenberger, Sputter Data, Technical Report IPP 9/82, Max-Planck Institut für Plasmaphysik, Garching, Germany, 1993.
- [7] J. Roth, Journal of Nuclear Materials **266-269**, 51–57 (1999).
- [8] M. Mayer, V. Philipps, P. Wienhold, H. Esser, J. von Seggern, et al., Journal of Nuclear Materials **290-293**, 381 – 388 (2001).
- [9] J. Roth, E. Tsitrone, A. Loarte, T. Loarer, G. Counsell, et al., Journal of Nuclear Materials **390-391**, 1–9 (2009).
- [10] K. Krieger, T. Lunt, R. Dux, A. Janzer, H. W. Müller, et al., Physica Scripta **T145**, 014067 (2011).
- [11] J. Coenen, G. Arnoux, B. Bazylev, G. Matthews, S. Jachmich, et al., Journal of Nuclear Materials (2014), submitted.

- [12] J. Riesch, T. Höschen, C. Linsmeier, S. Wurster, and J.-H. You, Physica Scripta **T159**, 014031 (2014).
- [13] R. Isler, R. Neidigh, and R. Cowan, Physics Letters A **63**(3), 295–297 (1977).
- [14] E. Hinnov and M. Mattioli, Phys. Lett. **A66**, 109 (1978).
- [15] A. Kallenbach, R. Neu, R. Dux, H.-U. Fahrbach, J. C. Fuchs, et al., Plasma Physics and Controlled Fusion **47**(12B), B207–B222 (2005).
- [16] <http://www.psfc.mit.edu/research/alcator/>.
- [17] B. Lipschultz, D. Pappas, B. LaBombard, J. Rice, D. Smith, et al., Nuclear Fusion **41**, 585 – 596 (2001).
- [18] <http://www.ipp.mpg.de/ippcms/de/pr/forschung/asdex/index>.
- [19] R. Neu, K. Asmussen, S. Deschka, A. Thoma, M. Bessenrodt-Weberpals, et al., Journal of Nuclear Materials **241–243**, 678–683 (1997).
- [20] R. Neu, V. Bobkov, R. Dux, J. C. Fuchs, O. Gruber, et al., Physica Scripta **T138**, 014038 (6pp) (2009).
- [21] <http://www.jet.efda.org/jet/>, 2014.
- [22] G. F. Matthews, S. Brezinsek, I. Chapman, J. Hobirk, L. D. Horton, et al., Physica Scripta **T159**, 014015 (2014).
- [23] F. Romanelli and JET EFDA contributors, Nuclear Fusion **53**(10), 104002 (2013).
- [24] R. Neu, G. Arnoux, M. Beurskens, V. Bobkov, S. Brezinsek, et al., Physics of Plasmas **20**(5) (2013).
- [25] <http://www.iter.org/>.
- [26] <http://west.cea.fr/>.
- [27] H.-S. Bosch, Die Physik der Alpha-Teilchen in einem Fusionsreaktor mit Deuterium-Tritium-Plasmen, Technical Report IPP-1-325 – Habilitationsschrift Humboldt-Univ. Berlin, Max-Planck-Institut für Plasmaphysik (IPP), Garching, 2000.
- [28] J. T. Hogan and D. L. Hillis, Nuclear Fusion **40**, 879–888 (2000).
- [29] ITER Physics Expert Groups, Nuclear Fusion **39**(12), 2175–2235 (1999).
- [30] V. Bobkov, F. Braun, R. Dux, A. Herrmann, A. Kallenbach, et al., Journal of Nuclear Materials **363–365**, 122–126 (2007).

- [31] R. Dux, V. Bobkov, N. Fedorczak, K. Iraschko, A. Kallenbach, et al., Journal of Nuclear Materials **363-365**, 112–116 (2007).
- [32] B. Lipschultz, Y. Lin, E. Marmar, D. Whyte, S. Wukitch, et al., Journal of Nuclear Materials **363-365**, 1110 – 1118 (2007).
- [33] S. Wukitch, B. LaBombard, Y. Lin, B. Lipschultz, E. Marmar, et al., Journal of Nuclear Materials **390-391**, 951 – 954 (2009).
- [34] V. Rohde, M. Balden, T. Lunt, and the ASDEX Upgrade Team, Physica Scripta **T138**, 014024 (5pp) (2009).
- [35] M. Balden, N. Endstrasser, P. Humrickhouse, V. Rohde, M. Rasinski, et al., Nuclear Fusion **54**(7), 073010 (2014).
- [36] A. Kallenbach, M. Bernert, R. Dux, L. Casali, T. Eich, et al., Plasma Physics and Controlled Fusion **55**(12), 124041 (2013).
- [37] A. Kallenbach, R. Dux, M. Mayer, R. Neu, T. Pütterich, et al., Nuclear Fusion **49**(4), 045007 (2009).
- [38] D. Reiter, G. H. Wolf, and H. Kever, Nuclear Fusion **30**(10), 2141–2155 (1990).
- [39] D. Post, R. Jensen, C. Tarter, W. Grasberger, and W. Lokke, At. Data Nucl. Data Tables **20**, 397–439 (1977).
- [40] W. J. Karzas and R. Latter, Astrophysical Journal Supplements **VI**, 167–212 (1961).
- [41] R. Dux, V. Bobkov, A. Herrmann, A. Janzer, A. Kallenbach, et al., Journal of Nuclear Materials **390-391**, 858–863 (2009).
- [42] K. Behringer, H. P. Summers, B. Denne, M. Forrest, and M. Stamp, Plasma Physics and Controlled Fusion **31**, 2059–2099 (1989).
- [43] A. Kallenbach, G. Fussmann, H.-M. Mayer, S. Pitcher, and ASDEX Upgrade Team, Plasma Physics and Controlled Fusion **36**(8), 1299–1306 (1994).
- [44] T. Pütterich, Investigations on Spectroscopic Diagnostic of High-Z Elements in Fusion Plasmas, Technical Report 10/29, IPP Garching, Germany, Apr. 2006, Doctoral thesis at Universität Augsburg.
- [45] R. J. Fonck, D. S. Darrow, and K. P. Jaehnig, Phys. Rev. A **29**(6), 3288–3309 (1984).
- [46] F. L. Hinton and S. K. Wong, Physics of Fluids (1958-1988) **28**(10), 3082–3098 (1985).

- [47] M. L. Reinke, I. H. Hutchinson, J. E. Rice, N. T. Howard, A. Bader, et al., Plasma Physics and Controlled Fusion **54**(4), 045004 (2012).
- [48] M. Bernert, *Analysis of the H-mode density limit in the ASDEX Upgrade tokamak using bolometry*, Phd thesis, LMU München, 2013, also IPP report 17/38.
- [49] M. Anton, M. J. Dutch, and H. Weisen, Review of Scientific Instruments **66**(7), 3762–3769 (1995).
- [50] K. Asmussen, K. B. Fournier, J. M. Laming, R. Neu, J. F. Seely, et al., Nuclear Fusion **38**(7), 967–986 (1998).
- [51] S. D. Loch, J. A. Ludlow, M. S. Pindzola, A. D. Whiteford, and D. C. Griffin, Physical Review A (Atomic, Molecular, and Optical Physics) **72**(5), 052716 (2005).
- [52] R. D. Cowan, *The Theory of Atomic Structure and Spectra (Los Alamos Series in Basic and Applied Sciences)*, University of California Press, California, 1981.
- [53] M. Gu, Astrophys. J. **582**, 1241–1250 (2003).
- [54] H. P. Summers, The ADAS User Manual, version 2.6 <http://adas.phys.strath.ac.uk> (2004).
- [55] G. J. van Rooij, J. W. Coenen, L. Aho-Mantila, S. Brezinsek, M. Clever, et al., Journal of Nuclear Materials **438**, S42–S47 (2013).
- [56] A. V. Chankin, D. P. Coster, and R. Dux, Plasma Physics and Controlled Fusion **56**(2), 025003 (2014).
- [57] G. Janeschitz, R. König, L. Lauro-Taroni, J. Lingertat, G. Matthews, et al., Journal of Nuclear Materials **196-198**, 380 – 385 (1992).
- [58] A. Geier, H. Maier, R. Neu, K. Krieger, and ASDEX Upgrade Team, Plasma Physics and Controlled Fusion **44**(10), 2091–2100 (2002).
- [59] K. Krieger, V. Rohde, R. Schwörer, K. Asmussen, C. García-Rosales, et al., Journal of Nuclear Materials **241-243**, 734–738 (1997).
- [60] D. Naujoks, K. Asmussen, M. Bessenrodt-Weberpals, S. Deschka, R. Dux, et al., Nuclear Fusion **36**(6), 671–687 (1996).
- [61] F. L. Hinton, Collisional Transport in Plasmas, in *Basic Plasma Physics I*, edited by A. A. Galeev and R. N. Sudan, Handbook of Plasma Physics, North-Holland, Amsterdam, 1st edition, 1983.

- [62] R. Dux, Neoclassical Transport, Advanced Lecture for PhD students, 2010.
- [63] A. G. Peeters, Physics of Plasmas **7**(1), 268–275 (2000).
- [64] R. Dux and A. G. Peeters, Nuclear Fusion **40**(10), 1721–1729 (2000).
- [65] A. G. Peeters, provided the NEOART code, 1998 (1998).
- [66] S. P. Hirshman and D. J. Sigmar, Nuclear Fusion **21**(9), 1079–1201 (1981).
- [67] W. A. Houlberg, K. C. Shaing, S. P. Hirshman, and M. C. Zarnstorff, Physics of Plasmas **4**(9), 3230–3241 (1997).
- [68] C. Angioni, P. Mantica, T. Pütterich, M. Valisa, M. Baruzzo, et al., Plasma Physics and Controlled Fusion (2014), accepted.
- [69] F. Casson, C. Angioni, E. Belli, R. Bilato, P. Mantica, et al., Plasma Physics and Controlled Fusion (2014), submitted.
- [70] P. A. Schneider, *Characterization and scaling of the tokamak edge transport barrier*, Phd thesis, LMU München, 2012, also IPP Report 10/42.
- [71] R. Neu, R. Dux, A. Kallenbach, T. Pütterich, M. Balden, et al., Nuclear Fusion **45**(3), 209–218 (2005).
- [72] R. Dux, A. Janzer, T. Pütterich, and ASDEX Upgrade Team, Nuclear Fusion **51**(5), 053002 (2011).
- [73] R. Neu, R. Dux, A. Geier, H. Greuner, K. Krieger, et al., Journal of Nuclear Materials **313–316**, 116–126 (2003).
- [74] M. Z. Tokar, J. Rapp, G. Bertschinger, L. Könen, A. Krämer-Flecken, et al., Nuclear Fusion **37**(12), 1691–1708 (1997).
- [75] R. Dux, R. Neu, A. G. Peeters, G. Pereverzev, A. Mück, et al., Plasma Physics and Controlled Fusion **45**(9), 1815–1825 (2003).
- [76] T. Nakano, Journal of Nuclear Materials **415**, S327 – S333 (2011).
- [77] A. Loarte, G. Huijsmans, S. Futatani, L. Baylor, T. Evans, et al., Nuclear Fusion **54**(3), 033007 (2014).
- [78] K. D. Marr, B. Lipschultz, P. J. Catto, R. M. McDermott, M. L. Reinke, et al., Plasma Physics and Controlled Fusion **52**(5), 055010 (2010).

- [79] R. M. Churchill, C. Theiler, B. Lipschultz, R. Dux, T. Putterich, et al., Review of Scientific Instruments **84**(9), 093505 (2013).
- [80] R. Dux, E. Fable, A. Loarte, A. Kukushkin, and ASDEX Upgrade team, Transport of tungsten in the H-mode edge transport barrier of ITER, in *Europhysics Conference Abstracts (CD-ROM, Proc. of the 40th EPS Conference on Plasma Physics, Espoo, Finland, 2013)*, edited by V. Naulin, C. Angioni, M. Borghesi, S. Ratynskaia, S. Poedts, et al., volume 37D of *ECA*, page P4.143, Geneva, 2013, European Physical Society.

At the end of my thesis I would like to thank everybody, who supported me, made this work possible or contributed directly or indirectly to the success of this work. In detail, I would like to thank

- **Prof. Dr. Hartmut Zohm, Prof. Dr. Harald Lesch and Prof. Dr. Ralf Bender** for enabling the possibility of my 'Habilitation'.
- **Prof. Dr. Ulrich Stroth** for giving me the opportunity to invest the extra time necessary.
- **Dr. habil. Ralph Dux**, for his support and advice and for sharing his insights, which were very useful to me.
- **Dr. habil. Jörg Stober**, for helpfully supporting my start into the world of lecturing.
- **Prof. Dr. Bruce Lipschultz**, for the warm welcome at PSFC and for the positive discussions on the physics of the plasma edge.
- **Prof. Dr. Hugh Summers, Dr. Martin O'Mullane**, for the enduring good collaboration on atomic data and for the cordial support.
- **Prof. Dr. Rudolf Neu**, for his enduring ability to broaden my horizon.
- **Prof. Dr. Arne Kallenbach**, for his supporting optimism and help to advertise my work.
- **Dr. Eleonora Viezzer, Mr. Marco Cavedon and Mr. Tomáš Odstrčil** for their outstanding work, of which also I could benefit.
- **Dr. Rachael McDermott** for the helpful discussions and her elaborate proof reading.
- **all colleagues**, both the ones that became friends and those who support me on a purely professional basis.
- **Mr. Andreas Bolland, Mr. Michael Rolffs and Mr. Alois Mayer** for the beneficial work on technical equipment and diagnostics.
- **the ASDEX Upgrade Team**, which earned the name 'team' by its uncomplicated and efficient way of collaboration.
- **My parents Mr. Egon und Mrs. Elfriede Pütterich** for their loving support. I dedicate this thesis to my dad, as I feel his strong support and love beyond his death.
- **My wife Birgit, and our daughters Anna and Marie** for their understanding of my working hours and the support and joy they provided not only during stressful times.